



HAL
open science

Etude des mécanismes d'excitation stochastique des oscillations stellaires par la convection turbulente

Réza Samadi

► **To cite this version:**

Réza Samadi. Etude des mécanismes d'excitation stochastique des oscillations stellaires par la convection turbulente. Astrophysique stellaire et solaire [astro-ph.SR]. Université Pierre et Marie Curie - Paris VI, 2012. tel-00761620

HAL Id: tel-00761620

<https://theses.hal.science/tel-00761620v1>

Submitted on 5 Dec 2012

HAL is a multi-disciplinary open access archive for the deposit and dissemination of scientific research documents, whether they are published or not. The documents may come from teaching and research institutions in France or abroad, or from public or private research centers.

L'archive ouverte pluridisciplinaire **HAL**, est destinée au dépôt et à la diffusion de documents scientifiques de niveau recherche, publiés ou non, émanant des établissements d'enseignement et de recherche français ou étrangers, des laboratoires publics ou privés.

UNIVERSITÉ PIERRE ET MARIE CURIE - PARIS 6

THÈSE D'HABILITATION A DIRIGER DES RECHERCHES

Spécialité : Astronomie et Astrophysique

Présentée par

Davoud Réza SAMADI

Titre :

Étude des mécanismes d'excitation stochastique des oscillations stellaires par la convection turbulente

Soutenue le 17 octobre 2012

Devant le jury composé de :

Président : Jean-Philippe Beaulieu

Rapporteurs : Bernd Freytag

John Leibacher

François Lignières

Examineurs : Thierry Appourchaux

Arlette Noels-Grotsch

Rubayat

آنان که محیط فضل و آداب شدند در جمع کمال شمع اصحاب شدند
ره زین شب تاریک نبروند برون گفتند فغانه ای و در خواب شدند

Ces océans de vertu et de science,
Ces flambeaux illuminant l'assemblée des parfaits,
N'ont pourtant point trouvé d'issue hors de cette nuit ténébreuse.
Ils ont raconté une histoire, et puis se sont endormis.

Traduction R. Lescot, tiré de l'"Anthologie de la poésie persane", Z. Safâ.

Omar Khayam (1048-1122)

L'astronome et mathématicien perse qui ne croyait pas au ciel.

Avant-propos

Le travail présenté dans ce mémoire représente 12 années de recherche. Il est important de rappeler que celui-ci repose sur un travail d'équipe. J'en profite donc pour remercier l'ensemble des collègues, étudiants et amis qui y ont apporté leurs pierres, petites ou grandes. Leur contribution scientifique sera en partie mise en lumière (le plus fidèlement j'espère !) dans ce mémoire notamment à travers les publications communes. Mais leur amitié, plus précieuse, ne peut se quantifier ...

Comme vous l'imaginez, ces 12 années passées ne sont pas limitées au seul travail de recherche. D'abord, du fait de mon statut spécifique (astronome-adjoint), j'ai investi une partie importante de mon temps sur des projets spatiaux (CoRoT, PLATO) et le travail que cela a représenté ne sera pas reproduit dans ce mémoire. J'ai assuré également des enseignements divers (voir C.V., page 257). Ensuite, comme vous le savez de nos jours malheureusement, un chercheur est amené à passer une part croissante de son temps à des activités administratives (remplir la paperasserie, faire des demandes de fric ... etc), techniques (développer des scripts, effectuer des sauvegardes, gérer les comptes, mettre à jour les OS.... etc), et logistiques (nettoyer son bureau, réserver hôtel et transport ...etc).

A ces activités, s'en sont ajoutées d'autres à partir de 8 juillet 2009, moins intellectuelles, souvent très terre-à-terre (biberons, couches, habillages, déshabillages ...) mais tellement intenses en émotions et sentiments ...

Table des matières

Rubayat

iii

Avant-propos

Chapitre 1

Introduction

1.1	Contexte et thématique de recherche	7
1.2	Qu’observe-t-on et à quoi ça sert ... ?	7
1.3	Bref historique sur le sujet	9
1.4	Mes travaux dans ce contexte	9

Chapitre 2

Des observables à la modélisation

2.1	Balance énergétique	11
2.2	Contraintes sismiques en terme de vitesse	12
2.2.1	Principe général	13
2.2.2	Cas du Soleil	14
2.2.3	Cas des autres étoiles	15
2.3	Contraintes sismiques en terme d’intensité	17

Chapitre 3

Modélisation de l’excitation stochastique

3.1	Fondements théoriques	20
3.1.1	L’équation d’onde inhomogène	20
3.1.2	Solution générale	22
3.1.3	Termes sources de forçage	23
3.1.4	Séparation d’échelle	24

3.1.5	Modèles de fermeture	25
3.1.6	Modèle de turbulence adopté	25
3.1.7	Formulation finale	26
3.2	Approches alternatives	28
3.2.1	Méthode de l’“équipartition” d’énergie	28
3.2.2	Méthode <i>ab initio</i>	29
3.3	Cas des modes non-radiaux	30
3.4	A propos de la contribution de l’entropie	31

Chapitre 4

Contraintes sur la convection turbulente

4.1	Spectres de la turbulence	33
4.1.1	Composante spatiale, $E(k)$	35
4.1.2	Composante fréquentielle, $\chi_k(\omega)$	37
4.2	Modèles de fermeture et anisotropie	41

Chapitre 5

Contraintes sur les modèles standards de structure stellaire

5.1	Contraintes sur les modèles locaux de convection	47
5.2	Importance de la pression turbulente	50
5.3	Rôle de l’abondance en métaux à la surface	51

Chapitre 6

Lois d’échelles sur les amplitudes

6.1	Taux d’excitation, \mathcal{P}	55
6.2	Amplitude en terme de vitesse, V	58
6.3	Amplitude en terme d’intensité, $\delta L/L$	59

Chapitre 7

Discussion et perspectives

7.1	Modélisation du forçage par la convection turbulente	63
7.1.1	Bases théoriques du modèle d’excitation stochastique	63
7.1.2	Amplitudes des modes dans les géantes rouges	64
7.1.3	Oscillations stochastiquement excitées dans les étoiles massives et les δ Scuti	66

7.1.4	Liens entre observables et physique des modes	66
7.2	Améliorer les modèles de structure stellaire	67
7.3	Perspectives observationnelles	69
7.3.1	CoRoT et <i>Kepler</i>	69
7.3.2	et après ?	70

Références bibliographiques **73**

Annexe A

Articles reproduits

<i>Solar-like oscillations in delta Scuti stars</i>		
	Samadi R., Goupil M.-J., Houdek G., 2002, A&A, 395, 563	87
<i>Numerical constraints on the model of stochastic excitation of solar-type oscillations</i>		
	Samadi R., Nordlund A., Stein R. F., Goupil M.-J., Roxburgh I., 2003, A&A, 403, 303	97
<i>Numerical 3D constraints on convective eddy time-correlations : Consequences for stochastic excitation of solar p modes</i>		
	Samadi R., Nordlund A., Stein R. F., Goupil M.-J., Roxburgh I., 2003, A&A, 403, 1129	107
<i>Inferred acoustic rates of solar p modes from several helioseismic instruments</i>		
	Baudin F., Samadi R., Goupil M.-J., Appourchaux T., Barban C., Boumier P., Chaplin W. J., Gouttebroze P., 2004, A&A, 433, 349	117
<i>Rotation profile inversion in solar-like stars. In the COROT framework</i>		
	Lochard J., Samadi R., Goupil M.-J., 2005, A&A, 438, 939	125
<i>Influence of local treatments of convection upon solar p mode excitation rates</i>		
	Samadi R., Kupka F., Goupil M.-J., Lebreton Y., van't Veer-Menneret C., 2006, A&A, 445, 233	135
<i>A closure model with plumes. I. The solar convection</i>		
	Belkacem K., Samadi R., Goupil M.-J., Kupka F., 2006, A&A, 460, 173	145
<i>A closure model with plumes. II. Application to the stochastic excitation of solar p modes</i>		
	Belkacem K., Samadi R., Goupil M.-J., Kupka F., Baudin F., 2006, A&A, 460, 183	157

<i>Excitation of solar-like oscillations across the HR diagram</i>	
Samadi R., Georgobiani D., Trampedach R., Goupil M.-J., Stein R. F., Nordlund A., 2007, A&A, 463, 297	165
<i>Modeling the excitation of acoustic modes in α Centauri A</i>	
Samadi R., Belkacem K., Goupil M.-J., Dupret M.-A., Kupka F., 2008, A&A, 489, 291	177
<i>Stochastic excitation of non-radial modes. I. High-angular-degree p modes</i>	
Belkacem K., Samadi R., Goupil M.-J., Dupret M.-A., 2008, A&A, 478, 163	187
<i>Stochastic excitation of nonradial modes. II. Are solar asymptotic gravity modes detectable ?</i>	
Belkacem K., Samadi R., Goupil M.-J., Dupret M.-A., Brun A. S., Baudin F., 2009, A&A, 494, 191	199
<i>Intrinsic photometric characterisation of stellar oscillations and granulation. Solar reference values and CoRoT response functions</i>	
Michel E., Samadi R., Baudin F., Barban C., Appourchaux T., Auvergne M., 2009, A&A, 495, 979	213
<i>The CoRoT target HD 49933 . I. Effect of the metal abundance on the mode excitation rates</i>	
Samadi R., Ludwig H.-G., Belkacem K., Goupil M. J., Dupret M.-A., 2010, A&A, 509A, 15	223
<i>The CoRoT target HD 49933 . II. Comparison of theoretical mode amplitudes with observations</i>	
Samadi R., Ludwig H.-G., Belkacem K., Goupil M. J., Benomar O., Mosser B., Dupret M.-A., Baudin F., Appourchaux T., Michel E., 2010, A&A, 509A, 16	231
<i>Stochastic excitation of gravity modes in massive main-sequence stars</i>	
Samadi R., Belkacem K., Goupil M. J., Dupret M.-A., Brun A. S., Noels A., 2010, Ap&SS, 328, 253	239
<i>Turbulent eddy-time-correlation in the solar convective zone</i>	
Belkacem K., Samadi R., Goupil M. J., Baudin F., Salabert D., Appourchaux T., 2010, A&A, 522L, 2	245
<i>Amplitudes of solar-like oscillations in red-giant stars : Evidences for non-adiabatic effects using CoRoT observations</i>	
Samadi R., Belkacem K., Dupret M.-A., Ludwig H.-G., Baudin F., Caffau E., Goupil M. J., Barban C., 2012, A&A, 543, 120	249

Annexe B
CURRICULUM VITAE

Annexe C
Publications

C.1 Journaux à comité de lecture	263
C.2 Autres journaux	269
C.3 Contributions invitées et revues	272
C.4 Ouvrages et chapitres d'ouvrages	272
C.5 Diffusion des connaissances	272
C.6 Notes techniques	272

Chapitre 1

Introduction

1.1 Contexte et thématique de recherche

Après le Soleil et la Lune, les étoiles sont les astres qu'un enfant âgé d'à peine trois ans remarque et questionne en levant son regard vers les cieux. Les questions qu'il se pose et les rêves qu'il construit sur ces objets sont peut-être similaires à ceux des premières consciences humaines.

Pour nous ces étoiles constituent, de manière plus pragmatique, un formidable laboratoire de physique sans équivalent sur Terre. Elles permettent, notamment, d'étudier des milieux hydrodynamiques dans des régimes extrêmement turbulents.

Mes activités de recherche ont pour cadre la physique stellaire et s'intéressent particulièrement aux propriétés de la convection turbulente que l'on rencontre dans diverses étoiles mais qui sont mal modélisées dans les codes de structure et d'évolution stellaire. Elles s'appuient sur la sismologie stellaire – cad l'étude des propriétés des oscillations – utilisée comme outil pour sonder la structure des étoiles et les phénomènes physiques qui y prennent place.

La sismologie stellaire (et donc aussi l'héliosismologie) consiste – classiquement – à mesurer et interpréter les fréquences des oscillations qui résonnent à travers la cavité que constitue l'étoile. L'interprétation des fréquences des oscillations fait principalement appel à des outils théoriques en sismologie qui ont été développés ces 30 dernières années. Celle-ci fournit principalement des informations précieuses sur la *structure* interne de l'étoile ; toutefois les contraintes qu'elle apporte sur les processus dynamiques prenant place au sein de l'étoile sont plus limitées. Une autre branche de la sismologie stellaire s'est développée plus récemment, au développement de laquelle j'ai contribué : elle concerne la mesure précise et l'interprétation des amplitudes et durées de vie des *oscillations de type solaire*, cad des oscillations de nature analogue à celles que l'on détecte sur le Soleil. Et, comme je tacherai de le montrer, cette nouvelle branche constitue potentiellement un formidable moyen pour sonder la convection turbulente dans les étoiles, notamment s'agissant de ces aspects *dynamiques*.

1.2 Qu'observe-t-on et à quoi ça sert ... ?

Les modes solaires sont caractérisés par des durées de vie finie (quelques jours) et des amplitudes très faibles (quelques cm/s en vitesse et quelques partie par millions [ppm] en terme

d'intensité). Leur durée de vie est la conséquence de divers processus complexes d'amortissement qui ne sont pas encore bien connus et modélisés. L'excitation de ces modes est attribuée à la convection turbulente et prend place dans la partie supérieure de l'enveloppe convective. Cette région est en effet le siège de mouvements convectifs vigoureux et – dans une certaine mesure – incohérents. Depuis les travaux pionniers de [Lighthill \[1952\]](#), nous savons qu'un milieu turbulent génère des fluctuations de pressions acoustiques et incohérentes, phénomène que l'on nomme également "bruit acoustique"¹ Une toute petite fraction de l'énergie cinétique contenue dans ces mouvements turbulents est transmise – via un processus *stochastique* (i.e. aléatoire) – dans les modes stationnaires de la cavité solaire. Ce forçage peu efficace est responsable des amplitudes faibles des modes acoustiques (modes p) observés à la surface du Soleil.

Comme nous allons le montrer, mesurer l'amplitude et la durée de vie des modes nous permet de quantifier l'énergie injectée par unité de seconde dans les modes (cette quantité sera par la suite notée \mathcal{P} ; elle s'exprime en Joule par seconde). La mesure de \mathcal{P} fournit des contraintes directes sur les processus d'excitation par la convection turbulente [[Libbrecht, 1988](#)]. Cependant, comme l'ont noté [Baudin et al. \[2005\]](#), même pour le Soleil, déterminer \mathcal{P} à partir des données sismiques est loin d'être une tâche triviale et le problème est encore plus ardu s'agissant des données stellaires [[Samadi et al., 2008](#)]. Nous discuterons donc dans le Chap. 2 les problèmes liés à la détermination de contraintes sismiques fiables sur \mathcal{P} .

Durant la décade passée, des oscillations analogues à celles du Soleil (que l'on nomme "oscillations de type solaire") ont été détectées *depuis le sol* dans quelques dizaines d'étoiles, situées dans diverses stades évolutifs et représentatives de divers masses et abondances de surface [voir la revue par [Bedding and Kjeldsen, 2007](#)]. Comme pour le Soleil, ces oscillations ont de très faibles amplitudes et des durées de vie finie. L'excitation de ces oscillations de type solaire sont également attribuées à la convection turbulente, et prend place dans les couches externes des étoiles dotées d'enveloppe convective.

Jusqu'à un passé récent, seules les données sismiques solaires étaient de qualité suffisante pour contraindre directement et indépendamment les processus d'excitation et d'amortissement. Depuis le lancement de la mission CoRoT (CNES) en décembre 2006, des contraintes de même nature et de très bonne qualité ont été – pour la première fois – disponibles pour d'autres étoiles que le Soleil. Grâce aux missions spatiales CoRoT² et *Kepler* (NASA), les amplitudes des oscillations de type solaires sont maintenant mesurées dans un échantillon conséquent d'étoiles. Ces mesures mettent en évidence le fait que les amplitudes et durées de vie de ces modes varient d'une étoile à l'autre suivant des lois d'échelles caractéristiques qui sont fonctions des paramètres fondamentaux des étoiles (luminosité, température effective, gravité de surface ... etc).

L'extension de ces deux missions vont permettre de consolider et d'enrichir encore le diagnostic sismique apporté par ce genre d'observations. Dans ce contexte très riche et en plein essor, mes travaux de recherche visent à interpréter et à modéliser de manière réaliste les amplitudes des oscillations de type solaire détectées dans diverses étoiles et – par ce biais – à établir des diagnostics sur les modèles de convection turbulente adaptés aux étoiles.

1. Terme faisant référence à des ondes acoustiques dont la phase et l'amplitude varient de manière aléatoire.

2. On trouvera dans [Michel and Baglin \[2012\]](#) un état des lieux concernant les observations CoRoT ainsi que les résultats associés.

1.3 Bref historique sur le sujet

Les oscillations solaires ont été détectées pour la première fois par [Leighton *et al.* \[1962\]](#). On pensait que ces oscillations pouvaient contribuer au chauffage de la couronne solaire [cf. [Stein and Leibacher, 1974](#)]. C'est dans le cadre de cette problématique que [Unno and Kato \[1962\]](#) ont étudiés la génération de bruit acoustique par les fluctuations incohérentes de la densité à la surface du soleil³. Par la suite, [Stein \[1967\]](#) a généralisé l'approche de [Lighthill \[1952\]](#) à des atmosphères stratifiées (situation évidemment adaptée au cas du Soleil et des étoiles en général). Il a ainsi montré que, contrairement aux termes de type quadrupolaire⁴, les termes de forçage de type monopolaire contribuent de manière négligeable à la génération du bruit acoustique. Parmi les termes quadrupolaires, le tenseur de Reynolds a été ainsi identifié comme étant le terme dominant pour la génération d'*onde* acoustique.

Ce n'est qu'au début des années 1970 que les oscillations solaires ont été clairement identifiées comme étant les modes propres acoustiques associés à la cavité solaire [[Ulrich, 1970](#); [Leibacher and Stein, 1971](#); [Deubner, 1975](#)]. Quelques années plus tard, [Goldreich and Keeley \[1977b, GK par la suite\]](#) ont proposé la première modélisation théorique de l'excitation stochastique de ces *modes propres* par la convection turbulente. Depuis ce travail pionnier, différentes améliorations ont été proposées [[Dolginov and Muslimov, 1984](#); [Balmforth, 1992a](#); [Goldreich and Kumar, 1990](#); [Goldreich *et al.*, 1994](#); [Samadi and Goupil, 2001](#); [Samadi *et al.*, 2003a](#); [Chaplin *et al.*, 2005](#); [Belkacem *et al.*, 2006b, 2008, 2010](#)]. Elles se distinguent les unes des autres par la nature des termes de forçage retenus ainsi que par la manière de modéliser la convection turbulente. En particulier, à partir des années 90, deux débats ont stimulé des recherches sur le sujet : L'un concerne l'importance ou non d'un forçage de nature thermique (liées aux fluctuations turbulentes de l'entropie, voir Chap. 3), et l'autre la manière de décrire les corrélations temporelles entre éléments turbulents (voir Chap. 4).

1.4 Mes travaux dans ce contexte

Dans le cadre des développements théoriques menés sur le sujet, mes travaux de thèse [[Samadi, 2000](#), soutenue le 8 décembre 2000] ont constitué une étape importante puisqu'ils ont permis d'élaborer une formulation théorique qui prend en compte – de manière consistante et en généralisant son rôle – la turbulence stellaire [[Samadi and Goupil, 2001](#)]. Depuis ces travaux, mes efforts ont cherché à mieux préciser le lien entre observables et modèles théoriques (Chap. 2), à consolider la modélisation des amplitudes, à établir des diagnostics sur la convection turbulente dans les étoiles (Chap. 4) ainsi que les modèles standards de structure stellaire (Chap. 5) et enfin à interpréter et modéliser les lois d'échelles sismiques portant sur les amplitudes des modes de type solaire (Chap. 6). Ce manuscrit expose les bases théoriques de l'excitation stochastique par la convection turbulente (Chap. 3) et résume l'ensemble des résultats obtenus dans ce contexte après ma thèse. Le Chap. 7 sera dédié à la discussion critique sur les modèles actuels, sur les problématiques ouvertes, et enfin les perspectives qui s'ouvrent dans ce contexte.

3. Cette forme de forçage est dit du type monopolaire car associé à des fluctuations de volume, donc de densité

4. Un terme de forçage est dit quadrupolaire lorsqu'il est associé à du cisaillement.

Chapitre 2

Des observables à la modélisation

Sommaire

2.1	Balance énergétique	11
2.2	Contraintes sismiques en terme de vitesse	12
2.2.1	Principe général	13
2.2.2	Cas du Soleil	14
2.2.3	Cas des autres étoiles	15
2.3	Contraintes sismiques en terme d'intensité	17

Articles reproduits dans ce mémoire (voir Appendice A) et auxquels ce chapitre se rapporte :

- “*Inferred acoustic rates of solar p modes from several helioseismic instruments*”, Baudin F., Samadi, R., Goupil M.-J., Appourchaux T., Barban C., Boumier P., Chaplin W. J., Gouttebroze P., 2004, A&A, 433, 349 [Page 117] ;
- “*Modeling the excitation of acoustic modes in α Centauri A*”, Samadi R., Belkacem K., Goupil M.-J., Dupret M.-A., Kupka F., 2008, A&A, 489, 291 [Page 177] ;
- “*Intrinsic photometric characterisation of stellar oscillations and granulation. Solar reference values and CoRoT response functions*”, Michel E., Samadi R., Baudin F., Barban C., Appourchaux T., Auvergne M., 2009, A&A, 495, 979 [Page 213].

2.1 Balance énergétique

Comme on va le mettre en évidence ici, l’amplitude d’un mode de type solaire résulte d’un équilibre entre excitation et amortissement. L’énergie (cinétique plus potentielle) contenue dans un mode est par définition la quantité⁵ :

$$E_{\text{osc}}(t) = \int d^3x \rho_0 \vec{v}_{\text{osc}}^2(\vec{r}, t) \quad (2.1)$$

5. Notez que cette définition suppose une équipartition entre énergie cinétique et potentielle.

où \vec{v}_{osc} correspond à la vitesse du mode à la position \vec{r} et au temps t , et ρ_0 est la densité à l'équilibre.

L'amortissement du mode opère à des échelles de temps très lent devant les échelles de temps associées au forçage par la convection turbulente. En effet, les modes solaires ont une durée de vie de l'ordre du jour tandis, dans la région où le forçage est le plus vigoureux (*i.e.* la partie supérieure de la zone convective), les éléments convectifs ont une durée de vie de l'ordre de la minute. Par conséquent, les processus d'amortissement et de forçage peuvent être découplés dans le temps. Nous allons supposer que l'amortissement – qu'elle qu'en soit son origine physique – est constant et linéaire, de sorte que :

$$\frac{d\vec{v}_{\text{osc}}(t)}{dt} = -\eta \vec{v}_{\text{osc}}(t) \quad (2.2)$$

où η est le taux (constant) d'amortissement et la dérivée temporelle dans Eq. (2.2) est appliquée sur des échelles de temps très longues devant les temps associés au forçage.

Soit \mathcal{P} l'énergie communiquée par unité de temps par une source d'excitation arbitraire (mais agissant sur des échelles temps très court devant $1/\eta$). En vertu des Eqs. (2.1) et (2.2), la variation de E_{osc} avec le temps est donnée par l'équation :

$$\frac{dE_{\text{osc}}}{dt}(t) = \mathcal{P} - 2\eta E_{\text{osc}}(t). \quad (2.3)$$

Les amplitudes des oscillations de type solaires sont connues pour être stables sur des échelles de temps très longs devant les temps caractéristiques liés aux processus d'excitation et d'amortissement, à savoir dans le cas du Soleil, de quelques minutes pour l'excitation et quelques jours pour l'amortissement. Dans ces conditions, la moyenne temporelle de l' Eq. (2.3) vérifie donc :

$$\overline{\frac{dE_{\text{osc}}}{dt}}(t) = 0, \quad (2.4)$$

où $\overline{(\)}$ correspond à une moyenne effectuée sur des temps très longs devant les temps caractéristiques de l'amortissement et du forçage par la convection turbulente . A partir des Eqs. (2.3) et (2.4), nous établissons immédiatement la relation :

$$\overline{E}_{\text{osc}} = \frac{\overline{\mathcal{P}}}{2\eta}. \quad (2.5)$$

La relation 2.5 met clairement en évidence que l'énergie d'un mode stable (et donc son amplitude) est contrôlée par un équilibre en excitation (\mathcal{P}) et amortissement (η). La difficulté majeure étant d'identifier et de modéliser les processus physiques à l'origine de l'excitation et de l'amortissement. Les processus liés à l'amortissement ne seront pas abordés dans ce mémoire (voir à ce sujet la revue récente que l'on doit à [Belkacem and Samadi \[2013\]](#)). Les processus d'excitation à l'oeuvre seront en revanche abordés en détail dans le présent document.

2.2 Contraintes sismiques en terme de vitesse

Nous établissons ici les liens (subtiles) entre les mesures sismiques des amplitudes et des durée de vie des mode et la quantité \mathcal{P} , laquelle, rappelons-le, permet de quantifier et donc contraindre les processus d'excitation.

2.2.1 Principe général

Le modèle théorique présenté dans le chapitre 3 nous conduit à écrire le déplacement d'un mode, $\delta\vec{r}_{\text{osc}}$, en terme d'une fonction propre adiabatique $\vec{\xi}$ et d'une amplitude instantanée $A(t)$ comme suit :

$$\delta\vec{r}_{\text{osc}} \equiv \frac{1}{2} \left(A(t) \vec{\xi}(\vec{r}) e^{-i\omega_{\text{osc}}t} + cc \right) \quad (2.6)$$

où cc fait référence au complexe conjugué, ω_{osc} est la fréquence (angulaire) du mode propre, et $A(t)$ l'amplitude instantanée résultant des effets combinés de l'excitation et de l'amortissement. Notez que puisque la fonction propre normalisée est arbitraire, l'amplitude *intrinsèque* du mode est au final fixée par le terme A , dont la valeur reste à déterminer (ceci sera l'objet du Chap. 3). La vitesse d'un mode est donc donnée par l'expression suivante :

$$\vec{v}_{\text{osc}}(\vec{r}, t) = \frac{d\delta\vec{r}_{\text{osc}}}{dt} = \frac{1}{2} (-i\omega_{\text{osc}} A(t) \vec{\xi}(\vec{r}) e^{-i\omega_{\text{osc}}t} + cc) . \quad (2.7)$$

A l'aide des Eqs. (2.7) et (2.1), nous établissons l'expression pour l'énergie moyenne du mode :

$$E_{\text{osc}} = \int d^3x \rho_0 \overline{v_{\text{osc}}^2} = \frac{1}{2} \overline{|A|^2} I \omega_{\text{osc}}^2 , \quad (2.8)$$

où

$$I \equiv \int_0^M d^3x \rho_0 \vec{\xi}^* \cdot \vec{\xi} \quad (2.9)$$

est par définition l'inertie du mode. Par soucis de simplification, nous allons dans la suite considérer uniquement des modes radiaux⁶. En vertu de l'Eq. (2.7), la vitesse quadratique moyenne du mode à la surface s'exprime (pour un mode radial) par la relation :

$$\overline{v_s^2}(r_h) = \frac{1}{2} \overline{|A|^2} \omega_{\text{osc}}^2 |\xi_r(r_h)|^2 \quad (2.10)$$

où ξ_r est la fonction propre de déplacement (radial) et r_h le rayon correspondant à la couche de surface où la vitesse du mode est mesurée. Comme on le verra dans la suite, il est pratique de définir la "masse" du mode (mode mass en anglais) comme :

$$\mathcal{M}(r_h) \equiv \frac{I}{|\xi_r(r_h)|^2} . \quad (2.11)$$

On notera que le calcul de \mathcal{M} (ainsi que de l'inertie I) repose, en vertu des Eqs. (2.9) et (2.11), sur un modèle de structure interne et nécessite la résolutions des modes propres associés. En vertu des Eqs. (2.8), (2.10), and (2.11), nous dérivons finalement la relation :

$$E_{\text{osc}} = \mathcal{M} \overline{v_s^2} . \quad (2.12)$$

6. Nous avons traité en détail le cas des modes radiaux dans [Belkacem et al. \[2008\]](#). Voir également la Sect. 3.3 du Chap. 3.

Il est important de noter que, bien que \mathcal{M} et v_s dépendent du choix de la couche r_h , E_{osc} est par définition intrinsèque au mode (voir Eq. (2.1)) et par conséquent ne dépend pas du lieu où celle-ci est mesurée. En revanche la quantité \mathcal{M} , que l'on nomme “masse du mode” du fait de sa dimension, n'est en aucun cas intrinsèque au mode car dépend du choix de la couche r_h . En vertu de l'Eq. (2.12), il s'agit simplement du coefficient de proportionnalité entre l'énergie cinétique et le carré de la vitesse (rms) à l'endroit où celle-ci est mesurée.

En combinant l'Eq. (2.5) avec l'Eq. (2.12), on aboutit finalement à la relation

$$\bar{v}_s^2(r_h, \omega_{\text{osc}}) = \frac{\mathcal{P}}{2\pi\mathcal{M}\Gamma} \quad (2.13)$$

où $\Gamma = \eta/\pi$ correspond à la largeur du mode. L'Eq. (2.13), témoigne à nouveau du fait que l'amplitude d'un mode résulte de l'équilibre entre l'excitation (\mathcal{P}) et l'amortissement ($\eta = \Gamma\pi$). Cependant, cette équation montre aussi que l'amplitude en terme de vitesse dépend de la “masse” du mode (ou de manière équivalente de l'inertie) : pour un forçage (\mathcal{P}) et un amortissement (η) donnés, plus la “masse” du mode est élevée, plus l'amplitude est faible.

Lorsque la résolution fréquentielle et le niveau signal-à-bruit sont suffisamment élevés, il est possible de résoudre le profil d'un mode dans le domaine Fourier et mesurer ainsi à la fois Γ et sa hauteur H dans le spectre de densité spectral (généralement exprimé en m^2/Hz). Dans ces conditions, v_s est donné par la relation [voir e.g. Chaplin *et al.*, 1998; Baudin *et al.*, 2005] :

$$v_s^2(r_h, \omega_{\text{osc}}) = \pi C_{\text{obs}} H \Gamma \quad (2.14)$$

où le coefficient C_{obs} prend en compte les conditions d'observations, notamment les effets géométriques [voir Baudin *et al.*, 2005]. A partir des Eqs. (2.13) et (2.14), on établit alors la relation qui relie \mathcal{P} aux mesures sismiques :

$$\mathcal{P}(\omega) = 2\pi\mathcal{M}\Gamma v_s^2 = 2\pi^2\mathcal{M}C_{\text{obs}}H\Gamma^2. \quad (2.15)$$

A condition de pouvoir mesurer Γ et H , il est alors possible de contraindre \mathcal{P} . Rappelons cependant que l'évaluation de \mathcal{P} à partir des observations fait intervenir des modèles puisque il est nécessaire d'évaluer \mathcal{M} (l'évaluation de cette quantité nécessitant un modèle de structure interne). Par ailleurs, il existe une forte anti-corrélation entre H et Γ qui engendre d'importants biais dans la mesure de ces deux quantités [voir e.g. Chaplin *et al.*, 1998; Chaplin and Basu, 2008].

2.2.2 Cas du Soleil

On traite ici de la qualité des mesures sismiques disponibles en héliosimologie pour la détermination des taux d'excitation des modes, \mathcal{P} .

A partir des données héliosismiques fournies par l'instrument GOLF à bord de SOHO ainsi que des réseaux sols BiSON et GONG, Baudin *et al.* [2005, article inséré en page 117] ont déterminé les taux d'excitation \mathcal{P} associés aux modes p solaires. Comme l'ont noté Baudin *et al.* [2005], la couche r_h à laquelle la masse du mode \mathcal{M} est évaluée doit être déterminé précisément pour obtenir des contraintes correctes sur les taux d'excitation \mathcal{P} (Eq. (2.15)), et à travers eux sur les processus de forçage. Chaque instrument utilise une raie spectrale donnée, qui se forme dans une région donnée de l'atmosphère. En fonction de la raie utilisée et de la (ou les)

position(s) dans la raie, la mesure Doppler est sensible à une région précise dans l’atmosphère. On considère en général que cette région correspond par défaut à la région de formation de la raie. Par exemple, l’instrument BiSON utilise la raie I du potassium (KI) laquelle se forme à une profondeur optique $\tau_{500\text{nm}} \approx 0.013$. Les profondeurs optiques associées à chaque raie spectrale utilisée par les différents instruments utilisés en héliosismologie sont renseignées dans Houdek [2006].

Les taux d’excitation \mathcal{P} calculés par Baudin *et al.* [2005] sont reproduits sur la Fig. 2.1 (panneau supérieur). Pour $\nu \lesssim 3.2$ mHz, $\mathcal{P}^{\text{GONG}}$ et $\mathcal{P}^{\text{BiSON}}$ sont mutuellement en accord, en revanche $\mathcal{P}^{\text{GOLF}}$ est systématiquement plus petit que $\mathcal{P}^{\text{GONG}}$ et $\mathcal{P}^{\text{BiSON}}$; les écarts demeurent toutefois à l’intérieur de la barre d’incertitude à $1\text{-}\sigma$. Les différences entre les jeux de données sont plus importantes à haute fréquence. Ceci peut être partiellement attribué au choix de la couche r_h à laquelle est évalué \mathcal{M} . En effet, la sensibilité de \mathcal{M} avec r_h est plus importante à haute fréquence, car les modes de hautes fréquences sont plus confinés à la surface que ne le sont les modes de basses fréquences. En revanche, à basse fréquence, le mode masse \mathcal{M} est beaucoup moins sensible au choix de la couche r_h . Par conséquent, le désaccord observé à basse fréquence entre GOLF et les deux autres jeux de données suggère que la calibration de l’instrument GOLF est dans une certaine mesure incorrecte [voir Baudin *et al.*, 2005]. On montre sur la Fig. 2.1 (panneau inférieur), $\mathcal{P}_{\text{GOLF}}$ multiplié par un facteur deux, choisi de telle sorte que, à basse fréquence, $\mathcal{P}_{\text{GOLF}}$ se raccorde à $\mathcal{P}^{\text{GONG}}$ et $\mathcal{P}^{\text{BiSON}}$. Quelque soit la fréquence, $\mathcal{P}^{\text{GONG}}$ et $\mathcal{P}^{\text{GOLF}}$ sont en accord tandis qu’à haute fréquence $\mathcal{P}^{\text{GONG}}$ est systématiquement plus bas que $\mathcal{P}^{\text{GOLF}}$ ou $\mathcal{P}^{\text{BiSON}}$. Ce résidu à haute fréquence est peut-être du à une évaluation imprécise de la couche r_h à laquelle les différents instruments sont sensibles, mais évaluer précisément la couche à laquelle un instrument donné effectue effectivement la mesure sismique est loin d’être un problème trivial [pour une discussion détaillée on se référera à Baudin *et al.*, 2005]. En particulier, confondre la région de formation d’une raie spectrale avec le lieux où cette raie est sensible aux oscillations est une simplification qui se doit d’être regardée de plus près [c.f. Eibe *et al.*, 2001]. Enfin, par ailleurs le calcul de la “masse” du mode (\mathcal{M}) s’effectue jusqu’à présent en supposant des modes adiabatiques, hypothèse évidemment non réaliste du fait de l’existence d’importants échanges énergétiques entre les modes et le milieu [cf. Belkacem and Samadi, 2013].

2.2.3 Cas des autres étoiles

Les mesures des oscillations de type solaire en terme de vitesse Doppler sont généralement effectuées avec des spectromètres dédiés à la sismologie stellaire et la recherche de planètes extra-solaires (comme par exemple UCLES, UVES, HARPS). Ces mesures Doppler utilisent un très grand nombre de raies spectrales, et ce à fin d’optimiser le niveau signal à bruit. Chaque raie spectrale se formant dans une région donnée de l’atmosphère, il est donc encore plus difficile que dans le cas solaire d’estimer la couche effective r_h à laquelle la mesure sismique s’effectue. Comme cela est discuté dans Samadi *et al.* [2008, ci-joint page 177], le calcul des vitesses des modes à la surface v_s (Eq. (2.13)), dépend – à travers la masse du mode (Eq. (2.11)) – significativement du choix de la couche r_h . Ceci est illustré sur la Fig. 2.2 dans le cas de l’étoile α Cen A.

Les mesures effectuées par Kjeldsen *et al.* [2008a] nous permettent cependant d’estimer la couche effective à laquelle s’effectue en général les mesures dans le cas stellaire. En effet, ces auteurs ont mesuré les modes solaires avec le spectromètre UCLES. Les amplitudes mesurées

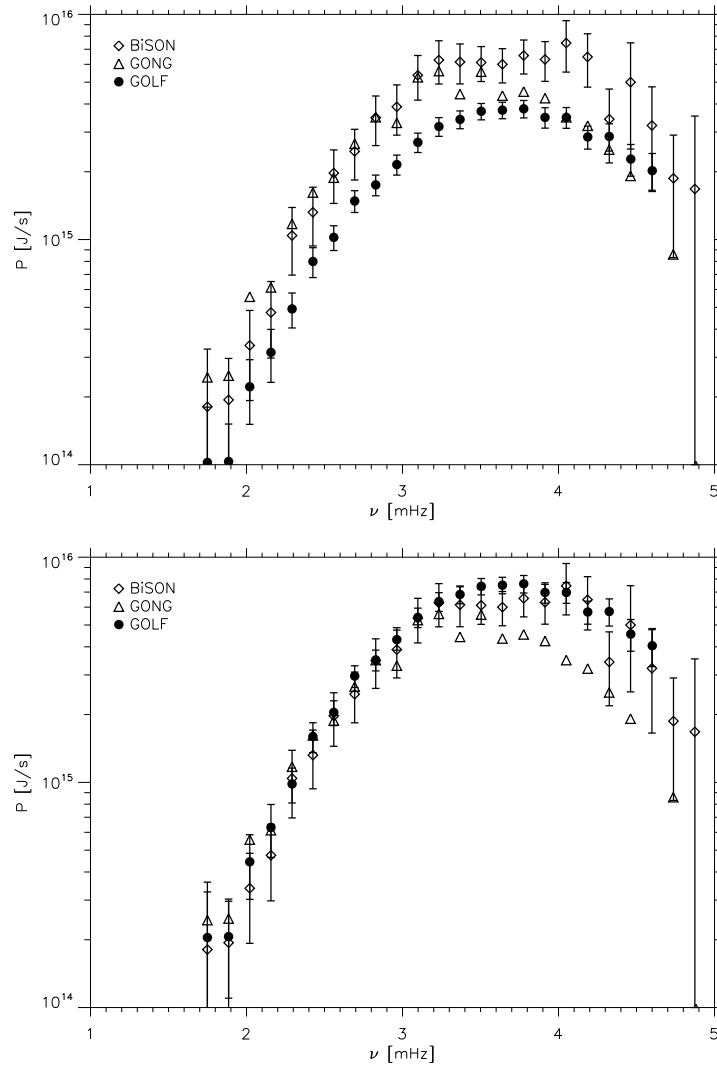


FIGURE 2.1 – **Panneau supérieur** : Taux d’excitation \mathcal{P} des modes p solaires en fonction de la fréquence. Les cercles pleins correspondent aux données sismiques issues de l’instrument SOHO/GOLF, les diamants au réseau sol BiSON et les triangles au réseau sol GONG. **Panneau inférieur** : Comme pour le panneau supérieur. Les taux d’excitation \mathcal{P} déduits des données GOLF ont ici été multipliés par un facteur deux, choisi de telle sorte que, à basse fréquence, ces données se raccordent au mieux aux données issues des réseaux BiSON et GONG.

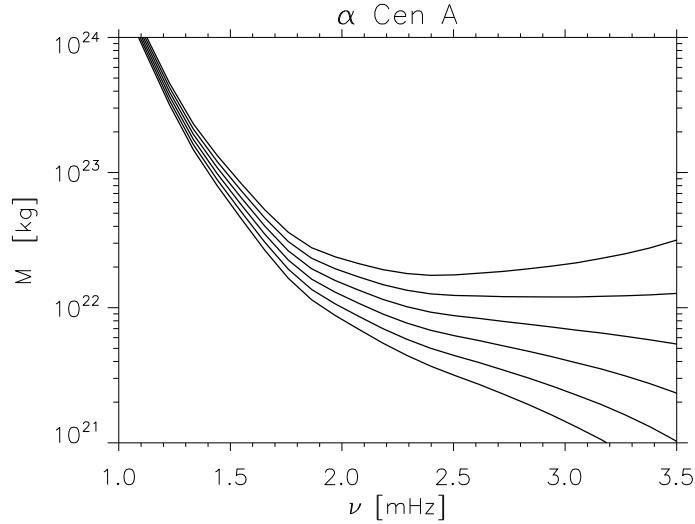


FIGURE 2.2 – Masses des modes (\mathcal{M}) calculées, dans le cas de l'étoile α Cen A, à différentes hauteurs h au dessus de la photosphère. La courbe supérieure correspond à la photosphère ($h = 0$ km) tandis que la courbe inférieure à la partie supérieure de l'atmosphère (à $h = 1000$ km). Le pas en h est de 200 km.

avec cet instrument sont légèrement plus faibles que celles mesurées avec le réseau BiSON. L'instrument de ce réseau utilise la raie du potassium (K) dont la région de formation est située à la profondeur optique $\tau_{500 \text{ nm}} \simeq 0.013$ (dans le continu). Les mesures faites par [Kjeldsen et al. \[2008a\]](#) suggèrent donc que les mesures sismiques effectuées dans le cas stellaire se situent légèrement en dessous de la région de formation du potassium, i.e. à une couche située légèrement en dessous de l'épaisseur optique $\tau_{500 \text{ nm}} \simeq 0.013$. Par conséquent, les amplitudes des modes stellaires sont, par *défaut*, évaluées au niveau de cette couche. Cependant, une approche plus rigoureuse prenant compte du fait que plusieurs raies spectrales sont utilisées et que la présence ainsi que le poids de chaque raie est en fait fonction de l'étoile considérée. Par ailleurs, comme dans le cas du Soleil (voir Sect. 2.2.2), il s'agit de distinguer le lieu de formation d'une raie donnée des régions où celle-ci est sensible à l'oscillation. L'ensemble de ces problématiques nécessite une étude spécifique.

2.3 Contraintes sismiques en terme d'intensité

Les missions spatiales CoRoT et *Kepler* détectent et mesurent des oscillations de type solaire sur un très grand nombre d'étoiles. Toutes ces mesures sont basées sur des mesures photométriques de très hautes précisions. Par conséquent, à fin de comparer les amplitudes théoriques avec les observations, il est nécessaire de considérer non plus les vitesses des modes mais les fluctuations d'intensité qu'elles induisent.

On note L la luminosité absolue de l'étoile. A chaque instant t donné, la fluctuation bolométrique, δL , induite par un mode d'oscillation est reliée à la variation Lagrangienne du rayon δR_* et à la fluctuation de la température effective δT_{eff} de l'étoile en vertu de la relation [[Dziem-](#)

blowski, 1977; Pesnell, 1990]

$$\frac{\delta L(t)}{L} = 4 \frac{\delta T_{\text{eff}}(t)}{T_{\text{eff}}} + 2 \frac{\delta R_*(t)}{R_*}. \quad (2.16)$$

Compte-tenu des vitesses caractéristiques des modes de type solaire (voir chapitre 6), les variations relatives de rayon, $\delta R_*(t)/R_*$, s'avèrent être négligeables devant les fluctuations d'intensités mesurées. On peut donc négliger le second terme à droite de l'Eq. (2.16) devant le premier. On préfère en général évaluer les amplitudes des modes en terme d'écart-type dans la mesure où, comme on l'a évoqué dans la section 2.1, l'amplitude d'un mode de type solaire résulte d'un forçage de nature stochastique (aléatoire) et qui, comme on le verra dans le Chap. 3, ne peut être évalué que de manière statistique. L'écart-type associé à $\delta L(t)$ s'exprime alors comme :

$$\left(\frac{\delta L}{L}\right)_{\text{rms}} = 4 \left(\frac{\delta T_{\text{eff}}}{T_{\text{eff}}}\right)_{\text{rms}}, \quad (2.17)$$

où les quantités avec l'indice 'rms' font références à des écart-types (en anglais : rms = root mean-square).

Il est à ce stade important de noter que les intensités mesurées par les instruments CoRoT et Kepler ne correspondent pas à des mesures bolométriques car elles sont limitées à une bande spectrale donnée. Ces bandes, relativement assez larges, sont centrées dans le visible. Les fluctuations d'intensité mesurées dans une bande spectrale donnée sont en fait fonction du spectre de l'étoile ainsi que de la bande passante de l'instrument [Michel *et al.*, 2009, ci-joint page 213].

Il est donc nécessaire de relier la fluctuation (relative) d'intensité mesurée par un instrument donné à la fluctuation bolométrique correspondante. De plus, le cas des modes non-radiaux doit être traité en tenant compte de la géométrie propre à ces modes. Nous avons établi dans Michel *et al.* [2009, ci-joint page 213] la relation entre fluctuations d'intensité mesurées (ou "apparentes") avec les fluctuations de température effective induites par un mode d'oscillation de degré ℓ donné, puis, à l'aide de l'Eq. (2.17) on relie ainsi fluctuations d'intensité "apparentes" aux fluctuations bolométriques δL_{rms} associées. Cette relation s'écrit pour un mode de degré ℓ donné comme :

$$\left(\frac{\delta I}{I}\right)_{\text{rms}} = R_\ell \left(\frac{\delta T_{\text{eff}}}{T_{\text{eff}}}\right)_{\text{rms}} = \frac{R_\ell}{4} \left(\frac{\delta L}{L}\right)_{\text{rms}}, \quad (2.18)$$

où le coefficient R_ℓ , dont l'expression est donnée dans Michel *et al.* [2009], dépend de la bande passante de l'instrument, du spectre de l'étoile (et à travers lui de sa température effective, gravité de surface et composition chimique) et enfin du degré ℓ du mode. Le coefficient R_ℓ , qui constitue la "fonction réponse" de l'instrument, permet donc de convertir l'amplitude mesurée par CoRoT ou Kepler [pour le cas de Kepler voir Ballot *et al.*, 2011], en terme d'amplitude bolométrique $\left(\frac{\delta L}{L}\right)_{\text{rms}}$, amplitude qui est par essence indépendante de l'instrument ainsi que de la géométrie du mode. Les valeurs obtenues pour le coefficient R_ℓ ont été au préalable validées dans le cas du Soleil à l'aide d'une comparaison entre des mesures effectuées dans différentes bandes passantes et des mesures bolométriques [voir Michel *et al.*, 2009].

Chapitre 3

Modélisation de l'excitation stochastique

Sommaire

3.1 Fondements théoriques	20
3.1.1 L'équation d'onde inhomogène	20
3.1.2 Solution générale	22
3.1.3 Termes sources de forçage	23
3.1.4 Séparation d'échelle	24
3.1.5 Modèles de fermeture	25
3.1.6 Modèle de turbulence adopté	25
3.1.7 Formulation finale	26
3.2 Approches alternatives	28
3.2.1 Méthode de l'“équipartition” d'énergie	28
3.2.2 Méthode <i>ab initio</i>	29
3.3 Cas des modes non-radiaux	30
3.4 A propos de la contribution de l'entropie	31

Articles reproduits dans ce mémoire (voir Appendice A) et auxquels ce chapitre se rapporte :

- “*Numerical constraints on the model of stochastic excitation of solar-type oscillations*”, Samadi R., Nordlund A., Stein R. F., Goupil M.-J., Roxburgh I., 2003, A&A, 403, 303 [Page 97];
- “*Numerical 3D constraints on convective eddy time-correlations : Consequences for stochastic excitation of solar p modes*”, Samadi R., Nordlund A., Stein R. F., Goupil M.-J., Roxburgh I., 2003, A&A, 403, 1129 [Page 107];
- “*Excitation of solar-like oscillations across the HR diagram*”, Samadi R., Georgobiani D., Trampedach R., Goupil M.-J., Stein R. F., Nordlund A., 2007, A&A, 463, 29 [Page 165];
- “*Stochastic excitation of non-radial modes. I. High-angular-degree p modes*”, Belkacem K., Samadi R., Goupil M.-J., Dupret M.-A., 2008, A&A, 478, 163 [Page 187];

- "Stochastic excitation of nonradial modes. II. Are solar asymptotic gravity modes detectable?", Belkacem K., Samadi R., Goupil M.-J., Dupret M.-A., Brun A. S., Baudin F., 2009, A&A, 494, 191 [Page 199];
- "Stochastic excitation of gravity modes in massive main-sequence stars", Samadi R., Belkacem K., Goupil M. J., Dupret M.-A., Brun A. S., Noels A., 2010, Ap&SS, 328, 253 [Page 239].

3.1 Fondements théoriques

3.1.1 L'équation d'onde inhomogène

La propagation d'une onde dans un milieu donné est régie par une équation dite de "propagation" (ou simplement équation d'onde). Si on ajoute à cette équation d'onde des conditions aux limites appropriées et que l'on résout le système, on peut alors déterminer les modes piégés dans la cavité. Cette équation ne permet pas à elle seule de déterminer l'amplitude et la durée de vie des modes. Résoudre les propriétés des modes (amplitude, durée de vie et fréquence) de manière pleinement consistante et complète nécessiterait de résoudre simultanément (cad de manière couplé) les trois équations fondamentales, à savoir : l'équation de continuité, de mouvement et d'énergie.

Les mécanismes d'amortissement dominants (que l'équation d'énergie permet en principe d'isoler) sont encore mal connus et sont modélisés de manière encore très simplifiée [voir à ce sujet par exemple la revue de [Belkacem and Samadi, 2013](#)]. Pour simplifier la résolution théorique du problème des amplitudes des modes de type solaire, on adopte en général l'approche proposée par [Goldreich and Keeley \[1977b\]](#), GK par la suite]. Celle-ci consiste à résoudre d'abord l'équation de "propagation" en supposant des modes adiabatiques et non forcés. La résolution de cette équation en tenant compte de conditions aux limites appropriées, fournit les modes propres adiabatiques. On ajoute alors à l'équation de "propagation" les termes de forçage. Ceci forme ce que l'on nomme l'équation d'onde *inhomogène*. On résout alors cette équation en s'appuyant sur les solutions de l'équation d'onde sans forçage.

On reproduit ci-après, dans ses grandes lignes, les étapes qui permettent d'établir et de résoudre l'équation d'onde inhomogène. Le développement plus détaillé est publié dans ma thèse de doctorat ⁷ [[Samadi, 2000](#), SPHd par la suite ou de manière plus concise dans [Samadi and Goupil \[2001\]](#)].

Chaque grandeur physique f (excepté la vitesse v) est décomposée comme suit sous la forme d'une grandeur à l'équilibre (f_0) et d'une fluctuation eulérienne : $f = f_0 + f_1$. Nous retiendrons par la suite uniquement les termes linéaires ou quadratiques en P_1 et ρ_1 , où P désigne la pression du gaz et ρ la densité. On néglige en revanche les fluctuations g_1 de la gravité g . S'agissant de la composante oscillante (*i.e.* celle associée au mode), il s'agit de l'approximation dite de Cowling qui est vérifiée pour les modes d'ordres élevés [c.f. [Cowling, 1941](#); [Ledoux and Walraven,](#)

7. On avisera le lecteur que deux corrections ont été apportées au manuscrit de thèse. Le manuscrit original ainsi que l'erratum associé sont téléchargeables à cette adresse : <http://tel.archives-ouvertes.fr/tel-00067734>. L'une de ces erreurs concerne une erreur analytique commise lors de la dérivation du terme de forçage associé au tenseur de Reynolds. Cette erreur a également été corrigée dans [Samadi et al. \[2005\]](#) et les conséquences de celles-ci discutées dans [Samadi et al. \[2007\]](#).

1958]. Cette approximation n'est toutefois pas indispensable, on l'adopte ici pour simplifier l'équation régissant la propagation des ondes. S'agissant des termes de forçages induits par g_1 , on montre qu'ils sont négligeables devant le terme de Reynolds. La perturbation de l'équation de mouvement et de continuité donne alors :

$$\frac{\partial \rho \vec{v}}{\partial t} + \vec{\nabla} : (\rho \vec{v} \vec{v}) + \vec{\nabla} P_1 - \rho_1 \vec{g}_0 = 0 \quad (3.1)$$

$$\frac{\partial \rho_1}{\partial t} + \vec{\nabla} \cdot (\rho \vec{v}) = 0 . \quad (3.2)$$

L'équation d'état perturbée s'écrit à l'ordre deux comme

$$P_1 = c_s^2 \rho_1 + \alpha_s s_1 + \alpha_{\rho\rho} \rho_1^2 + \alpha_{ss} s_1^2 + \alpha_{\rho s} \rho_1 s_1 , \quad (3.3)$$

où s est l'entropie, $\alpha_s = (\partial P / \partial s)_\rho$, $c_s = \Gamma_1 P_0 / \rho_0$ désigne la vitesse moyenne du son, $\Gamma_1 = (\partial \ln P / \partial \ln \rho)_s$ est l'indice adiabatique, $\alpha_{\rho\rho}$, α_{ss} et $\alpha_{\rho s}$ sont les dérivées partielles secondes de P en fonction de s et ρ . Il est important de noter que l'Eq. (3.3) suppose une composition chimique constante (ce qui est le cas dans une région convective) mais aussi un taux d'ionisation également constant.

La vitesse du fluide \vec{v} est décomposée sous la forme d'une composante $\delta \vec{v}_{\text{osc}}$ due au mode et de la composante \vec{u} associée à la turbulence :

$$\vec{v} = \vec{v}_{\text{osc}} + \vec{u} . \quad (3.4)$$

On se place en absence de la turbulence (i.e. $\vec{u} = 0$). En combinant l'Eq. (3.1) avec l'Eq. (3.2) puis en différenciant par rapport au temps, on aboutit à l'équation d'onde *homogène*

$$\left(\frac{\partial^2}{\partial t^2} - \vec{L} \right) \vec{v}_{\text{osc}} = 0 , \quad (3.5)$$

où L est l'opérateur linéaire régissant la propagation de l'onde [voir son expression dans SPhD, page 65]. Une expression plus générale ne reposant pas sur l'approximation de Cowling est en pratique utilisée. Si on ajoute à cette équation des conditions aux limites appropriées, cela donne les fonctions propres usuelles [Unno *et al.*, 1989]

$$\vec{L}(\vec{\xi}(\vec{r}, t)) = -\omega_{\text{osc}}^2 \vec{\xi}(\vec{r}, t) , \quad (3.6)$$

où ω_{osc} est la fréquence (angulaire) propre du mode et $\vec{\xi}(\vec{r}, t) \equiv e^{-i\omega_{\text{osc}} t} \vec{\xi}(\vec{r})$ le déplacement adiabatique propre.

On se replace maintenant en présence de la turbulence ($\vec{u} \neq \vec{0}$). En combinant l'Eq. (3.1) avec l'Eq. (3.2), en différenciant par rapport au temps, en négligeant les termes non-linéaires en \vec{v}_{osc} et enfin en supposant une turbulence incompressible ($\vec{\nabla} \cdot \vec{u} = 0$), on aboutit à l'équation d'onde inhomogène

$$\rho_0 \left(\frac{\partial^2}{\partial t^2} - \vec{L} \right) [\vec{v}_{\text{osc}}] + \vec{\mathcal{D}} [\vec{v}_{\text{osc}}] = \frac{\partial}{\partial t} \vec{\mathcal{S}} - \vec{\mathcal{C}} \quad (3.7)$$

avec

$$\vec{\mathcal{S}} \equiv \vec{\mathcal{S}}_R + \vec{\mathcal{S}}_S \quad (3.8)$$

$$\vec{\mathcal{S}}_R = \vec{\nabla} : (\rho_0 \vec{u} \vec{u}) - \vec{\nabla} : (\langle \rho_0 \vec{u} \vec{u} \rangle) \quad (3.9)$$

$$\vec{\mathcal{S}}_S = -\vec{\nabla} (\bar{\alpha}_s s_t) , \quad (3.10)$$

où s_t désigne les fluctuations *eulériennes* et turbulentes de l'entropie, et $\bar{\alpha}_s = \overline{(\partial P / \partial \rho)_s}$. Les termes \mathcal{S}_R (Eq. (3.9)) et \mathcal{S}_S (Eq. (3.10)) s'identifient comme deux termes de forçage, à savoir le terme du tenseur de Reynolds et un terme de forçage impliquant les fluctuations d'entropie. Le dernier terme \mathcal{C} rassemble les termes impliquant ρ_1 ainsi que les termes de second ordre issus de l'Eq. (3.3). Le terme \mathcal{C} contribue en principe au forçage. Cependant, on montre qu'il contribue de manière négligeable devant les contributions des termes \mathcal{S}_R et \mathcal{S}_S [voir les détails dans SPhD ou GK]. Enfin, l'opérateur $\vec{\mathcal{D}}$ apparaissant à droite de l'Eq. (3.2) couple le champ de vitesse turbulent (\vec{u}) à la vitesse du mode (\vec{v}_{osc}). Ce terme contribue (parmi d'autres mécanismes) à l'amortissement du mode. Il ne sera pas considéré sous sa forme, mais remplacé par la suite *a posteriori* en supposant des taux d'amortissement connus par ailleurs.

3.1.2 Solution générale

On revient maintenant dans le cas où la turbulence est présente. En présence de turbulence, on cherche les solutions générales (i.e. les solutions de l'équation d'onde inhomogène, Eq. (3.7)). C'est un problème classique : les solutions générales $\delta\vec{r}_{\text{osc}}(\vec{r}, t)$ (exprimées ici en terme de déplacement) sont recherchées sous la forme du produit de la solution de l'équation homogène (les fonctions propres adiabatiques, $\vec{\xi}(\vec{r}, t)$) et d'un terme $A(t)$, à savoir :

$$\delta\vec{r}_{\text{osc}} \equiv \frac{1}{2} \left(A(t) \vec{\xi}(\vec{r}), e^{-i\omega_{\text{osc}}t} + cc \right) \quad (3.11)$$

où cc fait référence au complexe conjugué, et $A(t)$ représente l'amplitude instantanée résultant des effets combinés de l'excitation et de l'amortissement.

En rappelant que $\vec{v}_{\text{osc}} = d\delta\vec{r}_{\text{osc}}/dt$, on a donc

$$\vec{v}_{\text{osc}}(\vec{r}, t) = \frac{1}{2} (-i\omega_{\text{osc}} A(t) \vec{\xi}(\vec{r}) e^{-i\omega_{\text{osc}}t} + cc), \quad (3.12)$$

où l'on a négligé la dérivée temporelle de A . Ceci se justifie par le fait que la période du mode ($2\pi/\omega_{\text{osc}}$) est en général beaucoup plus courte que sa durée de vie τ_{osc} , laquelle est inversement égale au taux d'amortissement ($\tau_{\text{osc}} = 1/\eta$).

En substituant l'Eq. (3.12) dans l'Eq. (3.7), on établit une équation différentielle pour $A(t)$ [voir son expression dans SPhD, page 67]. La résolution de cette équation différentielle donne la solution générale pour $A(t)$:

$$A(t) = \frac{ie^{-\eta t}}{2\omega_{\text{osc}}I} \int_{-\infty}^t dt' \int_{\mathcal{V}} d^3x e^{(\eta+i\omega_{\text{osc}})t'} \vec{\xi}^*(\vec{x}) \cdot \vec{\mathcal{S}}(\vec{x}, t') \quad (3.13)$$

où I est l'inertie du mode (voir Eq. (2.9)), et où l'intégration spatiale porte sur l'ensemble du volume stellaire, \mathcal{V} . Dans la mesure où les termes de forçage sont de nature aléatoire, A ne peut être évalué qu'en terme de moyenne quadratique, $\langle |A|^2 \rangle$. Cette moyenne statistique doit se comprendre comme étant effectuée sur un grand nombre (en principe infini) de réalisations indépendantes. A partir de Eq. (3.13) et avec l'aide de quelques simplifications détaillées dans SPhD, on peut établir l'expression

$$\langle |A|^2 \rangle = \frac{C^2}{8\eta(\omega_{\text{osc}}I)^2}, \quad (3.14)$$

avec

$$C^2 \equiv \int_{\mathcal{V}} d^3 x_0 \int_{-\infty}^{+\infty} d^3 r d\tau e^{-i\omega_{\text{osc}}\tau} \langle \vec{\xi}^* \cdot \vec{\mathcal{S}}_1 \vec{\xi} \cdot \vec{\mathcal{S}}_2 \rangle, \quad (3.15)$$

où η est le taux d'amortissement (que l'on peut, par exemple, déterminer à partir de mesures sismiques), I l'inertie du mode (Eq. (2.9)), \vec{x}_0 la position dans l'étoile où l'excitation est évaluée, \mathcal{S} les termes de forçage (Eqs. (3.8)-(3.10)), $\langle \cdot \rangle$ désigne une moyenne statistique, \vec{r} et τ deux longueurs de corrélations respectivement spatiales et temporelles associées à la turbulence locale, et enfin les indices 1 et 2 désignent deux positions spatiales et temporelles différentes, à savoir respectivement : $[\vec{x}_0 - \frac{\vec{r}}{2}, -\frac{\tau}{2}]$ et $[\vec{x}_0 + \frac{\vec{r}}{2}, \frac{\tau}{2}]$. Nous avons introduit dans l'Eq. (3.15) deux jeux de variables : (\vec{x}_0, t_0) et (\vec{r}, τ) . Les variables du premier sont désignées sous le terme de variables "lentes" tandis que celles du second sous le terme de variables "rapides", au sens où (\vec{x}_0, t_0) varient à des échelles spatiales et temporelles plus lentes que les variables (\vec{r}, τ) qui sont associées aux propriétés locales la turbulence.

En vertu des Eqs. (2.5), (2.8) et (3.14), le taux d'excitation théorique est finalement donné par l'expression :

$$\mathcal{P} = \frac{1}{8I} \int_{\mathcal{V}} d^3 x_0 \int_{-\infty}^{+\infty} d^3 r d\tau e^{-i\omega_{\text{osc}}\tau} \langle \vec{\xi}^* \cdot \vec{\mathcal{S}}_1 \vec{\xi} \cdot \vec{\mathcal{S}}_2 \rangle. \quad (3.16)$$

3.1.3 Termes sources de forçage

Le tenseur de Reynolds (Eq. (3.9)) a très tôt été identifié par [Lighthill \[1952\]](#) comme une source permettant la génération de "bruit acoustique". Ce terme a ensuite été considéré par GK comme la source d'excitation des *modes* acoustiques solaires (voir Sect. 1.3). Il représente un terme de forçage de nature mécanique et est considéré par la majorité des formulations théoriques comme la source dominante du forçage des oscillations de type solaire [[Goldreich and Keeley, 1977b](#); [Dolginov and Muslimov, 1984](#); [Balmforth, 1992a](#); [Stein and Nordlund, 2001](#); [Samadi et al., 2003a](#); [Chaplin et al., 2005](#)]. Cependant, comme cela a été pointé par [Osaki \[1990\]](#), les premiers calculs théoriques effectués par GK conduisent en fait à sous-estimer de manière importante (plusieurs ordres de grandeur) les amplitudes des modes solaires.

Afin d'expliquer ce désaccord, [Goldreich et al. \[1994\]](#), [GMK](#) par la suite] ont identifié les fluctuations *Lagrangienne* d'entropie comme une source additionnelle. Le terme source \mathcal{S}_S (Eq. (3.10)) fait apparaître, non pas la fluctuation Lagrangienne (δs_t par la suite), mais la fluctuation Eulérienne (s_t). Pour faire apparaître la première, il est nécessaire d'écrire la relation liant l'une à l'autre :

$$\frac{d\delta s_t}{dt} = \frac{\partial s_t}{\partial t} + \vec{u} \cdot \nabla (s_0 + s_t), \quad (3.17)$$

où s_0 est l'entropie à l'équilibre. On peut donc réécrire le terme source \mathcal{S}_S sous la forme :

$$\frac{\partial \vec{\mathcal{S}}_S}{\partial t} = -\vec{\nabla} \left(\frac{d}{dt} (\bar{\alpha}_s \delta s_t) - \bar{\alpha}_s \vec{u} \cdot \vec{\nabla} s_t \right), \quad (3.18)$$

où l'on a mis de côté le terme $\vec{u} \cdot \vec{\nabla} s_0$ dans la mesure où il ne contribue pas effectivement au forçage [voir GK ou SPhD]. L'intégration de l'Eq. (3.18) par rapport au temps donne alors le terme

\mathcal{S}_S . D'après GMK, le terme impliquant δs_t à droite de l'Eq. (3.18) serait la source dominante du forçage. Affirmation qui avait été initialement avancée par [Stein and Nordlund \[1991\]](#) à l'aide d'une simulation hydrodynamique 3D représentative des couches superficielles du Soleil, mais qui a été contredite plus tard par [Stein and Nordlund \[2001\]](#). Cependant, l'approche théorique proposée par GMK s'appuie sur l'hypothèse que la fluctuation d'entropie se comporte comme un scalaire passif. Une quantité physique f se comporte comme un scalaire passif lorsqu'elle obéit à une équation de diffusion [voir e.g. [Lesieur, 1997](#)] :

$$\frac{df}{dt} = \frac{\partial f}{\partial t} + \vec{u} \cdot \vec{\nabla} f = \chi \nabla^2 f, \quad (3.19)$$

où χ est un coefficient de diffusion. Comme cela a été montré dans SPhD, supposer que δs_t se comporte comme un scalaire passif conduit à un forçage nul. En revanche, il est montré dans SPhD que le terme $\bar{\alpha}_s \vec{u} \cdot \vec{\nabla} s_t$ dans le membre de droite de l'Eq. (3.18) contribue effectivement au forçage, à condition, toujours, de supposer que s_t se comporte comme un scalaire passif. Aussi, dans la formulation théorique de SPhD, le terme source lié à l'entropie se réduit à

$$\frac{\partial}{\partial t} \mathcal{S}_S = \vec{\nabla} \cdot (\bar{\alpha}_s \vec{u} \cdot \vec{\nabla} s_t). \quad (3.20)$$

Notez que le terme $\vec{u} \cdot \vec{\nabla} s_t$ à droite de l'Eq. (3.20) est un terme de nature advectif. Dans la mesure où il implique les fluctuations d'entropie, il peut être considéré comme un forçage thermique.

Ce terme source avait été initialement identifié par GK mais considéré par ces auteurs comme étant négligeable devant le terme de Reynolds (\mathcal{S}_R , Eq. (3.9)). Notons que les formulations théoriques proposées par [Balmforth \[1992a\]](#) et [Chaplin et al. \[2005\]](#) ne tiennent pas compte de ce terme. D'après [Samadi et al. \[2003a\]](#), ce terme n'est pas négligeable dans le cas du Soleil (environ $\sim 15\%$ de la puissance totale) mais demeure néanmoins petit devant \mathcal{S}_R (voir aussi Sect. 3.4).

Pour finir, notons que les termes \mathcal{S}_R et \mathcal{S}_S introduisent des termes croisés à travers l'Eq. (3.13). Cependant, en supposant comme GMK que s_t se comporte comme un scalaire passif ainsi qu'une turbulence *incompressible* (i.e. $\vec{\nabla} \cdot \vec{u} = 0$), on montre dans SPhD que ces termes croisés sont nuls. Toutefois, comme on le verra en Sect. 3.4, ces termes ne sont pas rigoureusement nuls et conduisent en fait à des compensations partielles entre \mathcal{S}_R et \mathcal{S}_S .

3.1.4 Séparation d'échelle

Comme on le voit dans l'intégrande à droite de l'Eq. (3.15), la fonction propre de déplacement $\vec{\xi}(\vec{r})$ est spatialement couplée avec la fonction source, \mathcal{S} . Pour établir une formulation qui puisse être évaluée de manière analytique, il est nécessaire de découpler spatialement $\vec{\xi}(\vec{r})$ de \mathcal{S} . C'est la raison pour laquelle toutes les formulations supposent implicitement ou explicitement cette forme de *séparation d'échelle*. En pratique, cela revient à supposer que les tourbillons turbulents qui contribuent effectivement au forçage ont des tailles beaucoup plus petite que la longueur d'onde associée au mode ainsi que à l'échelle de densité [voir les détails dans SPhD, section 4.7, page 76]. Cette approximation est pleinement justifiée lorsque le nombre de Mach turbulent M_t (défini comme étant égal au rapport entre u et la vitesse du son c_s) est petit. Cependant cela cesse d'être le cas dans la partie supérieure de la zone convective, à savoir dans la

région dite super-adiabatique où, M_t atteint dans le cas du Soleil une valeur proche de 0.3 (en moyenne sur les flots montants et descendants, M_t est même proche de un dans les panaches). Par ailleurs, pour les étoiles G et F situées sur la séquence principale, on s'attend à ce que M_t croît avec la température effective. D'après les modèles standards de structure stellaire, un maximum de M_t serait atteint pour des masses stellaires proches de $1.6 M_\odot$ [c.f. Houdek *et al.*, 1999]. Par conséquent, l'hypothèse d'une séparation d'échelle est une approximation sujette à caution en particulier pour les étoiles de type F (on se reportera à la discussion du Chap. 7).

3.1.5 Modèles de fermeture

La seconde intégrale à droite de l'Eq. (3.15) implique le terme $\langle \mathcal{S}_1 \mathcal{S}_2 \rangle$, qui correspond à un produit de corrélation à deux points (spatial et temporel) faisant intervenir les termes sources (Eqs. (3.9)-(3.10)). Par conséquent le terme source associé au tenseur de Reynolds, \mathcal{S}_R , fait intervenir des produits de corrélation à deux points de la forme $\langle (\vec{u} \vec{u})_1 (\vec{u} \vec{u})_2 \rangle$. De la même façon, le terme source associé à l'entropie, \mathcal{S}_S , fait intervenir des produits de corrélation de la forme $\langle (\vec{u} s_t)_1 (\vec{u} s_t)_2 \rangle$. Dans les deux cas, on a affaire à des produits d'ordre quatre impliquant des quantités turbulentes (à savoir \vec{u} et s_t).

Les moments d'ordre quatre sont solutions d'équations faisant intervenir des moments d'ordre cinq. A son tour, les moments d'ordre cinq sont solutions d'équations faisant intervenir des moments d'ordre six etc. C'est le problème classique de la fermeture des moments, autrement dit le problème de fermeture. Ce problème ne peut être résolu de manière analytique qu'en adoptant des modèles, que l'on nomme donc modèles de fermeture. Un modèle de fermeture simple est l'Approximation quasi-Normale (AqN par la suite) qui permet – à moindre frais – d'exprimer un moment d'ordre quatre en produits de moments d'ordre deux [c.f. e.g. Lesieur, 1997] :

$$\begin{aligned} \langle (u_i u_j)_1 (u_k u_l)_2 \rangle(\vec{r}, \tau) = & \langle (u_i u_j)_1 \rangle \langle (u_k u_l)_2 \rangle + \langle (u_i)_1 (u_l)_2 \rangle \langle (u_j)_1 (u_k)_2 \rangle \\ & + \langle (u_i)_1 (u_k)_2 \rangle \langle (u_j)_1 (u_l)_2 \rangle . \end{aligned} \quad (3.21)$$

Ce modèle de fermeture nous permet ainsi de “casser” un moment d'ordre quatre en deux moments d'ordre deux. Le système d'équation est ainsi fermé puisque que l'on a maintenant affaire uniquement à des moments d'ordre deux et inférieurs. La décomposition de l'Eq. (3.21) est strictement valide lorsque la vitesse est distribuée selon une loi Normale. On notera que le premier terme à droite de l'Eq. (3.21) s'annule avec le terme $\langle \vec{u} \vec{u} \rangle$ apparaissant dans l'Eq. (3.9) [voir Chaplin *et al.*, 2005]. Une expression similaire à l'Eq. (3.21) est établie pour le produit $\langle (\vec{u} s_t)_1 (\vec{u} s_t)_2 \rangle$ [voir SPhD, section 4.8.2, page 78].

3.1.6 Modèle de turbulence adopté

Les membres de droite de l'Eq. (3.21) correspondent à des produits de moments à deux points d'ordre deux de la forme $\langle (u_i)_1 (u_k)_2 \rangle$. Il s'agit donc maintenant d'adopter un modèle à même de reproduire ces derniers. Il est généralement plus commode de se placer dans le domaine Fourier en terme de fréquence, ω , et de nombre d'onde, k . Nous définissons ainsi $\phi_{i,j}$ comme la transformée de Fourier temporelle et spatiale du produit de corrélation $\langle (u_i)_1 (u_j)_2 \rangle$.

Pour un milieu turbulent homogène, incompressible et isotrope, on établit une relation entre $\phi_{i,j}(\vec{k}, \omega)$ et le spectre d'énergie cinétique ; cette relation s'écrit [voir e.g. [Batchelor, 1970](#)] :

$$\phi_{ij}(\vec{k}, \omega) = \frac{E(k, \omega)}{4\pi k^2} \left(\delta_{ij} - \frac{k_i k_j}{k^2} \right), \quad (3.22)$$

où $\delta_{i,j}$ désigne le symbole de Kronecker. En suivant [Stein \[1967\]](#), on décompose $E(k, \omega)$ comme

$$E(k, \omega) = E(k) \chi_k(\omega), \quad (3.23)$$

où $E(k)$ est la moyenne temporelle de l'énergie cinétique et $\chi_k(\omega)$ correspond à la composante en fréquence de $E(k, \omega)$. Comme on le verra dans la Sect. 4.1.2, $\chi_k(\omega)$ est une mesure de la corrélation temporelle entre tourbillons dans le domaine des fréquences et des nombres d'onde. On verra aussi que ce terme contrôle de manière déterminante l'efficacité du forçage.

On notera qu'une décomposition similaire à l'Eq. (3.23) est adoptée s'agissant du spectre associé aux fluctuations d'entropie ($E_s(k, \omega)$).

Les termes $\chi_k(\omega)$ et $E(k)$ satisfont par définition les conditions de normalisation suivante [voir e.g. [Tennekes and Lumley, 1982](#), Chap 8.1] :

$$\int_{-\infty}^{+\infty} d\omega \chi_k(\omega) = 1, \quad (3.24)$$

$$\int_0^{\infty} dk E(k) = \frac{1}{2} \langle \vec{u}^2 \rangle = \frac{\Phi}{2} \langle u_z^2 \rangle \equiv \frac{3}{2} u_0^2, \quad (3.25)$$

où u_z est la composante verticale de la vitesse, u_0 une vitesse caractéristique introduit par convection, et enfin $\Phi \equiv \langle u^2 \rangle / \langle u_z^2 \rangle$ est le facteur d'anisotropie introduit par [Gough \[1977\]](#). Des conditions de normalisation similaires sont adoptées pour les spectres associés aux fluctuations d'entropie.

3.1.7 Formulation finale

A partir de l'ensemble des approximations et hypothèses décrites plus haut, on établit l'expression finale donnant le taux d'excitation, \mathcal{P} , d'un mode *radial* donné [voir détails dans SPhD] :

$$\mathcal{P} = \frac{1}{8I} (C_R^2 + C_S^2) \quad (3.26)$$

où C_R^2 et C_S^2 correspondent aux contributions du terme de Reynolds et d'entropie. Ces contributions s'expriment :

$$C_R^2 = 4\pi^3 \mathcal{G} \int_0^M dm \rho_0 \left| \frac{d\xi_r}{dr} \right|^2 S_R(m, \omega_{\text{osc}}) \quad (3.27)$$

$$C_S^2 = \frac{4\pi^3 \mathcal{H}}{\omega_{\text{osc}}^2} \int_0^M dm \frac{\bar{\alpha}_s^2}{\rho_0} g_r(\xi_r, m) S_S(m, \omega_{\text{osc}}), \quad (3.28)$$

avec S_R et S_S les termes source associés respectivement au tenseur de Reynolds et terme d'entropie :

$$S_R = \int_0^\infty dk \frac{E^2(k, m)}{k^2} \int_{-\infty}^{+\infty} d\omega \chi_k(\omega_{\text{osc}} + \omega, m) \chi_k(\omega, m) \quad (3.29)$$

$$S_S = \int_0^\infty dk \frac{E_s(k, m)E(k, m)}{k^2} \int_{-\infty}^{+\infty} d\omega \chi_k(\omega_{\text{osc}} + \omega, m) \chi_k(\omega, m). \quad (3.30)$$

Dans les Eqs. (3.27) et (3.28), ρ_0 est la densité moyenne, \mathcal{G} et \mathcal{H} deux facteurs d'anisotropie [voir leur expression dans SPhD, annexe C, pages 145-146], et enfin $g_r(\xi_r, m)$ est une fonction qui implique la première et second dérivée spatiale de la fonction propre de déplacement, ξ_r [voir son expression dans SPhD, section 4.8.2, page 78]. Il est plus utile de réécrire les Eqs. (3.27) et (3.28) sous la forme :

$$C_R^2 = 4\pi^3 \mathcal{G} \int_0^M dm \frac{\rho_0 u_0^4}{k_0^3 \omega_0} \left| \frac{d\xi_r}{dr} \right|^2 \tilde{S}_R(m, \omega_{\text{osc}}), \quad (3.31)$$

$$C_S^2 = \frac{4\pi^3 \mathcal{H}}{\omega_{\text{osc}}^2} \int_0^M dm \frac{(\bar{\alpha}_s \tilde{s} u_0)^2}{\rho_0 k_0^3 \omega_0} g_r(\xi_r, m) \tilde{S}_s(m, \omega_{\text{osc}}), \quad (3.32)$$

où nous avons introduit les fonctions sources adimensionnelles $\tilde{S}_R \equiv (k_0^3 \omega_0 / u_0^4) S_R$ et $\tilde{S}_s \equiv (k_0^3 \omega_0 / (u_0^2 \tilde{s}^2)) S_S$, où \tilde{s} désigne l'écart-type de la fluctuations d'entropie. Ont également été introduits la fréquence caractéristique ω_0 ainsi que le nombre d'onde caractéristique k_0 ; ces derniers sont définis comme suit

$$\omega_0 \equiv k_0 u_0 \quad (3.33)$$

$$k_0 \equiv \frac{2\pi}{\Lambda}, \quad (3.34)$$

où Λ correspond à une échelle caractéristique (qui reste à définir et évaluer, voir Sect. 4.1.1) et u_0 est une vitesse caractéristique définie par l'Eq. (3.25). Pour un usage futur, il est également utile de définir le temps caractéristique τ_0 comme :

$$\tau_0 = \frac{2\pi}{k_0 u_0} = \frac{\Lambda}{u_0}. \quad (3.35)$$

On montre à partir de l'Eq. (3.31) que le forçage du au terme de Reynolds est localement proportionnel au flux d'énergie cinétique. En effet, le flux d'énergie cinétique, F_{kin} , est par définition égal à

$$F_{\text{kin}} \equiv w E_{\text{kin}} = w \left(\frac{1}{2} \rho_0 \bar{u}^2 \right) = \frac{3}{2} \sqrt{\frac{3}{\Phi}} \rho_0 u_0^3, \quad (3.36)$$

où $E_{\text{kin}} \equiv (1/2) \rho_0 \bar{u}^2$ est l'énergie cinétique par unité de volume. La substitution de l'Eq. (3.36) dans l'Eq. (3.31) permet d'écrire :

$$C_R^2 \propto \int_0^M dm F_{\text{kin}} \Lambda^4 \left| \frac{d\xi_r}{dr} \right|^2 \tilde{S}_R(m, \omega_{\text{osc}}). \quad (3.37)$$

S'agissant du terme de forçage thermique, S_S , on montre que celui-ci est localement proportionnel à F_{kin} ainsi qu'au carré du rapport F_c/F_{kin} où F_s est le flux convectif [voir la démonstration dans Samadi *et al.*, 2006, article inséré en page 135].

3.2 Approches alternatives

3.2.1 Méthode de l'“équipartition” d'énergie

Dans certaines conditions que l'on va dans la suite expliciter, il existe ce que certains nomment “équipartition” de l'énergie cinétique entre les tourbillons turbulents et les modes. Utiliser le terme “équipartition” est historique mais en fait inadéquat comme on le verra par la suite ; on devrait plutôt parler d'une “partition” constante ou universelle.

Pour établir cette “partition”, il faut supposer comme le proposait GK, que les modes acoustiques sont d'une part amortis exclusivement par la viscosité turbulente, *et*, d'autre part, excités par le seul terme de Reynolds (\mathcal{S}_R , Eq. (3.9)). Nous reproduisons ici leur démonstration de manière simplifiée en supposant des modes de fréquences ω_{osc} telles que $\omega_{\text{osc}} \tau_0 \lesssim 1$ où τ_0 désigne la durée de vie caractéristique des plus grosses cellules convective situées à l'extrémité de la région convective, là où celle-ci est la plus vigoureuse. De plus, nous négligerons comme le font GK le forçage thermique (\mathcal{S}_S , Eq. (3.28)).

En vertu des Eqs. (3.26) et (3.37), nous avons de manière très approximative et pour les modes acoustiques tels que $\omega_{\text{osc}} \tau_0 \lesssim 1$:

$$\mathcal{P} \propto \frac{1}{I} \int dm \left| \frac{d\xi_r}{dr} \right|^2 E_{\text{eddy}} \Lambda u_0, \quad (3.38)$$

où Λ est la taille caractéristique des plus gros tourbillons, u_0 leur vitesse caractéristique, $\tau_0 = \Lambda/u_0$ leur durée de vie caractéristique (Eq. (3.35)), et enfin $E_{\text{eddy}} = (3/2)\rho_0 u_0^2 \Lambda^3$ leur énergie cinétique. On désigne par k_{osc} le nombre d'onde radial associé au mode. Nous avons donc par définition de k_{osc} la relation $d\xi_r/dr = i k_{\text{osc}} \xi_r$. Par ailleurs, nous supposons que – dans la région d'excitation – les ondes acoustiques sont propagatives. Cette hypothèse implique : $\omega_{\text{osc}} = k_{\text{osc}} c_s$ où c_s est la vitesse du son. On peut alors simplifier l'Eq. (3.38) comme :

$$\mathcal{P} \propto \frac{\omega_{\text{osc}}^2}{I} \int dm \left(\frac{\xi_r}{c_s} \right)^2 E_{\text{eddy}} \Lambda u_0. \quad (3.39)$$

Dans la région de forçage, les termes E_{eddy} , u_0 , et c_s varient rapidement. Toutefois, par soucis de simplification, on supposera ces quantités constantes et on les évaluera au niveau de la couche où le forçage est le plus efficace, à savoir au niveau du pic super-adiabatique. L'intégration de l'Eq. (3.38) peut alors se simplifier comme

$$\mathcal{P} \propto \frac{1}{I} \left(\frac{\omega_{\text{osc}}}{c_s} \right)^2 E_{\text{eddy}} \Lambda u_0 \int dm \xi_r^2. \quad (3.40)$$

En utilisant la définition de l'inertie (Eq. (2.9)), on peut simplifier l'Eq. (3.40), ce qui donne :

$$\mathcal{P} \propto \left(\frac{\omega_{\text{osc}}}{c_s} \right)^2 E_{\text{eddy}} \Lambda u_0. \quad (3.41)$$

Lorsque la viscosité turbulente est la seule source d'amortissement, le taux d'amortissement η d'un mode est donné par la relation [Ledoux and Walraven, 1958; Goldreich and Keeley, 1977a]

$$\eta \propto \frac{1}{3I} \int dm \nu_t \left| r \frac{d}{dr} \left(\frac{\xi_r}{r} \right) \right|^2, \quad (3.42)$$

où ν_t est la viscosité turbulente. La prescription la plus simple pour ν_t nous est fournie par le concept d’“eddy-viscosity” qui donne $\nu_t = u_0 \lambda = \tau_0 u_0^2$ dans laquelle [voir par exemple [Lesieur, 1997](#), Chap. 1.1]. Le milieu turbulent est évidemment composé d’éléments de tailles différentes et hiérarchisées. Cependant, seuls les éléments tels que $\omega_{\text{osc}} \tau_\lambda \approx 1$ contribuent efficacement à l’amortissement (τ_λ correspondant à la durée de vie d’un élément de taille λ donné). Dans la mesure où l’on s’intéresse aux modes tels que $\omega_{\text{osc}} \tau_\lambda \lesssim 1$, seuls les plus gros tourbillons (qui ont une taille Λ) contribuent. Par conséquent, on adopte $\nu_t = u_0 \Lambda$. En utilisant les mêmes simplifications et hypothèses que celles utilisées pour établir l’Eq. (3.41), on peut simplifier l’Eq. (3.42) comme

$$\eta \propto \left(\frac{\omega_{\text{osc}}}{c_s} \right)^2 \Lambda u_0 . \quad (3.43)$$

A partir des Eqs. (2.5), (3.41) et (3.43), on peut exprimer l’énergie cinétique d’un mode :

$$E_{\text{osc}} \propto E_{\text{eddy}} . \quad (3.44)$$

L’Eq. (3.44) met en évidence une forme de “partition” d’énergie cinétique entre un mode acoustique donné et un tourbillon en résonance avec celui-ci. C’est sur la base de cette forme de ‘partition’ que [Christensen-Dalsgaard and Frandsen \[1983\]](#) ont établi la première évaluation quantitative des modes des oscillations de type solaires dans diverses étoiles.

L’Eq. (3.44) a été établie en supposant que les modes sont amortis par la viscosité turbulente. Cependant, comme l’a pointé [Osaki \[1990\]](#), les largeurs des modes solaires Γ (on a $\Gamma = \eta/\pi$) calculés par [Goldreich and Keeley \[1977a\]](#), i.e. en supposant un amortissement dû à la viscosité turbulente, sous-estiment de manière importante les observations solaires. En revanche, [Xiong et al. \[2000\]](#) montrent que la viscosité turbulente est bien la source dominante de l’amortissement. Comme cela a été discuté par [Belkacem and Samadi \[2013\]](#), il y’a à l’heure actuelle de grosses incertitudes concernant les mécanismes d’amortissement et les observations tendent à montrer que l’amortissement des modes n’est pas dominé par la viscosité turbulente. Si l’amortissement se révèle ne pas être dominé par la viscosité turbulente, alors dans ce cas il y’a aucune raison que la partition évoquée ici, et traduite par l’Eq. (3.44), se maintienne en général.

3.2.2 Méthode *ab initio*

Le modèle théorique présenté en Sect. 3.1 repose sur un nombre important d’approximations et d’hypothèses, en particulier concernant le traitement de la turbulence et des termes de forçage. Il existe pourtant une alternative plus fiable car reposant sur très peu d’hypothèses et d’approximations. Cette méthode a été proposée par [Nordlund and Stein \[2001\]](#). Dans cette approche, l’énergie injectée par unité de seconde dans un mode acoustique est évalué *directement* à l’aide de simulations hydrodynamiques 3D représentatives des surfaces des étoiles en calculant le travail (incohérent) effectué par la convection turbulente sur le mode acoustique. En pratique, le calcul de \mathcal{P} s’effectue numériquement à l’aide de l’Eq. (74) établie par [Nordlund and Stein \[2001\]](#) ; celle-ci s’exprime (en J s^{-1}) comme :

$$\mathcal{P}_{3\text{D}}(\omega_{\text{osc}}) = \frac{\omega_{\text{osc}}^2 \mathcal{S}}{8 \Delta v \mathcal{E}_{\omega_{\text{osc}}}} \left| \int_r dr \Delta \hat{P}_{\text{nad}}(r, \omega_{\text{osc}}) \frac{\partial \xi_r}{\partial r} \right|^2 , \quad (3.45)$$

où $\Delta\hat{P}_{\text{nad}}(r, \omega)$ est la transformée de Fourier discrète de la composante non-adiabatique de la pression totale (pression du gaz plus pression turbulente), $\Delta P_{\text{nad}}(r, t)$, laquelle est évaluée à la fréquence du mode $\omega_{\text{osc}} = 2\pi\nu_0$, ξ_r est la composante radiale de la fonction propre adiabatique, S la surface correspondant à la boîte de la simulation, $\Delta\nu = 1/T_s$ la résolution en fréquence de la simulation, T_s sa durée, et enfin $\mathcal{E}_{\omega_{\text{osc}}}$ est l'énergie cinétique normalisée du mode propre par unité de surface. $\mathcal{E}_{\omega_{\text{osc}}}$ est définie comme suit [Eq. (63) dans Nordlund and Stein, 2001] :

$$\mathcal{E}_{\omega_{\text{osc}}} = \frac{1}{2} \omega_{\text{osc}}^2 \int_r dr \xi_r^2 \rho \left(\frac{r}{R} \right)^2 . \quad (3.46)$$

L'Eq. (3.45) correspond au calcul du travail, PdV , associé aux fluctuations non-adiabatique du gaz et de la pression turbulente (termes diagonaux du tenseur de Reynolds). Contrairement à une approche analytique (telle que celle présentée en Sect. 3.1), la dérivation de l'Eq. (3.45) ne repose pas sur un modèle de la turbulence. Par exemple, la relation de l'Eq. (3.22) n'est plus nécessaire. Par ailleurs, il n'est pas non plus nécessaire de supposer que l'entropie est un scalaire passif. Cependant, comme pour le modèle théorique de la Sect. 3.1, ils supposent que ξ_r varie à une échelle plus grande que celle des tourbillons qui contribuent effectivement au forçage (il s'agit donc de la séparation d'échelle introduite dans la Sect. 3.1.4). Enfin, l'Eq. (3.45) suppose implicitement l'Approximation quasi-Normale (Eq. (3.21)).

L'Eq. (3.45) a été appliquée dans le cas du Soleil par Stein and Nordlund [2001]. Les auteurs ont abouti un relativement bon accord avec les mesures sismiques effectuées par Roca Cortés *et al.* [1999] à l'aide de l'instrument SOHO/GOLF.

Stein *et al.* [2004] ont par la suite calculé \mathcal{P}_{3D} (Eq. 3.45) pour un jeux de simulations 3D d'étoiles correspondant à des types K à F. Dans Samadi *et al.* [2007, article inséré en page 165] nous avons effectué la comparaison de leurs calculs avec ceux obtenus à partir du modèle d'excitation stochastique (Eqs. (3.26)-(3.30)). Des écarts systématiques ont été constatés. Ces derniers ont été attribués à la résolution insuffisante des simulations 3D calculées par Stein *et al.* [2004].

3.3 Cas des modes non-radiaux

Le modèle théorique présenté dans la Sect. 3.1 a été établi pour des modes radiaux uniquement. Toutefois, tant que le degré ℓ d'un mode reste faible ($\ell \ll 100$), le formalisme précédent reste applicable sous réserve de calculer et d'utiliser l'inertie I du mode en tenant compte de son degré ℓ . En effet, les déplacements de ceux-ci sont principalement radiaux dans la région où l'excitation est la plus vigoureuse (dans la partie supérieure de l'enveloppe convective). Le modèle cesse en revanche d'être valable pour les hauts degrés ($\ell \gtrsim 100$). En effet, les modes de hauts - degrés sont très confinés en surface et leur déplacement cesse d'être principalement radial. Du fait de leur géométrie très différente des modes radiaux ou de très faible degré, il est nécessaire d'en prendre compte de manière à quantifier correctement leur forçage par la convection turbulente. Par ailleurs, du fait à nouveau de leur géométrie, ces modes sondent non seulement les composantes radiales des termes de forçage, mais également leurs composantes horizontales. Par conséquent, la comparaison entre observations et modélisation pourrait à terme fournir des contraintes utiles sur l'anisotropie du milieu turbulent.

La généralisation aux cas des modes non-radiaux du formalisme présenté plus haut à été entreprise par [Belkacem et al. \[2008\]](#), article inséré en page 187]. Celle-ci nous a ensuite permis d'aborder l'excitation des modes de gravité (car ce sont des modes par essence non-radiaux). Nous avons d'abord considéré les modes solaires de gravité et montré que amplitudes attendues étaient légèrement en dessous des seuils de détection actuels [[Belkacem et al., 2009c](#), article inséré en page 199]. Nous avons ensuite appliqué ce formalisme au cas des étoiles massives. Nous avons montré que les étoiles massives de l'ordre de $10 M_{\odot}$ sont des candidats intéressants pour la détection de modes de gravité excités stochastiquement par la convection turbulente dans le coeur convectif ainsi que dans l'enveloppe convective associée à la région d'ionisation du Fer [[Samadi et al., 2009](#), article inséré en page 239]. De tels modes auraient été découverts récemment par [Neiner et al. \[2012\]](#) dans une étoile B. Toutefois, les estimations établies par [Samadi et al. \[2009\]](#) ne suffisent pas à expliquer les amplitudes mesurées. C'est pourquoi d'autres formes de mécanismes sont évoquées par [Neiner et al. \[2012\]](#).

3.4 A propos de la contribution de l'entropie

Le terme de forçage \mathcal{S}_S (Eq. (3.10)) lié aux fluctuations d'entropie a été, à partir des années 90, l'objet d'un débat (voir Sect. 3.1.3). La modélisation de ce terme telle qu'elle a été présentée dans la Sect. 3.1.3 repose sur des hypothèses qui sont sujettes à caution (voir la discussion dans le Chap. 7). Un moyen fiable d'en évaluer la contribution repose sur l'application de la méthode *ab initio* présentée en Sect. 3.2.2,

En appliquant cette méthode, [Stein and Nordlund \[2001\]](#) ont montré que la contribution du terme associée aux fluctuations d'entropie, \mathcal{S}_S reste faible devant la contribution du terme de Reynolds, \mathcal{S}_R . Ce résultat a été confirmé par [Samadi et al. \[2007\]](#), article inséré en page 165] sur la base du modèle théorique présenté en Sect. 3.1. De plus, [Samadi et al. \[2007\]](#) ont montré que la contribution relative du terme \mathcal{S}_S à la puissance totale augmente rapidement avec la température effective, T_{eff} . Par exemple, s'agissant de l'étoile HD 49333 qui est significativement plus chaude que le Soleil, la contribution relative du terme \mathcal{S}_S est d'environ 30 % [[Samadi et al., 2010b](#), article inséré en page 223] tandis qu'elle est de l'ordre de 15 % pour le Soleil [[Samadi et al., 2007](#)] ou pour l'étoile α Cen A [[Samadi et al., 2008](#)]. Les calculs effectués par [Stein et al. \[2004\]](#) sur la base de la méthode *ab initio* (Sect. 3.2.2) montrent une compensation partielle entre la pression turbulente (associée au terme de Reynolds) et les fluctuations non-adiabatiques de la pression du gaz (associées aux fluctuations d'entropie). Cette compensation augmente lorsque T_{eff} croît [voir [Stein et al., 2004](#)]. Dans le modèle théorique d'excitation stochastique (Sect. 3.1), les termes croisés entre le terme de Reynolds et le terme d'entropie se compensent rigoureusement en raison des hypothèses adoptées (voir Sect. 3.1.3). Comme cela a été initialement suggéré par [Houdek \[2006\]](#) et discuté par [Samadi et al. \[2010a\]](#), article inséré en page 231], l'existence d'une compensation partielle réduit l'amplitude des modes et peut ainsi améliorer l'accord avec les mesures sismiques effectuées sur les étoiles de type F, comme par exemple HD 49333. Cependant, il n'existe par encore de modélisation théorique de ce phénomène de compensation (voir Sect. 7 ainsi que la discussion dans [Samadi et al. \[2010a\]](#)).

Chapitre 4

Contraintes sur la convection turbulente

Sommaire

4.1 Spectres de la turbulence	33
4.1.1 Composante spatiale, $E(k)$	35
4.1.2 Composante fréquentielle, $\chi_k(\omega)$	37
4.2 Modèles de fermeture et anisotropie	41

Articles reproduits dans ce mémoire (voir Appendice A) et auxquels ce chapitre se rapporte :

- “*Numerical constraints on the model of stochastic excitation of solar-type oscillations*”, Samadi R., Nordlund A., Stein R. F., Goupil M.-J., Roxburgh I., 2003, A&A, 403, 303 [Page 97] ;
- “*Numerical 3D constraints on convective eddy time-correlations : Consequences for stochastic excitation of solar p modes*”, Samadi R., Nordlund A., Stein R. F., Goupil M.-J., Roxburgh I., 2003, A&A, 403, 1129 [Page 107] ;
- “*A closure model with plumes. I. The solar convection*”, Belkacem K., Samadi R., Goupil M.-J., Kupka F., 2006, A&A, 460, 173 [Page 145] ;
- “*A closure model with plumes. II. Application to the stochastic excitation of solar p modes*”, Belkacem K., Samadi R., Goupil M.-J., Kupka F., Baudin F., 2006, A&A, 460, 183 [Page 157] ;
- “*Modeling the excitation of acoustic modes in α Centauri A*”, Samadi R., Belkacem K., Goupil M.-J., Dupret M.-A., Kupka F., 2008, A&A, 489, 291 [Page 177] ;
- “*Turbulent eddy-time-correlation in the solar convective zone*”, Belkacem K., Samadi R., Goupil M. J., Baudin F., Salabert D., Appourchaux T., 2010, A&A, 522L, 2 [Page 245].

4.1 Spectres de la turbulence

Comme on l’a vu dans le Chap. 3, Sect. 3.1.6, deux quantités importantes pour la modélisation des amplitudes sont les produits de corrélation impliquant la vitesse et les fluctuations

d'entropie. Par exemple, s'agissant du terme de Reynolds, celui-ci implique le produit de corrélation $C_{ij}(\vec{x}_0, \vec{t}_0, \vec{r}, \vec{\tau}) \equiv \langle (u_i(\vec{x}_0 - \frac{\vec{r}}{2}, t_0 - \frac{\tau}{2}) u_j(\vec{x}_0 + \frac{\vec{r}}{2}, t_0 + \frac{\tau}{2})) \rangle$. On aborde dans cette section le problème de la modélisation de ce terme⁸. Au préalable, on met en évidence ici le lien entre ce produit de corrélation et les composantes spatiales et fréquentielle du spectre d'énergie cinétique.

On suppose par hypothèse une turbulence stationnaire et homogène, le produit de corrélation C_{ij} est donc invariant par translation par rapport aux variables "lentes"⁹ \vec{x}_0 et t_0 . On s'intéresse au spectre de l'énergie cinétique, i.e. la répartition de l'énergie cinétique dans le domaine Fourier en termes de nombre d'onde k et de fréquence ω . Ceci nous amène à définir ϕ_{ij} comme la transformée de Fourier de C_{ij} par rapport à τ et \vec{r} :

$$\phi_{ij}(\omega, \vec{k}) \equiv \int d\tau e^{i\tau\omega} \int d^3r e^{i\vec{k}\cdot\vec{r}} C_{ij}(\vec{r}, \tau). \quad (4.1)$$

Inversement, C_{ij} est relié à ϕ_{ij} à travers la transformée de Fourier inverse :

$$C_{ij} = \left(\frac{1}{2\pi}\right)^4 \int d\omega e^{-i\tau\omega} \int d^3k e^{-i\vec{k}\cdot\vec{r}} \phi_{ij}(\vec{k}, \omega). \quad (4.2)$$

L'énergie cinétique moyenne est par définition égale à :

$$\langle E \rangle \equiv \frac{1}{2} \sum_{i=1}^3 \langle u_{ii}^2 \rangle. \quad (4.3)$$

Celle-ci est reliée au produit de corrélation C_{ij} par la relation :

$$\langle E \rangle = \frac{1}{2} \sum_{i=1}^3 C_{ii}(\vec{r} = \vec{0}, \tau = 0). \quad (4.4)$$

En vertu de l'Eq. (4.2), on peut ainsi écrire :

$$\langle E \rangle = \frac{1}{2} \int d\omega \int d^3k \sum_{i=1}^3 \phi_{ii}(\vec{k}, \omega). \quad (4.5)$$

Dans le cas d'une turbulence isotrope, on a enfin :

$$\langle E \rangle = \int d\omega \int dk E(k, \omega). \quad (4.6)$$

où l'on définit la quantité $E(k, \omega) \equiv \frac{1}{2} 4\pi k^2 \left(\sum_{i=1}^3 \phi_{ii}(k, \omega) \right)$, qui correspond donc à la densité spectrale d'énergie cinétique. On montre que pour une turbulence incompressible, les composantes de ϕ_{ij} sont liées à $E(k, \omega)$ par la relation suivante [voir e.g. [Batchelor, 1970](#)] :

$$\phi_{ij}(k, \omega) = \frac{E(k, \omega)}{4\pi k^2} \left(\delta_{ij} - \frac{k_i k_j}{k^2} \right), \quad (4.7)$$

8. Le cas des produits de corrélations impliquant les fluctuations d'entropie ne sera par abordé ici mais discuté dans le Chap. 7.

9. Voir en Sect. 3.1.2 la signification de variables "lentes" dans ce contexte.

où $\delta_{i,j}$ désigne le symbole de Kronecker. On peut formellement décomposer $E(k, \omega)$ comme [Stein, 1967]

$$E(k, \omega) = E(k) \chi_k(\omega), \quad (4.8)$$

où $E(k)$ est la moyenne temporelle de l'énergie cinétique et $\chi_k(\omega)$ correspond à la composante en fréquence de $E(k, \omega)$, définie telle que :

$$\int_{-\infty}^{+\infty} d\omega \chi_k(\omega) = 1. \quad (4.9)$$

Notons que la décomposition de l'Eq. (4.8) est générale dans la mesure où la dépendance en k est reportée dans la composante fréquentielle $\chi_k(\omega)$.

La composante spatiale $E(k)$ correspond à la moyenne de l'énergie cinétique à l'échelle k . En effet, lorsque l'on combine les Eqs. (4.1) et (4.6) - (4.9), on a la relation

$$\langle E \rangle = \int d^3\vec{k} \frac{1}{4\pi k^2} E(k) = \int dk E(k) \quad (4.10)$$

Avec l'Eq. (4.10), le terme $E(k)$ s'interprète donc bien comme la densité d'énergie cinétique moyenne à l'échelle associée au nombre d'onde k .

Le terme $\chi_k(\omega)$ introduit dans l'Eq. (4.8), est une mesure, dans le domaine Fourier, de la corrélation temporelle entre tourbillons à l'échelle associée au nombre d'onde k . En effet notons $\mathcal{E}_{ij}(k, \tau)$ la transformée de Fourier spatiale de $C_{ij}(r, \tau)$. En vertu de la définition de ϕ_{ij} (Eq. (4.1)) et à l'aide des Eqs. (4.7)-(4.9), on établit donc :

$$\mathcal{E}_{ij}(\vec{k}, \tau) = \frac{1}{2\pi} \int d\omega e^{-i\omega\tau} \phi_{ij}(\vec{k}, \omega) = \frac{1}{2\pi} \frac{E(k)}{4\pi k^2} \left(\delta_{ij} - \frac{k_i k_j}{k^2} \right) \int d\omega e^{-i\omega\tau} \chi_k(\omega). \quad (4.11)$$

On a donc :

$$\chi_k(\omega) \propto \int d\tau e^{i\omega\tau} \mathcal{E}_{ij}(\vec{k}, \tau) \quad (4.12)$$

D'après Eq. (4.12), la composante fréquentielle $\chi_k(\omega)$ correspond – à un facteur de proportionnalité près – à la transformée de Fourier temporelle du produit de corrélation temporelle à l'échelle k . Ce terme fournit donc, dans le domaine Fourier, une mesure du produit de corrélation temporelle entre d'éléments de taille donnée.

Nous avons considéré différentes prescriptions concernant la composante spatiale $E(k)$ (voir Sect. 4.1.1) ainsi que la composante fréquentielle $\chi_k(\omega)$ (voir Sect. 4.1.2). Ces différentes prescriptions ont été utilisées pour calculer les taux d'excitation \mathcal{P} . Comme on va le voir dans la suite, la comparaison entre ces calculs théoriques et les observations nous ont permis de discriminer entre certaines de ces prescriptions.

4.1.1 Composante spatiale, $E(k)$

Deux approches sont généralement adoptées pour décrire $E(k)$. La plus classique est de considérer des formes analytiques déduites soit de considérations théoriques soit de manière purement empirique. Le spectre analytique le plus connu est le spectre dit de Kolmogorov [1941].

Originellement du à [Oboukhov \[1941\]](#), il a été établi en postulant que l'énergie se transmet des grandes échelles aux plus petites échelles à taux constant. D'autres spectre théoriques ont été également testé dans ce contexte (par exemple celui-proposé par [Spiegel \[1962\]](#)) ainsi que des spectres purement empiriques [e.g. [Musielak et al., 1994](#)]. Ces spectres diffèrent les uns des autres par la manière dont E varie avec k notamment aux grandes échelles proches de l'échelle d'injection dans la cascade turbulente. Toutes ces approches nécessitent quoi qu'il en soit une prescription concernant l'échelle caractéristique à laquelle l'énergie est injectée dans la cascade turbulente. Cette échelle est associée à un nombre d'onde que l'on notera par la suite k_0 .

Une autre approche consiste à déterminer $E(k)$ à l'aide de simulations hydrodynamiques 3D. Cette quantité est directement calculée à partir du champ de vitesse extrait de la simulation 3D [voir e.g. [Nordlund et al., 1997](#); [Samadi et al., 2003b](#)]. Elle fournit non seulement la variation de E avec k mais aussi et surtout le nombre d'onde caractéristique k_0 . Cette méthode est cependant très dépendante de la qualité de la simulation hydrodynamique 3D, surtout de sa résolution spatiale.

Ces deux approches ont été comparées dans [Samadi et al. \[2003b\]](#), article inséré en page 97]. Parmi les différentes formes analytiques testées, la plus proche d'une simulation 3D du Soleil est le spectre proposé par [Musielak et al. \[1994\]](#) de manière purement empirique sous le nom "Extended Kolmogorov Spectrum". Ce spectre croît aux grandes échelles comme k^{+1} , puis décroît dans le régime inertiel (i.e. la cascade turbulente) selon le spectre de Kolmogorov, i.e. comme $k^{-5/3}$. Cependant, étant donné la résolution spatiale limitée de cette simulation 3D solaire, le spectre de Kolmogorov est validé uniquement sur un intervalle en nombre d'onde restreint. Toutefois, l'essentiel de l'excitation des modes est due aux plus grandes échelles du spectre ; les échelles non résolues par les simulations 3D contribuent très peu au forçage.

Plus que la forme du spectre, la connaissance de l'échelle d'injection k_0 fixe de manière déterminante le niveau du forçage. En effet, les intégrantes des Eqs. (3.31) et (3.32) sont toutes deux proportionnelles à k_0^{-4} . Par conséquent, les taux d'excitation \mathcal{P} sont extrêmement sensibles au choix de cette échelle. Il n'existe pas de principe physique simple permettant de fixer cette échelle caractéristique. Celle-ci peut en revanche être déterminée à partir de simulations hydrodynamiques 3D. Cependant, par défaut, on évalue cette échelle en la supposant proportionnelle à la longueur de mélange, elle-même supposée proportionnelle à l'échelle de pression. On considère ainsi la relation :

$$k_0 = k_0^{\text{MLT}} \equiv \frac{2\pi}{\beta \Lambda_{\text{MLT}}}, \quad (4.13)$$

où $\Lambda_{\text{MLT}} = \alpha H_p$ est l'échelle de la longueur de mélange, α le paramètre de la longueur de mélange, H_p l'échelle de hauteur en pression, et enfin β un paramètre qui permet au final d'ajuster k_0 . Ce dernier paramètre peut, par exemple, être contraint à l'aide de simulations hydrodynamiques 3D. La simulation solaire mise en oeuvre par [Samadi et al. \[2003b\]](#) indique que, dans la partie supérieure de l'enveloppe convective solaire, $k_0 \simeq 3.6 \text{ Mm}^{-1}$. Ce nombre d'onde correspond à des échelles de l'ordre de 2 Mm, valeur compatible avec les mesures effectuées à la surface du Soleil [voir e.g. [Roudier and Muller, 1986](#); [Muller, 1989](#)]. Pour les autres étoiles, les simulations hydrodynamiques 3D sont rarement disponibles. Dans ce cas, k_0 est évalué sur la base de l'Eq. (4.13) en prenant pour le paramètre β la valeur ajustée dans le cas du Soleil. Une question sous-jacente est de savoir si cette prescription reste valable d'une étoile à une autre ¹⁰.

10. Les travaux menés par [Freytag et al. \[1997\]](#) et [Samadi et al. \[2008\]](#) tendent à montrer, qu'en première

4.1.2 Composante fréquentielle, $\chi_k(\omega)$

Les formulations théoriques adoptaient jusqu'à présent explicitement ou implicitement une forme Gaussienne pour la composante $\chi_k(\omega)$ [Goldreich and Keeley, 1977b; Dolginov and Muslimov, 1984; Goldreich *et al.*, 1994; Balmforth, 1992a; Samadi *et al.*, 2001; Chaplin *et al.*, 2005]. Cependant, les simulations hydrodynamiques 3D des couches superficielles du Soleil montrent que χ_k est plus proche d'une forme Lorentzienne qu'une Gaussienne [Samadi *et al.*, 2003a, article inséré en page 107]. Ce résultat est illustré sur la Fig. 4.1. En fait, comme l'a montré Sawford [1991], les produits de corrélation temporelle évalués dans un référentiel *Lagrangien* dépendent fortement du niveau de la turbulence, plus spécifiquement du nombre de Reynolds. En effet, Sawford [1991] montre que plus le nombre de Reynolds élevé, plus les produits de corrélation temporelle mettant en jeu la vitesse (*Lagrangienne*) tendent vers une exponentielle, i.e. vers une forme Lorentzienne dans le domaine Fourier. Ce comportement est également vérifiée par des simulations dans une description *Eulerienne* (l'approche adoptée dans le cas présent). En effet, nous avons montré dans Samadi *et al.* [2007, article inséré en page 165] qu'à l'échelle d'injection (i.e. $k \sim k_0$), χ_k dépend fortement de la résolution spatiale des simulations hydrodynamiques 3D. Lorsque cette résolution est faible, χ_k tend vers une forme Gaussienne ; elle tend au contraire vers une forme Lorentzienne lorsque la résolution est élevée. Ce résultat est illustré par comparaison des Fig. 4.2 et Fig. 4.1. D'autres expériences numériques vont dans le même sens. Ainsi, He *et al.* [2002] ont constaté que $\chi_k(\omega)$ décroît plus lentement avec ω dans les simulations du type Large Eddy Simulations (LES) que dans des simulations du type Direct Numerical Simulations (DNS). En résumé, il existe un ensemble de preuves tant théoriques que numériques qui montrent que, dans un milieu très turbulent (notre cas) et à l'échelle d'injection, χ_k tend effectivement vers une forme Lorentzienne, et que par voie de conséquence, l'utilisation d'une forme Gaussienne ne se justifie pas.

Comme l'ont montré Samadi *et al.* [2003a, article inséré en page 107], les taux d'excitation calculés en supposant une forme Gaussienne conduisent à sous-estimer de manière importante les observations sismiques solaires. En revanche, l'utilisation d'une forme Lorentzienne aboutit à un plutôt bon accord avec les données solaires. Un résultat similaire est établi par Samadi *et al.* [2008, article inséré en page 177] dans le cas de l'étoile α Cen A. Ces résultats sont illustrés sur la Fig. 4.4 (cas du Soleil) et la Fig. 4.4 (cas de l'étoile α Cen A).

Les calculs menés par Chaplin *et al.* [2005] confirment le fait qu'une forme Gaussienne conduit effectivement à sous-estimer de manière importante les observations sismiques solaires. En revanche, contrairement à Samadi *et al.* [2003a], leurs calculs basés sur une forme Lorentzienne pour χ_k conduisent à sur-estimer de manière importante l'énergie injectée dans les modes de basse fréquence ($\nu \lesssim 2$ mHz). Afin de reproduire leurs résultats et à titre d'illustration, nous avons effectué des calculs similaires en considérant un modèle solaire proche de celui utilisé par Chaplin *et al.* [2005] et en ne considérant, comme ces auteurs, uniquement le terme de Reynolds. Ce modèle calculé avec un code 1D de structure stellaire [voir détails dans Houdek *et al.*, 1999], couvre l'ensemble de l'enveloppe convective solaire¹¹. Le résultat du calcul en terme de taux d'excitation \mathcal{P} est présenté sur la Fig. 4.5. Les calculs basés sur une forme Gaussienne

approximation, l'échelle caractéristique des granules varie d'une étoile à l'autre en fonction de l'échelle de pression à la photosphère.

11. Contrairement aux simulations hydrodynamiques 3D évoquées plus haut qui se limitent aux couches les plus superficielles, i.e. sur une profondeur de 3 Mm dans le cas du Soleil.

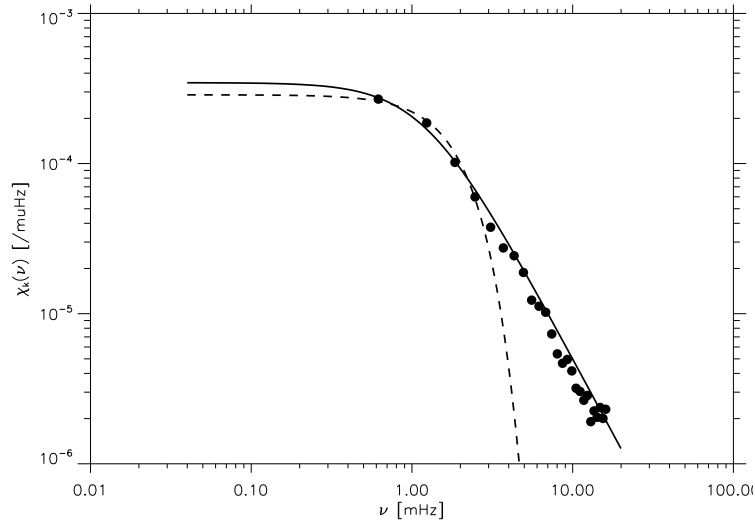


FIGURE 4.1 – χ_k en fonction de la fréquence $\nu = \omega/(2\pi)$. χ_k est tracé pour la couche où la vitesse convective est maximale et pour l'échelle k correspond au maximum de $E(k)$. Les cercles pleins représentent aux valeurs extraites à partir d'une simulation hydrodynamique 3D dotée d'une résolution horizontale ≈ 25 km [Samadi *et al.*, 2003a]. La courbe solide représente une fonction Lorentzienne et la courbe en pointillée à une fonction Gaussienne.

sous-estiment d'un facteur ~ 20 les puissances mesurées. Lorsqu'une forme Lorentzienne est utilisée, on constate que les puissances injectées dans les modes fréquence $\nu \lesssim 2$ mHz sont sévèrement sur-estimées. Il est important de noter que l'excitation des modes de fréquence $\nu \lesssim 2$ mHz s'étend sur une profondeur supérieure à celle des simulations 3D utilisées par Samadi *et al.* [2003a]. Il est donc normal que les calculs de ces derniers ne conduisent pas à une telle sur-estimation.

Les résultats de Chaplin *et al.* [2005] ont donc posé le problème de la validité de la forme Lorentzienne dans les couches profondes de l'enveloppe convective. Ce problème a récemment été résolu par Belkacem *et al.* [2010, article inséré en page 245]. En effet, les modes de basse fréquence sondent le domaine haute fréquence de la fonction χ_k . Dans ce régime la dynamique des éléments turbulents est dominée par l'advection par les éléments les plus énergétiques (qui ont une taille proche de l'échelle d'injection). C'est pourquoi on parle alors d'un phénomène de balayage bien connu en hydrodynamique des milieux turbulents [Kraichnan, 1964; Tennekes, 1975; Kaneda, 1993]. Ce phénomène se traduit dans le domaine Fourier par l'existence d'une fréquence de coupure au delà de laquelle χ_k tend rapidement vers zéro. Cette fréquence de coupure est proportionnelle au rapport entre la taille des éléments les plus énergétiques et leur vitesse. En introduisant cette fréquence de coupure dans la modélisation des amplitudes, Belkacem *et al.* [2010] ont résolu le problème de la sur-estimation des amplitudes des modes solaires de basse fréquence et ce faisant clos le débat en question.

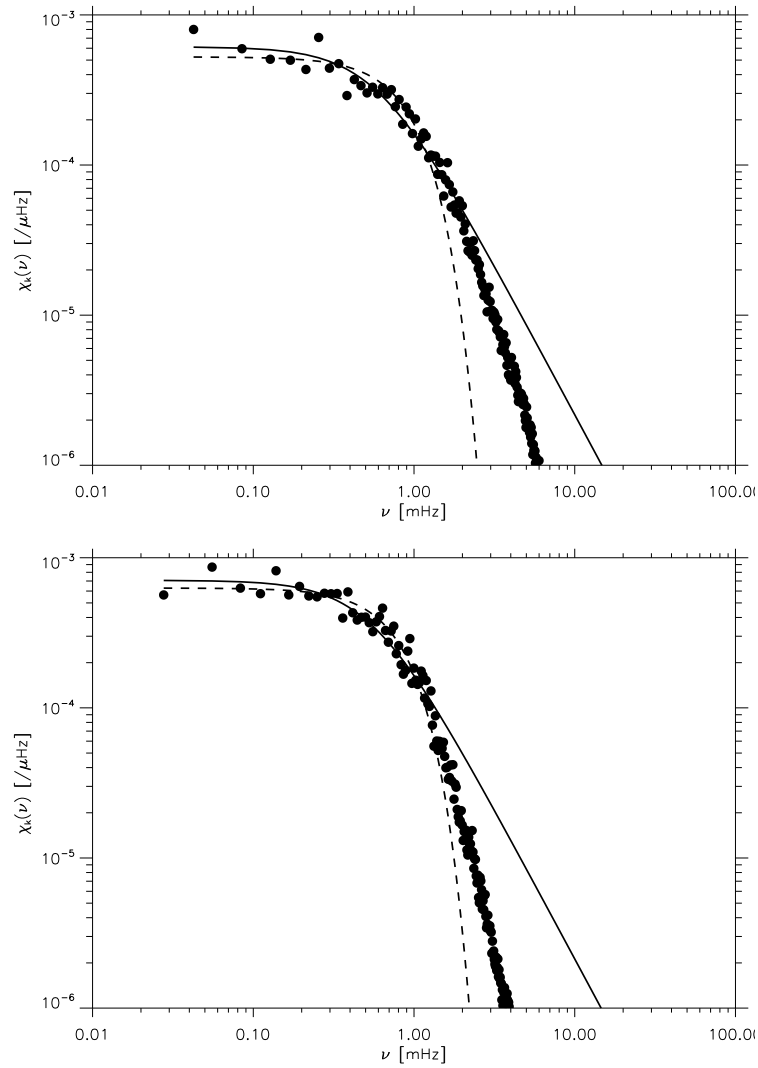


FIGURE 4.2 – **En haut** : Comme sur la Fig. 4.1 pour une simulation solaire 3D dotée d'une résolution horizontale de $\simeq 50$ km [Belkacem *et al.*, 2006a]. **En bas** : Comme sur le panneau supérieur pour une résolution horizontale de 120 km.

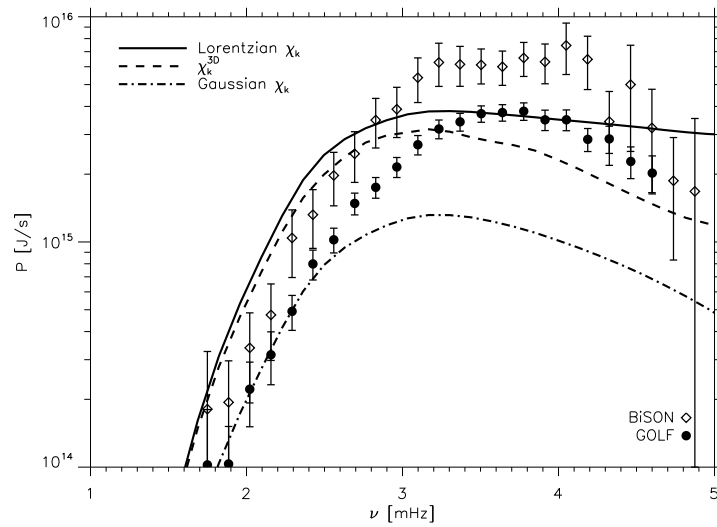


FIGURE 4.3 – Taux d’excitation (\mathcal{P}) des modes p solaires en fonction de la fréquence ν . Les cercles pleins (SOHO/GOLF) et les diamants (BiSON) correspondent aux données sismiques présentées dans le Chap. 2, Sect. 2.2.2, Fig. 2.1. Les courbes correspondent aux calculs théoriques effectués en adoptant différentes prescriptions pour χ_k : une forme Lorentzienne (trait plein) et une forme Gaussienne (trait pointillé).

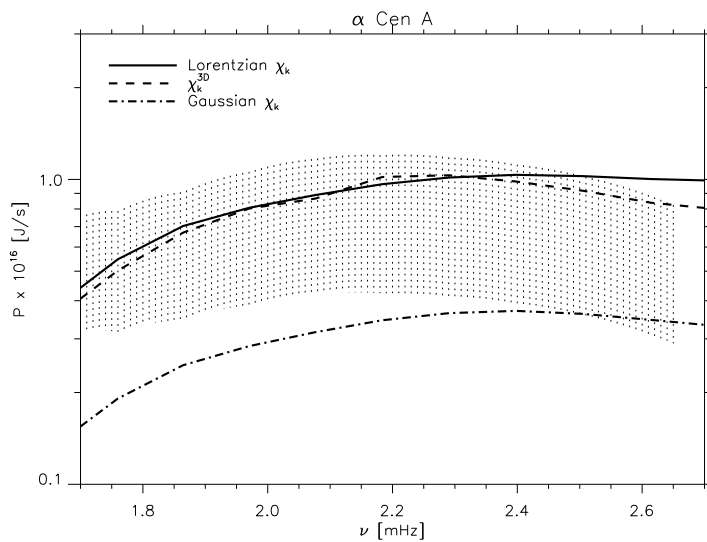


FIGURE 4.4 – Comme sur la Fig. 4.3 pour le cas de l’étoile α Cen A.

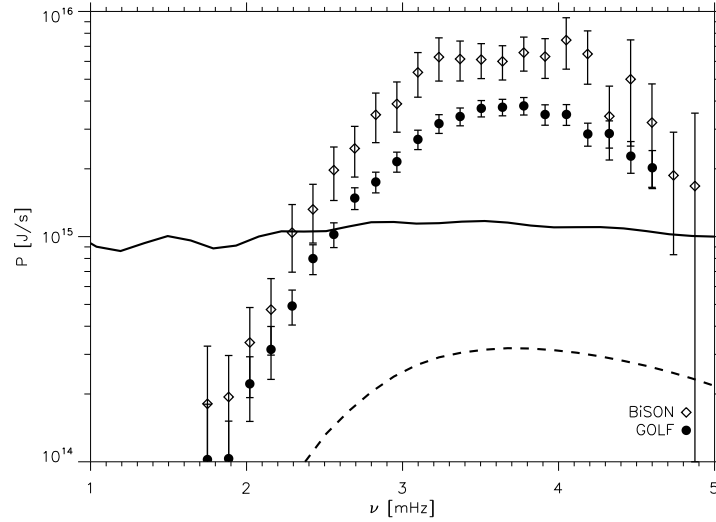


FIGURE 4.5 – Comme sur la Fig. 4.3. Les courbes correspondent ici aux calculs effectués dans les mêmes conditions que ceux réalisés par [Chaplin *et al.* \[2005\]](#) (voir texte). Deux prescriptions pour χ_k ont été considérées : une forme Lorentzienne (ligne en trait plein) et une forme Gaussienne (ligne en tiret-point). On a ici, comme [Chaplin *et al.* \[2005\]](#), considéré uniquement le forçage par le terme de Reynolds.

4.2 Modèles de fermeture et anisotropie

La décomposition de l'Eq. (3.21) suppose l'approximation quasi-normale (AQN). Cependant, l'écart à l'AQN est important dans un milieu fortement turbulent. Cette approximation est strictement valide dans le cas de quantités distribuées selon une distribution normale. Toutefois, la partie supérieure de l'enveloppe convective est un milieu turbulent composé de deux flots asymétriques l'un par rapport à l'autre : le flot montant (qui constitue les granules visibles à la surface) et le flot descendant (les plumes, qui se forment entre les granules). Par conséquent, dans un tel milieu, les distributions des vitesses et fluctuations de température sont asymétriques, ce qui viole de fait l'hypothèse de distribution normale et met en question l'usage de l'AQN dans ce contexte.

Comme l'ont vérifié [Belkacem *et al.* \[2006a\]](#), article inséré en page 145] et [Kupka and Robinson \[2007\]](#), l'écart à l'AQN est importante dans la partie supérieure de l'enveloppe convective du Soleil. En effet, cette approximation conduit à sous-estimer de $\approx 50\%$ le moment d'ordre quatre associé à la vitesse dans la région quasi-adiabatique de la simulation 3D solaire étudiée. Cet écart important a donc motivé un travail en vue d'aller au delà de l'AQN.

Rappelons tout d'abord que le terme que l'on cherche à modéliser, i.e. celui situé à gauche de l'Eq. (3.21), correspond à un produit de corrélation à *deux points* impliquant la vitesse, à savoir le terme : $\langle (u_i u_j)_1 (u_k u_l)_2 \rangle(r, \tau)$ où r et τ sont respectivement les longueurs de corrélation spatiales et temporelles. Lorsque que $r \rightarrow 0$ et $\tau \rightarrow 0$, ce terme se réduit à un produit de corrélation à *un point*, autrement dit ici à un moment d'ordre quatre (MOQ par la suite). Comme nous allons le voir, il est possible d'établir un modèle de fermeture pour ce MOQ qui ne repose

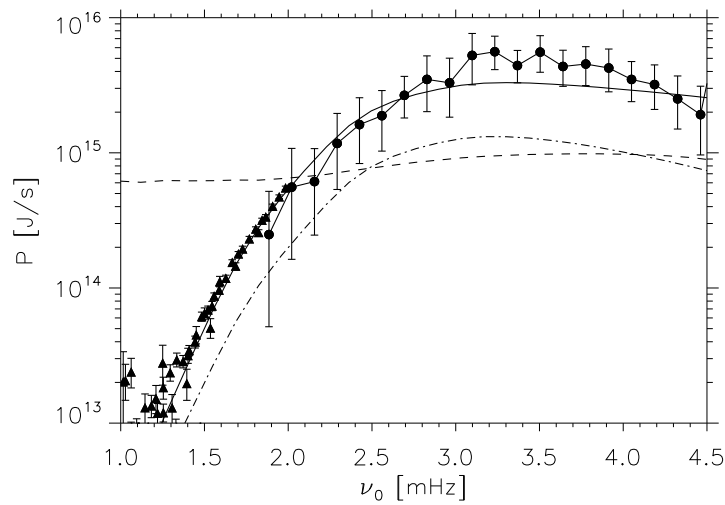


FIGURE 4.6 – Taux d’excitation (\mathcal{P}) des modes p solaires en fonction de la fréquence ν . Les cercles pleins et les triangles correspondent aux données sismiques issus du réseau GONG. Deux jeux de données sont présentés : des données basse fréquence (triangles) et des données plus haute fréquence (cercles). La courbe en trait plein correspond à un calcul semi-analytique utilisant des données extraites d’une simulation 3D solaire. Les autres courbes ont été obtenues en utilisant un modèle solaire 1D couvrant l’ensemble de l’enveloppe convective (voir texte). Les résultats de différentes prescriptions pour χ_k sont représentés : les courbes en trait plein et en tiret-point correspondent à une forme Lorentzienne tenant compte du phénomène de balayage (voir texte) et la courbe tiretée à une forme Lorentzienne pure.

pas sur l'AQN. Toutefois, il est au préalable nécessaire d'adopter une prescription permettant de relier un produit de corrélation à deux points à un produit (ou moment) à un point. Nous nous intéressons à des modes de bas degré, qui dans la région d'excitation se déplacent de manière principalement radiale. Nous avons donc besoin d'une prescription pour les produits de corrélation $\langle w_1^2 w_2^2 \rangle(r, \tau)$ et $\langle (w s_r)_1 (w s_r)_2 \rangle(r, \tau)$ où w correspond à la composante verticale de la vitesse.

Par défaut, [Belkacem et al. \[2006b\]](#) ont supposé que $\langle w_1^2 w_2^2 \rangle(r, \tau)$ varie en fonction de r et τ de la même façon que dans la AQN (Eq. (3.21)), à savoir comme suit :

$$\langle w_1^2 w_2^2 \rangle = \frac{\mathcal{K}_w}{3} \langle w_1^2 w_2^2 \rangle_{\text{QNA}}, \quad (4.14)$$

où \mathcal{K}_w est une constante et $\langle w_1^2 w_2^2 \rangle_{\text{QNA}}$ est le produit de corrélation à deux points donné en vertu de l'AQN. La prescription de l'Eq. (4.14) est brièvement discutée dans le Chap. 7. La contribution du terme de Reynolds (C_R^2 , Eq. (3.27)) se réécrit donc alors comme :

$$C_R^2 = 4\pi^3 \mathcal{G} \int_0^M dm \rho_0 \left(\frac{d\xi_r}{dr} \right)^2 \frac{\mathcal{K}_w}{3} S_R(m, \omega_{\text{osc}}). \quad (4.15)$$

Notons que la contribution due aux fluctuations d'entropie (C_S^2 , Eq. (3.28)) reste modélisée en supposant l'AQN. Cette inconsistance a toutefois un faible impact car la contribution du terme d'entropie est faible devant celle du au terme de Reynolds, du moins pour les étoiles pas trop chaudes (voir Sect. 3.4).

La constante \mathcal{K}_w dans l'Eq. (4.14) est déterminée dans la limite $r \rightarrow 0$ et $\tau \rightarrow 0$. Dans ce cas on a donc :

$$\langle w^4 \rangle = \frac{\mathcal{K}_w}{3} \langle w^4 \rangle_{\text{QNA}}, \quad (4.16)$$

où $\langle w^4 \rangle$ est par définition le MOQ associé à w , la composante verticale de la vitesse, tandis que $\langle w^4 \rangle_{\text{QNA}}$ est le MOQ donné par l'AQN (Eq. (3.21)). En vertu de l'Eq. (3.21) et dans la limite $r \rightarrow 0$ et $\tau \rightarrow 0$, on a donc :

$$\langle w^4 \rangle_{\text{QNA}} = 3 \langle w^2 \rangle^2. \quad (4.17)$$

A l'aide des Eqs. (4.16) et (4.17), on détermine la constante \mathcal{K}_w :

$$\mathcal{K}_w = 3 \frac{\langle w^4 \rangle}{\langle w^4 \rangle_{\text{QNA}}} = \frac{\langle w^4 \rangle}{\langle w^2 \rangle^2}, \quad (4.18)$$

constante qui est par définition le *Kurtosis*. Cette quantité mesure l'aplatissement de la fonction de densité de probabilité. Pour une distribution normale (cas de l'AQN), on a $\mathcal{K}_w = 3$. Le Kurtosis mesure l'écart du MOQ à l'AQN. Les simulations numériques 3D des couches superficielles du Soleil montrent que dans la région quasi-adiabatique, le Kurtosis est quasi constant et proche de la valeur six [[Belkacem et al., 2006a](#); [Kupka and Robinson, 2007](#)]. Il s'agit donc de développer un modèle de fermeture permettant de reproduire l'écart à la valeur "canonique" (i.e. $\mathcal{K}_w = 3$).

Des modèles de fermeture plus sophistiqués que la AQN ont été proposés. Parmi ceux-ci, celui connu sous le nom de modèle à deux flots [“two-scale mass flux model” [Gryanik and Hartmann, 2002](#)] est particulièrement adapté à notre contexte. Ce modèle tient en effet compte de l’existence de deux flots asymétriques (dans notre cas les granules montantes, et les plumes descendantes). Un tel modèle est toutefois limité à des flots quasi-laminaires ce qui n’est clairement pas le cas dans notre cas. Avec le modèle à deux flots proposé par [Gryanik and Hartmann \[2002\]](#), le Kurtosis \mathcal{K}_w s’écrit :

$$\mathcal{K}_w = (1 + S_w^2), \quad (4.19)$$

où le terme S_w est défini comme :

$$S_w \equiv \frac{\langle w^3 \rangle}{\langle w \rangle^{3/2}}. \quad (4.20)$$

Le terme S_w s’appelle le “biais” (“skewness” en anglais) et mesure l’asymétrie d’une distribution. Dans le modèle [Gryanik and Hartmann \[2002\]](#), S_w s’exprime comme :

$$S_w \equiv \frac{\langle w^3 \rangle}{\langle w \rangle^{3/2}} = \frac{1 - 2a}{\sqrt{a(1 - a)}}, \quad (4.21)$$

où a est la surface moyenne et relative occupée par les flots montants. Dans la limite de l’AQN, i.e. lorsque l’on a affaire à une distribution normale, nous avons nécessairement $S_w = 0$ (la distribution normale étant symétrique). Par conséquent, dans la limite de l’AQN, le Kurtosis donné par l’Eq. (4.19) ne tend pas vers la valeur canonique $\mathcal{K}_w = 3$ attendue pour une distribution normale. C’est la raison pour laquelle [Gryanik and Hartmann \[2002\]](#) ont proposé de modifier – “à la main” – l’Eq. (4.19) comme suit :

$$\mathcal{K}_w = 3 \left(1 + \frac{1}{3} S_w^2\right). \quad (4.22)$$

La Fig. 4.7 montre le MOQ obtenu à l’aide de l’Eq. (4.22) où S_w est déterminé à l’aide de l’Eq. (4.21). Comme on le voit, l’amélioration apportée par rapport à l’AQN est très modeste. En revanche, lorsque S_w est déterminé numériquement directement à partir de la simulation hydrodynamique 3D du Soleil, l’Eq. (4.22) reproduit assez correctement le MOQ dans la région quasi-adiabatique. Dans cette région, l’Eq. (4.22) constitue un modèle réaliste du Kurtosis \mathcal{K}_w sous réserve, toutefois, que le biais S_w soit correctement évalué [voir détails dans [Belkacem et al., 2006a](#); [Kupka and Robinson, 2007](#)].

Dans [Belkacem et al. \[2006a, article inséré en page 145\]](#), nous avons généralisé l’approche due à [Gryanik and Hartmann \[2002\]](#) en tenant en compte du biais introduit par la présence de deux flots asymétriques *et* de la turbulence au sein de chaque flot. Nous avons ainsi établi une expression plus précise pour S_w (voir son expression dans [Belkacem et al. \[2006a\]](#)). L’impact de ce modèle sur l’évaluation du Kurtosis \mathcal{K}_w donné par l’Eq. (4.22) est illustré sur la Fig. 4.7. Dans la région quasi-adiabatique, l’amélioration par rapport à l’AQN ou au modèle de [Gryanik and Hartmann \[2002\]](#) est substantielle.

Dans [Belkacem et al. \[2006b, article inséré en page 157\]](#), nous avons calculé le taux d’excitation, \mathcal{P} , des modes solaire en utilisant pour la contribution du terme de Reynolds l’Eq. (4.15)

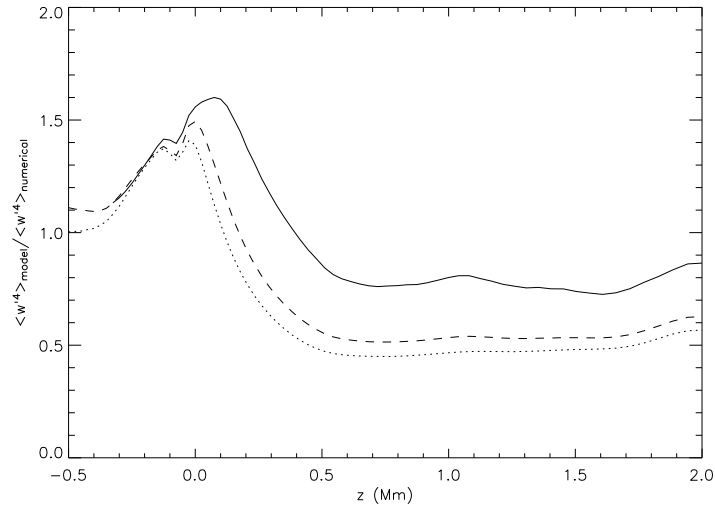


FIGURE 4.7 – Rapport entre le moment d’ordre quatre (MOQ) modélisé et celui extrait numériquement d’une simulation hydrodynamique 3D solaire. Le trait continu correspond au MOQ obtenu sur la base du modèle de fermeture proposé par [Belkacem et al. \[2006a\]](#), la courbe tiretée au modèle de [Gryanik and Hartmann \[2002\]](#) (Eq. (4.22) et Eq. (4.21)), et la courbe en pointillés au résultat obtenu avec l’AQN ($\mathcal{K}_w = 3$ et $\mathcal{S}_w = 0$).

dans laquelle le Kurtosis (K_w) est évalué avec les modèles de fermeture présentés plus haut. Le résultat est illustré sur la Fig. 4.8. Le maximum de \mathcal{P} est environ 30 % plus large lorsque l’on utilise le modèle de fermeture de [Belkacem et al. \[2006a\]](#) plutôt que l’AQN. Cette différence est plus grande que la contribution de l’entropie (environ 15 %, voir Sect. 3.4). Elle reste toutefois comparable aux différences entre les différents jeux de données sismiques (SOHO/GOLF, GONG, BiSON, voir Chap. 2).

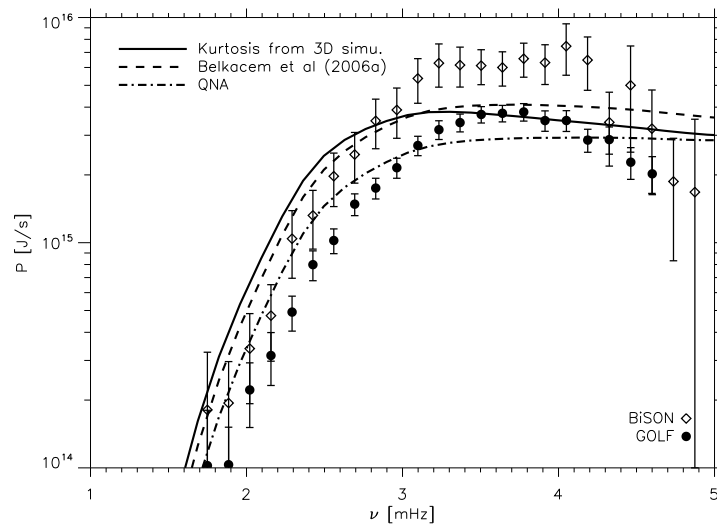


FIGURE 4.8 – Comme sur la Fig. 4.3. Les courbes correspondent aux calculs théoriques de \mathcal{P} pour lesquels la contribution du terme de Reynolds est évaluée sur la base de l’Eq. (4.15). Dans cette Eq. le Kurtosis (K_w) est évalué de différentes manières : la ligne continue correspond au calcul utilisant le Kurtosis évalué numériquement directement à partir d’une simulation hydrodynamique 3D solaire, la ligne tiretée au calcul basé sur le modèle de fermeture proposé par [Belkacem et al. \[2006a\]](#), et la ligne en tiret-point au calcul basé sur l’AQN ($\mathcal{K}_w = 3$ et $\mathcal{S}_w = 0$).

Chapitre 5

Contraintes sur les modèles standards de structure stellaire

Sommaire

5.1 Contraintes sur les modèles locaux de convection	47
5.2 Importance de la pression turbulente	50
5.3 Rôle de l'abondance en métaux à la surface	51

Articles reproduits dans ce mémoire (voir [Appendice A](#)) et auxquels ce chapitre se rapporte :

- “*Influence of local treatments of convection upon solar p mode excitation rates*”, Samadi R., Kupka F., Goupil M.-J., Lebreton Y., van’t Veer-Menneret C., 2006, *A&A*, 445, 233 [Page 135] ;
- “*Modeling the excitation of acoustic modes in α Centauri A*”, Samadi R., Belkacem K., Goupil M.-J., Dupret M.-A., Kupka F., 2008, *A&A*, 489, 291 [Page 177] ;
- “*The CoRoT target HD 49933. I. Effect of the metal abundance on the mode excitation rates*”, Samadi R., Ludwig H.-G., Belkacem K., Goupil M. J., Dupret M.-A., 2010, *A&A*, 509A, 15 [Page 223] ;
- “*The CoRoT target HD 49933. II. Comparison of theoretical mode amplitudes with observations*”, Samadi R., Ludwig H.-G., Belkacem K., Goupil M. J., Benomar O., Mosser B., Dupret M.-A., Baudin F., Appourchaux T., Michel E., 2010, *A&A*, 509A, 16 [Page 231].

5.1 Contraintes sur les modèles locaux de convection

Les formulations théoriques de la convection utilisées dans les modèles standards de structure stellaires ont pour objectif essentiel de reproduire la structure des régions convectives dans les étoiles. Dans la majeure partie de l'étoile le transport de l'énergie par la convection est extrêmement efficace de sorte que le mouvement de la matière s'effectue de manière quasi-adiabatique. Dans ces conditions, le gradient de température est très proche du gradient adiabatique. Le transport par la radiation étant dans ces régions directement proportionnel au gradient

de température (en vertu de l'équation de diffusion qui reste valable tant que le milieu est optiquement épais), le flux d'énergie et la stratification de ces régions sont complètement contraintes par le gradient de température adiabatique, dont la valeur est connue à partir de l'équation d'état et de la composition chimique. Il n'en est pas de même au voisinage de la surface visible. En effet, au voisinage de cette région les flots montants se refroidissent rapidement, de sorte que le transport convectif devient très inefficace et le gradient de température s'écarte significativement du gradient adiabatique¹². Pour compenser la chute rapide de la densité tout en transportant de manière convective l'énergie, les éléments montants doivent accroître leur vitesse de manière substantielle, ce qui rend le milieu particulièrement turbulent. Enfin, par ailleurs, le transfert radiatif ne plus être y traité dans l'approximation de diffusion. C'est principalement pour ces deux dernières raisons que le transport convectif est particulièrement difficile à modéliser dans cette région.

La théorie dite de "la longueur de mélange" [Biermann, 1932; Böhm-Vitense, 1958, MLT par la suite] a été la première formulation analytique de la convection qui a été appliquée pour modéliser les étoiles. Malgré tous ces nombreux défauts [voir à ce sujet la revue due à Zahn, 1991], elle est toujours utilisée dans de nombreux codes de structure et d'évolution stellaire, principalement pour des raisons de commodité¹³. Le modèle théorique proposé par Canuto, Goldman, & Mazzitelli [1996, CGM par la suite] est une alternative plus réaliste que la MLT puisqu'elle prend en compte la présence d'éléments turbulents de tailles différentes. Par ailleurs, comme la MLT, il s'agit d'une formulation locale et 1D de la convection, elle peut donc être très facilement intégrée dans les codes de structure stellaire.

Ces formulations locales de la convection dans les étoiles ont été testées et comparées en utilisant les positions des étoiles dans le diagramme Hertzsprung-Russell ou bien en effectuant l'analyse détaillée de raies spectrales. Toutefois, ces méthodes ne permettent pas de discriminer sans ambiguïtés entre la MLT et la théorie de CGM [voir Kupka *et al.*, 2009; Kupka, 2009]. En revanche, les fréquences des modes solaires offrent un diagnostic clair dans le cas du Soleil. En effet, les fréquences des modes permettent de sonder la structure. En particulier les modes de haute fréquence sont principalement confinés près de la surface. Ces modes sont donc indirectement sensibles aux caractéristiques d'un modèle de convection. Basu and Antia [1995] ont ainsi montré que les fréquences des modes solaires calculées avec un modèle solaire basé sur le modèle de CGM reproduisent mieux les fréquences observées que ne le fait la MLT.

Il existe toutefois un diagnostic plus direct et donc plus fort. C'est celui qui existe entre amplitudes des modes et vitesse des éléments convectifs. En effet, ce lien est mis en lumière par les Eqs. (3.31) et (3.32) ainsi que par le terme $\chi_k(\omega)$ apparaissant dans les Eqs. (3.29) et (3.30). On voit en effet que la vitesse caractéristique du flux convectif, u_0 , intervient directement dans l'expression pour le taux d'excitation \mathcal{P} . Par ailleurs, cette vitesse caractéristique contrôle le temps caractéristique τ_0 (Eq. (3.35)), qui contrôle le temps caractéristique de corrélation entre éléments turbulents, donc au final la largeur caractéristique du terme $\chi_k(\omega)$. Ce lien direct entre amplitudes des oscillations de type solaire et vitesse des éléments convectifs offre donc des diagnostics sur les modèles théoriques de convection. C'est pourquoi nous avons calculé dans Samadi *et al.* [2006, article inséré en page 135] les taux d'excitation solaires en utilisant des modèles solaires calculés avec différentes prescriptions pour le transport convectif, à savoir la

12. Dans cette région, le gradient de température est dit alors "super-adiabatique".

13. En particulier, pour son approche unidimensionnelle et locale du phénomène de transport convectif.

MLT et la formulation due à CGM.

Toutefois, comme on l'a noté plus haut, la partie supérieure de la région convective (région dite super-adiabatique) correspond à la région de transition entre l'enveloppe convective et la partie supérieure de l'atmosphère radiative. Dans cette région qui devient progressivement optiquement mince et le flux radiatif important, l'approximation de diffusion pour le flux radiatif cesse d'être valide. Il est donc nécessaire de traiter de manière plus réaliste, non seulement le flux convectif mais aussi le flux radiatif. C'est pourquoi nous avons donc comparé deux traitements différents du flux radiatif : l'un basé sur l'approximation dite d'Eddington¹⁴ et l'autre sur un modèle d'atmosphère plus réaliste calculé avec le code ATLAS 9 [Kurucz, 1993].

Au final, quatre modèles solaires différents ont été comparés [pour plus de détails on se reportera à Samadi *et al.*, 2006, article inséré en page 135]. Ces modèles sont désignés et décrits ci-dessous :

- EMLT : modèle calculé sur la base de la MLT et en traitant le flux radiatif dans l'approximation d'Eddington ;
- ECGM : modèle calculé sur la formulation de CGM pour la convection et en traitant le flux radiatif dans l'approximation d'Eddington ;
- KMLT : modèle calculé sur la base de la MLT que l'on a raccordé avec un modèle d'atmosphère calculé avec le code ATLAS 9 (connu également sous le nom code Kurucz) en utilisant la même prescription pour le transport convectif ;
- KCGM : modèle calculé sur la formulation de CGM que l'on a raccordé avec un modèle d'atmosphère calculé avec le code ATLAS 9 en utilisant la même prescription pour le transport convectif.

Pour les quatre modèles, on a ajusté la valeur du paramètre de la longueur de mélange (α) utilisée dans l'intérieur du modèle de telle sorte à ce que chaque modèle reproduise le rayon et la luminosité du Soleil. Pour les modèles KMLT et KCGM, la valeur de α utilisée dans le modèle d'atmosphère a été ajustée de manière à ce que celui-ci reproduise les raies de Balmer observées.

Comme le montre la Fig. 5.1, les variations des vitesses convectives obtenues avec ces quatre modèles sont très différentes les uns des autres dans la région super-adiabatique [pour l'interprétation de ces différences on se reportera à Samadi *et al.*, 2006]. Pour chaque modèle, on a ensuite calculé les taux d'excitation \mathcal{P} des modes solaires. La comparaison de ces taux d'excitation avec les contraintes sismiques est reproduite sur la Fig. 5.2. Comme le montre la figure, les taux d'excitation obtenus avec le traitement de la convection dû à CGM sont plus proches des observations que ne le sont ceux obtenus avec la MLT. Par ailleurs, cette figure montre que la sensibilité au traitement de l'atmosphère est plus grande avec la MLT qu'elle ne l'est avec la formulation de CGM.

Ce résultat montre que les amplitudes des modes permet de discriminer, dans le cas du Soleil, entre différents traitement de la convection. L'écart résiduel entre les données sismiques et les taux d'excitation obtenus avec la formulation de CGM reste important. Comme on l'a vu dans le Chap 4, il se réduit notablement lorsque l'on calcule \mathcal{P} en utilisant les données extraites de simulations hydrodynamiques 3D des couches superficielles du Soleil.

14. Approximation qui permet de fermer simplement le système d'équation pour le transfert radiatif.

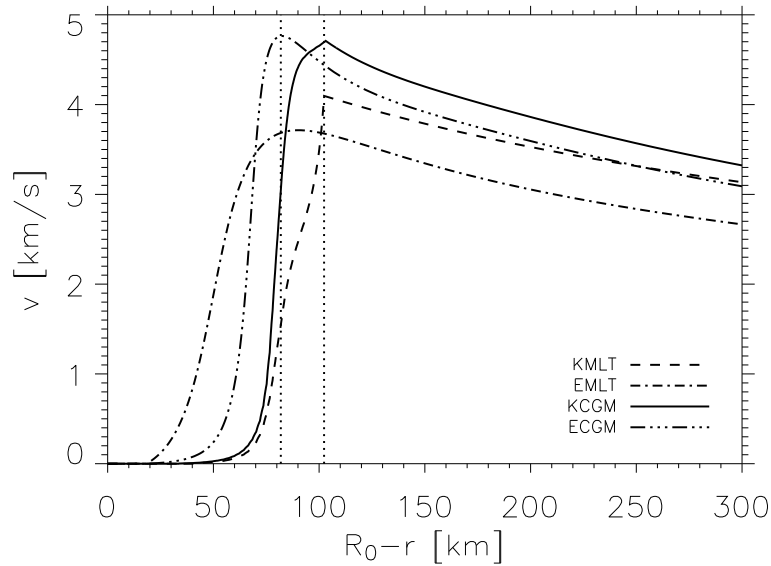


FIGURE 5.1 – Vitesses convectives en fonction de la distance $z = R_{\odot} - r$, où R_{\odot} correspond au rayon solaire et r à un rayon donné. Quatre modèles solaires sont comparés : EMLT, ECGM, KMLT, et KCGM (voir texte).

5.2 Importance de la pression turbulente

A l'aide d'une simulation hydrodynamique 3D des couches superficielles du Soleil, [Rosenthal et al. \[1999\]](#) ont montré que la prise en compte de la pression turbulente dans la modélisation des couches superficielles améliorerait notablement l'accord entre fréquences observées et théoriques. Dans cet esprit, nous avons dans [Samadi et al. \[2008, article inséré en page 177\]](#) cherché à mesurer l'effet de la prise en compte de la pression turbulente dans le modèle d'équilibre sur les taux d'excitation. Pour cela, nous avons construit deux modèles de structure représentatifs de l'étoile α Cen A. Un des modèles, que l'on désignera sous le terme "raccordé"¹⁵, a ses couches superficielles extraites d'une simulation hydrodynamique 3D tandis que ces couches internes sont obtenues avec le code de structure stellaire CESAM [[Morel and Lebreton, 2008](#)] en utilisant le traitement de la convection basée sur la MLT et en ignorant la pression turbulente. Le second modèle (que l'on désignera sous le terme de "standard") est construit intégralement à l'aide du code CESAM.

Les couches superficielles du modèle "raccordé" tient compte de la pression turbulente ce qui n'est pas le cas du modèle "standard". Ces deux modèles permettent donc de mesurer l'effet de la pression turbulente sur \mathcal{P} . Le résultat obtenu par [Samadi et al. \[2008\]](#) est reproduit sur la Fig. 5.3 où l'on a représenté, non pas \mathcal{P} mais le rapport \mathcal{P}/\mathcal{M} . En effet, en vertu de l'Eq. (2.15), déterminer \mathcal{P} à partir des données sismique requiert de modéliser la masse du mode \mathcal{M} . Cette dernière quantité dépend du modèle d'équilibre (voir Eq. (2.11)). En revanche, la détermination du rapport \mathcal{P}/\mathcal{M} à partir des données sismiques ne requiert pas d'hypothèse concernant le mo-

15. En anglais, de tels modèles ont été pour la première fois désignés par [Trampedach \[1997\]](#) sous le nom de "patched". Le procédé de fabrication de ce genre de modèles est détaillé dans [Trampedach \[1997\]](#) ainsi que dans [Samadi et al. \[2008\]](#).

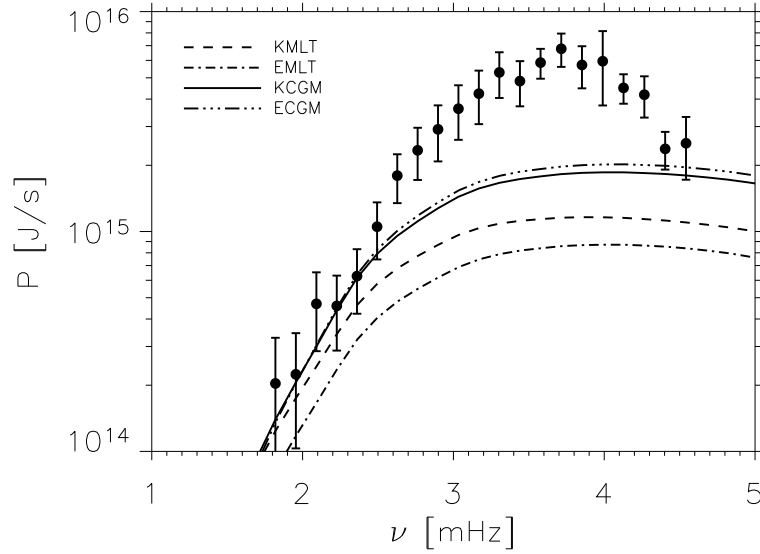


FIGURE 5.2 – Taux d’excitation \mathcal{P} des modes solaires en fonction de la fréquence ν . Les courbes correspondent aux valeurs obtenues avec les modèles solaires EMLT, ECGM, KMLT, et KCGM (voir texte ainsi que la Fig. 5.1). Les cercles pleins avec les barres d’erreurs verticales correspondent aux données sismiques solaires obtenues par [Chaplin *et al.* \[1998\]](#).

dèle d’équilibre ce qui permet donc de comparer les observations à des modèles d’équilibres qui prédiraient différentes valeurs pour \mathcal{M} .

Comme le montre la Fig. 5.3, le modèle “raccordé” donne des valeurs \mathcal{P}/\mathcal{M} plus proches des contraintes sismiques mesurées sur α Cen A que celles obtenues avec le modèle “standard”. Cela est principalement dû aux masses des modes \mathcal{M} (Eq. (2.11)). En effet, les masses des modes associées au modèle “raccordé” sont plus faibles que celles associées au modèle “standard”. Cela s’explique du fait que le modèle “raccordé” inclue la pression turbulente au niveau des couches supérieures dans lesquelles sont confinés les modes que l’on regarde. Cette pression turbulente s’ajoute à la pression du gaz. Elle fournit un support additionnel au poids des couches supérieures. Par conséquent, en présence de pression turbulente, le poids des couches supérieures peut être soutenu avec une pression du gaz plus faible et donc une densité inférieure à celle nécessaire pour le modèle “standard” [voir aussi [Nordlund and Stein, 1999](#); [Rosenthal *et al.*, 1999](#)]. Des densités plus faibles impliquent nécessairement des \mathcal{M} plus faibles, ce qui explique donc le résultat reproduit sur la Fig. 5.3.

5.3 Rôle de l’abondance en métaux à la surface

Dans [Samadi *et al.* \[2010b\]](#), article inséré en page 223], nous avons évalué l’effet d’une variation de l’abondance en métaux à la surface d’une étoile sur les taux d’excitation des oscillations de type solaire. Pour cela, nous avons mis en oeuvre deux simulations hydrodynamiques 3D représentatives de l’étoile CoRoT HD 49933. Cette étoile déjà connue, avant CoRoT, pour présenter des oscillations de type solaire [[Mosser *et al.*, 2005](#)], a été considérée ici du fait de sa faible abondance en fer ($[\text{Fe}/\text{H}]=-0.37$). L’une des deux simulations 3D (S0 par la suite) a

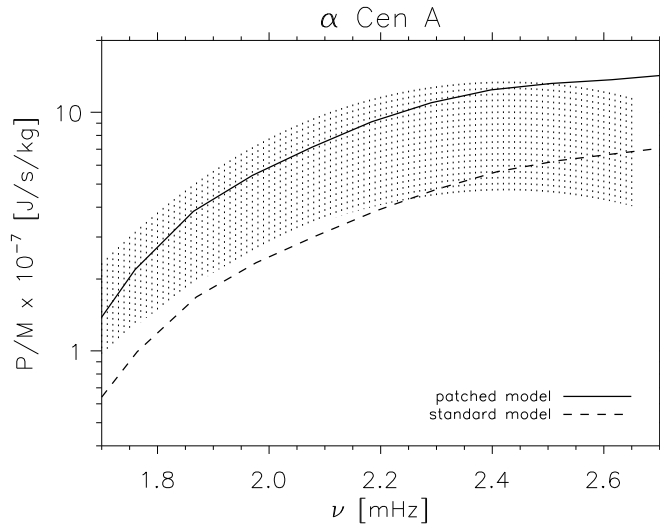


FIGURE 5.3 – Rapport \mathcal{P}/\mathcal{M} en fonction de la fréquence ν pour l'étoile α Cen A. Les lignes pointillées représentent le domaine correspondant aux mesures sismiques disponibles pour l'étoile α Cen A [voir détails dans Samadi *et al.*, 2008]. La courbe en trait plein correspond aux valeurs de \mathcal{P}/\mathcal{M} obtenues avec le modèle “raccordé” tandis que la courbe en pointillé aux valeurs correspond au modèle “standard”.

son abondance en métaux égale à celle du Soleil tandis que l'autre (S1 par la suite) a une abondance dix fois plus faible ($[\text{Fe}/\text{H}]=-1$). Pour chacune des simulations 3D nous avons construit un modèle “raccordé” associée et calculé les taux d'excitation des modes associés.

Comme cela est illustré sur la Fig. 5.4, les taux d'excitation \mathcal{P} obtenus avec le modèle S1 sont trois fois plus faibles que ceux obtenus avec le modèle S0. Cette différence s'explique du fait qu'une faible abondance en métaux à la surface implique une faible opacité du milieu, et par conséquent une plus forte densité à la surface de l'étoile [voir les détails dans Samadi *et al.*, 2010b]. Or pour transporter un flux convectif identique¹⁶, des vitesses convectives plus faibles sont suffisantes lorsque la densité est plus élevée. Enfin, des vitesses convectives plus faibles impliquent un forçage plus faible ; ceci explique donc le résultat illustré sur la Fig. 5.4.

Nous avons ensuite cherché à tester notre modélisation dans le cas de l'étoile HD 49933 observée par CoRoT et pour lesquelles des mesures précises des amplitudes et largeurs sont disponibles [Benomar *et al.*, 2009]. Cette étoile ayant une abondance en métaux intermédiaire entre celle de S0 et S1, nous avons au préalable établi une méthode permettant d'interpoler les taux d'excitation obtenus pour chacune de ces deux modèles 3D [voir les détails dans Samadi *et al.*, 2010b]. Le résultat de cette interpolation est reproduit sur la Fig. 5.4.

Avec les largeurs mesurées (Γ) et les taux d'excitation théoriques \mathcal{P} calculés pour HD 49933, nous avons évalué les vitesses des modes à l'aide de l'Eq. (2.13). Ces amplitudes en termes de vitesse ont ensuite été converties en termes de fluctuation d'intensité en adoptant l'approximation quasi-adiabatique (voir Chap. 6 Sect. 6.3). Les amplitudes en termes d'intensité ainsi obtenues ont été comparées dans Samadi *et al.* [2010a, article inséré en page 231] aux mesures

16. Les deux simulations 3D ayant la même température effective.

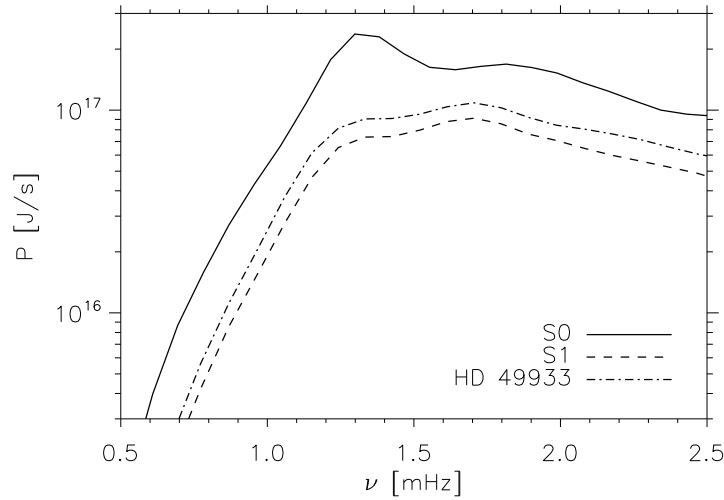


FIGURE 5.4 – Taux d’excitation \mathcal{P} calculés en fonction de la fréquence ν pour des modèles ayant une température effective et une gravité proche de celle de l’étoile CoRoT HD 49933. La courbe en trait plein correspond au modèle S0, celle en trait pointillé au modèle S1, et enfin celle en tiret-point au modèle doté de la même abondance en métaux que HD 49933 (voir texte).

sismiques effectuées par [Benomar *et al.* \[2009\]](#) à l’aide des données CoRoT. Le résultat de cette comparaison est reproduit sur la Fig. 5.5. Excepté à haute fréquence ($\nu \gtrsim 1.9$ mHz) où le désaccord important reste à expliquer (voir Chap. 7), les amplitudes théoriques sont en bon accord avec les mesures sismiques. La Fig. 5.5 montre aussi qu’ignorer la faible abondance en métaux de cette étoile conduit à surestimer de manière significative les amplitudes observées. Ce résultat illustre l’importance du rôle de l’abondance en métaux et donc de la nécessité de sa prise en compte.

L’effet de l’abondance en métaux sur les amplitudes semble avoir été observé de manière qualitative par [Stello and Gilliland \[2009\]](#) en comparant les amplitudes des modes de type solaire dans des amas globulaires caractérisés par des abondances en métaux différentes. Toutefois, une comparaison plus quantitative reste à effectuer. Pour cela il sera nécessaire de mesurer également les durées de vie des modes, car il s’agit de distinguer l’effet de l’abondance en métaux sur le forçage avec celui sur l’amortissement des modes.

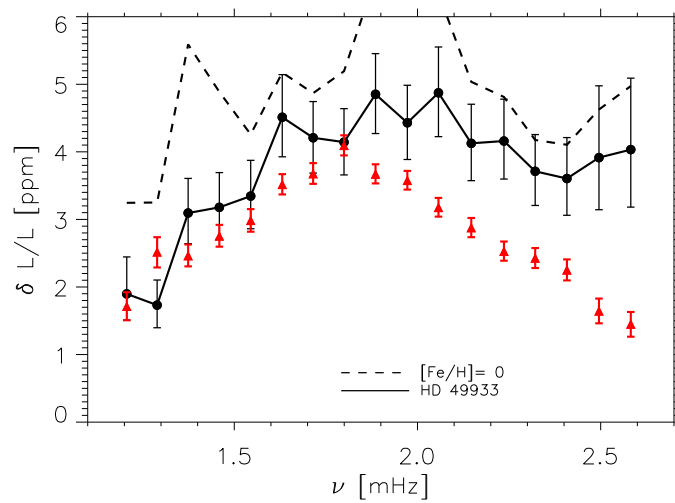


FIGURE 5.5 – Amplitudes bolométriques en fonction de la fréquence ν . Les triangles pleins et rouges correspondent aux mesures sismiques effectuées par [Benomar *et al.* \[2009\]](#) sur l'étoile HD 49933. Les cercles pleins connectés par la courbe en trait épais correspondent au calcul théorique établi en tenant compte de l'abondance en métaux de l'étoile HD 49933 ainsi que les largeurs des modes mesurées. La courbe en trait pointillé correspond au calcul théorique obtenu avec le modèle 3D S0, dont l'abondance en métaux est solaire.

Chapitre 6

Lois d'échelles sur les amplitudes

Sommaire

6.1 Taux d'excitation, \mathcal{P}	55
6.2 Amplitude en terme de vitesse, V	58
6.3 Amplitude en terme d'intensité, $\delta L/L$	59

Articles reproduits dans ce mémoire (voir Appendice A) et auxquels ce chapitre se rapporte :

- *Excitation of solar-like oscillations across the HR diagram*, Samadi R., Georgobiani D., Trampedach R., Goupil M.-J., Stein R. F., Nordlund A., 2007, A&A, 463, 297 [Page 165] ;
- *Amplitudes of solar-like oscillations in red-giant stars : Evidences for non-adiabatic effects using CoRoT observations*, Samadi R., Belkacem K., Dupret M.-A., Ludwig H.-G., Baudin F., Caffau E., Goupil M. J., Barban C., 2012, A&A, 543, 120 [Page 257].

6.1 Taux d'excitation, \mathcal{P}

A l'aide d'un jeu de modèles hydrodynamiques 3D représentatifs des surfaces d'étoiles situées sur la séquence principale, nous avons dans Samadi *et al.* [2007, article inséré en page 165] calculé le maximum des taux d'excitation (\mathcal{P}_{\max} par la suite). Différentes prescriptions pour la composante en fréquence χ_k ont été testées (voir la définition de χ_k dans le Chap. 4, Sect. 4.1.2), notamment une forme Lorentzienne et une forme Gaussienne. Les valeurs obtenues pour \mathcal{P}_{\max} sont reproduites sur la Fig. 6.1 en fonction du rapport L/M (L étant la luminosité et M la masse de l'étoile). On constate clairement que \mathcal{P}_{\max} varie selon une loi d'échelle de la forme $(L/M)^s$ où la pente s dépend de la prescription adoptée pour χ_k : $s = 3.1$ pour une forme Gaussienne et $s = 2.6$ pour une forme Lorentzienne. Le travail mené par Samadi *et al.* [2007] a été récemment étendu par Samadi *et al.* [2012, article inséré en page 257] aux cas des étoiles sous-géantes et géantes rouges. Ces derniers ont montré que la pente s se maintient à la valeur $s = 2.60 \pm 0.09$ lorsqu'une forme Lorentzienne est adoptée pour χ_k . En revanche, pour ces étoiles la différence entre une forme Lorentzienne et une Gaussienne est très tenue car on a $s = 2.69 \pm 0.06$ pour une forme Gaussienne.

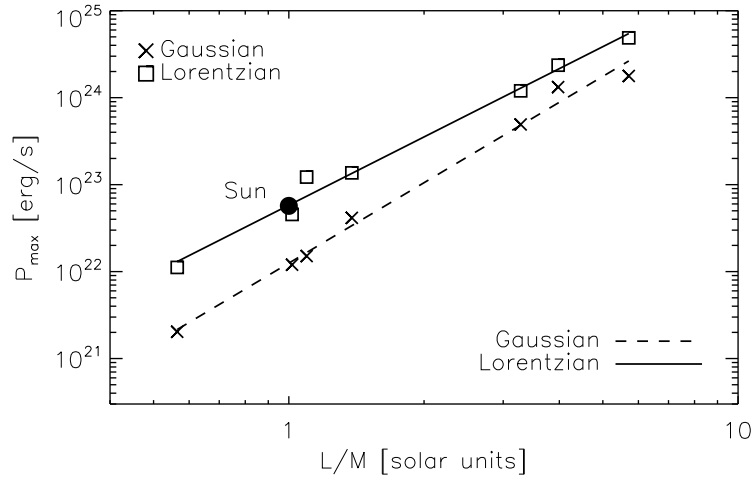


FIGURE 6.1 – Maximum des taux d’excitation, \mathcal{P}_{\max} , en fonction du rapport L/M . La courbe en trait plein correspond au calcul théorique basé sur une forme Lorentzienne pour χ_k tandis que la courbe en pointillé à celui basé sur une forme Gaussienne.

L’accroissement de \mathcal{P}_{\max} avec le rapport L/M n’est pas surprenant. En effet, notons d’abord que bien que L/M soit le rapport entre deux grandeurs globales pour l’étoile, ce rapport est également proportionnel à T_{eff}/g , où T_{eff} est la température effective de l’étoile et g sa gravité de surface¹⁷. Ensuite, comme on va le montrer maintenant, \mathcal{P}_{\max} dépend étroitement de T_{eff} et de g . En effet, l’Eq. (3.41) peut se réécrire comme :

$$\mathcal{P} \propto \left(\frac{\omega_{\text{osc}}}{c_s} \right)^2 F_{\text{kin}} \Lambda^4, \quad (6.1)$$

où

$$F_{\text{kin}} = \frac{3}{2} \rho_0 u_0^3 \quad (6.2)$$

est par définition le flux d’énergie cinétique par unité de volume¹⁸ et u_0 est une vitesse caractéristique donnée par l’Eq. (3.25).

En bonne approximation, l’échelle caractéristique Λ varie d’une étoile à une autre approximative selon l’échelle de pression H_p à la photosphère [voir Freytag *et al.*, 1997; Samadi *et al.*, 2008]. L’équilibre hydrostatique permet d’écrire que $P = \rho g H_p$, où P correspond à la pression totale (pression du gaz + pression turbulente). En supposant un gaz parfait, on a donc que $H_p \propto T/g$. La vitesse du son est donnée par la relation : $c_s^2 = \Gamma_1 P/\rho$. Par conséquent, en supposant à nouveau un gaz parfait, on a $c_s^2 \propto T$. A l’aide des relations précédentes, on peut alors

17. En effet, en vertu de la loi de Stefan, on a $L = 4\pi\sigma T_{\text{eff}}^4 R_*^2$ où σ est la constante de Stefan et R_* le rayon de l’étoile. De plus, la gravité à la surface est égale à $g = GM/R^2$ où G est la constante universelle de la gravitation. On a donc finalement $L/M \propto T_{\text{eff}}^4/g$.

18. Par soucis de simplification, on a supposé un milieu isotrope ; par voie de conséquence le flux d’énergie cinétique est égal dans les trois directions de l’espace.

simplifier l'Eq. (6.1) comme suit :

$$\mathcal{P} \propto \omega_{\text{osc}}^2 F_{\text{kin}} T^3 g^{-4} . \quad (6.3)$$

Dans le cadre de la théorie de la longueur de mélange (MLT), on peut montrer que le flux d'énergie cinétique F_{kin} est approximativement proportionnel au flux convectif F_c . En effet, dans le cadre de cette théorie, un élément convectif est accéléré par la force d'Archimède sur une longueur égale par définition à la longueur de mélange Λ_{MLT} . Un choix par défaut est de supposer que $\Lambda_{\text{MLT}} = \alpha H_p$ où α est ce qu'on appelle le paramètre de la longueur de mélange. L'énergie cinétique des éléments s'exprime alors comme [voir les notes de cours de [Bohm-Vitense, 1989](#)] :

$$E_{\text{eddy}} \equiv \frac{3}{2} \rho u_0^2 \Lambda^3 = g (\Delta\rho \Lambda^3) \Lambda , \quad (6.4)$$

où $\Delta\rho$ est la différence de densité entre l'élément en mouvement et le milieu ambiant. Dans l'approximation de Boussinesq, la perturbation de l'équation d'état se simplifie comme :

$$\frac{\Delta\rho}{\rho} \propto \frac{\Delta T}{T} \quad (6.5)$$

où ΔT correspond à la différence de température entre l'élément et le milieu ambiant.

Le flux convectif est par définition égal à

$$F_c \equiv u_0 (\rho C_p \Delta T) , \quad (6.6)$$

où $C_p = (\partial s / \partial \ln T)_p$. Finalement, en vertu de l'Eq. (6.2) et le jeu d'Eqs. (6.4)-(6.6), on en déduit que $F_{\text{kin}} \propto g \Lambda / T F_c$ et, puisque $\Lambda \propto T/g$, on a finalement $F_{\text{kin}} \propto F_c$.

Dans la région où le forçage est le plus efficace, le flux total d'énergie, F_{tot} , n'est plus transporté exclusivement par la convection. Cependant, de manière à établir une expression qui dépende simplement des paramètres de surface (T_{eff} et g), on suppose néanmoins que la totalité du flux est transporté par la convection ; par voie de conséquence on a donc $F_c \approx F_{\text{tot}} = \sigma T_{\text{eff}}^4 \propto g (L/M)$ où σ est la constante de Steffan. Finalement, en supposant que $T = T_{\text{eff}}$, on peut alors simplifier l'Eq. (6.3) comme suit :

$$\mathcal{P} \propto \omega_{\text{osc}}^2 T_{\text{eff}}^4 T^3 g^{-4} \approx \omega_{\text{osc}}^2 T_{\text{eff}}^7 g^{-4} . \quad (6.7)$$

Définissons maintenant $\nu_{\text{max}} = (\omega_{\text{osc}})_{\text{max}} / 2\pi$. Cette fréquence caractéristique correspond par définition à la position en fréquence du maximum de puissance (\mathcal{P}_{max}). Comme l'ont montré [Samadi et al. \[2012, article inséré en page 257\]](#), le maximum de puissance et d'amplitude coïncident. Par ailleurs, il a été établi tant du point de vue observationnel [[Bedding and Kjeldsen, 2003](#); [Stello et al., 2008, 2009](#); [Kallinger et al., 2009](#)] que théorique [[Belkacem et al., 2011](#)], que ν_{max} varie étroitement avec la fréquence de coupure ν_c , laquelle varie selon la loi d'échelle $g/T_{\text{eff}}^{1/2}$. Si on injecte cette dernière loi d'échelle dans l'Eq. (6.7), on en déduit alors la relation :

$$\mathcal{P}_{\text{max}} \propto T_{\text{eff}}^6 g^{-2} . \quad (6.8)$$

Au vue de l'Eq. (6.8), on voit que \mathcal{P}_{max} croît, comme on l'attendait, avec le flux total $F_{\text{tot}} = \sigma T_{\text{eff}}^4$ tandis qu'il décroît lorsque g croît. Ceci explique donc *qualitativement* la loi d'échelle de la forme $\mathcal{P}_{\text{max}} \propto (L/M)^s \propto (T_{\text{eff}}^4/g)^s$ établie par [Samadi et al. \[2007\]](#).

6.2 Amplitude en terme de vitesse, V

Sur la base des calculs théoriques effectués par [Christensen-Dalsgaard and Frandsen \[1983\]](#), [Kjeldsen and Bedding \[1995\]](#) ont établi la première loi d'échelle théorique pour les amplitudes maximum des modes en termes de vitesse (V_{\max} par la suite). Cette loi d'échelle est de la forme $V_{\max} \propto (L/M)^s$ où la pente $s \simeq 1$. Les calculs théoriques effectués par [Christensen-Dalsgaard and Frandsen \[1983\]](#) ont supposé qu'il existe une forme d'équipartition d'énergie entre les modes et les éléments convectifs (voir Chap 3., Sect. 3.2.1). Cependant, une condition nécessaire (mais par nécessairement suffisante) pour que cette forme d'équipartition se maintienne est que l'amortissement des modes soit dominé par la viscosité turbulente. Toutefois, comme cela avait été discuté dans le Chap.3 – Sect. 3.2.1, il est peu probable que cela soit le cas.

Depuis la loi d'échelle proposée par [Kjeldsen and Bedding \[1995\]](#), d'autres lois d'échelle théoriques ont été proposées et comparées aux données en vitesse Doppler. Nous présentons ci-dessous celle établie par [Samadi et al. \[2007\]](#), article inséré en page 165] pour les étoiles de la séquence principale et celle établie par [Samadi et al. \[2012\]](#), article inséré en page 257] pour les stades plus évolués.

Nous rappelons que la moyenne quadratique de la vitesse d'un mode à la surface est donnée par la relation (voir Eq. (2.13)) :

$$v^2(\nu_{\text{osc}}, r) = \frac{\tau(\nu_{\text{osc}})}{2} \frac{\mathcal{P}(\nu_{\text{osc}})}{\mathcal{M}(\nu_{\text{osc},r})} \quad (6.9)$$

où τ correspond à la durée de vie du mode (laquelle est inversement égale au taux d'amortissement η), r le rayon au niveau de l'atmosphère où la mesure de vitesse s'effectue, et \mathcal{M} la masse du mode (Eq. (2.11)). Notons que la masse du mode doit être en principe évaluée au niveau de la couche où s'effectue la mesure de vitesse Doppler. Cependant cette couche n'est pas bien connue (voir Chap. 2, Sect. 2.2.3) ; aussi, à titre de simplification, on évaluera \mathcal{M} à la photosphère (i.e. en $T = T_{\text{eff}}$).

Pour le Soleil, la fréquence ν_{\max} pour laquelle ν atteint son maximum (V_{\max}) coïncide avec la fréquence correspondant au plateau observé au niveau des durées de vie τ [voir [Belkacem et al., 2011](#)]. Par ailleurs, il a été montré par [Samadi et al. \[2012\]](#) que \mathcal{P} ainsi que le rapport $(\mathcal{P}/\mathcal{M})$ atteignent leur maximum également à la fréquence ν_{\max} . Par conséquent, une loi d'échelle pour V_{\max} repose donc simplement sur l'existence de lois d'échelles sur τ_{\max} , \mathcal{P}_{\max} et \mathcal{M}_{\max} où τ_{\max} , \mathcal{P}_{\max} , et \mathcal{M}_{\max} correspondent respectivement aux valeurs prises par τ , \mathcal{P} , et \mathcal{M} à la fréquence $\nu = \nu_{\max}$.

Une loi d'échelle théorique pour $\tau_{\max} \propto T_{\text{eff}}^{-10.8} g^{0.3}$ a été établie par [Belkacem et al. \[2012\]](#), voir aussi la revue due à [Belkacem and Samadi \[2013\]](#). S'agissant de \mathcal{P}_{\max} , on a présenté dans la Sect. 6.1 des lois d'échelle qui diffèrent selon le choix adopté pour χ_k . Nous nous tournons donc maintenant sur \mathcal{M}_{\max} . Nous avons établi dans [Samadi et al. \[2012\]](#) que pour les étoiles sous-géantes et géantes rouges \mathcal{M}_{\max} varie comme $\Delta\nu^{-p}$ avec $p = 2.0 \pm 0.1$ et $\Delta\nu$ désigne la grande séparation que l'on a supposé varier comme $\sqrt{M/R^3}$. Par conséquent, \mathcal{M}_{\max} varie selon l'inverse de la densité moyenne, i.e. $\langle\rho\rangle \propto (M/R^3)$. Pour les étoiles de la séquence principale, les calculs effectués par [Samadi et al. \[2007\]](#) conduisent à une pente $p = 1.3 \pm 0.2$. Ces deux relations entre \mathcal{M}_{\max} et $\langle\rho\rangle$ ne sont pas encore bien comprises. Toutefois, ces relations montrent – comme on s'y attendait – que \mathcal{M} dépend bien de la stratification de l'étoile. Enfin, comme

l'amplitude d'un mode est inversement proportionnel à la racine carré de \mathcal{M} , on voit comment cette amplitude est liée à la stratification en densité de l'étoile.

Lorsque l'on combine la loi d'échelle $\tau_{\max} \propto T_{\text{eff}}^{-10.8} g^{0.3}$, la loi d'échelle $\mathcal{P}_{\max} \propto (L/M)^s$ et enfin la loi d'échelle pour \mathcal{M}_{\max} , on obtient en vertu de l'Eq. (6.9) la loi d'échelle suivante :

$$V_{\max} \propto T_{\text{eff}}^{-5.4} g^{0.15} \left(\frac{L}{M}\right)^{s/2} \left(\frac{M}{R^3}\right)^{p/4}, \quad (6.10)$$

où $p = 1.3$ pour les étoiles de la séquence principale et $p = 2$ pour les étoiles plus évoluées (sous-géantes et géantes rouges), et $s = 2.6$ lorsqu'une forme Lorentzienne est adoptée. Dans la mesure où la grande séparation $\Delta\nu$ varie typiquement comme $(M/R^3)^{1/2}$ [voir e.g. [White et al., 2011](#)], que ν_{\max} varie comme $g/T_{\text{eff}}^{1/2}$ et que (L/M) est proportionnel à $T_{\text{eff}}^{7/2}/\nu_{\max}$ [voir [Baudin et al., 2011a,b](#)], Eq. 6.10 peut-être reformulée en utilisant les indices sismiques ν_{\max} et $\Delta\nu$ ainsi que T_{eff} :

$$V_{\max} \propto T_{\text{eff}}^{7/4 s - 5.32} \nu_{\max}^{0.15 - s/2} \Delta\nu^{p/2}. \quad (6.11)$$

La loi d'échelle donnée par l'Eq. 6.11 est comparée sur la Fig. 6.2 avec les mesures Doppler obtenues jusqu'à présent depuis le sol. Lorsqu'une forme Lorentzienne est adoptée pour χ_k (ce qui implique $s = 2.6$), la loi d'échelle pour V_{\max} reproduit plutôt bien les mesures sismiques effectuées sur les étoiles situées sur la séquence principale (i.e. celles pour lesquelles $\nu_{\max} \gtrsim 200 \mu\text{Hz}$). Ce n'est en revanche pas le cas pour les étoiles plus évoluées pour lesquelles les valeurs théoriques sont systématiquement situées en dessous des mesures. Des raisons possibles expliquant cet écart sont avancées et discutées dans [Samadi et al. \[2012\]](#) ainsi que dans le Chap. 7.

6.3 Amplitude en terme d'intensité, $\delta L/L$

Les mesures sismiques réalisées depuis l'espace (e.g. CoRoT et *Kepler*) reposent uniquement sur des mesures photométriques de haute précision. Pour comparer les amplitudes théoriques avec les mesures en intensité, il est donc nécessaire de convertir les vitesses des modes en fluctuations d'intensité. On considère pour cela la relation de l'Eq. (2.17) qui lie variations bolométriques, δL , aux variations de température effective δT_{eff} . Il est donc maintenant nécessaire de relier $(\delta T_{\text{eff}}/T_{\text{eff}})_{\text{rms}}$ (ou de manière équivalente $(\delta L/L)_{\text{rms}}$) à la vitesse quadratique moyenne v_{rms} . Pour cela, on introduit par convenance le coefficient adimensionnel ζ défini de telle sorte que :

$$(\delta L/L)_{\text{rms}} = 4 \left(\frac{\delta T_{\text{eff}}}{T_{\text{eff}}}\right)_{\text{rms}} = \zeta (\delta L/L)_{\text{rms},\odot} \left(\frac{v_{\text{rms}}}{v_{\text{rms},\odot}}\right) \quad (6.12)$$

où $(\delta L/L)_{\text{rms},\odot} = 2.53 \pm 0.11$ ppm est le maximum des amplitudes bolométriques solaires [[Michel et al., 2009](#), article inséré en page 213], $T_{\text{eff},\odot} = 5777$ K la température effective du Soleil, et $v_{\text{rms},\odot} = 18.5 \pm 1.5$ cm/s le maximum des vitesses des modes solaires [[Samadi et al., 2010a](#), article inséré en page 231].

Définissons maintenant $(\delta L/L)_{\text{max}}$ comme le maximum atteint par $(\delta L/L)_{\text{rms}}$. On cherche ici à établir une loi d'échelle pour $(\delta L/L)_{\text{max}}$. Comme on le voit dans l'Eq. (6.12), nous avons besoin

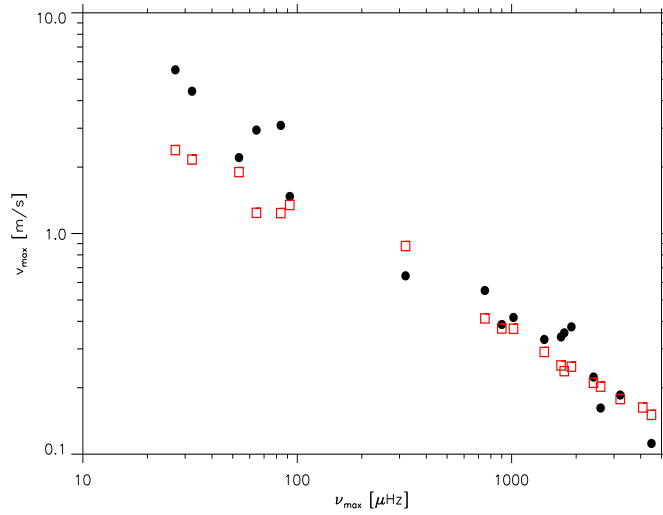


FIGURE 6.2 – Maximum des vitesses des modes V_{\max} en fonction de ν_{\max} . Les cercles pleins correspondent aux mesures sismiques tandis que les carrés rouges aux valeurs obtenues avec la loi d'échelle donnée par l'Eq. (6.11) en adoptant pour χ_k une forme Lorentzienne (ce qui implique $s = 2.6$). On a pris $p = 2.0$ pour les étoiles sous-géantes et géantes ($\nu_{\max} \lesssim 200 \mu\text{Hz}$) et $p = 1.3$ pour les étoiles de la séquence principale ($\nu_{\max} \gtrsim 200 \mu\text{Hz}$).

d'établir une loi d'échelle pour ζ dans la mesure où celle pour V_{rms} est donnée par l'Eq. (6.10) (ou de manière équivalente par l'Eq. (6.11)).

Un calcul consistant de la quantité ζ requierait de tenir compte de manière complète et réaliste les pertes d'énergie des modes. Ceci peut être effectué à l'aide de code de pulsation non-adiabatique prenant en compte le couplage entre oscillations, radiation et convection turbulente [voir à ce sujet la revue due à [Belkacem and Samadi, 2013](#)]. Cependant, de tels calculs ne sont pas triviaux et reposent encore sur de nombreuses simplifications. C'est la raison pour laquelle la relation quasi-adiabatique proposée par [Kjeldsen and Bedding \[1995\]](#) est généralement adoptée. En effet, si on suppose des modes adiabatiques ainsi qu'une atmosphère isotherme, on peut relier de manière aisée la vitesse V_{rms} d'un mode à la fluctuation d'intensité correspondante, δL . Cette approximation donne ainsi¹⁹ [voir [Kjeldsen and Bedding, 1995](#)] :

$$\zeta_{\text{K95}} = \sqrt{\frac{T_{\text{eff},\odot}}{T_{\text{eff}}}}. \quad (6.13)$$

Si on combine l' Eq. (6.13) avec l'Eq. (6.12), on obtient pour $(\delta L/L)_{\max}$ une loi d'échelle “quasi-adiabatique” :

$$(\delta L/L)_{\max} \propto T_{\text{eff}}^{-0.5} V_{\max}, \quad (6.14)$$

où la loi d'échelle pour V_{\max} est donnée par l'Eq. (6.11) (ou de manière équivalente par l'Eq. (6.10)).

19. La dérivation de l'Eq. (6.13) suppose que les modes sont propagatifs au niveau où ceux-ci sont mesurés. Toutefois, ce n'est pas le cas car les modes sont (en général) évanescents dans la partie visible de l'atmosphère.

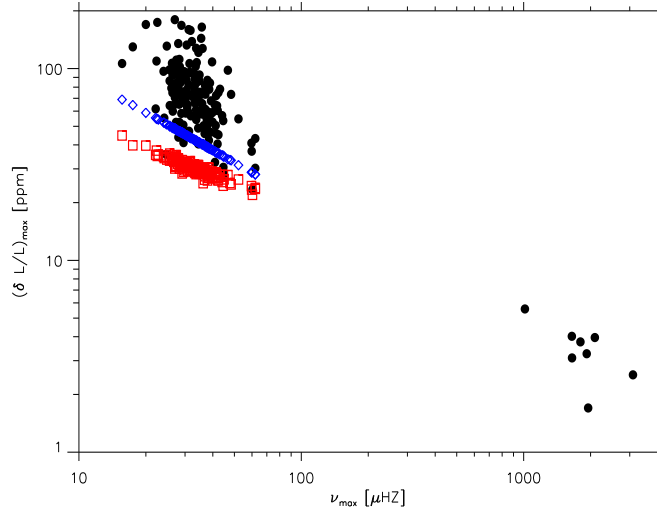


FIGURE 6.3 – Maximum des amplitudes bolométriques $(\delta L/L)_{\max}$ en fonction de ν_{\max} . Les cercles pleins situés en dessous de $\nu_{\max} = 200 \mu\text{Hz}$ correspondent aux mesures sismiques effectuées par [Baudin et al. \[2011a,b\]](#) sur un nombre important de géantes rouges observées par CoRoT, tandis que ceux situés au dessus $\nu_{\max} = 200 \mu\text{Hz}$ à des étoiles de la séquence principale observées avec CoRoT [voir [Baudin et al., 2011a,b](#)]. Les carrés rouges correspondent aux valeurs théoriques obtenues avec la loi d'échelle adiabatique donnée par l'Eq. (6.14) tandis que les diamants bleus à celles obtenues avec la loi d'échelle non-adiabatique donnée par l'Eq. (6.16).

Les amplitudes bolométriques calculées sur la base de l'Eq. (6.14) sont comparées dans la Fig. 6.3 avec les mesures sismiques effectuées par [Baudin et al. \[2011a,b\]](#) avec le satellite CoRoT pour des étoiles géantes rouges. Comme on peut le voir, la loi d'échelle “quasi-adiabatique” donnée de l'Eq. (6.14) sous-estime de manière importante les mesures sismiques fournies par l'instrument CoRoT.

Dans [Samadi et al. \[2012\]](#), nous avons calculé le coefficient ζ (Eq. (6.12)) en utilisant le code MAD permettant de résoudre les équations des modes non-adiabatiques [voir [Grigahcène et al., 2005](#)]. Ce calcul a permis d'établir que pour les étoiles évoluées (sous-géantes et géantes rouge) ζ varie selon la loi d'échelle :

$$\zeta_{\text{nad}} = \zeta_0 \left(\frac{L}{L_{\odot}} \frac{M_{\odot}}{M} \right)^{0.25}, \quad (6.15)$$

où $\zeta_0 = 0.59$. L'augmentation de ζ avec le rapport L/M n'est pas étonnant. En effet, les pertes d'énergies varient dimensionnellement comme L/M . Les étoiles évoluées sont caractérisées par des luminosités élevées. Par conséquent, on s'attend pour ces étoiles à un important écart à l'approximation quasi-adiabatique, autrement dit à un différence importante entre ζ_{nad} et ζ_{K95} .

Nous rappelons que L/M est proportionnel à $T_{\text{eff}}^{7/2}/\nu_{\max}$. Par conséquent, si on substitue l'Eq. (6.15) dans l'Eq. (6.12), on peut réécrire la loi d'échelle non-adiabatique pour $(\delta L/L)_{\max}$

comme²⁰

$$(\delta L/L)_{\max} \propto T_{\text{eff}}^{1.75} \nu_{\max}^{-0.25} V_{\max}, \quad (6.16)$$

où V_{\max} est donné par l'Eq. (6.11) avec $p = 2$ (cas des étoiles évoluées). Cette loi d'échelle est comparée sur la Fig. 6.3 avec les mesures sismiques effectuées avec les observations CoRoT. Comme on le voit sur la figure, les différences entre observations sont réduites par rapport au cas de la loi d'échelle adiabatique (Eq. (6.14)). Cependant, les différences résiduelles demeurent importantes. Des raisons possibles expliquant celles-ci sont discutées dans [Samadi *et al.*, 2012, voir aussi Chap. 7].

20. Cette loi d'échelle est valide uniquement pour les sous-géantes et géantes rouges, car on a utilisé l'Eq. (6.15) qui est valable uniquement pour $(L/M) \gtrsim 10$.

Chapitre 7

Discussion et perspectives

Tout d'abord, si vous avez lu tout ce qui précède articles inclus, bravo ! ... hum, mais peut-être êtes vous passé directement de l'introduction à ce chapitre ? Dans ce cas la discussion qui suit va en partie vous échapper alors retournez *fissa* en arrière !

7.1 Modélisation du forçage par la convection turbulente

7.1.1 Bases théoriques du modèle d'excitation stochastique

La modélisation des amplitudes des oscillations de type solaires reste très simplifiée puisque elle repose sur un certain nombre d'approximation et d'hypothèses, et, comme on va le rappeler ci-dessous, certaines sont partiellement ou complètement mises en défaut.

La prise en compte du forçage thermique (associé aux fluctuations d'entropie) repose actuellement sur l'hypothèse que les fluctuations d'entropie se comportent comme un scalaire passif (voir Chap. 3, Sect. 3.1.3). Par voie de conséquence, les termes croisés entre le terme de Reynolds et le terme d'entropie s'annulent. Supposer que les fluctuations d'entropie se comportent comme un scalaire passif est une *hypothèse forte* qui est mis à défaut dans la région super-adiabatique (là où le forçage thermique est maximal). En effet, rappelons d'abord qu'un scalaire passif vérifie par définition une équation de diffusion (voir Eq. (3.19)). Cette équation est rigoureusement valide lorsque le transfert d'énergie peut être traité dans l'approximation de diffusion et lorsque l'approximation de Bousinesq est applicable (impliquant donc un milieu quasi incompressible). Or, la région super-adiabatique correspond à la région de transition entre un milieu optiquement épais et un milieu optiquement mince, où, par conséquent, le flux radiatif ne peut plus être traité dans l'approximation de diffusion. Par ailleurs, dans cette région, le fluide cesse d'être quasi-incompressible. Par conséquent, dans cette région l'hypothèse d'un scalaire passif est clairement mis à défaut. S'affranchir de cette hypothèse, nécessiterait de prendre en compte de manière complète les pertes d'énergies, ce qui en dernier ressort nécessiterait de résoudre l'équation d'énergie de manière couplée avec l'équation d'onde inhomogène (voir Chap. 3, Eq. (3.1.1)). Dans ces conditions, la quantification du forçage ne devrait pas avoir de solution analytique et devrait donc être effectuée de manière numérique, par exemple en s'inspirant de l'approche suivie par Wachter and Kosovichev [2005] dans le cas de la propagation des ondes acoustiques à la surface du Soleil.

Une autre hypothèse importante concerne la séparation d'échelle. Celle-ci suppose que les éléments convectifs qui contribuent effectivement au forçage ont des tailles significativement plus petites que l'onde acoustique forcée par ceux-ci (voir Chap. 3, Sect. 3.1.4). Cette approximation est mise à défaut principalement pour les modes de haute fréquence et à nouveau dans la région super-adiabatique où le nombre de Mach turbulent atteint des valeurs élevées. Elle expliquerait en partie le désaccord observé à haute fréquence dans le cas du Soleil (voir Chap. 4, Sect. 4.1.2) et surtout dans le cas de l'étoile CoRoT HD 49933 (voir Chap. 5, Sect. 5.3). Cette séparation d'échelle peut cependant être évitée si le spectre d'énergie associé à la turbulence est couplé de manière appropriée avec la dépendance spatiale des modes (travail toujours en cours ...).

Enfin, comme on l'a vu dans le Chap. 4 Sect. 4.2, le modèle d'excitation stochastique repose encore sur une hypothèse concernant les produits de corrélation à deux points. En effet, on suppose que ces produits varient en fonction des longueurs de corrélation temporelle et spatiale comme les produits de corrélation donnés par l'approximation quasi-normale (voir Eq. (4.14) pour le produit de corrélation associé au terme de Reynolds). Cette hypothèse a été sommairement testée dans [Belkacem et al. \[2006b\]](#), article inséré en page 157]. En effet, seule la dépendance par rapport à la longueur de corrélation spatiale a été évaluée à l'aide d'une simulation hydrodynamique 3D solaire. Si cette approximation est qualitativement satisfaisante aux petites échelles, il n'en est pas du tout le cas pour les échelles comparables à celles des granules. Une étude numérique plus approfondie est nécessaire ; celle-ci devra en particulier évaluer l'impact de l'approximation actuelle sur les taux d'excitation. Enfin, la possibilité d'améliorer la modélisation théorique des produits à deux points doit être explorée.

7.1.2 Amplitudes des modes dans les géantes rouges

Pour les étoiles géantes rouges, l'écart constaté entre calculs théoriques et observations n'est pas encore bien compris (voir Chap. 6, Sect. 6.2 et 6.3). L'origine la plus probable viendrait de l'écart à l'hypothèse adiabatique adoptée pour calculer les modes propres. En effet, le calcul du forçage repose toujours sur l'hypothèse de modes adiabatiques. Or les simulations hydrodynamiques 3D montrent que le mode dominant piégé dans celles-ci s'écarte de manière importante, dans la région super-adiabatique, des modes équivalents calculés dans l'hypothèse adiabatique [[Samadi et al., 2013](#)]. Cet écart est comme on l'attend d'autant plus grand que l'étoile est évoluée (i.e. que le rapport L/M est élevé). Toutefois, la représentativité des modes piégés dans ces simulations se pose dans la mesure où ceux-ci s'écartent du régime linéaire [c.f. [Samadi et al., 2013](#)].

La résolution la plus complète et consistante possible consisterait à résoudre de manière couplée l'équation d'énergie avec l'équation d'onde inhomogène (comme on l'avait déjà noté plus haut s'agissant du terme de forçage thermique). La résolution de ces équations ne devrait être possible que de manière numérique et à l'aide de modèles de fermeture adaptés. Une alternative consiste à résoudre de manière découplée l'équation d'onde inhomogène (en supposant à ce niveau des modes adiabatiques) et l'équation d'onde homogène (sans terme de forçage mais en supposant des modes non-adiabatiques). Tandis que la résolution de la première utilise, depuis [Samadi et al. \[2007\]](#), des modèles "raccordés" (voir Chap. 5, Sect. 5.2), la seconde repose actuellement sur les codes non-adiabatiques qui tiennent en compte le couplage entre convection et pulsation, tels que le code MAD [[Grigahcène et al., 2005](#)] ou le code de Gough & Balmforth

[Gough, 1976, 1977; Balmforth, 1992c,b,a] ou celui de Xiong *et al.* [2000].

Hormis celui de Xiong *et al.* [2000], ces codes non-adiabatiques se basent sur la théorie de la longueur de mélange mais ne sont pas d'accord s'agissant des processus d'amortissement dominants [voir Belkacem and Samadi, 2013]. Une tentative de contraindre cette approche avec des simulations hydrodynamiques 3D a été proposée par Dupret *et al.* [2006a, voir aussi Dupret *et al.* [2006b]]. Les modes propres non-adiabatiques calculés avec le code MAD montrent des différences dans la partie supérieure de la région d'excitation. Cependant, contrairement aux cas des modes piégés dans les simulations hydrodynamiques 3D, ces différences ont un impact négligeable sur les taux d'excitation, ne permettant pas d'expliquer l'écart qui reste avec les observations effectuées sur les géantes rouges [voir la discussion dans Samadi *et al.*, 2013].

Toutefois, si le code MAD permet de reproduire correctement les lois d'échelles observées pour la durée de vie des modes [Belkacem *et al.*, 2012] et de réduire l'écart avec les amplitudes observées sur les géantes rouges (voir Chap. 6), cela se fait au prix de l'ajustement d'un paramètre libre²¹. En effet, ce dernier est ajusté d'un modèle à l'autre de manière à ce que pour un modèle donné, le plateau observé sur les durées de vie coïncide avec la fréquence du maximum [c.f. Belkacem *et al.*, 2012]. Cela enlève tout caractère prédictif à cette modélisation. Il s'agit donc de manière générale de progresser sur cette modélisation, tant du point de vue de la compréhension physique des processus dominant l'amortissement que de leur modélisation. Pour cela l'utilisation des simulations hydrodynamiques 3D adaptées est essentielle, d'une part pour permettre d'identifier les processus vraiment à l'oeuvre, et d'autre part pour guider la modélisation de ces processus en vue de leur introduction dans un code de pulsation.

Malgré ses relatifs succès pour les étoiles de la séquence principale, il n'est pas non plus exclu que pour une raison ou une autre le modèle de convection turbulente adoptée jusqu'à présent pour calculer le forçage (voir Chap. 4) soit mis à défaut pour les stades évolués. Un moyen de s'affranchir de ce modèle et donc tester cette hypothèse serait d'utiliser l'approche *ab initio* proposée par Nordlund and Stein [2001, voir Chap. 3 Sect. 3.2.2]. Si celle-ci se base toutefois sur des modes adiabatiques, elle permet avec un nombre limité d'hypothèses et d'approximations de calculer les taux d'excitation. Aussi, la mise en oeuvre de cette méthode fournirait un diagnostic supplémentaire.

Les données CoRoT et *Kepler* permettent de détecter des oscillations de type solaire dans un nombre important d'étoiles géantes rouges. Si la plus part de ces modes ont les amplitudes attendues, il n'est pas de même sur certaines géantes rouges. Celles-ci présentent des amplitudes plus faibles [Mosser *et al.*, 2012a]. Plus intrigant encore, nombreuses d'entre-elles ont des modes $\ell = 1$ avec des amplitudes relativement plus faibles que celles des modes radiaux [Mosser *et al.*, 2012a]. Ce fait observationnel n'est pas encore compris. La question est de savoir si ce fait est lié à l'inertie des modes ou une particularité des processus d'excitation ou d'amortissement.

Ces géantes rouges montrent également la présence de nombreux modes mixtes [Beck *et al.*, 2011; Bedding *et al.*, 2011; Mosser *et al.*, 2012b]. Ces modes, qui se propagent à la manière des modes p à la surface, se comportent comme des modes g à l'intérieur. De ce fait, ils permettent de sonder les coeurs de ces étoiles. Ils permettent notamment de distinguer les étoiles du clump (qui brûlent leur hélium dans le coeur), des étoiles géantes rouges qui brûlent en-

21. Ce paramètre est introduit dans l'équation pour les fluctuations lagrangienne de l'entropie pour éliminer les oscillations non physiques des fonctions propres [voir Grigahcène *et al.*, 2005].

core l'hydrogène en couche ; ou encore de sonder la rotation dans les couches les plus internes de l'étoile. Comme l'ont montré [Mosser et al. \[2012a\]](#), leur amplitudes ont une particularité étonnante : pour un ordre radial donné, la somme quadratique de leurs amplitudes égale approximativement l'amplitude du mode radial associé. Autrement dit il semble qu'il y'ait une forme d'équipartition d'énergie entre modes p pures et modes mixtes. Comme ces derniers se comportent comme des modes p pures dans l'enveloppe convective, on peut donc penser qu'ils sont excités et amortis de la même façon que leurs homologues p. Cela reste toutefois à vérifier. Si cela est effectivement le cas, alors cela signifierait que les inerties (ou masses) de ces modes assurent cette forme d'équipartition, pour une raison qui reste à expliquer.

7.1.3 Oscillations stochastiquement excitées dans les étoiles massives et les δ Scuti

La généralisation du formalisme d'excitation aux cas des modes non-radiaux a permis de traiter le cas de l'excitation des modes g dans le Soleil ainsi que dans d'autres étoiles (voir Chap. 3 Sect. 3.3). Nous avons montré dans [Samadi et al. \[2009\]](#), article inséré en page 239] que les étoiles massives de l'ordre de $10 M_{\odot}$ pouvait présenter des modes g avec des amplitudes non négligeables. [Neiner et al. \[2012\]](#) ont annoncé la détection de tels modes dans une étoile B. Toutefois, les amplitudes mesurées s'avèrent être plus grande d'un facteur un à deux par rapport à nos estimations [[Samadi et al., 2009](#)]. Ces estimations théoriques sont encore très incertaines car elles s'appuient sur la théorie de la longueur de mélange. Afin de consolider ces calculs, il est donc nécessaire d'utiliser des résultats de simulations hydrodynamiques 3D à la manière où cela avait été fait par [Belkacem et al. \[2009c\]](#), article inséré en page 199] dans le cas des modes g solaires. Parallèlement, d'autres raisons permettant d'expliquer les amplitudes observées doivent être explorées [c.f. [Neiner et al., 2012](#)].

La détection d'oscillations de type solaire a été annoncées par [Belkacem et al. \[2009d\]](#) dans une étoile massive déjà connue comme étant un pulsateur classique (l'étoile V1448 Aql). Cette détection trouve son support théorique chez [Belkacem et al. \[2009a\]](#) sans que toutefois le niveau des amplitudes mesurées puisse être expliqué. Depuis, des oscillations analogues ont été détectées dans d'autres étoiles massives [c.f. [Degroote et al., 2009, 2010](#)]. Des oscillations du même type auraient également été détectées par [Antoci et al. \[2011\]](#) sur étoile du type δ Scuti observées par *Kepler*. Si cette détection se confirme, elle confirmerait les prédictions théoriques antérieures [[Samadi et al., 2002](#), article inséré en page 87]

De manière générale, la découverte d'oscillations stochastiquement excitées (modes p ou g) dans les pulsateurs classiques ou les étoiles massives ouvre la voie vers une amélioration de notre connaissance de leur structure interne, notamment de leur zones convectives internes et superficielles.

7.1.4 Liens entre observables et physique des modes

Le Chap. 2 a mis en lumière les liens qui existent entre observables et caractéristiques intrinsèques des modes. Comme on l'a vu ces liens sont complexes à plusieurs titres.

Tout d'abord, il est nécessaire de modéliser de manière précise l'inertie et la masse d'un mode. Ceci nécessite des modèles d'équilibres réalistes, en particulier au niveau des couches

superficielles (voir aussi Chap. 5 Sect. 5.2), mais aussi la prise en compte du caractère non-adiabatique des modes, ce qui n'est pas le cas actuellement.

D'autre part, il est fondamental de préciser le lien entre la technique de mesure et les propriétés des modes mesurés à la surface de l'étoile (notamment du Soleil). Ce lien est particulièrement compliqué dans le cas des mesures Doppler effectuées sur les étoiles autres que le Soleil car plusieurs raies spectrales contribuent à la mesure dans une proportion qui reste à déterminer. Même si le cas du Soleil est plus simple du fait de l'utilisation d'une unique raie spectrale, il reste, comme on l'a vu, encore des désaccords incompris lorsque l'on compare les amplitudes déduites des mesures Doppler effectuées sur différents instruments dédiés à l'héliosismologie.

7.2 Améliorer les modèles de structure stellaire

Les modèles standards de structure et d'évolution stellaire sont encore très utilisés dans divers domaines de l'astrophysique. Outre évidemment la physique stellaire, c'est en particulier le cas aussi dans l'étude des populations stellaires et l'étude des planètes extrasolaires.

Un moyen unique pour sonder les intérieurs stellaires, et par là contraindre les modèles de structure et d'évolution des étoiles, consiste à utiliser la sismologie. Le diagnostic fourni par cette technique est cependant très sensible à la façon dont les couches de surfaces sont modélisées. En effet, la comparaison des fréquences des modes solaires avec les fréquences théoriques montre une différence qui croît avec la fréquence. Plus la fréquence d'un mode est élevée plus le mode est confiné à la surface. La différence croissante entre fréquences observées et théoriques reflète donc l'imperfection avec laquelle les modèles standards traitent les couches superficielles (voir Chap. 5) mais aussi à la façon de traiter les pulsations [voir e.g. Houdek, 2010; Grigahcène *et al.*, 2012]. Ce phénomène, que l'on désigne sous le nom d' "effet de surface", affecte la précision des mesures obtenues par le biais des mesures sismiques, ce qui en dernier ressort limite la portée du diagnostic sismique.

Comme on l'a vu dans le Chap. 5, les modèles d'évolution stellaire reposent sur des descriptions très approximatives des processus de transports, en particulier la convection dans les couches superficielles. En particulier, la majorité des modèles stellaires utilisés négligent la présence de la pression turbulente, dont l'importance relative croît à la surface des étoiles. Cette pression s'ajoute à la pression du gaz et modifie la structure de la surface. Comme l'ont montré Rosenthal *et al.* [1999], l'ignorer contribue de manière notable aux effets de surface évoqués plus haut.

Les simulations hydrodynamiques 3D des couches superficielles des étoiles sont actuellement les approches les plus réalistes qui soient. Toutefois, ces simulations lourdes sont difficiles à mettre en oeuvre et par conséquent ne permettent pas d'envisager la modélisation de la globalité de l'étoile, ni son évolution dans le temps. En revanche, couplées avec les modèles 1D d'intérieur stellaire, elles permettent de résoudre le problème de la modélisation des couches de surfaces tout en bénéficiant des intérêts des modèles 1D d'intérieur. Ce procédé consiste en fait à remplacer les couches superficielles des modèles 1D de structure stellaire par la stratification des couches de surface issues des simulations hydrodynamiques 3D. Il s'agit des modèles "hybrides" que l'on a décrit dans le Chap. 5.

Cependant, les simulations hydrodynamiques 3D disponibles étant trop peu nombreuses, il n'est pas possible de disposer d'une densité suffisante, ni pour un jeu suffisant de compositions

chimiques.

[Kjeldsen et al. \[2008b\]](#) ont proposé une méthode empirique pour corriger les fréquences des modes d’oscillation des effets de surface. Cependant cette méthode analytique bien que simple fait appel à un jeu de paramètres libres étalonnés à l’aide des données sismiques solaires. Une question que permettrait d’aborder les modèles “hybrides” est de savoir si cette forme analytique ainsi que les valeurs des paramètres étalonnés ont un caractère universel ou non ²².

Une alternative, à portée plus générale, consisterait à construire des modèles “hybrides” à partir d’une grille de simulations hydrodynamiques 3D pour des paramètres stellaires quelconques. Pour cela il s’agirait d’établir une procédure permettant d’effectuer une interpolation appropriée entre les modèles 3D disponibles. Les modèles hybrides ainsi construits seront utilisés pour calculer les taux d’excitation, d’amortissement et fréquence des oscillations de type solaire. La comparaison de ces calculs théoriques avec les observations permettra en retour de tester la qualité des modèles hybrides.

Une fois validée, la mise en oeuvre des modèles hybrides permettront de modéliser de manière réaliste les effets de surfaces et améliorer ainsi la détermination sismique des paramètres des étoiles. De plus la possibilité de calculer à la demande des modèles hybrides rendra l’utilisation de ce genre de modèles accessible à une large communauté.

Notons que des alternatives aux modèles hybrides existent. L’une d’elle consiste à inclure l’approche phénoménologique proposée par [Spiegel \[1963\]](#) et permettant de “mimer” la nature non-locale de la convection turbulente. Dans cette approche, la solution locale est considérée comme un terme source pour la solution non-locale obtenue en appliquant une loi de conservation pour le flux convectif. Dans un régime stationnaire, la solution non-locale pour le flux convectif s’écrit [voir [Spiegel, 1963](#)] :

$$\frac{d^2 F_{c,nl}}{d\xi^2} = b^2 (F_{t,nl} - F_{t,l}) \quad (7.1)$$

où $F_{t,l}$ est la solution locale pour le flux convectif (celui donné dans le cadre de la MLT), $F_{t,nl}$ sa solution non-locale, $d\xi = dr/l$, l la longueur de mélange et a est un paramètre libre. Une équation différentielle similaire est adoptée pour la pression turbulente, cette dernière faisant intervenir un paramètre libre b . Cette approche a pour l’instant été seulement implémentée par [Gough & Balmforth \[Gough, 1976, 1977; Balmforth, 1992c,b,a\]](#) dans des modèles d’enveloppe. De par sa nature non-locale, elle tient naturellement compte de la pénétration convective aux extrémités des régions convectives. Cette approche ne permet toutefois pas de remédier aux autres difficultés rencontrées dans la région super-adiabatique. Enfin, elle fait appel aux paramètres a et b qui sont susceptibles de varier le long du diagramme HR.

Une seconde approche plus consistante mais aussi plus difficile consisterait à développer un modèle de type “Reynolds stress”. Dans cette approche utilisée dans nombreuses applications en hydrodynamique, on considère l’équation de Navier Stokes moyennée horizontalement. Combiné avec l’équation d’énergie, l’équation d’état et l’équation de conservation de la masse, on forme alors un jeu d’équations 1D et temps dépendant [voir détails dans [Kupka, 1999; Kupka and Montgomery, 2002](#)]. Toutefois, pour être à même de fermer le système il est nécessaire d’adopter des modèles de fermeture adaptées aux cas des étoiles considérées, tels que ceux proposés par [Canuto and Dubovikov \[1998\]](#). Une fois fermées, ces équations sont résolues dans le

22. A ce sujet des résultats préliminaires ont été présentés dans [Goupil et al. \[2011\]](#).

temps jusqu'à atteindre la solution d'équilibre qui fournit alors le modèle d'équilibre pour la ou les régions convectives à un état donné de l'évolution stellaire (cet état étant fixé principalement par le brûlage des éléments au coeur). Cette approche tient compte de manière consistante de la nature non-locale de la convection. Elle a été appliquée avec succès par [Kupka and Montgomery \[2002\]](#) aux cas des étoiles de type A. Cependant le modèle de fermeture adoptée s'avère inapproprié pour les étoiles plus froides (type F ou plus froide), pour lesquelles la convection est plus efficace [voir [Kupka, 2007](#)]. Il s'agit donc de développer des modèles de fermetures adaptées, mais ça n'est pas une mince affaire.... Là encore les simulations hydrodynamiques 3D représentent un outil indispensable pour permettre à discriminer entre les différents modèles proposés ou qui seront développés dans l'avenir.

7.3 Perspectives observationnelles

7.3.1 CoRoT et Kepler

La mission spatiale CoRoT (CNES), lancée le 27 décembre 2006, est suffisamment précise pour détecter des oscillations de type solaire aussi faible que celles qui ont été détectées dans le Soleil il y'a maintenant plus de quarante ans [[Michel et al., 2008](#)]. Par ailleurs, du fait des observations longues (jusqu'à 150 jours) et continues qu'elle fournit, il a été possible pour la première fois avec CoRoT de mesurer *directement* la largeur (ou durée de vie) des modes [voir e.g. [Appourchaux et al., 2008](#)]. A la manière à ce qui a été fait par le passé avec le Soleil, il est donc depuis possible de contraindre simultanément et (quasi) indépendamment les processus d'excitation et d'amortissement des oscillations de type solaire, et par leur biais d'étudier la convection turbulente dans les étoiles ainsi que la physique des modes.

La mission spatiale *Kepler* (NASA) a suivi les pas de CoRoT à la suite de son lancement le 7 mars 2009. Grâce à leur qualité photométrique exceptionnelle et à la continuité à long terme des observations disponibles, ces deux missions permettent de détecter des modes de type solaire et d'en mesurer fréquences, amplitudes et durées de vie, et ceci dans une variété d'étoiles avec des caractéristiques diverses concernant leur statut évolutif, température effective, gravité de surface, composition chimique, champ magnétique, rotation etc. Ces observations ont déjà fourni des résultats majeurs [voir les revues dues à [Christensen-Dalsgaard and Thompson, 2011](#); [Michel and Baglin, 2012](#)]. Elles permettent d'envisager à terme des avancées prodigieuses sur la connaissance des intérieurs stellaires, en particulier des processus dynamiques qui y prennent place. Comme le disait je ne sais plus qui, on vit donc une époque *formidabile* !

Si on en revient à l'étude les amplitudes des modes, la poursuite de ces deux missions va nous permettre d'avancer encore sur l'étude de la convection turbulente et les phénomènes de couplage entre convection et oscillation. Mais, ces missions devraient nous permettre d'aborder les nouveaux sujets d'études avancés ci-dessous.

Certains pulsateurs de type solaire sont des étoiles jeunes présentant un haut niveau d'activité (par exemple HD 49933, HD 181420, HD 175726, HD 181906, ...). L'effet du champ magnétique sur les amplitudes des oscillations de type solaire a jusqu'à présent été ignoré. Un champ magnétique fort peut partiellement inhiber le transport convectif [c.f e.g. [Proctor and Weiss, 1982](#); [Vögler et al., 2005](#)]. Par ailleurs, un champ fort peut changer significativement la distribution spatiale d'énergie cinétique contenue dans la turbulence à petites échelles, rédui-

sant ainsi l'efficacité du forçage par la convection turbulente, en particulier à haute fréquence [c.f. [Jacoutot et al., 2008](#)]. A cet égard l'annonce par [Garcia et al. \[2010\]](#) de la découverte d'un cycle d'activité sur l'étoile CoRoT HD 49933 est particulièrement intéressante puisqu'elle montre qu'un cycle d'activité analogue à celui du Soleil existe et influence à la fois fréquences et amplitudes des modes. Enfin, l'étude menée par [Chaplin et al. \[2011\]](#) avec les données *Kepler* montre le lien entre niveau d'activité et amplitudes des modes. La mesure des durées de vie des modes au cours du temps permettrait de savoir si les variations observées des amplitudes ont un lien avec des variations du forçage ou de l'amortissement, ou sont simplement le fait de l'évolution des propriétés de la cavité stellaire.

Les étoiles plus jeunes que le Soleil sont en général des rotateurs plus rapides. [Belkacem et al. \[2009b\]](#) ont montré que la rotation ajoutait des termes additionnels de forçage. Cependant, pour les rotateurs modérés comme HD 49933 ces termes sont négligeables devant le terme de Reynolds ou même le terme de forçage thermique. En revanche, la présence de rotation modifie les propriétés des fonctions propres. A très basse fréquence ceci induit des taux d'excitation différents entre modes de nombre azimutal m différents [voir [Belkacem et al., 2009b](#)]. Pour un rotateur modéré comme HD 49933 l'effet demeure toutefois in-délectable. La durée et la qualité des données *Kepler* laissent cependant espérer la détection d'un tel effet, en particulier sur des rotateurs plus rapides que HD 49933.

7.3.2 et après ?

L'après CoRoT et *Kepler* est encore incertain en terme programmatique. Le projet de mission spatiale PLATO (ESA), s'il est sélectionné, représentera une relève ambitieuse. En effet, cette mission a pour objectif, *double*, de détecter – via la technique des transits – des planètes extra-solaires notamment des planètes analogues à la Terre située dans la zone “habitable” et de caractériser – via la sismologie stellaire – les propriétés (age, masse ... etc) des étoiles associées aux planètes détectées. Les deux techniques (transit planétaire et analyse sismique) qui seront utilisées *simultanément* sur les mêmes objets, reposeront sur des mesures photométriques de précision supérieure à celle atteinte par CoRoT et *Kepler* (à une magnitude donnée). Elles permettront d'étudier les systèmes planètes-étoiles grâce à l'apport essentiel de la sismologie.

Grâce a son très grand champ, elle atteindra son objectif sur des étoiles beaucoup plus brillantes que celles sur lesquelles CoRoT et *Kepler* sont capable de détecter des planètes. Ceci permettra de confirmer au sol la présente de candidats planètes mais aussi d'effectuer des observations plus directes des systèmes planètes-étoiles. La mission PLATO couvrira près de 50 % de la voûte céleste. Ceci permettra d'étudier un nombre gigantesque d'étoiles variées, notamment des étoiles situées dans des amas. Par rapport aux missions antérieures, cela représentera un saut quantitatif de plusieurs ordres de grandeur en terme de nombre de cibles.

Le saut quantitatif par rapport aux missions CoRoT et *Kepler* laisse naturellement espérer un saut qualitatif pour l'étude des systèmes exo-planétaires ainsi que la physique stellaire et l'étude des populations stellaires.

Après avoir passé différentes étapes de sélection, plus ou moins heureuses ... , PLATO reste en compétition pour la sélection d'une mission M3 par l'ESA en novembre 2013 pour un lancement prévu vers 2022.

En parallèle à ce projet, d'autres projets spatiaux analogues sont à l'étude. Comme les projets TESS (NASA), PLAVI (ESA), KEHOPS (ESA) Si le projet TESS (NASA) est d'ambi-

tion analogue à PLATO, les autres restent plus modestes, mais tout aussi incertains en terme de sélection.

Références bibliographiques

- V. Antoci, G. Handler, T. L. Campante, A. O. Thygesen, A. Moya, T. Kallinger, D. Stello, A. Grigahcène, H. Kjeldsen, T. R. Bedding, T. Lüftinger, J. Christensen-Dalsgaard, G. Cantanaro, A. Frasca, P. De Cat, K. Uytterhoeven, H. Bruntt, G. Houdek, D. W. Kurtz, P. Lenz, A. Kaiser, J. van Cleve, C. Allen, and B. D. Clarke. The excitation of solar-like oscillations in a δ Sct star by efficient envelope convection. *Nature*, 477 :570–573, September 2011.
- T. Appourchaux, E. Michel, M. Auvergne, A. Baglin, T. Toutain, F. Baudin, O. Benomar, W. J. Chaplin, S. Deheuvels, R. Samadi, G. A. Verner, P. Boumier, R. A. García, B. Mosser, J.-C. Hurlot, J. Ballot, C. Barban, Y. Elsworth, S. J. Jiménez-Reyes, H. Kjeldsen, C. Régulo, and I. W. Roxburgh. CoRoT sounds the stars : p-mode parameters of Sun-like oscillations on HD 49933. *A&A*, 488 :705–714, September 2008.
- J. Ballot, C. Barban, and C. van't Veer-Menneret. Visibilities and bolometric corrections for stellar oscillation modes observed by Kepler. *A&A*, 531 :A124, July 2011.
- N. J. Balmforth. Solar pulsational stability - part three - acoustical excitation by turbulent convection. *MNRAS*, 255 :639, April 1992.
- N. J. Balmforth. Solar pulsational stability - part two - pulsation frequencies. *MNRAS*, 255 :632, April 1992.
- N. J. Balmforth. Solar pulsational stability. i - pulsation-mode thermodynamics. *MNRAS*, 255 :603–649, April 1992.
- S. Basu and H. M. Antia. Helioseismic Test of Stellar Convection Theories. In R. K. Ulrich, E. J. Rhodes, Jr., and W. Dappen, editors, *GONG 1994. Helio- and Astro-Seismology from the Earth and Space*, volume 76 of *Astronomical Society of the Pacific Conference Series*, page 649, 1995.
- G. K. Batchelor. *The theory of homogeneous turbulence*. University Press, 1970.
- F. Baudin, R. Samadi, M.-J. Goupil, T. Appourchaux, C. Barban, P. Boumier, W. J. Chaplin, and P. Gouttebroze. Inferred acoustic rates of solar p modes from several helioseismic instruments. *A&A*, 433 :349–356, April 2005.
- F. Baudin, C. Barban, K. Belkacem, S. Hekker, T. Morel, R. Samadi, O. Benomar, M.-J. Goupil, F. Carrier, J. Ballot, S. Deheuvels, J. De Ridder, A. P. Hatzes, T. Kallinger, and W. W. Weiss. Amplitudes and lifetimes of solar-like oscillations observed by CoRoT. Red-giant versus main-sequence stars. *A&A*, 529 :A84, May 2011.

- F. Baudin, C. Barban, K. Belkacem, S. Hekker, T. Morel, R. Samadi, O. Benomar, M.-J. Goupil, F. Carrier, J. Ballot, S. Deheuvels, J. De Ridder, A. P. Hatzes, T. Kallinger, and W. W. Weiss. Amplitudes and lifetimes of solar-like oscillations observed by CoRoT (Corrigendum). Red-giant versus main-sequence stars. *A&A*, 535 :C1, November 2011.
- P. G. Beck, T. R. Bedding, B. Mosser, D. Stello, R. A. Garcia, T. Kallinger, S. Hekker, Y. Elsworth, S. Frandsen, F. Carrier, J. De Ridder, C. Aerts, T. R. White, D. Huber, M.-A. Dupret, J. Montalbán, A. Miglio, A. Noels, W. J. Chaplin, H. Kjeldsen, J. Christensen-Dalsgaard, R. L. Gilliland, T. M. Brown, S. D. Kawaler, S. Mathur, and J. M. Jenkins. Kepler Detected Gravity-Mode Period Spacings in a Red Giant Star. *Science*, 332 :205–, April 2011.
- T. R. Bedding and H. Kjeldsen. Solar-like Oscillations. *Publications of the Astronomical Society of Australia*, 20 :203–212, 2003.
- T. R. Bedding and H. Kjeldsen. Observations of solar-like oscillations. *Communications in Asteroseismology*, 150 :106, June 2007.
- T. R. Bedding, B. Mosser, D. Huber, J. Montalbán, P. Beck, J. Christensen-Dalsgaard, Y. P. Elsworth, R. A. García, A. Miglio, D. Stello, T. R. White, J. De Ridder, S. Hekker, C. Aerts, C. Barban, K. Belkacem, A.-M. Broomhall, T. M. Brown, D. L. Buzasi, F. Carrier, W. J. Chaplin, M. P. di Mauro, M.-A. Dupret, S. Frandsen, R. L. Gilliland, M.-J. Goupil, J. M. Jenkins, T. Kallinger, S. Kawaler, H. Kjeldsen, S. Mathur, A. Noels, V. S. Aguirre, and P. Ventura. Gravity modes as a way to distinguish between hydrogen- and helium-burning red giant stars. *Nature*, 471 :608–611, March 2011.
- K. Belkacem and R. Samadi. *Connections between stellar oscillations and turbulent convection*, volume in press of *Lecture Notes in Physics*, Berlin Springer Verlag. Springer Verlag, 2013.
- K. Belkacem, R. Samadi, M. J. Goupil, and F. Kupka. A closure model with plumes. I. The solar convection. *A&A*, 460 :173–182, December 2006.
- K. Belkacem, R. Samadi, M. J. Goupil, F. Kupka, and F. Baudin. A closure model with plumes. II. Application to the stochastic excitation of solar p modes. *A&A*, 460 :183–190, December 2006.
- K. Belkacem, R. Samadi, M.-J. Goupil, and M.-A. Dupret. Stochastic excitation of non-radial modes. I. High-angular-degree p modes. *A&A*, 478 :163–174, January 2008.
- K. Belkacem, M. A. Dupret, and A. Noels. Solar-like oscillations in massive main-sequence stars. I. Asteroseismic signatures of the driving and damping regions. *ArXiv e-prints*, November 2009.
- K. Belkacem, S. Mathis, M. J. Goupil, and R. Samadi. Mode excitation by turbulent convection in rotating stars. I. Effect of uniform rotation. *A&A*, 508 :345–353, December 2009.
- K. Belkacem, R. Samadi, M. J. Goupil, M. A. Dupret, A. S. Brun, and F. Baudin. Stochastic excitation of nonradial modes. II. Are solar asymptotic gravity modes detectable? *A&A*, 494 :191–204, January 2009.

-
- K. Belkacem, R. Samadi, M.-J. Goupil, L. Lefèvre, F. Baudin, S. Deheuvels, M.-A. Dupret, T. Appourchaux, R. Scuflaire, M. Auvergne, C. Catala, E. Michel, A. Miglio, J. Montalbán, A. Thoul, S. Talon, A. Baglin, and A. Noels. Solar-Like Oscillations in a Massive Star. *Science*, 324 :1540–, June 2009.
- K. Belkacem, R. Samadi, M. J. Goupil, F. Baudin, D. Salabert, and T. Appourchaux. Turbulent eddy-time-correlation in the solar convective zone. *A&A*, 522 :L2, November 2010.
- K. Belkacem, M. J. Goupil, M. A. Dupret, R. Samadi, F. Baudin, A. Noels, and B. Mosser. The underlying physical meaning of the $\nu_{max} - \nu_c$ relation. *A&A*, 530 :A142, June 2011.
- K. Belkacem, M. A. Dupret, F. Baudin, T. Appourchaux, J. P. Marques, and R. Samadi. Damping rates of solar-like oscillations across the HR diagram. Theoretical calculations confronted to CoRoT and Kepler observations. *A&A*, 540 :L7, April 2012.
- O. Benomar, F. Baudin, T. L. Campante, W. J. Chaplin, R. A. García, P. Gaulme, T. Toutain, G. A. Verner, T. Appourchaux, J. Ballot, C. Barban, Y. Elsworth, S. Mathur, B. Mosser, C. Régulo, I. W. Roxburgh, M. Auvergne, A. Baglin, C. Catala, E. Michel, and R. Samadi. A fresh look at the seismic spectrum of HD49933 : analysis of 180 days of CoRoT photometry. *A&A*, 507 :L13–L16, November 2009.
- L. Biermann. Untersuchungen über den inneren Aufbau der Sterne. IV. Konvektionszonen im Innern der Sterne. (Veröffentlichungen der Universitäts-Sternwarte Göttingen, Nr. 27.) Mit 5 Abbildungen. *Zeitschrift für Astrophysik*, 5 :117, 1932.
- E. Böhm-Vitense. *Zeitschr. Astrophys.*, 46 :108, 1958.
- E. Bohm-Vitense. *Introduction to stellar astrophysics*, volume 3. Cambridge University Press, 1989.
- V. M. Canuto and M. Dubovikov. Stellar Turbulent Convection. I. Theory. *ApJ*, 493 :834, January 1998.
- V. M. Canuto, I. Goldman, and I. Mazzitelli. Stellar turbulent convection : A self-consistent model. *ApJ*, 473 :550, December 1996.
- W. J. Chaplin and S. Basu. Perspectives in Global Helioseismology and the Road Ahead. *Solar Physics*, page 36, March 2008.
- W. J. Chaplin, Y. Elsworth, G. R. Isaak, R. Lines, C. P. McLeod, B. A. Miller, and R. New. "solar p-mode excitation : further insight from recent low-l bison helioseismological data". *MNRAS*, 298 :L7–L12, July 1998.
- W. J. Chaplin, G. Houdek, Y. Elsworth, D. O. Gough, G. R. Isaak, and R. New. On model predictions of the power spectral density of radial solar p modes. *MNRAS*, 360 :859–868, July 2005.

- W. J. Chaplin, T. R. Bedding, A. Bonanno, A.-M. Broomhall, R. A. García, S. Hekker, D. Huber, G. A. Verner, S. Basu, Y. Elsworth, G. Houdek, S. Mathur, B. Mosser, R. New, I. R. Stevens, T. Appourchaux, C. Karoff, T. S. Metcalfe, J. Molenda-Żakowicz, M. J. P. F. G. Monteiro, M. J. Thompson, J. Christensen-Dalsgaard, R. L. Gilliland, S. D. Kawaler, H. Kjeldsen, J. Ballot, O. Benomar, E. Corsaro, T. L. Campante, P. Gaulme, S. J. Hale, R. Handberg, E. Jarvis, C. Régulo, I. W. Roxburgh, D. Salabert, D. Stello, F. Mullally, J. Li, and W. Woehler. Evidence for the Impact of Stellar Activity on the Detectability of Solar-like Oscillations Observed by Kepler. *ApJ*, 732 :L5, May 2011.
- J. Christensen-Dalsgaard and S. Frandsen. Stellar 5 min oscillations. *Solar Physics*, 82 :469–486, 1983.
- J. Christensen-Dalsgaard and M. J. Thompson. Stellar hydrodynamics caught in the act : Asteroseismology with CoRoT and Kepler. In N. H. Brummell, A. S. Brun, M. S. Miesch, and Y. Ponty, editors, *IAU Symposium*, volume 271 of *IAU Symposium*, pages 32–61, August 2011.
- T. G. Cowling. The non-radial oscillations of polytropic stars. *MNRAS*, 101 :367, 1941.
- P. Degroote, M. Briquet, C. Catala, K. Uytterhoeven, K. Lefever, T. Morel, C. Aerts, F. Carrier, M. Auvergne, A. Baglin, and E. Michel. Evidence for nonlinear resonant mode coupling in the β Cephei star HD 180642 (V1449 Aquilae) from CoRoT photometry. *A&A*, 506 :111–123, October 2009.
- P. Degroote, M. Briquet, M. Auvergne, S. Simón-Díaz, C. Aerts, A. Noels, M. Rainer, M. Hareter, E. Poretti, L. Mahy, R. Oreiro, M. Vučković, K. Smolders, A. Baglin, F. Baudin, C. Catala, E. Michel, and R. Samadi. Detection of frequency spacings in the young O-type binary HD 46149 from CoRoT photometry. *A&A*, 519 :A38, September 2010.
- F. L. Deubner. Observations of low wavenumber nonradial eigenmodes of the sun. *A&A*, 44 :371–375, November 1975.
- A. Z. Dolginov and A. G. Muslimov. Nonradial stellar oscillations excited by turbulent convection. *Ap&SS*, 98 :15–36, January 1984.
- M. A. Dupret, C. Barban, M.-J. Goupil, R. Samadi, A. Grigahcène, and M. Gabriel. Theoretical damping rates and phase-lags for solar-like oscillations. In *Proceedings of SOHO 18/GONG 2006/HELAS I, Beyond the spherical Sun*, volume 624 of *ESA Special Publication*, October 2006.
- M.-A. Dupret, R. Samadi, A. Grigahcene, M.-J. Goupil, and M. Gabriel. Non-local time-dependent treatments of convection in A-G type stars. *Communications in Asteroseismology*, 147 :85–88, January 2006.
- W. Dziemblowski. Oscillations of giants and supergiants. *Acta Astronomica*, 27 :95–126, 1977.
- M. T. Eibe, P. Mein, T. Roudier, and M. Faurobert. Investigation of temperature and velocity fluctuations through the solar photosphere with the Na I D lines. *A&A*, 371 :1128–1136, June 2001.

-
- B. Freytag, H. Holweger, M. Steffen, and H.-G. Ludwig. On the Scale of Photospheric Convection. In F. Paresce, editor, *Science with the VLT Interferometer*, page 316, 1997.
- R. A. Garcia, J. Ballot, S. Mathur, D. Salabert, and C. Regulo. Signature of a magnetic activity cycle in HD49933 observed by CoRoT. *ArXiv e-prints*, December 2010.
- P. Goldreich and D. A. Keeley. "solar seismology. i - the stability of the solar p-modes". *ApJ*, 211 :934–942, February 1977.
- P. Goldreich and D. A. Keeley. Solar seismology. ii - the stochastic excitation of the solar p-modes by turbulent convection. *ApJ*, 212 :243–251, February 1977.
- P. Goldreich and P. Kumar. Wave generation by turbulent convection. *ApJ*, 363 :694–704, November 1990.
- P. Goldreich, N. Murray, and P. Kumar. Excitation of solar p-modes. *ApJ*, 424 :466–479, March 1994.
- D.O. Gough. In E.A. Spiegel and J.-P. Zahn, editors, *Problems of stellar convection*, volume 71 of *Lecture notes in physics*, page 15. Springer Verlag, 1976.
- D. O. Gough. Mixing-length theory for pulsating stars. *ApJ*, 214 :196–213, May 1977.
- M. J. Goupil, Y. Lebreton, J. P. Marques, R. Samadi, and F. Baudin. Open issues in probing interiors of solar-like oscillating main sequence stars 1. From the Sun to nearby suns. *Journal of Physics Conference Series*, 271(1) :012031, January 2011.
- A. Grigahcène, M.-A. Dupret, M. Gabriel, R. Garrido, and R. Scuflaire. Convection-pulsation coupling. I. A mixing-length perturbative theory. *A&A*, 434 :1055–1062, May 2005.
- A. Grigahcène, M.-A. Dupret, S. G. Sousa, M. J. P. F. G. Monteiro, R. Garrido, R. Scuflaire, and M. Gabriel. Towards an effective asteroseismology of solar-like stars : time-dependent convection effects on pulsation frequencies. *MNRAS*, page L422, March 2012.
- V.M. Gryanik and J. Hartmann. *J. Atmos. Sci.*, 59 :2729, 2002.
- G.-W. He, R. Rubinstein, and L.-P. Wang. Effects of subgrid-scale modeling on time correlations in large eddy simulation. *Physics of Fluids*, 14 :2186–2193, July 2002.
- G. Houdek, N. J. Balmforth, J. Christensen-Dalsgaard, and D. O. Gough. Amplitudes of stochastically excited oscillations in main-sequence stars. *A&A*, 351 :582–596, November 1999.
- G. Houdek. Stochastic excitation and damping of solar-like oscillations. In *Proceedings of SOHO 18/GONG 2006/HELAS I, Beyond the spherical Sun*, volume 624 of *ESA Special Publication*, pages Published on CDROM, p. 28.1, October 2006.
- G. Houdek. Convection and oscillations. *Astronomische Nachrichten*, 331 :998–1003, December 2010.

- L. Jacoutot, A. G. Kosovichev, A. Wray, and N. N. Mansour. Realistic Numerical Simulations of Solar Convection and Oscillations in Magnetic Regions. *ApJ*, 684 :L51–L54, September 2008.
- T. Kallinger, W. W. Weiss, J. De Ridder, S. Hekker, and C. Barban. Oscillating Red Giants in the CoRoT Exo-field : An Asteroseismic Radius and Mass Determination. In S. J. Murphy & M. S. Bessell, editor, *Astronomical Society of the Pacific Conference Series*, volume 404 of *Astronomical Society of the Pacific Conference Series*, page 307, August 2009.
- Y. Kaneda. Lagrangian and Eulerian time correlations in turbulence. *Physics of Fluids*, 5 :2835–2845, November 1993.
- H. Kjeldsen and T. R. Bedding. Amplitudes of stellar oscillations : the implications for asteroseismology. *A&A*, 293 :87–106, January 1995.
- H. Kjeldsen, T. R. Bedding, T. Arentoft, R. P. Butler, T. H. Dall, C. Karoff, L. L. Kiss, C. G. Tinney, and W. J. Chaplin. The Amplitude of Solar Oscillations Using Stellar Techniques. *ApJ*, 682 :1370–1375, August 2008.
- H. Kjeldsen, T. R. Bedding, and J. Christensen-Dalsgaard. Correcting Stellar Oscillation Frequencies for Near-Surface Effects. *ApJ*, 683 :L175–L178, August 2008.
- A. N Kolmogorov. *Dokl. Akad. Nauk SSSR*, 30 :299, 1941.
- R. H. Kraichnan. Kolmogorov’s Hypotheses and Eulerian Turbulence Theory. *Physics of Fluids*, 7 :1723–1734, November 1964.
- F. Kupka and M. H. Montgomery. A-star envelopes : a test of local and non-local models of convection. *MNRAS*, 330 :L6–L10, February 2002.
- F. Kupka and F. J. Robinson. On the effects of coherent structures on higher order moments in models of solar and stellar surface convection. *MNRAS*, 374 :305–322, January 2007.
- F. Kupka, K. Belkacem, J.-M. Goupil, and R. Samadi. Using p-mode excitation rates for probing convection in solar-like stars. *Communications in Asteroseismology*, 159 :24–26, March 2009.
- F. Kupka. Turbulent Convection : Comparing the Moment Equations to Numerical Simulations. *ApJ*, 526 :L45–L48, November 1999.
- F. Kupka. Some open questions concerning the modelling of non-locality in Reynolds stress type models of stellar convection. In F. Kupka, I. Roxburgh, and K. Chan, editors, *IAU Symposium*, volume 239 of *IAU Symposium*, pages 92–94, May 2007.
- F. Kupka. 3D stellar atmospheres for stellar structure models and asteroseismology. *MmSAI*, 80 :701, 2009.
- R. L. Kurucz. *SYNTHE spectrum synthesis programs and line data*. 1993.

-
- P. Ledoux and Th. Walraven. In Flugge S., editor, *Handbuch der Physik*, volume 51, page 353. Springer-Verlag (New York), 1958.
- J. W. Leibacher and R. F. Stein. A New Description of the Solar Five-Minute Oscillation. *Astrophys. Lett.*, 7 :191–192, 1971.
- R. B. Leighton, R. W. Noyes, and G. W. Simon. Velocity fields in the solar atmosphere. i. preliminary report. *ApJ*, 135 :474, March 1962.
- M. Lesieur. *Turbulence in fluids*. Kluwer Academic Publishers, 1997.
- K. G. Libbrecht. Solar p-mode phenomenology. *ApJ*, 334 :510–516, November 1988.
- M. J. Lighthill. On sound generated aerodynamically. *Proc. R. Soc. Lond.*, A211 :564, 1952.
- E. Michel and A. Baglin. Some CoRoT highlights - A grip on stellar physics and beyond. *ArXiv e-prints*, February 2012.
- E. Michel, A. Baglin, M. Auvergne, C. Catala, R. Samadi, F. Baudin, T. Appourchaux, C. Barban, W. Weiss, G. Berthomieu, P. Boumier, M.-A. Dupret, R. A. Garcia, M. Fridlund, R. Garrido, M.-J. Goupil, H. Kjeldsen, Y. Lebreton, B. Mosser, A. Grottsch-Noels, E. Janot-Pacheco, J. Provost, I. W. Roxburgh, A. Thoul, T. Toutain, D. Tiphene, S. Turck-Chieze, S. D. Vauclair, C. Aerts, G. Alecian, J. Ballot, S. Charpinet, A.-M. Hubert, F. Lignieres, P. Mathias, M. J. P. F. G. Monteiro, C. Neiner, and E. . Poretti. CoRoT measures solar-like oscillations and granulation in stars hotter than the Sun. *Science*, 322 :558–560, 2008.
- E. Michel, R. Samadi, F. Baudin, C. Barban, T. Appourchaux, and M. Auvergne. Intrinsic photometric characterisation of stellar oscillations and granulation. Solar reference values and CoRoT response functions. *A&A*, 495 :979–987, March 2009.
- P. Morel and Y. Lebreton. CESAM : a free code for stellar evolution calculations. *Ap&SS*, 316 :61–73, August 2008.
- B. Mosser, F. Bouchy, C. Catala, E. Michel, R. Samadi, F. Thévenin, P. Eggenberger, D. Sosnowska, C. Moutou, and A. Baglin. Seismology and activity of the F type star HD 49933. *A&A*, 431 :L13–L16, February 2005.
- B. Mosser, Y. Elsworth, S. Hekker, D. Huber, T. Kallinger, S. Mathur, K. Belkacem, M. J. Goupil, R. Samadi, C. Barban, T. R. Bedding, W. J. Chaplin, R. A. García, D. Stello, J. De Ridder, C. K. Middour, R. L. Morris, and E. V. Quintana. Characterization of the power excess of solar-like oscillations in red giants with Kepler. *A&A*, 537 :A30, January 2012.
- B. Mosser, M. J. Goupil, K. Belkacem, E. Michel, D. Stello, J. P. Marques, Y. Elsworth, C. Barban, P. G. Beck, T. R. Bedding, J. De Ridder, R. A. García, S. Hekker, T. Kallinger, R. Samadi, M. C. Stumpe, T. Barclay, and C. J. Burke. Probing the core structure and evolution of red giants using gravity-dominated mixed modes observed with Kepler. *A&A*, 540 :A143, April 2012.

- R. Muller. Granulation : Overview. In R.J. Rutten and G. Severino, editors, *Solar and Stellar Granulation*, page 101. Kluwer Academic Publishers, 1989.
- Z. E. Musielak, R. Rosner, R. F. Stein, and P. Ulmschneider. On sound generation by turbulent convection : A new look at old results. *ApJ*, 423 :474–487, March 1994.
- C. Neiner, M. Floquet, R. Samadi, F. Espinosa Lara, Y. Frémat, S. Mathis, B. Leroy, B. de Batz, M. Rainer, E. Poretti, P. Mathias, J. Guarro Fló, C. Buil, J. Ribeiro, E. Alecian, L. Andrade, M. Briquet, P. D. Diago, M. Emilio, J. Fabregat, J. Gutiérrez-Soto, A.-M. Hubert, E. Janot-Pacheco, C. Martayan, T. Semaan, J. Suso, and J. Zorec. Stochastic gravito-inertial modes discovered by CoRoT in the hot Be star HD 51452. *A&A*, 546 :A47, October 2012.
- Å. Nordlund and R. F. Stein. Convection Simulations. In A. Gimenez, E. F. Guinan, and B. Montesinos, editors, *Stellar Structure : Theory and Test of Connective Energy Transport*, volume 173 of *Astronomical Society of the Pacific Conference Series*, page 91, 1999.
- Å. Nordlund and R. F. Stein. Solar oscillations and convection. i. formalism for radial oscillations. *ApJ*, 546 :576–584, January 2001.
- A. Nordlund, H. C. Spruit, H.-G. Ludwig, and R. Trampedach. Is stellar granulation turbulence ? *A&A*, 328 :229–234, December 1997.
- A.M. Oboukhov. On the distribution of energy in the spectrum of turbulent flow. *Dokl. Akad. Sci. Nauk SSSR*, 32 :22–24, 1941.
- Y. Osaki. Excitation Mechanisms of Solar Oscillations. In Y. Osaki and H. Shibahashi, editors, *Progress of Seismology of the Sun and Stars*, volume 367 of *Lecture Notes in Physics*, Berlin Springer Verlag, page 75, 1990.
- W. D. Pesnell. Nonradial, nonadiabatic stellar pulsations. *ApJ*, 363 :227–233, November 1990.
- M. R. E. Proctor and N. O. Weiss. Magnetoconvection. *Reports of Progress in Physics*, 45 :1317–1379, November 1982.
- T. Roca Cortés, P. Montañés, P. L. Pallé, F. Pérez Hernández, A. Jiménez, C. Régulo, and The GOLF Team. Low L Solar p-Mode Oscillations Parameters and Convection. In A. Gimenez, E. F. Guinan, and B. Montesinos, editors, *Stellar Structure : Theory and Test of Connective Energy Transport*, volume 173 of *Astronomical Society of the Pacific Conference Series*, page 305, 1999.
- C. S. Rosenthal, J. Christensen-Dalsgaard, Å. Nordlund, R. F. Stein, and R. Trampedach. Convective contributions to the frequencies of solar oscillations. *A&A*, 351 :689–700, November 1999.
- T. Roudier and R. Muller. *Solar Phys.*, 107 :11, 1986.
- R. Samadi and M. J. Goupil. Excitation of stellar p-modes by turbulent convection. i. theoretical formulation. *A&A*, 370 :136–146, 2001.

-
- R. Samadi, M. J. Goupil, and Y. Lebreton. Excitation of stellar p-modes by turbulent convection. ii. the sun. *A&A*, 370 :147–156, 2001.
- R. Samadi, M.-J. Goupil, and G. Houdek. Solar-like oscillations in delta Scuti stars. *A&A*, 395 :563–571, November 2002.
- R. Samadi, Å. Nordlund, R. F. Stein, M. J. Goupil, and I. Roxburgh. Numerical 3D constraints on convective eddy time-correlations : Consequences for stochastic excitation of solar p modes. *A&A*, 404 :1129–1137, June 2003.
- R. Samadi, Å. Nordlund, R. F. Stein, M. J. Goupil, and I. Roxburgh. Numerical constraints on the model of stochastic excitation of solar-type oscillations. *A&A*, 403 :303–312, May 2003.
- R. Samadi, M.-J. Goupil, E. Alecian, F. Baudin, D. Georgobiani, R. Trampedach, R. Stein, and Å. Nordlund. Excitation of Solar-like Oscillations : From PMS to MS Stellar Models. *Astrophysics & Astronomy*, 26 :171, June 2005.
- R. Samadi, F. Kupka, M. J. Goupil, Y. Lebreton, and C. van’t Veer-Menneret. Influence of local treatments of convection upon solar p mode excitation rates. *A&A*, 445 :233–242, January 2006.
- R. Samadi, D. Georgobiani, R. Trampedach, M. J. Goupil, R. F. Stein, and Å. Nordlund. Excitation of solar-like oscillations across the HR diagram. *A&A*, 463 :297–308, February 2007.
- R. Samadi, K. Belkacem, M. J. Goupil, M.-A. Dupret, and F. Kupka. Modeling the excitation of acoustic modes in α Centauri A. *A&A*, 489 :291–299, October 2008.
- R. Samadi, K. Belkacem, M. J. Goupil, M.-A. Dupret, A. S. Brun, and A. Noels. Stochastic excitation of gravity modes in massive main-sequence stars. *Ap&SS*, page 240, December 2009.
- R. Samadi, H.-G. Ludwig, K. Belkacem, M. J. Goupil, O. Benomar, B. Mosser, M.-A. Dupret, F. Baudin, T. Appourchaux, and E. Michel. The CoRoT target HD 49933 . II. Comparison of theoretical mode amplitudes with observations. *A&A*, 509 :A16, January 2010.
- R. Samadi, H.-G. Ludwig, K. Belkacem, M. J. Goupil, and M.-A. Dupret. The CoRoT target HD 49933 . I. Effect of the metal abundance on the mode excitation rates. *A&A*, 509 :A15, January 2010.
- R. Samadi, K. Belkacem, M.-A. Dupret, H.-G. Ludwig, F. Baudin, E. Caffau, M.-J. Goupil, and C. Barban. Amplitudes of solar-like oscillations in red giant stars. Evidence for non-adiabatic effects using CoRoT observations. *A&A*, 543 :A120, July 2012.
- R. Samadi, K. Belkacem, M.-A. Dupret, M.-J. Goupil, H.-G. Ludwig, C. Barban, F. Baudin, and E. Caffau. Amplitudes of solar-like oscillations in red giants : departures from the quasi-adiabatic approximation. In *EPJ Web of Conferences*, volume in press, 2013.
- R. Samadi. *Excitation stochastique des oscillations stellaires. Application à la mission spatiale COROT*. PhD thesis, Université Paris 6, dec 2000.

- B. L. Sawford. Reynolds number effects in Lagrangian stochastic models of turbulent dispersion. *Physics of Fluids*, 3 :1577–1586, June 1991.
- E.A. Spiegel. Thermal turbulence at very small prandtl number. *J. Geophys. Res.*, 67 :3063, 1962.
- E. A. Spiegel. A generalization of the mixing-length theory of turbulent convection. *ApJ*, 138 :216, July 1963.
- R. F. Stein and J. Leibacher. Waves in the solar atmosphere. *ARA&A*, 12 :407–435, 1974.
- F Stein and A. Nordlund. in *Challenges to Theories of the Structure of Moderate-Mass Stars*, volume 195. ed D. Gough & J. Toomre (Springer-Verlag), 1991.
- R. F. Stein and Å. Nordlund. Solar oscillations and convection. ii. excitation of radial oscillations. *ApJ*, 546 :585–603, January 2001.
- R. Stein, D. Georgobiani, R. Trampedach, H.-G. Ludwig, and Å. Nordlund. Excitation of Radial P-Modes in the Sun and Stars. *Solar Physics*, 220 :229–243, April 2004.
- R. F. Stein. Generation of acoustic and gravity waves by turbulence in an isothermal stratified atmosphere. *Solar Physics*, 2 :385–432, 1967.
- D. Stello and R. L. Gilliland. Solar-like Oscillations in a Metal-poor Globular Cluster with the Hubble Space Telescope. *ApJ*, 700 :949–955, August 2009.
- D. Stello, H. Bruntt, H. Preston, and D. Buzasi. Oscillating K Giants with the WIRE Satellite : Determination of Their Asteroseismic Masses. *ApJ*, 674 :L53–L56, February 2008.
- D. Stello, W. J. Chaplin, S. Basu, Y. Elsworth, and T. R. Bedding. The relation between $\Delta\nu$ and ν_{\max} for solar-like oscillations. *MNRAS*, 400 :L80–L84, November 2009.
- H. Tennekes and J.L. Lumley. *A first course in turbulence*. MIT Press, 8th edition, 1982.
- H. Tennekes. Eulerian and lagrangian time microscales in isotropic turbulence. *Journal of Fluids Mechanics*, 67 :561–567, 1975.
- R. Trampedach. Master’s thesis, Master’s thesis, Aarhus University (1997), 1997.
- R. K. Ulrich. The five-minute oscillations on the solar surface. *ApJ*, 162 :993, December 1970.
- W. Unno and S. Kato. On the generation of acoustic noise from the turbulent atmosphere, i. *PASJ*, 14 :417, 1962.
- W. Unno, Y. Osaki, H. Ando, H. Saio, and H. Shibahashi. *Nonradial oscillations of stars*. Tokyo : University of Tokyo Press, 1989, 2nd ed., 1989.
- A. Vögler, S. Shelyag, M. Schüssler, F. Cattaneo, T. Emonet, and T. Linde. Simulations of magneto-convection in the solar photosphere. Equations, methods, and results of the MURaM code. *A&A*, 429 :335–351, January 2005.

-
- R. Wachter and A. G. Kosovichev. Properties of the Solar Acoustic Source Inferred from Non-adiabatic Oscillation Spectra. *ApJ*, 627 :550–561, July 2005.
- T. R. White, T. R. Bedding, D. Stello, J. Christensen-Dalsgaard, D. Huber, and H. Kjeldsen. Calculating Asteroseismic Diagrams for Solar-like Oscillations. *ApJ*, 743 :161, December 2011.
- D. R. Xiong, Q. L. Cheng, and L. Deng. Turbulent convection and pulsational stability of variable stars : non-adiabatic oscillations of the solar p-modes. *MNRAS*, 319 :1079–1093, December 2000.
- J.-P. Zahn. Convection and Turbulence in Stars. In C. B. De Loore, editor, *Late Stages of Stellar Evolution. Computational Methods in Astrophysical Hydrodynamics*, volume 373 of *Lecture Notes in Physics*, Berlin Springer Verlag, page 355, 1991.

Annexe A

Articles reproduits

Sommaire

<i>Solar-like oscillations in delta Scuti stars</i> Samadi R., Goupil M.-J., Houdek G., 2002, A&A, 395, 563	87
<i>Numerical constraints on the model of stochastic excitation of solar-type oscillations</i> Samadi R., Nordlund A., Stein R. F., Goupil M.-J., Roxburgh I., 2003, A&A, 403, 303	97
<i>Numerical 3D constraints on convective eddy time-correlations : Consequences for stochastic excitation of solar p modes</i> Samadi R., Nordlund A., Stein R. F., Goupil M.-J., Roxburgh I., 2003, A&A, 403, 1129	107
<i>Inferred acoustic rates of solar p modes from several helioseismic instruments</i> Baudin F., Samadi R., Goupil M.-J., Appourchaux T., Barban C., Boumier P., Chaplin W. J., Gouttebroze P., 2004, A&A, 433, 349	117
<i>Rotation profile inversion in solar-like stars. In the COROT framework</i> Lochard J., Samadi R., Goupil M.-J., 2005, A&A, 438, 939	125
<i>Influence of local treatments of convection upon solar p mode excitation rates</i> Samadi R., Kupka F., Goupil M.-J., Lebreton Y., van't Veer-Menneret C., 2006, A&A, 445, 233	135
<i>A closure model with plumes. I. The solar convection</i> Belkacem K., Samadi R., Goupil M.-J., Kupka F., 2006, A&A, 460, 173 .	145
<i>A closure model with plumes. II. Application to the stochastic excitation of solar p modes</i> Belkacem K., Samadi R., Goupil M.-J., Kupka F., Baudin F., 2006, A&A, 460, 183	157
<i>Excitation of solar-like oscillations across the HR diagram</i> Samadi R., Georgobiani D., Trampedach R., Goupil M.-J., Stein R. F., Nordlund A., 2007, A&A, 463, 297	165
<i>Modeling the excitation of acoustic modes in α Centauri A</i> Samadi R., Belkacem K., Goupil M.-J., Dupret M.-A., Kupka F., 2008, A&A, 489, 291	177
<i>Stochastic excitation of non-radial modes. I. High-angular-degree p modes</i> Belkacem K., Samadi R., Goupil M.-J., Dupret M.-A., 2008, A&A, 478, 163	187

<i>Stochastic excitation of nonradial modes. II. Are solar asymptotic gravity modes detectable ?</i>	
Belkacem K., Samadi R., Goupil M.-J., Dupret M.-A., Brun A. S., Baudin F., 2009, A&A, 494, 191	199
<i>Intrinsic photometric characterisation of stellar oscillations and granulation. Solar reference values and CoRoT response functions</i>	
Michel E., Samadi R., Baudin F., Barban C., Appourchaux T., Auvergne M., 2009, A&A, 495, 979	213
<i>The CoRoT target HD 49933 . I. Effect of the metal abundance on the mode excitation rates</i>	
Samadi R., Ludwig H.-G., Belkacem K., Goupil M. J., Dupret M.-A., 2010, A&A, 509A, 15	223
<i>The CoRoT target HD 49933 . II. Comparison of theoretical mode amplitudes with observations</i>	
Samadi R., Ludwig H.-G., Belkacem K., Goupil M. J., Benomar O., Mosser B., Dupret M.-A., Baudin F., Appourchaux T., Michel E., 2010, A&A, 509A, 16	231
<i>Stochastic excitation of gravity modes in massive main-sequence stars</i>	
Samadi R., Belkacem K., Goupil M. J., Dupret M.-A., Brun A. S., Noels A., 2010, Ap&SS, 328, 253	239
<i>Turbulent eddy-time-correlation in the solar convective zone</i>	
Belkacem K., Samadi R., Goupil M. J., Baudin F., Salabert D., Appourchaux T., 2010, A&A, 522L, 2	245
<i>Amplitudes of solar-like oscillations in red-giant stars : Evidences for non-adiabatic effects using CoRoT observations</i>	
Samadi R., Belkacem K., Dupret M.-A., Ludwig H.-G., Baudin F., Caffau E., Goupil M. J., Barban C., 2012, A&A, 543, 120	249

Les publications listées ci-dessus sont reproduites ci-après par ordre chronologique.

Solar-like oscillations in δ Scuti stars

R. Samadi^{1,2}, M.-J. Goupil², and G. Houdek³

¹ Astronomy Unit, Queen Mary, University of London, London E14NS, UK

² Observatoire de Paris, LESIA, CNRS FRE 2461, 92195 Meudon, France

³ Institute of Astronomy, University of Cambridge, Cambridge CB3 0HA, UK

Received 25 January 2002 / Accepted 5 September 2002

Abstract. Model computations of δ Scuti stars, located in the vicinity of the red edge of the classical instability strip, suggest amplitudes of solar-like oscillations larger than in cooler models located outside the instability strip. Solar-like amplitudes in our δ Scuti models are found to be large enough to be detectable with ground-based instruments provided they can be distinguished from the opacity-driven large-amplitude pulsations. There would be advantages in observing simultaneously opacity-driven and stochastically excited modes in the same star. We anticipate their possible detection in the context of the planned asteroseismic space missions, such as the French mission COROT (COnvection ROTation and planetary Transits). We propose known δ Scuti stars as potential candidates for the target selection of these upcoming space missions.

Key words. stars: interiors – stars: variables: δ Sct

1. Introduction

The δ Scuti stars are in general main sequence stars with masses between $1.5 M_{\odot}$ and $2.5 M_{\odot}$. They are located inside the classical instability strip (IS hereafter) where the κ -mechanism drives low-order radial and nonradial modes of low degree to measurable amplitudes (opacity-driven unstable modes). Only a small number of opacity-driven modes are observed in δ Scuti stars (for a review see e.g. Gautschy & Saio 1996), but their amplitudes, which are limited by nonlinear processes, are much larger than stochastically driven intrinsically stable solar-like p modes.

For main-sequence stars with surface convection zones, located outside the IS, model computations suggest all modes to be intrinsically stable but excited stochastically by turbulent convection; for models located near the red edge of the IS the predicted velocity amplitudes become as large as 15 times the solar value (Houdek et al. 1999). Moreover, these computations suggest that models located inside the IS can pulsate simultaneously with modes excited both by the κ -mechanism and by the turbulent velocity field.

Provided that many modes can be detected, high-frequency p modes are more easily identified than low frequency p modes. Hence there are advantages of observing simultaneously both types of modes in the same star. As a first step, high-frequency p modes can help to determine the fundamental stellar parameters (e.g., luminosity, effective temperature) more accurately, whereas low-frequency modes, which

are strongly sensitive to the properties of the deep layers of the star, can then be used as a diagnostic for the inner properties of the model. Such developments are outside the scope of the present paper and we only outline briefly the underlying idea.

The nearly regular frequency spacing of solar-like modes of high order (i.e., the large frequency separation) depends predominantly on the structure of the surface layers and consequently provides further constraints on the equilibrium models. Their degree l and azimuthal order m can be identified with the help of the classical echelle diagram method; this method was successfully tested by the simulation results of the COROT Seismic Working Group (Appourchaux 2002, personal communication); this severely constrains the fundamental stellar parameters (mass, age, chemical composition) of models for which the frequencies of computed oscillation modes are similar to the observed high-order modes (Berthomieu et al. 2002). Moreover, solar-type modes also provide information on the star's mean rotation rate.

A nearly regular spacing in frequency is also observed for opacity-driven low-frequency modes (Breger et al. 1999); the large separation of these low-frequency modes has to be similar between observations and theoretical models which satisfy also the properties of the observed high-frequency solar-type p modes. However, some of the opacity-driven modes deviate from the mean value of the large frequency separation; these modes are so-called mixed modes which provide details of the stellar core and of the precise evolutionary stage of the observed star (Unno et al. 1989 and references therein). This deviation from the mean value of the large frequency separation could suggest the presence of mixed modes. The problem

Send offprint requests to: R. Samadi,
e-mail: Reza.Samadi@obspm.fr

is further complicated by the fact that the rotational splitting frequency components are no longer equidistant for these fast rotators, i.e. these frequencies could erroneously be identified as frequencies of mixed modes. However, knowing the mean rotation rate from the high-frequency splittings of solar-type p modes, the frequency splittings of the low-frequency opacity-driven modes can be computed in the manner of Dziembowski & Goode (1992) (see also Soufi et al. 1998).

The understanding of the physics responsible for the return to stability of opacity-driven modes at the red edge of the IS is still in its infancy. As the star becomes cooler the extent of the surface convection zone increases, thereby making the effect of convection-pulsation coupling on mode stability progressively more important. Several authors have tried to model the location of the red edge, e.g., Baker & Gough (1979), Bono et al. (1995) for RR Lyrae stars and e.g., Houdek (1996) and Xiong & Deng (2001) for δ Scuti stars. Although the authors assumed various models for the time-dependent treatment of convection, they all concluded that convection dynamics crucially effect the location of the red edge; however, different results were reported as to whether the convective heat flux (e.g., Bono et al. 1995), the momentum flux (e.g., Houdek 1996) or turbulent viscosity (Xiong & Deng 2001) is the crucial agent for stabilizing the modes at the red edge. In all these investigations, the predicted position of the red edge depends crucially on the assumed convection parameters, such as the mixing-length parameter or whether acoustic emission is included or neglected in the equilibrium model (Houdek 2000).

Although it is possible from Fig. 13 of Houdek et al. (1999) to conclude that both types of modes can be excited simultaneously in the same star, amplitudes of stochastically excited modes for stars located inside the instability strip were not explicitly carried out by Houdek et al. (1999) and their possible detection were not addressed.

The aim of this paper is to demonstrate that models of stars, located inside the IS and near the red edge, can exhibit both opacity driven modes and solar-like oscillations with sufficiently large amplitudes to be detectable with today's ground-based instruments. Consequently the planned asteroseismology space missions, such as COROT (CONvection ROTation and planetary Transits, Baglin & The Corot Team 1998) or Eddington (Favata et al. 2000), will detect these oscillations even more easily.

Section 2 describes the equilibrium models, and the linear analysis results are discussed in Sect. 3, which are obtained from solving the equations of linear nonadiabatic oscillations in which convection is treated with the time-dependent, non-local formalism by Gough (1976, 1977, hereafter G'MLT). Furthermore, the effect of acoustic radiation in the equilibrium model on the stability properties is taken into account in the manner of Houdek (2000, and references therein). In this paper we consider only radial p modes.

Amplitudes of solar-like oscillations result from the balance between damping and stochastic driving by turbulence. The rate at which the turbulence injects energy into the p modes is estimated in the manner of Samadi & Goupil (2001, Paper I hereafter) and is discussed in Sect. 4.

Table 1. Stellar parameters for the envelope models A1, A2, B1, B2 and C; R is the stellar radius at the photosphere ($T = T_{\text{eff}}$), and ν_c is the acoustic cut-off frequency.

Model	T_{eff} [K]	$(b - y)_0$	R [R_{\odot}]	ν_c [mHz]	acoustic radiation
A1, A2	6839	0.235	2.40	1.4	included
B1, B2	6839	0.235	2.40	1.4	neglected
C	6650	0.262	2.54	1.3	neglected

Table 2. Acoustic emissivity coefficient Λ and Mach-number dependence Γ assumed in the acoustic radiation model for the stellar models A1 and A2.

Model	Λ	Γ
A1	100	5
A2	2000	7.5

In Sect. 5 we address the possibilities and conditions for detecting solar-type oscillations in δ Scuti stars with ground-based instruments and propose possible candidates, some of which are listed in the catalogue by Rodríguez et al. (2000). Conclusions are given in Sect. 6.

2. The stellar models

Equilibrium envelope models are computed in the manner of Houdek et al. (1999) using G'MLT formulation for convection. Integration starts at an optical depth of $\tau = 10^{-4}$ and ends at a radius fraction 0.2. Radiation is treated in the Eddington approximation and the atmosphere is assumed to be grey and plane parallel. In G'MLT formulation two more parameters, a and b , are introduced which control the spatial coherence of the ensemble of eddies contributing to the total heat and momentum fluxes (a), and the degree to which the turbulent fluxes are coupled to the local stratification (b). In this paper we choose $a^2 = 900$ and $b^2 = 2000$ in order to obtain stable modes in the frequency range in which the damping rates exhibit a local minimum (e.g., at about 1.1 mHz for model C; see Sect. 3 and Fig. 2). The mixing-length parameter α has been calibrated to a solar model to obtain the helioseismically inferred depth of the convection zone of 0.287 of the solar radius (Christensen-Dalsgaard et al. 1991).

All models assume solar chemical composition and have mass $M = 1.68 M_{\odot}$ and luminosity $L = 11.3 L_{\odot}$, but differ in effective temperature T_{eff} , and whether or not acoustic radiation is included in the equilibrium computations. Table 1 lists the fundamental stellar parameters of these models. The models A1, A2, B1 and B2 are hotter than model C and are located inside the IS and close to the red edge. Models A1 and A2 differ from models B1 and B2 by the inclusion of acoustic radiation by turbulence in the envelope calculations. In this model for acoustic radiation in the equilibrium model two more parameters are introduced (Houdek & Gough 1998): the emissivity coefficient Λ and the parameter Γ which describes the power-law dependence of the acoustic power emission on the turbulent Mach number. A Mach-number dependence of $\Gamma = 5$ assumes that acoustic emission is dominated by the energy-bearing

eddies; if acoustic emission is predominantly emitted by inertial-range eddies Γ has the value 7.5. Table 2 lists the values of Λ and Γ that are assumed in the models A1 and A2. The values for Λ provide for a solar model a similar value for the acoustic flux F_{ac} as the estimates of Stein (1968) and Musielak et al. (1994). For all the models, except for model B2, we assume for the mixing-length parameter the calibrated solar value $\alpha = 2.037$; for model B2 the value $\alpha = 1.5$ is assumed.

Figure 1 displays the locations of these models in the colour-magnitude diagram. Evolutionary tracks (dashed curves) are shown for models with various masses and are obtained with the CESAM code by Morel (1997) as described by Samadi et al. (2001a). The transformation from luminosity, effective temperature and surface gravity to absolute magnitude M_i and dereddened colour indices $(b - y)_0$ are obtained from the Basel Stellar Library (Lejeune et al. 1998). The blue and red edges of the fundamental radial modes (solid curves) are calculated in the manner of Houdek et al. (1999). The positions of the observed δ Scuti stars (filled circles) are taken from Rodríguez et al. (2000): absolute magnitudes, derived from Hipparcos distances and dereddened colour indices were kindly supplied by E. Rodríguez (2001, personal communication; see Rodríguez & Breger 2001, for details).

3. Stability analysis

The stability computations are as described in Houdek (2000, and references therein). In particular they include the Lagrangian perturbations of the turbulent fluxes (heat and momentum) according to Gough's (1977) time-dependent formulation. Assuming a temporal dependence, $\exp(-i\omega t)$, for the pulsations, the complex eigenfrequencies of the modes can be written as $\omega = \omega_r + i\omega_i$, which defines the cyclic pulsation frequency $\nu = \omega_r/2\pi$ and the damping/growth rate $\eta = -\omega_i/2\pi$. The outer boundary conditions are applied at the temperature minimum, the mechanical boundary condition being consistent with a perfectly reflecting surface; at the base of the envelope, conditions of adiabaticity and vanishing displacement are imposed.

For model C all the modes are found to be linearly stable (i.e., $\eta > 0$) as is expected for models lying well outside the IS. This is also found for the hotter model B1. For the model A1 (resp. A2) the first four (resp. three) radial modes, $n = 1, \dots, 4$ (resp. $n = 1, 2, 3$), are found to be overstable. With the inclusion of a model for the acoustic radiation in the equilibrium structure the efficacy with which convection transports the turbulent fluxes is decreased (see Houdek & Gough 1998). This leads to a decrease in the turbulent Mach number and to a consequent reduction of the stabilizing influence of the perturbed momentum flux on the mode damping. The driving eventually dominates over the damping leading to overstable modes.

Reducing α has a similar effect on mode stability than the inclusion of acoustic radiation in the equilibrium model (see Houdek & Gough 1998; Michel et al. 1998; Houdek 2000). The model B2 was computed with the smaller mixing-length parameter $\alpha = 1.5$, leading to overstable modes with radial orders $n = 1, 2, 3$.

Table 3. Frequency ν , damping/growth rate η and stability coefficient ω_i/ω_r for all overstable radial p modes predicted for the models A1, A2 and B2.

Model	n	ν [μ Hz]	η [nHz]	ω_i/ω_r $\times 10^{-6}$
A1	1	123	-0.03	0.25
	2	161	-0.31	1.92
	3	202	-4.14	20.48
	4	244	-3.90	15.97
A2	1	124	-0.04	0.36
	2	162	-0.40	2.47
	3	203	-1.27	6.25
B2	1	124	-0.04	0.34
	2	161	-0.31	1.95
	3	203	-0.83	4.09

Table 3 displays the frequency ν and damping/growth rate η for all overstable radial modes ($\eta < 0$) found in the models A1, A2 and B2.

Figure 2 displays the damping rates as function of frequency for all stable modes and for all stellar models. The coolest model C exhibits a sharp dip in η at about 1.1 mHz, which we moderated by applying a median filter with a width in frequency corresponding to nine radial modes; the result is plotted by the long-dashed curve in Fig. 2. This pronounced depression in η in model C is related to the structure of the outer superadiabatic boundary layer: with decreasing surface temperature the location of the superadiabatic boundary layer is shifted progressively deeper into the star. This modifies the thermodynamic properties of this boundary layer of finite thickness, in particular, the thermal relaxation time (Balmforth 1992). The thermodynamic coupling between the pulsations and the superadiabatic boundary layer becomes more efficient in cooler models, thereby promoting the depression in the damping rates by radiative processes (see Houdek et al. 1999).

4. Excitation rate and amplitude spectrum

The rms value of the mode surface velocity, v_s , is related to the damping rate, η , and to the rate at which energy is injected into the mode (excitation rate), P , by

$$v_s^2 = \xi_r^2(r_s) \frac{P}{2\eta I}, \quad (1)$$

where ξ_r is the radial displacement eigenfunction, r_s is the radius at which the surface velocities are measured and which we assume to be 200 km above T_{eff} , and the mode inertia I satisfies

$$I = \int_0^M \xi^* \cdot \xi \, dm. \quad (2)$$

The rate of energy injected into a mode is computed according to Paper I and is proportional to

$$P(\omega) \propto \int_0^M \rho w^3 \ell^4 \left(\frac{d\xi_r}{dr} \right)^2 \mathcal{S}(\omega, m) \, dm, \quad (3)$$

where ρ is the density, ℓ is the mixing length, and w is the vertical component of the rms velocity of the convective elements. The function $\mathcal{S}(\omega, m)$ describes approximately contributions from eddies with different sizes to the excitation rate P .

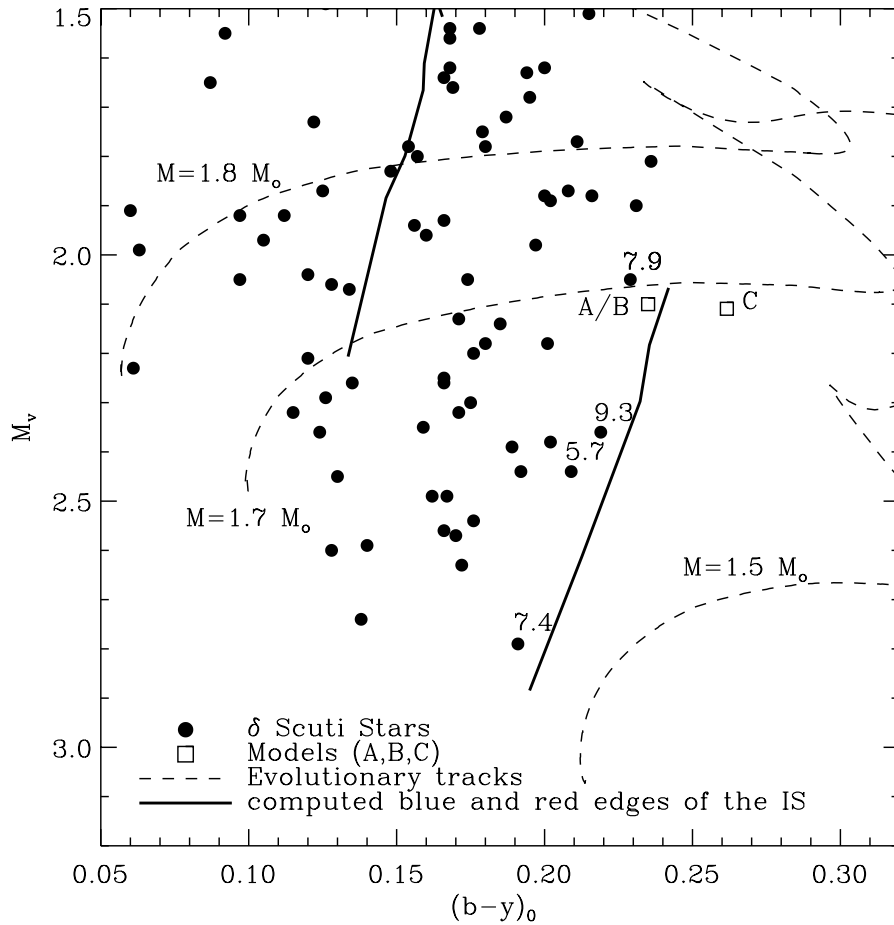


Fig. 1. Colour-magnitude diagram: filled circles display the positions of observed δ Scuti stars from the Rodríguez et al. (2000) catalogue. Squares indicate the positions of the models A1, A2, B1, B2 and C (see Table 1). Dashed curves show evolutionary tracks for models with masses $1.5 M_{\odot}$, $1.7 M_{\odot}$ and $1.8 M_{\odot}$. Solid curves display theoretical locations of the blue and red edges for the fundamental radial modes according to Houdek et al. (1999). Numbers associated with the symbols indicate apparent magnitudes V for selected observed δ Scuti stars.

Detailed expressions for $\mathcal{S}(\omega, m)$ were given in Paper I. For estimating \mathcal{S} , assumptions for the turbulent kinetic energy spectrum $E(k)$, and for the turbulent spectrum of the entropy fluctuations $E_s(k)$ have to be made, where k is the eddy wavenumber. In this paper we assume for $E(k)$ the “Nesis Kolmogorov Spectrum” (NKS hereafter) as discussed in Paper I. This turbulent spectrum is obtained from observations of the solar granulation by Nesis et al. (1993), and leads to the best agreement between a solar model using our stochastic excitation theory and solar measurements (Samadi et al. 2001b).

Results for the estimated excitation rate P are depicted in Fig. 3. For the models A1, A2 and B1 the excitation rate P is about one magnitude larger than for model C. This is a result of the larger convective velocities in the superadiabatic boundary layers of the models A1, A2 and B1 (see Fig. 4), which are all hotter than model C. The frequency dependence of P for the models A1 and B1 are similar as it is also the case for the models A2 and B2; the latter two models, however, are quite different from the first two models. This difference in the frequency dependence of P is a consequence of the different profiles of the convective velocities w (see Fig. 4); the profiles of w are similar for A2 and B2 but differ substantially from A1 and B1.

For the models A2 and B2 the efficacy of convection has been reduced severely by either including acoustic radiation in the equilibrium model (A2) or by reducing the mixing-length parameter α to a value much smaller than the calibrated value for a solar model (B2). This results in shallower superadiabatic regions and in larger superadiabatic temperature gradients; pulsation modes in A2 and B2 are therefore predominantly excited at the very top of the convection zone, whereas in the models A1 and B1 the modes are excited over a larger driving region. The two sets of values for Λ and Γ , listed in Table 2, provide in a solar model approximately the same value for the acoustic flux F_{ac} (see Sect. 2). In model A2 (which assumes $\Lambda = 2000$ and $\Gamma = 7.5$), however, F_{ac} is about three times larger than in model A1 (which assumes $\Lambda = 100$ and $\Gamma = 5$), and the associated velocities, plotted in Fig. 4, are correspondingly greater.

It is interesting to note that in Fig. 4 the convective velocities in the superadiabatic boundary layers of models A1 and A2 are somewhat larger than the others. Although including acoustic radiation in the mean stellar structure leads to a reduction of the maximum turbulent Mach number $M_t \equiv w/c$ (by $\sim 1.5\%$ for model A1 and $\sim 5\%$ for model A2 relative to B1), the whole structure of the outer layers changes too, thereby increasing

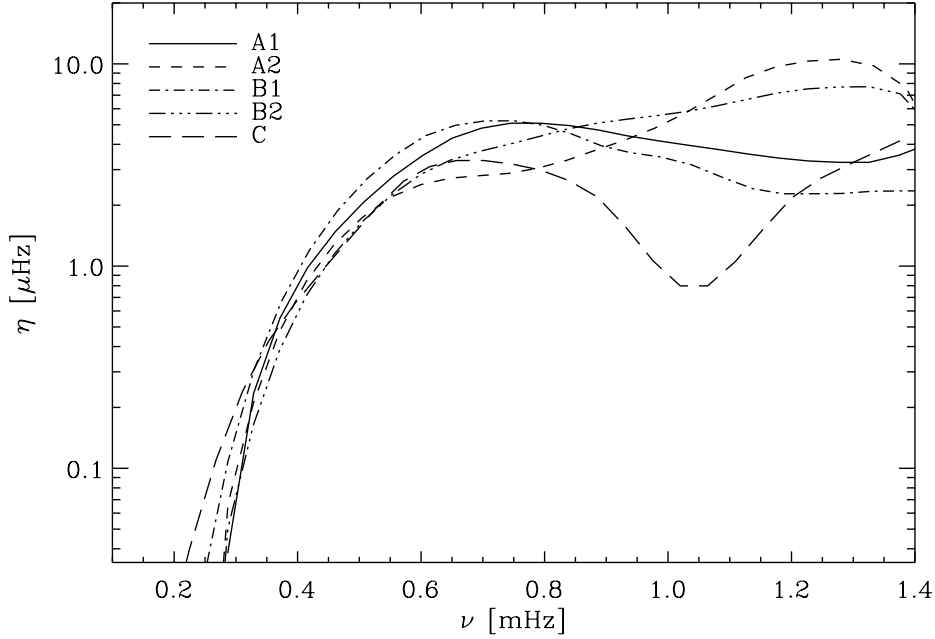


Fig. 2. Damping rates of stable radial p modes as function of frequency for all stellar models.

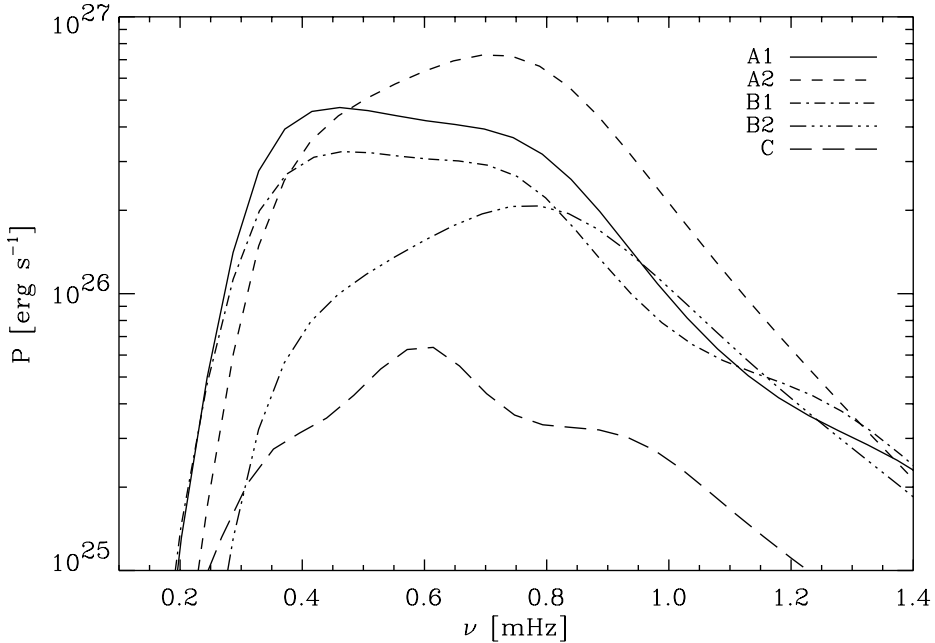


Fig. 3. Excitation rate P as function of frequency for all stellar models.

the locally defined adiabatic sound speed c . This leads to an increase of the convective velocities w in the very outer layers despite the decrease in M_1 .

The less smooth frequency dependence (wiggles) of P for $\nu \gtrsim 0.7 \mu\text{Hz}$ for model B1 (and model C) is related to the location and extent of the driving region: the radial eigenfunctions ξ_r vary rapidly with depth and frequency (particularly for the high-frequency modes). As discussed above, in the models A2 and B2 the modes are predominantly excited in a shallow region beneath the surface, where the expression $(d\xi_r/dr)^2$ (see

Eq. (3)) varies monotonically with frequency (Goldreich et al. 1994; Samadi et al. 2002), leading to the smooth frequency dependence of P for $\nu \gtrsim 0.7 \mu\text{Hz}$, as depicted in Fig. 3. The larger driving regions in the models B1 and C extend to layers where the expression $(d\xi_r/dr)^2$ no longer varies monotonically with frequency leading to the frequency-dependence of P as shown by the dot-dashed and long-dashed curves in Fig. 3.

In the top panel of Fig. 5 the surface velocity amplitudes v_s are depicted for all stellar models, computed according to Eq. (1). In the models A1, A2, B1 and B2 the amplitudes of

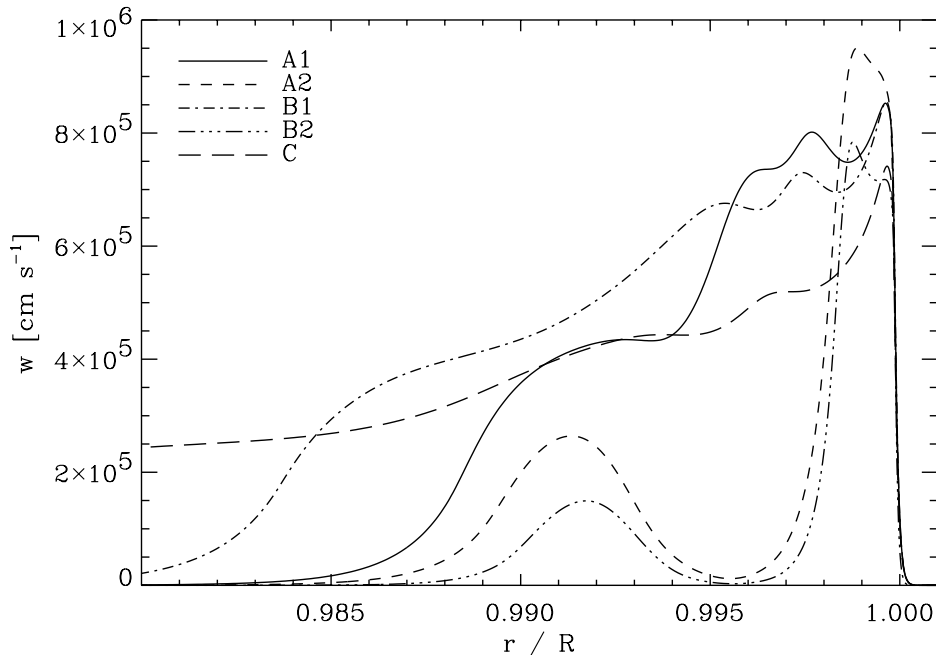


Fig. 4. Depth dependence of the vertical component of the convective velocity, with R being the radius at the photosphere ($T = T_{\text{eff}}$).

stochastically excited p modes are larger ($\sim 5\text{--}9\text{ ms}^{-1}$) than in model C ($\sim 2\text{ ms}^{-1}$).

For estimating the luminosity amplitudes the full nonadiabatic luminosity eigenfunctions have to be used. The relative luminosity amplitudes, $\delta L/L$, are linearly related to the velocity amplitudes, i.e. they are proportional to the ratio of the luminosity eigenfunction over the displacement eigenfunction. This ratio is determined by the solution of the nonadiabatic pulsation equations and is independent of a stochastic excitation model (see Houdek et al. 1999). In the middle panel of Fig. 5 the amplitude ratios, $\Delta L/\Delta v_s$, are plotted as a function of frequency for all stellar models. The shape of the amplitude ratios are in general similar between all the models with the smallest ratios predicted for the models A2 and A1. Only at the highest frequencies the amplitude ratios are considerably larger in A2 and B2; at high frequencies nonadiabatic effects due to radiative dissipation in the radiative zone, below the shallow surface convection zones in A2 and B2, lead to an increase in the amplitude of the luminosity eigenfunctions and consequently in the luminosity amplitudes. The velocity amplitudes in Fig. 5 are obtained 200 km above the photosphere ($T = T_{\text{eff}}$) and do increase by a factor of about two at the outermost meshpoint of the model, i.e. at an optical depth $\tau = 10^{-4}$.

We predict a maximum value of the luminosity amplitude $\delta L/L \sim 97$ ppm for model A1, $\delta L/L \sim 150$ ppm for model A2, $\delta L/L \sim 101$ ppm for model B1, $\delta L/L \sim 98$ ppm for model B2 and $\delta L/L \sim 84$ ppm for model C. These results are summarized in Table 4.

The dotted horizontal line in the middle panel of Fig. 5 represents an order-of-magnitude estimate of the amplitude ratio according to Kjeldsen & Bedding (1995):

$$\delta L/L \propto v_s T_{\text{eff}}^{-1/2}. \quad (4)$$

Kjeldsen & Bedding derived this expression for a purely radiative model assuming simplified proportional relations in the adiabatic approximation. This simplified scaling law suggests smaller values for the amplitude ratios and consequently leads to smaller luminosity amplitudes $\delta L/L$, particularly at high frequencies, where nonadiabatic effects are important. At a frequency $\nu \approx 1$ mHz, for example, the scaling law (4) predicts for model A1 a luminosity amplitude which is about three times smaller than that obtained from the nonadiabatic computation.

There is evidence that energy equipartition holds for the Sun (apparently fortuitously); an estimate of the total energy in the modes is, however, only possible for the Sun for which accurate data are available; using GONG data the total energy for modes with degrees $l = 0, \dots, 300$ and with radial order n up to 10 is found to be approximately $2 \times 10^6 E_0$, where $E_0 \sim 2 \times 10^{28}$ erg is the maximum value of the kinetic energy in a particular ridge (i.e. for a particular value of n) and which is independent of l (see Fig. 5 of Komm et al. 2000). The value 2×10^6 is also roughly equal to the number of granules on the solar surface, a result which supports the energy equipartition principle. In other stars, however, energy equipartition does not necessarily hold, because we have a nonequilibrium dynamical (yet statistically steady) system in which the damping and excitation is balanced in a nonlinear way by the energy input and output, i.e. it is not determined by equilibrium. In such a nonequilibrium situation there is no general physical principle limiting the ratio of the energy in the oscillation mode to the energy in the convection. Another facet of such a dynamical process is provided by the reaction of convection to the acoustical radiation; although the latter contributes towards augmenting the damping of an eddy, the resultant change of the background stratification is such as to augment the driving by even more, causing the convective velocities to increase.

Table 4. Maximum values of the estimated velocity, v_s , and luminosity, $\delta L/L$, amplitudes.

Model	v_s [ms^{-1}]	$\delta L/L$ [ppm]
A2	8.6	150
A1	7.9	97
B1	4.9	101
B2	5.5	98
C	2.0	84

It is perhaps interesting to mention that the acoustic energy flux generated by the fluctuating Reynolds stress of the turbulent velocity field is relatively small compared to the total energy flux carried by the convection; the ratio between the acoustic energy flux emitted by the energy-bearing eddies and the convective energy flux is proportional to M_t^2 with $\Gamma = 5$ for homogeneous, isotropic turbulence (see Lighthill 1952). The turbulent Mach number in δ Scuti stars is in general much smaller than unity and consequently this ratio is small. For the Sun this ratio is of the order of $\sim 10^{-3}$ (see e.g., Stein 1968). The acoustic flux emitted predominantly by inertial-range eddies is proportional to M_t^2 with $\Gamma = 15/2$ (see Goldreich & Kumar 1990), *i.e.* it scales with an even higher power of the Mach number (see also Sect. 2). Consequently the total amount of acoustic energy injected into the p modes is small compared to the energy carried by the convection. In a fully convective envelope the total energy flux (luminosity) is carried solely by the turbulent velocity field, *i.e.* in that case the luminosity is a measure of the total energy in the convection. Therefore the ratio between the energy supply rate for a particular mode and the luminosity, P/L , is proportional to the ratio between the energy in that mode and the total energy in the convection. In the Sun this ratio is of the order of $\sim 10^{-11}$ for the mode with the largest amplitude. In model A2 this ratio is $\sim 10^{-8}$, which is still small.

5. Observational constraints for detecting solar-type oscillations

There have been recent reports on the possible detection of solar-type oscillations in α Cen (HD 128620) by Bouchy & Carrier (2001), in β Hydri (HD 2151) by Bedding et al. (2001) and in Procyon A (HD 61421) by Martic et al. (1999; see also Barban et al. 1999), who obtained spectroscopic surface velocity measurements of these bright stars (the apparent magnitude $V = 2.80$ for β Hydri, $V = 0.34$ for Procyon and $V = -0.1$ for α Cen) from the ground. The maximum values of the observed peak-velocity amplitudes are of the order $\sim 35 \text{ cm s}^{-1}$ for α Cen, $\sim 50 \text{ cm s}^{-1}$ for β Hydri and $\sim 50 \text{ cm s}^{-1}$ for Procyon. Current ground-based instruments are able to detect oscillations with velocity amplitudes of the order predicted for our models A1, A2 and B1, B2, but only for stars with an apparent magnitude V of less than $\sim 3-4$ (Bouchy, personal communication). The HARPS (High-Accuracy Radial-velocity Planetary Search) project (Bouchy & Carrier 2001), for example, will be able to detect oscillations with our predicted velocity amplitudes for stars with an apparent magnitude smaller than $\sim 4-5$.

This detection threshold is still too small for detecting solar-type oscillations in δ Scuti stars located near the red edge of the IS, particularly in view of the fact that most of the currently known δ Scuti stars are even fainter. For example, the apparent magnitudes of known δ Scuti stars located nearest to the red edge (see Fig. 1) are between $V = 5.7$ and $V = 9.3$.

Future space missions with instruments dedicated to asteroseismology, however, will be able to detect solar-like oscillations in δ Scuti stars: the forthcoming space project COROT (Baglin & The Corot Team 1998), for example, will reach a noise level of 0.7 ppm (Auvergne & the COROT Team 2000) for a star with an apparent magnitude of $V = 6$, using photometric measurements. Therefore, in stars with similar magnitudes, COROT will be able to detect oscillation amplitudes as small as ~ 3 ppm, a value which is similar to that measured in the Sun. The instrument on COROT will be limited by the photon noise only for stars with magnitudes larger than $V \approx 9$: *i.e.*, for a star with magnitude $V \approx 8$ the detection threshold will be ~ 5 ppm. This threshold is small enough to detect and measure many solar-like oscillations in δ Scuti stars which are similar to the δ Scuti models considered in this paper.

6. Conclusion

We studied oscillation properties in δ Scuti stars located near the observed red edge of the classical instability strip. Such stars can pulsate with both opacity-driven modes and intrinsically stable stochastically driven (solar-like) modes. The estimated velocity amplitudes of the stochastically driven modes in our δ Scuti models are found to be larger than in cooler and pulsationally stable models lying outside the IS. This result supports the idea that solar-like oscillations in δ Scuti stars may be detected.

Including a model for the acoustic radiation in the equilibrium model results in a cooler red edge and does effect the properties of the excitation rate of p modes (see also Houdek & Gough 1998; Houdek 2000); in particular the pulsation amplitudes do become larger and are predicted to be largest for a model with the largest acoustic flux F_{ac} (*i.e.*, model A2). Moreover, for the δ Scuti models considered in this paper, overstable modes were predicted only if either acoustic emission in the mean stratification was included or if the mixing-length parameter was reduced to a value smaller than suggested by a calibrated solar model.

A potential target star should neither be too cool (*i.e.*, no opacity-driven modes) nor too hot (*i.e.*, stochastically excited modes with amplitudes too small to be detectable). We quantify this with the illustrative case of our δ Scuti models with a mass $M = 1.68 M_\odot$ and we identify the following δ Scuti stars from the Rodríguez et al. (2000) catalogue, located near the red edge, as potential candidates for the target selection of upcoming observing campaigns: HD57167, HD14147, HD208999 and HD105513.

Although the amplitudes of the solar-type oscillations, predicted in our δ Scuti models, are large enough to be detected from ground, today's ground-based instruments will detect such oscillations only in brighter δ Scuti stars with an apparent magnitude of up to $V \sim 3-4$ (Bouchy 2001, personal

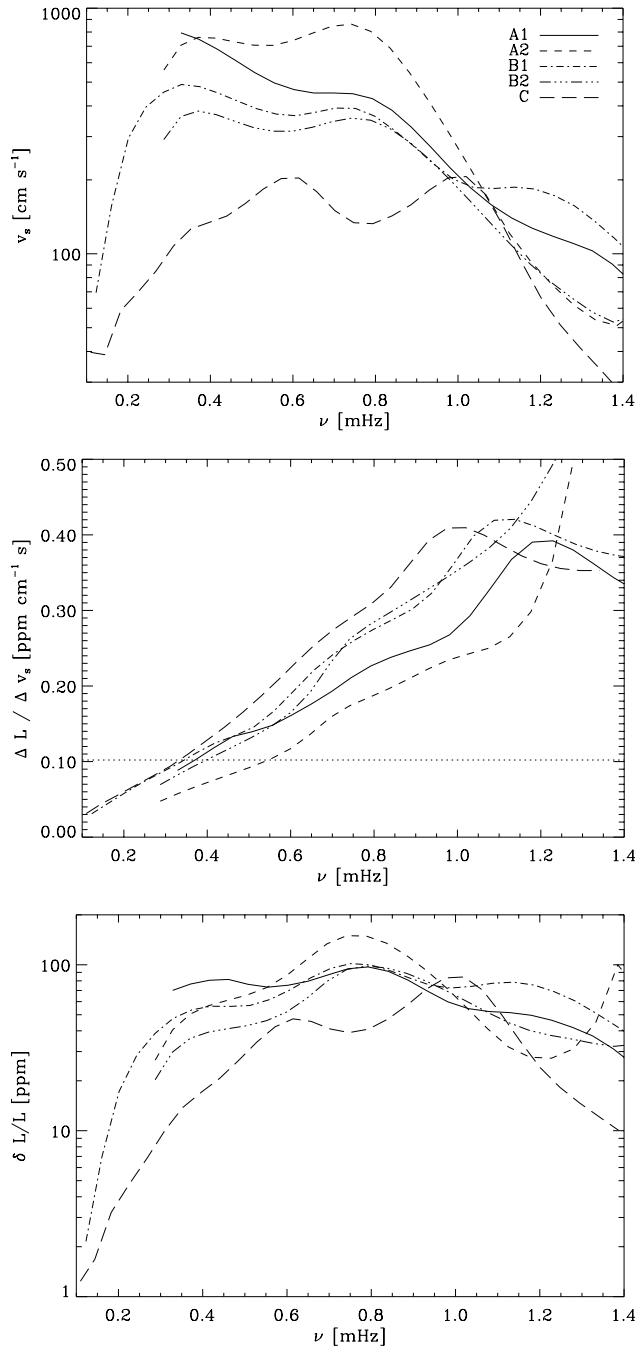


Fig. 5. Linear oscillation amplitudes of stable radial modes as a function of frequency. The top panel displays the surface velocity amplitudes and the middle panel the amplitude ratios, luminosity over velocity amplitudes, computed 200 km above the photosphere ($T = T_{\text{eff}}$). The dotted horizontal line represents the results for Kjeldsen & Bedding's (1995) scaling expression (4), assuming $T_{\text{eff}} = 6839$ K. In the bottom panel the luminosity amplitudes are depicted. In the middle and bottom panel the luminosity amplitudes are computed at the outermost meshpoint of the models.

communication). However, new ground-based observing campaigns, such as the HARPS project (Bouchy & Carrier 2001) will be able to detect stochastically excited oscillations in

δ Scuti stars with an apparent magnitude of up to $V \sim 4-5$. Unfortunately, there are no such bright stars in the Rodríguez et al. (2000) catalogue which are located near the red edge, although some bright stars near the red edge may have opacity-driven modes with amplitudes too small to be detectable with today's ground-based instruments and are therefore not classified as δ Scuti stars.

The forthcoming space missions for asteroseismology, such as COROT (Baglin & The Corot Team 1998) and Eddington (Favata et al. 2000) will be able to detect solar-like oscillations in faint δ Scuti stars. The large instrument on the Eddington spacecraft will measure stellar oscillations with amplitudes as small as 1.5 ppm in stars with an apparent magnitude of $V \approx 11$ assuming an observing period of 30 days. Moreover, Eddington's large field of view will allow it to monitor a large number of stars simultaneously. This will be helpful for detecting and classifying new δ Scuti stars and for measuring the location of the red edge of the IS with greater precision than it was possible before.

Acknowledgements. We thank E. Rodríguez for providing the δ Scuti data set in a convenient and immediate usable form, T. Lejeune for allowing us to use the Basel library and D. Cordier for providing it on the Internet. We thank A. Baglin for useful discussions on the COROT specifications, F. Bouchy for providing valuable information on the HARPS project and related experiments, and C. Catala and E. Michel for useful discussions on the possibilities of detecting new δ Scuti stars. We are grateful to Douglas Gough for very helpful discussions on stochastic mode excitation and to Mike Montgomery for improving the English. GH and RS acknowledge support by the Particle Physics and Astronomy Research Council of the UK. RS's work has been supported under the grant PPA/G/O/1998/00576.

References

- Auvergne, M., & the COROT Team 2000, in The Third MONS Workshop: Science Preparation and Target Selection, ed. T. C. Teixeira, T. Bedding (Aarhus University: Aarhus), 135
- Baglin, A., & The Corot Team 1998, in New Eyes to See Inside the Sun and Stars, ed. F.-L. Deubner, J. Christensen-Dalsgaard, & D.W. Kurtz (Kluwer: Dordrecht), IAU Symp. 185, 301
- Baker, N. H., & Gough, D. O. 1979, ApJ, 234, 232
- Balmforth, N. J. 1992, MNRAS, 255, 603
- Barban, C., Michel, E., Martic, M., et al. 1999, A&A, 350, 617
- Bedding, T. R., Butler, R., Kjeldsen, H., et al. 2001, ApJ, 549, L105
- Berthomieu and the COROT Seismic Working Group, in Proc. Asteroseismology Across the HR Diagram, 1-5 July 2002, Porto, in preparation
- Bono, G., Caputo, F., Castellani, V., et al. 1995, ApJ, 442, 159
- Bouchy, F., & Carrier, F. 2001, A&A, 374, L5
- Breger, M., Pamyatnykh, A. A., Pikall, H., & Garrido, R. 1999, A&A, 341, 151
- Christensen-Dalsgaard, J., Gough, D. O., & Thompson, M. J. 1991, ApJ, 378, 413
- Dziembowski, W. A., & Goode, P. R. 1992, ApJ, 394, 670
- Favata, F., Roxburgh, I., & Christensen-Dalsgaard, J. 2000, in The Third MONS Workshop: Science Preparation and Target Selection, ed. T. C. Teixeira, & T. Bedding (Aarhus University: Aarhus), 49
- Gautschi, A., & Saio, H. 1996, ARA&A, 34, 551
- Goldreich, P., & Kumar, P. 1990, ApJ, 363, 694

- Goldreich, P., Murray, N., & Kumar, P. 1994, *ApJ*, 424, 466
- Gough, D. 1976, in *Lecture notes in physics, Problems of stellar convection*, ed. E. Spiegel, & J.-P. Zahn (Springer: Berlin), vol. 71, 15
- Gough, D. O. 1977, *ApJ*, 214, 196
- Houdek, G. 1996, Ph.D. Thesis, Institut für Astronomie, Wien
- Houdek, G. 2000, in *Delta Scuti and Related Stars*, ed. M. Breger, & M. H. Montgomery (ASP: San Francisco), ASP Conf. Ser., 210, 454
- Houdek, G., & Gough, D. O. 1998, in *Proc. SOHO 6/GONG 98 Workshop, Structure and dynamics of the interior of the Sun and Sun-like stars*, ed. S. G. Korzennik, & A. Wilson (ESTEC: Noordwijk), ESA SP-418, vol. 2, 479
- Houdek, G., Balmforth, N. J., Christensen-Dalsgaard, J., & Gough, D. O. 1999, *A&A*, 351, 582
- Kjeldsen, H., & Bedding, T. R. 1995, *A&A*, 293, 87
- Komm, R. W., Howe, R., & Hill, F. 2000, *ApJ*, 543, 472
- Lejeune, T., Cuisinier, F., & Buser, R. 1998, *A&AS*, 130, 65
- Lighthill, M. J. 1952, *Proc. R. Soc. Lond.*, A211, 564
- Martic, M., Schmitt, J., Lebrun, J.-C., et al. 1999, *A&A*, 351, 993
- Michel, E., Hernández, M. M., Houdek, G., et al. 1999, *A&A*, 342, 153
- Morel, P. 1997, *A&AS*, 124, 597
- Musielak, Z. E., Rosner, R., Stein, R. F., & Ulmschneider, P. 1994, *ApJ*, 423, 474
- Nesis, A., Hanslmeier, A., Hammer, R., et al. 1993, *A&A*, 279, 599
- Rodríguez, E., & Breger, M. 2001, *A&A*, 366, 178
- Rodríguez, E., López-González, M. J., & López de Coca, P. 2000, *A&AS*, 144, 469
- Samadi, R., & Goupil, M.-J. 2001, *A&A*, 370, 136
- Samadi, R., Goupil, M.-J., & Lebreton, Y. 2001a, *A&A*, 370, 147
- Samadi, R., Houdek, G., Goupil, M.-J., Lebreton, Y., & Baglin, A. 2001b, in *1st Eddington Workshop: Stellar Structure and Habitable Planet Finding*, ESA SP-485, 87
- Samadi, R., Houdek, G., Goupil, M.-J., & Lebreton, Y. 2002, *A&A*, submitted
- Soufi, F., Goupil, M. J., & Dziembowski, W. A. 1998, *A&A*, 334, 911
- Stein, R. F. 1968, *ApJ*, 154, 297
- Unno, W., Osaki, Y., Ando, H., Saio, H., & Shibahashi, H. 1989, *Nonradial oscillations of stars* (Tokyo: University of Tokyo Press) 2nd ed.
- Xiong, D. R., & Deng, L. 2001, *MNRAS*, 324, 243

Numerical constraints on the model of stochastic excitation of solar-type oscillations

R. Samadi^{1,2}, Å. Nordlund³, R. F. Stein⁴, M. J. Goupil², and I. Roxburgh^{1,2}

¹ Astronomy Unit, Queen Mary, University of London, London E14NS, UK

² Observatoire de Paris, LESIA, CNRS UMR 8109, 92195 Meudon, France

³ Niels Bohr Institute for Astronomy Physics and Geophysics, Copenhagen, Denmark

⁴ Department of Physics and Astronomy, Michigan State University, East Lansing, Michigan, USA

Received 7 November 2002 / Accepted 7 March 2003

Abstract. Analyses of a 3D simulation of the upper layers of a solar convective envelope provide constraints on the physical quantities which enter the theoretical formulation of a stochastic excitation model of solar p modes, for instance the convective velocities and the turbulent kinetic energy spectrum. These constraints are then used to compute the acoustic excitation rate for solar p modes, P . The resulting values are found ~ 5 times larger than the values resulting from a computation in which convective velocities and entropy fluctuations are obtained with a 1D solar envelope model built with the time-dependent, nonlocal Gough (1977) extension of the mixing length formulation for convection (GMLT).

This difference is mainly due to the assumed mean anisotropy properties of the velocity field in the excitation region. The 3D simulation suggests much larger horizontal velocities compared to vertical ones than in the 1D GMLT solar model. The values of P obtained with the 3D simulation constraints however are still too small compared with the values inferred from solar observations.

Improvements in the description of the turbulent kinetic energy spectrum and its depth dependence yield further increased theoretical values of P which bring them closer to the observations. It is also found that the source of excitation arising from the advection of the turbulent fluctuations of entropy by the turbulent movements contributes ~ 65 – 75% to the excitation and therefore remains dominant over the Reynolds stress contribution. The derived theoretical values of P obtained with the 3D simulation constraints remain smaller by a factor ~ 3 compared with the solar observations. This shows that the stochastic excitation model still needs to be improved.

Key words. convection – turbulence – stars: oscillations – Sun: oscillations

1. Introduction

Solar-type oscillations are believed to be stochastically excited by turbulent convection in the near-surface layers of the star. The excitation is caused by turbulent convective motions which generate acoustic energy which in turn is injected into the p modes (e.g. Goldreich & Keeley 1977). Measurements of the acoustic energy injected into solar-like oscillations are among the goals of future space seismic missions such as the COROT (Baglin & The Corot Team 1998) and Eddington (Favata et al. 2000) missions. These seismic data will make it possible to constrain the theory of the oscillation excitation and damping, to provide valuable information about the properties of stellar convection, and hence to severely constrain stellar models.

Models for stochastic excitation of stellar p modes have been proposed by several authors, (e.g. Goldreich & Keeley 1977; Osaki 1990; Balmforth 1992a; Goldreich et al. 1994; Samadi & Goupil 2001). These theoretical approaches yield

the acoustic energy injected into solar-like oscillations. This offers the advantage of testing separately several properties entering the excitation mechanism which are not well understood or modeled.

Such approaches require simplifying assumptions which need to be validated before they can be used with confidence. They require an accurate knowledge of the properties of turbulent convection and, unfortunately, current observations of the solar granulation cannot provide a determination of the turbulent spectrum precise enough in the present context (Rieutord et al. 2000; Nordlund et al. 1997). On the theoretical side, theoretical models of turbulent convection, such as the mixing-length approaches or multiple size eddies approaches (e.g. Canuto & Mazzitelli 1991; Canuto et al. 1996), provide a too limited description of the characteristic scale length of the solar turbulent spectrum.

These theoretical formulations of stochastic excitation also involve scaling parameters which are determined to by the requirement that the computed values of the oscillation amplitudes give the best fit to the solar seismic measurements (e.g.

Send offprint requests to: R. Samadi,
e-mail: Reza.Samadi@obspm.fr

Houdek et al. 1999; Samadi et al. 2001, Paper II hereafter). When the scaling parameters are so adjusted, constraints and validation on the turbulent stellar medium can only come from seismic observations of other stars. Such accurate data on the excitation rates for other stars than the Sun are not yet available.

An alternative way is then to consider results from 3D numerical simulations. They indeed enable one to compute directly the rate at which p modes are excited (e.g. this was undertaken for the Sun by Stein & Nordlund 2001). Such methods are time consuming and do not easily allow massive computations of the excitation rate for stars with different temperatures and luminosities. They can provide quantities which can be implemented in a formulation for the excitation rate P . In any case we cannot avoid to use a 1D model for computing accurate eigenfrequencies for the whole observed frequency range.

The purpose of the present paper is to provide a better insight into the excitation model with a semianalytical approach but using a model of turbulence and values of the scaling parameters derived from a 3D simulation of the solar outer layers. We consider in this work the theoretical formulation of stochastic excitation by Samadi & Goupil (2001, hereafter Paper I, see also Samadi 2001 for a detailed summary) which includes a detailed treatment of turbulent convection. This formulation involves two scaling parameters which are related to the spatial and temporal characteristics of the turbulence model. Our final goal is to test the excitation model without adjusting these parameters and without the use of the mixing-length approach for estimating convective velocities and entropy fluctuations.

The paper is organized as follows: in Sect. 2 we briefly recall the adopted formulation for estimating the rate at which turbulent convection supplies energy to the p modes (excitation rate $P(\nu)$). We emphasize some assumptions and approximations entering this formulation.

In Sect. 3, a 3D numerical simulation of the upper part of the solar convection zone is used in order to determine the time averaged properties of turbulent convection: this provides constraints on the ingredients involved in the theoretical expression of the excitation rate, such as scaling parameters, velocity anisotropy factor, the values of convective velocities and entropy fluctuations and the k (wavenumber) dependence of the kinetic turbulent spectrum.

These constraints are then used in Sect. 4 to compute the excitation rate $P(\nu)$, for radial solar p modes. The results are compared with solar seismic observations as given in Chaplin et al. (1998) and with a 1D mixing-length model built according to Gough (1977)'s non-local formulation of the mixing-length theory (GMLT hereafter). In Sect. 5 we summarize our results and discuss some possible origins of the remaining discrepancies with solar seismic observations and results by Stein & Nordlund (2001).

2. Stochastic excitation

2.1. The excitation model

The rate at which turbulent motions of the convective elements supply energy to acoustic oscillation modes is computed as in Paper I. For a given mode with eigenfrequency ω_0 ,

the excitation rate can be written as (Eqs. (58) and (59) of Paper I):

$$P(\omega_0) = P_R + P_S \quad (1)$$

where

$$P_{R,S} = \frac{\pi^3}{2I} \int_0^M dm \rho_0 \frac{\Phi}{3} w^4 F_{R,S} \quad (2)$$

where ρ_0 is the mean averaged density, w is the rms value of the vertical component of the velocity,

$$I \equiv \int_0^M dm \xi_r^2 \quad (3)$$

is the mode inertia, ξ_r is the radial component of the fluid displacement adiabatic eigenfunction ξ , and Φ is an anisotropy factor. Following Gough (1977), we define

$$\Phi(z) \equiv \frac{\overline{\langle \mathbf{u}^2 \rangle} - \langle \mathbf{u} \rangle^2}{w^2} \quad (4)$$

where \mathbf{u} is the velocity field, $\langle \cdot \rangle$ denotes horizontal average and $\overline{(\cdot)}$ denotes time average. The mean vertical velocity, w , is defined as:

$$w^2 \equiv \overline{\langle u_z^2 \rangle} - \langle u_z \rangle^2. \quad (5)$$

P_R , P_S respectively account for the excitation by the Reynolds stress and for the excitation resulting from the advection of the entropy fluctuations by the turbulent velocity field (the so-called entropy source term). Here the entropy term (F_S) is an advective term which mixes turbulent pressure and entropy fluctuations. Expressions for F_R , F_S are:

$$F_R = f_R(\xi) S_R(\omega_0) \quad F_S = f_S(\xi) S_S(\omega_0) \quad (6)$$

with

$$f_R(\xi) = \mathcal{G} \frac{\Phi}{3} \left(\frac{d\xi_r}{dr} \right)^2 \quad (7)$$

$$f_S(\xi) = \mathcal{H} \left(\frac{\alpha_s \tilde{s}}{\rho_0 w} \right)^2 \frac{g_r(\xi_r, m)}{\omega_0^2} \quad (8)$$

where $\alpha_s = (\partial p / \partial s)_\rho$, p denotes the pressure and s the entropy, \tilde{s} is the rms value of the entropy fluctuations, and \mathcal{G} and \mathcal{H} are anisotropy factors. We assume that injection of acoustic energy into the modes is isotropic. This assumption implies $\mathcal{G} = 16/15$ and $\mathcal{H} = 4/3$ in Eqs. (7) and (8) above. Effects of the space averaged anisotropy in the driving process is investigated in Sect. 4.1.2.

The function $g_r(\xi_r, m)$ is defined as:

$$g_r(\xi_r, m) = \left(\frac{1}{\alpha_s} \frac{d\alpha_s}{dr} \frac{d\xi_r}{dr} - \frac{d^2 \xi_r}{dr^2} \right)^2. \quad (9)$$

One can show that the Reynolds contribution $-P_R-$ scales as $\Phi^2 w^4$ while the source term involving the entropy fluctuations $-P_S-$ scales as $\Phi w^2 \tilde{s}^2$. $P(\omega)$ is thus very dependent of the estimated values of w^2 , \tilde{s}^2 and Φ . The MLT provides estimates for w but Φ is a free parameter. For isotropic turbulence $\Phi = 3$, and in Böhm-Vitense (1958, BV-MLT hereafter) formulation $\Phi = 2$. In the present paper, unless otherwise stated, Φ is

given by a simulation of the upper part of the solar convective zone in Sect. 3.4 below.

For the driving sources in Eq. (6):

$$S_R = \int_0^\infty \frac{dk}{k^2} \frac{E(k, r)}{u_0^2} \frac{E(k, r)}{u_0^2} \chi_k(\omega_0) \quad (10)$$

$$S_S = \int_0^\infty \frac{dk}{k^2} \frac{E(k, r)}{u_0^2} \frac{E_s(k, r)}{\bar{s}^2} \times \int_{-\infty}^{+\infty} d\omega \chi_k(\omega_0 + \omega) \chi_k(\omega) . \quad (11)$$

$E(k)$ represents the kinetic energy spectrum associated with the turbulent velocity field and $E_s(k)$ models the spectrum of the turbulent entropy fluctuations, with k the eddy wavenumber. The time-dependent part of the turbulent spectrum is described by the function $\chi_k(\omega)$ which models the correlation time-scale of an eddy with wavenumber k . The quantity $u_0 \equiv \sqrt{\Phi/3} w$ is introduced for convenience (see Eq. (17)),

The above expression for P is mainly based on the assumption that the medium is incompressible. In other words, we adopt the Boussinesq approximation i.e. assume a homogeneous model for the turbulence and the excitation mechanism. We therefore neglect effects of the stratification in the excitation process.

2.2. The turbulence model

Let $k_0(r)$ be the wavenumber at which energy is injected into the turbulent cascade and the energy $E(k)$ is maximum. $k_0(r)$ is related to the mixing-length $\Lambda \equiv \alpha H_p$ by (Paper I):

$$k_0^{\text{MLT}}(r) \equiv \frac{2\pi}{\beta \Lambda(r)} = \frac{2\pi}{\beta \alpha H_p(r)}, \quad (12)$$

where β is a parameter of order unity, α is the mixing-length parameter and H_p is the pressure scale-height. This is a natural way to estimate k_0 as Λ is the characteristic length of the largest convective elements.

The Gaussian function is usually assumed for modeling $\chi_k(\omega)$ (e.g. Stein 1967; Goldreich & Keeley 1977) as a consequence of the turbulent nature of the medium where the stochastic excitation occurs. The Gaussian function takes the form

$$\chi_k(\omega) = \frac{1}{\omega_k \sqrt{\pi}} e^{-(\omega/\omega_k)^2}, \quad (13)$$

where ω_k is its linewidth.

Let τ_k be the characteristic time correlation length of an eddy of wavenumber k . Equation (13) corresponds in the time domain to a Gaussian function with linewidth equal to $2/\omega_k$. Then $\omega_k = 2/\tau_k$ for a Gaussian time spectrum.

The energy supply rate P crucially depends on the correlation time-scale τ_k (see Paper II). Following Balmforth (1992a) we define it as:

$$\tau_k = \lambda (k u_k)^{-1}, \quad (14)$$

where u_k is the velocity of an eddy with wavenumber k . The velocity u_k is obtained from the kinetic energy spectrum $E(k)$ (Stein 1967)

$$u_k^2 = \int_k^{2k} dk E(k). \quad (15)$$

$E(k)$ is normalised such that:

$$\int_0^\infty dk E(k) = \frac{1}{2} \langle \mathbf{u}^2 \rangle = \frac{3}{2} u_0^2(z) \quad (16)$$

where u_0 is introduced for convenience. According to Eqs. (4) and (16), u_0 and w are then related to each other by

$$\frac{3}{2} u_0^2 = \frac{1}{2} \Phi(z) w^2(z). \quad (17)$$

The parameter λ in Eq. (14) accounts for our lack of precise knowledge of the time correlation τ_k in stellar conditions. In the present paper, we assume $\lambda = 1$ while β (Eq. (12)) and $\Phi(z)$ (Eq. (4)) are given by a simulation of the upper part of the solar convective zone in Sect. 3.4 below.

2.3. Computations of the excitation rate $P(\omega)$

In practice, we compute the excitation rate $P(\omega)$ according to Eq. (1). The calculation requires the knowledge of several quantities which can be obtained either from a 1D model (Paper II) or at least partly from a 3D simulation. Comparison of the results using both options yields insights in the excitation mechanism and its modelling. Hence in the following:

- The velocity, entropy fluctuations, anisotropy and turbulent spectra E 's are obtained from a 3D simulation as described in the next section.

- The mean density, ρ_0 , the thermodynamic quantity α_s , the oscillation properties – eigenfrequencies and eigenfunctions – are calculated from a solar envelope equilibrium model and Balmforth (1992b)'s pulsation code. The envelope model is built with a treatment of convection as prescribed by the GMLT formulation and is computed in the manner of Balmforth (1992b) and Houdek et al. (1999). This solar envelope model (hereafter GMLT solar model) is identical to the one considered in Samadi et al. (2002, hereafter Paper III). In particular, it incorporates turbulent pressure (momentum flux) in the equilibrium model envelope. The entire envelope is integrated using the equations appropriate to the nonlocal mixing-length formulation by Gough (1976) and to the Eddington approximation to radiative transfer (Unno & Spiegel 1966). The equation of state included a detailed treatment of the ionization of C, N, and O, and a treatment of the ionization of the next seven most abundant elements (Christensen-Dalsgaard 1982), as well as “pressure ionization” by the method of Eggleton, Faulkner & Flannery (Eggleton et al. 1973). In this generalization of the mixing-length approach, two additional parameters, namely a and b , are introduced which control the spatial coherence of the ensemble of eddies contributing to the total heat and momentum fluxes (a), and the degree to which the turbulent fluxes are coupled to the local stratification (b). These convection parameters are calibrated to a solar model to obtain the helioseismically inferred depth of the solar convection zone of 0.287

of the solar radius (Christensen-Dalsgaard et al. 1991). The adopted value for the shape factor $\Phi = 1.3745$, a value which provides the best fit between computed solar damping rates and measurements by Chaplin et al. (1998) (see Houdek et al. 2001). The detailed equations describing the equilibrium and pulsation models were discussed by Balmforth (1992b) and by Houdek (1996).

For implementation in Eqs. (1)–(11), the quantities from the 3D simulation are interpolated at the GMLT model mesh points. The grid of mesh points of the simulated domain is matched with the GMLT one such that w in the 3D simulation has its maximum at the same layer as in the GMLT model. In the simulation, w peaks ~ 40 km above the layer at which the mean optical depth $\langle \tau \rangle$ is unity while in the GMLT model, w peaks ~ 130 km below the photosphere ($\langle \tau \rangle = 2/3$).

3. Constraints from the 3D simulation

We consider a 3D simulation of the upper part of the solar convective zone obtained with the 3D numerical code developed at the Niels Bohr Institute for Astronomy, Physics and Geophysics (Copenhagen, Denmark).

The simulated domain is 3.2 Mm deep and its surface is 6×6 Mm². The grid of mesh points is $256 \times 256 \times 163$, the total duration 27 min and the sampling time 30 s. Physical assumptions are described in Stein & Nordlund (1998).

Output of the simulation considered here are the velocity field $\mathbf{u}(x, y, z, t)$ and the entropy $s(x, y, z, t)$. They are used to determine the quantities \hat{s}^2 , $\Phi(z)$, $w(z)$, $E_s(k, z)$, $E(k, z)$ which enter the excitation rate through Eqs. (2), (7), (8), (10), (11).

3.1. Fourier transforms and averaging

We compute the 2D Fourier transform, along horizontal planes, of the velocity field \mathbf{u} and the entropy s , at each layer z . This provides $\hat{\mathbf{u}}(\mathbf{k}, z, t)$ and $\hat{s}(\mathbf{k}, z, t)$ where \mathbf{k} is the wavenumber along the horizontal plane. Next we integrate $\hat{\mathbf{u}}^2(\mathbf{k}, z, t)$ and $\hat{s}^2(\mathbf{k}, z, t)$ over circles with radius k at each given layer z . Finally take a time average of the various quantities over the time series. This yields $\hat{\mathbf{u}}(k, z)$ and $\hat{s}(k, z)$ where $k = \|\mathbf{k}\|$ is the wavenumber norm.

We define the time averaged kinetic energy spectrum $E(k, z)$ as:

$$E(k, z) = \begin{cases} \frac{1}{2} \hat{\mathbf{u}}^2(k, z) & \text{for } k > 0 \\ 0 & \text{for } k = 0 \end{cases} \quad (18)$$

and the time averaged spectrum of the entropy $E_s(k, z)$ as:

$$E_s(k, z) = \begin{cases} \frac{1}{2} \hat{s}^2(k, z) & \text{for } k > 0 \\ 0 & \text{for } k = 0. \end{cases} \quad (19)$$

From Parseval-Plancherel's relation, $E(k, z)$ and $E_s(k, z)$ satisfy:

$$\int_0^{+\infty} dk E(k, z) = \frac{1}{2} \overline{\langle \mathbf{u}^2 \rangle - \langle u_z \rangle^2} \equiv \frac{3}{2} u_0^2(z) \quad (20)$$

$$\int_0^{+\infty} dk E_s(k, z) = \frac{1}{2} \overline{\langle s^2 \rangle - \langle s \rangle^2} \equiv \frac{1}{2} \hat{s}^2(z)$$

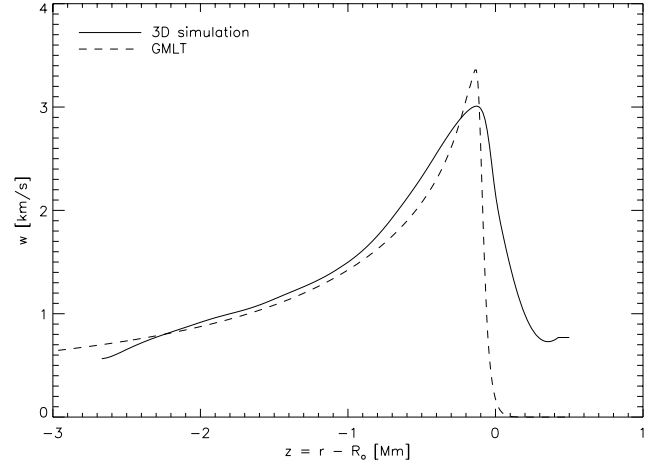


Fig. 1. The root mean square of the vertical component of the velocity ($w = \sqrt{\langle u_z^2 \rangle - \langle u_z \rangle^2}$) in the upper layers of a solar model is plotted versus depth for the 3D simulation (solid line) and for the 1D GMLT model (dashed line). The abscissa is the depth $z = r - R_\odot$ where R_\odot is the radius at the photosphere. The w maximum corresponds to the top of the superadiabatic region and is reached at the depth $z \approx -130$ km in the GMLT model. The grid of mesh points of the simulated domain is adjusted so that the w maxima of the 3D simulation and the GMLT coincide at the same layer.

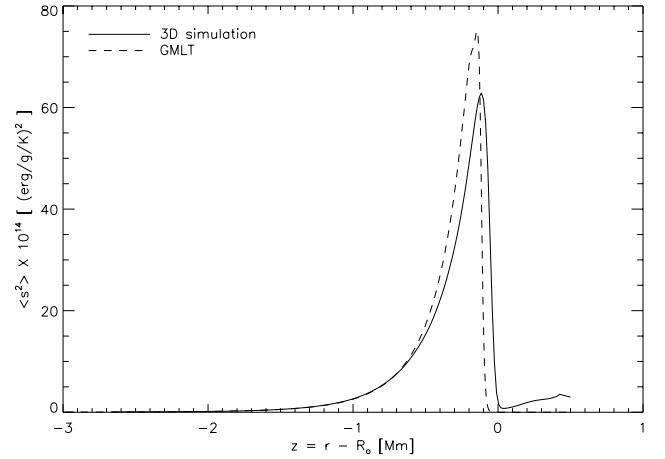


Fig. 2. Same as Fig. 1 for the mean square of the entropy fluctuations (\hat{s}^2). The peak is narrower than for the velocity w because \hat{s}^2 scales approximately as w^4 .

Hence the definitions of the energy spectra here involve zero mean velocity and entropy fluctuations.

3.2. Convective velocities and entropy fluctuations

Figures 1 and 2 present $w(z)$, $\hat{s}^2(z)$ versus depth for the 3D simulation. For comparison purpose, the plots also show w and \hat{s}^2 obtained with the GMLT solar model.

The vertical velocity GMLT w is larger at the top of superadiabatic region but smaller just beneath compared to values from the simulation. The GMLT \hat{s}^2 is larger than in the simulation ($\sim 20\%$). This explains that the relative contribution of the entropy source term to the excitation is overestimated with the

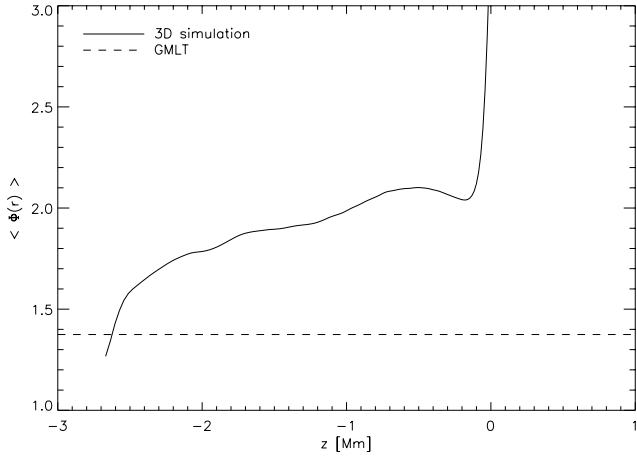


Fig. 3. Same as Fig. 1 for the anisotropy factor Φ versus z .

GMLT model (see Sect. 4.1.1). Differences between the GMLT and the simulation are likely to be related to differences in the convective efficiency: GMLT is less efficient than the 3D simulation. Indeed as pointed out by Houdek & Gough (2002), a single eddy approach such as the GMLT results in a larger peak for the superadiabatic gradient.

3.3. Velocity anisotropy at large scale

As it will be shown in Sect. 4.1.2, the value of Φ plays a crucial role in controlling the depth of the excitation region and therefore the total amount of acoustic energy injected into the oscillation modes.

Figure 3 displays the anisotropy factor Φ versus depth z for the 3D simulation. $\Phi(z)$ sharply decreases from the value $\Phi = 3$ at the top of the CZ down to $\Phi = 2$ and then slowly decreases to reach the value $\Phi \approx 1.3$ at the bottom of the simulation. The decrease of $\Phi(z)$ with depth is explained first by the onset of the convection and the formation of convective plumes at $z \sim 0$ and then by the *relative* increase in number of the plumes inward in the simulation. Indeed, plumes are highly anisotropic structures whereas turbulent cells are quite isotropic. The turbulent Mach number increases with z and reaches its maximum value at the top of the CZ. Therefore the fluid is more turbulent outward in the atmosphere. Consequently the number of turbulent isotropic cells increases with z up to the top of the CZ whereas the number of plumes remains roughly constant. The medium is thus more isotropic outward than inward.

In most of the excitation region, the value of $\Phi = 2$ consistent with the BV-MLT is in better agreement with the values of $\Phi(z)$ inferred from the simulation compared to the value $\Phi = 1.3745$ which must be imposed for the GMLT solar model in order to match the observed solar damping rates.

3.4. Turbulent kinetic energy spectrum $E(k)$

Variations of E and E_s with k at different depths z are depicted in Fig. 4. The spectra clearly show two regimes: at large scale (small values of k), the spectra increase approximately as k^{+1} which can roughly be explained using dimensional analysis.

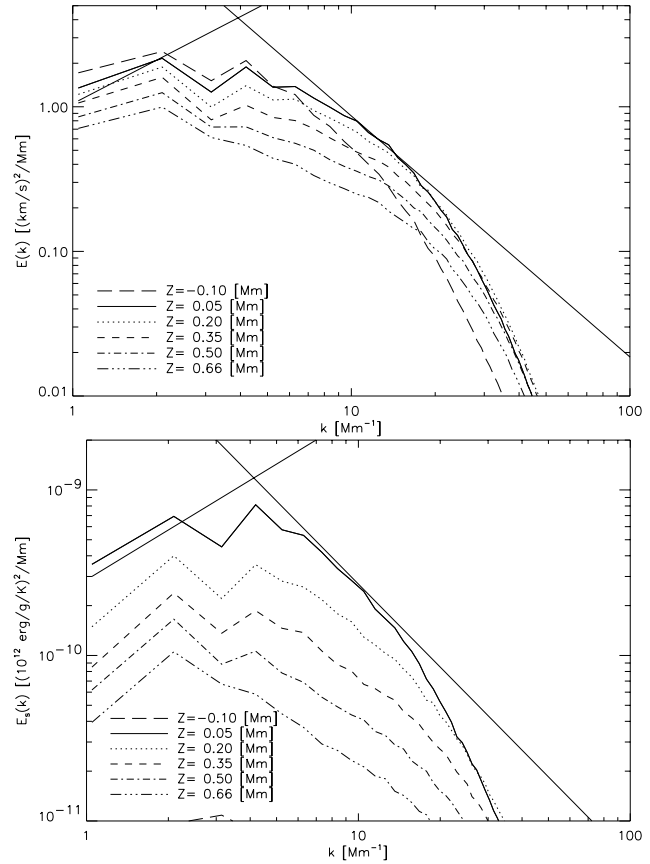


Fig. 4. Turbulent kinetic energy spectra E (top) and E_s (bottom) from the simulation are plotted versus k and for different depths z in the simulation. The straight solid lines delimitate the slopes k^1 and $k^{-5/3}$ of the EKS spectrum (Eq. (21)). Intersection of the slopes determines k_0^E , the scale of maximum energy at each depth z .

At small scale (large values of k), the spectra decrease very rapidly with k . The Kolmogorov law ($k^{-5/3}$) is observed only over a small k -range. Departures of the computed spectra from a Kolmogorov law at high values of k can be explained by the finite resolution of the simulation spatial grid.

The main characteristics of the kinetic spectrum $E(k, z) - k$ dependency – derived from the 3D simulation are approximately reproduced by an analytical expression which was considered by Musielak et al. (1994), namely the “Extended Kolmogorov Spectrum” (EKS hereafter) defined in Musielak et al. (1994) as:

$$E(k, z) = a \frac{u_0^2}{k_0^E} \begin{cases} \left(\frac{k}{k_0^E}\right)^{+1} & \text{for } k < k_0^E(z) \\ \left(\frac{k}{k_0^E}\right)^{-5/3} & \text{for } k > k_0^E(z) \end{cases} \quad (21)$$

where a is a normalisation factor which satisfies Eq. (20) and u_0 is defined according to Eq. (20). k_0^E is the scale of maximum energy in the energy spectrum.

At each layer, k_0^E is determined by imposing that the EKS, as defined above, matches the turbulent spectrum $E(k, z)$ calculated from the simulation as well as possible. This then

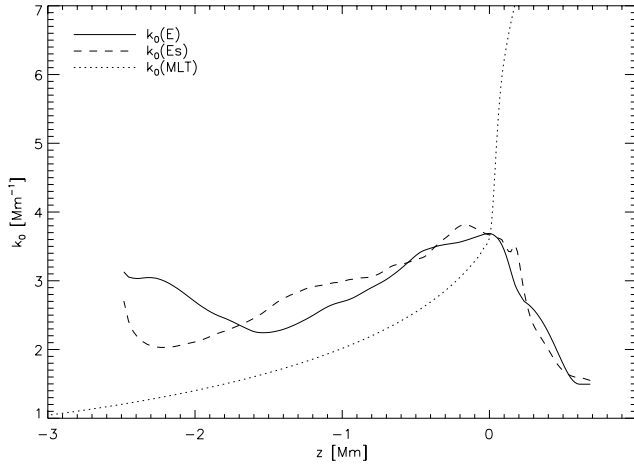


Fig. 5. The wavenumbers k_0^E (solid line) and k_0^{Es} (dashed line) are plotted versus z (k_0^E and k_0^{Es} are obtained by fitting, at each layer, the EKS (Eq. 21) to the computed spectra E and E_s of Fig. 4 resp., see text for details). The dotted line corresponds to $k_0^{MLT}(z)$ obtained according to Eq. (12). In computing $k_0^{MLT}(z)$, we assume $\beta = 3.48$ in order for k_0^{MLT} to match the value reached by k_0^E (solid line) at the layer $z \simeq -130$ km where w reaches its maximum ($k_0^E = 3.62$ Mm $^{-1}$ at that layer).

fixes the z dependency of k_0^E . A similar procedure is applied for $E_s(k, z)$ for which we introduce k_0^{Es} . All spectra satisfy their respective normalisation condition as given in Eq. (20).

For comparison, in Fig. 7, the “Nesis Kolmogorov Spectrum” (NKS hereafter) determined from solar observations of Nesis et al. (1993) is also shown. The NKS scales as k^{-5} in the energy injection region for $k < k_0^E$ and down to $k_{\min} = 0.7 k_0^E$. This spectrum does not agree with turbulent spectrum $E(k, z)$ calculated from the simulation. In particular, the NKS underestimates the velocity of the small size turbulent elements in the cascade ($k > k_0$) and overestimates the velocity of the turbulent with wavenumber $k \sim k_0^E$. As we will show in Sect. 4.2, differences between the EKS and the NKS have an important impact on $P(\omega)$.

If we assume that $k_0^E = k_0^{Es}$, one can show that $P(\omega)$ scales as k_0^{-4} . $P(\omega)$ is therefore very dependent on the values reached by $k_0(z)$ in the excitation region. Variation of $k_0(z)$ with depth is thus shown in Fig. 5 for E and E_s : k_0^E and k_0^{Es} vary slowly within the excitation region.

For comparison, in Fig. 5 we have also plotted $k_0^{MLT}(z)$, the MLT value for $k_0(z)$ according to Eq. (12). The scaling parameter β in the definition of k_0^{MLT} is determined such that k_0^{MLT} and k_0^E take the same value at the layer $z \simeq -130$ km where w reaches its maximum (and consequently the layer where the excitation is maximum). The derived value is $\beta = 3.48$.

k_0^{MLT} varies slowly with depth below the top of the superadiabatic region ($z \simeq -130$ km) but increases very rapidly above. Such a behavior is explained by the rapid decrease with z of the pressure scale height H_p (which enters in the definition of k_0^{MLT} , Eq. (12)) in the atmosphere.

Comparison between $k_0^{MLT}(z)$ and $k_0^E(z)$ shows that the mixing-length approach does not model satisfactorily the behavior of $k_0^E(z)$ in particular just above the layer at which w

reaches its maximum value. Consequences in terms of mode excitation are investigated in Sect. 4.3.

4. Consequences in term of p modes excitation

The acoustic energy supply rate P injected into the solar oscillations is related to the rms value v_s of surface velocity as:

$$P(\omega_0) = 2\eta \frac{I}{\xi_r^2(r_s)} v_s^2(\omega_0) \quad (22)$$

where η is the mode damping rate and r_s is the radius at which oscillations are measured.

We derive the “observed” P from Chaplin et al. (1998)’s seismic data according to Eq. (22) where the mode damping rate, η , and the mode surface velocity, v_s , are obtained from Chaplin et al. (1998)’s data. The mode mass $I/\xi_r^2(r_s)$ is given by the GMLT model and we adopt $r_s = R_\odot + 200$ km consistent with the observations.

Theoretical values of P are computed according to Eq. (1). In Eqs. (10) and (11) the integrations over k are performed from $k = k_{\min}$ (where k_{\min} depends on the adopted turbulent spectra E and E_s) to $k = 20 k_0$. We checked numerically that contributions to the excitation rate from turbulent elements with $k \gtrsim 20 k_0$ are negligible.

A Gaussian function is assumed for $\chi_k(\omega)$ in Eq. (10) and Eq. (11).

For the other quantities (w , \tilde{s}^2 , ϕ , k_0 , $E(k/k_0)$ and $E_s(k/k_0)$) involved in the expression for P we investigate several possible assumptions.

4.1. Convective velocities and large scale anisotropy

In this section, the excitation rate P (Eq. (1)) is computed with the following assumptions:

- the k -dependency E and E_s is given by the analytical form of Eq. (21), also called the EKS.
- $k_0^E = k_0^{Es} = k_0^{MLT}$ where $k_0^{MLT}(z)$ is given in Eq. (12) with $\beta = 3.48$ so that k_0^{MLT} takes the value reached by $k_0^E(z)$ (solid line, Fig. 5) at the layer $z \simeq -130$ km where w reaches its maximum.

For the quantities Φ , w and \tilde{s}^2 we investigate the effects of using either the values derived from the 3D simulation (see Sects. 3.2 and 3.3) or calculated with the GMLT solar model.

4.1.1. Convective velocities and entropy fluctuations

The values of w , \tilde{s}^2 and $\Phi(z)$ are fixed by the 3D simulation inside the simulation domain and by the 1D equilibrium model outside this domain. Either, if we impose zero values or if we assume quantities from the 1D MLT model, no sensitivity on the calculation of P is found.

Results are shown in Fig. 6 for P and for the relative contribution of the Reynolds stress to the total energy supply rate P . When the excitation rate $P(\nu)$ is computed with quantities derived from the 3D simulation as described in Sect. 2.3, the resulting excitation rate at maximum is found too small by a factor ~ 4 compared with the observations.

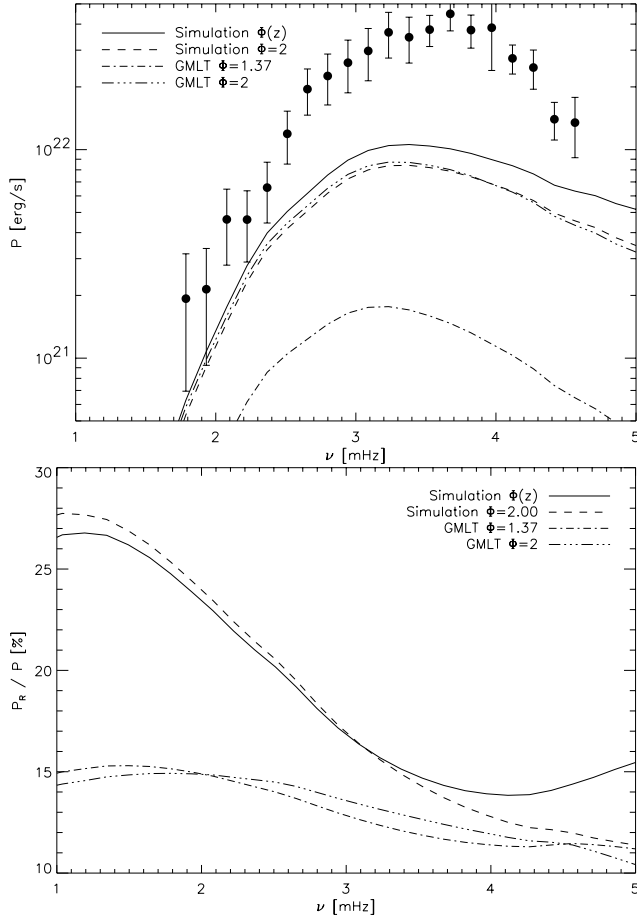


Fig. 6. Top: Rate P at which acoustic energy is injected into the solar radial modes. The filled dots represent P computed from Chaplin et al. (1998)’s solar seismic data according to Eq. (22). The curves represent theoretical values of P computed according Eq. (1) and for different computations of w , \tilde{s}^2 and $\Phi(z)$: Solid line: values of w , \tilde{s}^2 and $\Phi(z)$ are fixed by the 3D simulation inside the simulated domain and by the 1D equilibrium model outside this domain. Dashed line (– – –): same as solid line but fixing Φ to BV’s value $\Phi = 2$. Dot dashed line (– · – · –): values of w , \tilde{s}^2 and $\Phi (=1.37)$ are fixed by the 1D equilibrium model (GMLT). Three dots dashed line (– · · · – · · · –): same as the dot dashed line but fixing Φ to BV’s value $\Phi = 2$. **Bottom:** Same as top panel for the relative contribution of the Reynolds stress, P_R , to the total acoustic energy P .

Provided the appropriate value for Φ is given in the GMLT estimations (see Sect. 4.1.2 below), no significant difference is found in the excitation rate when computed with the values of w and \tilde{s}^2 from the simulation or their respective GMLT estimations.

The main effect is illustrated in the bottom panel of Fig. 6: the 3D simulation generates a larger relative contribution of the Reynolds stress to P than the GMLT model. This is explained as follows: within most part of the excitation region – except at the top of superadiabatic region – the values reached by w are larger whereas values reached by \tilde{s}^2 are smaller than their corresponding GMLT estimations.

4.1.2. Velocity anisotropy at large scales

The main consequence (in term of p modes excitation) of the differences between the time averaged properties of the convective region inferred from the 3D simulation and from the GMLT solar model (Fig. 6) is due to differences in their respective anisotropy factor Φ values (Fig. 3).

Within most of the excitation region, $\Phi(z)$ is found close to ~ 2 and thus larger than the value $\Phi = 1.37$ assumed for the 1D equilibrium model (see Sect. 3.3 and Fig. 3). Smaller values of Φ decrease the rms total convective velocity which results in larger values of τ_k (see Eqs. (14), (15)) and therefore in a smaller depth of excitation for a given mode frequency (see Paper III for more details). Smaller values of the rms total convective velocity also induce smaller values of E in the integrand of Eq. (1). Consequently, as it is illustrated in Fig. 6, the total amount of acoustic energy injected into the modes is ~ 5 times smaller for the constant value $\Phi = 1.37$ compared to the constant value $\Phi = 2$ (the relative contribution of the Reynolds stress to P is found ~ 2 times larger in the simulation).

The effect of the depth dependency of Φ on the mode excitation is small except at high frequency. This is illustrated in the bottom panel of Fig. 6 (compare the solid line with the dashed line). Just above the top of the superadiabatic region ($z \gtrsim -130$ km), $\Phi(z)$ increases rapidly with z until the value ≈ 3 (Fig. 3). Most of the injection of acoustic energy into the high frequency modes occurs at the top of superadiabatic region. The high frequency modes are therefore more sensitive to this rapid increase of $\Phi(z)$. As a consequence, the relative contribution of the Reynolds stress is larger for the high frequency modes than it is when assuming the constant value $\Phi = 2$.

4.2. Turbulent spectra

In this section we compare the excitation rate obtained assuming, for the turbulent spectra (E and E_s) either – the EKS spectrum (Eq. (21)) with slopes given by the 3D simulation as in the previous section – or assuming the NKS spectrum from solar observations of Nesis et al. (1993) (see also Paper I).

As in Sect. 4.1 we compute P using w , \tilde{s}^2 and Φ derived from the 3D simulation and assuming that $k_0^E = k_0^{E_s} = k_0^{\text{MLT}}$. The results are plotted in Fig. 8.

The NKS overestimates the maximum in P by a factor ~ 1.5 while the EKS underestimates it by a factor ~ 4 . This is because most of the kinetic energy in the NKS is concentrated at $k \sim k_0^E$ whereas in the EKS a large part of the energy is concentrated both at large scales ($k < k_0^E$) and at small scales ($k > k_0^E$).

4.3. Effects due to the stratification of the turbulent spectrum at large scale

In Sect. 3.4 we showed that the variations of k_0^E and $k_0^{E_s}$ with z deduced from the 3D simulation differ from the MLT estimation as given by Eq. (12) (see Fig. 5). Figure 9 presents the consequences of the z variations of k_0^E on the oscillation amplitudes (as the variations of k_0^E and $k_0^{E_s}$ with depth are quite similar we assume for the sake of simplicity that $k_0^{E_s}(z)$ is equal to $k_0^E(z)$).

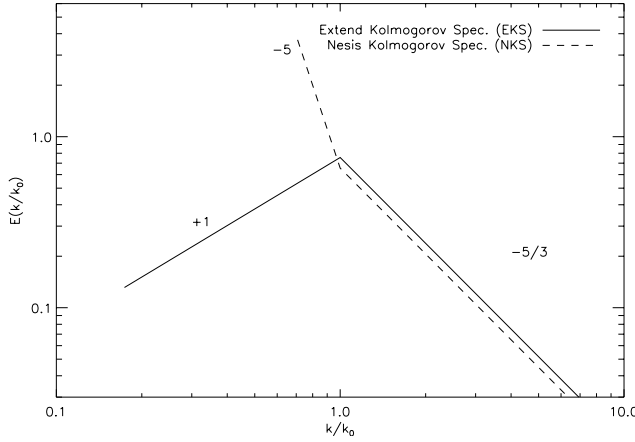


Fig. 7. The NKS and the EKS turbulent kinetic energy spectra are plotted versus the normalized wavenumber k/k_0 .

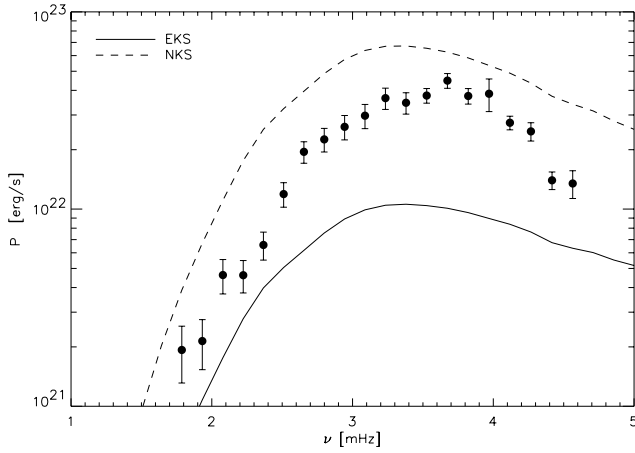


Fig. 8. Acoustic energy supply rate P computed according to Eq. (1) and assuming for $E(k)$ the EKS and the NKS plotted in Fig. 7. Dots represent the energy supply rate injected into the oscillations derived from the solar observations with the help of Eq. (22).

The z dependency of k_0^E causes the maximum of P to be larger than when assuming $k_0^E = k_0^{\text{MLT}}$ ($\sim 50\%$ larger). This is due to the fact that in most part of the excitation region k_0^{MLT} is smaller than k_0^E and $k_0^{E_s}$ except above the top of the superadiabatic region (see Fig. 5). A larger k_0^E results in a larger linewidth $\omega_k \equiv (ku_k)/\lambda$ for $\chi_k(\omega)$ hence in a larger amount of acoustic energy injected to the mode (see Eq. (13)).

Furthermore, at high frequency, P decreases with ν more rapidly than when assuming $k_0^E = k_0^{E_s} = k_0^{\text{MLT}}$. Taking into account the actual variation k_0^E with z instead of assuming $k_0^E = k_0^{\text{MLT}}$ makes then the ν -dependency of P at high frequency closer to that of the observed excitation spectrum. This is because, above the top of the superadiabatic region, k_0^E decreases with z whereas k_0^{MLT} increases with z . Indeed, the excitation of the high frequency modes occurs predominantly in the upper most part of the top of the superadiabatic region. As mentioned above the line width of $\chi_k(\omega)$ decreases with decreasing k_0 . Therefore the contribution of the term $\chi_k(\omega)$ to the excitation of high frequency mode is smaller when assuming

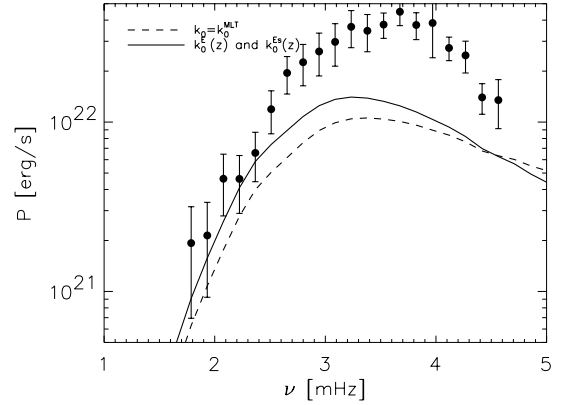


Fig. 9. Same as Fig. 6. Solid line: the variation of k_0^E and $k_0^{E_s}$ with z are obtained from the simulation (see Fig. 5 and Sect. 3.4). The dashed line is identical to the solid line of Fig. 6 where $k_0^E = k_0^{E_s} = k_0^{\text{MLT}}(z)$.

the actual variation of k_0^E with z than when assuming that k_0^E varies as k_0^{MLT} .

5. Summary and discussion

An analysis of a 3D simulation of the upper part of the solar convective zone provides time averaged constraints upon several physical parameters which enter the theoretical expression for the supply rate of energy, P , injected into the solar p modes. These constraints are:

- 1) the depth dependency: of u^2 , the mean square velocity – of w^2 , the mean square vertical component of the velocity – of \tilde{s}^2 , the mean square values of entropy fluctuations.
- 2) the wavenumber (k) dependency of E and E_s the turbulent kinetic energy spectrum and the turbulent entropy spectrum respectively.
- 3) the depth dependency of the wavenumbers k_0^E and $k_0^{E_s}$, the wavenumbers at which convective energy is maximum and is injected into the turbulent inertial ranges of the turbulent kinetic energy spectra E, E_s respectively.
- 4) the depth dependency of $\Phi = u^2/w^2$, the mean values of the anisotropy.

Differences between w^2 – and \tilde{s}^2 – and their respective GMLT estimations have only small consequences on the profile of the excitation rate $P(\omega)$. However the values reached by w^2 and \tilde{s}^2 with the 3D simulation are responsible for an increase of the relative contribution of the Reynolds stress to $P(\omega)$ by a factor ~ 1.5 at low frequency $\nu \lesssim 3$ mHz compared to the one obtained with the GMLT solar model. This is because the GMLT model overestimates \tilde{s}^2 by $\sim 20\%$ at the top of excitation region and underestimates w^2 within most part of the excitation region by up to $\sim 15\%$.

The energy distributions E and E_s over eddies with wavenumber k obtained in the simulation scale approximately as k^{-1} in the domain $k \lesssim k_0^E$. They therefore have approximately the same behavior as the “Extended Kolmogorov Spectrum” (EKS) defined in Musielak et al. (1994). In contrast, their k -dependencies significantly differ from those assumed in the Nesis Kolmogorov Spectrum (NKS) which scales as k^{-5} below k_0^E . The NKS predicts much larger maximum values for P

than does the EKS. This is because the NKS concentrates kinetic energy in the vicinity of k_0^E .

The 3D simulation indicates that $k_0^E \simeq 3.6 \text{ Mm}^{-1}$ at the top of excitation region. This corresponds to the horizontal size of the granulation ($\sim 2 \text{ Mm}$). It is worth noting that taking the depth dependency of $k_0(z)$ into account results in an increase of the maximum of P by as much as $\sim 50\%$ and brings these values even closer to the observations. On the other hand, only minor differences are seen on the frequency dependence of the excitation rates P when using the depth dependency of $k_0(z)$ from the simulation or assuming the form $k_0^{\text{MLT}} = 2\pi/\beta\Lambda$ with $\Lambda = \alpha H_p$ provided that β is adjusted in order for k_0^{MLT} to match the value reached by k_0^E at the layer where w reaches its maximum.

The excitation rate $P(\omega)$ is very sensitive to the value of Φ . In the GMLT formulation, the quantity Φ is a parameter which is adjusted in order to obtain the best fit between computed solar damping rates and the solar measurements: the adopted value is $\Phi = 1.37$ (see Houdek et al. 2001). On the other hand, the 3D simulation suggests a higher value within the excitation region ($\Phi \simeq 2$). Larger values of Φ result in an increase of the mode driving by the turbulent motions. We find that using the value $\Phi = 1.37$ underestimates $P(\omega)$ by a factor ~ 5 relatively to $P(\omega)$ computed with $\Phi(z)$ in the excitation region from the 3D simulation. On the other hand, using the GMLT formulation for the convective velocity with a value $\Phi \sim 2$, as suggested by the 3D simulation, yields a power $P(\omega)$ close to the one obtained by the 3D simulation. To fix ideas, the maximum amplitude is $\sim 4 \text{ cm/s}$, $\sim 8 \text{ cm/s}$, $\sim 10 \text{ cm/s}$ when calculated with GMLT and $\Phi = 1.37$, with GMLT and $\Phi = 2$ and when using velocities and $\Phi(z)$ derived from the 3D simulation respectively. These figures must be compared to the observed maximum amplitude $\sim 23 \text{ cm/s}$.

This shows that the values of Φ found for the solar GMLT model when adjusted to the damping rates is not compatible with the actual properties of the turbulent medium in the excitation region. An improvement could come from a consistent calculation which would assume a depth dependent $\Phi(z)$, as suggested by the simulations, in both damping rate and excitation rate computations. Damping rates are indeed expected to be sensitive to depths deeper than the excitation rate where smaller values of Φ are encountered and the simulation shows that the velocity anisotropy factor Φ decreases from 2 down to 1.3 from top of the superadiabatic region to bottom of the simulated solar region.

Without any adjustment of scaling parameters but using all the constraints inferred from the 3D simulation considered here, we find a maximum of P much larger (~ 5 times larger) than the P maximum obtained using a 1D GMLT solar model when Φ is fixed by the observed damping rates. It is also found that the so-called entropy source term, which arises from the advection of the turbulent fluctuations of entropy by the turbulent motions, is still the dominant source of the excitation. However its contribution to the excitation is now $\sim 65\text{--}75\%$ instead of $\sim 95\%$ as found in Paper II.

Our computation still underestimates by a factor ~ 3 the maximum value of P compared with the one derived from the solar seismic observations by Chaplin et al. (1998). Moreover

the decrease of P with ν at high frequency ($\nu \gtrsim 3.5 \text{ mHz}$) is found to be significantly smaller than the one inferred from the solar seismic observations, indicating a deficiency in the present modelling at high frequency.

As a final point, we discuss the model for the turbulent kinetic energy spectrum:

In Paper II the parameter λ and k_0^E were adjusted – given a turbulent spectrum $E(k)$ – so as to obtain the best possible agreement between computed and measured values of the maximum solar oscillation amplitude and its frequency position, as well as the frequency-dependence of the oscillation amplitudes. Adjustments of these scaling parameters led to a better agreement between computed values of P and the seismic observations when using the NKS than the EKS. However, the present results from a 3D simulation strongly suggest that the EKS is a better model for the solar turbulent kinetic energy spectrum.

The better agreement obtained with NKS than EKS when adjusting the free parameters is due to the fact that the NKS concentrates most of the kinetic energy in the vicinity of k_0^E . Indeed, the NKS predominantly excites the modes whose period are close to the characteristic lifetime of the eddies of wavenumber k_0^E , i.e. the modes with frequency close to the frequency at which P peaks ($\nu \sim 3 \text{ mHz}$). As a consequence, the amount of energy going into the high frequency modes is relatively smaller with the NKS than it is with the EKS. This explains why the NKS reproduces better the steep decrease with ν of P at high frequency and results in a value for k_0^E identical to that inferred from the simulation ($k_0^E \simeq 3.6 \text{ Mm}^{-1}$). In contrast, whatever the adjustment, the EKS reproduces neither the frequency dependence of P at high frequency nor the value $k_0^E \simeq 3.6 \text{ Mm}^{-1}$. Hence assuming that the 3D simulation yields the proper behavior of the solar kinetic energy spectrum, well modelled by the EKS, one is led to conclude that the excitation as given by the present stochastic excitation model is not efficient enough at large scales ($k \sim k_0$) and too efficient at small scales ($k > k_0$).

Discrepancies between our calculations and the observed excitation rates or the results by Stein & Nordlund (2001) are likely due to dynamic properties of turbulence which are not properly taken into account in the excitation model. Indeed, the dynamic properties of turbulence are modeled by the function χ_k . All current theoretical calculations of the excitation rates assume a Gaussian function for χ_k (e.g. Goldreich & Keeley 1977; Balmforth 1992a). The Gaussian model is likely to be at the origin of the current under-estimate of the rates at which solar p -modes are excited (see forthcoming paper Samadi et al. 2003). This may also explain the fact that we find that the entropy source term is dominant over the Reynolds stress contribution whereas Stein & Nordlund (2001) in their direct computations found the reverse. In a recent study based on a frequency analysis of the present simulation we investigate what model can correctly reproduce model χ_k in the frequency range where the acoustic energy injected into the solar p -modes is important (see forthcoming paper Samadi et al. 2003).

In the manner of Rosenthal et al. (1999) constraints from 3D simulation can be imposed to the 1D model. According to the authors, such constraints result in a better agreement

between the observed frequencies of the solar p -modes and the eigenfrequencies of the computed adiabatic oscillations. An improvement in the calculation of the excitation rates at solar-type oscillations could then also come from a more consistent calculation of the eigenmodes which would use such constrained 1D model.

Acknowledgements. We thank H.-G. Ludwig for valuable help in analyzing the simulated data. We are indebted to G. Houdek for providing us the solar model. We thank the referee (B. Dintrans) for his meaningful comments. RS's work has been supported in part by the Particle Physics and Astronomy Research Council of the UK under grant PPA/G/O/1998/00576.

References

- Baglin, A., & The Corot Team. 1998, in *New Eyes to See Inside the Sun and Stars*, IAU Symp., 185, 301
- Balmforth, N. J. 1992a, *MNRAS*, 255, 639
- Balmforth, N. J. 1992b, *MNRAS*, 255, 603
- Böhm-Vitense, E. 1958, *Z. Astrophys.*, 46, 108
- Canuto, V. M., Goldman, I., & Mazzitelli, I. 1996, *ApJ*, 473, 550
- Canuto, V. M., & Mazzitelli, I. 1991, *ApJ*, 370, 295
- Chaplin, W. J., Elsworth, Y., Isaak, G. R., et al. 1998, *MNRAS*, 298, L7
- Christensen-Dalsgaard, J. 1982, *MNRAS*, 199, 735
- Eggleton, P. P., Faulkner, J., & Flannery, B. P. 1973, *A&A*, 23, 325
- Favata, F., Roxburgh, I., & Christensen-Dalsgaard, J. 2000, in *The Third MONS Workshop: Science Preparation and Target Selection*, 49
- Goldreich, P., & Keeley, D. A. 1977, *ApJ*, 212, 243
- Goldreich, P., Murray, N., & Kumar, P. 1994, *ApJ*, 424, 466
- Gough, D. O. 1977, *ApJ*, 214, 196
- Houdek, G. 1996, Ph.D. Thesis, Institut für Astronomie, Wien
- Houdek, G., Balmforth, N. J., Christensen-Dalsgaard, J., & Gough, D. O. 1999, *A&A*, 351, 582
- Houdek, G., Chaplin, W. J., Appourchaux, T., et al. 2001, *MNRAS*, 327, 483
- Houdek, G., & Gough, D. O. 2002, *MNRAS*, 336, L65
- Musielak, Z. E., Rosner, R., Stein, R. F., & Ulmschneider, P. 1994, *ApJ*, 423, 474
- Nesis, A., Hanslmeier, A., Hammer, R., et al. 1993, *A&A*, 279, 599
- Nordlund, A., Spruit, H. C., Ludwig, H. G., & Trampedach, R. 1997, *A&A*, 328, 229
- Osaki, Y. 1990, in *Lecture Notes in Physics: Progress of Seismology of the Sun and Stars*, ed. Y. Osaki, & H. Shibahashi (Springer-Verlag), 75
- Rieutord, M., Roudier, T., Malherbe, J. M., & Rincon, F. 2000, *A&A*, 357, 1063
- Rosenthal, C. S., Christensen-Dalsgaard, J., Nordlund, Å., Stein, R. F., & Trampedach, R. 1999, *A&A*, 351, 689
- Samadi, R. 2001, in *SF2A-2001: Semaine de l'Astrophysique Française*, E148 [astro-ph/0108363]
- Samadi, R., & Goupil, M. 2001, *A&A*, 370, 136 (Paper I)
- Samadi, R., Goupil, M., & Lebreton, Y. 2001, *A&A*, 370, 147 (Paper II)
- Samadi, R., Houdek, G., Goupil, M.-J., & Lebreton, Y. 2002, *A&A*, submitted (Paper III)
- Samadi, R., Nordlund, Å., Stein, R., Goupil, M.-J., & Roxburgh, I. 2003, *A&A*, in press
- Stein, R. F. 1967, *Sol. Phys.*, 2, 385
- Stein, R. F., & Nordlund, A. 1998, *ApJ*, 499, 914
- Stein, R. F., & Nordlund, Å. 2001, *ApJ*, 546, 585
- Unno, W., & Spiegel, E. A. 1966, *PASJ*, 18, 85

Numerical 3D constraints on convective eddy time-correlations: Consequences for stochastic excitation of solar p modes

R. Samadi^{1,2}, Å. Nordlund³, R. F. Stein⁴, M. J. Goupil², and I. Roxburgh^{1,2}

¹ Astronomy Unit, Queen Mary, University of London, London E14NS, UK

² Observatoire de Paris, LESIA, CNRS UMR 8109, 92195 Meudon, France

³ Niels Bohr Institute for Astronomy, Physics, and Geophysics, Copenhagen, Denmark

⁴ Department of Physics and Astronomy, Michigan State University, Lansing, USA

Received 9 December 2002 / Accepted 30 March 2003

Abstract. A 3D simulation of the upper part of the solar convective zone is used to obtain information on the frequency component, χ_k , of the correlation product of the turbulent velocity field. This component plays an important role in the stochastic excitation of acoustic oscillations. A time analysis of the solar simulation shows that a Gaussian function does not correctly reproduce the ν -dependency of χ_k inferred from the 3D simulation in the frequency range where the acoustic energy injected into the solar p modes is important ($\nu \approx 2\text{--}4$ mHz). The ν -dependency of χ_k is fitted with different analytical functions which can then conveniently be used to compute the acoustic energy supply rate P injected into the solar radial oscillations. With constraints from a 3D simulation, adjustment of free parameters to solar data is no longer necessary and is not performed here. The result is compared with solar seismic data. Computed values of P obtained with the analytical function which fits best χ_k are found ~ 2.7 times larger than those obtained with the Gaussian model and reproduce better the solar seismic observations. This non-Gaussian description also leads to a Reynolds stress contribution of the same order as the one arising from the advection of the turbulent fluctuations of entropy by the turbulent motions. Some discrepancy between observed and computed P values still exist at high frequency and possible causes for this discrepancy are discussed.

Key words. convection – turbulence – stars: oscillations – Sun: oscillations

1. Introduction

Solar oscillations are believed to be stochastically excited by turbulent convection in the outer part of the Sun. The excitation is caused by turbulent convective motions which generate acoustic energy which in turn is injected into the p modes.

Models of stochastic excitation of stellar p modes have been proposed by several authors (e.g. Goldreich & Keeley 1977; Osaki 1990; Balmforth 1992; Goldreich et al. 1994). These models use simplified models to describe the dynamics of the turbulent medium. For instance these approaches (Goldreich & Keeley 1977; Balmforth 1992) assume a Gaussian function for representing χ_k , the frequency component of the correlation product of the turbulent velocity field. As pointed out by Samadi (2001), the way the component χ_k is modeled plays a crucial role in controlling the extent of the excitation region of a given mode and hence the total amount of acoustic energy injected into the mode. In the following, χ_k will also be referred to as *the dynamic model of turbulence* and *dynamic* will refer to time-dependence or frequency-dependence.

Direct computations of the rate at which the solar p modes are excited have been performed by Stein & Nordlund (2001) using 3D simulations of the upper part of the solar convective zone. They found good agreement between their numerical results and the solar seismic observations. This direct but time consuming approach did not address the role of the dynamic properties of the turbulent medium on the excitation mechanism.

In contrast semi-analytical formulations for $P(\nu)$ offer the advantage of testing *separately* several properties entering the excitation mechanism. Here we consider the formulation by Samadi & Goupil (2001, hereafter Paper I, see also Samadi 2001 for a summary) which includes a detailed treatment of the *time averaged* and *dynamic* properties of the turbulent convective medium.

The impact of the averaged properties have been investigated by Samadi et al. (2003). The authors used a 3D simulation of the upper part of the solar convective zone to constrain the averaged properties of the turbulent convective medium. The computed rates P at which the solar p modes are excited were found to be larger than those computed with a 1D mixing-length solar model but still *underestimate* the solar seismic data

Send offprint requests to: R. Samadi,
e-mail: reza.samadi@obspm.fr

by a factor ~ 2.5 . It was also found that the Reynolds tensor contributes about 20% of the total acoustic energy injected into the solar p modes, in contrast with direct 3D estimations (Stein & Nordlund 2001). These discrepancies were attributed to the assumed Gaussian function for the dynamic model of turbulence.

In the present paper we therefore derive an empirical dynamic model of turbulence obtained from a 3D simulation of the upper part of the solar convective zone and then study the consequences of using this model on the computed excitation rates P . We compare our computation with solar seismic data and finally obtain an improved model of stochastic excitation.

The paper is organised as follows: The basic theoretical background and notations are recalled in Sect. 2. In Sect. 3, a 3D simulation of the upper part of the solar convective zone is used to characterise χ_k in the domain where stochastic excitation takes place. The inferred ν -dependency of χ_k is compared with the Gaussian function and fitted with different non-Gaussian functions. These functions are then used in Sect. 4 to compute the excitation rate P for radial p modes. The results are compared with solar seismic observations as provided by Chaplin et al. (1998) and with computations in which the Gaussian function is assumed. Section 5 is dedicated to discussions and conclusions.

2. Stochastic excitation

2.1. The model of stochastic excitation

We consider the model of stochastic excitation as described in Paper I and assume here – as in Samadi et al. (2003) – that injection of acoustic energy into the modes is isotropic and consider only radial p modes. Accordingly, the rate at which a given mode with frequency ω_0 is excited can be written as:

$$P(\omega_0) = \frac{\pi^3}{2I} \int_0^M dm \frac{\Phi}{3} \rho_0 w^4 \left\{ \frac{16}{15} \frac{\Phi}{3} \left(\frac{d\xi_r}{dr} \right)^2 S_R + \frac{4}{3} \left(\frac{\alpha_s \tilde{s}}{\rho_0 w} \right)^2 \frac{g_r}{\omega_0^2} S_S \right\}. \quad (1)$$

In Eq. (1), ρ_0 is the mean density, ξ_r is the radial component of the fluid displacement adiabatic eigenfunction ξ , I is the mode inertia (Eq. (19)), $\alpha_s = (\partial p / \partial s)_\rho$ where p denotes the pressure and s the entropy, \tilde{s} is the rms value of the entropy fluctuations which are assumed to arise solely from turbulence, $g_r(\xi_r, r)$ is a function involving the first and the second derivatives of ξ_r with respect to r , Φ is a mean anisotropy factor defined by Gough (1977) as

$$\Phi(r) \equiv \frac{\overline{\langle \mathbf{u}^2 \rangle} - \langle u_z^2 \rangle}{w^2(r)} \quad (2)$$

where \mathbf{u} is the velocity field, $\langle . \rangle$ denotes horizontal average, $\overline{(\cdot)}$ denotes time average, and $w(r)$ is the mean vertical velocity ($w^2 \equiv \overline{\langle u_z^2 \rangle} - \langle u_z^2 \rangle$). Expressions for $g_r(\xi_r, r)$ are given in Samadi et al. (2003).

The driving sources $S_R(r, \omega_0)$ and $S_S(r, \omega_0)$ arise from the Reynolds stress and the entropy fluctuations respectively:

$$S_R(r, \omega_0) = \int_0^\infty \frac{dk}{k^2} \frac{E(k, r)}{u_0^2} \frac{E(k, r)}{u_0^2} \chi_k(\omega_0, r) \quad (3)$$

$$S_S(r, \omega_0) = \int_0^\infty \frac{dk}{k^2} \frac{E(k, r)}{u_0^2} \frac{E_s(k, r)}{\tilde{s}^2} \times \int_{-\infty}^{+\infty} d\omega \chi_k(\omega_0 + \omega, r) \chi_k(\omega, r) \quad (4)$$

where $u_0(r) \equiv \sqrt{\Phi/3} w$ is introduced for convenience, $E(k, r)$ is the time averaged turbulent kinetic energy spectrum, $E_s(k, r)$ is the time averaged turbulent spectrum associated with the entropy fluctuations and $\chi_k(\omega, r)$ is the frequency-dependent part of the correlation product of the turbulent velocity field (see Sect. 2.2). In order to simplify the notation, we drop the explicit r dependence of the quantities in Eqs. (1–4).

2.2. The dynamic model of turbulence

The dynamic model of turbulence is represented by $\chi_k(\omega)$. In order to give a precise meaning to $\chi_k(\omega)$, we recall first some theoretical relations. Excitation by Reynolds stresses involves $\phi_{i,j}(k, \omega)$, the Fourier transform of the second-order velocity correlations; here the indices i and j refer to any of the 3 directions of the velocity field. For incompressible, homogeneous and isotropic turbulence, $\phi_{i,j}(k, \omega)$ has the form (Batchelor 1970):

$$\phi_{ij}(k, \omega) = \frac{E(k, \omega)}{4\pi k^2} \left(\delta_{ij} - \frac{k_i k_j}{k^2} \right) \quad (5)$$

where $E(k, \omega)$ is the turbulent kinetic energy spectrum as a function of k and ω and δ_{ij} is the Kronecker tensor. Following Stein (1967), $E(k, \omega)$ is decomposed as

$$E(k, \omega) = E(k) \chi_k(\omega) \quad (6)$$

where $\chi_k(\omega)$ satisfies the normalisation condition (Tennekes & Lumley 1982, Chap. 8.1):

$$\int_{-\infty}^{+\infty} d\omega \chi_k(\omega) = 1. \quad (7)$$

According to the decomposition of Eq. (6), $\chi_k(\omega)$ is – at fixed k – the frequency component of $E(k, \omega)$.

According to Eqs. (5) and (6), $\chi_k(\omega)$ then represents the frequency dependence of $\phi_{i,j}(\mathbf{k}, \omega)$. In other words, $\chi_k(\omega)$ measures – in the frequency and k wavenumber domains – the evolution of the velocity correlation between two distant points of the turbulent medium.

The same decomposition of Eq. (7) is assumed for $E_s(k, \omega)$. This leads to introducing χ_k^s , the frequency-dependent part of the correlation product of the entropy fluctuation. For simplifying the computation of P , as in Paper I, we assume $\chi_k^s = \chi_k$. We have checked that χ_k^s and χ_k have almost the same behaviour in the region where excitation by entropy fluctuations is significant.

In the present work, we consider only the excitation of radial p modes. Let $E_z(k, \omega)$ be the vertical component of the

kinetic energy spectrum. We consider that $E_z(k, \omega)$ can be decomposed as $E(k, \omega)$ (Eq. (7)). For isotropic turbulence we then have $E(k, \omega) = 3 E_z(k, \omega)$, $E(k) = 3 E_z(k)$ and $\chi_k^z = \chi_k$, which is equivalent to stating that the averaged and dynamic properties of the velocity field are the same in all 3 directions.

The anisotropy factor Φ – introduced in the expression for P , Eq. (1) – partially takes into account the spatial and temporal anisotropy of the turbulence ($\Phi = 3$ corresponds to an isotropic turbulence). It has been found in Samadi et al. (2003) that $\Phi \approx 2$ within the region where most of the excitation occurs. This shows that the time and space averaged properties of the medium are indeed anisotropic. One can therefore expect that the dynamic properties of turbulence differ between the horizontal and vertical directions. As the excitation of radial p modes is predominantly governed by turbulent elements moving in the vertical direction, an open question is whether one should consider χ_k^z rather than χ_k in Eqs. (3) and (4) when taking into account the dynamic properties of the turbulence. In the present work, we therefore characterise both χ_k^z and χ_k from a 3D simulation and assess the consequences of using either χ_k^z or χ_k in the calculation of P .

2.3. A Gaussian function for χ_k

Stein (1967) and Musielak et al. (1994) suggested several analytical forms for $\chi_k(\omega)$. The Gaussian Function (GF hereafter) is the simplest choice and is defined as

$$\chi_k(\omega) = \frac{1}{\omega_k \sqrt{\pi}} e^{-(\omega/\omega_k)^2} \quad (8)$$

where ω_k is its linewidth.

In the time domain, the Gaussian function, Eq. (8), is the Fourier transform of a Gaussian function whose linewidth is equal to $2\tau_k$, where τ_k is a characteristic time correlation length. Hence ω_k and τ_k are related to each other as

$$\omega_k = \frac{2}{\tau_k}. \quad (9)$$

The characteristic time τ_k is usually associated with the characteristic correlation time-scale of an eddy with wavenumber k . As in Balmforth (1992), we define it as

$$\tau_k \equiv \frac{\lambda}{ku_k} \quad (10)$$

where the velocity u_k of the eddy with wave number k is related to the kinetic energy spectrum $E(k)$ by (Stein 1967)

$$u_k^2 = \int_k^{2k} dk E(k). \quad (11)$$

The parameter λ in Eq. (10) accounts for our lack of precise knowledge of the time correlation τ_k under stellar conditions.

In the calculation of P , a GF is usually assumed for χ_k (e.g. Goldreich & Keeley 1997, Balmforth 1992). This assumption is equivalent to supposing that two distant points in the turbulent medium are uncorrelated.

In Sect. 3, we use a 3D simulation of the upper part of the solar convective zone to derive the ν -dependencies of χ_k^z and χ_k . Inferred ν -dependencies of χ_k^z and χ_k are compared to that of the GF. We next determine several analytical forms for χ_k^z and χ_k that can better represent their ν -dependencies.

3. Constraints from the 3D simulation

The analysis of a 3D simulation of the upper part of the solar convective zone provides constraints for several physical parameters that enter the theoretical expression for the energy supply rate P injected into the solar p modes (Eq. (1)). The constraints may be considered to be of two types:

- *Static* constraints (*static* refers to spatial and time averages) determine the actual wavenumber dependency of $E(k, z)$, the kinetic turbulent spectrum, and $E_s(k, z)$, the turbulent spectrum associated with the entropy. The *static* constraints also determine the depth profile of the wavenumber k_0^E at which convective energy is injected into the turbulent inertial range of E (as in Samadi et al. 2003 we assume that the wavenumber $k_0^{E_s}$, at which convective energy is injected into the turbulent inertial range of E_s , is equal to k_0^E). They also provide the depth dependence of u^2 , the mean square velocity, w^2 , the mean square vertical component of the velocity, \bar{s}^2 , the mean square values of entropy fluctuations and $\Phi = u^2/w^2$, the mean values of the anisotropy studied in Samadi et al. (2003).
- The *dynamic* constraints, on the other hand, concern the frequency component χ_k and χ_k^z (see Sect. 2.2).

The static constraints have been established in Samadi et al. (2003). Here we investigate the dynamic constraints.

3.1. The 3D simulation

We study a 3D simulation of the upper part of the solar convection zone obtained with the 3D numerical code developed by Stein & Nordlund (1998).

The simulated domain is 3.2 Mm deep and its surface is 6×6 Mm². The grid of mesh points is $256 \times 256 \times 163$ (i.e. ~ 23 km \times 23 km \times 37 km), the total duration 27 mn and the sampling time 30s.

Outputs of the simulation considered in Samadi et al. (2003) are the velocity field $\mathbf{u}(x, y, z, t)$ and the entropy $s(x, y, z, t)$ where – as in Samadi et al. (2003) – $z = r - R_\odot$ and R_\odot is the radius at the photosphere (i.e. where $T = T_{\text{eff}}$). The quantities $\mathbf{u}(x, y, z, t)$ and $s(x, y, z, t)$ were used to determine the quantities $E(k, z)$, $E_s(k, z)$, w and \bar{s}^2 involved in the theoretical expression for the excitation rate P . In the present work we use the velocity field $\mathbf{u}(x, y, z, t)$ to characterise χ_k and χ_k^z .

3.2. Fourier transform

At five different layers of the simulated domain, we compute the 3D Fourier transform, with respect to time and in the horizontal plane, of the velocity field \mathbf{u} . These layers cover a region where modes with frequency $\nu \gtrsim 2$ mHz are predominantly excited.

This provides $\hat{\mathbf{u}}(\mathbf{k}, z, \nu)$ where \mathbf{k} is the wavenumber in the horizontal plane. Next we integrate $\hat{\mathbf{u}}^2(\mathbf{k}, z, \nu)$ over circles with radius $k = \|\mathbf{k}\|$ at each given layer z . This yields $\hat{\mathbf{u}}(k, z, \nu)$ and therefore $E(k, \nu, z) \equiv \hat{\mathbf{u}}^2(k, \nu, z)$. The quantity $\chi_k(\nu, z)$ is the

frequency component of $E(k, \nu, z)$, at fixed k . Hence, according to Eqs. (6) and (7), $\chi_k(\nu, z)$ is obtained from $E(k, \nu, z)$ as:

$$\chi_k(\nu, z) = \frac{E(k, \nu, z)}{\int d\nu E(k, \nu, z)} \quad (12)$$

where the integration over ν is performed over the frequency range $[-\nu_{\max}, \nu_{\max}]$ corresponding to the window of the Fourier analysis with respect to time ($\nu_{\max} \simeq 16$ mHz).

We proceed in the same manner for the vertical component of \mathbf{u} . This then provides $E_z(k, \nu, z) \equiv \hat{u}_z^2(k, \nu, z)$ and $\chi_k^z(\nu, z)$.

3.3. Inferred properties of χ_k and χ_k^z

Figure 1 presents $\chi_k(\nu)$ as it is obtained from the simulation for the wavenumber k at which $E(k, z)$ peaks ($k = k_0$).

At the top of the superadiabatic region (for instance $z = -0.4$ Mm in Fig. 1, this is the layer where the excitation is the largest), the GF does not correctly model $\chi_k(\nu)$ (see Fig. 1). However the discrepancies between the GF and the simulation data occur mostly above the solar cut-off frequency ($\nu \sim 5.5$ mHz). Discrepancies between the GF and the 3D simulation data have then minor consequences for the p modes excitation in this region. This is not the case deeper in the simulation where the largest discrepancies between the GF and the simulation data occur in the frequency range where the dominant amount of acoustic energy is injected into the p modes ($\nu \sim 2-4$ mHz).

To reproduce the shape of $\chi_k(\nu)$ obtained with the 3D simulation, one needs a function which at high frequency decreases more slowly than the GF. For modeling the ν -dependency of $\chi_k(\nu)$, we thus propose three analytical functions: the Lorentzian function (LF hereafter)

$$\chi_k(\omega) = \frac{1}{\pi\omega_k/2} \frac{1}{1 + (2\omega/\omega_k)^2}, \quad (13)$$

the Gaussian plus an Exponential Function (GEF hereafter)

$$\chi_k(\omega) = \frac{1}{2} \left(\frac{1}{\omega_k \sqrt{\pi}} e^{-(\omega/\omega_k)^2} + \frac{1}{2\omega_k} e^{-|\omega/\omega_k|} \right), \quad (14)$$

and the Gaussian plus a Lorentzian function (GLF hereafter)

$$\chi_k(\omega) = \frac{1}{2} \left(\frac{1}{\omega_k \sqrt{\pi}} e^{-(\omega/\omega_k)^2} + \frac{1}{\pi \omega_k} \frac{1}{1 + (\omega/\omega_k)^2} \right). \quad (15)$$

All these functions satisfy the condition of normalisation of Eq. (7).

We first assume a constant $\lambda = 1$. As shown in Fig. 1, all these non-Gaussian functions reproduce the ν -variation of χ_k better than that obtained using a GF.

In the middle of the excitation region (-0.5 Mm $\lesssim z \lesssim 0.0$ Mm) the overall best agreement is obtained with the LF. Below $z \sim -0.5$ Mm, the LF does not reproduce χ_k well enough but still reproduces its ν -variation better than the other models.

However we have so far assumed that λ (or equivalently the eddy time correlation) is depth independent, which is a strong assumption. When λ is allowed to vary with z , we find that decreasing the value of λ below $z \lesssim -0.5$ Mm, the LF best

models χ_k below $z \sim -0.5$ Mm (e.g. $\lambda = 1.6$ at $z = -0.64$ Mm and $\lambda \simeq 1.30$ at $z = -0.99$ Mm, see Fig. 2). This shows that the variation with depth of the characteristic time τ_k (or equivalently the characteristic frequency ω_k) is not correctly represented by the relations of Eqs. (10) and (11) when computed assuming a constant λ below $z \sim -0.5$ Mm; τ_k increases faster with depth than expected from the relations (10) and (11). It is however found in Sect. 4 that this feature has negligible effect on P .

The function χ_k^z also decreases with the frequency more slowly than the GF (see Fig. 1). Moreover, decreasing values of λ for $z \lesssim -0.5$ Mm provide a better fit of χ_k^z . But in contrast with χ_k , χ_k^z is overall better modeled with the GEF for $z \gtrsim -0.5$ Mm and with the GLF for $z \lesssim -0.5$ Mm rather than with the LF (not shown).

We conclude from the frequency analysis of the 3D simulation that the simple Gaussian function cannot correctly represent the actual dynamic properties of the turbulent medium. One may expect that the GF causes an underestimation of the acoustic energy injected into the solar p modes. Instead the frequency analysis favours a non-Gaussian function for χ_k^z and χ_k that decreases more slowly with ν than the GF.

4. Consequences in terms of p modes excitation

4.1. Computations of the excitation rate P

Computation of the excitation rate P is performed as in Samadi et al. (2003) except that here two analytical functions other than the GF are assumed for χ_k , as discussed in Sect. 3. The computation process is summarised as follows: The eigenfunctions (ξ_r) and their frequencies (ν) are computed with Balmforth's (1992) non-adiabatic code for a solar 1D mixing-length model based on Gough's (1977) non-local time-dependent formulation of convection.

The quantities Φ , w^2 and s^2 are obtained from the 3D simulation. The k -dependency of $E(k, z)$ is the Extended Kolmogorov Spectrum (EKS hereafter) defined as:

$$\begin{aligned} E(k) &\propto (k/k_0)^{+1} & \text{for } k_0 > k > k_{\min} \\ E(k) &\propto (k/k_0)^{-5/3} & \text{for } k > k_0. \end{aligned} \quad (16)$$

In Eq. (16), the wavenumber k_0 is the wavenumber at which $E(k)$ peaks and k_{\min} is the minimal wavenumber reached by the 3D simulation ($k_{\min} = 1.05$ Mm $^{-1}$). The variation with depth of k_0 is also given by the 3D simulation. The k -dependency of the EKS reproduces the global features of E arising from the 3D simulation. The same model is considered for $E_s(k, z)$. $E(k, z)$ and $E_s(k, z)$ satisfy the normalisation conditions:

$$\begin{aligned} \int_{k_{\min}}^{+\infty} dk E(k, z) &= 1/2 \Phi w^2 \\ \int_{k_{\min}}^{+\infty} dk E_s(k, z) &= 1/2 s^2. \end{aligned} \quad (17)$$

The total energy contained in $E(k, z)$ and $E_s(k, z)$, and their depth dependencies, are then obtained from the 3D simulation according to Eq. (17). These theoretical estimates for P are then

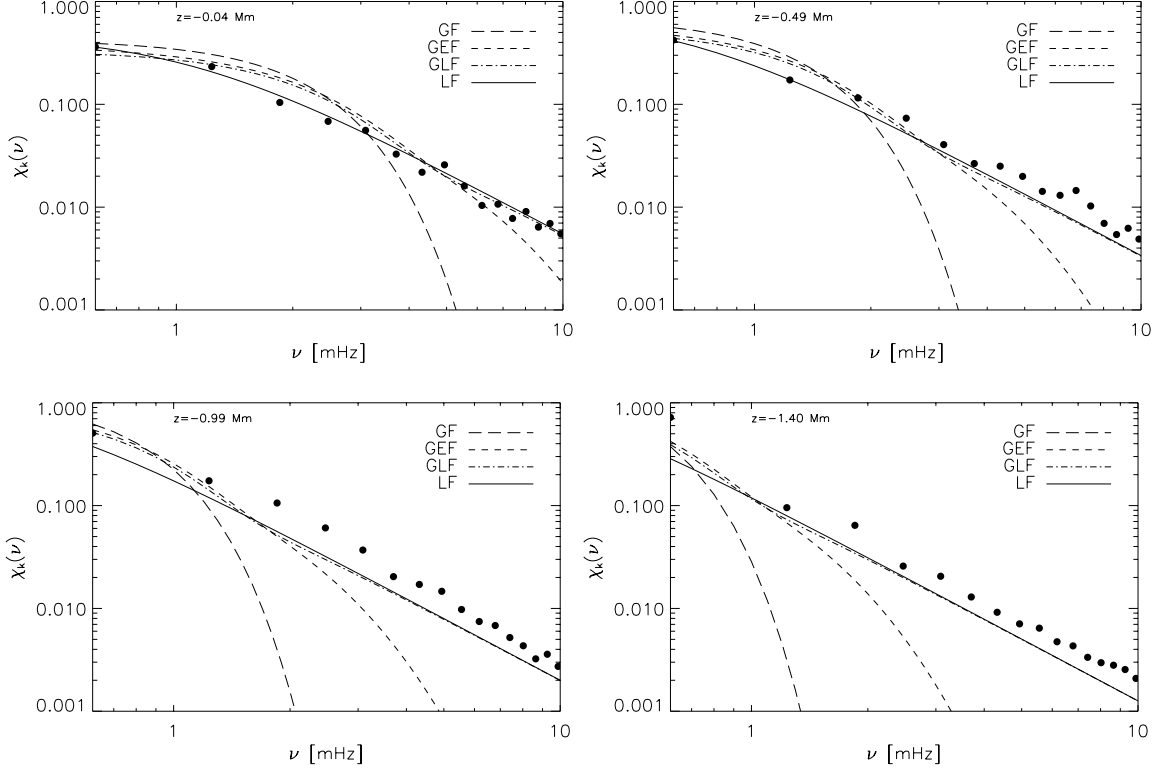


Fig. 1. The filled dots represent $\chi_k(\nu)$ obtained from the simulation for the wavenumber k_0 at which $E(k, z)$ peaks. The solid curves represent the Lorentzian function (LF, Eq. (13)), the dots-dashed curves the Gaussian Lorentzian function (GLF, Eq. (15)), the dashed curves the Gaussian Exponential function (GEF, Eq. (14)) and the long dashed curves the Gaussian function (GF, Eq. (8)). In these four analytical functions, $\lambda = 1$ is assumed for the calculation of ω_k (Eqs. (10) and (11)). Four different layers are considered: $z = -0.04$ Mm (the top of the superadiabatic region), $z = -0.49$ Mm, $z = -0.99$ Mm and $z = -1.40$ Mm.

compared with the “observed” P from Chaplin et al. (1998)’s seismic data, calculated according to the relation:

$$P(\omega_0) = 2\eta \frac{I}{\xi_r^2(r_s)} v_s^2(\omega_0) \quad (18)$$

where r_s is the radius at which oscillations are measured,

$$I \equiv \int_0^M dm \xi_r^2 \quad (19)$$

is the mode inertia and where the mode damping rate (η) and the mode surface velocity (v_s) are obtained from Chaplin et al. (1998). In Eq. (18), the mode mass $I/\xi_r^2(r_s)$ is given by the GMLT model and we adopt $r_s = R_\odot + 200$ km consistently with Chaplin et al. (1998)’s observations.

4.2. Comparisons with observations

We investigate the effect of using different analytical functions for χ_k (Sect. 3) in the computation of P . We first assume a constant value $\lambda = 1$. Results are shown in Fig. 3. Computations performed with the GF underestimate the observed P values by a factor ~ 2.7 . On the other hand, the LF, GEF and GLF choices result in larger values for the computed P than the GF one (~ 2 times larger). This brings them closer to the observations, compared with the GF choice for χ_k . The reason is that

all the non-Gaussian functions (the LF, the GEF and the GLF) – which indeed better model χ_k^z and χ_k from the 3D simulation than does the GF – decrease more slowly with ν than the GF in the frequency range where the mode amplitudes are large ($\nu \approx 2 - 4$ mHz). Consequently a larger amount of acoustic energy is injected into the modes with the non-Gaussian functions than with the GF.

In Sect. 3.3, the overall best models for χ_k were obtained with the LF and with decreasing values of λ below $z \sim -0.5$ Mm. We use a simple model for the depth variation of λ :

$$\begin{aligned} \lambda &= 1 && \text{for } z > -0.5 \text{ Mm} \\ \lambda &= 0.9 + 0.71(0.64\text{Mm} + z) && \text{for } -0.5 \geq z \geq -1 \text{ Mm} \\ \lambda &= 0.35 && \text{for } z < -1 \text{ Mm}. \end{aligned} \quad (20)$$

We have computed P according to the simple model of Eq. (20) and assuming the LF. We find no significant changes for P compared to the calculations in which a constant value $\lambda = 1$ is assumed (not shown).

In Sect. 3 we found that χ_k^z is better modelled with the GEF for $z \gtrsim -0.5$ Mm and with the GLF for $z \lesssim -0.5$ Mm rather than with the LF. However, as the stochastic excitation is the largest in the range $-0.5 \text{ Mm} \lesssim z \lesssim 0 \text{ Mm}$, we can assume the GEF in all the domain. The LF results in a value for P_{\max} slightly larger than the one resulting from the GEF

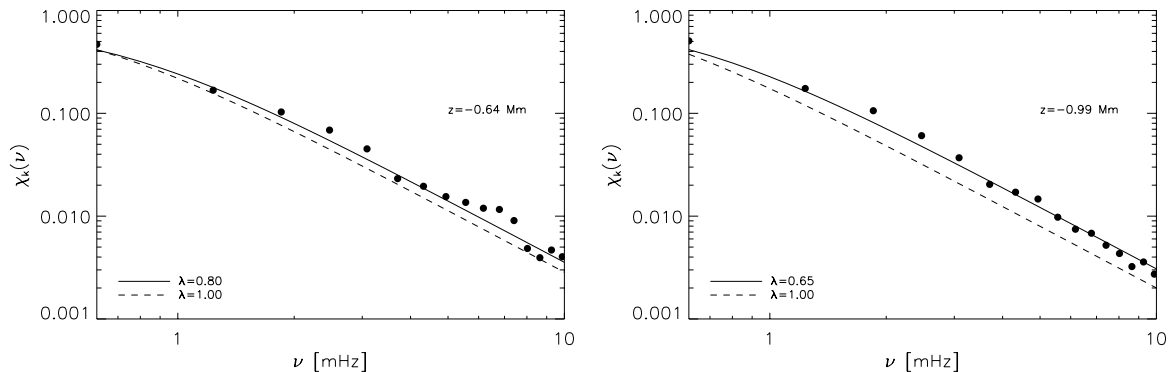


Fig. 2. As in Fig. 1, the filled dots represent $\chi_k(\nu, z)$ obtained from the simulation at two different layers: $z = -0.64$ Mm (left panel) and $z = -0.99$ Mm (right panel). The other curves represent the LF (Eq. (15)) with different assumptions for λ : The dashed curved correspond to $\lambda = 1$ and the solid curves correspond to $\lambda = 0.80$ at $z = -0.64$ Mm (left panel) and $\lambda = 0.65$ at $z = -0.99$ Mm (right panel).

(only ~ 1.2 larger). A better agreement is then obtained with the analytical functions which fits best χ_k (i.e. the LF) than the one which fits best χ_k^z (i.e. the GEF) in contrast with the intuitive idea mentioned in Sect. 2.2 that the excitation of radial p modes depends rather on the properties of χ_k^z than on those of χ_k .

In the frequency range where observational constraints are available, differences between results obtained with the different adopted non-Gaussian functions are of the same order as the actual error bars associated with the observed P values.

Below the frequency range of the observations – i.e. below $\nu \lesssim 1.8$ mHz – the differences between the different non-Gaussian functions are very large compared to the error bars (see bottom panel of Fig. 3). Those differences are related to differences in the ν -variation of the non-Gaussian models. Observational constraints at low frequency could therefore confirm that the LF is indeed the best representation for $\chi_k(\nu)$.

Important discrepancies still remain at high frequency ($\nu \gtrsim 3.5$ mHz). The excitation rate derived from the observations decreases as $\sim \nu^{-6.2}$ above $\nu \approx 3.5$ mHz whereas the computed P decreases as $\sim \nu^{-1}$ (see bottom panel of Fig. 3). Possible origins of this discrepancy are discussed in Sect. 5.5.

Another consequence of a non-Gaussian dependence of χ_k (or χ_k^z) with the frequency is a larger relative contribution of the Reynolds stress P_R to the mode excitation rate P . This is shown in Fig. 4. The GF generates a relative contribution of the Reynolds stress to the excitation (P_R/P) which is smaller than that obtained assuming a non-Gaussian function (e.g. for the LF, the relative contribution of P_R to the excitation is at least ~ 2 times larger than with the GF). Excitation by the entropy fluctuations takes place predominantly at the top of the excitation region over a thin layer ($\lesssim 0.2$ Mm) while that due to the Reynolds stress extends deeper below (~ 0.5 – 2 Mm). At the top of the excitation region, the discrepancy between the GF and χ_k inferred from the 3D simulation mainly occurs above $\nu \approx 5$ mHz and thus has a small impact on mode excitation. This is not the case deeper in the excitation region where the GF under-estimates χ_k in a frequency range increasing inward.

5. Conclusion and discussion

5.1. A Non-Gaussian eddy time correlation

In the present work we characterize *empirically* χ_k and of χ_k^z , the frequency components of the correlation product of the turbulent velocity field and of its vertical component respectively. A frequency analysis of a solar 3D simulation shows that at large scales ($k \sim k_0$) the Gaussian function significantly underestimates χ_k and χ_k^z in the frequency range ($\nu \approx 2$ – 4 mHz) where acoustic energy injected into the solar p modes is the largest.

As a result, the maximum value of P is found ~ 2.7 smaller than the solar seismic constraints.

This partly explains the *underestimate* of the values of solar p mode excitation rates obtained by Houdek et al. (1999) whose computations are based on the theoretical expression by Balmforth (1992) and the underestimate obtained by Samadi et al. (2003).

In order to reproduce the main properties of χ_k (or χ_k^z), one has to consider a model which must decrease more slowly with ν than the GF. We then assume for χ_k and χ_k^z three different simple analytical forms: the Lorentzian Function (LF), the so-called “Gaussian Exponential Function” (GEF, which is composed by the GF plus an exponential function) and the so-called “Gaussian Lorentzian Function” (GLF, which is composed by the GF plus a Lorentzian function).

From the top of the excitation region (which corresponds to the top of the superadiabatic region) down to the middle of the excitation region ($z \sim -0.5$ Mm where z is the distance to the radius at the photosphere), the best agreement between χ_k and the analytical approximations is obtained with the LF and with $\lambda = 1$. Deeper within the excitation region ($z \lesssim -0.5$ Mm), the agreement is better for $\lambda < 1$ and λ decreasing with depth.

The frequency dependencies of χ_k^z and χ_k are found to be very similar. However χ_k^z is best modeled by the GEF. As for χ_k , the agreement is better below $z \sim -0.5$ Mm with decreasing values of the parameter λ than with $\lambda = 1$.

Assuming a non-Gaussian function – either the LF, the GEF or the GLF – results in values for P_{\max} , the maximum of excitation power, which are ~ 2 times larger than when assuming the

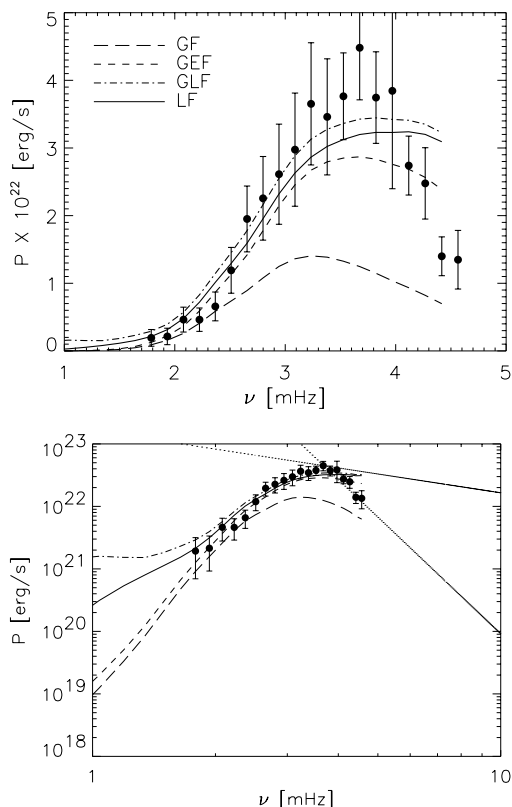


Fig. 3. Top: The curves correspond to computed values of $P(\nu)$ obtained with different analytical functions for $\chi_k(\nu)$: the GF (long dashed curve), the GEF (dashed curve), the GLF (dots-dashed curve) and the LF (solid curve). In all calculations, we assume $\lambda = 1$. The dots represent $P(\nu)$ derived from the amplitudes and line widths of the $\ell = 0$ p modes measured by Chaplin et al. (1998). **Bottom:** same as the top panel but P is plotted in a log-log representation as it is usually represented in the literature. The vertical and horizontal scales have been chosen for an easy comparison with equivalent plots found in Stein & Nordlund (2001). The lines with dots show two different power laws ν^p : one with $p = -6.2$ and the other with $p = -1$.

GF and brings P_{\max} much closer to the maximum of P derived from the solar seismic data of Chaplin et al. (1998).

We also find that taking into account the variation of λ with depth for z below -0.5 Mm does not significantly change the values of P . A constant value can then be assumed in the calculation of the solar p mode excitation rates. The constant value of λ on the other hand plays an important role and we find $\lambda = 1$.

We have investigated the sensitivity to the adopted representation for χ_k : Although the LF fits best the ν -variation of χ_k inferred from the 3D simulation, the GLF results in value for P_{\max} closer to the seismic constraints. However, the differences obtained with the different non-Gaussian approximations for χ_k are globally smaller than the actual error bars associated with the observations of Chaplin et al. (1998). On the other hand, below the frequency range where observational constraints on P are available (i.e. below $\nu \lesssim 1.8$ mHz), the differences between P obtained with different non-Gaussian functions are very large compared to the current error bars. Those

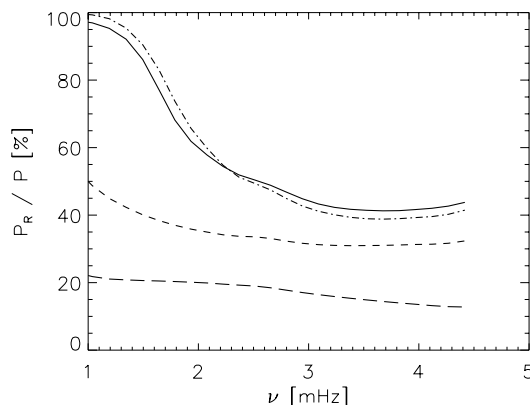


Fig. 4. Top: Same as Fig. 3 for the relative contribution of the Reynolds stress, P_R to the total acoustic energy P .

differences are directly related to the differences in the ν -variation of the non-Gaussian forms investigated in this work. This suggests that accurate enough data below this frequency range, could provide confirmation that the LF is indeed the best model for χ_k .

5.2. Relative contribution of the entropy fluctuations to the excitation

The non-Gaussian character of χ_k causes the excitation region to extend deeper (~ 500 km for modes of order $n = 20$) than with the GF (~ 200 km resp.). The largest entropy fluctuations mainly occur at the outermost part of the convective zone (CZ) over a very thin region (~ 100 km) while excitation by the Reynolds stress contribution occurs on a more extended region. Consequently the non-Gaussian property of χ_k leads to a relatively larger contribution of the Reynolds stress to the excitation than in the case of a GF. As a result, the Reynolds stress contribution is of the same order as the contribution arising from the advection of the turbulent fluctuations of entropy by the turbulent movements (the so-called entropy source term). This is in contrast with previous results (Samadi et al. 2001) based on the GF which concluded that the entropy source term dominates the Reynolds stress by about ~ 20 . It also differs with results by Goldreich et al. (1994) who found that the excitation arising directly from the entropy fluctuations dominates by about ~ 10 .

On the other hand, in Stein & Nordlund (2001), the excitation by turbulent pressure (Reynolds stress) is found dominant (~ 4 times larger) whereas here we find that the contribution of the entropy source term cannot be neglected. Whether this is the signature of some deficiency in the present excitation model is an open question.

5.3. Summary

We show that the usually adopted *Gaussian function* for χ_k is neither consistent with the properties of χ_k inferred from the 3D simulation nor does it reproduce the observed maximum of the solar p -modes excitation rates.

Following an empirical approach we improve the model of the convective eddy time-correlation χ_k which enters the current model of stochastic excitation. We then show that to reproduce *both* the ν -variation of χ_k as inferred from the 3D simulation and the observed maximum of the solar p -modes excitation rates one has to consider a non-Gaussian form which decreases at high frequency slower than the GF, as do the different non-Gaussian functions investigated here.

The use of non-Gaussian functions, for instance the LF, reproduces reasonably well the maximum value of the rate at which solar p -modes are excited *without any adjustments of free parameters or without introducing a scaling factor*, in contrast with previous approaches (e.g. Balmforth 1992; Goldreich et al. 1994; Samadi et al. 2001). We then solve the problem of the underestimation by the previous theoretical approaches. Furthermore the use of such a non-Gaussian form for χ_k makes the contribution of the turbulent pressure to the excitation much larger than in previous works making our results more consistent with that by Stein & Nordlund (2001).

Our investigation clearly emphasizes the *non-Gaussian character of the solar p modes excitation* as a result of the *non-Gaussian property of the convective eddies time-correlations*. It also shows that the dynamic properties of the solar turbulent convection inferred from the 3D simulation are consistent with the helioseismic data.

We stress that only simple non-Gaussian forms for χ_k have been investigated here. More sophisticated forms are likely to improve the agreement with the ν -dependency of χ_k (or χ_k^2). This would not affect the main conclusions presented in the present paper.

5.4. Possible origin of the non-Gaussian property of χ_k

We recall that χ_k measures the temporal evolution of the correlation between two points of the turbulent medium separated by a distance of $\sim 2\pi/k$. A Gaussian time-correlation means that the fluid motions in the medium are random in time. Departure from a Gaussian time-correlation at large scales ($k \sim k_0$) suggests that a strong correlation exists at that scale.

Downward plumes are likely to be responsible for the non-Gaussian behaviour of χ_k . Downward and upward convective motions are indeed highly asymmetric (Stein & Nordlund 1998): downward flows are associated with patterns (plumes) which are more coherent than the upward moving structures (Rieutord & Zahn 1995). The upward flows are associated with less coherent and more random structures (granules) characterised by a broad variety of sizes and lifetimes (Rieutord & Zahn 1995). The non-Gaussian behavior of χ_k can most probably be attributed to plumes. This however remains to be checked (work in progress).

5.5. Possible origin of the remaining discrepancy

Despite a clear improvement in the agreement between observed and theoretical excitation rates, important discrepancies between the computed P and the solar measurements still remain at high frequency $\nu \gtrsim 3.5$ mHz (see Sect. 4.2 and Fig. 3).

On the “observational side”, at high frequency, larger uncertainties for the damping rates η induce larger uncertainties on the derived supply energy rates.

On the theoretical side, part of the discrepancy might well be attributed to a poor description of the eigenfunctions at high frequency. Indeed, the discrepancies between the calculated eigenfrequencies and the observed ones are largest at high frequency ($\nu \gtrsim 3$ mHz). This indicates that the description of the eigenfunctions are less accurate at high frequency. As the expression for calculating P involves the first and second derivatives of the mode eigenfunction, the lack of accuracy in the calculation of the eigenfunctions has a larger impact on P at high frequencies than at small frequencies.

Other possible causes can perhaps be related to our simplified excitation model which assumes isotropic turbulence. Indeed the current theory assumes that the stochastic excitation is the same in all three directions, particularly between the ascending and descending flows. However the kinetic energy and entropy fluctuations are larger in the downward flows than in the upward flows (Stein & Nordlund 1998). Therefore the driving arising from the advection of the turbulent fluctuations of entropy by the turbulent movements differs significantly between the elements moving downwards and those moving upwards. As the entropy fluctuations are largest in the outermost part of the convective zone, the above mentioned asymmetry will predominantly affect the high frequency modes.

Moreover, it is also assumed that the total kinetic energy, E , is isotropically injected in all 3 directions. Excitation of the radial p modes results from the vertical component of the velocity. However at the top of the convective zone, the distribution of kinetic energy in $E(k, z)$ and in $E_z(k, z)$ are very different from each other. These differences may affect more strongly the high frequency modes. Consequences of these departures from the isotropic assumption need to be further investigated.

5.6. Perspectives

The non-Gaussian property of χ_k and its consequences for the stochastic excitation has been investigated so far only for the *Sun*. However such a non-Gaussian feature of the turbulence will most likely also be of importance for solar-like oscillating stars more massive than the Sun, provided our analysis is also valid for these stars. This can substantially change the excitation spectrum P for such stars compared to that which is currently predicted.

Therefore investigations of p mode excitation in hotter and more massive stars must be undertaken, which should proceed in two steps: first, the validity of the present results obtained in the solar case must be investigated for other stars with, for instance, the help of dedicated 3D simulations. The conclusions which will be drawn from this first step must be used in a second step to study the frequency dependence and the magnitude of P for different solar-like oscillating stars (see preliminary results in Samadi et al. 2002).

Future space missions such as COROT (Baglin & The Corot Team 1998), MOST (Matthews 1998) and Eddington (Favata et al. 2000) will provide high-quality data on seismic

observations. COROT will be the first mission that will provide high precision mode amplitudes and linewidths in other stars. This high-quality data will allow us to derive the excitation rate P and will provide improved observational constraints on the theory of stochastic excitation which is, at present, poorly constrained by observation.

Acknowledgements. We thank H.-G. Ludwig for useful discussions and valuable help in analysing the simulated data and we are indebted to G. Houdek for providing us the 1D solar model. We gratefully thank our referee (T. Appourchaux) for pertinent remarks which led to an improvement of the paper. RS's work has been supported in part by the Particle Physics and Astronomy Research Council of the UK under grant PPA/G/O/1998/00576.

References

- Baglin, A., & The Corot Team. 1998, in *New Eyes to See Inside the Sun and Stars*, IAU Symp., 185, 301
- Balmforth, N. J. 1992, *MNRAS*, 255, 639
- Batchelor, G. K. 1970, *The theory of homogeneous turbulence* (University Press)
- Chaplin, W. J., Elsworth, Y., Isaak, G. R., et al. 1998, *MNRAS*, 298, L7
- Favata, F., Roxburgh, I., & Christensen-Dalsgaard, J. 2000, in *The Third MONS Workshop: Science Preparation and Target Selection*, 49
- Goldreich, P., & Keeley, D. A. 1977, *ApJ*, 212, 243
- Goldreich, P., Murray, N., & Kumar, P. 1994, *ApJ*, 424, 466
- Gough, D. O. 1977, *ApJ*, 214, 196
- Houdek, G., Balmforth, N. J., Christensen-Dalsgaard, J., & Gough, D. O. 1999, *A&A*, 351, 582
- Matthews, J. M. 1998, in *Structure and Dynamics of the Interior of the Sun and Sun-like Stars*, 395
- Musielak, Z. E., Rosner, R., Stein, R. F., & Ulmschneider, P. 1994, *ApJ*, 423, 474
- Osaki, Y. 1990, in *Lecture Notes in Physics: Progress of Seismology of the Sun and Stars*, ed. Y. Osaki, & H. Shibahashi (Springer-Verlag), 75
- Rieutord, M., & Zahn, J.-P. 1995, *A&A*, 296, 127
- Samadi, R. 2001, in *SF2A-2001: Semaine de l'Astrophysique Francaise*, E148 [astro-ph/0108363]
- Samadi, R., Nordlund, Å., Stein, R., Goupil, M.-J., & Roxburgh, I. 2003, *A&A*, 403, 303
- Samadi, R., & Goupil, M. 2001, *A&A*, 370, 136 (Paper I)
- Samadi, R., Goupil, M., & Lebreton, Y. 2001, *A&A*, 370, 147
- Samadi, R., Nordlund, A., Stein, R. F., Goupil, M.-J., & Roxburgh, I. 2002, in *SF2A-2002: Semaine de l'Astrophysique Francaise*, meeting held in Paris, France, June 24–29, ed. F. Combes, & D. Barret (EDP Sciences)
- Stein, R. F. 1967, *Sol. Phys.*, 2, 385
- Stein, R. F., & Nordlund, A. 1998, *ApJ*, 499, 914
- Stein, R. F., & Nordlund, Å. 2001, *ApJ*, 546, 585
- Tennekes, H., & Lumley, J. 1982, *A first course in turbulence*, 8th edition (MIT Press)

Inferred acoustic rates of solar p modes from several helioseismic instruments

F. Baudin¹, R. Samadi^{2,3}, M.-J. Goupil², T. Appourchaux^{4,1}, C. Barban^{5,*},
P. Boumier¹, W. J. Chaplin⁶, and P. Gouttebroze¹

¹ Institut d'Astrophysique Spatiale, CNRS/Université Paris XI UMR 8617, 91405 Orsay Cedex, France
e-mail: frederic.baudin@ias.u-psud.fr

² Observatoire de Paris, LESIA, CNRS UMR 8109, 92195 Meudon, France

³ Observatório Astronómico UC, FCTUC, Coimbra, Portugal

⁴ European Space Agency, Research and Science Support Department, Science Payload and Advanced Concept Office,
PO Box 299, 2200Ag Noordwijk, The Netherlands

⁵ National Solar Observatory, 950 N. Cherry Avenue, Tucson AZ 85719, USA

⁶ School of Physics and Astronomy, University of Birmingham, Edgbaston, Birmingham B15 2TT, UK

Received 4 May 2004 / Accepted 13 November 2004

Abstract. Acoustic rates of excitation of solar p modes can be estimated from observations in order to place constraints on the modelling of the excitation process and the layers where it occurs in the star. For several reasons (including a poor signal to noise ratio and mode overlap), this estimation is difficult. In this work, we use three completely independent datasets to obtain robust estimates in the solar case for $\ell = 1$ modes. We also show that the height in the solar atmosphere where the modes are observed must be taken into account. Our three sets of results are shown to be consistent, particularly in the lower part of the p -mode spectrum (from 1.8 mHz to 2.8 mHz). At higher frequencies, the agreement is not as good, because of a larger dispersion of the measurements and also because of some systematic differences which might be due to observation height estimation or to a systematic influence of the noise.

Key words. Sun: oscillation – Sun: helioseismology

1. Introduction

Solar seismology has been used for many years to “sound out” the interior of the Sun through information provided by the acoustic resonances (the so-called p modes). More precisely, the frequencies of these resonances – which are usually extracted by the analysis of power frequency spectra – are governed by the physical conditions inside the Sun, and these can be “inverted” to infer these conditions (e.g., sound speed, density, rotation). In the last ten years, new ways of analysing the solar oscillations or extracting information from them have been developed, mainly in the field of local seismology (analysing local propagation of acoustic waves). However, globally coherent, or “classical” seismology, is also developing and giving rise to new results: for example Houdek et al. (2001) have used the width of the resonances to infer convection properties. Nevertheless, the outer layers of the Sun remain poorly described, as well as the convection in these layers.

Seismology can place constraints on the modelling of these layers, and on the convection which excites the acoustic resonances. Among others, Samadi & Goupil (2001) have

proposed such a model and compared the acoustic rates thereby predicted (see Sect. 2) with observations (Samadi et al. 2003). They found a good overall agreement when the input data of the theoretical model of stochastic excitation were constrained with a 3-D simulation of the Sun. However, even if the agreement is good for the lower part of the p -mode spectrum, some clear discrepancies remain at higher frequencies, which is unfortunately where the properties are most difficult to measure.

The excitation rate of low-frequency p modes is mainly dominated by inertia. In contrast, the excitation of high-frequency p modes is more sensitive to the nature of the source of excitation (either dynamical via Reynolds stresses or thermal via turbulent entropy fluctuations, see Goldreich et al. 1994; Samadi et al. 2001). The excitation rate at high frequencies also depends on the temporal properties of the turbulence in the outer layers of the star (Samadi et al. 2003). Observational constraints are needed for the modelling of such properties.

The estimation of the power and width of the acoustic resonances is subject to several sources of error. First, there is a large uncertainty in the measurement as the power spectrum of a resonance (or mode) has a large variance because of the stochastic nature of the excitation (see Sect. 6). Moreover, the absolute calibration in amplitude of a Doppler time

* *Present address:* Instituut voor Sterrenkunde, Katholieke Universiteit Leuven, Celestijnenlaan 200 B, 3001 Leuven, Belgium.

series is a complex problem (see Sect. 4). Another problem is to know exactly at which height in the solar atmosphere the modes are observed. Oscillations of the photosphere are measured in two ways: photometry in a given wavelength range, or Doppler measurements on a line formed in the photosphere (like the data used in this work). As the density drops rapidly with height in the solar atmosphere, the observed amplitude increases rapidly. Thus, a measurement of power is meaningful only if the altitude to which it corresponds is known. With a proper calibration, comparisons of the absolute power levels of models of mode excitation by convection are possible (whose results are strongly dependent on height; see Sect. 5).

Our aim in this paper is to obtain reliable measurements of the excitation rate of globally coherent, low-angular degree (or low- ℓ) modes. To have confidence in the results we have used three independent datasets (see Sect. 3) covering the same observation period, and then analysed these with the same method and software. We have been particularly careful in our extraction of the parameters at high frequencies (see Sect. 6). Furthermore, we have also taken into account in our analysis the observation heights in the solar atmosphere at which the three datasets were “taken”. As such, we have attempted to make available to modellers an internally consistent set of results.

2. Assessing excitation rates from seismic measurements

2.1. Relations between the mode excitation rate, line-width and surface velocity

The rate at which a p mode of frequency ν_0 is excited is expressed as in Goldreich et al. (1994):

$$P = 2\pi \Gamma E \quad (1)$$

where $\Gamma = 2\eta/2\pi$ is the linewidth of the mode and η is the damping rate. The averaged mode energy, E , is given by Samadi et al. (2001)

$$E = \mathcal{M}(r_s) v^2(\nu_0), \quad (2)$$

where $v^2(\nu_0)$ is the mean-square surface velocity of a *radial* mode. The mode mass is obtained from

$$\mathcal{M}(r_s) = \frac{I}{\xi_r^2(r_s)} \quad \text{with} \quad I \equiv \int_0^{M_\odot} dm \xi_r^* \cdot \xi \quad (3)$$

where I is the mode inertia, ξ is the eigenfunction for the fluid displacement, ξ_r its radial component and r_s is the radius at which oscillations are measured.

According to Eqs. (1) and (2), the excitation rate P can then be related to the seismic data by:

$$P(\nu_0) = 2\pi \Gamma \mathcal{M} v^2(\nu_0), \quad (4)$$

where the quantities Γ and v^2 are indeed obtained from the observations.

A pulsation code is used to compute the eigenfunctions, ξ , and the mode mass \mathcal{M} for a calibrated solar model (see Sect. 2.3). It is important to stress that the radius r_s , at which \mathcal{M} must be evaluated depends on the spectral line of the corresponding seismic measurement (see Sect. 5) and therefore on the observation set and instrument.

2.2. Determination of the mode surface velocity and line-width from the seismic measurements

To a first approximation, the mode profile in the observed power velocity spectrum, \mathcal{P}_L , can reasonably be assumed to be Lorentzian with a maximum power spectral density, or height, \mathcal{H} , and a linewidth at half maximum given by Γ . The mode profile is then written as:

$$\mathcal{P}_L(x) = \mathcal{H} \frac{1}{1+x^2} \quad \text{where} \quad x \equiv 2(\nu - \nu_0)/\Gamma. \quad (5)$$

The square of the mode velocity, v_L^2 – which will be used in evaluating Eq. (4) – results from the integration of the mode profile over the frequency ν :

$$v_L^2 = \int_{-\infty}^{+\infty} d\nu \mathcal{P}_L(\nu). \quad (6)$$

The integration is performed over $]-\infty, +\infty[$ to take into account both the negative and the positive side of the spectrum. In practice, the real velocity profile is modified by several effects such as the observational technique and geometrical effects. This is taken into account through a multiplicative factor C_{obs} , so that finally one has:

$$v_L^2 = \pi \mathcal{H} \Gamma C_{\text{obs}}. \quad (7)$$

In the actual observed velocity spectrum the solar p modes exhibit asymmetric profiles. This asymmetry is interpreted as due to the interaction between the resonant cavity mode and local emission from discrete sources (Duvall et al. 1993; Abrams & Kumar 1996). Nigam et al. (1998) developed a more sophisticated model by adding a correlation between the mode oscillation and the solar noise. After dropping an additional parameter, whose influence applies only far in the wings of the peak and which cannot be observed in the solar case because of the presence of noise and neighbour modes, and after some simplifying approximations, they modelled the power velocity spectrum as (hereafter Nigam’s profile):

$$\mathcal{P}_N(x) = \mathcal{H} \frac{(1+Bx)^2 + B^2}{1+x^2}, \quad (8)$$

where B is a parameter which controls the asymmetry and contains the effects of correlated noise and of the source. The corresponding mean square velocity of the Nigam profile is the integral of Eq. (8) over $x =]-\infty, +\infty[$. However, since the approximation performed by Nigam et al. (1998) in deriving Eq. (8) is valid only for $|Bx| \ll 1$, the formalism cannot be used when $|x| \gg 1$. In what follows, we obtain estimates of the \mathcal{H} and Γ by fitting the Nigam profile (Eq. (8)) to the data. However, we do so by restricting the fitting interval, which runs from $-x_0$ to x_0 , to $x_0 \leq 10$.

Once the quantities \mathcal{H} and Γ are determined, one needs to compute the velocity. The mean square velocity of the mode, v_N^2 , is then:

$$v_N^2 = \pi \mathcal{H} \Gamma C_{\text{obs}} (1 + \delta(B)) = v_L^2 (1 + \delta(B)), \quad (9)$$

with

$$\delta(B) = -1 + \frac{1}{\pi} \int_{-x_0}^{+x_0} dx \frac{(1 + Bx)^2 + B^2}{1 + x^2}. \quad (10)$$

The quantity δ depends on B , which in turn depends on ν_0 , and is found to be negligible for all the modes investigated here. For instance, at $\nu_0 \simeq 3.3$ mHz and with $x_0 \equiv 10$ (i.e., $|\nu - \nu_0| = 5\Gamma$) we have $B \sim -10^{-2}$ and $\delta \sim 0.05\%$. This last value must be compared with the relative errors associated with v^2 which are $\geq 20\%$. Therefore by estimating v^2 from Eq. (9) but neglecting the $\delta(B)$ we introduce a negligible error in the determination.

2.3. Mode mass calculation

The solar model we consider is calculated with the CESAM code (Morel 1997) and appropriate input physics, as described in detail in Lebreton et al. (1999). In particular, convection is modelled according to the classical mixing-length theory (Böhm-Vitense 1958, hereafter MLT) with a mixing-length $l = \alpha_c H_p$, where H_p is the pressure scale height and α_c is the mixing-length parameter. In contrast with Lebreton et al. (1999), the atmosphere is calculated assuming the Eddington classical gray atmosphere, and microscopic diffusion is included according to the simplified formalism of Michaud & Proffitt (1993). The calibration of the solar model in luminosity and radius for an age of 4.65 Gyr fixes the initial helium content $Y = 0.2751$, the metallicity $Z = 0.0196$ and the MLT parameter $\alpha_c = 1.76$.

The oscillation eigenfunctions, and hence the mode masses, \mathcal{M} , in Eq. (4) are next obtained with the adiabatic pulsation code of Tran Minh & Leon (1995) from the solar model.

In order to measure the influence of the treatment of convection and of the atmosphere, we have considered two additional solar models. One solar model assumes Canuto et al. (1996)'s local treatment of convection. The second has its atmosphere calculated assuming Kurucz's model, computed such as to provide a good agreement between synthetic and observed Balmer line profiles.

At fixed r_s , we find that the mode masses depend on the treatment of convection and on the treatment of the atmosphere but the associated changes in $\mathcal{M}(\nu)$ are found to be of the same order as the observational error bars associated with the excitation rates. As we are, here, mainly interested in the comparison between observations from different instruments, the effect of the adopted physics on \mathcal{M} does not influence the results.

3. The different data sets used

Three datasets were used in this work, each covering the 805-d period from 1996 April to 1998 June. This epoch coincides with a period of low activity on the Sun. The use of several sets allows a direct comparison, and an assessment of

the influence on the results of each observation method. The three time series come from the instrument GOLF (Global Oscillation at Low Frequencies, Gabriel et al. 1997) onboard the satellite SoHO, and from the ground-based networks BiSON (Birmingham Solar Oscillation Network, Chaplin et al. 1996) and GONG (Global Oscillation Network Group, Harvey et al. 1996). Each are velocity measurements integrated over the whole solar disc¹ sensitive to low-degree modes (mainly $\ell = 0, 1$ and 2). The analysis has been performed in the same way for the three sets (i.e., the same fitting algorithm).

An obvious difference between the datasets is the ‘‘duty cycle’’, or fraction of effective time for which observations are available. Interruptions can result from instrumental failures, and also from bad weather for the ground-based networks. Power levels in the Fourier (frequency) spectrum can be corrected to take account of these interruptions through a simple multiplication by the inverse of the duty cycle. However, as shown by Chaplin et al. (2003), this simple correction does not completely remove the bias in the fitted width and height parameters that is caused by the window. In this work, acoustic rates computed from BiSON and GONG spectra were therefore additionally corrected by a constant value of 9% for each 10% change in duty cycle, as indicated by Chaplin et al. (2003).

In addition to this, two aspects play an important role in the comparison of the three datasets. First, the absolute calibration of a Doppler time series is a delicate task. Among the seismic observables, frequencies are very accurately estimated (to some ppm), whereas amplitudes are not. One of the reasons for this is the difficulty in properly deriving the photospheric displacement from the spectro-photometric measurements performed by the instruments. The case of GOLF can be cited as a good example as, because of technical problems, Doppler shifts are estimated from only one wing of the selected atomic lines. However, the task is not much easier for the other two instruments (Hill, Leibacher, private communication). This is detailed in Sect. 4.

The second aspect of the problem of acoustic rate estimation is the height in the solar photosphere to which the observations correspond, as the amplitude of the modes varies with height. This is the old and complex problem of line formation in the solar atmosphere, illustrated by an abundant literature, and detailed in Sect. 5.

3.1. GOLF data

GOLF is based on a non-imaging spectrophotometer using the Na I D₁ (at 589.6 nm) and D₂ lines (at 589.0 nm) to measure the velocity of the photosphere. Because of technical problems (Gabriel et al. 1997), the velocity is derived from intensity measurements in only one wing of the lines (the blue wing for the period used here). The average position of the measurement points in the wing is 108 mÅ from the centre for the D₁ line, and 81 and 135 mÅ for the D₂ lines. To this must be added the value of the gravitational redshift for the sodium lines: 12.5 mÅ.

¹ GONG also provides imaged observations, but here we have used the whole disc data.

As GOLF is space-borne, the interruptions in the observations are very few, and the duty cycle reaches almost 100% over the total duration of the period of observation chosen here.

3.2. BiSON data

The BiSON instruments are also non-imaging spectrophotometers, but they work in the K I line at 769.9 nm. The intensity is measured in both wings, at typically ± 63 mÅ from the centre of the line (which presents a gravitational redshift of 16 mÅ).

Despite the use of six active sites spread widely in longitude, the network experiences some interruptions yielding a duty cycle of $\approx 74\%$ for the period used here.

3.3. GONG data

The GONG instrument is an imaging Fourier tachometer using Ni I at 676.8 nm, which measures velocity from the whole line, as described by Jones (1989). The time series used here is the $\ell = 0$ dataset (integration over 95% of the solar disc). Again, there are some gaps in network coverage giving a duty cycle for the period covered of about $\approx 82\%$.

4. Data calibration

The sensitivity of each instrument is not exactly the same: first, the geometrical visibility of the modes must be taken into account to compare those of different degree ℓ . The limb-darkening influences this parameter for the GOLF and BiSON spectrophotometers (see Appendix in Appourchaux et al. 2000; Christensen-Dalsgaard & Gough 1982), making it different for each instrument despite the fact that the geometry is intrinsic to the modes. In addition, GOLF and BiSON have their sensitivity influenced by the relative velocity of the instrument (due to the SoHO orbit for GOLF and to Earth orbit and rotation for BiSON, and to the gravitational redshift for both) and also by the solar rotation, as described by Christensen-Dalsgaard (1989). The impact of these effects on visibility gives rise to the so-called “Doppler imaging”. This yields a C_{obs} parameter (see Eq. (7)) for each spectrophotometer, and for each degree ℓ . Based on Appourchaux et al. (2000) and Christensen-Dalsgaard (1989) and on the limb-darkening description of Allen (1991), we have derived this parameter for GOLF and BiSON.

GONG is not a spectrophotometer but a Fourier tachometer. We have derived C_{obs} for the modes $\ell = 1$ and 2 from the value for $\ell = 0$ modes (given by F. Hill, private communication) and from their geometrical visibility.

All these values are listed in Table 1.

5. Observation heights

As mentioned in Sect. 2.1, the mass of the modes is one of the parameters needed to compute the excitation rate. As this mode mass is the mode inertia (an intrinsic characteristic) normalised by the displacement at the height where the wave is *observed*, this height must be properly estimated to derive correct values of the excitation rate. However, obtaining reliable formation

Table 1. Observational correction C_{obs} for the different instruments and modes (see Sect. 4).

	$\ell = 0$	$\ell = 1$	$\ell = 2$
GOLF	2.33	2.59	6.19
BiSON	2.99	3.38	8.41
GONG	3.27	3.88	10.91

heights of solar lines is a complex problem. In addition, each instrument analyses a well delimited part of the profile of the line, and as from the center of the line to the wings the height of formation varies by hundreds of km, the characteristics of each instrument must be taken into account. For the three relevant spectral lines used here, we have made use of Jones (1989) for GONG, and Bruls & Rutten (1992) for BiSON and GOLF. The work done by Jones is perfectly suited as it takes into account the manner in which GONG measurements are performed. On the other hand, the work of Bruls & Rutten is more general, but provides enough information to estimate the formation height of the K line of BiSON and the Na D₁ of GOLF. Unfortunately, this work does not include the neighbouring Na D₂ line.

We have taken these estimates as a first approach and are aware of their limitations. In addition to the missing D₂ line, some other aspects are neglected, e.g., integration over the entire solar disc and limb darkening effect. A complete and coherent treatment of the three lines, applied to the specific case of each instrument, is necessary but remains the next step for a future work.

It is not easy to define a formation height since physically it is not a single altitude in the solar atmosphere, but a range of contributing altitudes to the radiation of interest. The heights we extract from the literature must be considered only as estimates of the maximum of contribution. From Fig. 3 of Jones (1989), we have estimated the observation height of GONG at $h_{\text{GONG}} \approx 240$ km above the photosphere. Knowing the average position at which BiSON and GOLF measurements are made in the wings of K and Na lines, we have set $h_{\text{BiSON}} \approx 280$ km from Fig. 10 of Bruls & Rutten (1992), and $h_{\text{GOLF}} \approx 340$ km from their Fig. 11. Again, these estimates have to be taken as approximate, not only for the reasons already mentioned but also because they result from an average of different physical cases (the “hot” and “cool” models of Bruls & Rutten). More recently, Georgobiani et al. (2003) also showed that the definition of height is not trivial when comparing *geometrical* height and *optical* height.

The effect of height formation influences the determined acoustic rates, via the mode mass, mainly at high frequencies ($\nu \geq 3$ mHz); the effect is much weaker at lower frequencies (see Fig. 1). As such, this makes the interpretation of the results easier.

6. Measurements

The parameters necessary for the derivation of the acoustic rate are listed in Sect. 2. From the observations, two characteristics of the modes are needed: their width and their height in

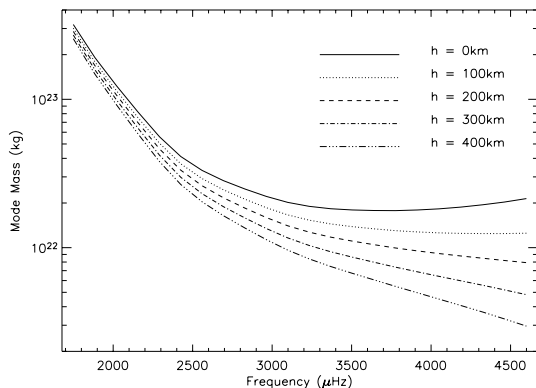


Fig. 1. Mode mass computed for different heights. Because the modes at higher frequencies are concentrated closer to the surface, the masses tend to decrease with increasing frequency. The increasing value of the eigenfunction ξ for larger heights gives the variation of mass versus height.

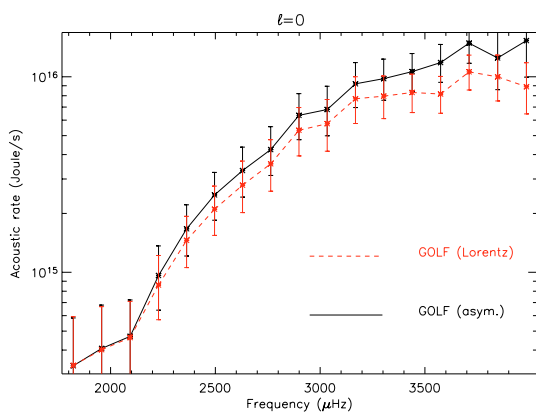


Fig. 2. Excitation rate computed from Lorentzian profiles and asymmetric profiles, showing a significant bias.

the power spectrum. They have been obtained by a classical fitting procedure applied in exactly the same manner to the three data sets. The modes are fitted using the asymmetric profile described by Nigam et al. (1998). This slight deformation of the peak is known to have a significant influence on frequency, but omitting it also leads to a bias in the determination of the acoustic rate, as shown in Fig. 2.

In the frequency interval from 2 to 3.5 mHz in the three datasets, the signal to noise ratio (SNR) is good and the fitting procedure extracts robust estimates of the mode parameters. However, as shown in Samadi et al. (2003), the high frequencies part (higher than 3.5 mHz) of the spectrum is interesting as observations and models tend to differ here. It is also the most difficult part of the spectrum to analyse, first because of the decreasing SNR, and second because of the increasing width of the modes. This makes the pairs $\ell = 0/2$ and $\ell = 1/3$ overlap. This in turn makes the fitting more difficult as cross-talk will appear between the modes.

To minimize the effect of cross-talk between neighbouring modes, as well as between the fitted parameters of a single mode, we modified the fitting strategy at high frequencies. The aim of these changes was to minimize the number of

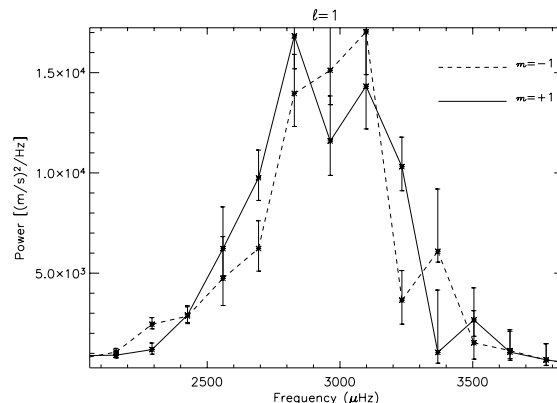


Fig. 3. Fitted heights for $m = \pm 1$ for $\ell = 1$ modes, which shows that the hypothesis of equal height for $|m| = \ell$ components is acceptable (error bars are 1σ).

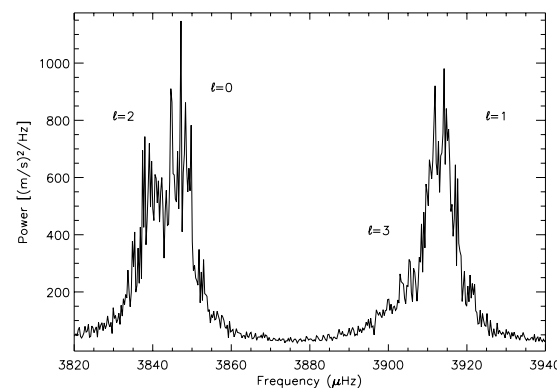


Fig. 4. Power spectrum at high frequencies from GOLF data, showing the overlapping pairs of modes.

fitted parameters; these were tested on the high SNR part of the spectrum and then applied at high frequencies. The changes applied can be something as simple as imposing the same amplitude for the $|m| = \ell$ components of a mode (see Fig. 3), or the same asymmetry for a pair $\ell = 0/2$ or $\ell = 1/3$ as shown by Thiery et al. (2000). However, at very high frequencies ($n \geq 29$), some more parameters have to be fixed in order to avoid poor convergence in the fits. First, we have chosen to restrict ourselves to the extracted $\ell = 1$ parameters, as full-disc observations are much less sensitive to $\ell = 3$ (see Fig. 4). The comparable heights of the $\ell = 0$ and $\ell = 2$ make this pair much more difficult to fit. Then, the strategy chosen here consisted of fixing the frequency difference in $\ell = 1/3$ pairs (leaving the $\ell = 1$ frequency to be fitted) in addition to fixing the relative height (from estimates done in the part of the spectrum with good SNR) of the $\ell = 3$ mode compared to that of the nearby $\ell = 1$ (which is fitted).

An additional way of improving the fitting is to use averaged power spectra. Instead of taking the power spectrum of the whole time series, one divides the series in N subsets, whose N spectra are averaged. It is the averaged spectrum that is then fitted. As the quantity of information is the same in both cases, no improvement should be expected in precision. Nevertheless, as the averaged spectrum has a reduced variance

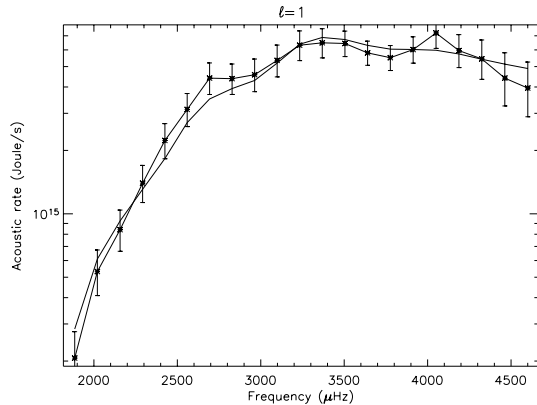


Fig. 5. Comparison of the excitation rate computed from the fitting procedure applied to a simulated spectrum (solid line) and the input excitation rate used for the simulation (crosses).

compared to the single (long) spectrum, and despite a poorer frequency resolution because of the shorter subsets, the fitting algorithm works better at high frequencies where the underlying shape of the peaks in the spectrum becomes then more evident. For this work, we averaged $N = 20$ spectra, each made from contiguous 40.25-d pieces. Uncertainties in the fitted parameters were computed according to Appourchaux (2003).

In order to check the reliability of the fitting, we performed a “blind” test using artificial data. The spectrum used is the main Hare-and-Hounds set of the Fitting at Low Angular-degree Group (FLAG)². One of us (WJC) generated the data for the fitter (FB) to analyse, with the basic underlying mode parameters unknown to the latter. As shown in Fig. 5, the output of the fitting procedure are in very good agreement with the input of the simulation, except at very high frequencies where a tendency to a slight underestimation is visible (but generally smaller than the error bars). Even if extensive simulations should be necessary to completely validate the fitting procedure, we consider that this first test is significant.

7. Results

7.1. Raw results

First, we compare the results for the acoustic rate of excitation of the modes, without any correction for the different observation heights in the solar atmosphere. The mode mass used was computed for an observation height of $h = 0$ km. This height is certainly not suited for any of the three instruments, but allows a comparison of the raw results in order to check for a possible bias due to the fitting procedure. Corrected results are shown and discussed in Sect. 7.2.

One can see from Fig. 6 that the independent measurements from the three helioseismic instruments coincide reasonably well. The error bars used in Fig. 6 are 1σ errors. The different measurements agree typically to within 1 or 2σ . The agreement between the different datasets is particularly convincing at low frequencies, except for an almost constant difference: in the range 2–3 mHz, the GOLF rate is systematically

² <http://bison.ph.bham.ac.uk/~wjc/Research/FLAG.html>

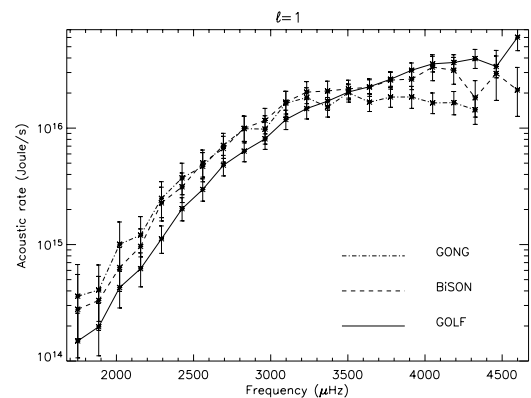


Fig. 6. Raw (no mass mode correction) acoustic rates for the three instruments.

lower than that of BiSON (by about 20% on average), whereas that of GONG is systematically higher ($\approx 15\%$). As mentioned in Sect. 5, mode mass does not make an important difference in this frequency range. The most likely origin of this discrepancy is an inaccurate absolute calibration of the three signals. However, we regard the level of agreement achieved as more than satisfactory given the complexities and uncertainties involved in the calibration.

At higher frequencies ($\nu \geq 3$ mHz), it is the difficulty in fitting the mode parameters (see Sect. 6) that is most problematic. Moreover, the mode mass correction is no longer negligible at these frequencies. However, despite a larger dispersion of the results, the GOLF rates are seen to be systematically higher than those of BiSON, most of which are in turn higher than those of GONG. This ordering is different from the one seen at low frequencies, and in fact reflects that of the observation heights of the three instruments. It is clearly necessary to correct for this effect.

7.2. Mode mass corrected results

The mode masses for the correction applied here were computed using the observation heights chosen in Sect. 5: $h_{\text{GONG}} \approx 240$ km, $h_{\text{BiSON}} \approx 280$ km and $h_{\text{GOLF}} \approx 340$ km. As expected, the correction does not make a large difference in the comparison of BiSON and GONG, as their observation heights are similar. Also foreseeable was the GOLF results were moved towards those of the other instruments, because of its higher observation height. However, the GOLF results remain higher than the others, particularly if one takes into account the apparent underestimation at low frequencies, which is certainly due to the absolute calibration as discussed in the next section.

8. Discussion

A first general conclusion that can be drawn from this work is that the excitation rate of solar p modes can be measured to relatively good accuracy. We have measured it from three completely independent datasets and found that the results were in agreement (without the need for speculative corrections). The discrepancies are of the order of 1σ (which corresponds to a

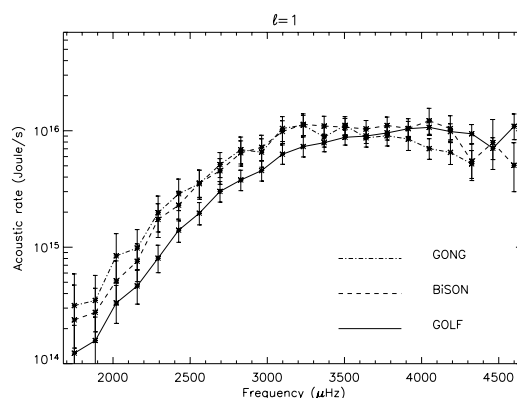
Table 2. Computed and measured (using GOLF data) parameters for $\ell = 1$ modes, including the mode mass correction for acoustic rates.

Mode identification	Frequency (μHz)	Mode mass (kg)	Height ($(\text{m/s})^2/\text{Hz}$)	Width (μHz)	Supply rate (Joule/s)
$n = 11 \ell = 1$	1749.33	2.64e+23	133.19	0.26	1.23e+14
$n = 12 \ell = 1$	1885.10	1.53e+23	256.89	0.28	1.58e+14
$n = 13 \ell = 1$	2020.83	9.58e+22	303.58	0.47	3.32e+14
$n = 14 \ell = 1$	2156.79	6.13e+22	516.56	0.54	4.65e+14
$n = 15 \ell = 1$	2292.03	4.02e+22	717.22	0.74	8.05e+14
$n = 16 \ell = 1$	2425.57	2.84e+22	1257.09	0.88	1.40e+15
$n = 17 \ell = 1$	2559.24	2.19e+22	1981.39	0.94	1.96e+15
$n = 18 \ell = 1$	2693.39	1.78e+22	3890.51	0.92	3.01e+15
$n = 19 \ell = 1$	2828.15	1.48e+22	5669.65	0.94	3.78e+15
$n = 20 \ell = 1$	2963.29	1.25e+22	11138.21	0.80	4.55e+15
$n = 21 \ell = 1$	3098.16	1.07e+22	9901.91	1.08	6.28e+15
$n = 22 \ell = 1$	3233.13	9.44e+21	12005.16	1.12	7.31e+15
$n = 23 \ell = 1$	3368.56	8.48e+21	5356.12	1.84	7.90e+15
$n = 24 \ell = 1$	3504.07	7.73e+21	2781.75	2.83	8.78e+15
$n = 25 \ell = 1$	3640.39	7.07e+21	1678.01	3.85	9.00e+15
$n = 26 \ell = 1$	3776.61	6.47e+21	831.83	5.90	9.57e+15
$n = 27 \ell = 1$	3913.49	5.95e+21	522.33	8.09	1.04e+16
$n = 28 \ell = 1$	4049.46	5.48e+21	331.52	10.73	1.07e+16
$n = 29 \ell = 1$	4186.98	5.05e+21	236.70	12.69	9.84e+15
$n = 30 \ell = 1$	4324.79	4.64e+21	147.81	16.39	9.42e+15
$n = 31 \ell = 1$	4462.08	4.25e+21	108.15	17.35	7.07e+15
$n = 32 \ell = 1$	4599.96	3.88e+21	78.85	26.42	1.09e+16

mean relative error of 22% for GOLF and 28% for BiSON and GONG) at low frequencies. These discrepancies can reach a level of 2 or 3σ at high frequencies, where the analysis is particularly difficult.

The level of agreement achieved has been possible by using a careful fitting of the data. The model fitted to the observations included an asymmetry in the peaks, since we found that the use of a Lorentzian profile yielded a small but systematic error. A strategy was adopted at high frequencies, where in the fitting of the $\ell = 1/\ell = 3$ pairs we used a fixed frequency difference and a fixed amplitude ratio. This gave robust fits despite the poor signal to noise ratio (SNR) and the large width of the peaks. A comparison with simulated data (the Hare-and-Hounds FLAG spectrum) validated this approach. However, extensive simulations would be necessary to estimate, for example, the influence of a poor SNR at high frequencies.

The agreement between the results from the three sets allows us to put constraints on the excitation rate. The excitation rate can be conveniently expressed as a power law: $P \propto \nu^\alpha$ (see for example Goldreich et al. 1994). At low frequencies, the exponent α mainly represents the inertia dependence of the excitation. At high frequencies, the excitation (and so the slope α) is strongly dependent on the adopted description of the turbulence. The three sets considered here yield similar values of α at low frequencies ($1.8 \text{ mHz} \leq \nu \leq 2.8 \text{ mHz}$): (7.7 ± 0.3) for GOLF; (7.5 ± 0.4) for BiSON; and (6.9 ± 0.4) for GONG. At higher frequencies ($3.3 \text{ mHz} \leq \nu \leq 4.8 \text{ mHz}$), the task is more difficult. First, the raw data (Fig. 6) – which have a positive, null and negative value for α – show the necessity of applying

**Fig. 7.** Mode mass corrected acoustic rates for the three instruments.

a mode mass correction to take account of the height of observation in the solar atmosphere. After the correction has been applied (Fig. 7), the three instruments yield α values of: (0.3 ± 0.5) for GOLF; (-2.1 ± 0.7) for BiSON; and (-2.3 ± 0.5) for GONG. This shows that the mode mass correction brings the GOLF results closer to those of BiSON and GONG.

However, there is still some residual high-frequency discrepancy. This suggests that more work is needed, in particular: (i) on the determination of the observation heights; and (ii) on the influence of the SNR on the measurements at high frequencies. If the Na line used by GOLF were higher than expected in the solar atmosphere, the mode mass correction would be

stronger and this might possibly make the GOLF results compatible with those of BiSON and GONG. Calculations based on the same hypothesis for radiative transfer in the solar atmosphere for the three atomic lines used are necessary to determine the three heights consistently. Moreover, these calculations must take into account the instrumental details in each case to allow an accurate determination. On the other hand, it must be noted that because of their lower-fill window functions, the SNR in the BiSON and GONG spectra is lower than for GOLF. The poor SNR in the Fourier spectra at high frequencies might bias the observed excitation rate. Extensive numerical simulations are needed to test the extent of this.

This work must be seen as a first step towards a better understanding of p -mode excitation and an improved description of convection in the outer layers of the Sun. The use of three different datasets shows that the estimation of the excitation rate is not trivial, as several instrument related effects must be taken into account. However, the results from the three instruments show that it is possible to provide reliable estimates. This is necessary to allow fruitful comparisons between models and observations and to obtain information on the excitation process (is it dominated by Reynolds stress or entropy fluctuation?) and on turbulent convection (for instance its dynamical properties such as the degree of correlation in the turbulent convection). This will be the aim of a following paper.

Acknowledgements. We would like to thank Frank Hill, John Leibacher, and Stuart Jefferies for helpful discussions, Yveline Lebreton for the computation of solar models, and Luca Bertello for providing the calibrated GOLF data. RS's work has been supported by Société de Secours des Amis des Sciences (Paris, France) and by Fundação para a Ciência e a Tecnologia (Portugal) under grant SFRH/BPD/11663/2002. GOLF is the result of the cooperative endeavours of many individuals, to whom we are deeply indebted. SoHO is a mission of international cooperation between ESA and NASA. We thank all those who have been, or are currently, involved in the BiSON project. BiSON is funded by the UK Particle Physics and Astronomy Research Council (PPARC). This work utilizes data obtained by the Global Oscillation Network Group (GONG) Program, managed by the National Solar Observatory, which is operated by AURA, Inc. under a cooperative agreement with the National Science Foundation. The data were acquired by instruments operated by the Big Bear Solar Observatory, High Altitude Observatory, Learmonth

Solar Observatory, Udaipur Solar Observatory, Instituto de Astrofísica de Canarias, and Cerro Tololo Interamerican Observatory.

References

- Abrams, D., & Kumar P. 1996, *ApJ*, 472, 882
 Allen, C. W. 1991, *Astrophysical Quantities*, 3rd ed.
 Appourchaux, T. 2003, *A&A*, 412, 903
 Appourchaux, T., Fröhlich, C., Andersen, B., et al. 2000, *ApJ*, 538, 401
 Böhm-Vitense, E. 1958, *Z. Astrophys.*, 46, 108
 Bruls, J. H. M. J., & Rutten, R. J. 1992, *A&A*, 265, 257
 Canuto, V. M., Goldman, I., & Mazzitelli, I. 1996, *ApJ*, 473, 550
 Chaplin, W. J., Elsworth, Y., Howe, R., et al. 1996, *Sol. Phys.*, 168, 1
 Chaplin, W. J., Elsworth, Y., Isaak, G. R., et al. 1998, *MNRAS*, 298, L7
 Chaplin, W. J., Elsworth, Y., Isaak, G. R., et al. 2003, *A&A*, 398, 305
 Christensen-Dalsgaard, J., & Gough, D. O. 1982, *MNRAS*, 198, 141
 Christensen-Dalsgaard, J. 1989, *MNRAS*, 239, 977
 Duvall, T. L., Jefferies, S. M., Harvey, J. W., Osaki, Y., & Pomerantz, M. A. 1993, *ApJ*, 410, 829
 Gabriel, A. H., Charra, J., Grec, G., et al. 1997, *Sol. Phys.*, 175, 207
 Georgobiani, D., Stein, R. F., Nordlund, Å. 2003, *ApJ*, 596, 698
 Goldreich, P., Murray, N., & Kumar, P. 1994, *ApJ*, 424, 466
 Harvey, J. W., Hill, F., Hubbard, R., et al. 1996, *Science*, 272, 1284
 Heiter, U., Kupka, F., van't Veer-Menneret, C., et al. 2002, *A&A*, 392, 619
 Houdek, G., Chaplin, W. J., Appourchaux, T., et al. 2001, *MNRAS*, 327, 483
 Jones, H. P. 1989, *Sol. Phys.*, 120, 211
 Kurucz, R. L. 1991, in *Stellar Atmospheres - Beyond Classical Models*, 441
 Lebreton, Y., Perrin, M., Cayrel, R., Baglin, A., & Fernandes, J. 1999, *A&A*, 350, 587
 Michaud, G., & Proffitt, C. R. 1993, in *Inside the Stars*, IAU Coll. 137, ASP Conf. Ser., 40, 246
 Morel, P. 1997, *A&AS*, 124, 597
 Nigam, R., Kosovichev, A. G., Scherrer, P. H., & Schou, J. 1998, *ApJ*, 495, L115
 Samadi, R., & Goupil, M.-J. 2001, *A&A*, 370, 136
 Samadi, R., Goupil, M.-J., & Lebreton, Y. 2001, *A&A*, 370, 147
 Samadi, R., Nordlund, Å., Stein, R. F., Goupil, M.-J., & Roxburgh, I. 2003, *A&A*, 404, 1129
 Thiery, S., Boumier, P., Gabriel, A. H., et al. 2000, *A&A*, 355, 743
 Tran Minh, F., & Leon, L. 1995, in *Physical Process in Astrophysics*, 219

Rotation profile inversion in solar-like stars

In the COROT framework

J. Lochard^{1,2}, R. Samadi², and M. J. Goupil²

¹ Institut d'Astrophysique Spatiale, Université Paris XI, 91405 Orsay Cedex, France
e-mail: jeremie.lochard@ias.u-psud.fr

² Observatoire de Paris, LESIA, CNRS UMR 8109, 92195 Meudon, France

Received 25 August 2004 / Accepted 3 February 2005

Abstract. The observation of a few mixed modes on solar-like oscillating stars would enable their rotation profile to be inverted with success. Here simulated data are used to show that it is possible to find models for solar-like stars that present stochastically excited mixed modes with detectable amplitudes. We take special care to build the mode set by computing the mode amplitudes and selecting those modes with amplitudes compatible with the performance of the forthcoming seismic space experiment, COROT. The frequency set is inverted for various cases where input and trial stellar models differ and where random noise is added to the splittings. We show it is possible to localize a rotation gradient and assess its magnitude. Moreover the use of inverse and forward procedures in parallel gives access to a large part of the profile. We provide several constraints to help the selection of such stars. One looks for a relatively evolved star (still on the main sequence) of $\approx 1.5 M_{\odot}$ and the rotation rate on the surface should not be too small.

Key words. stars: oscillations – stars: rotation

1. Introduction

Helioseismology has proven to be a powerful tool for probing the interior of the Sun. In particular the inversion of the solar eigenfrequencies has provided localized information on the internal structure and rotation of our star (Gough et al. 1996; Basu & Christensen-Dalsgaard 1997; Basu et al. 2000; Schou et al. 1998). Solar-like oscillations have now been detected for several other stars from the ground; α Cen A (Butler et al. 2004; Bedding et al. 2004), Procyon (Martić et al. 2004; Eggenberger et al. 2004), β Hydri (Bedding et al. 2002), η Bootis (Kjeldsen et al. 2003); for a review see (Bouchy & Carrier 2003; Bedding & Kjeldsen 2003). Furthermore, ongoing and forthcoming space seismic missions (MOST, COROT) should provide much more accurate data.

The tools developed for helioseismology can be adapted to study stellar interiors; however, the transition from helioseismology to asteroseismology is not an easy task. Stars other than the Sun are not spatially resolved. Because of averaging over the stellar surface, only oscillation modes with low degrees will be detected. The available mode sets will be much more restricted than in the solar case. Several studies have nevertheless explored what we can expect from inversion to probe the structure of solar-like stars; e.g. Basu (2003) has reviewed the different attempts in this field using simulated data sets.

These attempts to invert solar-like oscillations focused mostly on inversion for the structure of the star (sound speed,

density profile, etc.) It has been shown that structure inversion for solar-like stars is not as straightforward as for the Sun but remains possible. The success of the inversion is definitely linked to the number of observed modes bearing independent information, to the accuracy of the frequency measurement, but also to the quality of other observational constraints on the star, such as the basic stellar parameters which are usually poorly known. Rotational inversions based on simulated data sets have also been performed for δ Scuti stars, using opacity-driven modes (Goupil et al. 1996). It is expected that such inversions are unlikely to succeed with pure p mode oscillations (see Christensen-Dalsgaard 2004). Gough & Kosovichev (1993) showed successful rotational inversion results with solar-like oscillations; but the nature of the modes was not mentioned, and the relative error on the splittings was very small.

Obviously a restricted mode set and a degraded frequency resolution prevent the inversion process from providing comparable constraints on the stellar interiors to those on the solar interior. However we aim here at showing that for some specific stars, rotational inversion can be achieved using solar-like oscillations, primarily in the framework of the space seismic mission COROT. Indeed some stars must present a few mixed modes in the high frequency regime where modes are usually pure p modes (see Christensen-Dalsgaard 2004). These mixed modes present dual characteristics as they have kinetic energy both in the inner regions of the star (g mode nature) and in the

outer layers (p mode nature). Such modes may have already been observed for the star η Boo (Christensen-Dalsgaard et al. 1995; Guenther & Demarque 1996; Di Mauro et al. 2003). We expect that observation of such modes might help to determine the variation of the rotation profile along the radius and localize some possible strong rotational gradient. This information would be valuable in providing useful constraints for the modelling of the angular momentum transport mechanisms inside the star.

To establish what one can expect from rotational inversion with low degree, high radial order modes, we needed to construct artificial “observational” datasets comprised of rotational splittings. To do so, we began selecting a stellar model and generating the frequencies and the rotational kernels associated with its eigenmodes; see Sect. 3. In this selection, our main criterion was *the existence of a few mixed modes in the stochastically excited frequency range*. As the mode set is crucial to the success of the inversion (Basu et al. 2002), we took special care in its selection (Sect. 4). We first formulated an a priori mode rejection process based on criteria such as the degree and the physical nature of the modes. Then we computed the oscillation amplitudes for the remaining modes according to our current knowledge of the excitation and damping processes. We also determined a detection threshold according to the expected performance of COROT. Amplitudes of the modes were then compared to the COROT threshold to select the set of modes (Sect. 4). Assuming a slow rotation with a given rotational profile, we then computed the rotational splittings which were optionally contaminated with random noise.

We then inverted the rotational splittings using the SOLA inversion technique (Sect. 2) for three different cases, from the ideal to a more realistic case: 1) inversion of the splittings using the input kernels; 2) inversion of the same splittings using trial kernels, i.e. kernels computed from a stellar model differing from the input model used to build the rotational splittings, where the trial model was selected according to observational constraints such as the location of the model in the HR diagram and the large and small frequency separations; 3) inversion with trial kernels and splittings contaminated by noise. The results of these inversions for rotation – $\Omega(r)$ – are presented in Sect. 5.

2. SOLA inversion technique

For slow rotators, the rotational splitting of an (ℓ, n) mode ($\delta\omega_{n,\ell}$) is related to the rotational rate along the radius, $\Omega(r)$, as follows:

$$\delta\omega_{n,\ell} = \int_0^1 k_{n,\ell}(r) \Omega(r) dr + \epsilon_{n,\ell}, \quad (1)$$

where $k_{n,\ell}(r)$ is the rotational kernel and $\epsilon_{n,\ell}$ the error associated with the (n, ℓ) mode (Christensen-Dalsgaard 1998). Pure p mode rotational kernels are not highly localized, so that the splittings only provide an average of the rotation rate over their widths.

We use here the SOLA inversion method (Pijpers & Thompson 1994), which aims at constructing an *inversion*

kernel $K(r_0, r)$ localized in r_0 built as a linear combination of the rotational kernels, i.e.:

$$K(r_0, r) = \sum_j c_j(r_0) k_j(r), \quad (2)$$

where the subscript j denotes the (n, ℓ) indices of the mode. $K(r_0, r)$ is sought to match a pre-selected target function $\mathcal{J}(r_0, r)$ as close by as possible, while keeping the effects of the data errors low. The aim is to minimize the following combination of the distance between K and \mathcal{J} and the data error propagation:

$$\int_0^1 (\mathcal{J}(r_0, r) - K(r_0, r))^2 dr + \mu \sum_{ij} E_{ij} c_i c_j, \quad (3)$$

where μ is a trade-off parameter to set the relative weight between the first and second terms in Eq. (3). E is the error variance-covariance matrix of the observed frequencies. Combining Eqs. (2) and (1) yields the average rotation rate around r_0 :

$$\langle \Omega \rangle_{r_0} \equiv \sum_j c_j \delta\omega_j = \int_0^1 K(r_0, r) \Omega(r) dr + \sum_j c_j(r_0) \epsilon_j. \quad (4)$$

The target function is chosen here as a Gaussian with width Δ :

$$\mathcal{J}(r_0, r) = \frac{1}{N} \exp\left(-\left(\frac{r-r_0}{\Delta}\right)^2\right) \quad (5)$$

where N is a normalization factor. The error on $\langle \Omega \rangle_{r_0}$ is $\sum_j c_j \epsilon_j$, with ϵ_j the errors on the observed splittings $\delta\omega_j$. For errors on the splittings independent of frequency (ϵ), the error magnification can be expressed as follows:

$$\Lambda(r_0) = \left(\sum_j [c_j(r_0)]^2 \right)^{1/2}. \quad (6)$$

In this case, the error on $\langle \Omega \rangle_{r_0}$ is:

$$\sigma_{\Omega(r_0)} = \Lambda(r_0) \epsilon. \quad (7)$$

Hereafter rotation rates are normalized to the surface rotation rate Ω_{surf} . Thus the errors are normalized as well.

3. Stellar modelling

Our stellar models were computed with the CESAM stellar evolution code (Morel 1997). This computation assumed the EFF equation of state, OPAL opacities (Iglesias & Rogers 1996), the classical theory for convection (MLT), and the NACRE nuclear reaction rates (Gautier & Morel 1997). Diffusion and rotation were neglected in the stellar model computations.

In the next sections the choice of the mass and the age of the stellar models is motivated by the expected amplitudes and the nature of the oscillation modes respectively. A correct choice of these parameters ensures that mixed modes exist in the stochastically excited frequency range. Numerical calculations showed that for main sequence stars with mass lower than $1.50 M_{\odot}$, mixed modes are less likely to appear in the appropriate frequency range. As a typical case, our input model had the

following parameters: $M = 1.55 M_{\odot}$, while the initial hydrogen and helium abundances were $X_0 = 0.705$ and $Y_0 = 0.275$. The mixing-length parameter was set to $\alpha = 1.76$, and no overshoot was included for this model ($\alpha_{\text{ov}} = 0$). Our input model was on the main sequence with a central hydrogen abundance $X_c = 0.10$. The input model and its evolutionary track are represented in Fig. 3. The input rotation profile, $\Omega(r)$, used in this study was built a posteriori, assuming local conservation of angular momentum.

4. Selection of the mode set

The ability to recover the correct rotation profile with an inversion process is strongly linked to the available mode set. To make this study as realistic as possible we selected the mode set on the basis of the expected amplitudes of the modes and of the constraints imposed by performance of the space seismic mission COROT (launch in 2006).

4.1. A priori selection

We selected a priori specific modes according to their nature and degree, ℓ , since the quality of the inversion kernels depends on these properties. The depths which the modes probe depend very much on the nature of the modes. Pure p modes mainly probe the outer layers of the star where most of their kinetic energy is concentrated. Gravity modes – also named g modes – have most of their energy in the deep interior. Their large inertia are responsible for their very small amplitudes on the surface. For this reason their detection seems unlikely (see Unno et al. 1989). However, for sufficiently massive stars the convective core recedes with evolution, which leads to an increase in the chemical composition gradient at the edge of the core. This gradient is directly involved in the expression of the Brunt-Väissälä frequency N . Figure 2 shows that N^2 increases at the edge of the core with the age of the star. For relatively evolved stars, modes with mixed nature appear. These *mixed* modes present a g mode character in the deep interior and a p mode character in the outer part of the star. They share their kinetic energy between these two regions, the degree of their “mixedness” depends on their fraction of energy in these regions. Some of these modes showing a dual nature have inertia that allows them to be detected, thus making it possible to probe the star at low radii.

We chose here to reject the pure gravity modes from our mode set and to keep only pure p modes and those *mixed* modes with a rather low mixed character *i.e.* with their p mode nature dominating over their g mode nature.

The apparent amplitude of a mode is an average of the mode amplitude over the stellar surface, which strongly depends on the degree ℓ of the mode. The observable amplitude decreases with ℓ . The forthcoming space missions, such as COROT, are expected to measure modes with $\ell \leq 3$. According to Libbrecht (1992) the signal to noise ratio and the uncertainty on the eigenfrequency determinations are linked; thus the frequencies of $\ell = 3$ modes may be determined with a rather low precision. We therefore restrained ourselves to $\ell = 1, 2$ modes.

4.2. Amplitude computation

For these a priori selected modes, the *root mean square* amplitudes in terms of velocity, v was calculated from the acoustic excitation rate P and damping rate η , itself obtained from the tables of Houdek et al. (1999), calculated on the basis of Gough (1977a,b)’s non-local and time-dependent formulation of convection. We used the closest available model from the input model in Houdek’s table of mass and temperature ($M = 1.50 M_{\odot}$ and $T_{\text{eff}} = 6400$ K).

Excitation rates were computed according to the model of stochastic excitation by Samadi & Goupil (2001). The calculations assumed a Lorentzian function for modelling the convective eddy time-correlations (see Samadi et al. 2003). For simplicity, we used the adiabatic assumption formulated by Kjeldsen & Bedding (1995) to deduce the *root mean square of the intrinsic* mode amplitudes in terms of luminosity fluctuations $(\delta L/L)_{\text{intrinsic}}$ from their velocity v according to:

$$\left(\frac{\delta L}{L}\right)_{\text{intrinsic,max}} = \left(\frac{\delta L}{L}\right)_{\odot,\text{intrinsic,max}} \frac{V_{\text{max}}}{V_{\text{max}}^{\odot}} \sqrt{\frac{T_{\text{eff},\odot}}{T_{\text{eff}}}}. \quad (8)$$

One should point out that this relation has been established for bolometric amplitudes while COROT observes only in a finite bandwidth. Although this bandwidth is optimized for solar-like stars, the actual amplitudes are expected to be very similar to the bolometric ones. For the Sun we took the rms values $(\delta L/L)_{\odot,\text{max}} \simeq 4$ ppm (see Kjeldsen & Bedding 1995, Table 2; Barban et al. 2004) and $V_{\text{max}}^{\odot} \simeq 27$ cm/s according to Chaplin et al. (1998)’s seismic observations. As the adiabatic assumption is not correct in the outer layers of a star, we performed a rough comparison with what is available in the literature (Houdek et al. 1999). At a high frequency, the adiabatic assumption underestimates the amplitudes compared to Houdek’s results, so it is quite conservative in this case. At a low frequency a rough estimate showed that the adiabatic approach overestimates the amplitudes of the luminosity fluctuations; thus considering the non-adiabatic assumption would result in the present case losing one mode with a mixed character from the final mode set. This has no severe consequence for the inversion results. At the worst, it would mean that the present results are relevant for a star that is only a little more massive or evolved than our case.

Strictly speaking the theory underlying the excitation and damping rate computations used here is valid only for radial pure p modes. Only non-radial modes present rotational splittings but the $\ell = 1, 2$ modes are quasi-radial in the zone where the excitation occurs. They are excited in the same manner as the radial modes. Then, as the excitation rate is proportional to the inverse of the mode inertia I , the excitation rates of the non-radial modes P_{ℓ} can be deduced from those of the radial ones P_0 according to the relation:

$$\frac{P_{\ell}}{P_0} \simeq \frac{I_0}{I_{\ell}} \quad (9)$$

for pure p and low ℓ degree modes $I_0/I_{\ell} \simeq 1$. To some extent, it is the same for the damping rates. Indeed according to Balmforth (1992), the main contribution to damping is due to

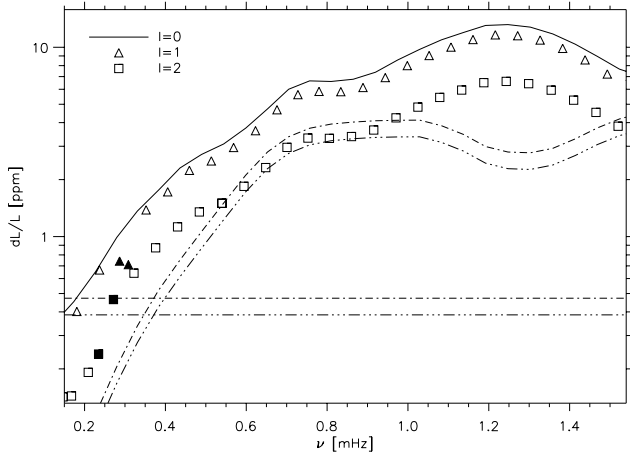


Fig. 1. Apparent mode amplitudes in terms of relative luminosity variations for $\ell = 0, 1, 2$. The solid line shows the amplitude of the radial modes; the triangle and square symbols represent the $\ell = 1$ and $\ell = 2$ modes respectively. The filled symbols represent the mixed modes. The horizontal lines correspond to Eq. (15) and apply to modes whose widths are smaller than the frequency bin in the Fourier domain (i.e. modes with $\nu \lesssim 0.4$ mHz). The upper line (dashed-dot) corresponds to $SNR_\infty = 9$ (confidence level: 99%) and the lower one (dashed-dot-dot-dot) to $SNR_\infty = 6$ (confidence level: 95%). The frequency-dependent thresholds apply to the other modes and correspond to Eq. (18) computed with $SNR = 9$ (dashed-dot line) and $SNR = 6$ (dashed-dot-dot-dot line).

convection and occurs mainly in the uppermost part of the convection zone where the modes are quasi-radial. Then we can deduce η_ℓ from η_0 using the relation:

$$\frac{\eta_\ell}{\eta_0} \approx \frac{I_0}{I_\ell} \quad (10)$$

with η being the damping rates. In the region where excitation and damping of the modes takes place, the mixed modes have the characteristics of pure p modes. Thus Eqs. (9) and (10) also apply to mixed modes.

The intrinsic amplitude $\left(\frac{\delta L}{L}\right)_{\text{intrinsic}}$ and the apparent amplitude $\left(\frac{\delta L}{L}\right)_\ell$ of a mode with a degree ℓ are related by:

$$\left(\frac{\delta L}{L}\right)_\ell = S_\ell * \left(\frac{\delta L}{L}\right)_{\text{intrinsic},\ell} \quad (11)$$

where S_ℓ is the spatial filtering function (see Christensen-Dalsgaard 1998). We used here the filtering functions used for the VIRGO instrument aboard SOHO spacecraft (Appourchaux et al. 1997), which observes the Sun as a star and monitors its luminosity variations as COROT and future asteroseismology space missions will do for other stars. $S_{\ell=1}$ and $S_{\ell=2}$ were set to 0.9 and 0.5 respectively, these coefficients depend on the angle between the rotation axis of the star and the line of sight. As an illustrative case we take the solar values. Figure 1 presents the apparent amplitudes of the luminosity variations for the $\ell = 0, 1, 2$ modes. The mixed modes are found at low frequency, and their amplitudes clearly depart from those of the pure p modes, while their smaller amplitudes are due to their larger inertia.

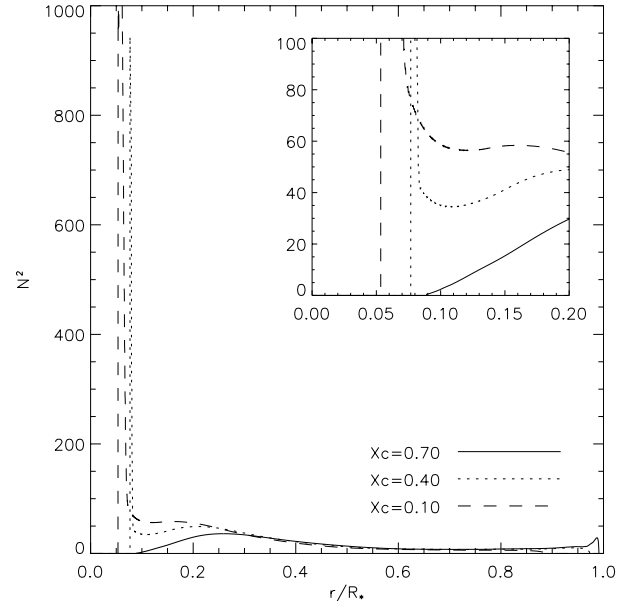


Fig. 2. Squared normalized Väissälä frequency for $1.55 M_\odot$ models at different evolutionary stages. The Väissälä frequency is normalized by $(G \langle \rho \rangle / \pi)^{1/2}$ with $\langle \rho \rangle$ the mean density and G the gravitational constant. The solid line corresponds to the ZAMS model (the hydrogen abundance in the core is $X_c = 0.7$), the dotted line to an $X_c = 0.4$ model. The dashed line represents the Väissälä frequency for an $X_c = 0.10$ model. In the insert frame, we focus on the deep interior, where one can see that along evolution, at the edge of the core, a cavity where g modes can be trapped develops in the high frequency regime.

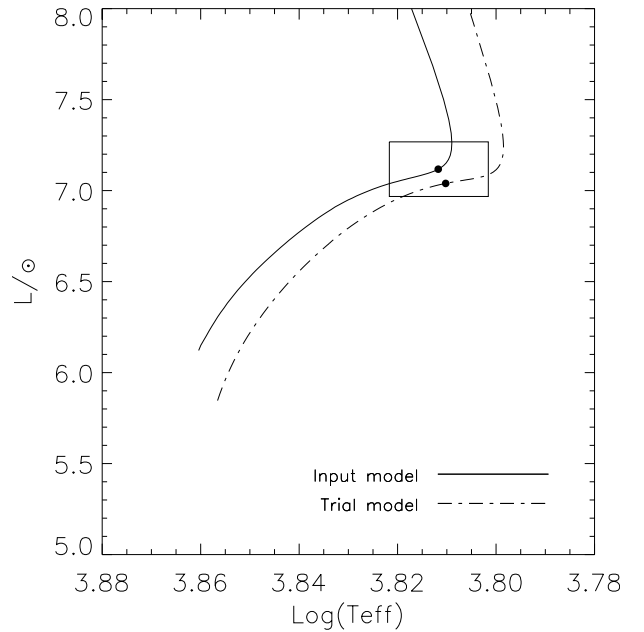


Fig. 3. Hertzsprung-Russell diagram with the evolutionary tracks of the input model (solid line) and the trial model (dashed line). Both models are represented by the black points on the tracks. The box materializes the typical uncertainties in determination of the luminosity and effective temperature.

4.3. COROT detection threshold and frequency accuracy

Our detection threshold was based on COROT specifications. The white noise level over 5 days of observation will be 0.61 ppm for a star of magnitude 5.7 (Auvergne & COROT Team 2000); consequently the level of the photon noise in the power spectrum B is (see Berthomieu et al. 2001):

$$B = (0.61 \text{ ppm})^2 5 \text{ days} = \frac{(0.61 \text{ ppm})^2}{2.3 \mu\text{Hz}} (\text{ppm})^2 \text{ s}. \quad (12)$$

To set the threshold and to determine the precision at which a mode frequency can be measured, two distinct cases must be considered depending on the widths of the modes versus the frequency resolution of the spectrum (also refer to Berthomieu et al. 2001).

4.3.1. Modes with long lifetimes

Modes with lifetimes longer than the observation time have their widths in the frequency domain smaller than the frequency bin and hence correspond to a single peak in the power spectrum with height H_∞ given by (see Berthomieu et al. 2001):

$$H_\infty = \frac{T_{\text{obs}}}{2} (\delta L/L)^2 (\text{ppm})^2 \text{ s}, \quad (13)$$

where $\delta L/L$ is the *root mean square* of the observed *apparent* mode amplitude in intensity as defined in Eq. (11).

The corresponding signal to noise ratio (SNR hereafter) in the *power* spectrum, SNR_∞ , is then according to Eqs. (13) and (12):

$$SNR_\infty \equiv \frac{H_\infty}{B} = \frac{1}{2} \frac{(\delta L/L)^2 T_{\text{obs}}}{(0.61 \text{ ppm})^2 5 \text{ days}} \quad (14)$$

where T_{obs} is expressed in unit of days. We stress that the SNR is expressed in terms of power (i.e. in terms of the square of the mode amplitude) because theoretical evaluations of the mode amplitudes (see Sect. 4.2) are derived in terms of mean square. A possible alternative is to define a signal to noise in terms of amplitude as in Kjeldsen & Frandsen (1992).

The value of SNR_∞ does not affect the precision of frequency determination. Indeed, for long lifetimes, whatever the value of SNR_∞ , the uncertainty on the frequency determination corresponds to the size of the bin, that is, to $0.08 \mu\text{Hz}$ for $T_{\text{obs}} = 150$ days. However the value of SNR_∞ sets the confidence level for the detection of an eigenmode. For $SNR_\infty = 9$, the confidence level reached is 99%.

For modes with long lifetimes, the detection threshold is from Eq. (14) then:

$$\left(\frac{\delta L}{L}\right)_{\infty, \text{threshold}} = \sqrt{2 SNR_\infty \frac{5 \text{ days}}{T_{\text{obs}}}} 0.61 \text{ ppm}. \quad (15)$$

For $SNR_\infty = 9$ (confidence level: 99%), the threshold (Eq. (15)) is equal to ≈ 0.47 ppm, and for $SNR_\infty = 6$ (confidence level: 95%) it is equal to ≈ 0.39 ppm. These thresholds are shown in Fig. 1 by horizontal dashed lines and are relevant for modes

whose widths are smaller than a single frequency bin, viz., modes below $\nu \approx 0.4$ mHz. Mixed modes are shown in Fig. 1 with filled symbols. Two $\ell = 1$ modes lie above the $SNR_\infty = 9$ threshold, while another $\ell = 2$ stands between the $SNR_\infty = 9$ and $SNR_\infty = 6$ thresholds. The first two modes are detected with a 99% confidence level and the latter with a level above 95%.

4.3.2. Modes with short lifetimes

For a mode with lifetime shorter than the observation time, the amplitude in the Fourier domain spreads over several frequency bins. In a first approximation the mode profile in the power spectrum is Lorentzian. The mean squared apparent amplitude of a mode is the integral over the peak profile. Consequently the height of the Lorentzian profile H is linked to the mode apparent amplitude $\delta L/L$ and its width through the following relation (in $\text{ppm}^2/\mu\text{Hz}$) (see e.g. Baudin et al. 2005)

$$H = \frac{(\delta L/L)^2}{\pi \Gamma} \quad (16)$$

where $\Gamma = \eta/\pi$ is the mode line-width in μHz with η the damping rate. According to Eqs. (12) and (16) the signal to noise ratio (SNR) then becomes:

$$SNR \equiv \frac{H}{B} = \frac{(\delta L/L)^2}{(0.61 \text{ ppm})^2} \frac{2.3 \mu\text{Hz}}{\pi \Gamma}. \quad (17)$$

Again, for $SNR_\infty = 9$, the mode is detected with a confidence level of $\sim 99\%$. Thus from Eq. (17) the detection threshold for modes with short lifetimes is:

$$\left(\frac{\delta L}{L}\right)_{\text{threshold}} = \sqrt{SNR \frac{\pi \Gamma}{2.3 \mu\text{Hz}}} 0.61 \text{ ppm}. \quad (18)$$

Hence, for $SNR = 9$, a mode with amplitude $\delta L/L > (\delta L/L)_{\text{threshold}}$ is detected with a confidence level better than 99%. The threshold given by Eq. (18) is plotted in Fig. 1 for $SNR = 9$ and $SNR = 6$. Only modes with $SNR \geq 6$ were kept. Most of the modes were detected with a confidence level better than 99%; however, few $\ell = 2$ modes were detected with a confidence level between 99% and 95%.

Note that the threshold depends only on Γ ; as the width depends on the mode, the threshold also varies with frequency. We point out that Eqs. (16) and (12) assume that the Fourier transform is normalized with respect to $T_{\text{obs}}^{-1/2}$, where T_{obs} is the duration of observation. This is why Eqs. (16) and (12) are independent of T_{obs} . However whatever the choice of normalization, Eqs. (17) and (18) do not depend on T_{obs} . Increasing the duration of observation does not increase the SNR but does decrease the stochastic fluctuations of the mode profile leading to better precision when determining of the mode frequency. Indeed Eq. (2) in Libbrecht (1992) gives the precision at which the frequency of a mode – with a life time shorter than the observation time – can be measured for a given SNR . This precision depends on the observation time (T_{obs}), on the mode line-width (Γ), and also on the SNR Eq. (17). Among the remaining modes with short lifetimes, the precision in frequency ranged between $\sim 0.05 \mu\text{Hz}$ and $\sim 0.3 \mu\text{Hz}$, according to Libbrecht (1992)'s formula.

4.4. Final set

The selection above left us with a set of 50 $\ell = 1, 2$ modes among which 3 were mixed modes. For these modes, we computed the associated rotational splittings according to Eq. (1) and assumed local conservation of angular momentum in the star. At high frequency, the widths of the modes increase. This might make the determination of the rotational splittings less accurate and some of the corresponding splitting useless; however, modes at such a frequency have very redundant kernels. The loss of their splittings does not affect the inversion results. In Sect. 5 below, we discuss the inversion results in cases of a set of splittings free of noise and one set contaminated with random noise. For short lifetime modes the error bars on the splittings were deduced from Eq. (2) in Libbrecht (1992). For modes with long lifetime, the error bars were set to the frequency bin.

5. Results of inversion

In this study we proceeded in 3 steps, successively aiming at more realistic conditions.

5.1. Optimal case

We first inverted the rotational splittings of our simulated data set, using the associated rotational kernels issued from the input model for k_j in Eq. (2). These are the optimal conditions, to check how far we can recover the rotational profile. The modes become evanescent in the convective core for intermediate mass stars and it was not possible to recover the rotational information in that specific region. On the other hand, Fig. 6a shows that we properly retrieved the rotation rate from the edge of the core ($0.07 r/R_*$) to $\approx 0.30 r/R_*$ with R_* the star radius. It was found that a few mixed modes only are sufficient to construct localized rotational kernels close to the core.

At intermediate radii, i.e. from ≈ 0.30 to $0.70 r/R_*$, it was not possible to construct localized inversion kernels. Neither pure p modes nor mixed modes have enough energy at intermediate radii, as their rotational kernels do not peak in these regions.

Further up in the outer layers of the star, p modes were sensitive to the rotation. The rotational kernels differ much more with the degree ℓ of the mode than with the mode frequency. As we assumed that we had access only to $\ell = 1$ and 2, the available p mode rotational kernels were too redundant to enable to construct localized inversion kernels. To obtain an estimate of the rotation rate in these layers, we are left with the forward method. As in Soufi et al. (1998), one can write the r -dependent rotational profile $\Omega(r)$ as:

$$\Omega(r) = \bar{\Omega}(1 + \eta(r)) \quad (19)$$

where $\bar{\Omega}$ is the mean rotation rate. A rigid body rotation corresponds to $\eta(r) = 0$. One can then write Eq. (1) as follows:

$$\delta\omega_{n,\ell} = \bar{\Omega} \int_0^1 k_{n,\ell}(r) dr + \bar{\Omega} \int_0^1 k_{n,\ell}(r) \eta(r) dr \quad (20)$$

and

$$\int_0^1 k_{n,\ell}(r) dr = 1 - C_{n\ell}, \quad (21)$$

where $C_{n\ell}$ is the Ledoux constant in the inertial frame (see Unno et al. 1989, Eq. (19.46)). For pure p modes, $C_{n\ell}$ can be neglected with regard to 1. In the outer part of the star, rotation is expected to be almost rigid, i.e. $\eta(r) \approx 0$. Thus the mean rotation rate in these layers can be expressed as:

$$\bar{\Omega} \sim \langle \delta\omega_{n,\ell} \rangle. \quad (22)$$

We selected a subset of rotational splittings of pure p modes in the asymptotic frequency range (32 modes). We then computed the mean value of the subset. The extent of the pure p mode kernels lead to a value which is an average over a large region. This mean value of the rotation rate is represented in Fig. 6a at $r/R_* = 0.78$. The horizontal error bar extended between 0.55 to 1 stellar radius and was determined so that more than 95% of the kernel energy is located within this range for the subset of modes used for the forward computation. The vertical bar is the linear average of the errors on the splittings. One notices that the rotational rate obtained by forward computing is overestimated. This shift is linked to the relatively small extent of the rotational kernels in the deep interior where the rotational rate increases.

5.2. Inversion with trial kernels

The stellar model used in the inversion process is not expected to represent the real star exactly. This departure from reality also exists for the rotational kernels used for the inversion process. In our simulated experiment, therefore, we must assume that the rotational kernels issued from computed models would not match the real ones exactly. To study the impact of differences between the true and trial kernels, we inverted the splittings with rotational kernels associated with a stellar model differing from the input one. The input or reference model is the model described in Sect. 3. The trial model was determined as for a blind experiment, i.e. by trying to approach our reference model as close as possible.

We used two steps to constrain the trial model. The first step consisted in getting as close as possible to the input model using the HR diagram information. As for real observations, we drew an error box around the input model in the HR diagram with typical observational uncertainties ($\sigma_{T_{\text{eff}}} = 150$ K and $\sigma_{L/L_\odot} = 0.15$, Fig. 3). We built several models with various initial parameters and retained only those consistent with the error box. Then the asteroseismic constraints enabled us to make a selection among the remaining trial models. The comparison of the large and small separations of the trial and input models, as defined in Eqs. (23) and (24) below, gave additional constraints. The large separation – Eq. (23) – is mostly linked to the overall structure of the star and to its mean density. The small separation – Eq. (24) – is related to the chemical composition gradient close to the core, giving hints about the evolutionary stage of the reference model (see Christensen-Dalsgaard 2004).

$$\Delta\nu_{n,\ell} = \nu_{n,\ell} - \nu_{n-1,\ell} \quad (23)$$

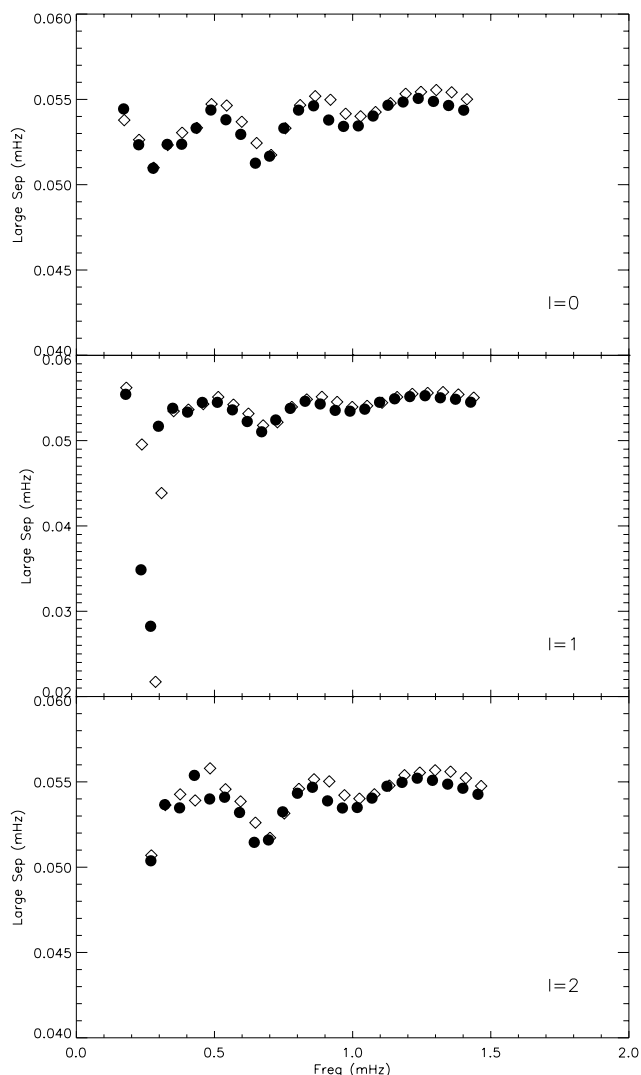


Fig. 4. Comparison of the large separations for the input and the trial models; see Eq. (23). Diamonds represent the large separation of the input model and filled circles correspond to that of the trial model. Each panel corresponds to a given degree ℓ (top panel: $\ell = 0$ to bottom panel: $\ell = 2$).

$$\delta\nu_{02} = \nu_{0,n} - \nu_{2,n-1}. \quad (24)$$

For several models within the HR diagram error box, we could reproduce the large separation reasonably well (see Fig. 4). However, we could recover the small separation only over a part of the frequency range (see Fig. 5). We gave priority to the model reproducing the small separation in the interval 0.5–1 mHz, as we were mainly interested in low frequency modes; modes above 1 mHz indeed produce very redundant rotational kernels. Eventually we selected the most appropriate model according to these criteria: $M = 1.52 M_{\odot}$, $X_0 = 0.7$, $Y_0 = 0.28$, $\alpha = 1.8$, and an overshoot parameter $\alpha_{\text{ov}} = 0.1$.

As was already the case when using the input kernels for the inversion, we recovered the rotational profile only partially. However, in this case the retrieved rates depart from the original profile, see Fig. 6b, although still in an acceptable way.

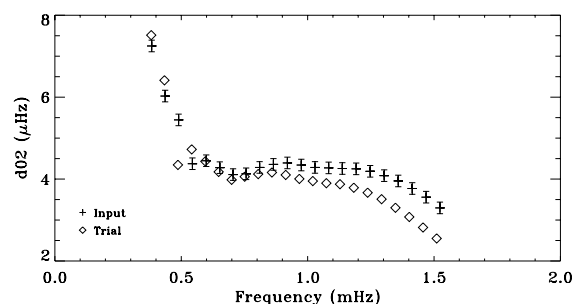


Fig. 5. Comparison of the small separations between $\ell = 0, 2$ – see Eq. (24) – for the input (crosses with associated error bars) and the trial models (diamonds).

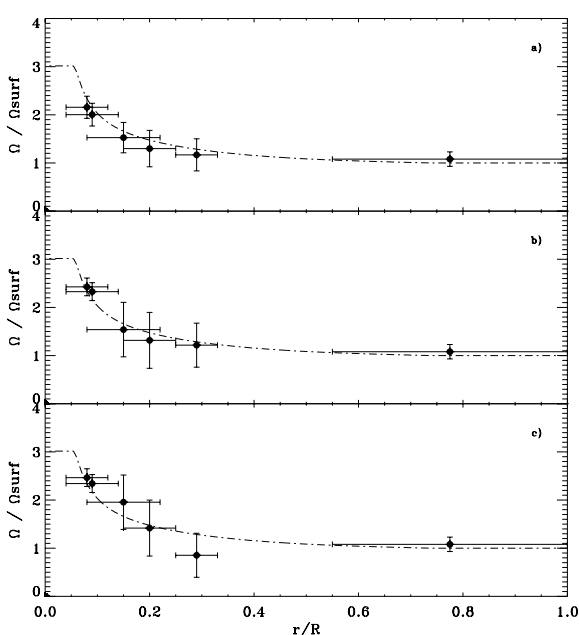


Fig. 6. Rotational profiles along the normalized radius of the stellar model. The dashed line represents the input rotation profile. The inverted rotation profiles are represented by black dots and their associated error bars: **a)** input rotational kernels, no noise included; **b)** trial rotational kernels, no noise included; **c)** one typical realization for trial rotational kernels, noise included ($V_{\text{surf}} = 30 \text{ km s}^{-1}$, $\epsilon = 0.08 \mu\text{Hz}$). In each panel, the point at $0.75 r/R_*$ is derived from the forward computation (see Sect. 5.1). The vertical error bar represent a 1σ error bars; the horizontal bars correspond to the width of the inversion kernels.

As previously, we used the forward computation to derive an estimate of the outer region rotation rate.

5.3. Inversion with trial kernels and splittings including random errors

Finally, the third case used the trial kernels and rotational splittings with random noise added prior to inversion. The noise was gaussian and several variance values were used corresponding to the COROT specifications and assumed surface rotation rates between 20 and 30 km s^{-1} . The recovered rates for one typical realization are shown in Fig. 6c. The retrieved rates based on

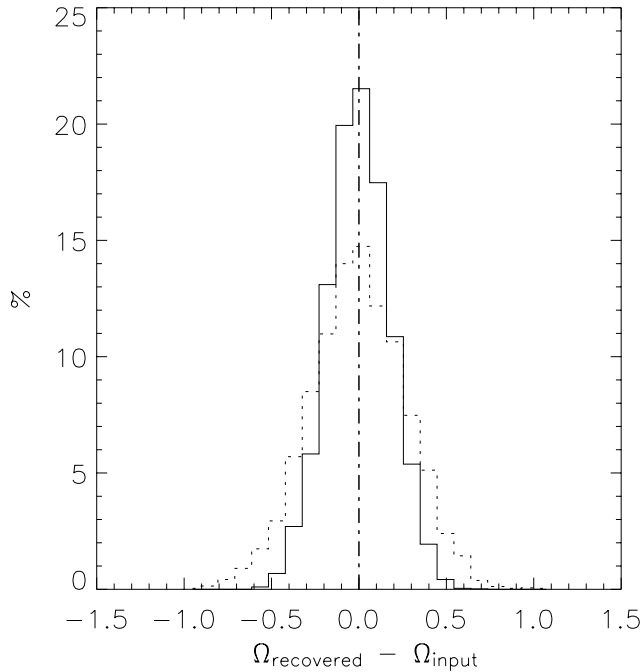


Fig. 7. Histogram of the differences between the recovered and input rotation rates at $r/R_* = 0.08$, both rates were normalized to the surface rotation rate. The full and dashed lines correspond to $V_{\text{surface}} = 30 \text{ km s}^{-1}$ and $V_{\text{surface}} = 20 \text{ km s}^{-1}$, respectively. The vertical line corresponds to zero bias. The bins were set to $0.1 \Omega_{\text{surface}}$.

the set of splittings with random noise generally differ by a few percent from the retrieved rates based on noise-free splittings.

To test the efficiency of the inversion process in the presence of noise, we created 5000 realizations of noisy splittings and inverted them. In Fig. 7 we plotted the histogram of the difference between the recovered and the initial rates at a given radius for several uncertainty levels.

We first checked the validity of the error bars on the rotational rates retrieved by inversion shown in Fig. 6. These uncertainties, expressed in Eq. (7), correspond to magnification of the initial errors on the measured splittings through the inversion process. If unbiased they should match the dispersion of the 5000 recovered rates. We thus compared the standard deviation of these rates to the propagated errors and found that they matched extremely well at every radius. This shows that the errors bars are estimated without bias.

Secondly, we calculated the averages of the recovered rates at each radius over the 5000 realizations and compared them to the input rates. If there were no bias, mean value of the difference between the retrieved and the input rotation rates would be zero. There actually is a small nonzero difference at each inversion radius, which is identical to the departure between the input and the output rates when the inversion was processed without random noise. This bias is due to the finite widths of the inversion kernels, which set the ultimate limit in retrieving the input rotation rate.

In Fig. 6c, the vertical error bars correspond to 1σ normalized uncertainties on the rotation rate, which were computed

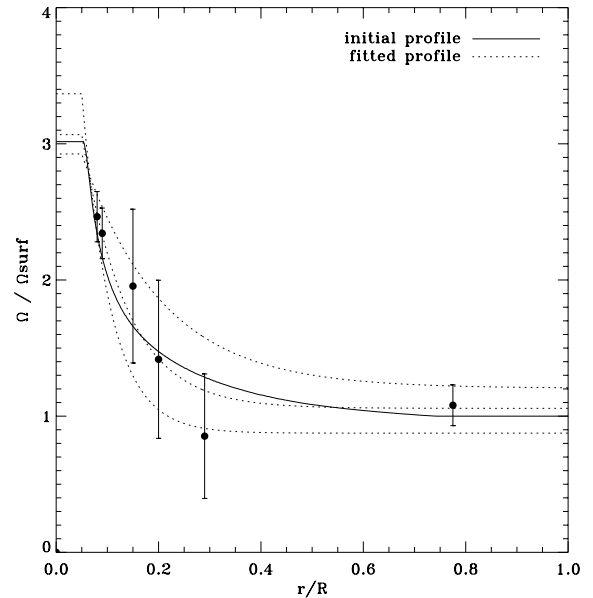


Fig. 8. Input and fitted rotational profiles. The full line curve stands for the initial rotational profile. The dotted curves fit the retrieved points of Fig. 6c. The middle one fits the central values, the two others fit the extreme values of the error bars.

assuming uncertainties on the splittings presented in Sect. 4.4 for a star rotating with a surface velocity of $V_{\text{surface}} = 30 \text{ km s}^{-1}$. This σ value corresponds in Fig. 7 to the half-width of the distribution. In the best case -with full line ($V_{\text{surface}} = 30 \text{ km s}^{-1}$)- only a few percent of the random realizations in the tail of the gaussian distribution give misleading rotation rates. In the second case in Fig. 7 - dashed line - the 1σ normalized error already corresponds to a large departure by the inverted rotation rate compared to the true value. In the conservative case, where we consider 3σ error bars, a rotation gradient can still be measured - if large enough - in the best case in Fig. 7. This is probably no longer possible in the worst case where the error bars strongly degrade our ability to estimate a rotational gradient.

As a final step, we estimated how discriminating the inversion is for reconstructing the rotational profile. We fitted the retrieved points with a decreasing exponential function. Figure 8 shows the mean and extreme profiles one could derive from the rates recovered in Fig. 6c where a random noise had been added to the splittings. We then computed the rotational splittings corresponding to these three profiles (mean and extreme). In Fig. 9 we plotted the input splittings - noise included - with black dots. The shaded area spans the values of the splittings computed from the extreme fitted profiles in Fig. 8. The input and the forward rotational splittings agree within the error bars.

This last step - i.e. computing the splittings from the recovered rotation rates - must be seen as a way to check the reliability of the inversion results. Inverted rotational profiles departing too much from the original will lead to computed splittings that do not match the true ones.

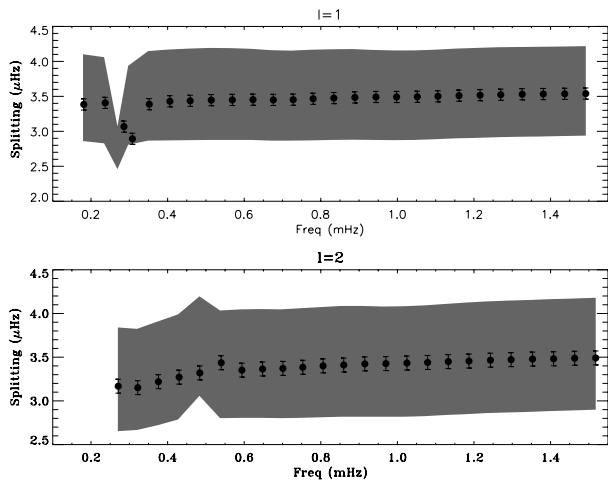


Fig. 9. Input and retrieved rotational splittings. The black dots represent the input splittings to which random noise was added, as in Fig. 6c. The shaded zone represents the range in which the solutions can be obtained by forward computation from the different fitted profiles in Fig. 8.

6. Discussion

As is well known, it is not possible to construct localized kernels for rotation with mode sets limited to $\ell = 1, 2$ and containing only pure p modes. Introducing $\ell = 3$ modes in the set improves the quality of the inversion kernels but does not provide enough diversity in the shapes of the rotational kernels to extract localized information at outer radii. However, we show here that stars exist which can present solar-like oscillations with a few mixed modes of detectable amplitudes. This presence in the mode set enables us to recover localized information on the rotation rate at several radii close to the core, leading to an estimate of the expected gradient.

As seen in Sect. 5.2, an important step is to model the observed star so as to build rotational kernels as close as possible to the real star. Combining the HR diagram and asteroseismic information (large and small separations) strongly constrains the model to be used to build the kernels. Accurate determination of stellar parameters, such as the luminosity and the effective temperature, is crucial at this step in the process.

We show that the inverse and forward procedures in stellar conditions are complementary and should be used in parallel. At low radii the inversion indeed provides localized and reliable information on the rotation rate and its evolution along the radius. In the outer part of the star the redundancy of the pure p mode rotational kernels does not allow us to build localized inversion kernels. Thus we derive the average rotation rate in this region directly from the splittings. Besides, the forward method can also be useful for checking the reliability of the rates retrieved by inversion. From the recovered points one can draw a rough rotational profile and use it to compute the splittings. By comparing the computed and the observed splittings it is possible to discard spurious profiles.

In short, a successful inversion of the rotational profile requires that the star fulfills several constraints. First, it has to be relatively evolved in order to have a receding convective

core so that avoided crossing occurs in the proper frequency range (roughly for $X_{\text{core}} \leq 0.2$). Secondly, the mass range, which yields mixed modes with large enough amplitude to be detected, spreads from $\approx 1.5 M_{\odot}$ up to masses that place the star in the instability strip of the HR-diagram, although studying stars above this upper mass limit is beyond the scope of this paper. For stars less massive than $\approx 1.5 M_{\odot}$, it is unlikely that mixed modes are detectable within the stochastically excited frequency domain. One must see the present results as prospecting. Some assumptions such as the adiabatic one – see Sect. 4.2 – might be too optimistic, in this case mixed modes will be detected in solar-like oscillations for stars with slightly higher mass or at more evolved stages than the one presented in this paper.

Finally, the surface rotation rate of the “ideal” target star should not be too small so that the splittings can be determined with a good accuracy and that the relative errors on the splittings remain small enough. We must add that important physical effects have been neglected here. One will probably, for instance, have to consider the effects of rotation and of the magnetic field on the large and small frequency spacings (Dziembowski & Goupil 1998). Moreover for faster rotators above $V_{\text{surf}} \approx 20\text{--}30 \text{ km s}^{-1}$ higher order effects on the rotational splittings will have to be considered.

Acknowledgements. The authors are grateful to Pr. Dziembowski for fruitful discussions and relevant comments. We thank T. Appourchaux, F. Baudin, P. Boumier, E. Michel for useful remarks, and A. Mazumdar for improving the English. We also thank the anonymous referee for valuable comments and for his help in improving the manuscript.

References

- Appourchaux, T., Andersen, B., Frohlich, C., et al. 1997, *Sol. Phys.*, 170, 27
- Auvergne, M., & COROT Team. 2000, in *The Third MONS Workshop: Science Preparation and Target Selection*, 135
- Balmforth, N. J. 1992, *MNRAS*, 255, 603
- Barban, C., Hill, F., & Kras, S. 2004, *ApJ*, 602, 516
- Basu, S. 2003, *Ap&SS*, 284, 153
- Basu, S., & Christensen-Dalsgaard, J. 1997, *A&A*, 322, L5
- Basu, S., Pinsonneault, M. H., & Bahcall, J. N. 2000, *ApJ*, 529, 1084
- Basu, S., Christensen-Dalsgaard, J., & Thompson, M. J. 2002, in *ESA SP-485: Stellar Structure and Habitable Planet Finding*, 249
- Baudin, F., Samadi, R., Goupil, M., et al. 2005, *A&A* 433, 349
- Bedding, T. R., & Kjeldsen, H. 2003, *PASA*, 20, 203
- Bedding, T. R., Kjeldsen, H., Baldry, I. K., et al. 2002, in *ASP Conf. Ser.*, 259: IAU Coll., 185: Radial and Nonradial Pulsations as Probes of Stellar Physics, 464
- Bedding, T. R., Kjeldsen, H., Butler, R. P., et al. 2004, *ApJ*, 614, 380
- Berthomieu, G., Toutain, T., Gonczi, G., et al. 2001, in *Proc. of the SOHO 10/GONG 2000 Workshop: Helio- and asteroseismology at the dawn of the millennium*, 2–6 October 2000, Santa Cruz de Tenerife, Tenerife, Spain. ed. A. Wilson, Scientific coordination by P. L. Pallé (Noordwijk: ESA Publications Division), ESA SP-464, 411
- Bouchy, F., & Carrier, F. 2003, *Ap&SS*, 284, 21
- Butler, R. P., Bedding, T. R., Kjeldsen, H., et al. 2004, *ApJ*, 600, L75

- Chaplin, W. J., Elsworth, Y., Isaak, G. R., et al. 1998, *MNRAS*, 298, L7
- Christensen-Dalsgaard, J. 1998, *Lecture notes on stellar oscillations* (Institut for Fysik og Astronomi, Aarhus Universitet)
- Christensen-Dalsgaard, J. 2004, *Sol. Phys.*, 220, 137
- Christensen-Dalsgaard, J., Bedding, T. R., & Kjeldsen, H. 1995, *ApJ*, 443, L29
- Di Mauro, M. P., Christensen-Dalsgaard, J., Kjeldsen, H., Bedding, T. R., & Paternò, L. 2003, *A&A*, 404, 341
- Dziembowski, W. A., & Goupil, M.-J. 1998, in *The First MONS Workshop: Science with a Small Space Telescope*, held in Aarhus, Denmark, June 29–30, 1998, ed. H. Kjeldsen, & T. R. Bedding, Aarhus Universitet, 69
- Eggenberger, P., Carrier, F., Bouchy, F., & Blecha, A. 2004, *A&A*, 422, 247
- Gautier, D., & Morel, P. 1997, *A&A*, 323, L9
- Gough, D. 1977a, in *Problems of Stellar Convection*, IAU Coll., 38, 15
- Gough, D. O. 1977b, *ApJ*, 214, 196
- Gough, D. O., & Kosovichev, A. G. 1993, in *ASP Conf. Ser.*, 40: IAU Colloq. 137: Inside the Stars, 541
- Gough, D. O., Kosovichev, A. G., Toomre, J., et al. 1996, *Science*, 272, 1296
- Goupil, M.-J., Dziembowski, W. A., Goode, P. R., & Michel, E. 1996, *A&A*, 305, 487
- Guenther, D. B., & Demarque, P. 1996, *ApJ*, 456, 798
- Houdek, G., Balmforth, N. J., Christensen-Dalsgaard, J., & Gough, D. O. 1999, *A&A*, 351, 582
- Iglesias, C. A., & Rogers, F. J. 1996, *ApJ*, 464, 943
- Kjeldsen, H., & Bedding, T. R. 1995, *A&A*, 293, 87
- Kjeldsen, H., Bedding, T. R., Baldry, I. K., et al. 2003, *AJ*, 126, 1483
- Kjeldsen, H., & Frandsen, S. 1992, *PASP*, 104, 413
- Libbrecht, K. G. 1992, *ApJ*, 387, 712
- Martić, M., Lebrun, J.-C., Appourchaux, T., & Korzennik, S. G. 2004, *A&A*, 418, 295
- Morel, P. 1997, *A&AS*, 124, 597
- Pijpers, F. P., & Thompson, M. J. 1994, *A&A*, 281, 231
- Samadi, R., & Goupil, M.-J. 2001, *A&A*, 370, 136
- Samadi, R., Nordlund, Å., Stein, R. F., Goupil, M. J., & Roxburgh, I. 2003, *A&A*, 404, 1129
- Schou, J., Antia, H. M., Basu, S., et al. 1998, *ApJ*, 505, 390
- Soufi, F., Goupil, M. J., & Dziembowski, W. A. 1998, *A&A*, 334, 911
- Unno, W., Osaki, Y., Ando, H., Saio, H., & Shibahashi, H. 1989, *Nonradial oscillations of stars*, *Nonradial oscillations of stars* (Tokyo: University of Tokyo Press), 2nd ed.

Influence of local treatments of convection upon solar p mode excitation rates

R. Samadi^{1,2}, F. Kupka³, M. J. Goupil¹, Y. Lebreton⁴, and C. van't Veer-Menneret⁴

¹ Observatoire de Paris, LESIA, CNRS UMR 8109, 92195 Meudon, France
e-mail: Reza.Samadi@obspm.fr

² Observatório Astronómico UC, Coimbra, Portugal

³ Max-Planck-Institute for Astrophysics, Karl-Schwarzschild Str. 1, 85741 Garching

⁴ Observatoire de Paris, GEPI, CNRS UMR 8111, 92195 Meudon, France

Received 18 February 2005 / Accepted 3 July 2005

ABSTRACT

We compute the rates P at which acoustic energy is injected into the solar radial p modes for several solar models. The solar models are computed with two different local treatments of convection: the classical mixing-length theory (MLT) and the formulation by Canuto et al. (1996, ApJ, 473, 550, CGM). Among the models investigated here, our best models reproduce both (i) the solar radius and the solar luminosity at solar age and (ii) the observed Balmer line profiles. For the MLT treatment, the rates P do significantly depend on the properties of the atmosphere, whereas for the CGM treatment, the dependence of P on the properties of the atmosphere is found to be smaller than the error bars attached to the seismic measurements. The excitation rates P for modes associated with the MLT models are significantly underestimated compared with the solar seismic constraints. The CGM models yield values for P closer to the seismic data than do the MLT models. We conclude that the solar p -mode excitation rates provide valuable constraints and, according to the present investigation, clearly favor the CGM treatment with respect to the MLT, although neither of them yields values of P as close to the observations as recently found for 3D numerical simulations.

Key words. convection – turbulence – Sun: atmosphere – stars: atmospheres – Sun: oscillations – radiative transfer

1. Introduction

In the outermost part of the convective zone (CZ) of intermediate mass stars, convection is highly superadiabatic because of the rapid radiative heat gains and losses of the convective fluid. In that region, entropy fluctuations are the largest, and the resulting decrease in the convective transport efficiency is compensated for by a large increase in the eddy motions, which is responsible for the oscillation mode driving. Modelling inefficient convection is complex. 3D numerical simulations are now being performed but remain still very time-consuming. Hence for massive stellar computations, 1D stellar models are used in which only simple prescriptions of convection are implemented.

Among these simplified treatments, the Canuto & Mazzitelli (1991, CM91 hereafter) approach differs from the classic mixing length approach (MLT hereafter) in that it takes the contribution of eddies with different sizes into account in the calculation of the convective flux and velocity, while keeping the computational expenses as low as the MLT. An improved version was proposed by Canuto et al. (1996, CGM hereafter), which takes into account the feedback of the turbulence on the energy input from the source which generates turbulent convection. These multi-eddy convection models

are usually referred to as Full Spectrum of Turbulence (FST) models.

Several non-local formulations of convection have also been proposed (Gough 1977; Xiong 1978, 1985; Canuto 1992, 1993; Canuto & Dubovikov 1998). However, we focus here on the effects of proposed improvements in the description of the energy spectrum and therefore consider only local treatments and compare FST models with MLT ones.

Any model of convection must satisfy several observational constraints provided by our Sun: the solar radius at the solar age, the Balmer line profiles, and the *uvby* color indices. The MLT, CM91's, and CGM's local treatments have been confronted to these observational constraints (e.g. Fuhrmann et al. 1993, 1994; van't Veer-Menneret & Megessier 1996; Smalley & Kupka 1997; Bernkopf 1998; Heiter et al. 2002; Montalbán et al. 2004). One main result is that these observational quantities are more sensitive to the adopted value of the convective scale length of the eddies than to the formulation of convection.

Solar seismic observations provide strong additional constraints. Comparisons of theoretical oscillation frequencies with observed solar ones have shown for instance that significant improvement in the agreement between observation and model at high frequency and degree ℓ can be achieved with 3D simulations (Rosenthal et al. 1999). We are interested here

in amplitudes of oscillation that can also bring several constraints on the convective process in the outer solar envelope. Indeed, the amplitudes of solar-like oscillations result from a balance between excitation and damping. Measurements of the oscillation mode growth rates (through their line-widths) and of the mode amplitudes enable the evaluation of the excitation rates P . Excitation of solar-like oscillations is known to be both due to turbulent convective motions through the driving by the turbulent Reynolds stresses (see Goldreich & Keeley 1977; Balmforth 1992; Samadi & Goupil 2001) and due to the advection of turbulent entropy fluctuations by the turbulent movements (see Samadi & Goupil 2001). The excitation rates P are thus directly related to the velocity of the convective elements and to the amount of thermal energy advected by convective motions (i.e. the convective flux). The excitation rates then depend crucially on the way the convective velocity and flux are modelled (see Houdek et al. 1999). Solar seismic measurements therefore provide – through a model of mode excitation – additional constraints on the stellar convective properties. In this framework, the goal of the present paper is to investigate the influence of different local treatments of convection on the calculation of the rates at which energy is injected into the solar radial p modes and to compare our results with the solar seismic constraints.

For this purpose we compute two calibrated solar models with the Böhm-Vitense formulation of the MLT (Böhm-Vitense 1958, hereafter BV) and with the CGM multi-eddy convection treatment. In each case, the same convection formulation is adopted for the interior *and* the model atmosphere. Models for the internal structure are built so as to reproduce the solar radius and the solar luminosity at the solar age. The atmosphere of each model is constructed using a $T(\tau)$ law which is derived from a Kurucz's model atmosphere (Kurucz 1993) computed with the same convection formulation (as described in Heiter et al. 2002). These model atmospheres are built in order to provide the best agreement between synthetic and observed Balmer line profiles (as in van't Veer-Menneret & Megessier 1996, for the MLT treatment) (Sect. 2). The matching of the model atmosphere with the interior model is performed – in the manner of Morel et al. (1994) – by ensuring the continuity of the temperature gradient, ∇ , and of the convective flux in a transition region between the interior and the atmosphere.

We also compute two models with an Eddington gray atmosphere, one with the MLT treatment and the second with the CGM formulation. These two additional models are considered for comparison purpose only. Indeed, they have an atmosphere with the same mixing-length parameter as in the interior and do not reproduce the Balmer line profiles. As a consequence, in contrast with the interior models including a Kurucz's atmosphere as described above, their atmospheres do not fulfill constraints on the properties of the convection at the surface.

Calculation of the excitation rates requires the computation of the convective flux, F_c , and of the convective velocity, v . This is done in Sect. 3 by paying special attention to the problem of the transition region. Indeed, the continuity of ∇ and of F_c through the transition region imposes a spatial variation of the mixing-length parameter in the transition region. This variable mixing-length parameter is then used in Sect. 3 to compute v .

Note that our approach, which is used here to compute v and P , is different from that of Schlattl et al. (1997), who built stellar models that assume a spatially varying mixing-length parameter, with a spatial variation imposed a priori from a comparison to 2D numerical simulations of convection, in order to compute p mode frequencies.

As a last step (Sect. 4), we compute the adiabatic eigenmodes and the excitation rates P for each model. The adopted model of excitation is that of Samadi & Goupil (2001, Paper I hereafter) in which the characteristic wavenumber k_0 , the wavenumber dependency of the turbulent spectra, as well as the frequency component (χ_k) of the correlation product of the turbulent velocity field are constrained with a 3D simulation of the Sun as in Samadi et al. (2003c, Paper II hereafter) and Samadi et al. (2003b, Paper III hereafter). Comparison with solar seismic constraints then allows us to conclude about the best local treatment of convection in the solar case (Sect. 5).

2. Solar models

All solar models discussed here are computed with the CESAM code (Morel 1997) including the following input physics and numerical features:

1. Equation of state (EOS): CEFF EOS (Christensen-Dalsgaard & Däppen 1992).
2. Opacities: OPAL (Iglesias & Rogers 1996) data, complemented by Alexander & Ferguson (1994) data for $T \lesssim 10^4$ K, both sets of data being given for Grevesse & Noels (1993) solar mixture.
3. Thermonuclear reaction rates: Caughlan & Fowler (1988).
4. Convection: either MLT or CGM's formalism. The same convection formalism has been used in the interior and in the model atmosphere.
5. Microscopic diffusion: all models include microscopic diffusion of helium and heavy elements calculated according to the simplified formalism of Michaud & Proffitt (1993), where heavy elements are treated as trace elements.
6. Chemical composition and mixing length parameter for convection: the Grevesse & Noels (1993) heavy elements solar mixture has been adopted. The constraint that solar models have the observed solar luminosity and radius at solar age yields the initial helium content Y_0 and the mixing length parameter of the interior model α_i (solar model calibration). Microscopic diffusion modifies the surface composition, therefore the initial ratio of heavy elements to hydrogen (Z/X)₀ is adjusted so as to get the ratio (Z/X)_⊙ = 0.0245 at solar age.
7. The models were calculated with 285 shells in the atmosphere and about 2000 shells in the interior.

The CGM formulation of convection is implemented according to Heiter et al. (2002). In contrast with Heiter et al. (2002), we use a characteristic scale length of convection for the two formulations which is the mixing-length $\Lambda = \alpha H_p$, where H_p is the pressure scale height and α the mixing-length parameter, which can be different in the interior and in the atmosphere.

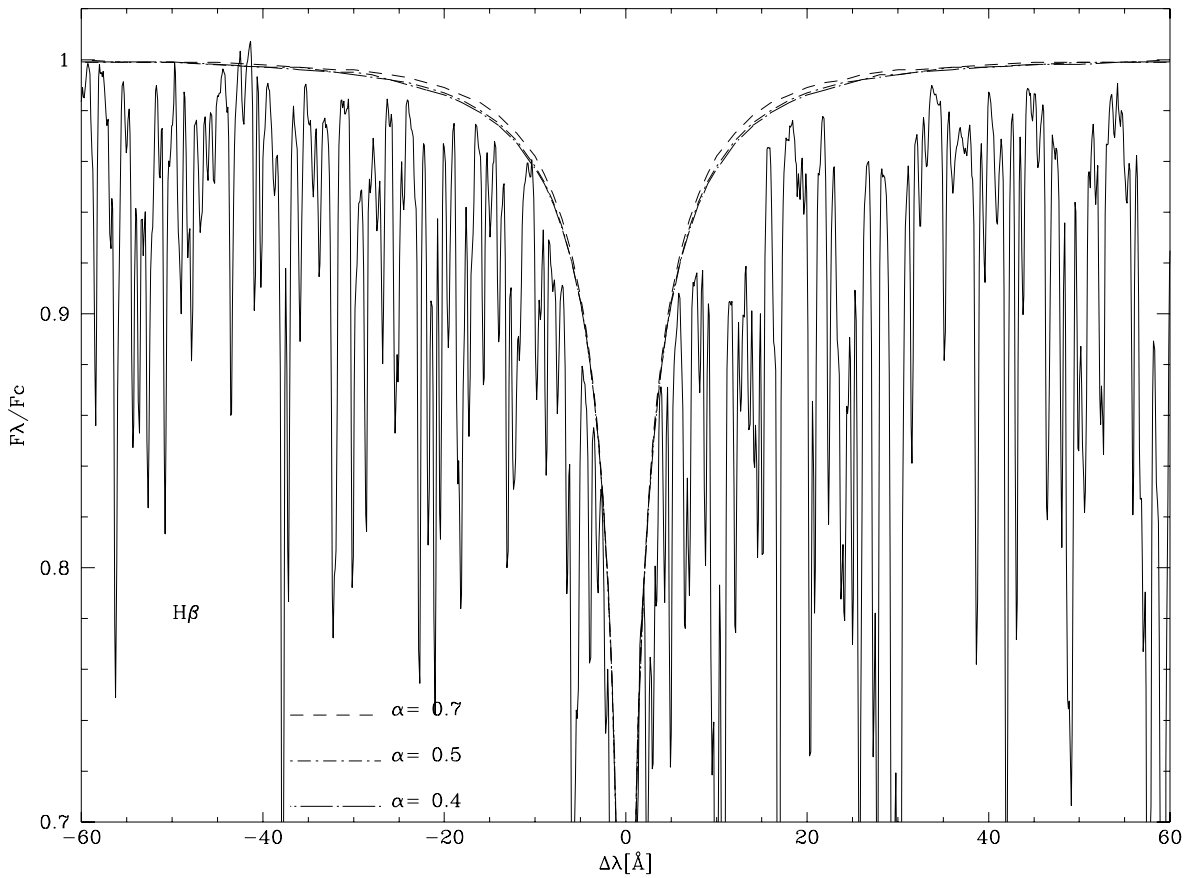


Fig. 1. The observed solar $H\beta$ profile is compared to theoretical ones computed with CGM models and assuming different values for α_a . Abscissae are distances in \AA from the line center, and ordinates are the flux in the profile normalized to the continuum. The large scatter is due to the presence of many spectral lines which overlap and cause an apparent enlargement of the true profile.

2.1. The “Kurucz models” (KMLT and KCGM models)

We consider here two stellar models: one computed with the MLT formulation of convection and the second one with the CGM formulation. They will be labelled hereafter as KMLT model and KCGM model, respectively.

Treatment of the atmosphere: the model atmospheres of those models are computed using the ATLAS 9 code (Kurucz 1993) as described in Heiter et al. (2002). Solar model atmospheres are built assuming different values for α_a , the mixing-length parameter assumed for the model atmosphere: $\alpha_a = 0.4, 0.5, 0.6, 0.7$. The model atmospheres with $\alpha_a = 0.4$ and $\alpha_a = 0.5$ provide the best agreement between synthetic and observed $H\beta$ Balmer line profiles for the two formulations of convection. This is shown in Fig. 1 for the CGM model atmosphere. For the MLT treatment, see Fuhrmann et al. (1993, 1994) and van’t Veer-Menneret & Megessier (1996). Above $\alpha_a \approx 0.6$, the synthetic profile rapidly departs from the observed one, as well as the effective temperature T_{eff} from the known solar T_{eff} .

There are no significant differences for the $H\beta$ Balmer line profile between the model atmospheres with $\alpha_a = 0.4$ and $\alpha_a = 0.5$. Among those model atmospheres we adopt arbitrarily those with $\alpha_a = 0.5$. Indeed, choosing the model atmospheres

with $\alpha_a = 0.4$ instead of $\alpha_a = 0.5$ will not change the conclusions of this article. For each formulation of convection we then obtain a $T(\tau)$ law.

The atmospheres of the KMLT and KCGM stellar models are recomputed according to the procedure described in Morel et al. (1994) from the $T(\tau)$ -laws mentioned above; the fit between interior (where the diffusion approximation is valid) and atmosphere is performed in a region where $\tau_1 \lesssim \tau \lesssim \tau_2$ (an acceptable range of values for τ_1 and τ_2 is discussed below). In the interior region where $\tau \gtrsim \tau_2$, the temperature gradient ∇_i is obtained from the MLT or CGM formalism. In the atmospheric region, where $\tau \lesssim \tau_1$, the temperature gradient ∇_a is computed using the $T - \tau$ law of the model atmosphere built with the same model of convection as in the interior. In the transition region, where $\tau_1 \lesssim \tau \lesssim \tau_2$, in order to ensure the continuity of the temperature gradient, ∇ is obtained by a linear interpolation of ∇_i and ∇_a as a function of the optical depth as follows:

$$\nabla = \beta(\tau)\nabla_a + (1 - \beta(\tau))\nabla_i \quad (1)$$

where $\beta(\tau) = (\tau_2 - \tau)/(\tau_2 - \tau_1)$.

Once the temperature gradients of the interior and the atmosphere are linked together in the transition region according to Eq. (1), we compute *afterward* in that region the convective

flux and an *equivalent* mixing-length parameter (i.e. a depth-dependent mixing-length parameter) as explained in Sect. 3.

Acceptable ranges for τ_1 and τ_2 : using a Newton-Raphson scheme, ∇_i is adjusted in order that $F_c^{(i)} + F_{\text{rad}}^{(i)} = L_\odot/4\pi r^2$, where L_\odot is the luminosity of the Sun and $F_{\text{rad}}^{(i)}$ is the radiative flux of the internal model. Calculation of $F_c^{(i)}$ assumes the diffusion approximation for the radiative transfer for F_{rad} . This approximation is valid at rather high values of τ , typically $\tau \gtrsim 10$ (see Morel et al. 1994). Therefore, τ_1 cannot be much smaller than $\tau \simeq 10$. Otherwise, ∇_i will have an unrealistic contribution to ∇ below $\tau \simeq 10$. On the other hand, for the calculation of $F_c^{(a)}$, the radiative flux F_{rad} is based on a Kurucz's model atmosphere, which treats the radiative transfer more realistically than the diffusion approximation.

The Kurucz model atmosphere is based on the Kurucz (1992, 1993) opacity tables which are given up to $T \simeq 2 \times 10^5$ K and $P = 10^8$ dyn cm $^{-2}$. As a consequence, τ_2 cannot be larger than $\tau \simeq 10^{7.5}$, i.e. layers for which $T \simeq 30\,000$ K. In order to ensure a satisfactory continuity of the temperature gradient, τ_2 must be sufficiently larger than τ_1 . On the other hand, the transition region should be as small as possible; i.e. $\tau_2 - \tau_1$ must be as small as possible. The main constraint for this region is thus to avoid discontinuities between the interior and the atmosphere. It is defined through an empirical procedure rather than based on a strict physical theory.

In practice, we find that $\tau_1 = 4$ is the minimal acceptable value for τ_1 ; below this value the bias introduced by the diffusion approximation has a significant effect on F_c . In addition, we find that above $\tau_2 \simeq 50$, the convective velocity v (see Sect. 3.2) shows a pronounced “kink” at $\tau = \tau_2$ for the CGM model (see Fig. 3, such a “kink” is also observed for F_c , but it is less pronounced). On the other hand, the choice of $\tau_2 = 20$ avoids the angular point. For the MLT model, whatever the value of τ_2 , v shows such a feature. This is a consequence of the much higher values of the mixing length parameter required in the interior in order to still obtain the correct solar radius, if a lower value of α is also used in regions further within the envelope. The requirement of matching R_\odot hence provides a more stringent upper limit for the choice of τ_2 (cf. also the discussion in Montalbán et al. 2004 on the computation of solar entropy as a function of radius). In the following, we will consider $\tau_1 = 4$ and $\tau_2 = 20$ as our optimal choice.

Calibration: the mixing-length parameter α_i for the internal structure, Y_0 , and $(Z/X)_0$ are adjusted such that the stellar model simultaneously reproduces the solar radius, the solar luminosity, and the observed ratio $(Z/X)_\odot = 0.0245$ at the solar age. The calibration yields $(Z/X)_0 = 0.0279$ and $Y_0 = 0.275$. At solar age, the helium abundance in the convection zone is $Y = 0.246$, in reasonable agreement with the value $Y = 0.249 \pm 0.003$ obtained from seismology (Basu 1997). Table 1 gives the calibrated values of the mixing-length parameters α_i for each complete solar model. The radius resulting from the adjustment of α_i , as well as the size of the convective zone, are given in Table 2. All the interior models have a depth of the convective zone of $\simeq 0.286 R_\odot$, which is in good agreement with the value of $0.287 \pm 0.003 R_\odot$ determined seismically by Christensen-Dalsgaard et al. (1991).

Table 1. Values of the mixing-length parameters of the KCGM and KMLT models: α_i (for the interior) and α_a (for the model atmosphere). α_i results from the calibration of the full model while α_a is fixed (see Sect. 2.1).

model	α_i	α_a
KMLT	2.51	0.50
KCGM	0.78	0.50

Table 2. $\Delta R \equiv R - R_\odot$, where R_\odot is the radius at the photosphere (i.e. at $T = T_{\text{eff}}$), and depth of the convective zone (CZ) for the KCGM and KMLT models. These quantities are given with respect to the solar radius R_\odot (we assume the Guenther et al. (1992) value of R_\odot).

model	$\Delta R/R_\odot$	depth CZ
KMLT	-10^{-6}	0.2860
KCGM	$5 \cdot 10^{-6}$	0.2859

Table 3. Values of the the mixing-length parameter α of the ECGM and EMLT models obtained for calibrated solar models.

model	α
EMLT	1.76
ECGM	0.69

2.2. Eddington approximation based models (EMLT and ECGM models)

For comparison purposes, we consider two additional stellar models here with an Eddington classical gray atmosphere instead of the Kurucz atmosphere models described in Sect. 2.1. One of these models assumes the MLT formulation of convection and the other the CGM formulation. In the following they will be labelled as EMLT model and ECGM model, respectively. The mixing-length parameter α of these models (the same α in the interior as in the atmosphere) is adjusted in order to reproduce the solar luminosity and radius at the solar age. However, as mentioned in the introduction, these models do not reproduce the Balmer line profiles. Table 3 gives the calibrated values of the mixing-length parameters.

2.3. Comments

With the CGM treatment, α_i is found to be less than one and closer to $\alpha_a = 0.5$. In contrast, with the MLT treatment the value of α_i is much larger than $\alpha_a = 0.5$.

The CGM models result in a much lower value for the mixing-length parameter (α_i for the KCGM model and α for the ECGM model) than the MLT models, because the convection in nearly adiabatic regions is more efficient with the CGM formulation than with the MLT one. Indeed, for the same value of the mixing-length parameter and in the region of high convective efficiency (below the superadiabatic region), the CGM treatment predicts a convective flux ten times larger than the MLT one for a given superadiabatic gradient. In a solar model, this behavior results in a gradient closer to the adiabatic one below a smaller superadiabatic zone in comparison to the MLT case (Canuto et al. 1996). At the top of the quasi-adiabatic

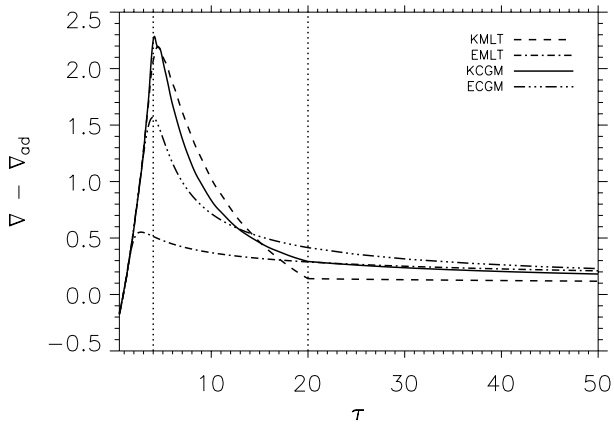


Fig. 2. The superadiabatic gradient $\nabla - \nabla_{\text{ad}}$ is plotted versus the optical depth τ in the outer region for the KMLT model (dashed line), EMLT model (dot-dashed line), ECGM model (dot-dot-dot-dashed line), and KCGM model (solid line). The dotted vertical lines correspond to the layers where $\tau = \tau_1 = 4$ and $\tau = \tau_2 = 20$, respectively, and delimit the transition region.

region, energy is predominantly transported by convection, such that $F_c \approx F$ where F_c is the convective flux and F the total energy flux. Above, convective transport is no longer efficient ($F_c < F$). Therefore, the solar energy flux F at the top of the quasi-adiabatic region can be reproduced for the CGM models with a lower value of the mixing-length parameter than the one required for the MLT.

The superadiabatic gradients are displayed in Fig. 2 as a function of τ . The angular point observed in $\nabla - \nabla_{\text{ad}}$ at the optical depth $\tau \approx 20$ for the KMLT model corresponds to the matching point; i.e. at $R_\odot - r \approx 100$ km, where R_\odot is the solar radius at the photosphere, defined to be where $\tau = 2/3$ and calibrated at the precision level given in Table 2. It results from the large difference between α_i and α_a . This difference is much smaller for the KCGM model, and therefore the “kink” at $\tau \approx 20$ is much less pronounced.

Our last comment concerns the large difference in the value of the mixing-length parameter between the KMLT and the EMLT models. Both models differ only by the structure of their uppermost layers located 50–100 km below the photosphere (see Fig. 3, middle), which represent a tiny fraction of the convection zone depth. The KMLT has a model atmosphere in which convection is much less efficient than that of the EMLT model as a consequence of the fact that $\alpha_a = 0.5$ in the Kurucz’s model atmosphere (see Sect. 2.1). This is why the superadiabatic gradient, $\nabla - \nabla_{\text{ad}}$, at that depth reaches much higher values for the KMLT model than for the EMLT model. Now if $\nabla - \nabla_{\text{ad}}$ from two models are vastly different, so is the entropy jump of both. Hence, if a certain entropy of the interior convection zone and thus a certain radius of the convection zone are to be matched, a much more drastic change in α is required with the KMLT model to avoid to large an entropy jump (see a detailed discussion in Montalbán et al. 2004).

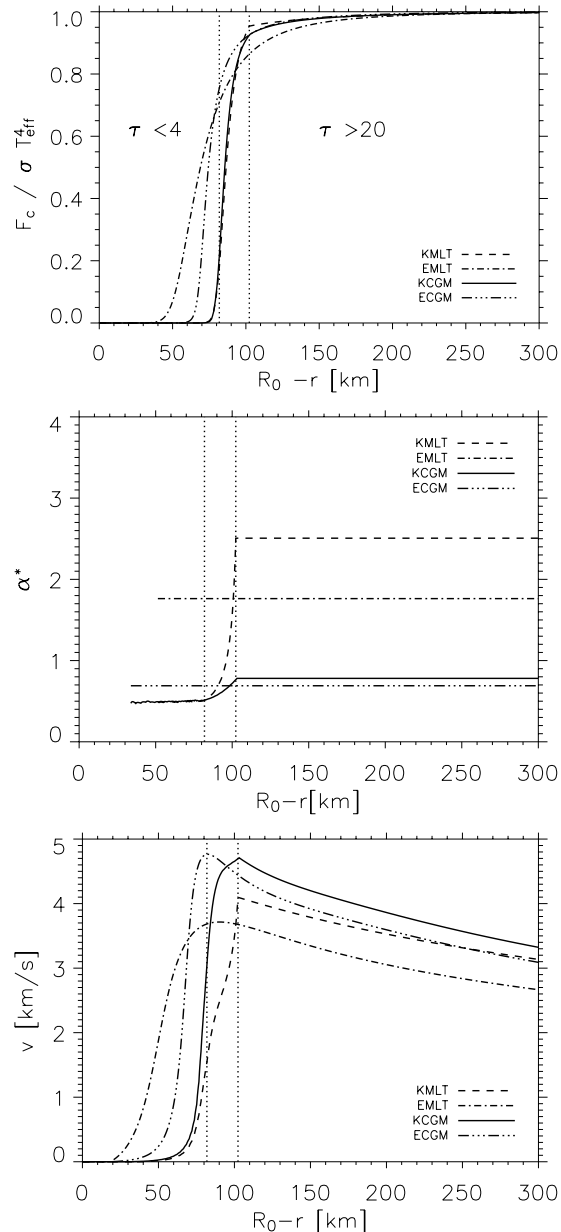


Fig. 3. Top: F_c is plotted versus $R_\odot - r$ for the KMLT model (dashed curve), EMLT model (dot-dashed line), ECGM model (dot-dot-dot-dashed line), and KCGM model (solid line). As in Fig. 2, the dotted vertical lines delimit the transition region. Middle: same as the top panel for α^* (see Sect. 3.2). Bottom: same as the top panel for the root mean square of the convective velocity, v .

3. Convective velocity and entropy fluctuations

3.1. Convective flux

Part of the mode excitation rates stems from the advection of turbulent entropy fluctuations by turbulent motions (the so-called “entropy source term”). This term scales – see Paper I – as $\alpha_s^2 \langle s_t^2 \rangle u_0^2$, where s_t represents the entropy fluctuations due to turbulent convection, $\alpha_s \equiv (\partial p / \partial s)_\rho$, ρ , s , and p are, respectively, the density, the entropy and the pressure, $\langle \rangle$, denotes

spatial and time average, $u_0^2 \equiv 1/3 \langle u^2 \rangle$, where \mathbf{u} is the velocity field associated with the turbulence. The factor $1/3$ arises from the simplifying assumption made in Paper I that the acoustic emission is injected into the p -mode isotropically in all three directions.

The “entropy source term” scales as the square of the convective flux F_c . Indeed, we show (see Appendix A) that it scales as $(\alpha_s/\rho_0 T_0)^2 (\bar{\Phi}/3) F_c^2$, where T_0 and ρ_0 are the mean temperature and density, respectively, and $\bar{\Phi}$ is the spatially averaged anisotropy factor, which is defined as (Gough 1977):

$$\bar{\Phi}(r) \equiv \frac{\langle u^2 \rangle}{\langle u_z^2 \rangle} \equiv \frac{v^2}{w^2} \quad (2)$$

where u_z is the vertical component of \mathbf{u} , and v and w are defined as $v^2 \equiv \langle u^2 \rangle$ and $w^2 \equiv \langle u_z^2 \rangle$, respectively.

For the CGM formulation, F_c is computed according to Eqs. (2) and (17)–(21) in Heiter et al. (2002), and for the MLT treatment, it is calculated according to Eq. (14.118) in Cox (1968, Chap. 14).

F_c can be viewed as function of α and ∇ , $F_c = h(\nabla, \alpha)$, where h is given by the adopted model of convection.

ECGM and EMLT models: for these two models only one mixing-length parameter is involved and F_c can directly be retrieved from α and ∇ .

KCGM and KMLT models: in the outer region ($\tau < \tau_1$), as well as in the interior region ($\tau > \tau_2$), values of F_c can be directly retrieved from α and ∇ . In the transition region ($\tau_1 < \tau < \tau_2$), however, we have to deal with two functions for the convective flux: $F_c^{(i)} = h(\nabla_i, \alpha_i)$, the convective flux calculated as in the interior, and $F_c^{(a)} = h(\nabla_a, \alpha_a)$, the convective flux calculated for the atmosphere. As a result of Eq. (1), the convective flux F_c of the model in the transition region can be related to $F_c^{(i)}$ and $F_c^{(a)}$ as follows:

$$F_c = \lambda(\tau)F_c^{(a)} + (1 - \lambda(\tau))F_c^{(i)} \quad (3)$$

where $\lambda(\tau)$ is – like $\beta(\tau)$ (Eq. (1)) – a function of τ , which ensures the continuity of the convective flux. This function must decrease with τ and must fulfill $\lambda(\tau) = 1$ for $\tau \leq \tau_1$ and $\lambda(\tau) = 0$ for $\tau \geq \tau_2$. We point out that both $F_c^{(i)}$ and $F_c^{(a)}$ fulfill $F_c + F_{\text{rad}} = L_\odot/4\pi r^2$ at any optical depth τ . Just as for $\beta(\tau)$, the choice $\lambda(\tau)$ is rather arbitrary. As for the case of ∇ (Eq. (1)), we assume $\lambda(\tau) = \beta(\tau) = (\tau_2 - \tau)/(\tau_2 - \tau_1)$ for $\tau_1 < \tau < \tau_2$. Figure 3 shows F_c as a function of τ for the KMLT and KCGM models.

Calculation of the driving by the entropy source term requires, in addition to the convective flux (F_c), a model for the mean anisotropy ($\bar{\Phi}$). In the CGM model of convection, the expressions for v^2 and F_c do not depend explicitly on the mean anisotropy factor $\bar{\Phi}$. However, CGM adopt a model of anisotropy which fixes the ratio $x \equiv k_h/k_v$, where k_h and k_v are the horizontal and vertical wavenumbers associated with the eddy of wavenumber k (note that $k^2 = k_h^2 + k_v^2$). As a result of that model, for the largest scales $x = 1/2$, while it increases quadratically with the total wavenumber k for the smaller scales. Let us define $\Phi(k) \equiv u^2(k)/u_z^2(k)$, a k -dependent anisotropy factor. For an incompressible fluid – a property assumed by the models investigated here (see also CM91) – one

can show that $\Phi(k) = 1 + x^{-1}$. Hence $x = 1/2$ implies $\Phi = 3$, i.e. an isotropic velocity field. As a result of its functional dependence on k , from the larger scales ($k \sim k_0$) to the smaller scales ($k \gg k_0$) $\Phi(k)$ decreases in the CGM model from ~ 3 towards ~ 1 . However, we recall that the model of stochastic excitation (MSE) we consider is basically isotropic. The anisotropy is taken into account only at large scales through Gough’s mean anisotropy factor ($\bar{\Phi}$). Therefore, although CGM’s treatment adopts a model where the anisotropy varies with k , we are left with the inconsistency that the turbulent spectrum, $E(k)$, assumed for the MSE (see Sect. 4.1), is isotropic along the turbulent cascade. A possible anisotropy is only taken into account at large scales through $\bar{\Phi}$. But as the modes are predominantly excited by turbulent eddies with $k \sim k_0$, which carry most of the kinetic energy, this approximation is not expected to affect our prediction significantly. Hence, we assume $\bar{\Phi} = 3$ for the CGM models in the discussion given below.

3.2. Convective velocity

Driving of the oscillation modes by the Reynolds term is proportional to $\rho_0 v^4$.

Like the convective flux, the convective velocity v can be viewed as a function of ∇ and α , i.e. $v = f(\nabla, \alpha)$, where the function f depends on the formulation of convection. For the CGM treatment, $v = f(\nabla, \alpha)$ is computed according to Eqs. (88)–(90) of CGM. For the MLT approach, we first compute $w(\nabla, \alpha)$ according to Eq. (14.110) of Cox (1968, Chap. 14). We then deduce $v = f(\nabla, \alpha)$ from Eq. (2) with $\bar{\Phi} = 2$ consistently with BV’s formulation of the MLT (see Gough 1977).

ECGM and EMLT models: as for the convective flux, v can be retrieved from α and ∇ .

KCGM and KMLT models: in the outer region (i.e. $\tau < \tau_1$), as well as in the inner region ($\tau > \tau_2$), only one α and one ∇ are defined. In those regions v is computed as $v = f(\nabla, \alpha)$. However, in the transition region we must deal with two different values of α (namely α_i and ∇_i from the inner region and α_a and ∇_a from the atmosphere) and v is not a linear function of α . We thus face the difficulty of properly defining a convective velocity consistent with F_c (Eq. (3)) in this region.

We proceed as follows: $\nabla(\tau)$ and $F_c(\tau)$ are defined by Eqs. (1) and (3), respectively. Then, at fixed ∇ and τ , we define an *equivalent mixing-length parameter*, α^* , such that $F_c = h(\nabla, \alpha^*)$. This parameter is variable with depth. We next compute $v = f(\nabla(\tau), \alpha^*)$ which is thus consistent with F_c of Eq. (3).

Figure 3 (middle and bottom) shows α^* and v as a function of depth. For the MLT models, our calculation of v assumes $\bar{\Phi} = 2$, which is consistent with BV’s formulation of the MLT (see Gough 1977), and for the CGM models it assumes $\bar{\Phi} = 3$.

3.3. Comments

As shown in Fig. 3, the EMLT and KMLT models have very different convective structures: up until close to the top of the superadiabatic region (located at $R_\odot - r \sim 70$ km for those

models), the EMLT model results in a convective velocity and convective flux smaller than those of the KMLT model. This is a consequence of the fact that $\alpha^{\text{EMLT}} < \alpha_i^{\text{KMLT}}$ (see Tables 1 and 3). On the other hand, the EMLT model results in larger v and F_c above the top of the superadiabatic region because $\alpha^{\text{EMLT}} > \alpha_a^{\text{KMLT}} = 0.5$.

In contrast with the MLT models, the KCGM and ECGM models have rather similar convective structures. Indeed, v^{KCGM} and v^{ECGM} (F_c^{KCGM} and F_c^{ECGM} resp.) have very similar shapes. This in turn is a consequence of the fact that the CGM models require values of α_i^{KCGM} and of α^{ECGM} close to that one required for the atmosphere ($\alpha_a = 0.5$).

For the KMLT model, there is a pronounced “kink” at the bottom boundary of the transition region (i.e. at $\tau = 20$ or $R_\odot - r = 100$ km), especially for v . For the KCGM model, the “kink” is much less important. These features are directly connected with the angular point observed for ∇ in that layer (see Sect. 2.3 and Fig. 2).

At the bottom of the transition region (i.e. at $\tau = \tau_2$), for both the KMLT and KCGM models, $\alpha^*(\tau)$ reaches – as expected – the “interior” value of the mixing-length parameter (i.e. α_i), namely: $\alpha_i^{\text{KCGM}} = 0.78$ and $\alpha_i^{\text{KMLT}} = 2.51$. At the top of the transition region (i.e. at $\tau = \tau_1$), $\alpha^*(\tau)$ reaches for both the KCGM and KMLT models the asymptotic value $\alpha^* \simeq 0.50$.

4. Calculation of the solar p mode excitation rates

4.1. Procedure

We compute the rate P at which acoustic energy is injected into solar radial p -modes according to the theoretical model of stochastic excitation of Paper I, and assume here – as in Paper II and Paper III – that injection of acoustic energy into the modes is isotropic and consider only radial p modes. The rate at which a given mode with frequency $\omega_0 = 2\pi\nu_0$ is excited is then calculated with the set of Eqs. (1)–(11) of Paper III and Eq. (3) of Samadi et al. (2005).

The calculation requires the knowledge of three different types of quantities. First of all, quantities which are related to the average properties of the medium:

- the mean density ρ , α_s (Eq. (A.5)), the mean square convective velocity v^2 , and the mean square of the entropy fluctuations s^2 (Eq. (A.6)). They are obtained from the equilibrium models as explained in Sect. 3.

Secondly, quantities which are related to the oscillation modes:

- the eigenfunctions ξ_r and the eigenfrequency ν . They are computed with the adiabatic pulsation code FILOU (Tran Minh & Leon 1995) for each model.

Finally, quantities which are related to the properties of the turbulent flow:

- the wavenumber (k) dependency of E , i.e. the turbulent kinetic energy spectrum;
- the values and depth dependency of k_0 , the wavenumber at which the convective energy has its maximum and is “injected” into the inertial range of the turbulent kinetic energy spectrum E ;

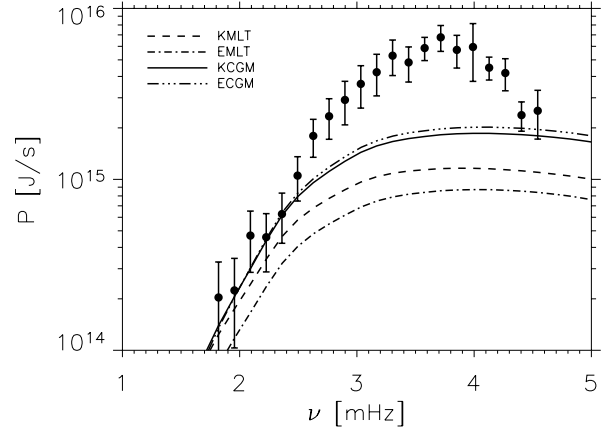


Fig. 4. The computed solar p mode excitation rates, $P(\nu)$, are plotted versus the frequency for the KMLT (dashed line), EMLT (dot-dashed line), ECGM (dot-dot-dot-dashed line), and KCGM (solid line) models. The filled circles represent the “observed” solar values of $P(\nu)$ derived – according to Eq. (4) – from the amplitudes and line widths of the $\ell = 0$ p -modes measured by Chaplin et al. (1998).

- the ν -dependency of χ_k , the frequency component of the auto-correlation product of the turbulent velocity field.

According to the results in Papers II and III obtained on the basis of a 3D numerical solar granulation simulation, the k -dependency of $E(k, \nu)$ is approximately reproduced by an analytical spectrum called “Extended Kolmogorov Spectrum” (EKS) and defined in Musielak et al. (1994). The ν -dependency of χ_k is found to be better modelled with a Lorentzian function rather than by a Gaussian function, which is usually assumed for χ_k (see Paper III). Within most parts of the excitation region, the spatially averaged anisotropy factor $\bar{\Phi}$ is found almost constant with a value of $\bar{\Phi} \sim 2$ in agreement with BV’s value.

At the top of the superadiabatic region, it was found that $k_0 \sim 3.6 \text{ Mm}^{-1}$ and that k_0 decreases slowly inwards with depth (see Paper II). A good approximation for our region of interest within the Sun is to assume a constant k_0 .

4.2. Comparison with the observations

Results for P are presented in Fig. 4. The theoretical estimates for P are compared with the “observed” P_{obs} , calculated from the seismic data of Chaplin et al. (1998) according to the relation:

$$P_{\text{obs}}(\nu) = 2\pi\Gamma \frac{I}{\xi_r^2(r_s)} v_s^2(\nu) = 2\pi\Gamma \mathcal{M} v_s^2(\nu), \quad (4)$$

where: ν is the mode frequency; r_s is the radius at which oscillations are measured;

$$I \equiv \int_0^{\mathcal{M}} dm \xi_r^2 \quad (5)$$

is the mode inertia; $\mathcal{M} = I/\xi_r^2(r_s)$ is the mode mass; and finally Γ and v_s are the mode line-width and the mode surface velocity, respectively, and are obtained from Chaplin et al. (1998). We point out that, according to the definition of Eq. (4), the derived value of P_{obs} depends on the model one considers through

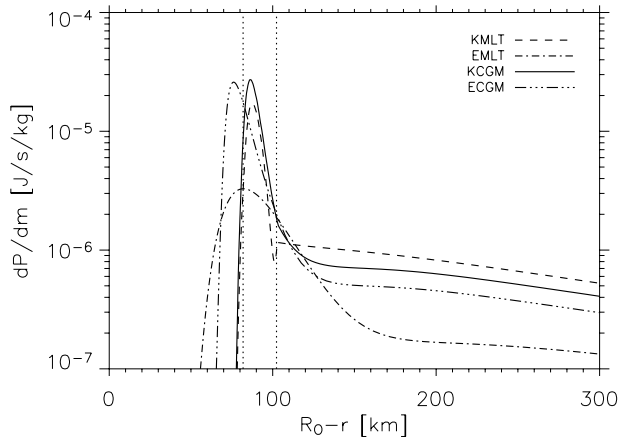


Fig. 5. The integrand dP/dm (Eq. (2) of Paper II) is plotted versus $R_{\odot} - r$ for a mode with order $n = 20$ ($n = 1$ being the fundamental mode) for the KMLT model (dashed line), EMLT model (dot-dashed line), ECGM model (dot-dot-dot-dashed line), and KCGM model (solid line).

\mathcal{M} . Indeed, for a given mode, \mathcal{M} – a priori – differs from one model to another. However, the mode masses of the models we consider here are very close to each other such that the changes on P_{obs} due to the use of the mode mass of the different models are not significant compared to the error bars attached to the measurements. For each mode, we can then compute a unique value for P_{obs} and compare the values of P obtained for the different models to each other and to P_{obs} . We choose to derive \mathcal{M} from the radial eigenfunctions ξ_r computed for the KCGM model and adopt $r_s = R_{\odot} + 200$ km consistently with the Chaplin et al. (1998) observations.

As shown in Fig. 4, differences between P_{KCGM} and P_{ECGM} are found smaller than the error bars associated with P_{obs} from Chaplin et al. (1998). This is a consequence of the fact that the ECGM and KCGM models present very similar convective structures (see Sect. 3.3 and Fig. 3). On the other hand, P_{KMLT} is found significantly larger than P_{EMLT} as a consequence of the fact that the KMLT models result in larger ν and F_c values than the EMLT ones (see Sect. 3.3 and Fig. 3) for $\tau \gtrsim 10 \dots 20$.

Furthermore, P_{KCGM} and P_{ECGM} are found closer to P_{obs} than P_{KMLT} . However, above $\nu \gtrsim 2.5$ mHz, differences between P_{obs} and P_{KCGM} (or P_{ECGM}) remain important. The origin of this discrepancy is discussed in Sect. 5.

For the KCGM and ECGM models, we have so far assumed $\bar{\Phi} = 3$. According to Eq. (A.6), assuming $\bar{\Phi} = 2$ – a value which is consistent with results from the 3D solar simulation – results in a driving by the entropy source smaller by a factor $\sim 2/3$ compared to the case $\bar{\Phi} = 3$. This decrease, however, remains small compared to the difference in P between the different models and hence does not influence our main results.

We present in Fig. 5 the integrand dP/dm (Eq. (2) of Paper II) corresponding to the excitation rate P of a mode of order $n = 20$. The plot is done for the four solar models. For three of the four models the extent of the region where most of the excitation takes place is very thin (less than 50 km). Obviously, this is the consequence of the very shallow extent of the superadiabatic region (see Fig. 2). This tiny extent of the

excitation region strongly contrasts with the one found in Stein & Nordlund (2001) and in Paper III. For instance, those authors found a size of the order of ~ 500 km for a mode of the same order. This discrepancy is attributed to the local nature of the convective treatments investigated in this work (see Sect. 5). Note that in Fig. 5 the EMLT model, with its large value of α for the entire superadiabatic region, predicts a broader excitation region than the other models. This is due to a smaller superadiabatic peak. However, in this model the transport of convective heat occurs with a smaller convective velocity and hence, as expected, the excitation is smaller than for the other models. We note here that despite the EMLT model results in a temperature structure closer to the numerical simulations (smaller superadiabatic peak), the predicted excitation amplitudes are smaller than for the other models investigated here and are the most discrepant in comparison with the data. This confirms that excitation rates provide a decisive additional test for convection models.

5. Conclusions

We have computed the rates P at which acoustic energy is injected into the solar radial p modes for several solar models. The solar models are computed with two different local treatments of convection: MLT and CGM.

For one set of solar models (EMLT and ECGM models), the atmosphere is gray and assumes Eddington’s approximation. The models assume only one mixing-length parameter value and reproduce the solar radius at solar age but not the Balmer line profiles. For a second set of models (KMLT and KCGM models), the atmosphere is built using a $T(\tau)$ law which was obtained from a Kurucz’s model atmosphere computed with the same local treatment of convection. The mixing-length parameter in the model atmosphere is chosen so as to provide good agreement between synthetic and observed Balmer line profiles, while the mixing-length parameter in the interior model is calibrated so that the model reproduces the solar radius at solar age.

Both the KMLT and the KCGM models reproduce the Balmer line profile and the solar radius and luminosity but – as shown in Figs. 2–4 – the CGM models model the transition between the region of high convective efficiency (the interior) and the region of low efficiency (the atmosphere) in a more realistic way than do the MLT models, as they reproduce the observed excitation rate P more closely and predict a smoother transition region. Furthermore, the KMLT model requires a change of the mixing-length by a factor of five in a layer of ~ 20 km thickness, which is significantly less than a pressure scale height (~ 300 km). Given the meaning of alpha, this means that the mixing-length varies from about 150 km to 750 km in a layer of ~ 20 km thickness (!), which does not make much sense from a physical point of view. On the other hand, the KCGM model does not require such large change in α .

For the MLT treatment, the oscillation excitation rates, P , do significantly depend on the properties of the atmospheres investigated here. Indeed, differences in P between the EMLT model and the KMLT model are found to be very large. On the other hand, for the CGM treatment, differences in P between

the ECGM and the KCGM models are very small compared to the error bars attached to the seismic measurements. This result shows that an Eddington gray atmosphere can be assumed for the calculation of P when the CGM formulation is adopted. This would be particularly convenient in the case of massive computations of P for a large set of stellar models.

For the EMLT and KMLT models, P is significantly underestimated compared to the solar seismic constraints obtained from the Chaplin et al. (1998) measurements. KCGM and ECGM models yield values for P closer to the seismic data than the EMLT and KMLT models. Constraints on the H_β Balmer line profile and on the solar radius can be satisfied by the two formulations (MLT and CGM), provided that the mixing-length parameters α_1 and α_a are suitably adjusted. Once the above constraints are satisfied, the solar seismic data provide additional valuable constraints and, according to the present investigation (focussed on local approaches), they clearly favor the CGM treatment.

Our calculations are based here on Grevesse & Noels (1993)'s solar abundances. There was recently a change in these values (see Asplund et al. 2004, 2005) with quite some implications for the internal structure of the Sun (see Basu & Antia 2004; Montalbán et al. 2004; Bahcall et al. 2005; Antia & Basu 2005). Then the implication for the calculation of the excitation rates (P) must in principle be tested consistently by changing the solar mixture both in the interior and the atmosphere (work in progress). However, we expect small changes in P . Indeed, as a first step we calculated a solar model having the low metallicity $Z/X = 0.0171$ inferred from the new Asplund et al. (2004)'s revised solar abundances, in which the interior calculation is based on the detailed Asplund et al. mixture and associated opacities, while the atmosphere considers the low metallicity but keeps the Grevesse & Noels (1993)'s solar abundances and associated opacities. Changes in P smaller than $\sim 10\%$ – much smaller than the errors bars ($\sim 20\%$) associated with the current measurements – were obtained.

The remaining discrepancy above $\nu \gtrsim 2.5$ mHz between computed and observed P (Fig. 4) is attributed to the assumption of locality in the present treatment of convection. As a matter of fact, Samadi et al. (2003b, Paper III) have succeeded in reproducing the seismic constraints much better using constraints from a 3D solar granulation simulation. One reason for this improvement is that convection is intrinsically a non-local phenomenon. In the terminology of classical turbulence modelling, the eddies located at different layers contribute to the convective flux of a given layer (cf. also the discussion in Houdek 1996). Hence, a non-local description of convection is expected to predict a more extended superadiabatic region. This is suggested, for instance, by the comparison of our present results with that of Paper II. Non-local theories – such as those by Gough (1977) and by Canuto & Dubovikov (1998) – also support this explanation by typically predicting a smaller temperature gradient in the superadiabatic region than the local theories do (see Houdek 1996; Kupka & Montgomery 2002), and thus a more extended superadiabatic region as well. Another property of solar granulation caused by non-locality is the observed asymmetry between the areas covered by up- and downflows. This allows for a lower root mean square

velocity while larger velocities (and thus more effective mode driving) can be reached in the downflows with their much higher velocities (note that such an asymmetry can be accounted for through non-local models as proposed by Canuto & Dubovikov (1998, see also Kupka & Montgomery 2002), although in a more simplified manner). On the other hand, the local models studied here cannot account for the different properties of up- and downflow areas at all. Hence, the superadiabatic region in these models is physically different from the one expected from non-local models and found in numerical simulations. Solar modes above $\nu \gtrsim 2$ mHz, however, are predominantly excited in the superadiabatic region (Paper III). A larger amount of acoustic energy is then injected into those modes when convection is treated – as is in the 3D simulation or on the base of a non-local theory – in a more realistic manner than through local theories.

The results presented here so far only concern our Sun. Samadi et al. (2003a) found that P scales as $(L/M)^s$ where s is the slope of the power law and L and M are the mass and luminosity of their computed 1D stellar models. By building a set of stellar models with the MLT and another one with Gough's (1977) non-local formulation of convection, the authors found that the slope s is quite sensitive to the 1D treatment of convection. In this respect, it would be interesting to compare the influence of the CGM formulation or of Canuto & Dubovikov's (1998) non-local convection treatment on the value of s and to test whether or not measurements of P can – for stars other than the Sun – distinguish the best 1D treatment of convection.

Acknowledgements. R.S.'s work was supported in part by the Particle Physics and Astronomy Research Council of the UK under grant PPA/G/O/1998/00576 (who also supported FK), by the Société de Secours des Amis des Sciences (Paris, France) and by Fundação para a Ciência e a Tecnologia (Portugal) under grant SFRH/BPD/11663/2002. We thank Achim Weiss for having carefully read this manuscript and R. Kurucz for giving access to the ATLAS9 code and associated data. Finally we thank the referee for his judicious suggestions.

Appendix A: Relation between the entropy fluctuations and the convective flux

As in Paper I, we relate the entropy fluctuations, s_t , to temperature fluctuations, θ , as follows:

$$s_t = \frac{c_p}{T_0} \theta, \quad (\text{A.1})$$

where T_0 is the mean temperature and $c_p = (\partial s / \partial \ln T)_p$. Hence, the mean square of the entropy fluctuations, $\langle s_t^2 \rangle$, can be expressed as

$$\langle s_t^2 \rangle \approx \left(\frac{c_p}{T_0} \right)^2 \langle \theta^2 \rangle. \quad (\text{A.2})$$

The convective flux is related to θ and u_z , the vertical component of convective velocity, as

$$F_c \approx \rho_0 c_p \langle u_z \theta \rangle, \quad (\text{A.3})$$

where ρ_0 is the mean density. We furthermore assume, consistently with the adopted quasi-normal approximation in Paper I, that $\langle u_z s_t \rangle^2$ can be decomposed as

$$\langle u_z s_t \rangle^2 = \langle u_z^2 \rangle \langle s_t^2 \rangle = w^2 \langle s_t^2 \rangle. \quad (\text{A.4})$$

Finally, one can show that

$$\alpha_s \equiv \left(\frac{\partial p}{\partial s} \right)_\rho = \rho_0 T_0 \Gamma_1 \nabla_{\text{ad}}, \quad (\text{A.5})$$

where s is the entropy and p the pressure, T_0 is the mean temperature, $\Gamma_1 = (\partial \ln p / \partial \ln \rho)_s$ is the adiabatic exponent, and $\nabla_{\text{ad}} = (\partial \ln T / \partial \ln p)_s$ is the adiabatic temperature gradient.

The mean square of the entropy fluctuations can then be deduced from the set of Eqs. (A.1)–(A.5) and (2):

$$\langle s_t^2 \rangle \approx \frac{\bar{\Phi}}{3} \left(\frac{F_c}{\rho_0 T_0 u_0} \right)^2, \quad (\text{A.6})$$

where $\bar{\Phi}$ is the spatially averaged anisotropy factor, which is defined in Eq. (2). Driving by the entropy source term is then proportional to $(\alpha_s / \rho_0 T_0)^2 (\bar{\Phi} / 3) F_c^2$ – see Paper I – and thus scales like the square of F_c .

References

- Antia, H. M., & Basu, S. 2005, *ApJ*, 620L, 129
- Alexander, D. R., & Ferguson, J. W. 1994, *ApJ*, 437, 879
- Asplund, M., Grevesse, N., Sauval, A. J., et al. 2004, *A&A*, 417, 751
- Asplund, M., Grevesse, N., & Sauval, A. J. 2005, in *Cosmic Abundances as Records of Stellar Evolution and Nucleosynthesis*, ASP Conf. Ser., 336, 25 [arXiv:astro-ph/0410214]
- Bahcall, J. N., Basu, S., Pinsonneault, M., & Serenelli, A. M. 2005, *ApJ*, 618, 1049
- Balmforth, N. J. 1992, *MNRAS*, 255, 639
- Basu, S. 1997, *MNRAS*, 288, 572
- Basu, S., & Antia, H. M. 2004, *ApJ*, 606L, 85
- Bernkopf, J. 1998, *A&A*, 332, 127
- Böhm-Vitense, E. 1958, *Zeitschr. Astrophys.*, 46, 108
- Canuto, V. M. 1992, *ApJ*, 392, 218
- Canuto, V. M. 1993, *ApJ*, 416, 331
- Canuto, V. M., & Mazzitelli, I. 1991, *ApJ*, 370, 295 (CM)
- Canuto, V. M., & Dubovikov, M. 1998, *ApJ*, 493, 834
- Canuto, V. M., Goldman, I., & Mazzitelli, I. 1996, *ApJ*, 473, 550 (CGM)
- Caughlan, G. R., & Fowler, W. A. 1988, *Atomic Data and Nuclear Data Tables*, 40, 283
- Chaplin, W. J., Elsworth, Y., Isaak, G. R., et al. 1998, *MNRAS*, 298, L7
- Christensen-Dalsgaard, J., & Daeppen, W. 1992, *A&AR*, 4, 267
- Christensen-Dalsgaard, J., Gough, D. O., & Thompson, M. J. 1991, *ApJ*, 378, 413
- Cox, J. 1968, *Principles of stellar structure* (Gordon and Breach)
- Fuhrmann, K., Axer, M., & Gehren, T. 1993, *A&A*, 271, 451
- Fuhrmann, K., Axer, M., & Gehren, T. 1994, *A&A*, 285, 585
- Goldreich, P., & Keeley, D. A. 1977, *ApJ*, 212, 243
- Gough, D. O. 1977, *ApJ*, 214, 196
- Grevesse, N., & Noels, A. 1993, in *Origin and Evolution of the Elements*, ed. N. Prantzos, E. Vangioni-Flam, & M. Cassé (Cambridge University Press), 15
- Guenther, D. B., Demarque, P., Kim, Y.-C., & Pinsonneault, M. H. 1992, *ApJ*, 387, 372
- Heiter, U., Kupka, F., van't Veer-Menneret, C., et al. 2002, *A&A*, 392, 619
- Houdek, G. 1996, Ph.D. Thesis, Institut für Astronomie, Wien
- Houdek, G., Balmforth, N. J., Christensen-Dalsgaard, J., & Gough, D. O. 1999, *A&A*, 351, 582
- Iglesias, C. A., & Rogers, F. J. 1996, *ApJ*, 464, 943
- Kupka, F., & Montgomery, M. H. 2002, *MNRAS*, 330, L6
- Kurucz, R. L. 1992, *Rev. Mex. Astron. Astrofis.*, 23, 45
- Kurucz, R. L. 1993, CD-ROM 13, Cambridge, SAO
- Michaud, G., & Proffitt, C. R. 1993, in *IAU Colloq.*, 137, *Inside the Stars*, ASP Conf. Ser., 40, 246
- Montalbán, J., D'Antona, F., Kupka, F., & Heiter, U. 2004, *A&A*, 416, 1081
- Montalbán, J., Miglio, A., Noels, A., Grevesse, N., & di Mauro, M. P. 2004, in *Proc. SOHO, 14, Helio- and Asteroseismology: Towards a Golden Future*, ESA SP-559, 574
- Morel, P. 1997, *A&AS*, 124, 597
- Morel, P., van't Veer, C., Provost, J., et al. 1994, *A&A*, 286, 91
- Musielak, Z. E., Rosner, R., Stein, R. F., & Ulmschneider, P. 1994, *ApJ*, 423, 474
- Rosenthal, C. S., Christensen-Dalsgaard, J., Nordlund, Å., Stein, R. F., & Trampedach, R. 1999, *A&A*, 351, 689
- Samadi, R., & Goupil, M. J. 2001, *A&A*, 370, 136 (Paper I)
- Samadi, R., Goupil, M. J., Lebreton, Y., Nordlund, Å., & Baudin, F. 2003a, *Ap&SS*, 284, 221
- Samadi, R., Nordlund, Å., Stein, R. F., Goupil, M. J., & Roxburgh, I. 2003b, *A&A*, 404, 1129 (Paper III)
- Samadi, R., Nordlund, Å., Stein, R. F., Goupil, M. J., & Roxburgh, I. 2003c, *A&A*, 403, 303 (Paper II)
- Samadi, R., Georgobiani, D., Trampedach, R., et al. 2005, *A&A*, submitted
- Schlattl, H., Weiss, A., & Ludwig, H.-G. 1997, *A&A*, 322, 646
- Smalley, B., & Kupka, F. 1997, *A&A*, 328, 349
- Stein, R. F., & Nordlund, Å. 2001, *ApJ*, 546, 585
- Tran Minh, F., & Leon, L. 1995, in *Physical Process in Astrophysics*, 219
- van't Veer-Menneret, C., & Megessier, C. 1996, *A&A*, 309, 879
- Xiong, D. R. 1978, *Chin. Astron.*, 2, 118
- Xiong, D. R. 1985, *A&A*, 150, 133

A closure model with plumes

I. The solar convection^{*}

K. Belkacem¹, R. Samadi¹, M. J. Goupil¹, and F. Kupka²

¹ Observatoire de Paris, LESIA, CNRS UMR 8109, 92195 Meudon, France

e-mail: Kevin.Belkacem@obspm.fr

² Max-Planck-Institute for Astrophysics, Karl-Schwarzschild Str. 1, 85741 Garching, Germany

Received 5 April 2006 / Accepted 18 August 2006

ABSTRACT

Context. Oscillations of stellar p modes, excited by turbulent convection, are investigated. In the uppermost part of the solar convection zone, radiative cooling is responsible for the formation of turbulent plumes, hence the medium is modelled with downdrafts and updrafts.

Aims. We take into account the asymmetry of the up- and downflows created by turbulent plumes through an adapted closure model. In a companion paper, we apply it to the formalism of excitation of solar p modes developed by Samadi & Goupil (2001).

Methods. Using results from 3D numerical simulations of the uppermost part of the solar convection zone, we show that the two-scale mass-flux model (TFM) is valid only for quasi-laminar or highly skewed flows (Gryanik & Hartmann 2002) and does not reproduce turbulent properties of the medium such as velocity-correlation products. We build a generalized two-scale mass-flux Model (GTFM) model that takes both the skew introduced by the presence of two flows *and* the effects of turbulence in each flow into account. In order to apply the GTFM to the solar case, we introduce the plume dynamics as modelled by Rieutord & Zahn (1995) and construct a closure model with plumes (CMP).

Results. The CMP enables expressing the third- and fourth-order correlation products in terms of second-order ones. When compared with 3D simulation results, the CMP improves the agreement for the fourth-order moments by a factor of two approximately compared with the use of the quasi-normal approximation or a skewness computed with the classical TFM.

Conclusions. The asymmetry of turbulent convection in the solar case has an important impact on the vertical-velocity fourth-order moment, which has to be accounted for by models. The CMP is a significant improvement and is expected to improve the modelling of solar p -mode excitation.

Key words. convection – turbulence – Sun: oscillations

1. Introduction

In the uppermost part of the solar convective zone, turbulent entropy fluctuations and motions of eddies drive acoustic oscillations. 3D numerical simulations of the stellar turbulent outer layers have been used to compute the excitation rates of solar-like oscillation modes (Nordlund & Stein 2001). As an alternative approach, semi-analytical modelling can provide an understanding of the physical processes involved in the excitation of p modes: in this case, it is indeed rather easy to isolate the different physical mechanisms at work in the excitation process and to assess their effects. Various semi-analytical approaches have been developed by several authors (Goldreich & Keeley 1977; Goldreich et al. 1994; Balmforth 1992; Samadi & Goupil 2001); they differ from each other by the nature of the assumed excitation sources, by the assumed simplifications and approximations, and also by the way the turbulent convection is described (see the review by Stein et al. 2004). Among the different theoretical approaches, that of Samadi & Goupil (2001) includes a detailed treatment of turbulent convection, which enables us to investigate different assumptions about turbulent convection in the outer layers of stars (Samadi et al. 2005). In this approach, the analytical expression for the acoustic power supplied to the

p modes involves fourth-order correlation functions of the turbulent Reynolds stress and the entropy source term, which for the sake of simplicity are expressed in terms of second-order moments by means of a closure model.

The most commonly used closure model at the level of fourth-order moments (FOM) is the *Quasi-Normal Approximation* (QNA), which is valid for a Gaussian probability distribution function (see Lesieur 1997) and was first introduced by Millionshchikov (1941). The QNA is rather simple and convenient to implement. However, Ogura (1963) has shown that such a closure could lead to part of the kinetic energy spectrum becoming negative. In this paper, we confirm the results of Kupka & Robinson (2006, hereafter KR2006), namely that this approximation indeed provides a poor description of the physical processes involved in solar turbulent convection.

Mass flux models (e.g., Randall et al. 1992; Abdella & McFarlane 1997) explicitly take the effects of *updrafts* and *downdrafts* on the correlation products into account. The presence of two well-defined flow directions then introduces an additional contribution when averaging the fluctuating quantities, since averages of fluctuating quantities over each individual flow differ from averages over the total flow. For applications in atmospheric sciences, the mass-flux model for convection has recently been improved by Gryanik & Hartmann (2002, hereafter GH2002). Their motivation has been to account for the fact

^{*} Appendix A is only available in electronic form at <http://www.aanda.org>

that horizontal scales of temperature and velocity fluctuations are different (hence their improvements lead to a “two-scale mass-flux model” (TFM)) as well as to understand and measure the effects of the skewness of their distribution. According to GH2002, mass-flux models, which also include the TFM, underestimate the FOM by as much as 70%. Therefore, such models clearly miss some important physical effects present in convective flows. Gryanik & Hartmann (2002) and Gryanik et al. (2005) studied the asymptotic limits of TFM which led the authors to propose an interpolation between the QNA and the limit of large skewness provided by the TFM. This new parametrization permits a much better description of the FOM for convection in the atmosphere of the Earth (GH2002). We show that for their parametrization to be applicable to the case of solar convection, a more realistic estimate for the skewnesses of velocity and temperature fluctuations is required than that provided by the TFM itself (Sect. 2).

The parametrization of GH2002 requires the knowledge of the skewnesses and second-order moments to compute FOM. These have to be provided either by measurements, by another model, or by numerical simulations. In the present paper we do not aim to construct a complete model to compute these quantities, which is the goal of the Reynolds stress approach (e.g., Canuto 1992; Canuto & Dubovikov 1998). Rather, we aim to analyze the shortcomings of the TFM and suggest improvements using numerical simulations of solar convection as a guideline. The conclusions drawn from this analysis are used to derive a model for fourth-order moments in terms of second-order moments that can be used in computations of solar p -mode excitation rates.

To proceed with the latter, we developed a formulation of the TFM that takes the effects of turbulence in each flow into account. This generalized TFM model (hereafter GTFM) is useful for both the superadiabatic and adiabatic outer solar layers. This formulation can actually be applied in other contexts than just the excitation of solar p modes as long as the convective system is composed of two flows.

The GTFM is more general and realistic than the TFM, but it requires the knowledge of additional properties of both the turbulent upwards and downwards flows. We choose to determine these properties by means of a plume model. Turbulent plumes are created at the upper boundary of the convection zone, where radiative cooling becomes dominant and where the flow reaches the stable atmosphere. In this region the updrafts become cooler and stop their ascent. This cooler flow is more dense than its environment and it triggers the formation of turbulent plumes (Stein & Nordlund 1998). As shown by Rieutord & Zahn (1995), these structures drive the dynamics of the flow; hence, to construct a closure model, we study the plume dynamics developed by Rieutord & Zahn (1995, hereafter RZ95). This makes it possible to build a *closure model with plumes (CMP)*, which is valid in the solar quasi-adiabatic convective region. In a companion paper (Belkacem et al. 2006, hereafter Paper II), we generalize this one-point correlation model to a two-points correlation model and calculate the power injected into solar p modes.

The paper is organised as follows: Sect. 2 introduces the TFM. Its validity is then tested with a 3D numerical simulation of the uppermost part of the solar convection region. In Sect. 3, we extend the TFM formulation (GTFM) in order to take into account turbulent properties of both upward and downward flows. We next investigate the asymptotic limits of the GTFM. In Sect. 4, we construct the CMP with the help of the RZ95 plume model. We test the validity of this model with results from the 3D simulation and show that the use of the plume model limits

the validity of the CMP to the quasi-adiabatic zone. The CMP is then used to obtain analytical expressions for the third- and fourth-order moments. Section 5 is dedicated to discussions and conclusions.

2. The two-scale mass-flux model

2.1. The model

The TFM considers a convective medium composed of upward and downward flows that are horizontally averaged. The presence of two flows introduces the possibility of a non-zero skewness for the moments of turbulent quantities when averages are done globally over the whole system. The TFM was developed in order to take into account this non-zero skewness.

Any averaged turbulent quantity ϕ can be split into two parts, one associated with the updrafts and the other with the downdrafts:

$$\langle \phi \rangle = a \langle \phi \rangle_u + (1 - a) \langle \phi \rangle_d, \quad (1)$$

where $\langle \rangle$ denotes ensemble spatial (in the horizontal plane) and time averages. $\langle \phi \rangle_u$ and $\langle \phi \rangle_d$ are the averages for the upflow and downflow, respectively. a and $1 - a$ are the mean fractional area occupied by the updrafts and downdrafts, respectively (Randall et al. 1992; Gryanik & Hartmann 2002; Canuto & Dubovikov 1998).

Fluctuating quantities defined as $\phi' = \phi - \langle \phi \rangle$ can be rigorously written as: $\langle \phi' \rangle = a \langle \phi' \rangle_u + (1 - a) \langle \phi' \rangle_d$, where the subscripts u and d are meant for upflow and downflow, respectively. For vertical velocity fluctuations w' , one then writes:

$$\langle w' \rangle = a \langle w' \rangle_u + (1 - a) \langle w' \rangle_d. \quad (2)$$

GH2002 propose to make the same decomposition for temperature fluctuations (θ'); thus, hot and cold regions are considered separately. This step was motivated by the observation that for the case of atmospheric boundary layer the characteristic horizontal scales of velocity and temperature fluctuations are different from each other and by the fact that the plain mass flux average Eq. (1) violates certain symmetries between velocity and temperature fluctuations. Indeed, hot and cold regions do not necessarily coincide with updrafts and downdrafts, respectively. Hence, a second quantity (b), the mean fractional area occupied by warm drafts, is introduced, and in most cases, $a \neq b$ (thus the name TFM). Then,

$$\langle \theta' \rangle = b \langle \theta' \rangle_h + (1 - b) \langle \theta' \rangle_c. \quad (3)$$

Furthermore, the TFM defines the velocity fluctuations inside the upflow (w'_u) and downflow (w'_d), respectively, as:

$$w'_u = w_u - \langle w \rangle \quad \text{and} \quad w'_d = w_d - \langle w \rangle. \quad (4)$$

Similarly, for the temperature fluctuations inside hot (θ'_h) and cold (θ'_c) regions, respectively, one has

$$\theta'_h = \theta_h - \langle \theta \rangle \quad \text{and} \quad \theta'_c = \theta_c - \langle \theta \rangle. \quad (5)$$

The quantities w_u , w_d , θ_h , and θ_c are the averages of velocity and temperature, respectively, over all updrafts (w_u), downdrafts (w_d), hot (θ_h) drafts, and cold (θ_c) drafts. Clearly, averages of the four fluctuating quantities in Eqs. (4) and (5) do not vanish because the average of a quantity over the whole flow differs from the average over one single (up or down, hot or cold) draft.

It is expected that the differences between the updrafts and downdrafts lead to a probability distribution function (PDF) that is no longer symmetric with respect to vanishing velocities and

temperature differences. As the third-order moments ($\langle w'^3 \rangle$ and $\langle \theta'^3 \rangle$) vanish when the PDF is symmetric, their values provide a measure for the deviation from a symmetric PDF. The skewnesses are defined as:

$$S_w = \frac{\langle w'^3 \rangle}{\langle w'^2 \rangle^{3/2}} \quad \text{and} \quad S_\theta = \frac{\langle \theta'^3 \rangle}{\langle \theta'^2 \rangle^{3/2}}, \quad (6)$$

respectively, for the vertical velocity and temperature fluctuations. In order to compute expressions for higher order moments in terms of velocity and temperature fluctuations, Eqs. (4) and (5), GH2002 followed Randall et al. (1992), using an additional simplifying approximation, i.e.,

$$\langle \phi^n \rangle \approx \langle \phi \rangle^n, \quad (7)$$

where $\phi = \{w'_{u,d}, \theta'_{h,c}\}$. This approximation neglects the contributions of fluctuations within the up- and downdrafts and differences in temperature and velocity between the individual drafts.

Given this approximation and the known second-order moments, the TFM provides third-order moments as follows (see GH2002):

$$\begin{aligned} \langle w'^2 \theta' \rangle &= S_w \langle w'^2 \rangle^{1/2} \langle w' \theta' \rangle \\ \langle w' \theta'^2 \rangle &= S_\theta \langle \theta'^2 \rangle^{1/2} \langle w' \theta' \rangle \end{aligned} \quad (8)$$

and FOMs as:

$$\begin{aligned} \langle w'^4 \rangle &= (1 + S_w^2) \langle w'^2 \rangle^2 \\ \langle \theta'^4 \rangle &= (1 + S_\theta^2) \langle \theta'^2 \rangle^2 \\ \langle w'^3 \theta' \rangle &= (1 + S_w^2) \langle w'^2 \rangle \langle w' \theta' \rangle \\ \langle w' \theta'^3 \rangle &= (1 + S_\theta^2) \langle \theta'^2 \rangle \langle w' \theta' \rangle. \end{aligned} \quad (9)$$

The skewnesses S_w and S_θ (Eq. (6)) are related to a and b through

$$S_w = \frac{1 - 2a}{\sqrt{a(1 - a)}} \quad \text{and} \quad S_\theta = \frac{1 - 2b}{\sqrt{b(1 - b)}} \quad (10)$$

(GH2002; see also Randall et al. 1992, for the case of S_w).

In the following we consider only vertical-velocity moments. Assuming $S_w = S_\theta = 0$ in Eq. (9) gives:

$$\langle w'^4 \rangle = \langle w'^2 \rangle^2. \quad (11)$$

Such a result is not consistent with a quasi-normal (Gaussian) PDF. Indeed, when w' follows a normal distribution, then (Lesieur 1997):

$$S_w = S_\theta = 0 \quad \text{and} \quad \langle w'^4 \rangle = 3 \langle w'^2 \rangle^2. \quad (12)$$

GH2002 found that the two-scale mass-flux average, Eqs. (8)–(10), underestimates both skewness and fourth-order moments as measured by aircraft data for planetary boundary layer convection (see their Figs. 4 and 7). To account for the omitted contributions from fluctuations within and between the up- and downdrafts, they suggested generalizing the TFM by building the fourth-order moments as an interpolation between two asymptotic regimes:

- $S_w = 0$, assuming the quasi-normal approximation (QNA) limit that is valid for a Gaussian PDF, and
- $S_w \gg 1$, the large skewness limit (GH2002).

GH2002 hence proposed:

$$\begin{aligned} \langle w'^4 \rangle &= 3 \left(1 + \frac{1}{3} S_w^2 \right) \langle w'^2 \rangle^2 \\ \langle \theta'^4 \rangle &= 3 \left(1 + \frac{1}{3} S_\theta^2 \right) \langle \theta'^2 \rangle^2 \\ \langle w'^3 \theta' \rangle &= 3 \left(1 + \frac{1}{3} S_w^2 \right) \langle w'^2 \rangle \langle w' \theta' \rangle \\ \langle w' \theta'^3 \rangle &= 3 \left(1 + \frac{1}{3} S_\theta^2 \right) \langle \theta'^2 \rangle \langle w' \theta' \rangle. \end{aligned} \quad (13)$$

Corresponding expressions for other FOMs ($\langle w'^2 \theta'^2 \rangle$) and those including horizontal velocities) can be found in Gryanik et al. (2005, hereafter GH2005).

2.2. Validation with a 3D numerical simulation of the solar external layers

We consider the uppermost part of the solar turbulent convection. Turbulent plumes are known to exist within this region (Cattaneo et al. 1991; Stein & Nordlund 1998). Here, we test the validity of the TFM using 3D numerical simulations of these upper solar layers. The geometry is plane-parallel with a physical size of 6 Mm \times 6 Mm \times 3 Mm. The upper boundary corresponds to a convectively stable atmosphere and the lower one to a quasi-adiabatic convection zone. The 3D simulations used in this work were obtained with Stein & Nordlund's 3D numerical code (Stein & Nordlund 1998). Two simulations with different spatial grids were considered: 253 \times 253 \times 163 and 125 \times 125 \times 82.

Averages and moments of the velocity and temperature fluctuations were computed in a two-stage process:

a is given as the number of grid points per layer with upwards directed vertical velocity divided by the total number of points in that layer. The instantaneous value of b is obtained in a similar manner, comparing the temperature at a given point in a layer with its horizontal average. Moments related to updrafts were obtained from horizontal averaging, using only those grid points at which vertical velocity was directed upwards at the given instant in time, and likewise, quantities related to downdrafts were obtained from horizontal averaging using only those grid points at which vertical velocity was directed downwards. In a second step, time averages were performed over a sufficiently long period of time such that averages no longer depended on the integration time beyond a few percent.

— *Calculation of the skewnesses:* computations of the mean fractional area of the upflow (a) and downflow ($1 - a$), as well those of the warm (b) and cold ($1 - b$) drafts from the numerical 3D simulations (Fig. 1), show that the upper part of the solar convection zone can be divided into three parts: the stable atmosphere, the superadiabatic zone, and the quasi-adiabatic zone. In the convectively stable atmosphere ($z < 0$ Mm, where $z = 0$ is approximately at the bottom of the photosphere and $z = -0.5$ Mm is the uppermost boundary of the simulation), there are no asymmetric motions. In the superadiabatic zone ($0 < z < 0.5$ Mm), from the top downwards, the departure from symmetry for the flows strongly increases (Fig. 1), and the skewnesses, S_w and S_θ , significantly differ from zero (Fig. 2). Hence, one must expect a non-negligible departure from the QNA, which is explained by radiative cooling creating turbulent plumes. In the quasi-adiabatic zone, plumes have already been formed and no additional asymmetry is therefore created. Hence,

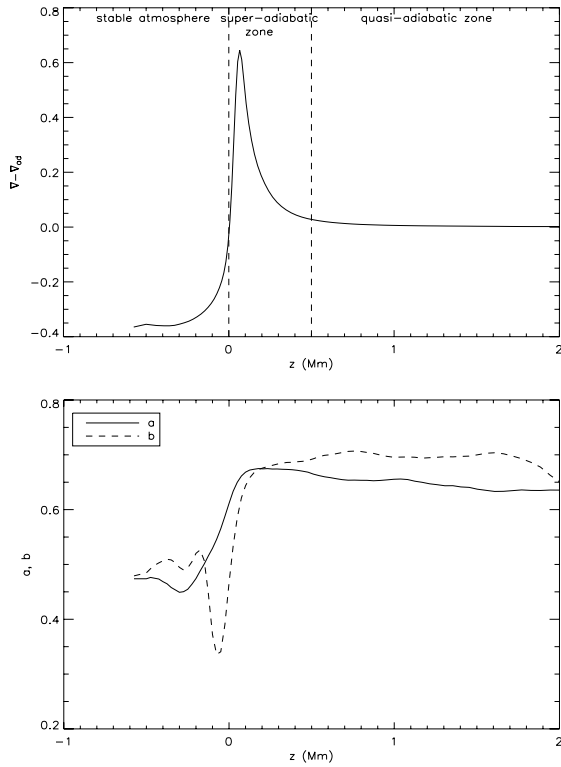


Fig. 1. On the top, the superadiabatic gradient ($\nabla - \nabla_{ad}$) is plotted versus the depth (z). The reference depth ($z = 0$ Mm) corresponds to the photosphere. At the bottom, the mean fractional area of the upflow (a) and the warm drafts (b) are given. To calculate these quantities the upflow and downflow are separated using the sign of w' as a criterion. The same is done for the warm and cold drafts.

the asymmetry remains large and constant ($a \approx b \approx 0.7$) and the skewnesses show a constant departure from $S_w = S_\theta = 0$.

The last two regions are of interest in this work because both show a departure from the quasi-normal PDF in terms of fluctuating vertical velocity and temperature. The comparison of the above numerical results with the results from the classical TFM (Eq. (9)) and the TFM model (Fig. 2) shows that Eq. (10) fails to reproduce the behaviour of the skewnesses from the 3D simulation (as was also found by Gryanik & Hartmann 2002 for convection in the atmosphere of the Earth, see their Fig. 4).

— *Detailed comparison of a fourth-order moment:* the GH2002 interpolation relation Eq. (14) combined with the TFM relation for skewness, Eq. (10), shows only a slight improvement of the QNA description for the FOM $\langle w'^4 \rangle$, when compared to the numerical result (Fig. 3).

To conclude, it seems that a physical process is missing in the quasi-adiabatic convective zone. To explain such a disagreement between the numerical results and the TFM, we must come back to its main approximation (see Eq. (7)). For $n = 2$, Eq. (7) yields:

$$\langle w'^2 \rangle - \langle w' \rangle^2 \approx 0 \quad \langle \theta'^2 \rangle - \langle \theta' \rangle^2 \approx 0. \quad (14)$$

Hence, the TFM assumes that the variances of the fluctuations of vertical velocity and temperature within and among individual drafts vanish, and the detailed turbulent nature of the flows themselves does not have to be taken into account. In order to compensate for the shortcoming of Eq. (9) and thus the consequences of the approximation Eq. (7) on the model predictions, Gryanik & Hartmann (2002) proposed a more general interpolation

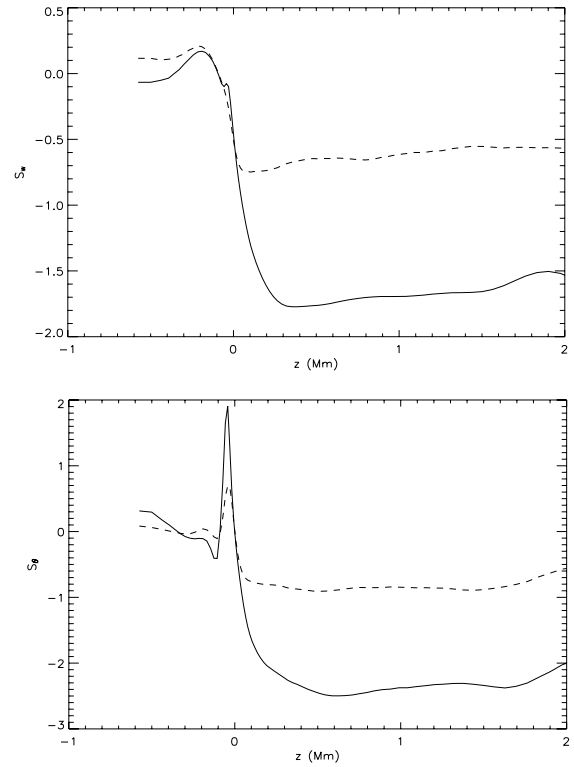


Fig. 2. The skewnesses S_w (on the top) and S_θ (on the bottom) are plotted versus the depth (z). Solid lines represent direct calculation from the 3D numerical simulation (Eq. (6)) and dashed lines represent the skewnesses calculated using the TFM model (Eq. (10)).

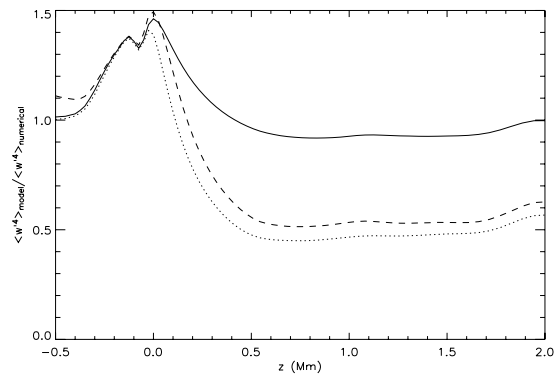


Fig. 3. Fourth-order moment ($\langle w'^4 \rangle$) as a function of depth (z) normalized to the FOM, as calculated directly from the simulation. The solid line denotes the moment calculated using Eq. (14) with S_w taken directly from the simulation; the dashed line shows the result if S_w is instead taken from Eq. (10), as in the TFM case; and the dotted line is the QNA (Eq. (26)). Equations (14) and (26) involve second-order moments that are computed using the numerical simulation.

relation (Eq. (14)) that uses Eq. (9) only for one of two asymptotic limits.

As seen above, Eq. (10) fails to describe the numerical results. The question therefore is whether the interpolated relation (Eq. (14)) is still valid, provided a correct value for the skewness is used. Hence, we assess the validity of Eq. (14) by inserting the value of S_w directly given by the 3D numerical result. The result is shown in Fig. 3 as well. This is the model that Gryanik & Hartmann (2002) proposed to be used instead of the TFM

itself and its associated relation for the skewnesses, Eq. (10). We obtain an accurate description of the FOM $\langle w'^4 \rangle$ in the quasi-adiabatic region, but not in the superadiabatic zone, where the interpolated relation does not seem well adapted (cf. KR2006 for a more detailed discussion).

3. The generalized two-scale mass-flux model

3.1. Theoretical formulation

Here we remove the approximation of Eq. (7) and instead consider the exact expression:

$$\langle w'^m \rangle = a \langle w'^m \rangle_u + (1-a) \langle w'^m \rangle_d. \quad (15)$$

Our main idea is to separate the effect of the skewness introduced by the presence of two flows from the effect of the turbulence that occurs in each individual flow. We note that in a geophysical context Siebesma & Cuijpers (1995) and Petersen et al. (1999) studied the transport properties of classical mass-flux models that also involved a separation of large-scale and turbulent components. Here, we start from the more recent viewpoint of the TFM by Gryanik & Hartmann (2002) and Gryanik et al. (2005), which takes into account that updrafts and downdrafts are not strictly correlated with hot and cold drafts, respectively. As a first step we define the intrinsic fluctuations within one of the flows as:

$$\tilde{w}'_j = w_j - \langle w \rangle_j, \quad (16)$$

where $j = \{u, d\}$. They are fluctuations with vanishing averages. To express w'_j in terms of \tilde{w}'_j (Eq. (4)), we write:

$$w'_j = \tilde{w}'_j + \langle w \rangle_j - \langle w \rangle. \quad (17)$$

Applying the decomposition of Eq. (1) to $\langle w \rangle$ in the above expression yields:

$$\begin{aligned} w'_u &= \tilde{w}'_u + (1-a) \delta w \\ w'_d &= \tilde{w}'_d - a \delta w \end{aligned} \quad (18)$$

with

$$\delta w = \langle w \rangle_u - \langle w \rangle_d = |\langle w \rangle_u| + |\langle w \rangle_d|, \quad (19)$$

because $\langle w \rangle_u > 0$ and $\langle w \rangle_d < 0$.

Inserting Eq. (18) into Eq. (15) for $n = 2, 3$ yields:

$$\langle w'^2 \rangle = a(1-a) \delta w^2 + a \langle \tilde{w}'^2 \rangle_u + (1-a) \langle \tilde{w}'^2 \rangle_d \quad (20)$$

$$\begin{aligned} \langle w'^3 \rangle &= a(1-a)(1-2a) \delta w^3 + a \langle \tilde{w}'^3 \rangle_u + (1-a) \langle \tilde{w}'^3 \rangle_d \\ &\quad + 3a(1-a) \left[\langle \tilde{w}'^2 \rangle_u - \langle \tilde{w}'^2 \rangle_d \right] \delta w. \end{aligned} \quad (21)$$

The third-order moment (Eq. (21)), which is related to the skewness (see Eq. (6)), is composed of four contributions:

- the first term is the expression derived by Gryanik & Hartmann (2002). It is a measure of the skewness introduced by the presence of two flows;
- the second and third terms represent the asymmetry of the PDF within each flow induced by turbulence;
- the fourth term measures the difference of the fluctuating velocity dispersion. Hence, if one of them is larger than the other, the PDF becomes asymmetric.

The description of the turbulence in individual flows that has been neglected in the TFM is included in the present formulation through the last three terms in Eq. (21).

We next focus on the fourth-order moment $\langle w'^4 \rangle$, which is of interest in the context of stochastic excitation of solar p modes (see Paper II). Then setting $n = 4$ in Eq. (15), we have:

$$\begin{aligned} \langle w'^4 \rangle &= a(1-a)(1-3a+3a^2) \delta w^4 \\ &\quad + 6a(1-a) \left[(1-a) \langle \tilde{w}'^2 \rangle_u + a \langle \tilde{w}'^2 \rangle_d \right] \delta w^2 \\ &\quad + 4a(1-a) \left[\langle \tilde{w}'^3 \rangle_u - \langle \tilde{w}'^3 \rangle_d \right] \delta w \\ &\quad + a \langle \tilde{w}'^4 \rangle_u + (1-a) \langle \tilde{w}'^4 \rangle_d. \end{aligned} \quad (22)$$

We stress that the TFM is recovered from the present generalized formulation when proper fluctuations (i.e., turbulence) within and among the individual drafts are neglected, i.e., $\langle \tilde{w}'^m \rangle = 0$.

The same decomposition can be performed in terms of temperature fluctuations. As the calculation is symmetrical in w', a and θ', b , we hence have:

$$\begin{aligned} \langle \theta'^2 \rangle &= b(1-b) \delta \theta^2 \\ &\quad + b \langle \tilde{\theta}'^2 \rangle_h + (1-b) \langle \tilde{\theta}'^2 \rangle_c \\ \langle \theta'^3 \rangle &= b(1-b)(1-2b) \delta \theta^3 \\ &\quad + b \langle \tilde{\theta}'^3 \rangle_h + (1-b) \langle \tilde{\theta}'^3 \rangle_c \\ &\quad + 3b(1-b) \left[\langle \tilde{\theta}'^2 \rangle_h - \langle \tilde{\theta}'^2 \rangle_c \right] \delta \theta \\ \langle \theta'^4 \rangle &= b(1-b)(1-3b+3b^2) \delta \theta^4 \\ &\quad + 6b(1-b) \left[(1-b) \langle \tilde{\theta}'^3 \rangle_h + b \langle \tilde{\theta}'^2 \rangle_c \right] \delta \theta^2 \\ &\quad + 4b(1-b) \left[\langle \tilde{\theta}'^3 \rangle_h - \langle \tilde{\theta}'^3 \rangle_c \right] \delta \theta \\ &\quad + b \langle \tilde{\theta}'^4 \rangle_h + (1-b) \langle \tilde{\theta}'^4 \rangle_c. \end{aligned} \quad (23)$$

The next step consists of the derivation of the cross terms $\langle w' \theta' \rangle$, $\langle w'^2 \theta'^2 \rangle$, $\langle w'^2 \theta' \rangle$ and $\langle w' \theta'^2 \rangle$; it is convenient to define the coefficients a_{uh}, a_{uc} so as to take into account the four types of flow (see also GH2005):

- warm updraft, a_{uh}
- cold updraft, $a_{uc} = a - a_{uh}$
- warm downdraft, $a_{dh} = b - a_{uh}$
- cold downdraft, $a_{dc} = 1 - b - a_{uc}$.

Expressions for the third and fourth cross-correlation moments are given in Appendix A.

The generalized TFM has the advantage of isolating the skewness introduced by the two flows (as measured by S_w and S_θ in Eq. (10)) from the effects of turbulence in each of the flows (as measured for instance by the two terms \tilde{w}'^2_u and \tilde{w}'^2_d). The GTFM allows us to take the effects of turbulence into account. We note that a small value of the kurtosis can occur only if proper fluctuations lead to negligibly small deviations from the root mean square average. Such a flow pattern consisting of clearly defined up- and downflows as well as hot and cold areas with a kurtosis $K_w \gtrsim 1$ can be considered as representing a *quasi-laminar state*. We stress that for the quasi-laminar case, Eq. (9) remains exact; thus the kurtosis becomes:

$$K_w = \frac{\langle w'^4 \rangle}{\langle w'^2 \rangle^2} = (1 + S_w^2) \quad \text{with} \quad S_w = \frac{1-2a}{\sqrt{a(1-a)}}. \quad (24)$$

For $a = 0.5$, one obtains $K_w = 1$, which is far from the value for a Gaussian PDF ($K_w = 3$). To take into account turbulence within

the up- and downdrafts, one can use Eq. (14) (see Sect. 2.2) with the skewness $S_w = \langle w'^3 \rangle / \langle w'^2 \rangle^{3/2}$ from the GTFM. In this case we obtain:

$$K_w = 3 \left(1 + \frac{1}{3} S_w^2 \right). \quad (25)$$

This implies that a (moderately small) non-vanishing skewness will make the value of K_w closer to three than in the quasi-laminar case. In the solar case, in the quasi-isentropic zone $S_w^2 \approx 4$ (Fig. 2), hence $K_w \approx 3 + 4/3$. In the physical picture underlying Eq. (14), turbulence prevents the PDF from being too far from a Gaussian one ($K_w \rightarrow 3$).

We notice that one important source of turbulence that can be considered responsible for at least part of the fluctuations in a draft – in addition to those created by the radiative processes on top of the convection zone – is related to shearing stresses between the up- and downdrafts. However, the investigation of the sources of turbulence is beyond the scope of the present work. Those mechanisms certainly play an important role in both the small scale velocity and the thermal fluctuations. Their study is definitely desirable in the future. One should also note that the splitting approach of the GTFM is valid and can be used for any convective system, provided that it is composed of two flows. As it is unclosed, it must be seen as a good basis for building a closure model.

3.2. Asymptotic limits

In the following, we study the asymptotic limits of the GTFM, focusing on the fourth-order moment $\langle w'^4 \rangle$. The standard mass flux model is easily recovered when setting the proper moments to zero: $\langle \tilde{w}'^n \rangle = 0$ in Eqs. (20)–(22). The same holds for the TFM, Eqs. (8)–(9), which is recovered, if in addition $\langle \tilde{\theta}'^n \rangle = 0$ in Eq. (23) (cf. Eqs. (7) and (8) in Gryanik & Hartmann 2002). We now turn to the QNA limit and the limit for large skewness, which are more interesting as they are used by Gryanik & Hartmann (2002) and Gryanik et al. (2005) in order to corroborate the interpolation formula Eq. (14).

3.2.1. The quasi-normal limit

To obtain the QNA (Eq. (12)), it is necessary that $S_w = 0$, but it is not sufficient. In fact, a vanishing skewness only shows that the PDF is symmetric, *but not that the PDF is Gaussian*. Further conditions are necessary:

- the moments must have zero mean, which implies $|\langle w \rangle_u| = |\langle w \rangle_d| = 0$ from Eqs. (2) and (18);
- for the QNA to apply to the whole system, one must assume that the QNA is valid for each flow;
- we must also assume that $a = 0.5$;
- the turbulent pressure must be the same in the upflow and downflow. Otherwise the skewness (S_w) is different from zero, according to Eq. (21), and the consequence is an asymmetric PDF, which is not consistent with the quasi-normal assumption. So the condition $\langle \tilde{w}'^2 \rangle_u = \langle \tilde{w}'^2 \rangle_d$ is required.

Then starting with Eq. (22), we find:

$$\begin{aligned} \langle w'^4 \rangle &= a \langle \tilde{w}'^4 \rangle_u + (1-a) \langle \tilde{w}'^4 \rangle_d \\ &= \frac{3}{2} \langle \tilde{w}'^2 \rangle_u^2 + \frac{3}{2} \langle \tilde{w}'^2 \rangle_d^2, \end{aligned}$$

and finally

$$\langle w'^4 \rangle = 3 \langle w'^2 \rangle^2, \quad (26)$$

which is the expression for the fourth order moment in the QNA. Note that the TFM (Sect. 2) is unable to properly recover the QNA. Within the GTFM the QNA results from two terms, $\langle \tilde{w}'^4 \rangle_u$ and $\langle \tilde{w}'^4 \rangle_d$, which are related to the intrinsic turbulence in each flow, but these are neglected in the TFM. This example also demonstrates that for a convective flow, the deviation of a PDF from a Gaussian one cannot be modelled by the TFM without further modifications of that model (even if $a = 0.5$).

3.2.2. The large skewness limit

Gryanik et al. (2005) have shown that the TFM must be recovered when considering a convective system with large skewness. Then, for $S_w \gg 1$, the expression for $\langle w'^4 \rangle$ in Eq. (14) becomes:

$$\langle w'^4 \rangle \approx S_w^2 \langle w'^2 \rangle^2. \quad (27)$$

The large skewness limit physically corresponds to either $a \approx 1$ or $a \approx 0$. Indeed, it means that one of the two flows dominates over the other one in terms of mean fractional area in the horizontal plane. Thus, due to conservation of mass, the mean vertical velocity becomes large such that $\delta w \gg 1 \text{ m s}^{-1}$ in the solar case (see Sect. 4, Eq. (41)).

In Eq. (22), the term proportional to δw^4 , which measures the effects introduced by an asymmetric flow, dominates and leads to the TFM expression for the fourth-order moment $\langle w'^4 \rangle$:

$$\langle w'^4 \rangle = a(1-a) \left(a^3 + (1-a)^3 \right) \delta w^4. \quad (28)$$

Gryanik & Hartmann (2002) demonstrated that this expression leads to the relation:

$$\langle w'^4 \rangle = (1 + S^2) \langle w'^2 \rangle^2 \approx S^2 \langle w'^2 \rangle^2 \text{ for } S \gg 1, \quad (29)$$

where, as in Eq. (10), $S = (1-2a)/\sqrt{a(1-a)}$. The same would result if the exact function S_w were taken in this limit instead of its approximation, Eq. (10).

Hence, the GTFM enables us to show that the asymptotic limits used by Gryanik & Hartmann (2002) to motivate the interpolated expressions for the FOMs (Eq. (14)) are limiting cases for a flow that consists of a coherent part with two components (up- and downdrafts), which themselves are subject to turbulence (cf. the discussion of the GH2002 model in KR2006). In Sect. 2.2 we have shown, using the 3D numerical simulation, that this interpolation is valid provided the skewness is taken directly from the 3D simulation. This property can be understood using the GTFM, as it permits us to obtain the different ingredients of the interpolation formula of Gryanik & Hartmann (2002) from Eq. (22) and the individual contributions to Eq. (22), can be analyzed using numerical simulations.

4. The closure model with plumes

Section 2.2 confirmed the conclusion by KR2006 that the interpolated relations in Eq. (14) proposed by Gryanik & Hartmann (2002) could be adapted for the solar case provided that the skewnesses are appropriately calculated. Using the GTFM to model skewnesses, Eq. (21) shows that the skewness S_w , for instance, depends on six quantities: δw , $\langle \tilde{w}'^3 \rangle_{u,d}$, $\langle \tilde{w}'^2 \rangle_{u,d}$, and a . As shown below, some of the terms in S_w turn out to be negligible in the quasi-adiabatic convective region because plumes are more turbulent in the downflow than in the upflow (Stein & Nordlund 1998). The remaining dominant terms are modelled hereafter by a plume model (Rieutord & Zahn 1995) in the quasi-adiabatic convective region, where the CMP is valid.

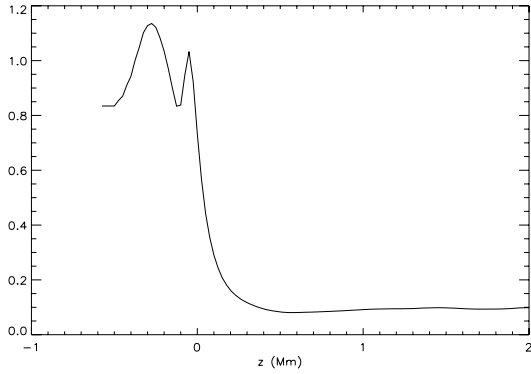


Fig. 4. Second-order moment of the upflow over that of the downflow ($\langle \tilde{w}'^2 \rangle_u / \langle \tilde{w}'^2 \rangle_d$) as a function of depth, calculated directly from the simulation. Upflow and downflow are determined according to the sign of w' .

4.1. Turbulence in upflows and downflows

In Fig. 4, we compare the second-order moments of both flows. These quantities are of the same order of magnitude in the upper part, above the photosphere. From the photosphere, the ratio $\langle \tilde{w}'^2 \rangle_u / \langle \tilde{w}'^2 \rangle_d$ then sharply decreases, with increasing depth (z). Hence, contributions to the skewness (S_w), involving $\langle \tilde{w}'^2 \rangle_u$ (Eqs. (20) and (21)) can be neglected in comparison with those involving $\langle \tilde{w}'^2 \rangle_d$ in the quasi-adiabatic part of the convection zone. The third-order moments $\langle \tilde{w}'^3 \rangle_d$ and $\langle \tilde{w}'^3 \rangle_u$ can also be discarded (see Fig. 5) because their contributions are negligible.

The skewness S_w then becomes:

$$S_w = \frac{a(1-a)}{\langle w'^2 \rangle^{3/2}} \left((1-2a)\delta w^2 - 3\langle \tilde{w}'^2 \rangle_d \right) \delta w, \quad (30)$$

where δw is given by Eq. (19). Hence, only $\langle \tilde{w}'^2 \rangle_d$ and δw remain to be modelled. Similarly, the 3D calculations show that the cool medium is more turbulent than the hot one and that third-order moments for the temperature fluctuations can be neglected. Then the expression for S_θ becomes:

$$S_\theta = b(1-b) \frac{1}{\langle \theta'^2 \rangle^{3/2}} \left((1-2b)\delta\theta^2 - 3\langle \tilde{\theta}'^2 \rangle_c \right) \delta\theta, \quad (31)$$

where the quantities $\delta\theta = \langle \theta \rangle_h - \langle \theta \rangle_c$ and $\langle \tilde{\theta}'^2 \rangle_c$ must be modelled.

Note that in the QNA limit $\delta w = 0$, so that for the expression Eq. (30), $S_w = 0$, and according to Eq. (14),

$$\langle w'^4 \rangle = 3\langle w'^2 \rangle^2.$$

However, because we have assumed $\langle \tilde{w}'^2 \rangle_u \ll \langle \tilde{w}'^2 \rangle_d$ when deriving the expression S_w , rigorously speaking, S_w does not tend correctly to zero in the QNA limit. Such an expression therefore cannot be used in the case of a near QNA regime. In our case, we have shown in Sect. 2.2 that the medium is far from the QNA limit in the quasi-adiabatic zone, and hence the expression Eq. (30) can be safely used.

To proceed further, $\langle \tilde{w}'^2 \rangle_d$ and $\langle \tilde{\theta}'^2 \rangle_c$ are written in a more suitable form. We neglect $\langle \tilde{w}'^2 \rangle_u$ in Eq. (20) for $\langle w'^2 \rangle$, and $\langle \tilde{\theta}'^2 \rangle_h$ in Eq. (23) for $\langle \theta'^2 \rangle$. This yields:

$$\begin{aligned} \langle w'^2 \rangle &= a(1-a)\delta w^2 + (1-a)\langle \tilde{w}'^2 \rangle_d \\ \langle \theta'^2 \rangle &= b(1-b)\delta\theta^2 + (1-b)\langle \tilde{\theta}'^2 \rangle_c. \end{aligned} \quad (32)$$

We then derive expressions for $\langle \tilde{w}'^2 \rangle_d$ and $\langle \tilde{\theta}'^2 \rangle_c$ in terms of $\langle w'^2 \rangle$, δw , and $\langle \theta'^2 \rangle$, $\delta\theta$, respectively (see Eq. (32)). Inserting them into Eqs. (30) and (31), one then obtains:

$$S_w = \frac{1}{\langle w'^2 \rangle^{3/2}} a \left((1-a)(1-5a)\delta w^2 - 3\langle w'^2 \rangle \right) \delta w \quad (33)$$

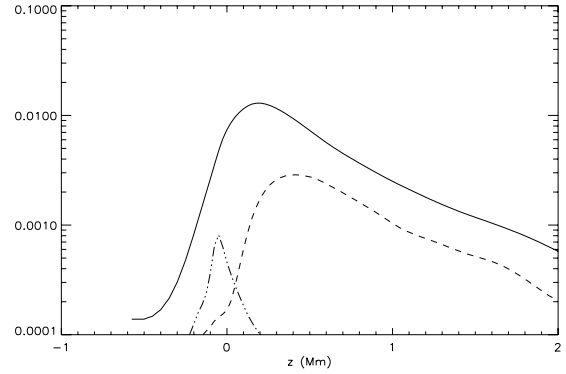


Fig. 5. The terms $3a(1-a)\langle \tilde{w}'^2 \rangle_d \delta w$ (solid line), $a\langle \tilde{w}'^3 \rangle_u$ (dot-dot-dashed line), and $(1-a)\langle \tilde{w}'^3 \rangle_d$ (dashed line) are plotted versus the depth (z). From Eq. (21), the dominant terms remains $3a(1-a)\langle \tilde{w}'^2 \rangle_d \delta w$. This justifies the assumptions that the terms involving third-order moments can be neglected in the quasi-adiabatic zone.

and

$$S_\theta = \frac{1}{\langle \theta'^2 \rangle^{3/2}} b \left((1-b)(1-5b)\delta\theta^2 - 3\langle \theta'^2 \rangle \right) \delta\theta. \quad (34)$$

We assume that the second-order moments ($\langle w'^2 \rangle$ and $\langle \theta'^2 \rangle$) are known. In the present work, they are computed from the 3D numerical simulation. In principle, they could also be taken from a convection model such as the mixing-length theory. The last step then is to determine δw and $\delta\theta$ (as well as a and b). As δw is the difference between the mean velocities of upward and downward flows, it is possible to model it by means of a plume model. This approach is also used to determine $\delta\theta$.

4.2. The plume model

4.2.1. Determination of δw

We use the model of plumes developed by Rieutord & Zahn (1995). The plume is considered in an axisymmetric geometry with a Gaussian horizontal profile for the vertical velocity (w_d), the fluctuations of enthalpy (δh), and density ($\delta\rho$) such that

$$\begin{aligned} w_d(r, z) &= V(z) \exp(-r^2/b_p^2), \\ \delta\rho(r, z) &= \Delta\rho(z) \exp(-r^2/b_p^2), \text{ and} \\ \delta h(r, z) &= \Delta h(z) \exp(-r^2/b_p^2). \end{aligned} \quad (35)$$

where $b_p(z)$ is the radius of the plume. We assume, as in RZ95, an isentropic and polytropic envelope structure, hence

$$\begin{aligned} \rho(z) &= \rho_0 (z/z_0)^q, \\ T(z) &= T_0 (z/z_0), \end{aligned} \quad (36)$$

where q is the polytropic coefficient. ρ_0 and T_0 are the density and temperature at depth $z = z_0$, and z_0 is the reference depth that corresponds to the base of the convective region.

In Fig. 6, we show that the mean velocity of upflow and downflow in the quasi-adiabatic convection zone both obey a power law in $(z/z_0)^r$. We therefore assume a power law for the mean velocity of the downflow (i.e., the plumes). Then

$$\langle w \rangle_d = w_{d0} \left(\frac{z}{z_0} \right)^r \quad (37)$$

with

$$w_{d0} = \left(\frac{12F}{\beta_0^2 \pi \rho_0 g z_0^2} \right)^{1/3}, \quad (38)$$

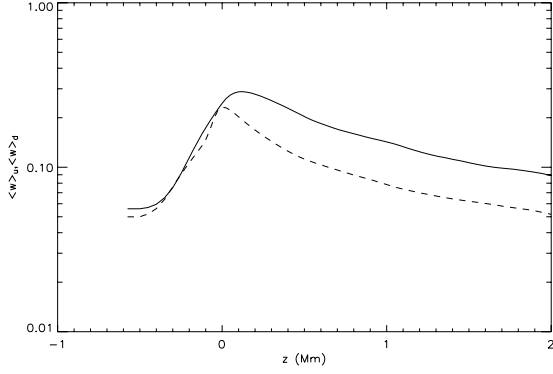


Fig. 6. Mean velocity profile of the upflow (dashed line) and downflow (solid line) as a function of the depth. Note that the peak at $z = 0.1$ Mm corresponds to the maximum turbulent pressure. The use of power laws limits the validity of the CMP to the quasi-adiabatic zone, as is implied by the deviation of the profiles from power laws in the superadiabatic region.

Table 1. Solar values of plume model parameters (from RZ95).

β_0	≈ 0.1
ρ_0	190 kg m^{-3}
L_\odot	$3.9 \times 10^{26} \text{ W}$
z_0	$\approx 2 \times 10^8 \text{ m}$
g_\odot	270 m s^{-2}

(RZ95), where $r = (-q + 1)/3$, $\beta_0 = 3\alpha/(q + 2)$, and $\alpha = 0.083$ is the entrainment constant for a Gaussian profile (Turner 1986). F is the convective energy flux and g is the gravitational acceleration. In Table 1, we list solar values of the previously introduced parameters taken from RZ95. These values are used in the present paper except for F , which is taken from the 3D numerical simulation (as explained below). For a monoatomic perfect gas, one has $q = 3/2$, hence $r = -1/6$. However, our 3D numerical simulations indicate a value of r closer to 0. The reason is likely that there is radiative cooling. Hence, $\gamma\Gamma = c_p/c_v$, where γ is the polytropic index ($q = 1/(\gamma - 1)$).

Following Rieutord & Zahn (1995), we assume that all the convective energy flux is transported by the plume, thus

$$F = L_\odot/N, \quad (39)$$

where N is the number of plumes in the shell at $h = R_\odot - z$. We find $N \approx 6 \times 10^6$ from the 3D numerical simulation. To obtain such a result, one has to use the relation between a and N :

$$a = N\pi b_p^2/4\pi h^2, \quad (40)$$

where (a) is mean fractional area of the upflow, $h = R_\odot - z$, and b_p is the radius of a plume. (b_p) and a are taken from the 3D numerical simulation. We assume $a = 0.7$, as taken from Fig. 1, which shows that the mean fractional area a is roughly constant in the quasi-adiabatic convection zone. The plume radius, b_p , is estimated at the top of the simulated box, which corresponds to the photosphere.

At this stage, we have modeled the downdrafts, but not yet the updrafts. The 3D numerical simulations show that mean velocities of upflow and downflow obey the *same* power law (Fig. 6). This can be explained as follows: from the conservation of the mass flux one has

$$\langle \rho w \rangle = a \langle \rho w \rangle_u + (1 - a) \langle \rho w \rangle_d = 0. \quad (41)$$

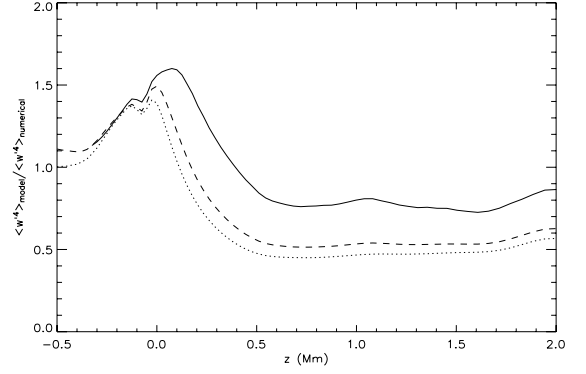


Fig. 7. Fourth-order moment $\langle w^4 \rangle$ as a function of depth z normalized to the FOM calculated directly from numerical simulations. The solid line shows $\langle w^4 \rangle$ calculated using the CMP model, the dashed line is the moment as obtained from Eq. (14) with Eq. (10) for S_w , and the dotted line is the QNA, Eq. (26).

Fluctuating parts of densities in up and downflows are neglected such that $\rho_u \approx \langle \rho \rangle_u$ and $\rho_d \approx \langle \rho \rangle_d$ (see Fig. 2b of RZ95). Thus,

$$\langle w \rangle_u = - \frac{(1 - a) \langle \rho \rangle_d}{a \langle \rho \rangle_u} \langle w \rangle_d. \quad (42)$$

Then, assuming that $\langle \rho \rangle_u = \rho_{u0}(z/z_0)^q$ and $\langle \rho \rangle_d = \rho_{d0}(z/z_0)^q$ obey the same power law as in Eq. (36):

$$\langle w \rangle_u \approx - \frac{(1 - a) \rho_{d0}}{a \rho_{u0}} \langle w \rangle_d. \quad (43)$$

ρ_{u0} and ρ_{d0} are the values at the reference depth z_0 . We set $a \approx 0.7$ (see Fig. 1), which is the value obtained in the quasi-adiabatic zone from the 3D numerical simulation. Assuming further that $\rho_{d0}/\rho_{u0} \approx 1$, one obtains

$$|\langle w \rangle_u| \approx 0.45 |\langle w \rangle_d|, \quad (44)$$

which is approximately what is seen in Fig. 6.

4.2.2. Skewness S_w and the fourth-order moment

We use Eq. (33) for the skewness with

$$\delta w = (\langle w_u \rangle - \langle w_d \rangle) \approx 1.45 w_{d0}. \quad (45)$$

The vertical depth of the computation box is narrow in comparison with the reference depth z_0 , thus δw varies only weakly with z . Hence, we assume $r = 0$ in the solar case. The fourth-order moment $\langle w^4 \rangle$ can then be computed by means of the interpolated relation Eq. (14). In Fig. 7, we show the resulting $\langle w^4 \rangle$. The CMP clearly is an improvement compared to the QNA and the TFM expression for S_w , Eq. (10) combined with Eq. (14), by at least a factor two in the quasi-adiabatic zone. The FOM in the superadiabatic zone is overestimated. Indeed, as mentioned above, the CMP is not able to describe such a zone mainly because the assumptions of Sect. 4.1 are not valid. Note that it is possible to use the same procedure to compute any other third- and fourth-order moment.

4.2.3. Determination of $\delta\theta$

Similarly to the procedure in the previous section, we evaluate $\langle \tilde{\theta}^2 \rangle$ with the help of Eqs. (32) and (34). We therefore need to

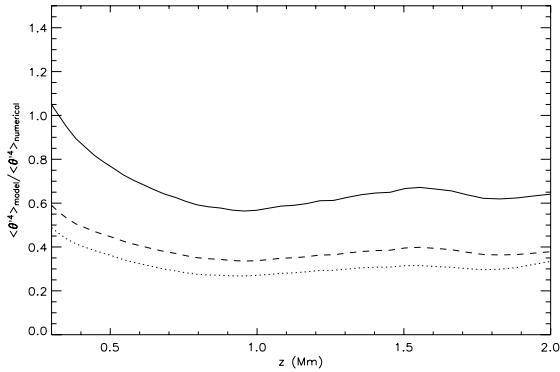


Fig. 8. Fourth-order moment $\langle \theta^4 \rangle$ as a function of depth z normalized to the directly numerically calculated FOM. In solid lines the moment stems from $\langle \theta^4 \rangle$ calculated using the CMP model, the dashed line is the moment as obtained from Eqs. (14) and (10) for S_θ and the dotted line is the QNA.

determine $\delta\theta$. The temperature profile is more sensitive to departure from adiabaticity than the velocity profile. It is therefore not suitable to assume an isentropic envelope. Such an approximation can still be used in the downflow, but not for the upflow, which is far from being adiabatic due to radiative cooling. Then, for the sake of simplicity, we assume a power law to obtain $\delta\theta$:

$$\delta\theta \approx \delta\theta_0 \left(\frac{z}{z_0} \right)^m. \quad (46)$$

For $z > 1$ Mm in the simulated box ($z = 0$ Mm denotes the photosphere), one derives $m = -1.5$, $\delta\theta_0 \approx 170$ K from the 3D numerical simulation. Using the power law (Eq. (46)) with $m = -1.5$, the skewness S_θ can be calculated using Eq. (34). In Fig. 8, we present the fourth-order moment $\langle \theta^4 \rangle$ computed using the CMP, and as expected, the description of the FOM is improved. In the deeper part of the convection zone (i.e., the adiabatic region), $\delta\theta$ is easier to model because Eq. (36) can be used and the difference $\delta\theta$ becomes a power law. From Eqs. (8), (14), (33), and (34) all the third- and fourth-order moments can be modelled with the CMP.

4.2.4. Summary: the CMP in a nutshell

In practice, one uses the CMP to compute $\langle w^4 \rangle$ by means of the interpolation formula Eq. (14), where the second-order moment $\langle w^2 \rangle$ is supposed to be known and where the skewness S_w is computed from Eq. (33). In the latter expression, δw is determined using the plume model through Eq. (45) and using Eqs. (37) to (40) with appropriate values of parameters for the case studied (in the present paper we used the values from Table 1, which are suitable for the solar case). Here, $a(z)$, N , b_p , and other input quantities are taken from the 3D numerical simulation. When the CMP is used to obtain the other third- and fourth-order moments, additional quantities have to be determined, namely b and m in Eq. (46) for S_θ (see Eq. (34)).

5. Conclusions

With the help of 3D numerical simulations of the upper part of the solar convective region, we have shown that the QNA and the TFM fail to describe the fourth-order velocity and temperature correlation moments, if merely used on their own. These results

confirm KR2006 and geophysical studies (Gryanik & Hartmann 2002) and led us to generalize the TFM in order to take the effects of the turbulent properties of the up- and downflows explicitly into account (GTFM). We point out that the GTFM can be used in other contexts than the solar one as long as the convective system can be described with two turbulent flows.

One might wonder whether it is likely that the CMP and the model for p mode excitation developed in Paper II are generally applicable to solar-like stars. To answer this question requires further work, but results on important ingredients of these models are encouraging. The case of convection in the planetary boundary layer of the atmosphere of the earth was already discussed in GH2002. Their interpolation model for FOMs has meanwhile been investigated for the case of convection in the ocean (Losch 2004) and solar granulation (Kupka & Robinson 2006, who also study the case of a K dwarf; preliminary results were published in Kupka & Hillebrandt 2005). We corroborate the latter here with simulations for solar granulation based on more realistic boundary conditions. The overall conclusion that can be drawn from these studies is that, at least away from the boundary layers of convection zones, the FOMs in purely convective flows can be estimated according to the interpolation model by GH2002 with an accuracy typically in the range of 20% to 30%, whereas the QNA is off by a factor of two to three. For the superadiabatic layer, the discrepancies of the QNA remain the same in any case of the same size.

We focused here on the solar case, more precisely a region that is nearly adiabatic, just below the superadiabatic zone where the acoustic modes are excited. As indicated by the 3D simulations, the coherent downdrafts, called plumes, are more turbulent than the upflow. In addition, we use the plume model developed by RZ95 to estimate the upward and downward mean velocities. With these additional approximations, the GTFM yields a closure model, the CMP, which can be applied in the quasi-adiabatic zone (located just below the superadiabatic one). Comparisons of calculations based on the CMP with direct calculations from the 3D numerical simulations show a good agreement. Hence, the CMP provides an analytical closure for third- and fourth-order moments. These moments are expressed in a simple way and require only the knowledge of the second-order moments and the parameters of the plume model. We stress that the CMP involves four parameters: the number of plumes in the considered shell (i.e., near the photosphere), the exponent of the power law for the mean vertical velocity of plumes, the law to describe the temperature difference between the two flows, and the mean fractional area of the updrafts and hot drafts.

A study of the dependence of the results on these parameters is in progress. For instance, an increase of a will imply an increase of S_w in Eq. (33), and hence of the fourth-order moment $\langle w^4 \rangle$. Nevertheless, it is extremely difficult to deduce the behaviour of the system, since from Eq. (41) a variation of a changes the velocities of the flows. Instead, one could use a set of numerical simulations to study the effect of a change of the parameter a . In a companion paper, we use the CMP in a semi-analytical approach to calculate the power supplied to the solar p modes. It is found that the power is quite significantly affected by the adopted closure model.

Our final aim is to apply the CMP to the study of stochastic excitation of solar-like p modes in stars other than the Sun. It will be necessary to assess the validity of the CMP approximations to extend their application to stellar conditions different from the solar case. This will also require investigating the dependence of the parameters entering the CMP, for instance, on the effective temperature of the star (work which is in progress). As pointed

out in Sect. 4, the CMP is valid only in the quasi-adiabatic zone due to the power laws used to model the plume dynamics. This will be discussed further in the companion paper in which the present model will be used in the superadiabatic zone in order to propose a new closure for the calculation of stellar p modes.

Finally, we note that in the present work we do not take the effect of differential rotation and meridional circulation into account. However, recent helioseismic investigations (Schou et al. 2002; Zhao & Kosovichev 2004) have shown that variability of those large-scale flows gradually affects wavelength and frequencies, leading to a redistribution of the observed power spectrum (Shergelashvili & Poedts 2005; Hindman et al. 2005). Hence, it could have an indirect effect on the amplitudes of p modes. Furthermore, large-scale laminar non-uniform flows can have a significant effect on the formation of the coherent structures and intrinsic turbulence (Miesch et al. 2000; Brun & Toomre 2002; Rempel 2005). To what extent they can affect solar p mode amplitudes, through the closure model and the Reynolds stresses, remains to be investigated.

Acknowledgements. We are indebted to J. Leibacher for his careful reading of the manuscript and his helpful remarks. We thank J. P. Zahn and F. Lignières for useful discussions and comments. F.K. is grateful to V. M. Gryanik and J. Hartmann for discussions on their model and their observational data. We also thank the anonymous referee for valuable comments that helped to improve the manuscript.

We thank Å. Nordlund and R. F. Stein for making their code available to us. Their code was made at the National Center for Supercomputer Applications and Michigan State University and supported by grants from NASA and NSF.

References

- Abdella, K., & McFarlane, N. 1997, *J. Atm. Sci.*, 54, 1850
 Balmforth, N. J. 1992, *MNRAS*, 255, 639

- Belkacem, K., Samadi, R., Goupil, M., Kupka, F., & Baudin, F. 2006, *A&A*, 460, 183
 Brun, A. S., & Toomre, J. 2002, *ApJ*, 570, 865
 Canuto, V. M. 1992, *ApJ*, 392, 218
 Canuto, V. M., & Dubovikov, M. 1998, *ApJ*, 493, 834
 Cattaneo, F., Brummell, N. H., Toomre, J., Malagoli, A., & Hurlburt, N. E. 1991, *ApJ*, 370, 282
 Goldreich, P., & Keeley, D. A. 1977, *ApJ*, 212, 243
 Goldreich, P., Murray, N., & Kumar, P. 1994, *ApJ*, 424, 466
 Gryanik, V. M., & Hartmann, J. 2002, *J. Atm. Sci.*, 59, 2729
 Gryanik, V. M., Hartmann, J., Raasch, S., & Schröter, M. 2005, *J. Atm. Sci.*, 62, 2632
 Hindman, B. W., Gough, D., Thompson, M. J., & Toomre, J. 2005, *ApJ*, 621, 512
 Kupka, F., & Hillebrandt, W. 2005, Workshop on Interdisciplinary Aspects of Turbulence
 Kupka, F., & Robinson, F. 2006, *MNRAS*, in press
 Lesieur, M. 1997, *Turbulence in fluids* (Kluwer Academic Publishers)
 Losch, M. 2004, *Geophys. Res. Lett.*, 31, 23301
 Miesch, M. S., Elliott, J. R., Toomre, J., et al. 2000, *ApJ*, 532, 593
 Millionshchikov, M. D. 1941, *Doklady Acad. Nauk SSSR*, 32, 611
 Nordlund, Å., & Stein, R. F. 2001, *ApJ*, 546, 576
 Ogura, Y. 1963, *J. Fluid Mech.*, 16, 33
 Petersen, A. C., Beets, C., van Dop, H., Dyuinkerke, P. G., & Pier Siebesma, A. 1999, *J. Atm. Sci.*, 56, 37
 Randall, D. A., Shao, Q., & Moeng, C.-H. 1992, *J. Atm. Sci.*, 49, 1903
 Rempel, M. 2005, *ApJ*, 631, 1286
 Rieutord, M., & Zahn, J.-P. 1995, *A&A*, 296, 127
 Samadi, R., & Goupil, M. 2001, *A&A*, 370, 136
 Samadi, R., Goupil, M.-J., Alecian, E., et al. 2005, *J. Astrophys. Atr.*, 26, 171
 Schou, J., Howe, R., Basu, S., et al. 2002, *ApJ*, 567, 1234
 Shergelashvili, B. M., & Poedts, S. 2005, *A&A*, 438, 1083
 Siebesma, A. P., & Cuijpers, J. W. M. 1995, *J. Atmos. Sci.*, 52, 650
 Stein, R., Georgobiani, D., Trampedach, R., Ludwig, H.-G., & Nordlund, Å. 2004, *Sol. Phys.*, 220, 229
 Stein, R. F., & Nordlund, A. 1998, *ApJ*, 499, 914
 Turner, J. S. 1986, *J. Fluid Mech.*, 173, 431
 Zhao, J., & Kosovichev, A. G. 2004, *ApJ*, 603, 776

Online Material

Appendix A: Cross-correlation moments

As explained in Sect. 3.1, we provide the cross-correlation moments:

$$\langle w'\theta' \rangle = a_{uh}\langle \tilde{w}'\tilde{\theta}' \rangle_{u,h} + a_{uc}\langle \tilde{w}'\tilde{\theta}' \rangle_{u,c} + a_{dc}\langle \tilde{w}'\tilde{\theta}' \rangle_{d,c} + a_{dh}\langle \tilde{w}'\tilde{\theta}' \rangle_{d,h} + \eta\delta w\delta\theta \quad (\text{A.1})$$

$$\langle w'^2\theta' \rangle = a_{uh}\langle \tilde{w}'^2\tilde{\theta}' \rangle_{u,h} + a_{uc}\langle \tilde{w}'^2\tilde{\theta}' \rangle_{u,c} + a_{dh}\langle \tilde{w}'^2\tilde{\theta}' \rangle_{d,h} + a_{dc}\langle \tilde{w}'^2\tilde{\theta}' \rangle_{d,c} + \beta_1\delta\theta + \beta_2\delta w + \beta_3\delta w^2\delta\theta \quad (\text{A.2})$$

$$\langle w'\theta'^2 \rangle = a_{uh}\langle \tilde{w}'\tilde{\theta}'^2 \rangle_{u,h} + a_{uc}\langle \tilde{w}'\tilde{\theta}'^2 \rangle_{u,c} + a_{dh}\langle \tilde{w}'\tilde{\theta}'^2 \rangle_{d,h} + a_{dc}\langle \tilde{w}'\tilde{\theta}'^2 \rangle_{d,c} + \gamma_1\delta w + \gamma_2\delta\theta + \gamma_3\delta w\delta\theta^2 \quad (\text{A.3})$$

$$\langle w'^2\theta'^2 \rangle = a_{uh}\langle \tilde{w}'^2\tilde{\theta}'^2 \rangle_{u,h} + a_{uc}\langle \tilde{w}'^2\tilde{\theta}'^2 \rangle_{u,c} + a_{dh}\langle \tilde{w}'^2\tilde{\theta}'^2 \rangle_{d,h} + a_{dc}\langle \tilde{w}'^2\tilde{\theta}'^2 \rangle_{d,c} + \phi_1\delta\theta + \phi_2\delta w + \phi_3\delta\theta^2 + \phi_4\delta w^2 + \phi_5\delta w\delta\theta + \phi_6\delta w^2\delta\theta^2 \quad (\text{A.4})$$

where:

$$\eta = \left[a_{uh}(1-a)(1-b) - a_{uc}b(1-a) + a_{dc}ab - a_{dh}a(1-b) \right]$$

$$\beta_1 = \left[a_{uh}(1-b) - a_{uc}b \right] \langle \tilde{w}'^2 \rangle_u + \left[a_{dh}(1-b) - a_{dc}b \right] \langle \tilde{w}'^2 \rangle_d$$

$$\beta_2 = 2 \left[a_{uh}\langle \tilde{w}'\tilde{\theta}' \rangle_{u,h} + a_{uc}\langle \tilde{w}'\tilde{\theta}' \rangle_{u,c} - a(\langle w'\theta' \rangle - \eta) \right]$$

$$\beta_3 = \left[a_{uh}(1-a)^2(1-b) - a_{uc}b(1-a)^2 + a_{dh}a^2(1-b) - a_{dc}a^2b \right]$$

$$\gamma_1 = \left[a_{uh}(1-a) - a_{dh}a \right] \langle \tilde{\theta}'^2 \rangle_h$$

$$+ \left[a_{uc}(1-a) - a_{dc}a \right] \langle \tilde{\theta}'^2 \rangle_c$$

$$\gamma_2 = 2 \left[a_{uh}\langle \tilde{w}'\tilde{\theta}' \rangle_{u,h} + a_{dh}\langle \tilde{w}'\tilde{\theta}' \rangle_{d,h} - b(\langle w'\theta' \rangle - \eta) \right]$$

$$\gamma_3 = \left[a_{uh}(1-a)(1-b)^2 - a_{uc}b^2(1-a) - a_{dh}a(1-b)^2 - a_{dc}ab^2 \right]$$

$$\phi_1 = 2 \left[a_{uh}\langle \tilde{w}'^2\tilde{\theta}' \rangle_{u,h} + a_{dh}\langle \tilde{w}'^2\tilde{\theta}' \rangle_{d,h} - b(\langle w'^2\theta' \rangle - \beta_1 - \beta_2 - \beta_3) \right]$$

$$\phi_2 = 2 \left[a_{uh}\langle \tilde{w}'\tilde{\theta}'^2 \rangle_{u,h} + a_{uc}\langle \tilde{w}'\tilde{\theta}'^2 \rangle_{u,c} - a(\langle w'\theta'^2 \rangle - \gamma_1 - \gamma_2 - \gamma_3) \right]$$

$$\phi_3 = \left[a_{uh}(1-b)^2 - a_{uc}b^2 \right] \langle \tilde{w}'^2 \rangle_u + \left[a_{dh}(1-b)^2 - a_{dc}b^2 \right] \langle \tilde{w}'^2 \rangle_d$$

$$\phi_4 = \left[a_{uh}(1-a)^2 - a_{dh}a^2 \right] \langle \tilde{\theta}'^2 \rangle_h + \left[a_{uc}(1-a)^2 - a_{dc}a^2 \right] \langle \tilde{\theta}'^2 \rangle_c$$

$$\phi_5 = 4 \left[a_{uh}(1-a)(1-b)\langle \tilde{w}'\tilde{\theta}' \rangle_{u,h} - a_{uc}b(1-a)\langle \tilde{w}'\tilde{\theta}' \rangle_{u,c} - a_{dh}a(1-b)\langle \tilde{w}'\tilde{\theta}' \rangle_{d,h} + a_{dc}ab\langle \tilde{w}'\tilde{\theta}' \rangle_{d,c} \right]$$

$$\phi_6 = \left[a_{uh}(1-a)^2(1-b)^2 + a_{uc}(1-a)^2b^2 + a_{dh}a^2(1-b)^2 + a_{dc}a^2b^2 \right].$$

A closure model with plumes

II. Application to the stochastic excitation of solar p modes

K. Belkacem¹, R. Samadi¹, M. J. Goupil¹, F. Kupka², and F. Baudin³

¹ Observatoire de Paris, LESIA, CNRS UMR 8109, 92195 Meudon, France

e-mail: Kevin.Belkacem@obspm.fr

² Max-Planck-Institute for Astrophysics, Karl-Schwarzschild Str. 1, 85741 Garching, Germany

³ Institut d'Astrophysique Spatiale, CNRS/Université Paris XI UMR 8617, 91405 Orsay Cedex, France

Received 5 April 2006 / Accepted 22 June 2006

ABSTRACT

Context. Amplitudes of stellar p modes result from a balance between excitation and damping processes taking place in the uppermost part of convective zones in solar-type stars and can therefore be used as a seismic diagnostic for the physical properties of these external layers.

Aims. Our goal is to improve the theoretical modelling of stochastic excitation of p modes by turbulent convection.

Methods. With the help of the closure model with plume (CMP) developed in a companion paper, we refine the theoretical description of the excitation by the turbulent Reynolds stress term. The CMP is generalized for two-point correlation products so as to apply it to the formalism developed by Samadi & Goupil (2001, A&A, 370, 136). The excitation source terms are then computed with this improvement, and a comparison with solar data from the GOLF instrument is performed.

Results. The present model provides a significant improvement when comparing absolute values of theoretical amplitudes with observational data. It gives rise to a frequency dependence of the power supplied to solar p modes, which agrees with GOLF observations. It is shown that the asymmetry of the turbulent convection zone (up and downflows) plays a major role in the excitation processes. Despite an increase in the Reynolds stress term contribution due to our improved description, an additional source of excitation, identified as the entropy source term, is still necessary for reproducing the observational data.

Conclusions. Theoretical excitation rates in the frequency range $\nu \in [2.5 \text{ mHz}, 4 \text{ mHz}]$ now are in agreement with the observational data from the GOLF instrument. However, at lower frequencies, it exhibits small discrepancies at the maximum level of a few per cent. Improvements are likely to come from a better physical description of the excitation by entropy fluctuations in the superadiabatic zone.

Key words. convection – turbulence – Sun: oscillations

1. Introduction

Amplitudes of solar-like oscillations result from a balance between excitation and damping. Excitation is attributed to turbulent motions that excite the p modes. In the uppermost part of the convection zone, entropy fluctuations and eddy motions drive oscillations. In this region, convection becomes inefficient and there is an increase of the eddy velocities and entropy fluctuations. Solar-like oscillations are mainly excited in such a region, thus a theoretical model of the excitation processes is a powerful tool in understanding the properties of the convective zones of solar-type stars. Goldreich & Keeley (1977) have proposed a model for the excitation process using the turbulent Reynolds stress and deduced an estimation of the power supplied to the p modes. The underestimation of the excitation rates by around a factor 10^3 compared to the observed solar values (Osaki 1990) led to alternative formulations (Goldreich & Kumar 1990; Goldreich et al. 1994). Another source of excitation was identified by Goldreich et al. (1994): the so-called entropy source term. Its contribution cannot be neglected, even though Stein & Nordlund (2001) have shown that excitation from the Reynolds stress remains dominant in comparison with the entropy fluctuation source term.

Samadi & Goupil (2001) propose a generalized formalism, taking the Reynolds and entropic fluctuation source terms into account. This approach allows investigation of the effects of several models of turbulence (Samadi et al. 2003b,a) by expressing the source terms as functions of the turbulent kinetic energy spectrum and the time-correlation function.

A confrontation of this model with data from the BiSON instrument (data from Chaplin et al. 1998) led to the conclusion that the theoretical predictions were in good agreement with the observations (Samadi et al. 2003a). Nevertheless, observational data from the GOLF instrument and a study of the BiSON data indicate that some discrepancies remain between the theoretical computation and observational data. In Samadi & Goupil (2001) (see also Samadi et al. 2005), one of the main assumptions is the quasi-normal approximation (QNA), which is useful for correlation functions of the turbulent Reynolds stress and the entropy fluctuation source terms (Samadi & Goupil 2001).

The uppermost part of the convection zone being a turbulent convective system composed of two flows, the probability distribution function of the fluctuations of the vertical velocity and temperature does not follow a Gaussian law (Lesieur 1997). Thus, the use of the QNA, which is exact for a normal distribution, becomes a doubtful approximation.

In a companion paper (Belkacem et al. 2006, hereafter Paper I), we propose another approach in order to build a closure model that expresses fourth-order correlation functions in terms of the second-order ones. This alternative approach consists in considering the convection zone as composed of two flows (the updrafts and downdrafts). Starting from the Gryanik & Hartmann (2002) approach, we develop a generalized two-scale mass-flux model (GTFM) that takes the physical properties of each flow into account. Then a theoretical description of the plumes developed by Rieutord & Zahn (1995) is used to construct the closure model with plumes (CMP). This model is valid for one-point correlation functions and in the quasi-adiabatic zone. However, what is needed here is a closure model for two-point correlation functions. In the present paper, we then propose a simple way to obtain this closure model to use it for calculating of the excitation rates according to Samadi & Goupil (2001). Only the Reynolds stress source term is corrected, mainly because it is the dominant term (Stein & Nordlund 2001; Samadi et al. 2003a). The entropy fluctuations are considered in the same way as explained in Samadi & Goupil (2001) (i.e. using the QNA approximation).

The paper is organized as follows: the theoretical model of stochastic excitation of p modes is briefly summarized in Sect. 2. In Sect. 3, the closure model with plume (CMP) is generalized for two-point correlation products and implemented into the formalism of Samadi & Goupil (2001). In Sect. 4, the calculation of theoretical power is explained. In Sect. 5, GOLF observational data are presented together with the derivation of observable quantities. A comparison between the theoretical power and heights computed as described in Sect. 4 with the corresponding observed quantities defined in Sect. 5 is performed in Sect. 6. Section 7 is dedicated to discussions and conclusions.

2. A model for stochastic excitation of solar-like p modes

The theoretical model of stochastic excitation considered here is basically that of Samadi & Goupil (2001; see also Samadi et al. 2005). It takes two sources into account that drive the resonant modes of the stellar cavity. The first one is related to the Reynolds stress tensor and as such represents a mechanical source of excitation. The second one is caused by the advection of the turbulent fluctuations of entropy by the turbulent motions (the so-called “entropy source term”) and thus represents a thermal source of excitation (Goldreich et al. 1994; Stein & Nordlund 2001).

The power fed into each mode, P , is given by (see e.g. Samadi et al. 2001):

$$P \equiv \frac{dE}{dt} = 2\eta E = \eta \langle |A|^2 \rangle I \omega_0^2, \quad (1)$$

where $\langle \rangle$ denotes the ensemble average, $\langle |A|^2 \rangle$ the mean square amplitude, η the damping rate, and E the energy that is defined as

$$E = \frac{1}{2} \langle |A|^2 \rangle I \omega_0^2 \quad (2)$$

where I is the mode inertia and ω_0 is the oscillation eigenfrequency (see Samadi & Goupil 2001, for details).

The mean square amplitude, as explained in Samadi & Goupil (2001), is

$$\langle |A|^2 \rangle = \frac{1}{8\eta(I\omega_0)^2} (C_R^2 + C_S^2) \quad (3)$$

where C_R^2 and C_S^2 are the turbulent Reynolds stress and entropy contributions, respectively. Their expressions for radial modes are given by

$$C_R^2 = \int d^3x_0 \rho_0^2 f_r \int_{-\infty}^{+\infty} d\tau e^{-i\omega_0\tau} \int d^3r \langle w_1^2 w_2^2 \rangle \quad (4)$$

$$C_S^2 = \int d^3x_0 g_r \int_{-\infty}^{+\infty} d\tau e^{-i\omega_0\tau} \int d^3r \langle (ws_r)_1 (ws_r)_2 \rangle \quad (5)$$

where w is the vertical component of the velocity, s_r the turbulent entropy fluctuation and $f_r(\xi_r, m) \equiv \left(\frac{\partial \xi_r}{\partial r}\right)^2$, where ξ_r is the radial component of the eigenfunction, and g_r a function that involves the first and second derivatives of ξ_r (see Eq. (9) of Samadi et al. 2003b). Quantities labelled with 1 and 2 denote two spatial and temporal positions, hence $\langle w_1^2 w_2^2 \rangle$ and $\langle (ws_r)_1 (ws_r)_2 \rangle$ correspond to two-point fourth-order correlation products. These correlation products are usually approximated by expressions involving second-order products only (closure model). In Samadi & Goupil (2001), the simplest approximation was used i.e. the quasi-normal hypothesis. We study here consequences of using a closure model closer to reality (i.e. the CMP from Paper I). Both are recalled in the next section.

3. Closure models

3.1. The quasi-normal approximation

The QNA (Lesieur 1997, Chap. VII-2) is adopted in Samadi & Goupil (2001) as a convenient means to decompose the fourth-order velocity correlations in terms of a product of second-order vertical velocity correlations, that is, one uses

$$\begin{aligned} \langle w_1^2 w_2^2 \rangle_{\text{QNA}} &= 2 \langle w_1 w_2 \rangle^2 + \langle w_1^2 \rangle \langle w_2^2 \rangle \\ \langle (ws_r)_1 (ws_r)_2 \rangle_{\text{QNA}} &= \langle w_1 w_2 \rangle \langle s_{r1} s_{r2} \rangle, \end{aligned} \quad (6)$$

where s_r is considered as a passive scalar.

This approximation (Eq. (6)) remains strictly valid for normally distributed fluctuating quantities with zero mean. As shown by Kraichnan (1957) in the context of turbulent flows and Stein (1967) in the solar context, the cumulant (the deviation from the QNA) can be large and therefore not negligible. The CMP presented in Paper I was shown to be a significant improvement on the QNA for the one-point correlation products. However, we need two-point correlation products here (see Eqs. (4) and (5)). A generalization of the CMP for two-point correlation products is therefore developed in Sect. 3.2 below.

The second-order correlation products in Eq. (6) are expressed in the Fourier domain (\mathbf{k}, ω) where \mathbf{k} and ω are the wavenumber and the frequency associated with a turbulent element (see Samadi & Goupil 2001, for details).

3.2. The closure model with plumes

The closure model with plumes (see Paper I) has been established only for one-point correlation products. Here we generalize the CMP to two-point correlation products. We start in Fig. 1 by comparing the correlation product $\langle w_1^2 w_2^2 \rangle$ calculated directly from 3D numerical simulations obtained from the Stein & Nordlund code (see Sect. 4) with those calculated using Eq. (6) of the QNA with second-order correlation products taken from the 3D simulation. The question is whether the modelling of the \mathbf{k} dependency on the two-point correlation function by the QNA can be used. For the sake of simplicity, we assume that the QNA can be used for the ω dependency.

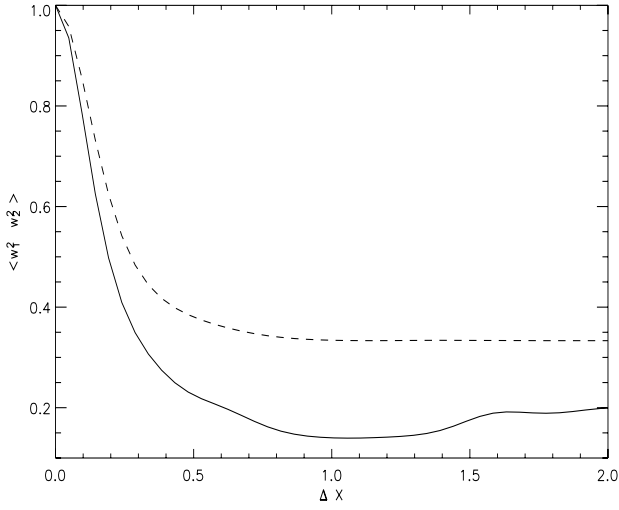


Fig. 1. Fourth-order correlation function calculated in the quasi-adiabatic zone directly from the 3D numerical simulation (solid line) and using the QNA approximation (Eq. (6); dashed lines). The fourth-order moments are presented as a function of the correlation length (ΔX), and the two curves are normalized so as to emphasise only their k dependency.

The correlation products $\langle w_1^2 w_2^2 \rangle$ in Fig. 1 are normalized so as to compare only the k dependency of these quantities. In the quasi-adiabatic region, the line width at half-maximum of the QNA and the numerical product are roughly the same. Discrepancies at high values of ΔX (the correlation length) are expected to have a negligible influence on the correlation product. Hence, we assume that the modelling of the k dependency on the two-point correlation product by the QNA is valid due to a small difference between the line width at half-maximum. Hence it is legitimate to use the (k, ω) dependency given by the QNA. One then needs only to correct the value of the correlation product at $(k = \mathbf{0}, \omega = 0)$ (which corresponds to the one point correlation function) with the CMP (see Paper I) for the turbulent Reynolds stress term contribution. We use the interpolation formula of Gryanik & Hartmann (2002) for the FOM of the velocity (Paper I, Eq. (13))

$$\langle w_1^2 w_2^2 \rangle_{\text{CMP}} = \left(1 + \frac{1}{3} S_w^2 \right) \langle w_1^2 w_2^2 \rangle_{\text{QNA}}, \quad (7)$$

with $\langle w_1^2 w_2^2 \rangle_{\text{QNA}}$ given by Eq. (6) the skewness S_w is calculated from the CMP (see Paper I for details).

In Fig. 2, calculations using Eqs. (6) and (7) are compared to the direct numerical correlation product. The above generalization of the CMP to two-point correlation products provides a good approximation mainly in the quasi-adiabatic region where the CMP is the more accurate one (see Paper I). The k dependence is approximatively modelled by the QNA (Fig. 1) except for large correlation lengths ($\Delta X > 0.2$ Mm), but these contribute only negligibly to $\langle w_1^2 w_2^2 \rangle$. However, in the superadiabatic zone, the generalization of the CMP and the QNA both fail to describe the two-point correlation function. In that zone, the temperature gradient is varying quickly, which is not the case in the CMP. In the plume model (Paper I) the temperature gradient appears only through a polytropic law, and for sake of simplicity we assume an isentropic atmosphere. In addition, for modelling the FOM (w^4), the interpolated formula derived by Gryanik & Hartmann (2002) (Paper I, Eq. (13)) is not valid in the superadiabatic zone. Thus, in this zone the treatment of

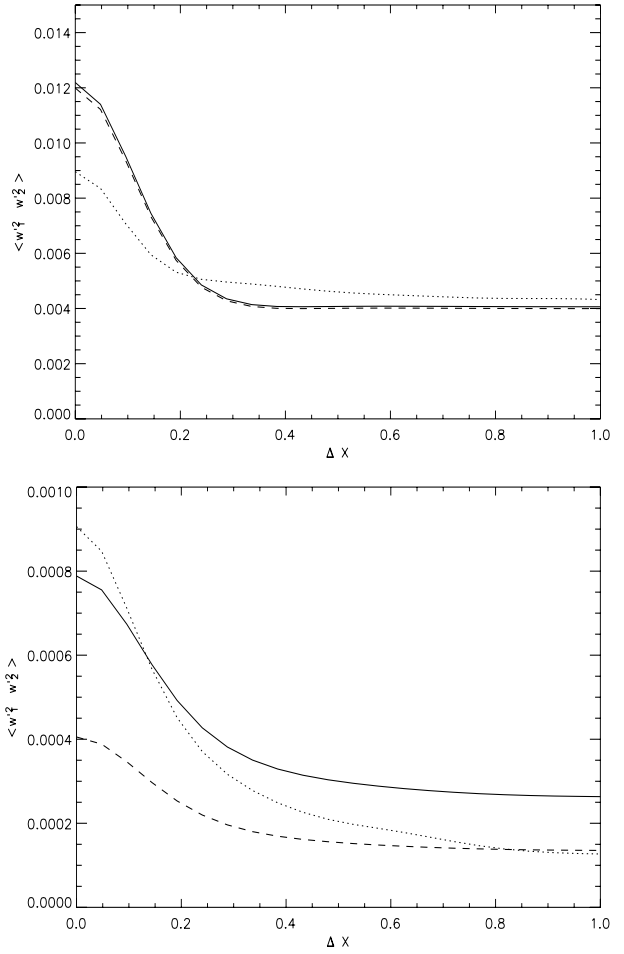


Fig. 2. Fourth-order correlation function calculated in the superadiabatic zone (at the top) and in the quasi-adiabatic zone (at the bottom) directly from the 3D numerical simulation (dotted line), using the QNA approximation (Eq. (6); dashed lines) and using the CMP (Eq. (7); solid line).

Eqs. (6) and (7) will introduce an energy excess injected into high-frequency p modes.

4. Calculation of the theoretical p mode excitation rates

The rate (P) at which energy is injected per unit time into a mode is calculated according to the set of Eqs. (4)–(6) when the QNA is used and Eqs. (4)–(7) using the CMP (see Sect. 4.1). The calculation thus requires the knowledge of four different types of quantities:

- 1) quantities that are related to the oscillation modes: the eigenfunctions (ξ_r) and associated eigenfrequencies (ω_0);
- 2) quantities that are related to the spatial and time-averaged properties of the medium: the density ρ_0 , the vertical velocity \bar{w} , the entropy \bar{s} , and $\alpha_s = \partial P_0 / \partial \bar{s}$;
- 3) quantities that contain information about spatial and temporal correlations of the convective fluctuations: $E(k)$, $E_s(k)$, and $\chi_k(\omega)$;
- 4) quantities that take anisotropies into account: a and Φ . The value of a is the mean horizontal fractional area of the updrafts (see Paper I), whereas Φ measures the anisotropy of

turbulence and is defined according to Gough (1977; see also Samadi & Goupil 2001, for details) as:

$$\Phi = \frac{\langle w^2 \rangle}{\langle u^2 \rangle}, \quad (8)$$

where $u^2 = w^2 + u_h^2$ and u_h is the horizontal velocity.

Both a and Φ are necessary to describe the flow because a measures the geometric anisotropy between up and downflows while Φ corresponds to the measure of the velocity anisotropies. However, these two quantities are linked because of mass conservation. An explicit relation can be easily derived between them using the formalism developed in Paper I to obtain

$$\Phi = \frac{a(1-a)\delta w^2 + a\langle \tilde{w}^2 \rangle_u + (1-a)\langle \tilde{w}^2 \rangle_d}{a(1-a)\delta w^2 + a\langle \tilde{u}^2 \rangle_u + (1-a)\langle \tilde{u}^2 \rangle_d} \quad (9)$$

where the $\tilde{\cdot}$ refers to the velocities of only one flow (updraft or downdraft) and δw is defined as in Paper I. For consistency reason, a and Φ are provided by the 3D numerical simulation.

4.1. The solar case

Calculations of the eigenfrequencies and eigenfunctions (in point 1) above) are performed as in Samadi et al. (2003b) on the basis of a 1D solar model built according to Gough's (1977) non-local formulation of the mixing-length theory (GMLT hereafter).

The spatial and time-averaged quantities in point 2) are obtained from a 3D simulation of the solar surface. The 3D simulations used in this work were built with Stein & Nordlund's 3D numerical code (see Stein & Nordlund 1998; Samadi et al. 2003a). Two simulations with different spatial mesh grids are considered, namely $253 \times 253 \times 163$ and $125 \times 125 \times 82$, in order to verify that the results are not sensitive to the spatial mesh resolution.

Finally, for the quantities in point 3) the total kinetic energy contained in the turbulent kinetic spectrum, $E(k)$, its depth dependence, and its k -dependence are obtained directly from a 3D simulation of the uppermost part of the solar convective zone. It was found in Samadi et al. (2003a) from 3D simulations that a Gaussian – usually used for modelling χ_k – is inadequate: a Lorentzian fits the frequency dependence of χ_k best. Hence, we adopt a Lorentzian here for χ_k .

4.2. Calculation of the power injected into the solar p modes with the CMP

We use the generalized CMP for two-point correlation functions presented in Sect. 3.2 (Eq. (7)) to model the Reynolds-stress source term. By replacing Eq. (6) with Eq. (7) in Eq. (4), the calculation of C_R^2 (as in Samadi & Goupil 2001) yields:

$$C_R^2 = \frac{64}{15} \pi^3 \int_0^M dm \left(1 + \frac{1}{3} S_w^2\right) \rho_0 \left(\frac{d\xi_r}{dr}\right)^2 \int_0^\infty dk \times \int_{-\infty}^\infty d\omega \frac{E^2(k)}{k^4} \chi_k(\omega_0 + \omega, r) \chi_k(\omega, r). \quad (10)$$

Equation (10) shows that the CMP causes an increase in the power injected into p modes in comparison with calculation using only the QNA. On the other hand, the entropy source term, C_S^2 , is still computed using the QNA closure model (see Samadi & Goupil 2001, for details).

5. Observational data and inferring observed excitation rates

The observational data set selected here for comparison with theoretical calculations was obtained with the GOLF instrument, onboard SOHO. GOLF (Gabriel et al. 1997) is a spectrometer measuring velocities of the photosphere integrated over the whole solar disc. Its location on the space platform yields a very good signal-to-noise ratio and also continuous observations (the actual duty cycle reaches almost 100%). This latter characteristic greatly improves the signal to noise ratio in the Fourier spectrum.

However, GOLF suffers from some technical problems, which restricts the measurements to one wing of the Na D₁ line instead of both wings. This results in a more difficult absolute calibration of the measured velocity and thus a possible bias (which does not exceed 20% in terms of the acoustic rate of excitation). Characteristics of the data set used here are described in Baudin et al. (2005).

These observations correspond to two periods when GOLF was observing in the same instrumental configuration (blue wing of the Na line) with a duration of 805 and 668 days, starting on April 11, 1996 and November 11, 2002, respectively. The level of solar activity was different during these two periods, but the measured excitation rate shows no dependence on activity, as the increase in width compensates for the decrease in height of the peaks, as shown by Chaplin et al. (2000) or Jiménez-Reyes et al. (2003).

The GOLF results were compared to BiSON observations and are compatible with them over a wide frequency range. A discrepancy appears at high frequency ($\nu > 3.2$ mHz). As the height and width of peaks in the Fourier spectrum are affected by the presence of noise and gaps in the data (see Chaplin et al. 2003), GOLF was chosen for the comparison model/observations. We consider only the $\ell = 1$ modes for which their properties (line-width, amplitude) are more accurately determined than the $\ell = 0$ modes (see Baudin et al. 2005, for details).

In order to compare theoretical results and observational data, the mode excitation rates are inferred from the observations according to the relation

$$P_{\text{obs}}(\omega_0) = 2\pi \Gamma_\nu \mathcal{M} v_s^2(\omega_0) \quad (11)$$

where $\mathcal{M} \equiv I/\xi_r^2(h)$ is the mode mass, h the height above the photosphere where oscillations are measured, $\Gamma_\nu = \eta/\pi$ the mode linewidth at half maximum (in Hz), and v_s^2 the mean square of the mode surface velocity. The last is derived from the observations according to

$$v_s^2 = \pi H \Gamma_\nu C_{\text{obs}} \quad (12)$$

where H is the maximum height of the mode profile in the power spectrum and C_{obs} the multiplicative constant factor that depends on the observation technique (see Baudin et al. 2005). Equation (12) supposes that the mode line profiles are symmetric, but it is well known that the mode profile deviates from a Lorentzian. However, Baudin et al. (2005) show that this equation is accurate enough for the evaluation of the mean square of the mode velocity, Eq. (12). On the other hand, the mode asymmetry is taken into account when determining mode line widths from observational data.

The mode mass is very sensitive to altitude at high frequency (see Fig. 1 of Baudin et al. 2005), so the layer (h) where the mode mass is evaluated must be properly estimated to derive correct values of the excitation rates. Indeed, solar seismic observations

in Doppler velocity are usually measured from a given spectral line. The layer where oscillations are measured then depends on the height where the line is formed. The GOLF instrument uses the Na I D 1 and D 2 lines whose height of formation is estimated at the height $h \approx 340$ km (see Baudin et al. 2005).

As an alternative to comparing theoretical results and observational data, Chaplin et al. (2005) propose to derive the maximum height of the mode profile (H) from the theoretical excitation rates and the observed mode line width according to the relation:

$$H = \frac{P}{2\pi^2 M \Gamma_\nu^2 C_{\text{obs}}}, \quad (13)$$

where $C_{\text{obs}} = 2.59$ for $\ell = 1$ modes.

Representation of the excitation rates themselves (Eq. (11)) emphasises disagreement at high frequencies, whereas disagreement at low frequency is more apparent with a representation using the profile height (Eq. (13)). Note that in the case of the observable height, only the slopes are the meaningful quantities, as the amplitude magnitude depends on the phase of the solar cycle when the observations were recorded.

As the maximum height H strongly depends on the observation technique, one cannot compare values of H coming from two different instruments. In Fig. 6, we therefore plot the product HC_{obs} , a quantity that is less dependent on the observational data (but still through M). Note that for ease of notation, HC_{obs} is noted H in the following.

It is important to stress that the mode height (H) calculated from the theoretical excitation rates (Eq. (11)) depends on the observations through the line width Γ_ν . This is why in Figs. 5 and 6 error bars appear in the theoretical results. In any case, the observational data can be characterised by at least three main features that the theoretical calculations (see above) must reproduce:

1. the frequency dependence from low to medium frequencies ($\nu < 3$ mHz);
2. the maximum of amplitude at 3 mHz for H and the slope for frequencies between 3 and 4 mHz or a nearly flat maximum between $\nu \approx 3.8$ mHz and 4 mHz for P ;
3. the slope at very high frequencies $\nu > 4$ mHz.

6. Comparison between theoretical and observed excitation rates

6.1. Turbulent Reynolds stress contribution

Figure 3 compares the observed power P injected into solar p modes with the theoretical one computed with only the turbulent Reynolds stress term assuming either the CMP or the QNA closure models. Figure 4 shows the associated heights H as computed according to Eq. (13). The comparison shows that the closure model has a significant effect on the resulting excitation rates. Indeed, the CMP induces an increase in the energy injected into the mode by about a factor two in comparison with the QNA closure model and brings the theoretical excitation rates closer to the observational ones. This energy increase is not uniform in terms of frequencies, due to the variation in the skewness with the depth (z) (see Paper I for details) and to the fact that the mean square velocity amplitudes of the turbulent elements decrease with depth. Indeed, at the top of the convection zone where the highest frequency modes are confined, the inefficiency of the convective transport causes an increase in the

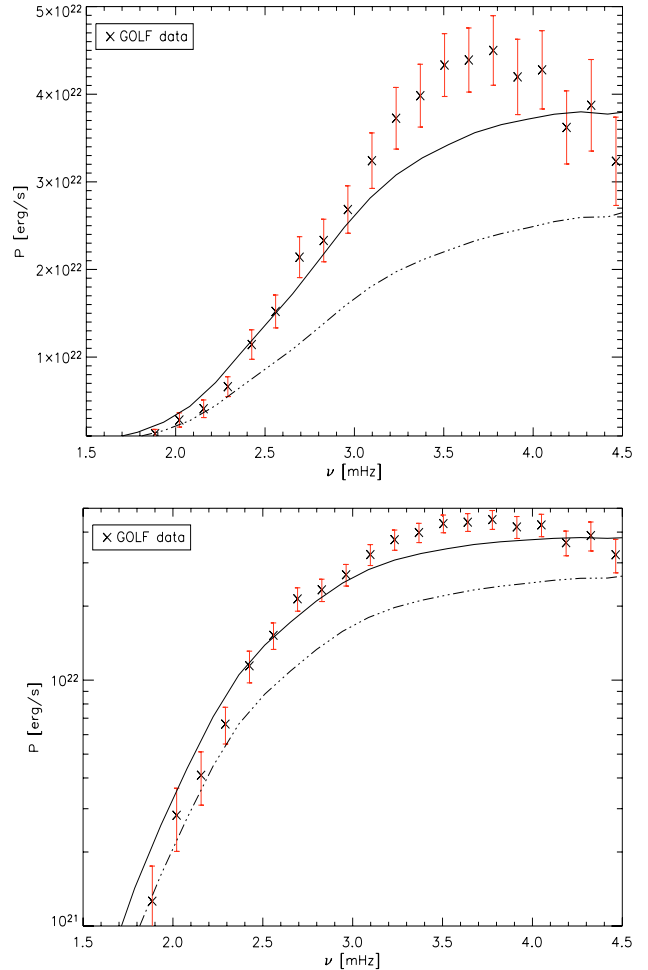


Fig. 3. Rate P at which acoustic energy is injected into the solar radial modes. *Only the Reynolds stress contribution is computed.* Cross dots represent P computed from Baudin et al. (2005) solar seismic data from the GOLF instrument (see Sect. 5). The associated error bars take into account uncertainties both from the line width (Γ_ν) and from the maximum height of the mode profile (H). The curves represent theoretical values of P computed as explained in Sect. 4: dash-dotted lines correspond to the calculation of P using the QNA closure model, and solid lines represent P using the CMP for the Reynolds stress term. We present the results in linear (at the top) and logarithmic scale (at the bottom).

velocities. Thus the effect of the flow anisotropy becomes dominant for such high-frequency modes.

At low frequencies ($\nu < 2.5$ mHz), the turbulent Reynolds stress contribution reproduces the observed power P (Fig. 3) within the observational uncertainties. As best emphasised in Fig. 4, it is possible that the theoretical results are slightly over-estimated, although this remains within the observational error bars.

At intermediate frequencies ($3 < \nu < 4$ mHz), the turbulent Reynolds stress term is not sufficient to reproduce the observations, so the additional excitation coming from entropy fluctuations is necessary.

At high frequencies ($\nu > 4$ mHz), Observational data seem to indicate a decrease in the power, which is not reproduced by the theoretical power.

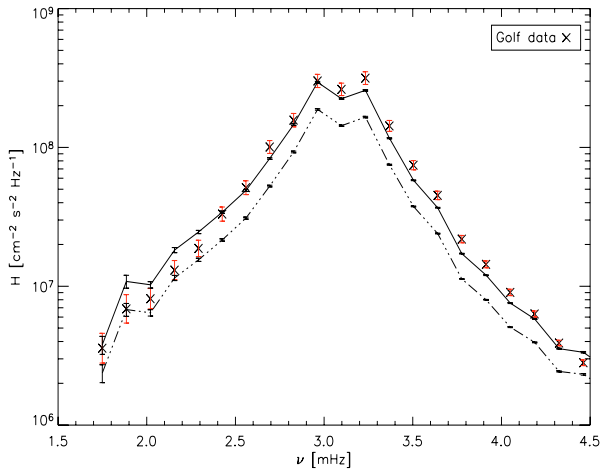


Fig. 4. Mode height H calculated as explained in Sect. 5 using only the Reynolds stress contribution. The solid (resp. dash-dotted) line represents H calculated with the CMP (resp. QNA) closure model, and cross-dots represent GOLF data with associated error bars. Error bars associated with the curves are due to mode line widths that are taken from observations (see Eq. (13)).

6.2. Adding the entropy fluctuation contribution

To proceed further, we add the C_2^S contribution (Eq. (5)). Results for the excitation rate and the maximum height are presented in Fig. 5. The additional (positive) entropy contribution causes an overall increase in the excitation rates as shown in Fig. 5. The theoretical modelling now reproduces the maximum of the power supplied to the modes when compared with the observational data. For the frequency behaviour of the excitation rate and height, Fig. 5 show:

At low frequency ($\nu \in [1.6 \text{ mHz}; 3 \text{ mHz}]$). We pointed out in Sect. 6.1 that the contribution from the Reynolds stress term can be sufficient for reproducing the GOLF data, perhaps even overestimating it. The combination of both Reynolds stress and entropy fluctuation is too large compared with the observation, and the resulting slope differs from the observational one in this frequency domain. Note however, that in Fig. 5 error bars represent 1σ error bars (Fig. 5).

For intermediate and high frequencies ($\nu \in [3; 4] \text{ mHz}$), the Reynolds (CMP) and entropy excitation model reproduces the ν variation in P . This is confirmed with the H representation (Fig. 5 at the bottom). However from a theoretical point of view, the description of the behaviour at high frequencies ($\nu > 4 \text{ mHz}$) is more complicated because these p modes are mainly excited in the superadiabatic zone, which is difficult to model properly. On the observational side, it must be kept in mind that even data with a signal-to-noise ratio as good as GOLF lead to linewidths difficult to measure at high frequencies.

7. Discussions and conclusions

We use a closure model (CMP, Paper I) that is more realistic than the usual QNA approximation to model the correlation products in a semi-analytical description of the excitation process of solar p modes. The present excitation model gives the theoretical slope of the power at intermediate and high frequencies ($\nu \in [2.5 \text{ mHz}; 4 \text{ mHz}]$), which agrees with the observed data. We also find that including the CMP causes a global increase in the injected power. This brings the power computed with the

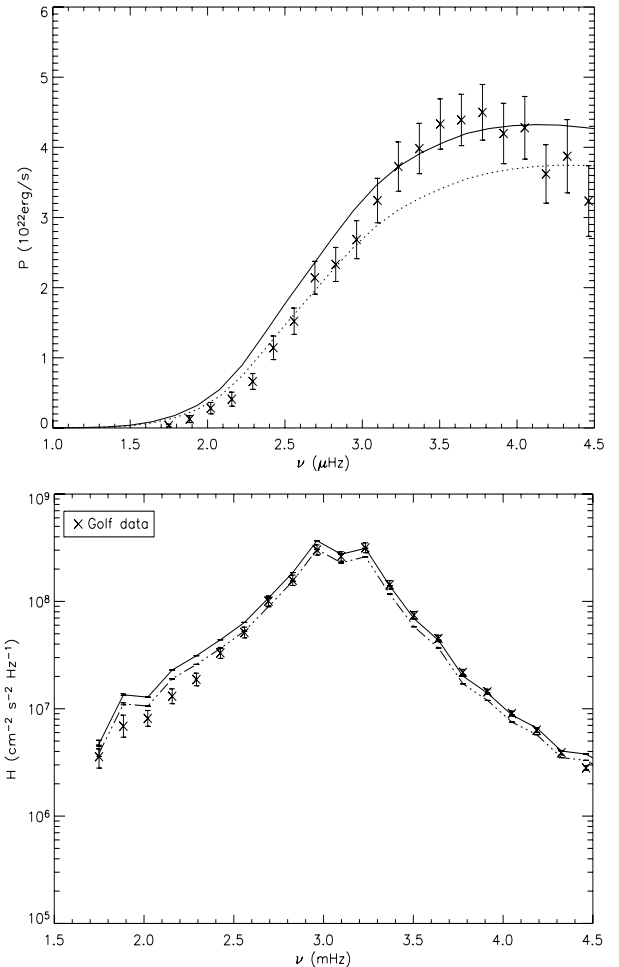


Fig. 5. Top: rate (P) at which acoustic energy is injected into the solar radial modes as a function of frequency. Cross dots represent P computed from the Baudin et al. (2005) solar seismic data from the GOLF instrument (see Sect. 5). The curves represent theoretical values of P computed as explained in Sect. 4: the solid line represents P using both the Reynolds stress (using the CMP) and entropy source contributions. The dotted line corresponds to the calculation for the Reynolds stress term only (using the CMP). Bottom: mode height (H) calculated as explained in Sect. 5. The solid line represents H calculated with the CMP closure model, using the Reynolds stress and entropy fluctuation contributions. The dotted line represents H computed with the CMP closure model, using only the Reynolds stress contribution. Cross-dots represent GOLF data with the associated error bars. Error bars associated with the curves are due to mode line widths that are taken from observations (see Eq. (13)). Only observations near minimum solar activity have been used, and they correspond to the second period as explained in Sect. 5.

Reynolds stress contribution alone closer to (although, at intermediate frequency, still below) the observations. On the other hand, the power obtained by including both the Reynolds stress and the entropy fluctuation contributions reproduces the observations at the maximum of the excitation rates. The comparison can now be made in linear scale, hence at lower frequencies there is still a small over-estimation (which amounts roughly to a few per cents and the errors bars represent 1σ error bars). The reason for this overestimation cannot be attributed to the CMP. Indeed, the Reynolds stress contribution was compared to the

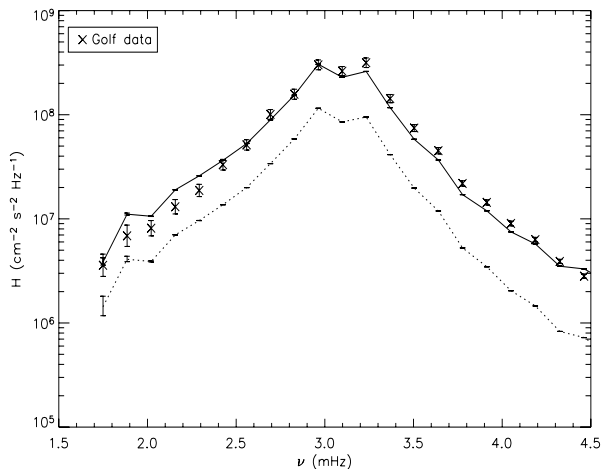


Fig. 6. Mode height H calculated as explained in Sect. 5 using only the Reynolds stress contribution. Solid lines represent H calculated with the CMP closure model and dots-line is the same except that a Gaussian is used for χ_k . Crosses represent GOLF data with associated error bars. Error bars associated with the curves are due to mode line widths which are taken from observation (see Eq. (13)).

3D numerical simulation (see Paper I), and the one-point fourth-order moment $\langle w^4 \rangle$ was found to agree with the simulation result. The remaining departure from the numerical simulation shows that the CMP actually underestimates the FOM in the quasi-adiabatic region, so correcting for this bias would result in an even larger overestimation of the power.

Various sources of discrepancies are likely to exist: the separation of scales used in the formalism that consists in assuming that the stratification and the oscillations have characteristic scale lengths larger than the eddies contributing to the excitation (see Samadi & Goupil 2001, for details). The physical description of the outer layers in the 1D solar model can also play an important role directly through the velocity and indirectly through the eigenfunctions. In this paper, we use Gough's (1977) non-local formulation of the mixing-length theory which shows an improvement in comparison with the local formulations in terms of the maximum of power P (Samadi et al. 2006) by about a few percent. Concerning the excitation model itself, some improvements in the modelling of Reynolds and entropy contributions that ought to be investigated are outlined below.

7.1. Turbulent Reynolds stress tensor contribution shortages

At low frequencies, a possibly small overestimation of the Reynolds stress contribution can be attributed to the frequency dependent factor (χ_k , see Eq. (10) in Sect. 4.1). Chaplin et al. (2005) use a Gaussian χ_k whereas Samadi et al. (2003b) use a Lorentzian factor. In Fig. 6, we present the calculation assuming a Gaussian and a Lorentzian for χ_k . As shown there, the frequency-dependent factor χ_k is likely between these two regimes. In the quasi-adiabatic convection zone, plumes are well-formed, and the convective system must be treated as composed of two flows (see Paper I). Hence, the upflows that are less turbulent can be modelled by a white noise (Gaussian), but downflows are turbulent creating a departure from a Gaussian. We expect this effect to cause a decrease in the theoretical power and bring it closer to the observation. A rough idea can be obtained by taking this effect into account as follows: we split the computation of the power supplied into the modes into two

parts. Those parts correspond to upflow (χ_k : Gaussian) and to downflows (χ_k : Lorentzian). The result indicates a decrease in the power at low frequency, which brings the theoretical power closer to the observation. This is true mainly for low-frequency modes, which are less sensitive to the superadiabatic zone where plumes are formed, because this region cannot be modelled by such a simple model. This issue needs further investigation.

7.2. Entropy source contribution shortages

In the present model, the turbulent entropy fluctuations are assumed to behave as a passive scalar, in other words, the entropy fluctuations are assumed to be advected by the turbulent velocity field without dissipation. It means that the entropy field does not have any effect on the velocity field.

This assumption associated with the QNA has the advantage of simplifying the closure of the fourth-order moments involving the entropy fluctuations (see Eq. (3.1)). However the biases introduced by this assumption remain to be evaluated. If the biases turn out to be large, alternative models must be developed.

7.3. Perspectives

Finally, we stress that there is an additional dependency, the coefficient a , which is the mean fractional area of updraft on the horizontal plane (see Eq. (9)). It is a measure of the asymmetry of the flows and a small variation in its value plays a major role on the excitation rates. This parameter has been fixed here using the results of 3-D simulations. The influence of parameter a is very important, as a small variation of its value leads to an increase in power P through the skewness S_w (see Paper I). It is beyond the scope of this paper to estimate the true effect of a variation in this parameter because its value is linked to the physical properties of the flows through, for instance, conservation of the mass flux. Hence a consistent approach is to investigate a set of different numerical simulations.

The CMP closure model, indeed, strongly depends on the structure of the upper convection zone, which again emphasises that the structure of this region is very important in the theoretical prediction of the power injected into the p modes, because the skew introduced by the asymmetry increases with the departure of a from the value 0.5. It is then possible to obtain physical constraints on the asymmetry of the convection zone flows.

To understand what can affect a is therefore an important issue, and in near future it will be necessary to study the variation in a with the type of star and from a hydrodynamical point of view to determine what the main processes that are responsible for this asymmetry. One interesting issue is the influence of a magnetic field on this parameter: as described by Weiss et al. (2002) and Vögler et al. (2005), the effect of a strong magnetic field induces a reduction in the typical length scale of convection, as well as the structure of the flows (hence the value of a).

The study of the mean fractional area a as a function of the magnetic field intensity therefore represents an interesting perspective for characterising B from the excitation rates, at least for stars with an expectedly strong magnetic field.

Acknowledgements. We are indebted to J. Leibacher for his careful reading of the manuscript and his helpful remarks. We thank Å Nordlund and R. F. Stein for making their code available to us. Their code was made at the National Center for Supercomputer Applications and Michigan State University and supported by grants from NASA and NSF.

References

- Baudin, F., Samadi, R., Goupil, M.-J., et al. 2005, *A&A*, 433, 349
Belkacem, K., Samadi, R., Goupil, M., & Kupka, F. 2006, *A&A*, 460, 173
Chaplin, W. J., Elsworth, Y., Isaak, G. R., et al. 1998, *MNRAS*, 298, L7
Chaplin, W. J., Elsworth, Y., Isaak, G. R., Miller, B. A., & New, R. 2000, *MNRAS*, 313, 32
Chaplin, W. J., Houdek, G., Elsworth, Y., et al. 2005, *MNRAS*, 360, 859
Gabriel, A. H., Charra, J., Grec, G., et al. 1997, *Sol. Phys.*, 175, 207
Goldreich, P., & Keeley, D. A. 1977, *ApJ*, 212, 243
Goldreich, P., & Kumar, P. 1990, *ApJ*, 363, 694
Goldreich, P., Murray, N., & Kumar, P. 1994, *ApJ*, 424, 466
Gough, D. O. 1977, *ApJ*, 214, 196
Gryanik, V. M., & Hartmann, J. 2002, *J. Atm. Sci.*, 59, 2729
Jiménez-Reyes, S. J., García, R. A., Jiménez, A., & Chaplin, W. J. 2003, *ApJ*, 595, 446
Kraichnan, R. H. 1957, *Phys. Rev.*, 107, 1485
Lesieur, M. 1997, *Turbulence in fluids* (Kluwer Academic Publishers)
Osaki, Y. 1990, in *Lecture Notes in Physics: Progress of Seismology of the Sun and Stars*, ed. Y. Osaki, & H. Shibahashi (Springer-Verlag), 75
Rieutord, M., & Zahn, J.-P. 1995, *A&A*, 296, 127
Samadi, R., & Goupil, M. 2001, *A&A*, 370, 136
Samadi, R., Goupil, M., & Lebreton, Y. 2001, *A&A*, 370, 147
Samadi, R., Nordlund, Å., Stein, R. F., Goupil, M. J., & Roxburgh, I. 2003a, *A&A*, 404, 1129
Samadi, R., Nordlund, Å., Stein, R. F., Goupil, M. J., & Roxburgh, I. 2003b, *A&A*, 403, 303
Samadi, R., Kupka, F., Goupil, M. J., Lebreton, Y., & van't Veer-Menneret, C. 2006, *A&A*, 445, 233
Stein, R. F. 1967, *Sol. Phys.*, 2, 385
Stein, R. F., & Nordlund, A. 1998, *ApJ*, 499, 914
Stein, R. F., & Nordlund, Å. 2001, *ApJ*, 546, 585
Vögler, A., Shelyag, S., Schüssler, M., et al. 2005, *A&A*, 429, 335
Weiss, N. O., Proctor, M. R. E., & Brownjohn, D. P. 2002, *MNRAS*, 337, 293

Excitation of solar-like oscillations across the HR diagram

R. Samadi^{1,2}, D. Georgobiani³, R. Trampedach⁴, M. J. Goupil², R. F. Stein⁵, and Å. Nordlund⁶

¹ Observatório Astronómico UC, Coimbra, Portugal
e-mail: Reza.Samadi@obspm.fr

² Observatoire de Paris, LESIA, CNRS UMR 8109, 92195 Meudon, France

³ Center for Turbulence Research, Stanford University NASA Ames Research Center, Moffett Field, USA

⁴ Research School of Astronomy and Astrophysics, Mt. Stromlo Observatory, Cotter Road, Weston ACT 2611, Australia

⁵ Department of Physics and Astronomy, Michigan State University, Lansing, USA

⁶ Niels Bohr Institute for Astronomy Physics and Geophysics, Copenhagen, Denmark

Received 6 September 2006 / Accepted 14 November 2006

ABSTRACT

Aims. We extend semi-analytical computations of excitation rates for solar oscillation modes to those of other solar-like oscillating stars to compare them with recent observations

Methods. Numerical 3D simulations of surface convective zones of several solar-type oscillating stars are used to characterize the turbulent spectra as well as to constrain the convective velocities and turbulent entropy fluctuations in the uppermost part of the convective zone of such stars. These constraints, coupled with a theoretical model for stochastic excitation, provide the rate \mathcal{P} at which energy is injected into the p-modes by turbulent convection. These energy rates are compared with those derived directly from the 3D simulations.

Results. The excitation rates obtained from the 3D simulations are systematically lower than those computed from the semi-analytical excitation model. We find that \mathcal{P}_{\max} , the \mathcal{P} maximum, scales as $(L/M)^s$ where s is the slope of the power law and L and M are the mass and luminosity of the 1D stellar model built consistently with the associated 3D simulation. The slope is found to depend significantly on the adopted form of χ_k , the eddy time-correlation; using a Lorentzian, χ_k^L , results in $s = 2.6$, whereas a Gaussian, χ_k^G , gives $s = 3.1$. Finally, values of V_{\max} , the maximum in the mode velocity, are estimated from the computed power laws for \mathcal{P}_{\max} and we find that V_{\max} increases as $(L/M)^{sv}$. Comparisons with the currently available ground-based observations show that the computations assuming a Lorentzian χ_k yield a slope, sv , closer to the observed one than the slope obtained when assuming a Gaussian. We show that the spatial resolution of the 3D simulations must be high enough to obtain accurate computed energy rates.

Key words. convection – turbulence – Sun: oscillations – Hertzsprung-Russell (HR) and C-M – stars: variables: general – methods: numerical

1. Introduction

Stars with masses $M \lesssim 2 M_{\odot}$ have upper convective zones where stochastic excitation of p-modes by turbulent convection takes place as in the case of the Sun. As such, these stars are often referred to as *solar-like oscillating stars*. One of the major goals of the future space seismology mission CoRoT (Baglin & The Corot Team 1998), is to measure the amplitudes and the line-widths of these stochastically driven modes. From the measurements of the mode line-widths and amplitudes, it is possible to infer the rates at which acoustic modes are excited (see e.g. Baudin et al. 2005). Such measurements will then provide valuable constraints on the theory of stellar oscillation excitation and damping. In turn, improved models of excitation and damping will provide valuable information about convection in the outer layers of solar-like stars.

The mechanism of stochastic excitation has been modeled by several authors (e.g. Goldreich & Keeley 1977; Osaki 1990; Balmforth 1992; Goldreich et al. 1994; Samadi & Goupil 2001, for a review see Stein et al. 2004). These models yield the energy rate, \mathcal{P} , at which p-modes are excited by turbulent convection but require an accurate knowledge of the time averaged and – above all – the *dynamic* properties of turbulent convection.

Eddy time-correlations. In the approach of Samadi & Goupil (2001, hereafter Paper I), the *dynamic* properties of turbulent convection are represented by χ_k , the frequency component of the auto-correlation product of the turbulent velocity field; χ_k can be related to the convective eddy time-correlations. Samadi et al. (2003b, hereafter Paper III) have shown that the Gaussian function usually used for modeling χ_k is inappropriate and is at the origin of the under-estimation of the computed maximum value of the solar p-modes excitation rates when compared with the observations. On the other hand, the authors have shown that a Lorentzian profile provides the best fit to the frequency dependency of χ_k as inferred from a 3D simulation of the Sun. Indeed, values of \mathcal{P} computed with the model of stochastic excitation of Paper I and using a Lorentzian for $\chi_k = \chi_k^L$ is better at reproducing the solar seismic observations whereas a Gaussian function, χ_k^G , under-estimates the amplitudes of solar p-modes. Provided that such a non-Gaussian model for χ_k is assumed, the model of stochastic excitation is – for the Sun – rather satisfactory. An open question, which we address in the present paper, is whether such non-Gaussian behavior also stands for other solar-like oscillating stars and what consequences arise for the theoretical excitation rates, \mathcal{P} .

Stochastic excitation in stars more luminous than the Sun. In the last five years, solar-like oscillations have been detected

in several stars (see for instance the review by Bedding & Kjeldsen 2003). Theoretical calculations result in an *overestimation* of their amplitudes (see Kjeldsen & Bedding 2001; Houdek & Gough 2002). For instance, using Gough's (1976, 1977) non-local and time dependent treatment of convection, Houdek et al. (1999) have calculated expected values of V_{\max} , the maximum oscillation amplitudes, for different solar-like oscillating stars. Their calculations, based on a simplified excitation model, imply that V_{\max} of solar-type oscillations scale as $(L/M)^{1.5}$ where L and M are the luminosity and mass of the star (see Houdek & Gough 2002, hereafter HG02). A similar scaling law was empirically found earlier by Kjeldsen & Bedding (1995). As pointed out by HG02, all these scaling laws overestimate the observed amplitudes of solar-like oscillating stars hotter and more massive than the Sun (e.g. β Hydri, η Bootis, Procyon, ξ Hydrae). As the mode amplitude results from a balance between excitation and damping, this *overestimation* of the mode amplitudes can be attributed either to an overestimation of the excitation rates or an underestimation of the damping rates. In turn, any overestimation of the excitation rates can be attributed either to the excitation model *itself* or to the underlying convection model.

All the related physical processes are complex and difficult to model. The present excitation model therefore uses a number of approximations such as the assumption of incompressibility, and the scale length separation between the modes and the turbulent eddies exciting the modes. It has been shown that the current excitation model is valid in the case of the *Sun* (Paper III), but its validity in a broader region of the HR-diagram has not been confirmed until now.

Testing the validity of the theoretical model of stochastic excitation with the help of 3D simulations of the outer layers of stellar models is the main goal of the present paper. For that purpose, we compare the p-mode excitation rates for stars with different temperatures and luminosities as obtained by direct calculations and by the semi-analytical method as outlined below.

Numerical 3D simulations enable one to compute directly the excitation rates of p-modes for stars with various temperatures and luminosities. For instance this was already undertaken for the Sun by Stein & Nordlund (2001) using the numerical approach introduced in Nordlund & Stein (2001). Such calculations will next be called "direct calculations". They are time-consuming and do not easily allow massive computations of the excitation rates for stars with different temperatures and luminosities. On the other hand, an excitation model offers the advantage of testing separately several properties entering the excitation mechanism which are not well understood or modeled. Furthermore, once it is validated, it can be used for a large set of 1D models of stars.

As it was done for the Sun in Samadi et al. (2003c, hereafter Paper II) and Paper III, 3D simulations can also provide quantities which can be implemented in a formulation for the excitation rate \mathcal{P} , thus avoiding the use of the mixing-length approach with the related free parameters, and assumptions about the turbulent spectra. Such calculations will next be called "semi-analytical calculations".

We stress however that in any case, we cannot avoid the use of 1D models for computing accurate eigen-frequencies for the whole observed frequency range. In the present paper, the 1D models are constructed to be as consistent as possible with their corresponding 3D simulations, as described in Sect. 3.

This paper is organized as follows: in Sect. 2 we present the methods considered here for computing \mathcal{P} , that is the so-called "direct" method based on Nordlund & Stein's (2001) approach (Sect. 2.1) and the so-called "semi-analytical" method based on

the approach from Paper I, with modifications as presented in Papers II and III and in the present paper (Sect. 2.2).

Comparisons between direct and semi-analytical calculations of the excitation rates are performed in seven representative cases of solar-like oscillating stars. The seven 3D simulations all have the same number of mesh points. Section 3 describes these simulations and their associated 1D stellar models.

The 3D simulations provide constraints on quantities related to the convective fluctuations, in particular the eddy time-correlation function, χ_k , which, as stressed above, plays an important role in the excitation of solar p-modes. The function χ_k is therefore inferred from each simulation and compared with simple analytical function (Sect. 4).

Computations of the excitation rates of their associated p-modes are next undertaken in Sect. 5 using both the direct approach and the semi-analytical approach. In the semi-analytical method, we employ model parameters as derived from the 3D simulations in Sect. 4.

In Sect. 5.2 we derive the expected scaling laws for \mathcal{P}_{\max} , the maximum in \mathcal{P} , as a function of L/M with both the direct and semi-analytical methods and compare the results. This allows us to investigate the implications of such power laws for the expected values of V_{\max} and to compare our results with the seismic observations of solar-like oscillations in Sect. 5.3. We also compare with previous theoretical results (e.g. Kjeldsen & Bedding 1995; Houdek & Gough 2002).

We finally assess the validity of the present stochastic excitation model and discuss the importance of the choice of the model for χ_k in Sect. 6.

2. Calculation of the p-mode excitation rates

2.1. The direct method

The energy input per unit time into a given stellar acoustic mode is calculated numerically according to Eq. (74) of Nordlund & Stein (2001) multiplied by \mathcal{S} , the area of the simulation box, to get the excitation rate (in erg s^{-1}):

$$\mathcal{P}(\omega_0) = \frac{\omega_0^2 \mathcal{S}}{8 \Delta \nu \mathcal{E}_{\omega_0}} \left| \int_r dr \Delta \hat{P}_{\text{nad}}(r, \omega_0) \frac{\partial \xi_r}{\partial r} \right|^2 \quad (1)$$

where $\Delta \hat{P}_{\text{nad}}(r, \omega)$ is the discrete Fourier component of the non-adiabatic pressure fluctuations, $\Delta P_{\text{nad}}(r, t)$, estimated at the mode eigenfrequency $\omega_0 = 2\pi\nu_0$, ξ_r is the radial component of the mode displacement eigenfunction, $\Delta \nu = 1/T$ the frequency resolution corresponding to the total simulation time T and \mathcal{E}_{ω_0} is the mode energy per unit surface area defined in Nordlund & Stein (2001, their Eq. (63)) as:

$$\mathcal{E}_{\omega_0} = \frac{1}{2} \omega_0^2 \int_r dr \xi_r^2 \rho \left(\frac{r}{R} \right)^2. \quad (2)$$

Note that Eq. (1) corresponds to the direct calculation of PdV work of the non-adiabatic gas and turbulent pressure (entropy and Reynolds stress) fluctuations on the modes. The energy in the denominator of Eq. (1) is essentially the mode mass. The additional factor which turns it into energy is the mode squared amplitude which is arbitrary and cancels the mode squared amplitude in the numerator. For a given driving (i.e. PdV work), the variation of the mode energy is inversely proportional to the mode energy (see Sect. 3.2 of Nordlund & Stein 2001). Hence, for a given driving, the larger the mode energy (i.e., the mode mass or mode inertia) the smaller the excitation rate.

In Eq. (1) the non-adiabatic Lagrangian pressure fluctuation, $\Delta\hat{P}_{\text{nad}}(r, \omega)$, is calculated as the following: we first compute the non-adiabatic pressure fluctuations $\Delta P_{\text{nad}}(r, t)$ according to Eq. (A.3) in Appendix A. We then perform the temporal Fourier transform of $\Delta P_{\text{nad}}(r, t)$ at each depth r to get $\Delta\hat{P}_{\text{nad}}(r, \omega)$.

The mode displacement eigenfunction $\xi_r(r)$ and the mode eigenfrequency ω_0 are calculated as explained in Sect. 3. Its vertical derivative, $\partial\xi_r/\partial r$, is normalized by the mode energy per unit surface area, \mathcal{E}_{ω_0} , and then multiplied by $\Delta\hat{P}_{\text{nad}}$. The result is integrated over the simulation depth, squared and divided by $8\Delta v$. We next multiply the result by the area of the simulation box (S) to obtain \mathcal{P} , the total excitation rates in erg s^{-1} for the entire star. Indeed the nonadiabatic pressure fluctuations are uncorrelated on large scales, so that average ΔP_{nad}^2 is inversely proportional to the area. Multiplication by the area of the stellar simulation gives the excitation rates for the entire star as long as the domain size is sufficiently large to include several granules.

2.2. The semi-analytical method

Calculations of excitation rates by the semi-analytical method are based on a model of stochastic excitation. The excitation model we consider is the same as presented in Paper I. In this model of excitation and in contrast to previous models (e.g. Goldreich & Keeley 1977; Balmforth 1992; Goldreich et al. 1994), the driving by turbulent convection is ensured not only by the Reynolds stress tensor but also by the advection of the turbulent fluctuations of entropy by the turbulent movements (the so-called entropy source term).

As in Paper I, we consider only radial p-modes. We do not expect any significant differences for low ℓ degree modes. Indeed, in the region where the excitation takes place, the low ℓ degree modes have the same behavior as the radial modes. Only for very high ℓ degree modes ($\ell \gg 100$) – which will not be seen in stars other than the Sun – can a significant effect be expected, as is quantitatively confirmed (work in progress).

The excitation rates are computed as in Paper II, except for the change detailed below. The rate at which a given mode with frequency $\omega_0 = 2\pi\nu_0$ is excited is then calculated with the set of Eqs. (1)–(11) of Paper II. These equations are based on the excitation model of Paper I, but assume that injection of acoustic energy into the modes is isotropic. However, Eq. (10) of Paper II must be corrected for an analytical error (see Samadi et al. 2005). This yields the following correct expression for Eq. (10) of Paper II:

$$S_R(r, \omega_0) = \int_0^\infty \frac{dk}{k^2} \frac{E(k, r)}{u_0^2} \frac{E(k, r)}{u_0^2} \times \int_{-\infty}^{+\infty} d\omega \chi_k(\omega_0 + \omega, r) \chi_k(\omega, r) \quad (3)$$

where $u_0 = \sqrt{\Phi/3} \bar{u}$, Φ is Gough's (1977) anisotropy factor, \bar{u} is the rms value of \mathbf{u} , the turbulent velocity field, k the wavenumber and $\chi_k(\omega)$ is the frequency component of the correlation product of \mathbf{u} .

The method then requires the knowledge of a number of input parameters which are of three different types:

- 1) Quantities which are related to the oscillation modes: the eigenfunctions (ξ_r) and associated eigen-frequencies (ω_0).
- 2) Quantities which are related to the spatial and time averaged properties of the medium: the mean density (ρ_0), $\alpha_s \equiv \langle (\partial p / \partial s)_\rho \rangle$ – where s is the entropy, p the gas pressure and $\langle \dots \rangle$ denotes horizontal and time averages – the mean square

of the vertical component of the convective velocity, $\langle w^2 \rangle$, the mean square of the entropy fluctuations, $\langle \tilde{s}^2 \rangle$, and the mean anisotropy, Φ (Eq. (2) of Paper II).

- 3) Quantities which contain information about spatial and temporal auto-correlations of the convective fluctuations: the spatial spectrum of the turbulent kinetic energy and entropy fluctuations, $E(k)$ and $E_s(k)$, respectively, as well as the temporal spectrum of the correlation product of the turbulent velocity field, χ_k .

Eigen-frequencies and eigenfunctions (in 1) above) are computed with the adiabatic pulsation code ADIPLS (Christensen-Dalsgaard & Berthomieu 1991) for each of the 1D models associated with the 3D simulations (see Sect. 3).

The spatial and time averaged quantities (in 2) and 3) above) are obtained from the 3D simulations in the manner of Paper II. For $E(k)$, however, we use the actual spectrum as calculated from the 3D simulations and not an analytical fit as was done in Paper II. However as in Paper II, we assume for $E_s(k)$ the k -dependency of $E(k)$ (we have checked this assumption for one simulation and found no significant change in \mathcal{P}).

For each simulation, we determine χ_k as in Paper III (cf. Sect. 4). Each χ_k is then compared with various analytical forms, among which some were investigated in Paper III. Finally we select the analytical forms which are the closest to the behavior of χ_k and use them, in Sect. 5, to compute \mathcal{P} .

3. The convection simulations and their associated 1D models

Numerical simulations of surface convection for seven different solar-like stars were performed by Trampedach et al. (1999). These hydrodynamical simulations are characterized by the effective temperature, T_{eff} and acceleration of gravity, g , as listed in Table 1. The solar simulation with the same input physics and number of mesh points is included for comparison purposes. The surface gravity is an input parameter, while the effective temperature is adjusted by changing the entropy of the inflowing gas at the bottom boundary. The simulations have $50 \times 50 \times 82$ grid points. All of the models have solar-like chemical composition, with hydrogen abundance $X = 0.703$ and metal abundance $Z = 0.0145$. The simulation time-series all cover at least five periods of the primary p-modes (highest amplitude, one node at the bottom boundary), and as such should be sufficiently long.

The convection simulations are shallow (only a few percent of the stellar radius) and therefore contain only few modes. To obtain mode eigenfunctions, the simulated domains are augmented by 1D envelope models in the interior by means of the stellar envelope code by Christensen-Dalsgaard & Frandsen (1983a). Convection in the envelope models is based on the mixing-length formalism (Böhm-Vitense 1958).

Trampedach et al. (2006a) fit 1D stellar envelopes to average stratifications of the seven convection simulations by matching temperature and density at a common pressure point near the bottom of the simulations. The fitting parameters are the mixing-length parameter, α , and a form-factor, β , in the expression for turbulent pressure: $P_{\text{turb}}^{\text{1D}} = \beta \rho u_{\text{MLT}}^2$, where u_{MLT} is the convective velocities predicted by the mixing-length formulation. A consistent matching of the simulations and 1D envelopes is achieved by using the same equation of state (EOS) by Däppen et al. (1988, also referred to as the MHD EOS, with reference to Mihalas, Hummer, and Däppen) and opacity distribution functions (ODF) by Kurucz (1992a,b), and also by using T - τ relations derived from the simulations (Trampedach et al. 2006b).

Table 1. Characteristics of the convection 3D simulations: t_{sim} is the duration of the relaxed simulations used in the present analysis, H_p is the pressure scale height at the surface, L_h the size of the box in the horizontal direction, C_s the sound speed and t_s the sound travel time across H_p . All the simulations have a spatial grid of $50 \times 50 \times 82$.

Star	t_{sim} [min]	size [Mm ³]	$\log g$	T_{eff} [K]	H_p [km]	L_h/H_p	C_s [km s ⁻¹]	t_s [s]	t_{sim}/t_s
α Cen B	59	$4.0 \times 4.0 \times 2.2$	4.5568	5363	95.	42.1	7.49	12.72	278.3
Sun	96	$6.0 \times 6.0 \times 3.4$	4.4377	5802	134	44.8	7.78	17.30	332.9
Star A	80	$11.6 \times 11.6 \times 6.4$	4.0946	4851	316	36.7	7.98	39.66	121.0
α Cen A	44	$8.9 \times 8.8 \times 5.1$	4.2946	5768	189	47.1	7.81	24.17	109.2
Star B	110	$20.7 \times 20.7 \times 11.3$	4.0350	6167	359	57.7	7.76	46.29	142.6
Procyon	119	$20.7 \times 20.7 \times 10.9$	4.0350	6470	380	54.5	7.52	50.50	141.4
η Boo	141	$36.9 \times 36.9 \times 16.3$	3.7534	6023	709	52.0	7.40	96.13	88.0

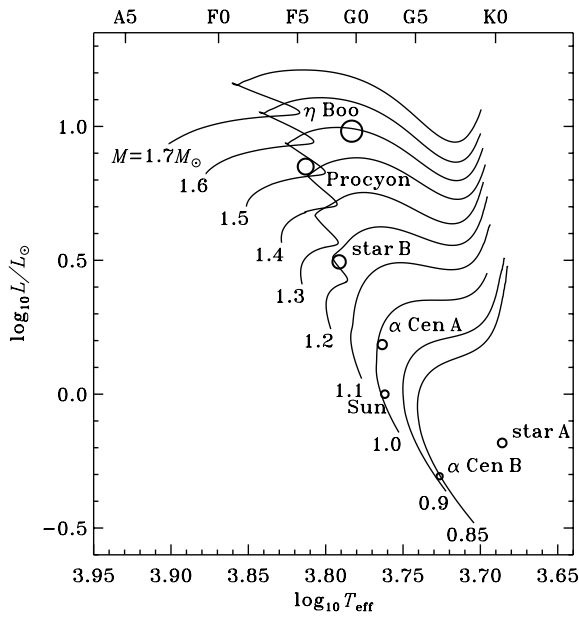


Fig. 1. Location of the convection simulations in the HR diagram. The symbol sizes vary proportionally to the stellar radii. Evolutionary tracks of stars, with masses as indicated, were calculated on the base of Christensen-Dalsgaard's stellar evolutionary code (Christensen-Dalsgaard 1982; Christensen-Dalsgaard & Frandsen 1983a).

The average stratifications of the 3D simulations, augmented by the fitted 1D envelope models in the interior, were used as the basis for the eigenmode calculations using the adiabatic pulsation code by Christensen-Dalsgaard & Berthomieu (1991). These combinations of averaged 3D simulations and matched 1D envelope models will, from hereon, be referred to as the 1D models.

The positions of the models in the HR diagram are presented in Fig. 1 and their global parameters are listed in Table 2. Five of the seven models correspond to actual stars, while Star A and Star B are merely sets of atmospheric parameters; their masses and luminosities are therefore assigned somewhat arbitrarily (the L/M -ratios, only depending on T_{eff} and g , are of course not arbitrary).

4. Inferred properties of χ_k

For each simulation, $\chi_k(\omega)$ is computed over the whole wavenumber (k) range covered by the simulations and at different layers within the region where modes are excited. We present the results at the layer where the excitation is maximum,

Table 2. Fundamental parameters of the 1D-models associated with the 3D simulations of Table 1.

Star	T_{eff} [K]	M/M_\odot	R/R_\odot	L/L_\odot	LM_\odot/ML_\odot
α Cen B	5363	0.90	0.827	0.51	0.56
Sun	5802	1.00	1.000	1.02	1.02
Star A	4852	0.60	1.150	0.66	1.10
α Cen A	5768	1.08	1.228	1.50	1.38
Star B	6167	1.24	1.769	4.07	3.28
Procyon	6470	1.75	2.102	6.96	3.98
η Boo	6023	1.63	2.805	9.31	5.71

i.e., where u_0 is maximum, and for two representative wavenumbers: $k = k_{\text{max}}$ at which $E(k)$ peaks and $k = 10 k_{\text{min}}$, where k_{min} is the first non-zero wavenumber of the simulations. Indeed, the amount of acoustic energy going into a given mode is largest at this layer and at the wavenumber $k \approx k_{\text{max}}$, provided that the mode frequency satisfies: $\omega_0 \lesssim (k_{\text{max}} u_0)$. Above $\omega_0 \sim k_{\text{max}} u_0$, the efficiency of the excitation decreases rapidly. Therefore low and intermediate frequency modes (i.e., $\omega_0 \lesssim k_{\text{max}} u_0$) are predominantly excited at $k \approx k_{\text{max}}$. On the other hand, high frequency modes are predominantly excited by small-scale fluctuations, i.e. at large k . The exact choice of the representative large wavenumber is quite arbitrary; however it cannot be too large because of the limited number of mesh points $k \lesssim 25 k_{\text{min}}$ and in any case, the excitation is negligible above $k \approx 20 k_{\text{min}}$. We thus chose the intermediate wavenumber $k = 10 k_{\text{min}}$. Figure 2 presents χ_k as obtained from the 3D simulations of Procyon, α Cen B and the Sun, at the layer where u_0 is maximum and for the wavenumber k_{max} . Although defined as a function of ω , for convenience, χ_k is plotted as a function of $\nu = \omega/2\pi$ throughout this paper. Figure 3 displays χ_k for $k = 10 k_{\text{min}}$. Results for the other simulations are not shown, as the results for Procyon, α Cen B and the Sun correspond to three representative cases.

In practice, it is not easy to implement directly in the excitation model the ν -variation of χ_k inferred from the 3D simulations. An alternative and convenient way to compute \mathcal{P} is to use simple analytical functions for χ_k which are chosen so as to best represent the 3D results. We then compare χ_k computed with the 3D simulations with the following simple analytical forms: the Gaussian form

$$\chi_k^G(\omega) = \frac{1}{\omega_k \sqrt{\pi}} e^{-(\omega/\omega_k)^2}, \quad (4)$$

the Lorentzian form

$$\chi_k^L(\omega) = \frac{1}{\pi \omega_k / 2} \frac{1}{1 + (2\omega/\omega_k)^2}, \quad (5)$$

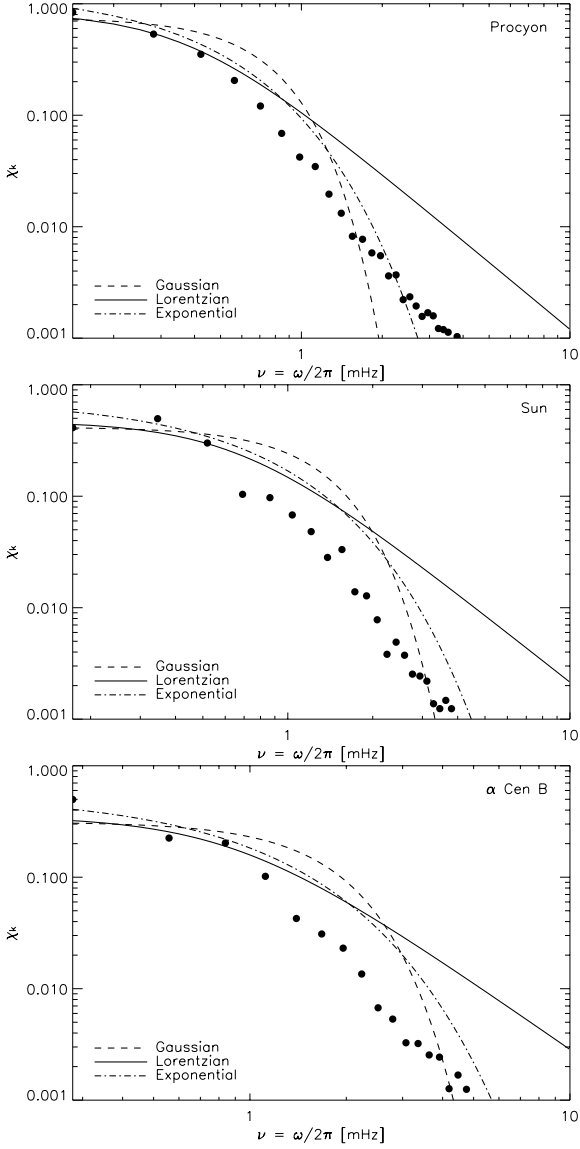


Fig. 2. The filled dots represent χ_k obtained from the 3D simulations for the wavenumber k at which $E(k)$ is maximum and at the layer where the excitation is maximum in the simulation. The results are presented for three simulations: Procyon (*top*), the Sun (*middle*) and α Cen B (*bottom*). The solid curves represent the Lorentzian form Eq. (5), the dashed curves the Gaussian form Eq. (4), and the dot dashed curves the exponential form Eq. (6).

and the exponential form

$$\chi_k^E(\omega) = \frac{1}{\omega_k} e^{-|\omega/\omega_k|}. \quad (6)$$

In Eqs. (4)–(6), ω_k is the line-width of the analytical function and is related to the velocity u_k of the eddy with wave number k as:

$$\omega_k \equiv 2ku_k. \quad (7)$$

In Eq. (7), u_k is calculated from the kinetic energy spectrum $E(k)$ as (Stein 1967)

$$u_k^2 = \int_k^{2k} dk E(k). \quad (8)$$

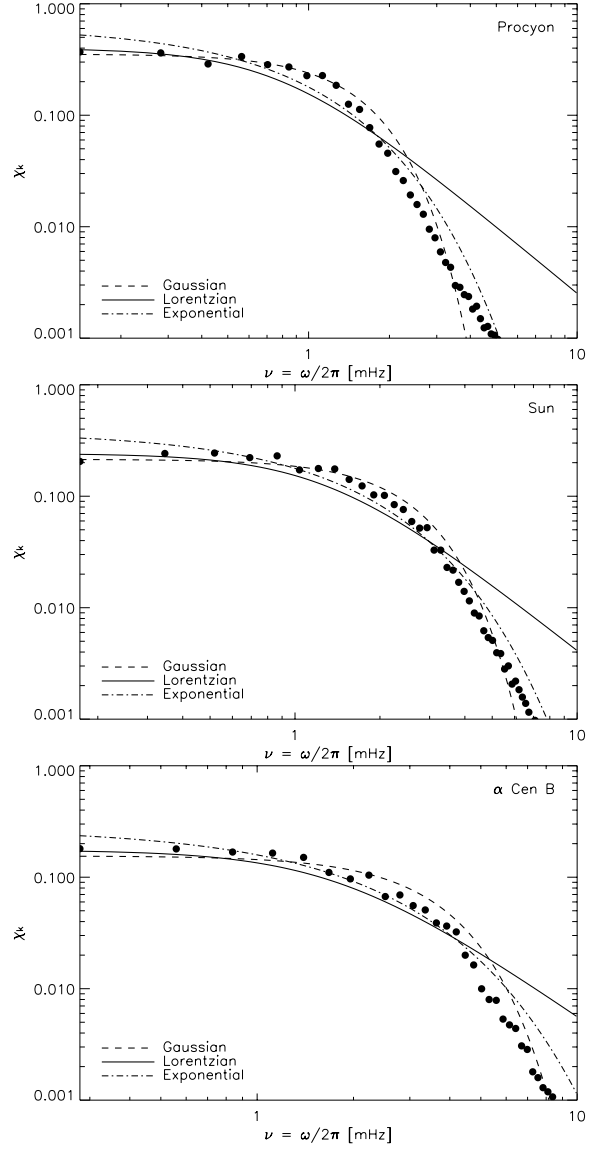


Fig. 3. Same as Fig. 2 for $k = 10 k_{\min}$ where k_{\min} is the first non-zero wavenumber of the simulation.

As shown in Figs. 2 and 3, the Lorentzian χ_k^L does not reproduce the ν -variation of χ_k satisfactorily. This is particularly true for the solar case. This contrast with the results of Paper III where it was found that χ_k^L reproduces nicely – at the wavenumber where E is maximum – the ν -variation of χ_k inferred from the solar simulation investigated in Paper III. These differences in the results for the solar case can be explained by the low spatial resolution of the present solar simulation compared with that of Paper III. Indeed we have compared different solar simulations with different spatial resolution and found that the ν -variation of χ_k converges to that of χ_k^L as the spatial resolution increases (not shown here). This dependency of χ_k with spatial resolution of the simulation is likely to hold for the non-solar simulations as well. This result then suggests that χ_k is in fact best represented by the Lorentzian form, χ_k^L .

As a consequence, realistic excitation rates evaluated directly for a convection simulation should be based on simulations with higher spatial resolution. However the main goal of the present work is to test the excitation model, which can be done with the

present set of simulations. Indeed, we only need to use as inputs for the excitation model the quantities related to the turbulent convection ($E(k), \chi_k, \dots$) as they are in the simulations, no matter how the real properties of χ_k are.

For the present set of simulations, we compare three analytical forms of χ_k : Lorentzian, Gaussian and exponential. For large k , χ_k is overall best modeled by a Gaussian (see Fig. 3 for $k = 10 k_{\min}$). For small k (see Fig. 2 for $k = k_{\max}$) both the exponential and the Gaussian are closer to χ_k than the Lorentzian.

For a given simulation, depending on the frequency, differences between $\chi_k(\nu)$ and the analytical forms are more or less pronounced.

The discrepancy between $\chi_k(\nu)$ inferred from the 3D simulations and the exponential or the Gaussian forms vary systematically with stellar parameters; decreasing as the convection gets more forceful, as measured by, e.g., the turbulent-to-total-pressure ratio. Of the three simulations illustrated in Fig. 2, Procyon has the largest and α Cen B has the smallest $P_{\text{turb}}/P_{\text{tot}}$ ratio.

As a whole for the different simulations and scale lengths k , we conclude that the ν -variation of χ_k in the present set of simulations lies between that of a Gaussian and an exponential. However, neither of them is completely satisfactory. Actually a recent detailed study by Georgobiani et al. (2006, in preparation) tends to show that χ_k cannot systematically be represented at all wavenumbers by a simple form such as a Gaussian, an exponential or a Lorentzian, but rather needs a more generalized power law. Hence, more sophisticated fits closer to the simulated ν -variation of χ_k could have been considered, but for the sake of simplicity we chose to limit ourselves to the three forms presented here.

5. p-mode excitation rates across the HR diagram

5.1. Excitation rate spectra ($\mathcal{P}(\nu)$)

For each simulation, the rates \mathcal{P} at which the p-modes of the associated 1D models are excited are computed both directly from the 3D simulations and with the semi-analytical method (see Sect. 2). In this section, the semi-analytical calculations are based on two analytical forms of χ_k : a Gaussian and an exponential form as described in Sect. 4. The Lorentzian form as introduced in Sect. 4 is not investigated in the present section. Indeed our purpose here is to test the model of stochastic excitation by using constraints from the 3D simulations, and a Lorentzian behaviour is never obtained in the present 3D simulations.

The results of the calculations of \mathcal{P} using both methods are presented in Fig. 4 for the six most representative simulations. In order to remove the large scattering in the direct calculations, we perform a running mean over five frequency bins. The results of this averaging are shown by dot-dashed lines. The choice of five frequency bins is somewhat arbitrary. However we notice that between 2 to 10 frequency bins, the maximum and the shape of the spectrum do not significantly change.

Comparisons between direct and semi-analytical calculations using either χ_k^G or χ_k^E all show systematic differences: the excitation rates obtained with the direct calculations are systematically lower than those resulting from the semi-analytical method. These systematic differences are likely due to the too low spatial resolution of the 3D simulations which are used here (see Sect. 5.2 below).

At high frequency, the use of χ_k^E instead of χ_k^G results in larger \mathcal{P} for all stars. This arises from the fact that χ_k^E spreads slightly more energy at high frequency than χ_k^G does (see Fig. 2).

The largest difference between the two types of calculation (direct versus semi-analytical) is seen in the case of Procyon. Indeed, the simulation of Procyon shows a pronounced depression around $\nu \sim 1.5$ mHz. Such a depression is not seen in the semi-analytical calculations. The origin of this depression has not been clearly identified yet but is perhaps related to some interference between the turbulence and the acoustic waves which manifests itself in the pressure fluctuations in the 3D work integral but is not included in the semi-analytical description.

5.2. Influence of the 3D simulation characteristics

In order to assess the influence of the spatial resolution of the simulation on our results, we have at our disposal three other solar 3D simulations, with a grid of $253 \times 253 \times 163$, $125 \times 125 \times 82$ and $50 \times 50 \times 82$ (hereafter S1), and a duration of ~ 42 min, 70 min and 100 min, respectively.

We have computed the p-modes excitation rates according to the direct method for those three simulations. For each of those simulations we have also computed the excitation rates according to the semi-analytical method assuming either a Lorentzian χ_k or a Gaussian χ_k .

As shown in Fig. 5 (top), the excitation rates computed according to the direct calculation increase as the spatial resolution of the 3D simulation increases. The excitation rates computed with the 3D simulations with the two highest spatial resolutions reach approximately the same mean amplitude level, indicating that this level of spatial resolution is sufficient for the direct calculations.

We note that as the spatial resolution increases, the semi-analytical calculations using a Lorentzian χ_k decrease by a factor ~ 2 (not shown here). The differences in the semi-analytical calculations based on the $253 \times 253 \times 163$ simulation and the $125 \times 125 \times 82$ simulation are found very small, indicating that this level of spatial resolution is sufficient for the semi-analytical calculations too.

Finally, we note that the excitation rates obtained for the $50 \times 50 \times 82$ solar simulation (S1) are approximately two times smaller than excitation rates for the $50 \times 50 \times 82$ solar simulation otherwise used throughout this work (S0 hereafter). This difference is attributed to the fact that the two simulations do not correspond to the same realization. Indeed, as a test, we have extended the duration of the simulation S1 up to 500 min. The full time series has then been divided into subsets of equal duration of 100 min and p-mode excitation rates have been computed for each subset. We find that the maximum in the p-modes excitation rates $\mathcal{P}(\nu)$ oscillates from a subset to another about a mean value. The observed variations are large: the maximum in $\mathcal{P}(\nu)$ can be larger (smaller resp.) by ~ 1.5 (0.5 resp.) times the maximum in the power spectrum obtained by averaging the power spectra of all subsets. Hence we find that at low spatial resolution, different realizations yield excitation rates that are scattered about a mean value at each frequency. This dispersion is likely to be responsible for the factor of two difference between the excitation rate maxima obtained for the two realizations S0 and S1. This type of dependency of \mathcal{P} – with the starting time of the time series and its duration – is expected to be smaller for simulations with resolution higher than $50 \times 50 \times 82$, because of the larger number of excitation sources there. This will be studied in a subsequent work.

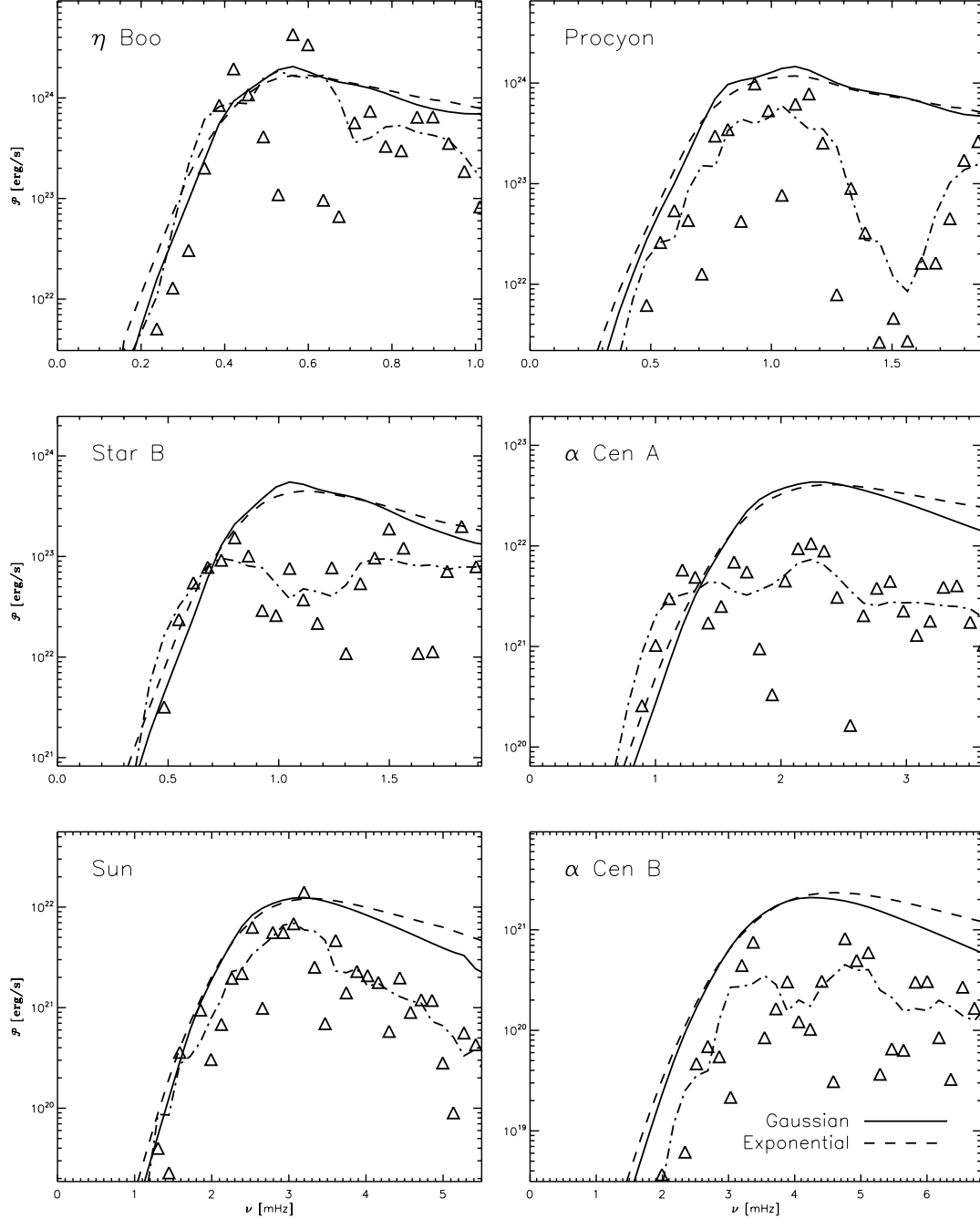


Fig. 4. Excitation rates, \mathcal{P} , are presented as functions of mode frequency for six of the seven convection simulations listed in Tables 1 and 2. Each triangle corresponds to a single evaluation of the 3D work integral estimated for a given eigenfrequency according to Eq. (1). The dot-dashed lines correspond to a running mean of the triangle symbols performed over five frequencies. The solid and dashed lines correspond to the excitation rates calculated with the semi-analytical method and using the Gaussian and the exponential forms of χ_k , respectively. All results shown are obtained as the sum of contributions from the two sources of excitation: excitation by the turbulent pressure and excitation by the non-adiabatic gas pressure.

5.3. Eddy-time correlation: Lorentzian versus Gaussian

As seen in Sect 5.2 above, the characteristics of the simulations influence the semi-analytical calculations of the mode excitation rates (through the input parameters which enter the semi-analytical calculations and which are taken from the 3D simulation). We want to compare the results of the semi-analytical calculations using χ_k^L with the semi-analytical calculations using

χ_k^G . It is then necessary to insert the 3D inputs in these calculations coming from simulations with the highest quality, here the highest available resolution.

Figure 5 (bottom) compares semi-analytical calculations using a Lorentzian χ_k with those using a Gaussian χ_k . All these semi-analytical calculations are here based on the energy spectrum of the simulation with the spatial resolution of $253 \times 253 \times 163$ (see Sect. 5.2).

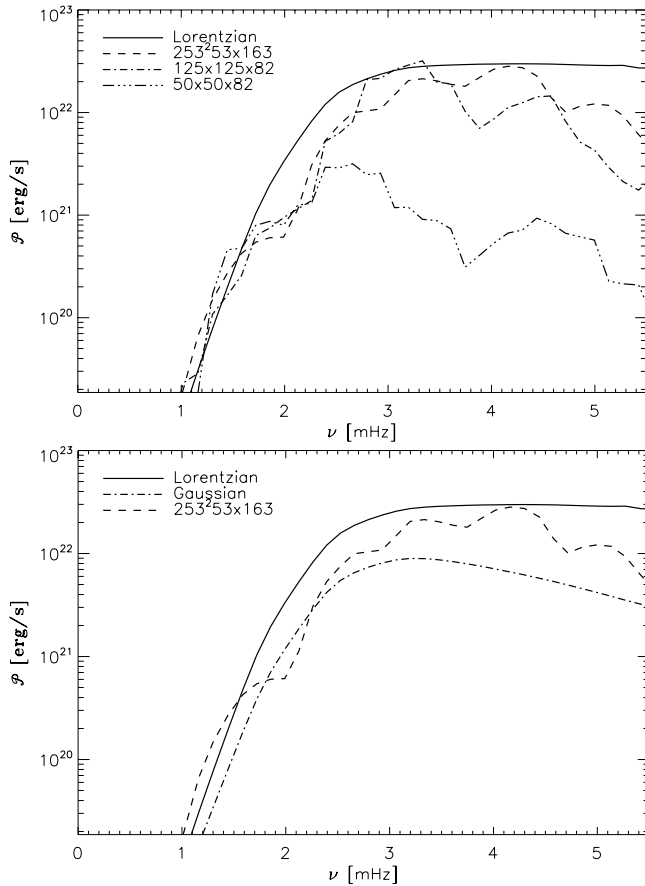


Fig. 5. *Top:* as in Fig. 4 for solar simulations only. The solid line corresponds to the semi-analytical calculations based on a Lorentzian χ_k and a simulation with a spatial resolution of $253 \times 253 \times 82$. The other lines are running means over five frequencies of the direct calculation based on solar simulations with different spatial resolution: $253 \times 253 \times 82$ (dashed line), $125 \times 125 \times 82$ (dot dashed line) and $50 \times 50 \times 82$ (dot dot dashed line). *Bottom:* the solid and dashed lines have the same meaning as in the top figure. The dot-dashed line corresponds to the semi-analytical calculations based on a Gaussian χ_k .

The average level of the excitation rates calculated according to the direct method and with the simulation with the highest spatial resolution is in between the semi-analytical calculations based on Lorentzian χ_k and those based on a Gaussian χ_k , nevertheless they are in general slightly closer to the semi-analytical calculations based on Lorentzian χ_k . This result is discussed in Sect. 6.2.1.

5.4. Maximum of \mathcal{P} as a function of L/M

Figure 6 shows \mathcal{P}_{\max} , the maximum in \mathcal{P} , as a function of L/M for the direct and the semi-analytical calculations.

The same systematic differences between the direct and the semi-analytical calculations as seen in Fig. 4 are of course observed here. Note that the differences slightly decrease with increasing values of L/M .

We have also computed the excitation rate with the semi-analytical method using χ_k^L . The maximum excitation rate as evaluated with χ_k^L is systematically larger than both the direct calculations and the semi-analytical results based on χ_k^G or χ_k^E .

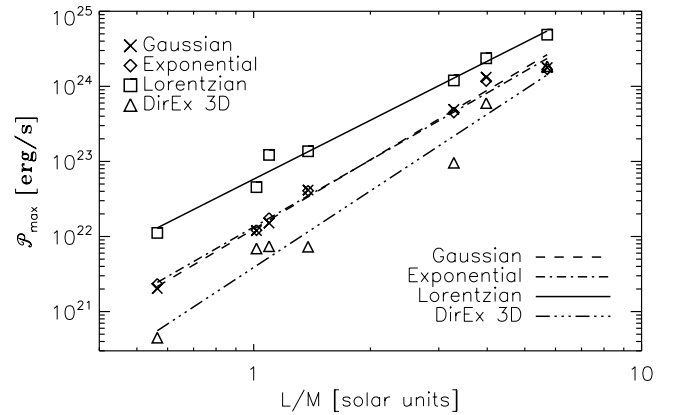


Fig. 6. \mathcal{P}_{\max} versus L/M where L is the luminosity and M is the mass of the 1D models associated with the 3D simulations. The triangles correspond to the direct calculations (labeled as “DirEx 3D” in the legend), and the other symbols correspond to the semi-analytical calculations using the three forms of χ_k : the crosses assume a Gaussian, the diamonds an exponential and the squares a Lorentzian, respectively. Each set of \mathcal{P}_{\max} is fitted by a power law of the form $(L/M)^s$ where s is the slope of the power law. The line-styles correspond to the three semi-analytical cases and the direct calculations, as indicated in the lower right corner of the plot.

Table 3. Values found for the slopes s (see Sect. 5.4) and sv (see Sect. 5.5). “Method” is the method considered for the calculations of \mathcal{P} .

Method	χ_k	s	sv
direct	—	3.4	—
semi-analytical	Gaussian	3.1	1.0
semi-analytical	exponential	3.0	0.9
semi-analytical	Lorentzian	2.6	0.7

In the solar case, \mathcal{P}_{\max} is found to be closer to the value derived from recent helioseismic data (Baudin et al. 2005) when using a Lorentzian compared to a Gaussian (see also Belkacem et al. 2006b, B06b hereafter). The “observed” excitation rates are derived from the velocity observations V as follows:

$$\mathcal{P} = 2\pi \Gamma_\nu \mathcal{M}(h) V^2 \quad (9)$$

where \mathcal{M} is the mode mass, V is the mode velocity amplitude and h is the height above the photosphere where the mode mass is evaluated. The mode line width at half maximum in Hz, $\Gamma_\nu = \eta/\pi$, (η is the mode amplitude damping rate in s^{-1}) is determined observationally in the solar case.

Using the recent helioseismic measurements of V and Γ_ν by Baudin et al. (2005) and the mode mass computed here for our solar model at the height $h = 340$ km (cf. Baudin et al. 2005), we find $\mathcal{P}_{\max,\odot} = 6.5 \pm 0.7 \times 10^{22} \text{ erg s}^{-1}$. This value must be compared with those found with χ_k^L and χ_k^G , namely $\mathcal{P}_{\max,\odot}^L = 4.9 \times 10^{22} \text{ erg s}^{-1}$ and $\mathcal{P}_{\max,\odot}^G = 1.2 \times 10^{22} \text{ erg s}^{-1}$ respectively.

Scaling laws: All sets of calculations can be reasonably well fitted with a scaling law of the form $\mathcal{P}_{\max} \propto (L/M)^s$ where s is a slope which depends on the considered set of calculations. Values found for s are summarized in Table 3.

• For the semi-analytical calculations, we find $s = 2.6$ using χ_k^L , $s = 3.0$ using χ_k^E and $s = 3.1$ for the Gaussian form.

The Lorentzian form results in a power law with a smaller slope than the Gaussian. This can be understood as follows: a Gaussian decreases more rapidly with ν than a Lorentzian. As the ratio L/M of a main sequence star increases, the mode frequencies shift to lower values. Hence p-modes of stars with large values of L/M receive *relatively* more acoustic energy when adopting a Gaussian rather than a Lorentzian χ_k . It is worthwhile to note that even though the ratio L/M is the ratio of two global stellar quantities, it nevertheless characterizes essentially the stellar surface layers where the mode excitation is located since $L/M \propto T_{\text{eff}}^4/g$.

- For the set of direct calculations, some scatter exists as a consequence of the large statistical fluctuations in \mathcal{P}_{max} and a linear regression gives $s = 3.4$. As expected, this value is rather close to that found with the semi-analytical calculations using either χ_k^G or χ_k^E .

5.5. Maximum of the mode amplitudes (V_{max}) as a function of L/M

The theoretical oscillation velocity amplitudes V can be computed according to Eq. (9). The calculation requires the knowledge of the excitation rates, \mathcal{P} , damping rates, η , and mode mass, \mathcal{M} . Although it is possible – in principle – to compute the convective dampings from the 3D simulations (Nordlund & Stein 2001), it is a difficult task which is under progress. However, using for instance Gough’s Mixing-Length Theory (1976; 1977, G’MLT hereafter), it is possible to compute η and \mathcal{P} for different stellar models of given L , M and deduce V_{max} , the maximum of the mode amplitudes, as a function of L/M at the cost of some inconsistencies.

In Samadi et al. (2001), calculations of the damping rates η based on G’MLT were performed for stellar models with different values of L and M . Although these stellar models are not the same as those considered here, it is still possible, for a crude estimate, to determine the dependency of V_{max} with L/M .

Hence we proceed as follows: for each stellar model computed in Samadi et al. (2001), we derive the values of η and \mathcal{M} at the frequency ν_{max} at which the maximum amplitude is expected. From the stars for which solar-like oscillations have been detected, Bedding & Kjeldsen (2003) have shown that this frequency is proportional to the cut-off frequency. Hence we determine $\nu_{\text{max}} = (\nu_c/\nu_{c,\odot})\nu_{\text{max},\odot}$ where ν_c is the cut-off frequency of a given model and the symbol \odot refers to solar quantities ($\nu_{\text{max},\odot} \approx 3.2$ mHz and $\nu_{c,\odot} \approx 5.5$ mHz). We then obtain (η_{max} \mathcal{M}_{max}) as a function of L and M .

On the other hand, in Sect. 5.4, we have established \mathcal{P}_{max} as a function of L and M . Then, according to Eq. (9), we can determine $V_{\text{max}}(L, M)$ for the different power laws of \mathcal{P}_{max} .

We are interested here in the slope (i.e. variation with L/M) of V_{max} and not its absolute magnitude, therefore we scale the theoretical and observed V_{max} with a same normalization value which is taken as the solar value $V_{\text{max},\odot} = 33.1 \pm 0.9$ cm s⁻¹ as determined recently by Baudin et al. (2005).

We find that V_{max} increases as $(L/M)^{sv}$ with different values for sv depending on the assumptions for χ_k . The values of sv are summarized in Table 3 and illustrated in Fig. 7. We find $sv \approx 0.7$ with χ_k^L and $sv \approx 1.0$ with χ_k^G .

These scaling laws must be compared with observations of a few stars for which solar-like oscillations have been detected in Doppler velocity. The observed V_{max} are taken from Table 1 of HG02, except for η Boo, ζ Her A, β Vir, HD 49933 and μ Ara, for which we use the V_{max} quoted by Carrier et al. (2003), Martić et al. (2001), Martić et al. (2004), Mosser et al. (2005) and

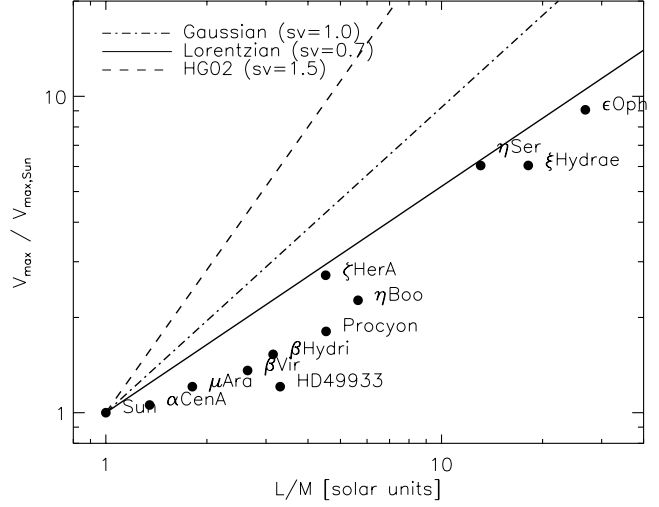


Fig. 7. Same as Fig. 6 for $V_{\text{max}}/V_{\text{max},\odot}$, the maximum of the mode amplitudes relative to the observed solar value ($V_{\text{max},\odot} = 33.1 \pm 0.9$ cm s⁻¹). The filled symbols correspond to the stars for which solar-like oscillations have been detected in Doppler velocity. The lines – except the dashed line – correspond to the power laws obtained from the predicted scaling laws for \mathcal{P}_{max} (Fig. 6) and estimated values of the damping rates η_{max} (see text for details). Results for two different eddy time-correlation functions, χ_k , are presented: Lorentzian (solid line) and Gaussian (dot-dashed line) functions. For comparison the dashed line shows the result by HG02. Values of the slope sv are given on the plot and in Table 3.

Bouchy et al. (2005) respectively and ϵ Oph and η Ser quoted by Barban et al. (2004).

Figure 7 shows that the observations also indicate a monotonic logarithmic increase of V_{max} with L/M despite a large dispersion which may at least partly arise from different origins of the data sets. For the observations we find a “slope” $sv \approx 0.7$. This is close to the theoretical slope obtained when adopting χ_k^L and definitely lower than the slopes obtained when adopting χ_k^G or adopted by HG02.

6. Summary and discussion

One goal of the present work has been to validate the model of stochastic excitation presented in Paper I. The result of this test is summarized in Sect. 6.1. A second goal has been to study the properties of the turbulent eddy time-correlation, χ_k , and the importance for the calculation of the excitation rates, \mathcal{P} , of the adopted form of χ_k . Section 6.2 deals with this subject.

6.1. Validation of the excitation model

In order to check the validity of the excitation model, seven 3D simulations of stars, including the Sun, have been considered. For each simulation, we calculated the p-mode excitation rates, \mathcal{P} , using two methods: the semi-analytical excitation model (cf. Sect. 2.2) that we are testing, and a direct calculation as detailed in Sect. 2. In the latter method, the work performed by the pressure fluctuations on the p-modes is calculated directly from the 3D simulations.

In the semi-analytical method, \mathcal{P} is computed according to the excitation model of Paper I. The calculation uses, as input, information from the 3D simulations as for instance the eddy

time-correlation (χ_k) and the kinetic energy spectra ($E(k)$). However although χ_k has been computed for each simulation, in practice for simplifying the problem of implementation as well as for comparison purpose with Paper III, we chose to represent the ν variation of χ_k with simple analytical functions. It is found that the ν -variation of χ_k in the present simulations lies loosely between that of an exponential and a Gaussian. We then perform the validation test of the excitation model using those two forms of χ_k .

We find that using either χ_k^G or χ_k^E in the semi-analytical calculations of \mathcal{P} results in systematically higher excitation rates than those obtained with direct 3D calculations. These systematic differences are attributed to the low spatial resolution of our present set of simulations. Indeed we have shown here that using solar simulations with different spatial resolutions, the resulting excitation rates increase with increasing spatial resolution.

We have next investigated the dependence of \mathcal{P}_{\max} with L/M (See Fig. 6), where L and M are the stellar luminosity and mass respectively. As in previous works based on a purely theoretical approach (e.g. Samadi et al. 2003a), we find that \mathcal{P}_{\max} scales approximatively as $(L/M)^s$ where s is the slope of the scaling law: we find $s = 3.4$ with the direct calculations and $s = 3.2$ and $s = 3.1$ with the semi-analytical calculations using χ_k^G and χ_k^E respectively. This indicates a general agreement between the scaling properties of both types of calculations, which validates to some extent the adopted excitation model across the domain of the HR diagram studied here.

For the sake of simplicity, only simple analytical forms for χ_k have been investigated here. We expect that the use of more sophisticated forms for χ_k would reduce the dispersion between the analytical and direct calculations, but would not affect the conclusions of the present paper.

6.2. The eddy time-correlation spectra, χ_k

The slope s of the scaling law for \mathcal{P}_{\max} , is found to depend significantly on the adopted analytical form for χ_k . The semi-analytical calculations using the Lorentzian form for χ_k results in a significantly smaller slope s than those based on the Gaussian or the exponential or from direct calculations (see Table 3).

Except for the Sun, independent and accurate enough constraints on *both* the mode damping rates and the mode excitation rates are not yet available. We are then left to perform comparison between predicted and observed mode amplitudes. Unfortunately, obtaining tight constraints on χ_k using comparison between predicted and observed mode amplitudes is hampered by large uncertainties in the theoretical estimates of the damping rates. It is therefore currently difficult to derive the excitation rates \mathcal{P} for the few stars for which solar-like oscillations have been detected (see Samadi et al. 2004). The future space mission COROT (Baglin & The Corot Team 1998) will provide high-quality data on seismic observations. Indeed the COROT mission will be the first mission that will provide *both* high precision mode amplitudes and line-widths for stars other than the Sun. It will then be possible to use the observed damping rates and to derive the excitation rate \mathcal{P} free of the uncertainties associated with a theoretical computation of damping rates. In particular, it will be possible to determine \mathcal{P}_{\max} as a function of L and M from the observed stars. Such observations will provide valuable constraints for our models for χ_k .

We can, nevertheless, already give some arguments below in favor of the Lorentzian being the correct description for χ_k .

6.2.1. Solar case

In the 3D simulations studied here, including that of the Sun, the inferred ν dependency of χ_k is far from a Lorentzian, in contrast to that found with the solar 3D simulation investigated in Paper III. However, by investigating solar simulations with different resolutions, we find that, as the spatial resolution increases, χ_k tends towards a Lorentzian ν -dependency. This explanation is likely to stand for non-solar simulations too, but has not yet been confirmed (work in progress).

Furthermore, as shown in Fig. 5, bottom, the direct calculations obtained with the simulation with the highest spatial resolution available is slightly closer to the semi-analytical calculations using the Lorentzian form than those using the Gaussian one.

Independently of the resolution (if large enough of course), a Lorentzian χ_k predicts larger values for \mathcal{P}_{\max} than a Gaussian or an exponential do. In particular in the solar case, the semi-analytical calculation using χ_k^L results in a \mathcal{P}_{\max} closer to the helioseismic constraints derived by Baudin et al. (2005) compared to using χ_k^G or χ_k^E . This latter result is in agreement with that of Paper III.

Part of the remaining discrepancies with the helioseismic constraints are attributed to the adopted closure model according to Belkacem et al. (2006b, B06b hereafter). Indeed, theoretical models of stochastic excitation adopt the quasi-normal approximation (QNA). As shown in B06b, the skew introduced by the QNA result in a under-estimation of the solar p mode excitation rates. When the so-called closure model with plumes proposed by Belkacem et al. (2006a) is adopted, new semi-theoretical calculations fit rather well the recent helioseismic constraints derived by Baudin et al. (2005, see B06b).

6.2.2. V_{\max} as a function of L/M

Consequences of the predicted power laws for \mathcal{P}_{\max} have also been crudely investigated here for the expected value of V_{\max} , the maximum value of the mode velocity (Fig. 7). Calculations of V_{\max} from \mathcal{P}_{\max} require the knowledge of the mode damping rates, η , which cannot be fully determined from the simulations. We are then led to use theoretical calculations of the damping rates. We consider here those performed by Samadi et al. (2001) which are based on Gough's (1976; 1977) non-local and time-dependent formulation of convection. From those values of η and the different power laws for \mathcal{P}_{\max} expected values of V_{\max} are obtained.

We find, as in Houdek & Gough (2002, HG02), that V_{\max} scales as $(L/M)^{sv}$. Calculations by HG02 result in $sv \approx 1.5$. Our semi-analytical calculations of \mathcal{P}_{\max} based on a Gaussian χ_k result in a slightly smaller slope ($sv \approx 1.0$). On the other hand, using a Lorentzian χ_k results in a slope $sv \approx 0.7$ which is closer to that derived from the few stars for which oscillation amplitudes have been measured.

From this result, we conclude that the problem of the over-estimation of the amplitudes of the solar-like oscillating stars more luminous than the Sun is related to the choice of the model for χ_k . Indeed, previous theoretical calculations by Houdek et al. (1999) are based on the assumption of a Gaussian χ_k . As shown here, the Gaussian assumption results in a larger slope sv than the Lorentzian χ_k . This is the reason why Houdek et al. (1999) over-estimate V_{\max} for $L/M > L_{\odot}/M_{\odot}$.

On the other hand, if one assumes $\chi_k = \chi_k^L$, a scaling factor is no longer required to reproduce \mathcal{P}_{\max} for the solar p-modes. Moreover, as a consequence of the smaller slope, sv , resulting

from a Lorentzian χ_k , the predicted amplitudes for other stars match the observations better.

This result further indicates that a Lorentzian is the better choice for χ_k , as was also concluded in Paper III.

Departures of the theoretical curve from the observed points in Fig. 7 can be attributed to several causes which remain to be investigated:

- 1) A major uncertainty comes from the computed damping rates as no accurate enough observations are available yet to validate them. As V results from the balance between \mathcal{P} and η , the slope sv can also depend on the variation of η with L/M . Thus, the large differences in sv between the seismic observations and the calculations based on χ_k^G can also be, a priori, attributed to an incorrect evaluation of the damping rates. However η_{\max} – the value of the damping rate at the frequency ν_{\max} at which the maximum amplitude is expected – does not follow a clear scaling law with L/M . We have looked at the η_{\max} variation in our set of G’MLT models and found no clear dependence of η_{\max} on L/M but rather a dispersion.
- 2) The observed stars in Fig. 7 have somewhat different chemical compositions; this can cause some scatter in the relation $V_{\max}-L/M$ which has not been taken into account here. All the simulations investigated in the present work employ a solar metal abundance. The metallicity has a direct impact on the opacity and the EOS. Both in turn affect the internal structure and are also decisive for the transition from convection to radiation in the photosphere and therefore determine the structure of the super-adiabatic region. Hence, the properties of the super-adiabatic region, relevant for the excitation rates, differ for stars located at the same position in the HR diagram (e.g., same T_{eff} and same g) but with different metal abundances. Consequently the excitation of p-modes for such stars probably differ, although it remains to be seen to what extent. A differential investigation of the metallicity effect is planned for the future.

6.3. Relative contribution of the turbulent pressure

Another issue concerns the *relative contribution of the turbulent pressure*. The excitation of solar-like oscillations is generally attributed to the turbulent pressure (i.e. Reynolds stress) and the entropy fluctuations (i.e. non-adiabatic gas pressure fluctuations) and occurs in the super-adiabatic region where those two terms are the largest. In Paper III, it was found that the two driving sources are of the same order of magnitude, in contradiction with the results by Stein & Nordlund (2001) who found – based on their 3D numerical simulations of convection – that the turbulent pressure is the dominant contribution to the excitation. The discrepancy is removed here as we used a corrected version of the formulation of the contribution of the Reynolds stress of Paper I (see Eq. (3)), leading to a larger contribution from the Reynolds stress.

For the Sun, assuming χ_k^L (χ_k^G resp.), we now find that the Reynolds stress contribution is 5 times (3 times resp.) larger than that due to the entropy fluctuations (non-adiabatic gas-pressure fluctuations). Hence, the Reynolds stress is indeed the dominant source of excitation in agreement with the results of Stein & Nordlund (2001). The best agreement with the latter results is obtained with a Lorentzian χ_k .

However, we find that the relative contribution from Reynolds stresses decreases rapidly with (L/M) . For instance, in

the simulation of Procyon, the Reynolds stress represents only $\sim 30\%$ of the total excitation rate.

From that, we conclude that the excitation by entropy fluctuations cannot be neglected, especially for stars more luminous than the Sun.

Acknowledgements. R.S.’s work has been supported by Société de Secours des Amis des Sciences (Paris, France) and by Fundação para a Ciência e a Tecnologia (Portugal) under grant SFRH/BPD/11663/2002. R.F.S. is supported by NASA grants NAG 5 12450 and NNG04GB92G and by NSF grant AST0205500. We thank the referee, Mathias Steffen, for his judicious suggestions which helped improve this manuscript.

Appendix A: Calculation of the non adiabatic pressure fluctuations

The adiabatic variation of the gas pressure does not contribute to the $\Delta(PdV)$ work over an oscillation period as it is in phase with the volume (or density) variation. In practice, however, it is beneficial for the accuracy of the computation of excitation to subtract the adiabatic part of the gas pressure fluctuation, since it reduces the coherent part. That part gives zero contribution only in the limit of infinite time, or for an exact integer number of periods. However, in practice, it gives rise to a random (or noisy) contribution. Indeed, as we deal with a lot of different modes it is hard to find a time-interval which is an integer number of periods of each and all of the modes at the same time.

The Lagrangian variations of gas pressure, ΔP_{gas} must satisfy

$$\Delta P_{\text{gas}} = \frac{\Gamma_1 P_{\text{gas}}}{\rho} \Delta \rho + \frac{\partial P_{\text{gas}}}{\partial S} \Delta S \quad (\text{A.1})$$

where P_{gas} , ρ and S are the gas pressure the density and the entropy respectively and where the operator Δ represents the *pseudo* Lagrangian fluctuations of a given quantity. The concept of pseudo Lagrangian fluctuations is introduced in Nordlund & Stein (2001). Accordingly we derive the non-adiabatic gas pressure fluctuations as:

$$\Delta P_{\text{gas,nad}}(\mathbf{r}, t) \equiv \Delta P_{\text{gas}} - c_s^2 \Delta \rho \quad (\text{A.2})$$

where $c_s^2 \equiv \Gamma_1 P_{\text{gas}}/\rho$ is the sound speed.

However, what we want to subtract off from ΔP_{gas} is that part of the pressure variation that is due to adiabatic compression and expansion due to the particular *radial wave modes* (i.e. the low amplitude perturbation of $\rho(r)$ on top of the possibly large variations horizontally of $\rho(r)$ that $\rho(r)$ is an average of).

To find the nonadiabatic pressure fluctuations, we start with calculations of horizontal averages of the primary quantities, P_{gas} , P_{turb} , ρ and c_s^2 . We convert these averages to the pseudo-Lagrangian frame of reference, in which the net mass flux vanishes. We then compute fluctuations of the resulting quantities with respect to time, i.e., subtract their time averages:

$$\begin{aligned} \Delta P_{\text{gas}} &= \langle P_{\text{gas}} \rangle_{\text{h}} - \langle P_{\text{gas}} \rangle_{\text{h,t}} \\ \Delta P_{\text{turb}} &= \langle P_{\text{turb}} \rangle_{\text{h}} - \langle P_{\text{turb}} \rangle_{\text{h,t}} \\ \Delta \rho &= \langle \rho \rangle_{\text{h}} - \langle \rho \rangle_{\text{h,t}}. \end{aligned}$$

Here, $\langle \rangle_{\text{h}}$ refers to horizontal average and $\langle \rangle_{\text{h,t}}$ refers to consequent time average performed on a horizontally averaged quantity. Finally, the non-adiabatic fluctuations of the *total* pressure (that is gas + turbulent pressure) are:

$$\begin{aligned} \Delta P_{\text{nad}} &= \Delta P_{\text{gas,nad}} + \Delta P_{\text{turb}} \\ &= \Delta P - \langle c_s^2 \rangle_{\text{h,t}} \Delta \rho \end{aligned} \quad (\text{A.3})$$

where $\Delta P \equiv \Delta P_{\text{gas}} + \Delta P_{\text{turb}}$.

References

- Baglin, A., & The Corot Team. 1998, in IAU Symp.: New Eyes to See Inside the Sun and Stars, 185, 301
- Balmforth, N. J. 1992, MNRAS, 255, 639
- Barban, C., de Ridder, J., Mazumdar, A., et al. 2004, in Proceedings of the SOHO 14 / GONG 2004 Workshop (ESA SP-559): Helio- and Asteroseismology: Towards a Golden Future, ed. D. Danesy, 113
- Baudin, F., Samadi, R., Goupil, M.-J., et al. 2005, A&A, 433, 349
- Bedding, T. R., & Kjeldsen, H. 2003, Pub. Astron. Soc. Aust., 20, 203
- Belkacem, K., Samadi, R., Goupil, M., & Kupka, F. 2006a, A&A, 460, 173
- Belkacem, K., Samadi, R., Goupil, M., & Kupka, F. 2006b, A&A, 460, 183 (B06b)
- Böhm-Vitense, E. 1958, Z. Astrophys., 46, 108
- Bouchy, F., Bazot, M., Santos, N. C., Vauclair, S., & Sosnowska, D. 2005, A&A, 440, 609
- Carrier, F., Bouchy, F., & Eggenberger, P. 2003, in Asteroseismology across the HR diagram, ed. M. J. Thompson, M. S. Cunha, & M. J. P. F. G. Monteiro, CDROM (Kluwer Acad.), 284 315
- Christensen-Dalsgaard, J. 1982, MNRAS, 199, 735
- Christensen-Dalsgaard, J., & Berthomieu, G. 1991, Theory of solar oscillations, Solar interior and atmosphere (A92-36201 14-92) (Tucson, AZ: University of Arizona Press), 401
- Christensen-Dalsgaard, J., & Frandsen, S. 1983a, Sol. Phys., 82, 165
- Christensen-Dalsgaard, J., & Frandsen, S. 1983b, Sol. Phys., 82, 469
- Däppen, W., Mihalas, D., Hummer, D. G., & Mihalas, B. W. 1988, ApJ, 332, 261
- Georgobiani, D., Stein, R., & Nordlund, Å. 2006, ApJ (submitted)
- Goldreich, P., & Keeley, D. A. 1977, ApJ, 212, 243
- Goldreich, P., Murray, N., & Kumar, P. 1994, ApJ, 424, 466
- Gough, D. 1976, in Lecture notes in physics, Problems of stellar convection, ed. E. Spiegel, & J.-P. Zahn (Springer Verlag), 71, 15
- Gough, D. O. 1977, ApJ, 214, 196
- Houdek, G., Balmforth, N. J., Christensen-Dalsgaard, J., & Gough, D. O. 1999, A&A, 351, 582
- Houdek, G., & Gough, D. O. 2002, MNRAS, 336, L65 (HG02)
- Kjeldsen, H., & Bedding, T. R. 1995, A&A, 293, 87
- Kjeldsen, H., & Bedding, T. R. 2001, Proceedings of the SOHO 10/GONG 2000 Workshop (ESA SP): Helio- and asteroseismology at the dawn of the millennium, ed. A. Wilson, 464, 361
- Kurucz, R. L. 1992a, Rev. Mex. Astron. Astrofis., 23, 45
- Kurucz, R. L. 1992b, Rev. Mex. Astron. Astrofis., 23, 181
- Martić, M., Lebrun, J. C., Schmitt, J., Appourchaux, T., & Bertaux, J. L. 2001, in ESA SP SOHO 10/GONG 2000 Workshop: Helio- and Asteroseismology at the Dawn of the Millennium, 464, 431
- Martić, M., Lebrun, J., Appourchaux, T., & Schmitt, J. 2004, in Proc. of the SOHO 14 / GONG 2004 Workshop (ESA SP): Helio- and Asteroseismology: Towards a Golden Future, ed. D. Danesy, 559, 563
- Mosser, B., Bouchy, F., Catala, C., et al. 2005, A&A, 431, L13
- Nordlund, Å., & Stein, R. F. 2001, ApJ, 546, 576
- Osaki, Y. 1990, in Lecture Notes in Physics: Progress of Seismology of the Sun and Stars, ed. Y. Osaki, & H. Shibahashi (Springer-Verlag), 75
- Samadi, R., & Goupil, M. . 2001, A&A, 370, 136 (Paper I)
- Samadi, R., Houdek, G., Goupil, M.-J., Lebreton, Y., & Baglin, A. 2001, in 1st Eddington Workshop (ESA SP-485): Stellar Structure and Habitable Planet Finding, [arXiv:astro-ph/0109174], 87
- Samadi, R., Goupil, M. J., Lebreton, Y., Nordlund, Å., & Baudin, F. 2003a, Ap&SS, 284, 221
- Samadi, R., Nordlund, Å., Stein, R. F., Goupil, M. J., & Roxburgh, I. 2003b, A&A, 404, 1129 (Paper III)
- Samadi, R., Nordlund, Å., Stein, R. F., Goupil, M. J., & Roxburgh, I. 2003c, A&A, 403, 303 (Paper II)
- Samadi, R., Goupil, M. J., Baudin, F., et al. 2004, in Proc. of the SOHO 14 / GONG 2004 Workshop (ESA SP): Helio- and Asteroseismology: Towards a Golden Future, ed. D. Danesy, 559, 615 [arXiv:astro-ph/0409325]
- Samadi, R., Goupil, M.-J., Alecian, E., et al. 2005, JA&A, 26, 171
- Stein, R., Georgobiani, D., Trampedach, R., Ludwig, H.-G., & Nordlund, Å. 2004, Sol. Phys., 220, 229
- Stein, R. F. 1967, Sol. Phys. 2, 385
- Stein, R. F., & Nordlund, Å. 2001, ApJ, 546, 585
- Trampedach, R., Stein, R. F., Christensen-Dalsgaard, J., & Nordlund, Å. 1999, in ASPC Ser., 233
- Trampedach, R., Christensen-Dalsgaard, J., Nordlund, Å., & Stein, R. F. 2006a, ApJ, submitted
- Trampedach, R., Stein, R. F., Christensen-Dalsgaard, J., & Nordlund, Å. 2006b, ApJ, in preparation

Modeling the excitation of acoustic modes in α Centauri A

R. Samadi¹, K. Belkacem¹, M. J. Goupil¹, M.-A. Dupret¹, and F. Kupka²

¹ Observatoire de Paris, LESIA, CNRS UMR 8109, 92195 Meudon, France
e-mail: reza.Samadi@obspm.fr

² Max-Planck-Institute for Astrophysics, Karl-Schwarzschild Str. 1, 85748 Garching, Germany

Received 26 September 2007 / Accepted 30 May 2008

ABSTRACT

From different seismic observations we infer the energy supplied per unit of time by turbulent convection to the acoustic modes of α Centauri A (HD 128620), a star that is similar but not identical to the Sun. The inferred rates of energy supplied to the modes (i.e. mode excitation rates) are found to be significantly higher than in the Sun. They are compared with those computed with an excitation model that includes two sources of driving, the Reynolds stress contribution and the advection of entropy fluctuations. The model also uses a closure model, the Closure Model with Plumes (CMP hereafter), that takes the asymmetry between the up- and down-flows (i.e. the granules and plumes, respectively) into account. Different prescriptions for the eddy-time correlation function are also compared to observational data. Calculations based on a Gaussian eddy-time correlation underestimate excitation rates compared with the values derived from observations for α Centauri A. On the other hand, calculations based on a Lorentzian eddy-time correlation lie within the observational error bars. This confirms results in the solar case. Compared to the helioseismic data, those obtained for α Centauri A constitute an additional support for our model of excitation. We show that mode masses must be computed taking turbulent pressure into account. Finally, we emphasize the need for more accurate seismic measurements in order to distinguish between the CMP closure model and the quasi-normal approximation in the case of α Centauri A, as well as to confirm or not the need to include the excitation by the entropy fluctuations.

Key words. convection – turbulence – stars: oscillations – stars: atmospheres

1. Introduction

The star α Centauri A is the most promising after the Sun for constraining the modeling of p-mode excitation by turbulent convection. Indeed, due to its proximity and its binarity, the fundamental parameters of α Centauri A (effective temperature, luminosity, metallicity, gravity, radius) are quite well known. For this reason this star and its companion (α Cen B) have been extensively studied (see for instance the most recent modeling by Miglio & Montalbán (2005) and the references therein). As pointed out by Samadi et al. (2007a), the detection of p-modes and the measurement of their amplitudes as well as their mode linewidths (i.e. lifetime), from α Centauri A enable the rates at which energy is supplied to the acoustic modes for this star to be derived. These observational constraints can then be used to check models of p-mode excitation by turbulent convection.

Such comparisons were first undertaken in the case of the Sun by various authors (see the recent review by Houdek 2006). They enable different models of stochastic excitation of acoustic modes to be tested as well as different models of turbulent convection (see e.g. Samadi et al. 2006). Among those theoretical prescriptions, we consider that one of Samadi & Goupil (2001) with the improvements proposed by Samadi et al. (2003) and Belkacem et al. (2006b). It was shown by Samadi et al. (2003) that the way the eddy time correlation is modeled plays an important role in the efficiency of excitation. Indeed, calculations of the mode excitation rates, \mathcal{P} , that use a Lorentzian eddy-time correlation function reproduce helioseismic data better than those using a Gaussian one. In addition, Belkacem et al. (2006b), in the case of the Sun, show that excitation rates computed using an adapted closure model that takes the presence of plumes into

account reproduce the solar observations much better than the calculations based on the classical quasi-normal approximation (Millionshchikov 1941).

An alternative theoretical model of the excitation of acoustic modes by turbulent convection proposed by Chaplin et al. (2005) differs from that by Samadi & Goupil (2001) in several ways: it does not take the driving by the advection of the entropy fluctuations by the velocity field into account. They only use the classical quasi-normal approximation. More importantly, these authors claim that a Gaussian eddy-time correlation function reproduces one the frequency dependence of mode excitation rates inferred from helioseismic data better than a Lorentzian one. However, they are led to introduce a factor to their model by which they multiply their formulation to reproduce the maximum of the solar mode excitation rates.

A second opportunity is provided by α Centauri A for testing various assumptions in the modeling of the p-mode excitation: the amplitudes of the acoustic modes detected in α Centauri A were derived by Butler et al. (2004) using spectrometric data. From those data, an estimate of the averaged mode linewidths has been first proposed by Bedding et al. (2004) and more recently updated in Kjeldsen et al. (2005). Using a different method and data from the WIRE satellite, Fletcher et al. (2006) propose a new estimate of the averaged mode linewidths that differ significantly from the one derived by Kjeldsen et al. (2005). Indeed, the two data sets place the mode lifetime between 2.2 days (Kjeldsen et al. 2005) and 3.9 days (Fletcher et al. 2006). For comparison, the averaged mode life time derived for the Sun by Bedding et al. (2004) in a similar way as for α Centauri A by Kjeldsen et al. (2005) is about two days.

Samadi et al. (2007a) inferred the p-mode excitation rates \mathcal{P} from those sets of seismic constraints. They find that they are significantly larger than those associated with the solar p-modes. Furthermore, \mathcal{P} peaks in the frequency domain ~ 2.2 – 2.6 mHz, while it peaks at the frequency $\nu_{\max} \sim 3.8$ mHz in the case of the Sun.

Although the spectroscopic characteristics ($T_{\text{eff}} = 5810$ K, $\log g = 4.305$) of α Centauri A are close to those of the Sun ($T_{\text{eff}} = 5780$ K, $\log g = 4.438$), the seismic signatures are quite different. Consequently, finding agreement between predicted and observed excitation rates would be a nontrivial result, providing additional support for the theory.

A preliminary comparison with theoretical calculations obtained in the manner of Belkacem et al. (2006a) was carried out by Samadi et al. (2007a). Discrepancies between the excitation rates inferred from the observations and the theoretical calculations were found. We update this study here by proceeding in a similar way as in Rosenthal et al. (1999). Indeed, these authors have built a solar 1D model where the surface layers are taken directly from a fully compressible 3D hydrodynamical numerical model. We refer here to such a 1D model as a “patched” model. Rosenthal et al. (1999) have obtained a much better agreement between observed and theoretical eigenfrequencies of the Sun computed for such a “patched” 1D model than for a “standard” 1D model based on the standard mixing-length theory with no turbulent pressure included. Following Rosenthal et al. (1999), we built such a “patched” model to derive adiabatic mode radial eigen-displacements (ξ_r) and mode inertia (I). We used them to compute the mode excitation rates, which we compared with excitation rates computed using ξ_r and I obtained with a “standard” 1D model.

The paper is organized as follows: in Sect. 2 we describe our procedure for computing the mode excitation rates for the specific case of α Centauri A. We then describe in Sect. 3 the way the mode excitation rates are inferred from seismic observations of α Centauri A. In Sect. 4, we compare theoretical calculations of \mathcal{P} with those inferred from the seismic data obtained for α Centauri A. We compare and explain in Sect. 5 the differences between α Centauri A and the Sun. Finally, Sects. 6 and 7 are devoted to the discussion and conclusions, respectively.

2. Modeling the excitation of p-modes

2.1. General formulation

Because the theoretical model of stochastic excitation is basically that of Samadi & Goupil (2001; see also Samadi et al. 2005) with the improvements of Belkacem et al. (2006a,b), we recall only some key features here. The model takes two driving sources into account. The first one is related to the Reynolds stress tensor and, as such, represents a mechanical source of excitation. The second one is caused by the advection of the turbulent fluctuations of entropy by the turbulent motions (the so-called “entropy source term”) and thus represents a thermal source of excitation (Goldreich et al. 1994; Stein & Nordlund 2001). The power fed into each radial mode, \mathcal{P} , is given by

$$\mathcal{P} = \frac{1}{8I} (C_{\text{R}}^2 + C_{\text{S}}^2), \quad (1)$$

where C_{R}^2 and C_{S}^2 are the turbulent Reynolds stress and entropy contributions, respectively and

$$I = \int_0^M dm |\xi_r|^2 \quad (2)$$

is the mode inertia, ξ_r is the adiabatic radial mode displacement and M the mass of the star. The expressions for C_{R}^2 and C_{S}^2 are given for a radial mode with frequency ω_0 by

$$C_{\text{R}}^2 = \frac{64\pi^3}{15} \int dm \rho_0 f_r \left(1 + \frac{1}{3} S_w^2\right) S_{\text{R}}(\omega_0), \quad (3)$$

$$C_{\text{S}}^2 = \frac{16\pi^3}{3\omega_0^2} \int dm \frac{\alpha_s^2}{\rho_0} g_r S_{\text{S}}(\omega_0), \quad (4)$$

where we have defined

$$S_{\text{R}}(\omega_0) = \int \frac{dk}{k^2} E^2(k) \int d\omega \chi_k(\omega + \omega_0) \chi_k(\omega), \quad (5)$$

$$S_{\text{S}}(\omega_0) = \int \frac{dk}{k^2} E(k) E_s(k) \int d\omega \chi_k(\omega + \omega_0) \chi_k(\omega), \quad (6)$$

where $f_r \equiv (d\xi_r/dr)^2$, and g_r is a function that involves the first and the second derivatives of ξ_r . Then, $E(k)$ is the spatial turbulent kinetic energy spectrum, $E_s(k)$ the spectrum associated with the entropy fluctuations, χ_k the time correlation function of the eddies, $\alpha_s = (\partial P/\partial s)_\rho$ where s is the entropy, P the gas pressure, ρ the density, ρ_0 the equilibrium density profile, and ω_0 the eigenfrequency.

Finally, $S_w \equiv \langle w^3 \rangle / (\langle w^2 \rangle)^{3/2}$ is the skewness and w the vertical component of the velocity (see Belkacem et al. 2006a,b, for details). Indeed, the expression of Eq. (3) depends on the closure model used to express the fourth-order moments involved in the theory in terms of the second-order ones. The most commonly used closure model at the level of fourth-order moments is the quasi-normal approximation (QNA). Such an assumption leads to a vanishing skewness S_w . However, in the solar case, the deviation from the QNA stems from the presence of turbulent plumes. Taking both the effect of the skewness introduced by the presence of two flows and the effect of turbulence onto each flow into account Belkacem et al. (2006a) thus propose a new closure model, which leads to a non-vanishing skewness, S_w , in Eq. (3). In the present work, S_w is then obtained directly from the 3D numerical model.

Calculation of the mode excitation rates is performed essentially in the manner of Belkacem et al. (2006b) as explained in Samadi et al. (2007a) in the specific case of α Centauri A: all required quantities, except the mode eigenfunctions ξ_r and mode inertia I , are directly obtained from a 3D simulation of the outer layers of α Centauri A, whose characteristics are described in Sect. 2.2 below.

The mode displacement ξ_r and mode inertia I must be computed from a global 1D equilibrium model. We chose to study two such equilibrium models which are described in Sect. 2.3. Finally, eigenfrequencies and eigenfunctions are computed using the adiabatic pulsation code ADIPLS (Christensen-Dalsgaard & Berthomieu 1991).

2.2. The 3D hydrodynamical model of the outer layers of α Centauri A

We consider the 3D hydrodynamical model of the outer layers of α Centauri A computed by Samadi et al. (2007a) using the Stein & Nordlund (1998) code. The assumed micro-physics (e.g. the equation of state and the opacity table) are explained in Samadi et al. (2007b). The hydrogen, helium, and metal abundances are solar, and the chemical mixture of the heavy elements is set according to the Grevesse & Noels (1993) mixture.

The 3D model associated with α Centauri A has a horizontal size of 8.17 Mm \times 8.17 Mm and a vertical size of 4.31 Mm. The

grid is $125 \times 125 \times 82$. As pointed out by Samadi et al. (2007b), this spatial resolution is sufficient for calculating the p-mode excitation rates. The simulation duration is 323 min, while the acoustic depth of the simulation is 410 s and the characteristic eddy turnover time is ~ 20 min (see Sect. 5). The duration of the simulation then represents ~ 47 sound travels across the simulated domain and about 15 eddy turnover times.

The effective temperature T_{eff} is adjusted to $5809 \text{ K} \pm 15$, in good agreement with the value $T_{\text{eff}} = 5810 \text{ K} \pm 50$ adopted by Miglio & Montalbán (2005). The gravity is set to $\log g = 4.305$ to exactly match the value ($\log g = 4.305 \pm 0.005$) inferred from the precise measurements of the mass and the radius of the star (see the related references in Miglio & Montalbán 2005).

2.3. 1D models

2.3.1. Standard model

The first 1D equilibrium model has the effective temperature and the gravity of α Centauri A and is built by requiring that, for the temperature at the bottom of the 3D simulation box, the 1D model has the same pressure and density as the 3D simulation (see Fig. 1). The 3D simulation is therefore used to constrain this 1D equilibrium model such that its interior structure is compatible with the second 1D model described later on, in Sect. 2.3.2 (see also Fig. 1). Convection in the 1D model is described according to Böhm-Vitense (1958)’s mixing-length local theory of convection (MLT) and turbulent pressure is ignored. Microscopic diffusion of helium and heavy elements are treated according to the simplified formalism of Michaud & Proffitt (1993). We assume a solar abundance to be consistent with the 3D model.

The mixing-length parameter, α , the age, the mass (M), the initial helium abundance (Y_0), and the initial $(Z/X)_0$ ratio where X and Z are the hydrogen and metal mass fractions, respectively, are fitted such that the model simultaneously reproduces the effective temperature of the star, its gravity, the solar composition, and the temperature-pressure relation at the bottom of the 3D simulation box. The outer layers of this model, which matter here, then have the stratification given by a standard MLT model. This model is referred to as standard hereafter.

The matching results in $\alpha = 1.694$. For comparison, the same matching performed for a solar 3D simulation results in $\alpha = 1.899$. The mass of the standard model is $M = 1.012 M_{\odot}$ and the radius $R = 1.1722 R_{\odot}$. They are slightly less than expected for this star, namely $M = 1.105 \pm 0.007 M_{\odot}$ and $R = 1.224 \pm 0.003 R_{\odot}$ (see Miglio & Montalbán 2005). This is because we have assumed a solar abundance for consistency with the 3D model. A global 1D model with the iron-to-hydrogen abundance ($[\text{Fe}/\text{H}]$) of α Centauri A (namely $[\text{Fe}/\text{H}] = 0.2$), would have the expected mass and radius of the star.

Slightly different R , M and $[\text{Fe}/\text{H}]$ values might have some influence on the mode excitation rates (\mathcal{P}). To measure the effect of having an R , M and $[\text{Fe}/\text{H}]$ different than required for α Centauri A, we computed two global models. The first model has an abundance $[\text{Fe}/\text{H}] = 0.2$ and the second has a solar abundance. Both models have the effective temperature and gravity of α Centauri A. In contrast with the “standard” model described above, we do not match these models with the 3D model. The model with $[\text{Fe}/\text{H}] = 0.2$ almost has the radius and the mass expected for α Centauri A, while the second has almost the same R and M as the standard model investigated here. We find that \mathcal{P} changes between the two models by less than $\sim 5\%$; this is much less than the uncertainties associated with the observations.

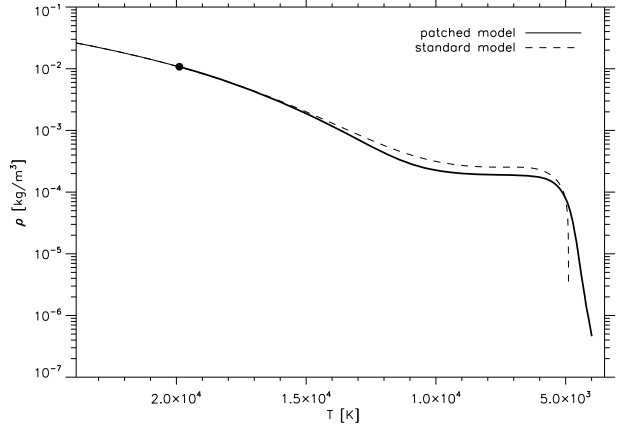


Fig. 1. Density as a function of the temperature. The solid line corresponds to the “patched” model and the dashed line to the “standard” model. The thick solid line is the part of the patched model obtained from the 3D simulation. The filled circle shows the position of the bottom of the 3D simulation box.

2.3.2. “Patched” model

To consider a more realistic description of the superadiabatic outer layers, we built a 1D global model, following Trampedach (1997, see also Samadi et al. 2007b), in which the outer layers are replaced by the averaged 3D simulation (see Fig. 1).

“Standard” and 3D models share the same microphysics but mainly differ in the way convective motions and radiative transfer are treated. In the 3D model convective motions are treated by solving the Navier-Stokes equation while in the standard model convective motions are modeled according to the mixing-length model of convection and no turbulent pressure is included in the hydrostatic equation. In the standard model, radiative transfer is gray and assumes the Eddington approximation. In the 3D model, radiative transfer is explicitly solved in LTE for four opacity bins (see details in Stein & Nordlund 1998).

The interior of the “patched” model is the same as in the standard model and does not include the turbulent pressure. At the bottom of the 3D simulation box, turbulent pressure is already negligible ($\sim 0.6\%$ of the total pressure). Then, neglecting it in the interior has negligible effects on the properties of the eigenfunctions considered here. This global model will be referred to as a patched model. Note that this patched model has the same total mass and a radius very close to that of the standard model, namely $R = 1.1726 R_{\odot}$.

The stratifications in density of the patched and standard models are compared in Fig. 1. At the top of the convective region, we see that the density is lower in the patched model compared to the standard model. This is because the patched model includes turbulent pressure that provides additional support against gravity: accordingly, the patched model has lower gas pressure at a given total pressure (P_{tot}). Now, since $T(P_{\text{tot}})$ is the same with and without turbulent pressure, the patched model has a lower density at a given temperature than the standard model.

Because the treatment of photospheric radiative transfer is not (and in practice cannot be) identical between a 3D calculation and a 1D model in the atmosphere, small differences in the stratifications of the very outer layers exist between the two models as seen in Fig. 1. In any case these differences do not play any significant role in the quantities that matter here, such as inertia. Note that some explanations about the differences seen

between the outer layers of 3D models and 1D models have been proposed by e.g. Nordlund & Stein (1999) and Rosenthal et al. (1999).

3. Inferring the excitation rates from seismic constraints

Mode excitation rates are derived from seismic observations according to the relation

$$\mathcal{P}(\nu) = 2\pi \mathcal{M} \Gamma (v/S_0)^2 \quad (7)$$

where $\mathcal{M} = I/\xi_r^2(r_h)$ is the mode mass evaluated at the layer $r_h \equiv R + h$ in the atmosphere where the mode is measured in radial velocity, R the radius at the photosphere (i.e. at $T = T_{\text{eff}}$), h the height above the photosphere, Γ the mode full width at half maximum (in ν), $v(r_h, \nu)$ is the rms apparent velocity amplitude of the mode at the layer r_h , $\nu = \omega_0/2\pi$ the mode frequency, and S_0 the visibility factor of the $\ell = 0$ mode.

Kjeldsen et al. (2005) have derived the apparent amplitude velocity spectrum, $v(\nu)$ of the modes detected in α Centauri A. However, their spectrum corresponds to amplitudes normalized to the mean of $\ell = 0$ and 1 modes rather than to $\ell = 0$. Furthermore, they do not take the mode visibilities into account. Recently, Kjeldsen et al. (2008) have derived the (apparent) amplitudes of the modes, normalized to the $\ell = 0$ modes and taking both the mode visibilities and limb-darkening effects into account. Finally, to derive the *intrinsic* mode amplitudes, we divide $v(\nu)$ by $S_0 = 0.712$, the visibility factor of the $\ell = 0$ modes observed in velocity (Kjeldsen et al. 2008). For the mode linewidth, Γ , we use the averaged values provided by Kjeldsen et al. (2005) and Fletcher et al. (2006).

Concerning mode masses, \mathcal{M} , as discussed in Sect. 6, it is not trivial to determine the height h where the Doppler velocities are predominantly measured. As we do not know the height representative of the observations precisely, we evaluate the mode masses – by default – at the optical depth $\tau_{500 \text{ nm}} \simeq 0.013$, which corresponds to the depth where the potassium (K) spectral line is formed (but see Sect. 6 for a discussion). This optical depth corresponds to $h = 470$ km.

Neither the standard nor the patched models have exactly the radius and the mass expected for α Centauri A (see Sect. 2.3.1). However, this inconsistency only has a negligible effect on the mode mass $\mathcal{M} = I/\xi_r^2$. Indeed, since the eigenmode displacement, ξ_r , is directly proportional to R , the mode inertia I scales as R^2 (see Eq. (2)). Accordingly, the ratio I/ξ_r^2 is almost insensitive to a small change in R . Furthermore, we checked that \mathcal{M} is also insensitive to a small change in M .

4. Comparison between observations and modeling

We first compare theoretical calculations of \mathcal{P} performed with eigenfunctions computed with the *patched* equilibrium model with those computed using the *standard* equilibrium model (see Sect. 2.2). However, eigenmodes computed with those two models do not have the same inertia and hence not the same mode masses \mathcal{M} . Thus, we instead compare the ratios \mathcal{P}/\mathcal{M} . As shown in Fig. 2, theoretical calculations that use the *patched* model lie well inside the observed domain of the seismic constraints. On the other hand, using the *standard* model leads to underestimated theoretical values compared to the two sets of seismic constraints.

When comparing the integrands of the *product* $\mathcal{P}\mathcal{M}$ – excitation power times mode mass – between the patched and standard

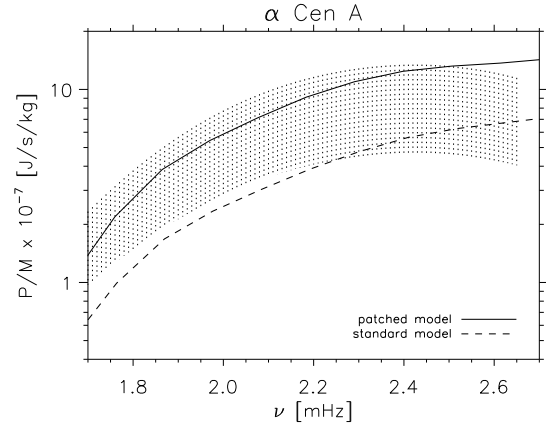


Fig. 2. Ratio of the rates \mathcal{P} at which energy is injected into p-modes to mode masses (\mathcal{M}) for α Centauri A. The dashed area represents the observed domain for $\mathcal{P}/\mathcal{M} = 2\pi \Gamma (v/S_0)^2$ as a function of ν . This domain is defined by merging the uncertainties associated with two independently derived values of Γ and with the mode amplitudes v (Eq. (7)). The solid (resp. dashed) line corresponds to computed excitation rates with the eigenmodes obtained using the “patched” (resp. “standard”) 1D global model. All calculations here use the CMP and the Lorentzian function (LF) for the eddy time-correlation function χ_k in Eqs. (5) and (6).

equilibrium models, we find that they are quite similar. On the other hand, the mode masses \mathcal{M} are quite different for the two equilibrium models in the domain 1–3 mHz where the modes are mostly excited. This is due to the turbulent pressure that is present in the patched model and ignored in the standard model. At a given radius in the super-adiabatic region, the patched model has a lower gas pressure and density (see Fig. 1). As a consequence, inertia of the modes, which are confined within the super-adiabatic region where the turbulent pressure has its maximum, are less for the patched model than for the standard model; accordingly, the *ratios* \mathcal{P}/\mathcal{M} , which are inversely proportional to the squared mode mass \mathcal{M}^2 , are about two times higher for the patched model.

In Fig. 3, we compare two sets of calculations for a patched stellar model that assumes two different prescriptions for the eddy-time correlation function (χ_k) and two different closure models, namely the QNA and the Closure Model with Plumes (CMP hereafter) in the excitation model. The theoretical calculations based on a Lorentzian χ_k and the CMP closure model lie inside the range allowed by the two sets of seismic constraints. The differences between calculations based on the CMP and on the QNA are found smaller than the differences between the two data sets. On the other hand, calculations based on a Gaussian χ_k yields significantly underestimated values compared to the seismic constraints.

Note that Samadi et al. (2007a) found a discrepancy between theoretical calculations and observations. Part of this discrepancy was due to the horizontal size of the simulation box being set to that of the solar simulation used in Belkacem et al. (2006b). Indeed, the kinetic energy spectrum E involved in the expression for S_R and S_S in Eqs. (5) and (6) must be normalized with respect to the horizontal size of the simulation box, as done here. Furthermore, the mode inertia considered by Samadi et al. (2007a) were computed for a standard MLT model (i.e. no turbulent pressure included) instead of using a patched model as is done here. As shown in Fig. 2, this results in an underestimation of the ratio \mathcal{P}/\mathcal{M} by a factor of about two (see Fig. 2).

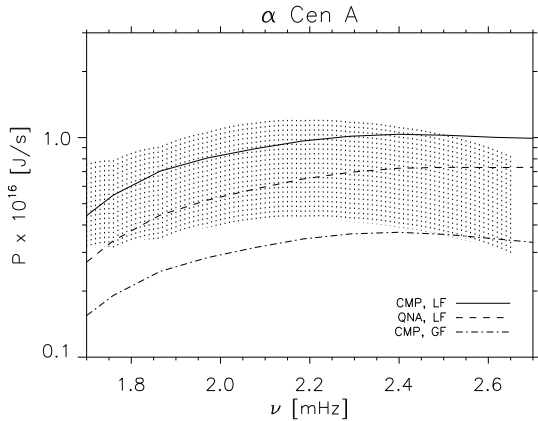


Fig. 3. Rates \mathcal{P} at which energy is injected into the p-modes of α Centauri A. The dashed area has the same meaning as in Fig. 2. The lines correspond to different theoretical calculations (all using a patched model): the solid line uses the Lorentzian function (LF) and the CMP, the dashed line uses the LF and the QNA closure model, the dot-dashed line uses the Gaussian function (GF) and the CMP.

5. Differences between α Centauri A and the Sun

5.1. Excitation rates

Figure 4 compares the excitation rates, \mathcal{P} , inferred for α Centauri A with those inferred from helioseismic measurements obtained for the Sun. For α Centauri A, excitation rates are obtained from the seismic measurements as explained in Sect. 3.

For the Sun we consider the helioseismic data studied by Baudin et al. (2005). We use here solar mode masses obtained with a patched model computed as for α Centauri A in Sect. 2. Mode masses are evaluated for the optical depth $\tau \approx 5 \times 10^{-4}$ since SOHO/GOLF observations are based on the Na D1 and D2 spectral lines (see Houdek 2006).

We find $\mathcal{P}_{\max, \odot} \approx 3.5 \pm 0.4 \times 10^{15}$ [J/s]. The excitation rates inferred for α Centauri A with mode masses \mathcal{M} evaluated at the optical depth associated with the potassium line ($\tau \approx 0.013$) give $\mathcal{P}_{\max} = 8.25 \pm 1.0 \times 10^{15}$ [J/s]. This is about 2.3 ± 0.3 times larger than $\mathcal{P}_{\max, \odot}$. If mode masses are evaluated at the photosphere ($h = 0, T = T_{\text{eff}}$), we obtain $\mathcal{P}_{\max} = 15.9 \pm 8.0 \times 10^{15}$ [J/s]. In that case this is about $\sim 4.4 \pm 2$ times larger than $\mathcal{P}_{\max, \odot}$.

As seen in Fig. 4, the frequency where \mathcal{P} peaks is ~ 2.4 mHz for α Centauri A. For comparison, in the solar case, \mathcal{P} peaks around 3.8 mHz. Clearly, the modes in α Centauri A are excited at a lower frequency compared to the solar modes. Note also that the frequency domain where the derivation of \mathcal{P} is possible from the available seismic data is much smaller for α Centauri A than for the Sun. This is obviously because the quality of the seismic data is much lower for α Centauri A than for the Sun.

5.2. Excitation rates as a function of depth

Figure 5 shows the integrand $d\mathcal{P}/dm$ of the excitation rates (Eq. (1), (3), (4)) as a function of the temperature for the mode for which \mathcal{P} is maximum in the Sun and in α Centauri A. The top panel shows the contribution of the Reynolds stress ($d\mathcal{P}_R/dm$) and the bottom panel the contribution of the entropy fluctuations ($d\mathcal{P}_S/dm$). Excitation due to the Reynolds stress is maximum where the rms value of velocity, u , peaks. Excitation due to the entropy fluctuations is maximum where \tilde{s} , the rms value of the entropy fluctuations, peaks. Figure 5 shows that the excitation

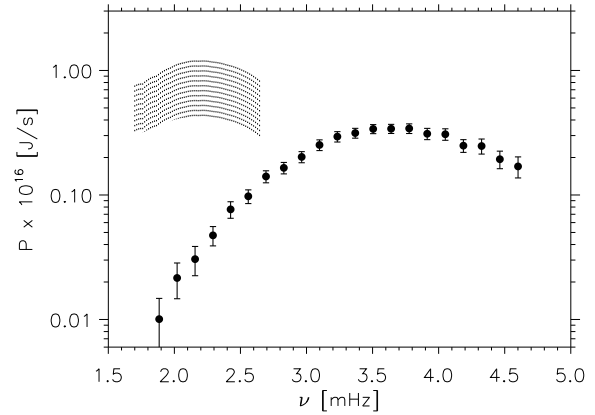


Fig. 4. Excitation rates \mathcal{P} inferred from seismic data according to Eq. (7). Filled circles correspond to the helioseismic constraints obtained by Baudin et al. (2005). The dashed area represents the observed domain for the excitation rates derived for α Centauri A.

rate is larger for α Centauri A than for the Sun and occurs over a slightly more extended region in α Centauri A than in the Sun.

The excitation due to the entropy fluctuations occurs in a more shallow region compared to the Reynolds stress. For α Centauri A, the relative contribution of the entropy fluctuations to the total excitation is $\approx 18\%$, which is similar to the Sun ($\approx 15\%$). Hence, in both cases the excitation due to the Reynolds stress remains the dominant contribution.

5.3. Differences in the characteristic properties of convection

To summarize, we find that \mathcal{P} is significantly larger in α Centauri A than in the Sun. Furthermore, \mathcal{P} peaks at lower frequency. As shown below, all these seismic differences can be attributed to differences in the characteristic properties of convection between α Centauri A and the Sun.

5.3.1. Why \mathcal{P} is larger for α Centauri A?

At a given layer, the power supplied to the modes by the Reynolds stress is proportional – per unit mass – to $\rho_0 u^3 \Lambda^4$ where Λ is the characteristic eddy size and u the rms value of the velocity (see Samadi & Goupil 2001). The flux of the kinetic energy, F_{kin} , is proportional to $\rho_0 u^3$. Hence, the greater F_{kin} or Λ , the greater the driving by the Reynolds stress.

The power supplied to the modes by the so-called entropy source term is proportional – per unit mass – to $\rho_0 u^3 \Lambda^4 \mathcal{R}^2 / (\tau_\Lambda \omega_0)^2$ where ω_0 is the mode frequency, $\tau_\Lambda \sim \Lambda/u$ is the characteristic eddy turn over time, and finally $\mathcal{R} \propto F_{\text{conv}}/F_{\text{kin}}$ where $F_{\text{conv}} \propto \omega \alpha_s \tilde{s}$ is the convective flux and \tilde{s} is the rms of entropy fluctuations (see Samadi et al. 2006). The higher \mathcal{R} , the higher the relative contribution of the entropy source to the excitation. The driving is maximum for mode frequency (see, e.g., Samadi & Goupil 2001)

$$\omega_0 \sim 2\pi/\tau_\Lambda. \quad (8)$$

Hence, at the mode frequency $\omega_0 \sim 2\pi/\tau_\Lambda$, the higher the ratio $F_{\text{conv}}/F_{\text{kin}}$, the greater the relative contribution of the entropy source term to the total excitation rate.

As a summary, for both Reynolds stress and entropy contributions, the larger the characteristic scale length (Λ) or the higher the kinetic energy (F_{kin}), the greater the excitation. Furthermore, the higher \mathcal{R} , the greater the relative contribution

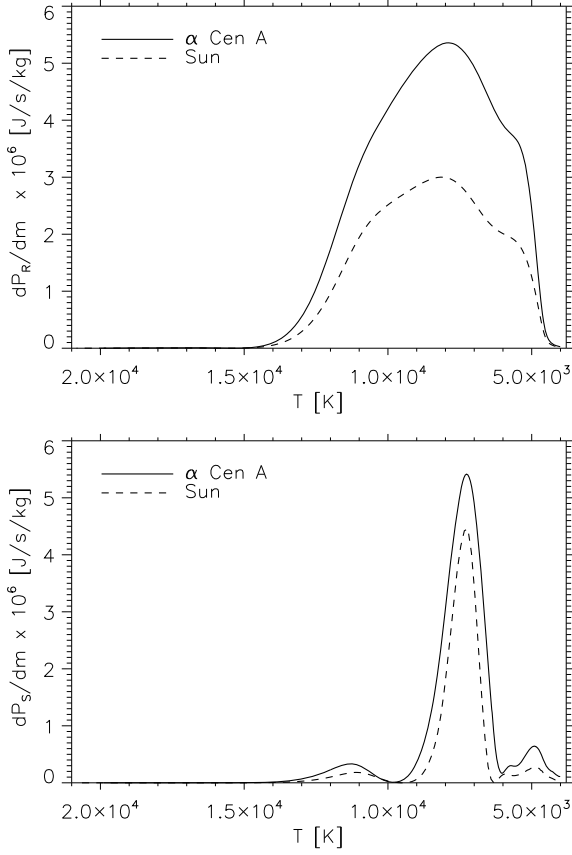


Fig. 5. *Top:* the integrand dP_R/dm (Eq. (1)) associated with the contribution of the Reynolds stress to the excitation is plotted as a function of the horizontally and temporally averaged temperature in the simulation box for the mode for which \mathcal{P} is maximum. The solid line corresponds to the 3D simulation associated with α Centauri A and the dashed line to the one associated with the Sun. *Bottom:* as the top panel for dP_S/dm , the integrand associated with the contribution due to the entropy fluctuations.

of the entropy source term to the excitation. We study the differences in Λ , F_{kin} , and \mathcal{R} between the Sun and α Centauri A below.

Kinetic energy flux (F_{kin}):

The maximum in u is up to $\sim 10\%$ greater in the 3D simulation associated with α Centauri A than in the solar one. However, the differences in the flux of kinetic energy, F_{kin} , between the 3D simulations associated with α Centauri A and the solar one are small ($\lesssim 10\%$). This small effect on F_{kin} despite its cubic dependence on u is due to the lower ρ_0 for a layer with the same average T in the simulation for α Centauri A as compared to the simulation for the Sun. The lower ρ_0 in turn is a consequence of the lower surface gravity of α Cen A compared to the Sun.

Relative contribution of the entropy source term:

We also find that \bar{s} is $\sim 25\%$ greater in the 3D simulation associated with α Centauri A. However, the convective flux, $F_{\text{conv}} \propto w \alpha_s \bar{s}$, in the 3D simulation associated with α Centauri A is very close to that of the solar simulation. This is not surprising since the two stars have almost the same effective temperature. Furthermore, as pointed out above, the differences in F_{kin} between α Centauri A and the Sun are small. As a consequence $\mathcal{R} \propto F_{\text{conv}}/F_{\text{kin}}$ does not differ between α Centauri A and the Sun. This explains why the contribution of the entropy term

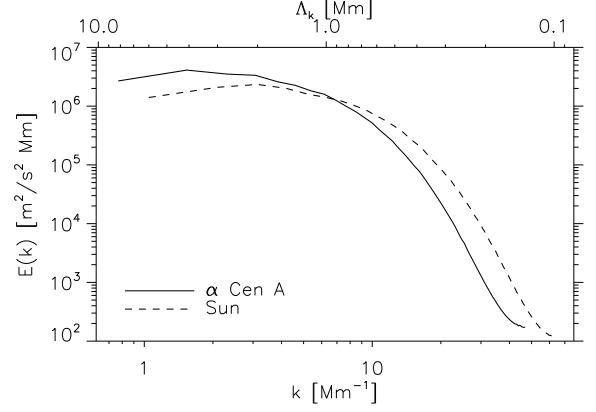


Fig. 6. The kinetic energy spectrum, E , as a function of the horizontal wavenumber k (lower axis) and the scale length $\Lambda_k = 2\pi/k$ (upper axis) for the layer where u is maximum. The solid line corresponds to the 3D simulation associated with α Centauri A and the dashed line to the one associated with the Sun.

relative to the Reynolds stress is similar between α Centauri A and the Sun.

Characteristic scale length (Λ):

Figure 6 shows the kinetic energy spectrum E as a function of the horizontal wavenumber k and the scale length $\Lambda_k = 2\pi/k$ for the layer where u is maximum. As seen in Fig. 6, for the 3D simulation associated with α Centauri A, E is maximum at a larger scale length compared to the solar simulation. Then, the eddies have a larger characteristic scale length in α Centauri A than in the Sun. This explains why the excitation of p-modes is significantly stronger for α Centauri A than for the Sun.

Since the number of grid points is the same for both simulations, the α Centauri A simulation has a larger physical grid size, thus a smaller maximum wavenumber, and in turn the cut-off in the spectrum occurs at a lower k . This explains the earlier drop-off of $E(k)$ for α Centauri A in Fig. 6. For that reason the high wavenumber part (beyond a k value of about 15 Mm^{-1} , or a Λ_k less than 0.4 Mm) should not be compared directly. On the other hand, the scaling chosen in Fig. 7 allows a direct comparison.

We point out that the characteristic scale length, Λ , scales as the pressure scale height. Indeed, we have plotted in Fig. 7 the kinetic energy spectrum, E , as a function of kH_p where H_p is the pressure height at the layer where u is maximum. Except at small scale lengths, we see that the k -dependency of the spectrum is almost the same between the simulation associated with α Centauri A and the solar one.

The ratio between $H_p^{\alpha \text{ cen A}}$ and H_p^{\odot} ($H_p^{\alpha \text{ cen A}}/H_p^{\odot} \simeq 1.38$) is very close to the ratio $g_{\odot}/g_{\alpha \text{ cen A}}$ ($\simeq 1.36$). This is obviously related to the fact that $H_p = P/\rho g \propto T/g$. Accordingly, since $\mathcal{P} \propto \Lambda^4$ (see above), we then have $\mathcal{P}/\mathcal{P}_{\odot} \propto (\Lambda/\Lambda_{\odot})^4 \propto (H_p^{\alpha \text{ cen A}}/H_p^{\odot})^4 \propto (g_{\alpha \text{ cen A}}/g_{\odot})^4 \sim 3.4$. For comparison, excitation rates computed for α Centauri A are two times greater than in the Sun.

5.3.2. Why \mathcal{P} peaks at lower frequency?

The characteristic eddy turnover time can be estimated as the quantity $\bar{\tau} \sim L_h/u$ where L_h is the horizontal extent of the 3D model and u the velocity at a given layer. At the layer where u is maximum, we find that $\bar{\tau}$, evaluated at the layer where u peaks, is larger in α Centauri A (~ 30 min) than in the Sun (~ 23 min).

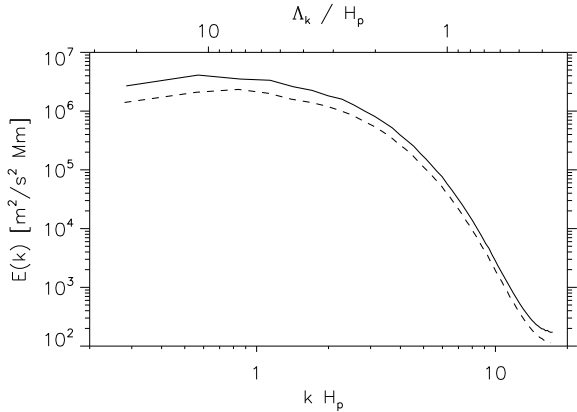


Fig. 7. The kinetic energy spectrum, E , as a function of $k H_p$ (lower axis) and Λ_k/H_p (upper axis) for the layer where u is maximum. The lines used have the same meaning as in Fig. 6.

This explains that for α Centauri A \mathcal{P} peaks at lower frequency than in the Sun ($\omega_0 \sim 2\pi/\bar{\tau}$, cf. Eq. (8)).

Both u and Λ are larger for α Centauri A than for the Sun. However, the net result is a larger $\bar{\tau}$ for α Centauri A.

5.3.3. Interpretation

The differences in characteristics of convection between α Centauri A and the Sun can be understood as follows: as seen in Sect. 5.3.1, the characteristic size Λ is mainly controlled by $H_p \propto T/g$ (for a given composition). The surface gravity for α Centauri A is $\sim 35\%$ times weaker than for the Sun while the effective temperature is very similar to that of the Sun. Consequently, Λ is larger than in the Sun. Furthermore because of the lower gravity, the density at the photosphere is lower than in the Sun. Hence, to transport the same amount of energy per unit surface area by convection, the convective cells must have higher speed (u).

6. Discussion

6.1. Effect of chemical composition

The star α Centauri A has an iron-to-hydrogen abundance of $[\text{Fe}/\text{H}] = 0.2$ (see Miglio & Montalbán 2005). The 3D simulation considered here has a solar abundance. Preliminary work tends to show that, at the given effective temperature, a 3D simulation with a metal abundance 10 times less than the solar one results in mode excitation rates ~ 2 times smaller. This can be understood as follows: the radiative flux is larger for a low metallicity than in a medium with a solar metallicity. In that case, to transport the same amount of energy, convection is less vigorous (i.e. lower flux of kinetic energy, F_{kin}), leading to a lower efficiency of the driving. If we extrapolate this preliminary result, we can expect that mode excitation rates ought to increase with $[\text{Fe}/\text{H}]$. A quantitative estimate of the expected increase must be performed, however, in particular for α Centauri A, which will require computing a 3D simulation with a non-solar abundance representative of the surface layers of the star (in progress).

6.2. Estimation of mode mass

Mode masses must be evaluated at the layer in the atmosphere where the acoustic modes are predominantly measured. The

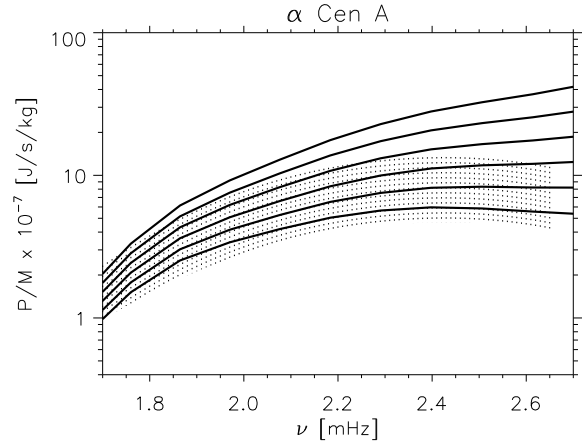


Fig. 8. Ratio of the rates \mathcal{P} at which energy is injected into the p-modes to the mode masses (\mathcal{M}) for α Centauri A. The dashed area represents the observed domain for $\mathcal{P}/\mathcal{M} = 2\pi\Gamma(v/S_0)^2$ as a function of ν (see Sect. 3). The solid lines correspond to the ratio \mathcal{P}/\mathcal{M} where the excitation rates, \mathcal{P} , are calculated according to Eq. (1) and the mode masses, \mathcal{M} , are evaluated at different heights h above the photosphere. The lower curve corresponds to the photosphere ($h = 0$) and the upper curve to the top of the atmosphere ($h = 1000$ km). The step in h is 200 km.

result of a comparison with seismic constraints significantly depends on the effective heights h where mode masses are evaluated. Indeed, we plot in Fig. 8 the ratio \mathcal{P}/\mathcal{M} for mode masses evaluated at different heights h in the atmosphere, namely from $h = 0$ (the photosphere) up to the top of the simulated domain ($h \approx 1000$ km). This ratio is compared to the quantity $2\pi\Gamma(v/S_0)^2$ obtained from the seismic constraints (Eq. (7)). For $h \gtrsim 600$ km (i.e. for optical depth $\lesssim 0.005$), the ratio \mathcal{P}/\mathcal{M} is outside the observational domain.

Seismic observations of α Centauri A were performed using UCLES and UVES spectrographs. UVES and UCLES use a similar technique to measure the acoustic modes (Bedding, private communication). Like other spectrographs dedicated to stellar seismic measurements, the UCLES instrument uses a large number of spectral lines to reach a high enough signal-to-noise ratio. In the case of stellar seismic measurements, it is then more difficult than for helioseismic observations to estimate the effective height h (for the solar case see, e.g., Baudin et al. 2005). A recent work by Kjeldsen et al. (2008) allows us to estimate the value for an effective h . Indeed, the authors have found that solar modes measured with the UCLES spectrograph have amplitudes slightly less than those measured by the BiSON network. The instruments of the BiSON network use the potassium (K) spectral line, which is formed at an optical depth $\tau_{500\text{ nm}} \approx 0.013$ (see Houdek 2006). The Kjeldsen et al. (2008) results then suggest that acoustic modes measured by UCLES are measured at an effective height (h) slightly below the formation depth of the K line, i.e. at optical depth slightly above $\tau_{500\text{ nm}} \approx 0.013$. Accordingly, we have evaluated the mode masses at that optical depth, which corresponds to $h = 470$ km.

A more rigorous approach would be to compute an effective mode mass by appropriately weighting the different mode masses associated with the different spectral lines that contribute to the seismic measurement. To infer accurate mode excitation rates from the seismic data of α Centauri A, the mode masses representative of the observation technique and the spectral lines of α Centauri A must be derived. This is, however, beyond the scope of this paper.

7. Conclusions

Theoretical estimations for the energy supplied per unit of time by turbulent convection (\mathcal{P}) to α Centauri A acoustic modes were compared to values obtained from observations. This allows us to draw the following conclusions.

7.1. Differences with the Sun

Although α Centauri A has an effective temperature very close to that of the Sun, we find here that the p-mode excitation rates \mathcal{P} inferred from the seismic constraints obtained for α Centauri A are about two times higher than in the Sun. These differences are attributed to the fact that the eddies in α Centauri A have a larger characteristic size (Λ) than in the Sun. This is related to the weaker surface gravity of α Centauri A.

Furthermore, the p-mode excitation rates for α Centauri A are maximum at lower frequencies than in the Sun. This behavior is related to the eddies having a longer turnover time as a result of a larger Λ .

The seismic characteristics of the p-modes detected in α Centauri A significantly differ from that of the Sun. They can therefore provide additional constraints on the model of stochastic excitation.

7.2. Inferred versus modeled excitation rates

Our modeling gives rise to excitation rates within the error bars associated with the observational constraints. We stress that this modeling was undertaken for α Centauri A *independently* from the solar case, i.e. without using a formulation fitted on the helioseismic data as is the case, for instance, for the Sun in [Chaplin et al. \(2005\)](#) or in the case for α Centauri A in [Houdek \(2002\)](#). The seismic constraints from α Centauri A then provide a clear validation of the basic underlying physical assumptions included in the theoretical model of stochastic excitation, at least for stars that are not too different from the Sun.

7.3. Constraints on the description of turbulence: eddy-time correlation

We find that our theoretical estimations of \mathcal{P} , which assume a Lorentzian eddy-time correlation function (χ_k) and the CMP proposed by [Belkacem et al. \(2006a\)](#), lie in the observed domain. On the other hand, when a Gaussian function is chosen for χ_k , \mathcal{P} is significantly underestimated. The comparison with the seismic data for α Centauri A confirms the results for the solar case obtained by [Samadi et al. \(2003\)](#) that χ_k significantly departs from a Gaussian. As in [Samadi et al. \(2003\)](#), we attribute the departure of χ_k from a Gaussian to diving plumes (i.e. down-flows), which are more turbulent than granules (i.e. the up-flows). This result confirms that a Lorentzian function is a more adequate description for the eddy-time correlation than a Gaussian.

7.4. Constraints on the modeling of turbulent convection in the equilibrium stellar model

Calculations involving eigenfunctions computed on the basis of a global 1D model that includes a realistic description of the outer layers of the star (taken from 3D simulations) reproduce much better (see Fig. 2) the seismic data than calculations that use eigenfunctions computed with a standard stellar model built with the MLT and ignoring turbulent pressure. This is because a model that includes turbulent pressure results in higher mode

masses \mathcal{M} than a model that ignores turbulent pressure. This can be understood as follows. Within the super-adiabatic region, a model that includes turbulent pressure provides an additional support against gravity, hence has a lower gas pressure and density (see Fig. 1) than a model that does not include turbulent pressure. As a consequence, mode inertia (hence mode masses) are then larger in a model that includes turbulent pressure.

These conclusion are similar to that obtained in the Sun. Indeed, the mode masses considered by [Belkacem et al. \(2006b\)](#) in the case of the Sun were obtained with a 1D model computed using the [Gough \(1977\)](#) non-local mixing-length formulation of convection. The model thus includes turbulent pressure. We do not observe significant differences between excitation rates obtained with this non-local model and those obtained with a “patched” solar computed as described here in the case of α Centauri A. On the other hand, excitation rates computed with mode masses obtained with a “standard” solar model (that is, with no turbulent pressure included) or with a model in which turbulent pressure is included according to the MLT significantly under-estimate the helioseismic constraints.

These results tell that one must compute mode masses from 1D models that include turbulent pressure using a 3D hydrodynamical model or using a non-local description of convection.

7.5. Need for improved data sets

As shown by [Samadi et al. \(2003\)](#) in the case of the Sun, contribution of the entropy fluctuations to the excitation cannot be neglected. Furthermore, recently, [Belkacem et al. \(2006b\)](#) have shown that theoretical calculations based on the CMP result in a better agreement with the helioseismic constraints than those based on QNA.

However, in the case of α Centauri A, differences between theoretical calculations that use the CMP and those based on the QNA (see Fig. 3), as well as differences between calculations including driving by entropy fluctuations and those that do not include it (not shown), are of the same order as the observational uncertainties associated with the two data sets. The present seismic constraints therefore are unable to distinguish between these assumptions. This emphasizes the need for more accurate seismic data for α Centauri A.

Acknowledgements. F.K.’s work was possible thanks to a one month grant provided by Observatoire de Paris. We thank T. Bedding for providing us the amplitude spectrum of α Centauri A obtained from the UVES and UCLES spectrographs. We thank Å. Nordlund, R. F. Stein, and R. Trampedach for making their 3D simulation code available. Finally, we thank the referee (M. Steffen) for his useful remarks.

References

- Baudin, F., Samadi, R., Goupil, M.-J., et al. 2005, *A&A*, 433, 349
- Bedding, T. R., Kjeldsen, H., Butler, R. P., et al. 2004, *ApJ*, 614, 380
- Belkacem, K., Samadi, R., Goupil, M. J., & Kupka, F. 2006a, *A&A*, 460, 173
- Belkacem, K., Samadi, R., Goupil, M. J., Kupka, F., & Baudin, F. 2006b, *A&A*, 460, 183
- Böhm-Vitense, E. 1958, *Z. Astrophys.*, 46, 108
- Butler, R. P., Bedding, T. R., Kjeldsen, H., et al. 2004, *ApJ*, 600, L75
- Chaplin, W. J., Houdek, G., Elsworth, Y., et al. 2005, *MNRAS*, 360, 859
- Christensen-Dalsgaard, J., & Berthomieu, G. 1991, *Theory of solar oscillations, Solar interior and atmosphere (A92-36201 14-92)* (Tucson, AZ: University of Arizona Press), 401
- Fletcher, S. T., Chaplin, W. J., Elsworth, Y., Schou, J., & Buzasi, D. 2006, *MNRAS*, 824
- Goldreich, P., Murray, N., & Kumar, P. 1994, *ApJ*, 424, 466
- Gough, D. O. 1977, *ApJ*, 214, 196
- Grevesse, N., & Noels, A. 1993, in *Origin and Evolution of the Elements*, ed. N. Prantzos, E. Vangioni-Flam, & M. Cassé (Cambridge University Press), 15

- Houdek, G. 2002, in *Radial and Nonradial Pulsations as Probes of Stellar Physics*, ed. C. Aerts, T. R. Bedding, & J. Christensen-Dalsgaard, IAU Colloq., 185447, ASP Conf. Ser., 259
- Houdek, G. 2006, in *Proceedings of SOHO 18/GONG 2006/HELAS I, Beyond the spherical Sun*, Published on CDROM, ESA SP, 624, 28.1
- Kjeldsen, H., Bedding, T. R., Butler, R. P., et al. 2005, *ApJ*, 635, 1281
- Kjeldsen, H., Bedding, T. R., Arentoft, T., et al. 2008, *ApJ*, 682, 1370
- Michaud, G., & Proffitt, C. R. 1993, in *Inside the Stars*, IAU Colloq., 137, ASP Conf. Ser., 40, 246
- Miglio, A., & Montalbán, J. 2005, *A&A*, 441, 615
- Millionshchikov, M. D. 1941, *Doklady Acad. Nauk SSSR*, 32, 611
- Nordlund, Å., & Stein, R. F. 1999, in *Stellar Structure: Theory and Test of Connective Energy Transport*, ed. A. Gimenez, E. F. Guinan, & B. Montesinos, ASP Conf. Ser., 173, 91
- Rosenthal, C. S., Christensen-Dalsgaard, J., Nordlund, Å., Stein, R. F., & Trampedach, R. 1999, *A&A*, 351, 689
- Samadi, R., Belkacem, K., Goupil, M.-J., Kupka, F., & Dupret, M.-A. 2007a, in ed. F. Kupka, I. Roxburgh, & K. Chan, IAU Symp., 239, 349
- Samadi, R., Georgobiani, D., Trampedach, R., et al. 2007b, *A&A*, 463, 297
- Samadi, R., & Goupil, M. 2001, *A&A*, 370, 136
- Samadi, R., Goupil, M.-J., Alecian, E., et al. 2005, *A&A*, 26, 171
- Samadi, R., Kupka, F., Goupil, M. J., Lebreton, Y., & van't Veer-Menneret, C. 2006, *A&A*, 445, 233
- Samadi, R., Nordlund, Å., Stein, R. F., Goupil, M. J., & Roxburgh, I. 2003, *A&A*, 404, 1129
- Stein, R. F., & Nordlund, A. 1998, *ApJ*, 499, 914
- Stein, R. F., & Nordlund, Å. 2001, *ApJ*, 546, 585
- Trampedach, R. 1997, Master's thesis, Aarhus University

Stochastic excitation of non-radial modes

I. High-angular-degree p modes

K. Belkacem, R. Samadi, M.-J. Goupil, and M.-A. Dupret

Observatoire de Paris, LESIA, CNRS UMR 8109, 92190 Meudon, France
e-mail: Kevin.Belkacem@obspm.fr

Received 2 May 2007 / Accepted 3 October 2007

ABSTRACT

Context. Turbulent motions in stellar convection zones generate acoustic energy, part of which is then supplied to normal modes of the star. Their amplitudes result from a balance between the efficiencies of excitation and damping processes in the convection zones.

Aims. We develop a formalism that provides the excitation rates of non-radial global modes excited by turbulent convection. As a first application, we estimated the impact of non-radial effects on excitation rates and amplitudes of the high-angular-degree modes that are observed on the Sun.

Methods. A model of stochastic excitation by turbulent convection was developed to compute the excitation rates and then successfully applied to solar radial modes. We generalise this approach to the case of non-radial global modes. This enables us to estimate the energy supplied to high- (ℓ) acoustic modes. Qualitative arguments, as well as numerical calculations, are used to illustrate the results.

Results. We find that non-radial effects for p modes are non-negligible:

- For high- n modes (i.e. typically $n > 3$) and for high values of ℓ , the power supplied to the oscillations depends on the mode inertia.
- For low- n modes, independent of the value of ℓ , the excitation is dominated by the non-radial components of the Reynolds stress term.

Conclusions. Our numerical investigation of high- ℓ p modes shows that the validity of the present formalism is limited to $\ell < 500$ due to the spatial separation of scale assumption. Thus, a model for very high- ℓ p -mode excitation rates calls for further theoretical developments; however, the formalism is valid for solar g modes, which will be investigated in a paper in preparation.

Key words. convection – turbulence – Sun: oscillations

1. Introduction

Amplitudes of solar-like oscillations result from a balance between stochastic excitation and damping in the outermost layers of the convection zone, which extends nearly to the surface of the star. Accurate measurements of the rate at which acoustic energy is supplied to the solar p modes are available from ground-based observations (GONG, BiSON), as well as from spacecraft (SOHO/GOLF and MDI). From those measurements and a comparison with theoretical models, it has been possible to demonstrate that excitation is due to eddy motions in the uppermost part of the convection zone and by advection of entropy fluctuations.

Stochastic excitation of *radial* modes by turbulent convection has been investigated by means of several semi-analytical approaches (Goldreich & Keeley 1977; Goldreich et al. 1994; Balmforth 1992; Samadi & Goupil 2001), they differ from each other in the nature of the assumed excitation sources, the assumed simplifications and approximations, and also by the way the turbulent convection is described (see reviews by Stein et al. 2004; Houdek 2006). Two major mechanisms have nevertheless been identified as driving the resonant p modes of the stellar cavity: the first is related to the Reynolds stress tensor and, as such, represents a mechanical source of excitation; the second is caused by the advection of turbulent fluctuations of entropy by turbulent motions (the entropy source term), and as such it represents a thermal source of excitation (Goldreich et al. 1994; Stein & Nordlund 2001). Samadi & Goupil (2001, hereafter Paper I) proposed a generalised formalism, taking the Reynolds and

entropy fluctuation source terms into account. In this model, the source terms are written as functions of the turbulent kinetic energy spectrum and the temporal-correlation function. This allowed us to investigate several possible models of turbulence (Samadi et al. 2003a,b). The results were compared with GOLF data for radial modes, and the theoretical values were found to be in good agreement with the observations (Samadi et al. 2003b). Part of the remaining discrepancies has recently been removed by taking into account the asymmetry introduced by turbulent plumes (Belkacem et al. 2006a,b).

In this paper we take an additional step by extending the Samadi & Goupil (2001) formalism to the case of non-radial global modes. This will enable us to estimate the excitation rates for a wide variety of p and g modes excited in different types of stars. The present model provides the energy supplied to the modes by turbulence in inner, as well as outer, stellar convective regions, provided the turbulent model appropriate for the relevant region is used. Studies of the stochastic excitation of solar radial modes (Samadi et al. 2003a,b) have given us access mainly to the radial properties of turbulence. The present generalised formalism enables us to take the horizontal properties of turbulence into account (through the non-radial components of the Reynolds stress contribution) in the outermost part of the convective zone.

In the Sun, high-angular-degree p modes (as high as one thousand) have been detected (e.g., Korzenik et al. 2004). From an observational point of view, Woodard et al. (2001) found that the energy supplied to the mode increases with ℓ , but that above

some high- ℓ value, which depends on the radial order n (see Woodard et al. 2001, Fig. 2), the energy decreases with increasing ℓ . They mention the possibility of an unmodelled mechanism of damping. Hence one of the motivations of this work is to investigate such an issue. As a first step, we develop here a theoretical model of the stochastic excitation taking the ℓ -dependence of the source terms into account to seek a physical meaning for such a behaviour of the amplitudes.

Modelling of the mechanisms responsible for exciting non-radial modes is useful not only for high- ℓ acoustic modes but also for gravity modes, which are intrinsically non-radial. As for p modes, g modes are stochastically excited by turbulent convection; the main difference is that the dominant restoring force for g modes is buoyancy. We, however, stress that convective penetration is another possible excitation mechanism for g modes (e.g. Dintrans et al. 2005). Such modes are trapped in the radiative interior of the Sun, so their detection promises closer knowledge of the deep solar interior. However, they are evanescent in the convection zone; thus, their amplitudes at the surface are very small and their detection remains controversial. A theoretical prediction of their amplitudes is thus an important issue. It requires an estimation of the excitation rates but also of the damping rates. Unlike p modes, the damping rates cannot be inferred from observations, and this introduces considerable uncertainties; e.g., theoretical estimates of the g -mode amplitudes (Gough 1985; Kumar et al. 1996) differ from each other by orders of magnitudes, as pointed out by Christensen-Dalsgaard (2002). We thus stress that the present work focuses on the excitation rates – damping rates are not investigated. A specific study of gravity modes will be considered in a forthcoming paper.

The paper is organised as follows: Sect. 2 introduces the general formalism, and a detailed derivation of the Reynolds and entropy source terms is provided. In Sect. 3, we demonstrate that the formalism of Samadi & Goupil (2001) is a special case and an asymptotic limit of the present model. In Sect. 4, we use qualitative arguments to determine the different contributions to the excitation rates and identify the dominant terms involving the angular degree (ℓ). Section 5 presents the numerical results where excitation rates are presented. Section 6 discusses the limitations of the model and some conclusions are formulated in Sect. 7.

2. General formulation

Following Paper I, we start from the perturbed momentum and continuity equation

$$\frac{\partial(\rho_0 + \rho_1)\mathbf{v}}{\partial t} + \nabla \cdot (\rho_0 \mathbf{v}\mathbf{v}) = -\nabla p_1 + \rho_1 \mathbf{g}_0 + \rho_0 \mathbf{g}_1 + \rho_1 \mathbf{g}_1, \quad (1)$$

$$\frac{\partial \rho_1}{\partial t} + \nabla \cdot ((\rho_0 + \rho_1)\mathbf{v}) = 0 \quad (2)$$

where ρ is the density, p the pressure, and \mathbf{g} the gravity. The subscripts 1 and 0 denote Eulerian perturbations and equilibrium quantities, respectively, except for velocity where the subscript 1 has been dropped for ease of notation. In the following, the velocity field is split into two contributions, namely the oscillation velocity (\mathbf{v}_{osc}) and the turbulent velocity field (\mathbf{u}), such that $\mathbf{v} = \mathbf{v}_{\text{osc}} + \mathbf{u}$. For a given mode, the fluid displacement can be written as

$$\delta \mathbf{r}_{\text{osc}} = \frac{1}{2} \left(A(t) \boldsymbol{\xi}(\mathbf{r}) e^{-i\omega_0 t} + c.c. \right), \quad (3)$$

where ω_0 is the eigenfrequency, $\boldsymbol{\xi}(\mathbf{r})$ the displacement eigenfunction in the absence of turbulence, $A(t)$ the amplitude due to the turbulent forcing, and $c.c.$ denotes the complex conjugate. The power (P) injected into the modes is related to the mean-squared amplitude ($\langle |A|^2 \rangle$) by (see Paper I)

$$P = \eta \langle |A|^2 \rangle I \omega_0^2, \quad (4)$$

where the operator $\langle \rangle$ denotes a statistical average performed on an infinite number of independent realisations, η is the damping rate, and I is the mode inertia.

We use the temporal WKB assumption, i.e. that $A(t)$ is slowly varying with respect to the oscillation period, $\eta \approx d \ln A(t) / dt \ll \omega_0$ (see Paper I for details). Under this assumption, using Eq. (3) with Eqs. (1) and (2) (see Paper I) yields:

$$\frac{dA(t)}{dt} + \eta A(t) = \frac{1}{2\omega_0^2 I} \int d^3x \boldsymbol{\xi}^* \cdot \frac{\partial \mathbf{S}}{\partial t} e^{i\omega_0 t}, \quad (5)$$

where d^3x is the volume element and $\mathbf{S} = -(\mathbf{f}_t + \nabla h_t + \mathbf{g}_t)$ the excitation source terms. Temporal derivatives appearing in Eq. (5) are

- The Reynolds stress contribution

$$\frac{\partial f_t}{\partial t} = -\frac{\partial}{\partial t} (\nabla : (\rho_0 \mathbf{u}\mathbf{u})), \quad (6)$$

where \mathbf{u} is the turbulent component of the velocity field.

- The entropy term

$$\frac{\partial}{\partial t} \nabla h_t = -\nabla \left(\alpha_s \frac{d\delta s_t}{dt} - \alpha_s \mathbf{u} \cdot \nabla s_t \right), \quad (7)$$

where δs_t is the turbulent Lagrangian fluctuation of the entropy ($\alpha_s = dp_1 / ds_t$) and p_1 denotes the Eulerian pressure fluctuations.

The last term in the right hand side of Eq. (7) represents the advection of entropy fluctuations by turbulent motion and, as such, is a thermal driving. Note that it was shown in Belkacem et al. (2006b) that this term is needed to reproduce the maximum in the amplitude as a function of frequency in the case of solar radial p modes.

- The fluctuating gravity term

$$\frac{\partial g_t}{\partial t} = \frac{\partial \rho_1 g_1}{\partial t}, \quad (8)$$

where g_1 is the fluctuation of gravity due to the turbulent field. This contribution can be shown to be negligible and will not be considered in detail here for p modes.

Several other excitation source terms appear on the right hand side of Eq. (1). However, as shown in Paper I, their contributions are negligible since they are linear in terms of turbulent fluctuations.¹

From Eq. (5), one obtains the mean-squared amplitude

$$\begin{aligned} \langle |A|^2(t) \rangle &= \frac{e^{-2\eta t}}{4(\omega_0 I)^2} \int_{-\infty}^t dt_1 dt_2 \\ &\times \int d^3r_1 d^3r_2 e^{\eta(t_1+t_2)+i\omega_0(t_1-t_2)} \\ &\times \langle (\boldsymbol{\xi}^*(\mathbf{r}_1) \cdot \mathbf{S}(\mathbf{r}_1, t_1)) (\boldsymbol{\xi}(\mathbf{r}_2) \cdot \mathbf{S}^*(\mathbf{r}_2, t_2)) \rangle, \end{aligned} \quad (9)$$

¹ Linear terms are defined as the product of an equilibrium quantity and a fluctuating one.

where subscripts 1 and 2 denote two spatial and temporal locations. To proceed further, it is convenient to define the following coordinates:

$$\begin{aligned} \mathbf{x}_0 &= \frac{\mathbf{r}_2 + \mathbf{r}_1}{2} & t_0 &= \frac{t_1 + t_2}{2} \\ \mathbf{r} &= \mathbf{r}_2 - \mathbf{r}_1 & \tau &= t_2 - t_1 \end{aligned}$$

where \mathbf{x}_0 and t_0 are the average space-time position and \mathbf{r} and τ are related to the local turbulence.

In the following, ∇_0 is the large-scale derivative associated with \mathbf{x}_0 , ∇_r is the small-scale one associated with \mathbf{r} , and the derivative operators ∇_1 and ∇_2 are associated with \mathbf{r}_1 and \mathbf{r}_2 , respectively. The mean-squared amplitude can be rewritten in terms of the new coordinates as

$$\begin{aligned} \langle |A|^2(t) \rangle &= \frac{1}{4(\omega_0 I)^2} \\ &\times \int_{-\infty}^t dt_0 e^{2\eta(t_0-t)} \int_{2(t_0-t)}^{2(t-t_0)} d\tau \int d^3x_0 d^3r e^{-i\omega_0\tau} \\ &\times \left\langle \left(\boldsymbol{\xi}^* \cdot \mathcal{S} \left[\mathbf{x}_0 - \frac{\mathbf{r}}{2}, t_0 - \frac{\tau}{2} \right] \right) \left(\boldsymbol{\xi} \cdot \mathcal{S}^* \left[\mathbf{x}_0 + \frac{\mathbf{r}}{2}, t_0 + \frac{\tau}{2} \right] \right) \right\rangle. \end{aligned} \quad (10)$$

Subscripts 1 and 2 are the values taken at the spatial and temporal positions $[\mathbf{x}_0 - \frac{\mathbf{r}}{2}, -\frac{\tau}{2}]$ and $[\mathbf{x}_0 + \frac{\mathbf{r}}{2}, \frac{\tau}{2}]$ respectively. In the excitation region, the eddy lifetime is much smaller than the oscillation lifetime ($\sim 1/\eta$) of p modes such that the integration over τ can be extended to infinity. Hence all time integrations over τ are understood to be performed over the range $]-\infty, +\infty[$.

We assume a stationary turbulence, therefore the source term (\mathcal{S}) in Eq.(10) is invariant to translation in t_0 . Integration over t_0 in Eq.(10) and using the definition of \mathcal{S} (Eq. (6), Eqs. (7) and (8) yields

$$\langle |A|^2 \rangle = \frac{1}{8\eta(\omega_0 I)^2} (C_R^2 + C_S^2 + C_{RS}), \quad (11)$$

where C_R^2 and C_S^2 are the turbulent Reynolds stress and entropy fluctuation contributions whose expressions are, respectively,

– the Reynolds source term:

$$\begin{aligned} C_R^2 &= \int d^3x_0 \int_{-\infty}^{+\infty} d\tau e^{-i\omega_0\tau} \int d^3r \\ &\times \left\langle \left(\rho_0 u_j u_i \nabla_0^j \xi^i \right)' \left(\rho_0 u_l u_m \nabla_0^l \xi^{*m} \right)'' \right\rangle \end{aligned} \quad (12)$$

where a *separation of scales* is assumed, i.e. that the spatial variation of the eigenfunctions is large compared to the typical length scale of turbulence (see Sect. 6 for a detailed discussion).

– the entropy contribution

$$\begin{aligned} C_S^2 &= \int d^3x_0 \int_{-\infty}^{+\infty} d\tau e^{-i\omega_0\tau} \int d^3r \\ &\times \left\langle \left(h_l \nabla_0^l \xi^i \right)_1 \left(h_l \nabla_0^l \xi^{*i} \right)_2 \right\rangle, \end{aligned} \quad (13)$$

where C_{RS} is the cross-source term representing interference between source terms. For p modes, C_{RS} turn out to be negligible because it involves third-order correlation products that are small and strictly vanish under the QNA assumption (Belkacem et al. 2006b).

2.1. Turbulent Reynolds stress contribution

Equation (12) is first rewritten as

$$\begin{aligned} C_R^2 &= \int d^3x_0 \int_{-\infty}^{+\infty} d\tau e^{-i\omega_0\tau} \int d^3r \rho_0^2 \\ &\times \nabla_0^j \xi^i \left\langle \left(u_j u_i \right)_1 \left(u_l u_m \right)_2 \right\rangle \nabla_0^l \xi^{*m}. \end{aligned} \quad (14)$$

The fourth-order moment is then approximated assuming the quasi-normal approximation (QNA, Lesieur 1997, Chap. VII-2) as in Paper I. The QNA is a convenient means of decomposing the fourth-order velocity correlations in terms of a product of second-order velocity correlations; that is, one uses

$$\begin{aligned} \langle \left(u_i u_j \right)_1 \left(u_l u_m \right)_2 \rangle &= \langle \left(u_i u_j \right)_1 \rangle \langle \left(u_l u_m \right)_2 \rangle \\ &+ \langle \left(u_i \right)_1 \left(u_l \right)_2 \rangle \langle \left(u_j \right)_1 \left(u_m \right)_2 \rangle \\ &+ \langle \left(u_i \right)_1 \left(u_m \right)_2 \rangle \langle \left(u_j \right)_1 \left(u_l \right)_2 \rangle. \end{aligned} \quad (15)$$

A better approximation is the closure model with plumes (Belkacem et al. 2006a,b) which can be adapted to the present formalism in order to take the presence of up and downdrafts in the solar convection zone into account.

It is then possible to express the Fourier transform (FT) of the resulting second-order moments in term of the turbulent kinetic and entropy energy spectrum (see Paper I for details)

$$\phi_{ij} = FT(\langle u_i u_j \rangle) = \frac{E(k, \omega)}{4\pi k^2} \left(\delta_{ij} - \frac{k_i k_j}{k^2} \right), \quad (16)$$

where $E(k, \omega)$ is the turbulent kinetic energy spectrum.

The turbulent Reynolds term Eq.(12) takes the following general expression under the assumption of isotropic turbulence:

$$C_R^2 = \pi^2 \int d^3x_0 \left(\rho_0^2 b_{ij}^* b_{lm} \right) S_{(R)}^{ijlm}(\omega_0) \quad (17)$$

where

$$\begin{aligned} S_{(R)}^{ijlm} &= \int_{-\infty}^{+\infty} d\omega \int d^3k \left(T^{ijlm} + T^{ijml} \right) \\ &\times \frac{E^2(k)}{k^4} \chi_k(\omega_0 + \omega) \chi_k(\omega) \end{aligned} \quad (18)$$

$$T^{ijlm} = \left(\delta^{il} - \frac{k^i k^l}{k^2} \right) \left(\delta^{jm} - \frac{k^j k^m}{k^2} \right) \quad (19)$$

$$b_{ij} \equiv \mathbf{e}_i \cdot (\nabla_0 : \boldsymbol{\xi}) \cdot \mathbf{e}_j \quad (20)$$

where $\{\mathbf{e}_i\}$ are the spherical coordinate unit vectors, (\mathbf{k}, ω) are the wavenumber and frequency associated with the turbulent eddies and turbulent kinetic energy spectrum $E(\mathbf{k}, \omega)$, which is expressed as the product $E(\mathbf{k})\chi_k(\omega)$ for isotropic turbulence (Lesieur 1997). The kinetic energy spectrum $E(k)$ is normalized as

$$\int_0^\infty dk E(k) = \frac{1}{2} \Phi w^2 \quad (21)$$

where w is an estimate for the vertical convective velocity and Φ is a factor introduced by Gough (1977) to take anisotropy effects into account. A detailed discussion of the temporal correlation function (χ_k) is addressed in Samadi et al. (2003b).

The contribution of the Reynolds stress can thus be written as (see Appendix A.1)

$$C_R^2 = 4\pi^3 \int dm \rho_0 R(r) S_R(\omega_0), \quad (22)$$

with

$$\begin{aligned}
 R(r) = & \frac{16}{15} \left| \frac{d\xi_r}{dr} \right|^2 + \frac{44}{15} \left| \frac{\xi_r}{r} \right|^2 + \frac{4}{5} \left(\frac{\xi_r^*}{r} \frac{d\xi_r}{dr} + c.c. \right) \\
 & + L^2 \left(\frac{11}{15} |\zeta_r|^2 - \frac{22}{15} \frac{\xi_r^* \xi_h}{r^2} + c.c. \right) \\
 & - \frac{2}{5} L^2 \left(\frac{d\xi_r^*}{dr} \frac{\xi_h}{r} + c.c. \right) \\
 & + \left| \frac{\xi_h}{r} \right|^2 \left(\frac{16}{15} L^4 + \frac{8}{5} \mathcal{F}_{\ell,|m|} - \frac{2}{3} L^2 \right)
 \end{aligned} \quad (23)$$

where we have defined

$$L^2 = \ell(\ell + 1) \quad (24)$$

$$\zeta_r \equiv \frac{d\xi_h}{dr} + \frac{1}{r}(\xi_r - \xi_h) \quad (25)$$

$$\mathcal{F}_{\ell,|m|} = \frac{|m|(2\ell + 1)}{2} (\ell(\ell + 1) - (m^2 + 1)) \quad (26)$$

$$S_{\mathbf{R}}(\omega_0) = \int \frac{dk}{k^2} E^2(k) \int d\omega \chi_k(\omega + \omega_0) \chi_k(\omega). \quad (27)$$

Note that in the present work, nonradial effects are taken only into account through Eq. (23). A more complete description would require including anisotropic turbulence effects in Eq. (18), but this is beyond the scope of the present paper.

2.2. Entropy fluctuations contribution

The entropy source term is computed as for the Reynolds contribution in Sect. 2.1. Then Eq. (13) becomes

$$C_S^2 = \frac{2\pi^2}{\omega_0^2} \int d^3x_0 \alpha_s^2 h^{ij} S_{ij}^{(S)}(\omega_0), \quad (28)$$

where

$$S_{ij}^{(S)}(\omega_0) = \int d^3k T_{ij} \frac{E(k)}{k^2} \frac{E_s(k)}{k^2} \int d\omega \chi_k(\omega_0 + \omega) \chi_k(\omega)$$

with

$$T_{ij} = \left(\delta_{ij} - \frac{k_i k_j}{k^2} \right), \quad (29)$$

where $E_s(k)$ is the entropy spectrum (see Paper I), and

$$\begin{aligned}
 h^{ij} = & |C|^2 \nabla_1^i (\ln |\alpha_s|) \nabla_2^j (\ln |\alpha_s|) \\
 & - C^* \nabla_1^i (\ln |\alpha_s|) \nabla_2^j (C) \\
 & - C \nabla_1^i (\ln |\alpha_s|) \nabla_2^j (C^*) + \nabla_1^i (C^*) \nabla_2^j (C),
 \end{aligned} \quad (30)$$

where $C \equiv \nabla \cdot \xi$ is the mode compressibility.

The final expression for the contribution of entropy fluctuations reduces to (see Appendix A.2)

$$C_S^2 = \frac{4\pi^3 \mathcal{H}}{\omega_0^2} \int d^3x_0 \alpha_s^2 (A_\ell + B_\ell) \mathcal{S}_S(\omega_0), \quad (31)$$

where \mathcal{H} is the anisotropy factor introduced in Paper I which, in the current assumption (isotropic turbulence), is equal to 4/3. In addition,

$$A_\ell \equiv \frac{1}{r^2} \left| D_\ell \frac{d(\ln |\alpha_s|)}{d \ln r} - \frac{dD_\ell}{d \ln r} \right|^2 \quad (32)$$

$$B_\ell \equiv \frac{1}{r^2} L^2 |D_\ell|^2 \quad (33)$$

$$S_S(\omega_0) \equiv \int \frac{dk}{k^4} E(k) E_s(k) \int d\omega \chi_k(\omega_0 + \omega) \chi_k(\omega) \quad (34)$$

where

$$D_\ell(r, \ell) \equiv D_r - \frac{L^2}{r} \xi_h, \quad D_r \equiv \frac{1}{r^2} \frac{d}{dr} (r^2 \xi_r). \quad (35)$$

3. The radial case

We show in this section that we recover the results of Paper I providing that:

- we restrict ourselves to the radial case by setting $\ell = 0$ ($\xi_h = 0$), and
- we assume a plane-parallel atmosphere.

In the entropy source term (C_S^2), the mode compressibility for a radial mode becomes

$$C = -\frac{\delta\rho}{\rho} = \frac{1}{r^2} \frac{d(r^2 \xi_r)}{dr} Y_{\ell,m} \quad (36)$$

and from Eqs. (32) and (33), one then has

$$A_{\ell=0} = \frac{1}{r^2} \left| D_r \frac{d}{d \ln r} \ln |\alpha_s| - \frac{dD_r}{d \ln r} \right|^2 \quad (37)$$

$$B_{\ell=0} = 0. \quad (38)$$

We thus obtain (Eq. (31))

$$\begin{aligned}
 C_S^2 = & \frac{4\pi^3 \mathcal{H}}{\omega_0^2} \int d^3x_0 \alpha_s^2 \\
 & \times \frac{1}{r^2} \left| D_r \frac{d \ln |\alpha_s|}{d \ln r} - \frac{dD_r}{d \ln r} \right|^2 \mathcal{S}_S(\omega_0).
 \end{aligned} \quad (39)$$

For the Reynolds stress contribution, Eq. (22) reduces to

$$\begin{aligned}
 C_R^2 = & 4\pi^3 \int d^3x_0 \rho_0^2 \\
 & \times \left(\frac{16}{15} \left| \frac{d\xi_r}{dr} \right|^2 + \frac{44}{15} \left| \frac{\xi_r}{r} \right|^2 + \frac{4}{5} \frac{\xi_r^*}{r} \frac{d\xi_r}{dr} + c.c. \right) \mathcal{S}_R(\omega_0).
 \end{aligned} \quad (40)$$

To proceed further, we use the plane-parallel approximation. It is justified (for p modes) by the fact that excitation takes place in the uppermost part of the convection zone ($r/R \approx 1$). It is valid when the condition $r k_{\text{osc}} \gg 1$ is fulfilled in the excitation region (k_{osc} being the local wavenumber), i.e. where excitation is dominant. Consequently,

$$\left| \frac{d\xi_r}{dr} \right| \gg \left| \frac{\xi_r}{r} \right|. \quad (41)$$

The validity of this inequality has been numerically verified and is discussed in Sect. 4 (Eq. (49))

With Eqs. (41), (39) and (40) simplify as

$$\begin{aligned}
 C_S^2 = & \frac{4\pi^3 \mathcal{H}}{\omega_0^2} \int d^3x_0 \alpha_s^2 \\
 & \times \frac{1}{r^2} \left| \frac{d\xi_r}{dr} \frac{d \ln |\alpha_s|}{d \ln r} - \frac{d}{d \ln r} \left(\frac{d\xi_r}{dr} \right) \right|^2 \mathcal{S}_S(\omega_0)
 \end{aligned} \quad (42)$$

$$C_R^2 = \frac{64}{15} \pi^3 \int d^3x_0 \rho_0^2 \left| \frac{d\xi_r}{dr} \right|^2 \mathcal{S}_R(\omega_0). \quad (43)$$

These are the expressions obtained by Paper I and Samadi et al. (2005) for the radial modes in a plane-parallel geometry.

4. Horizontal effects on the Reynolds and entropy source terms

We derive asymptotic expressions for the excitation source terms (Eqs. (22) and (31)) in order to identify the major nonradial contributors to the excitation rates in the solar case.

4.1. The ℓ dependence of the eigenfunctions

Let us consider the equation of continuity and the transverse component of the equation of motion for the oscillations. Let us neglect the Lagrangian pressure variation and Eulerian gravitational potential variation at $r = R$ (the surface). The ratio of the horizontal to the vertical displacement at the surface boundary is then approximately given by (Unno et al. 1989, p. 105)

$$\frac{\xi_h}{\xi_r} \approx \sigma^{-2}, \quad (44)$$

where σ is the dimensionless frequency defined by

$$\sigma^2 = \frac{R^3}{GM} \omega^2, \quad (45)$$

where ω is the angular frequency of the mode, R the star radius, and M its mass. Frequencies of solar p modes then range between $\sigma \approx 10$ and $\sigma \approx 50$ ($\nu \in [1, 5]$ mHz). Hence, for the solar oscillations, one always has

$$|\xi_r| \gg |\xi_h|. \quad (46)$$

However Eqs. (23) and (35) involve coefficients depending on the angular degree (ℓ). We then also consider the ratio

$$L^2 \frac{\xi_h}{\xi_r} \approx L^2 \sigma^{-2}. \quad (47)$$

Equation (47) is of order of unity for $\ell \sim \sigma$. For example, for a typical frequency of 3 mHz, one cannot neglect the horizontal effect $L^2 \frac{\xi_h}{\xi_r}$ in front of $\frac{\xi_h}{\xi_r}$ for values of ℓ equal or greater than 30.

In what follows, we introduce the complex number f , which is the degree of non-adiabaticity, defined by the relation

$$f = \frac{\delta p/p}{\Gamma_1 \delta \rho/\rho}. \quad (48)$$

Note that $f = 1$ for adiabatic oscillations.

Let now compare the derivatives. Under the same assumptions above, neglecting the term in $(p/\rho)d(\delta p/p)/dr$ in the radial component of the equation of motion (standard mechanical boundary condition), one gets, near the surface,

$$\begin{aligned} \frac{d\xi_r}{dr} / \left(\frac{\xi_r}{r} \right) &\approx (f\Gamma_1)^{-1} [\sigma^2 + 2 + (L^2/\sigma^2 - 2)(f\Gamma_1 - 1)] \\ &\approx \sigma^2 / (f\Gamma_1). \end{aligned} \quad (49)$$

Hence, we always have $|\partial \xi_r / \partial r| \gg |\xi_r / r|$ in the excitation region (except near a node of $\partial \xi_r / \partial r$). Similar to Eq. (44), one can assume

$$\frac{d\xi_h}{dr} / \frac{d\xi_r}{dr} \approx \sigma^{-2}. \quad (50)$$

In fact, comparing Eq. (50) with the numerically-computed eigenfunctions shows that it holds even better than Eq. (44) in the excitation region.

Finally, we can group the different terms of Eqs. (23) and (31) into four sets

$$S_1 = \left| \frac{d\xi_r}{dr} \right|^2 \approx \sigma^4 \left| \frac{\xi_r}{r} \right|^2, \quad (51)$$

$$S_2 = L^4 \left| \frac{\xi_h}{r} \right|^2 \approx \frac{\ell^4}{\sigma^4} \left| \frac{\xi_r}{r} \right|^2, \quad (52)$$

$$\begin{aligned} S_3 &= \left\{ L^2 \left| \frac{d\xi_r}{dr} \right| \left| \frac{\xi_h}{r} \right|, L^2 \left| \frac{d\xi_h}{dr} \right|^2, L^2 \left| \frac{d\xi_h}{dr} \right| \left| \frac{\xi_r}{r} \right| \right\} \\ &\approx \ell^2 \left| \frac{\xi_r}{r} \right|^2, \end{aligned} \quad (53)$$

$$S_4 = \left\{ \left| \frac{\xi_r}{r} \right|^2, \left| \frac{1}{r} \frac{d|\xi_r|^2}{dr} \right|, L^2 \left| \frac{\xi_r}{r} \right| \left| \frac{\xi_h}{r} \right| \right\}. \quad (54)$$

The terms in S_4 are always negligible compared to the others. At fixed frequency (σ) we have thus:

$$S_1 \gg S_3 \gg S_4 \gg S_2 \text{ for } \ell \ll \sigma \quad (55)$$

$$S_1 \gg S_3 \gg S_4 \approx S_2 \text{ for } \ell \approx \sigma \quad (56)$$

$$S_1 \approx S_3 \approx S_2 \gg S_4 \text{ for } \ell \approx \sigma^2 \quad (57)$$

$$S_2 \gg S_3 \gg S_1 \gg S_4 \text{ for } \ell \gg \sigma^2. \quad (58)$$

In conclusion, the contribution of the horizontal displacement terms (S_2, S_3) begins to dominate the excitation for $\ell \gg \sigma^2$.

4.2. Source terms as functions of ℓ

Reynolds stress contribution:

We start by isolating non-radial effects in the range $\ell \in [0; 500]$. Note that the limit $\ell = 500$ is justified in Sect. 6.1 by the limit of validity for the present formalism. We investigate two cases, $\ell \ll \sigma^2$ and $\ell \approx \sigma^2$ respectively. The condition for which $\ell \approx \sigma^2$ is satisfied for around the f mode for $\ell > 50$ and in the gap between the g_1 and f mode, for $\ell < 50$.

Using the set of inequalities Eqs. (55) to (58), for a typical frequency of 3 mHz (i.e. $\sigma \approx 30$), $R(r)$ (Eq. 23) becomes for high- n modes ($\ell \ll \sigma^2$):

$$R(r) \approx \frac{16}{15} \left| \frac{d\xi_r}{dr} \right|^2. \quad (59)$$

Hence, for high- n acoustic modes one can use Eq. (59) instead of Eq. (23), and in terms of the excitation source term, the formalism reduces to the radial case for $\ell < 500$ and high- n modes.

For low- n modes ($\ell \approx \sigma^2$, i.e. for instance $\sigma \approx 10$) some additional dependency must be retained (see Eq. (57)). One gets

$$\begin{aligned} R(r) &\approx \frac{16}{15} \left| \frac{d\xi_r}{dr} \right|^2 + \frac{16}{15} L^4 \left| \frac{\xi_h}{r} \right|^2 - \frac{2}{5} L^2 \left(\frac{d\xi_r^*}{dr} \frac{\xi_h}{r} + c.c \right) \\ &\quad + \frac{11}{15} L^2 |\zeta_r|^2. \end{aligned} \quad (60)$$

The additional terms correspond to the non-diagonal contributions of the tensor $\nabla : \xi$ appearing in the Reynolds stress term C_R^* because we are in the range $\ell \approx \sigma^2$ (see Eq. (57)). The radial and transverse components of the divergence of the displacement nearly cancel so that $\delta \rho / \rho$ takes its minimum values. This is due to the fact that they are nearly divergence-free, i.e.

$$\nabla \cdot \xi = D_\ell Y_\ell^m \approx \frac{d\xi_r}{dr} - L^2 \frac{\xi_h}{r} \approx 0. \quad (61)$$

As the divergence of the mode corresponds to the diagonal part of the tensor $\nabla : \xi$, one can then expect that the excitation rate decreases (through the terms in $d\xi_r^*/dr \times \xi_h/r$ in Eq. (60)). However, such a decrease is compensated for by the non-radial component of the tensor (ζ_r^2 in Eq. (60)). Thus, for low- n p modes there is a balance between the effect of incompressibility that tends to diminish the efficiency of the excitation and the non-diagonal components of the tensor $\nabla : \xi$ that tend to increase it.

Entropy contribution:

Numerical investigation shows that the non-radial component of the entropy source term does not affect the excitation rates significantly except for $\ell > 1000$, which is out of the validity domain of the present formalism (see Sect. 6.1). The non-radial effects appear through the mode compressibility, $L^2 |D_\ell|^2$ (Eq. (33)). From Eq. (57) one can show that non-radial contributions play a non-negligible role for low- n modes. However, such low-frequency modes are not enough localised in the superadiabatic zone, where the entropy source term is maximum, to be efficiently excited by this contribution.

5. Numerical estimations for a solar model

5.1. Computation of the theoretical excitation rates

In the following, we compute the excitation rates of p modes for a solar model. The rate (P) at which energy is injected into a mode per unit time is calculated according to the set of Eqs. (11)–(13). The calculation thus requires knowledge of four different types of quantities:

- 1) Quantities related to the oscillation modes: the eigenfunctions (ξ_r, ξ_h) and associated eigenfrequencies (ω_0).
- 2) Quantities related to the spatial and time-averaged properties of the medium: the density (ρ_0), the vertical velocity (\tilde{w}), the entropy (\tilde{s}), and $\alpha_s = \partial P_1 / \partial \tilde{s}$.
- 3) Quantities that contain information about spatial and temporal correlations of the convective fluctuations: $E(k)$, $E_s(k)$, and $\chi_k(\omega)$.
- 4) A quantity that takes anisotropy into account: Φ measures the anisotropy of the turbulence and is defined according to Gough (1977) (see also Paper I for details) as:

$$\Phi = \frac{\langle u^2 \rangle}{\langle w^2 \rangle}, \quad (62)$$

where $u^2 = w^2 + u_h^2$ and u_h is the horizontal velocity.

To be consistent with the current assumption of isotropic turbulence, we assume $\Phi = 3$.

Eigenfrequencies and eigenfunctions (in point 1) above) were computed using the adiabatic pulsation code OSC (Boury et al. 1975). The solar structure model used for these computations (quantities in point 2) was obtained using the stellar evolution code CESAM (Morel 1997) for the interior, and a Kurucz (1993) model for the atmosphere. The interior-atmosphere match point was chosen at $\log \tau = 0.1$ (above the convective envelope). The pulsation computations used the full model (interior+ atmosphere). In the interior model, we used the OPAL opacities (Iglesias & Rogers 1996) extended to low temperatures with the opacities of Alexander & Ferguson (1994), and the CEFF equation of state (Christensen-Dalsgaard & Daeppen 1992). Convection is included according to a Böhm-Vitense mixing-length formalism (see Samadi et al. 2006, for details), from

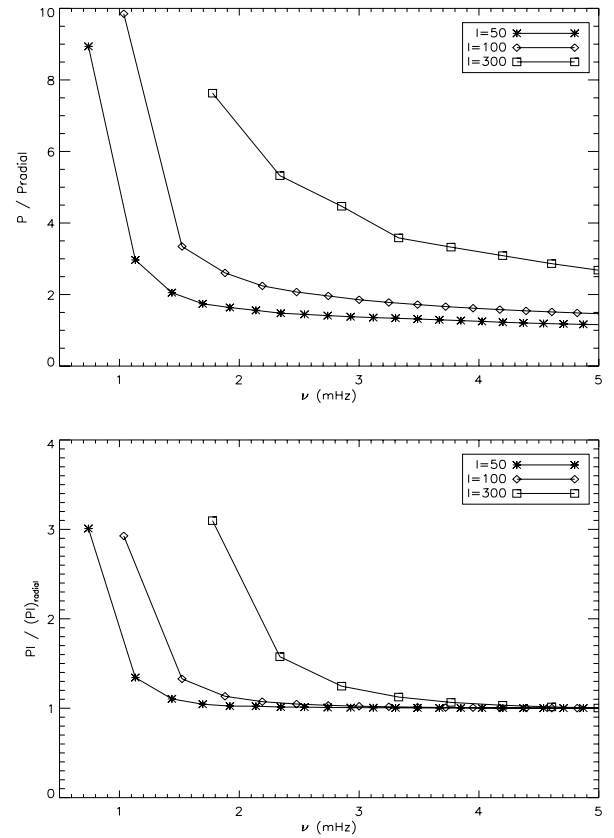


Fig. 1. Top: the rate (P) at which energy is supplied to each ℓ, n mode for $\ell = 50, 100, 300$ is divided by the excitation rate (P_{radial}) obtained for the $\ell = 0, n$ mode. Computation of the theoretical excitation rates is performed as explained in Sect. 5.1. Bottom: ratio $P I / (P I)_{\text{radial}}$ where I is the mode inertia.

which \tilde{w} is computed. The Φ value is set to 2 in the calculation. This is not completely consistent as we assume isotropic turbulence (i.e. $\Phi = 3$). This does not, however, affect the conclusions of the present paper, as all results on nonradial excitation rates are normalized to the radial ones. Note also that the equilibrium model does not include turbulent pressure. These two limitations are of small importance here as our investigation in this first work on nonradial modes remains essentially qualitative.

Finally, for the quantities in point 3, the total kinetic energy contained in the turbulent kinetic spectrum ($E(k)$) is obtained following Samadi et al. (2006).

5.2. Excitation rates

The rate (P) at which energy is supplied to the modes is plotted in Fig. 1, normalized to the radial excitation rate (P_{rad}). It is seen that the higher the ℓ , the more energy is supplied to the mode. This is explained by additional contributions (compared to the radial case) due to mode inertia, the spherical symmetry (departure from the plane-parallel assumption), and the contribution of horizontal excitation. Note that, as discussed in Sect. 3 (see Eq. (41)), the departure from the plane-parallel

approximation is negligible for p modes. Then, to discuss the other two contributions, one can rewrite Eq. (4) as

$$P = \left(\frac{|\xi_r(R)|^2}{8I} \right) \times \left(\frac{C_R^2 + C_S^2}{|\xi_r(R)|^2} \right), \quad (63)$$

where $|\xi_r(R)|$ is taken at the photosphere. Note that both terms of the product (Eq. (63)) are independent of the normalization of the eigenfunctions. Thus, as shown by Eq. (63), the power supplied to the modes is composed of two contributions that both depend on ℓ . The first is due to the mode inertia, which is defined as

$$I = \int_0^M dm |\xi|^2 = \int_0^R (|\xi_r|^2 + L^2 |\xi_h|^2) r^2 \rho_0 dr. \quad (64)$$

High- ℓ modes present a lower inertia despite the L^2 contribution in Eq. (64) because they are confined high in the atmosphere where the density is lower than in deeper layers.

The second term of the product Eq. (63) depends on the non-radial effects through the excitation source terms (Eqs. (31) and (22)). To investigate this quantity independent of the mode mass (defined as $I/|\xi_r(R)|^2$), we plot the ratio $PI/(PI)_{\text{radial}}$ in Fig. 1. One can then discuss two types of modes, namely low- n (≤ 3) and high- n (>3) modes (see Fig. 1).

- For high- n modes, non-radial effects play a minor role in the excitation source terms. The dominant effect (see Fig. 1) is due to the mode inertia as discussed above.
- For lower values of n , there is a contribution to the excitation rates due to the horizontal terms in Eq. (22).

Thus, contrary to high- n modes, the term $\frac{d\xi_r}{dr}$ in $R(r)$ (Eq. (23)) is no longer dominant in front of the terms involving ξ_h for low-order modes. Turbulence then supplies more energy to the low-frequency modes due to horizontal contributions, which explains the higher excitation rates for low- n modes as seen in Fig. 1. We stress that there is still turbulent energy that is supplied to the modes despite their nearly divergence-free nature. For such modes, the non-diagonal part of the tensor $\nabla : \xi$, which is related to the shear of the mode, compensates for and dominates the diagonal part, which is related to the mode compression.

5.3. Surface velocities

Another quantity of interest is the theoretical surface velocity, which can be compared to observational data. We compute the mean-squared surface velocity for each mode according to the relation (Baudin et al. 2005):

$$v_s^2(\omega_0) = \frac{P(\omega_0)}{2\pi\Gamma_v\mathcal{M}} \quad (65)$$

where $\mathcal{M} \equiv I/\xi_r^2(h)$ is the mode mass, h the height above the photosphere where oscillations are measured, $\Gamma_v = \eta/\pi$ the mode linewidth at half maximum (in Hz), and v_s^2 is the mean square of the mode surface velocity. Equation (65) involves the damping rates ($\eta = \pi\Gamma_v$) inferred from observational data in the solar case for low- ℓ modes (see Baudin et al. 2005, for details). We then assume that the damping rates are roughly the same as for the $\ell = 0$ modes. Such an assumption is supported for low- ℓ modes ($\ell \approx 50$) as shown by Barban et al. (2004).

Figure 2 displays the surface velocities for $\ell = 0, 20$, and 50. Note that the surface velocities are normalized to the maximum velocity of the $\ell = 0$ modes ($V_0 \approx 8.5 \text{ cm s}^{-1}$ using MLT). This

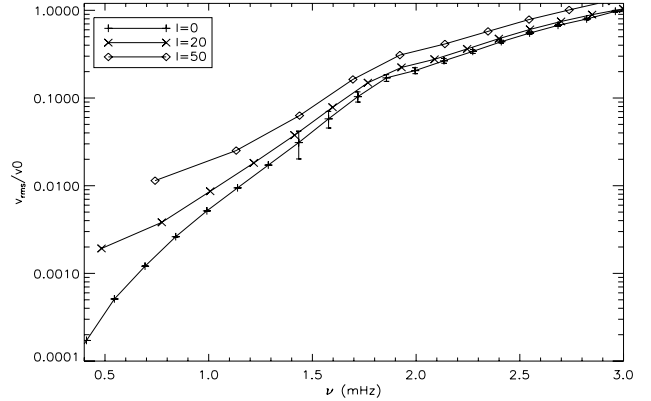


Fig. 2. Surface rms velocities of $\ell = 0, 20, 50$ modes calculated using Eq. (65) and normalized to the maximum velocity of the radial modes (see text). Note that the damping rates are taken from GOLF (Baudin et al. 2005) and are chosen to be the same for all angular degrees (ℓ). Three σ error bars derived from GOLF are plotted on the $\ell = 0$ curve.

choice is motivated by the dependence of the absolute values of velocities on the convective model that is used, and it is certainly imperfect. However, its influence disappears when considering differential effects. As an indication, 3σ error bars estimated from GOLF for the $\ell = 0$ modes are plotted (see Baudin et al. 2005, for details). The differences between the radial and non-radial computations are indeed larger than the $\ell = 0$ uncertainties for $\ell > 20$. For a more significant comparison, error bars for non-radial modes should be used, but they are difficult to determine with confidence (work in progress). For ℓ larger than 50, we do not give surface velocities; as derived, those here depend on the assumption of approximately constant damping rate that is not confirmed for $\ell > 50$.

When available, observational data should allow us to investigate the two regimes that have been emphasised in Sect. 5.2, namely the high- and low- n modes.

6. Discussion

6.1. The separation of scales

The main assumption in this general formalism appears in Eq. (11), where it has been assumed that the spatial variation of the eigenfunctions is large compared to the typical length scale of turbulence, leading to what we call *the separation of scales*. In order to test this assumption, one must compare the oscillation wavelength to the turbulent one or, equivalently, the wavenumbers. To this end, we use the dispersion relation (see Unno et al. 1989)

$$k_r^2 = \frac{\omega^2}{c_s^2} \left(1 - \frac{S_\ell^2}{\omega^2} \right) \left(1 - \frac{N^2}{\omega^2} \right) \quad \text{and} \quad k_h^2 = \frac{L^2}{r^2} \quad (66)$$

where N is the buoyancy frequency, S_ℓ the Lamb frequency, and k_r, k_h the radial and horizontal oscillation wavenumbers, respectively, and $L^2 = \ell(\ell + 1)$.

For the turbulent wavenumber, we choose to use, as a lower limit, the convective wavenumber $k_{\text{conv}} = 2\pi/L_c$, where L_c is the typical convective length scale. Thus, the assumption of separation of scales is fulfilled, provided

$$k_{r,h}/k_{\text{conv}} \ll 1. \quad (67)$$

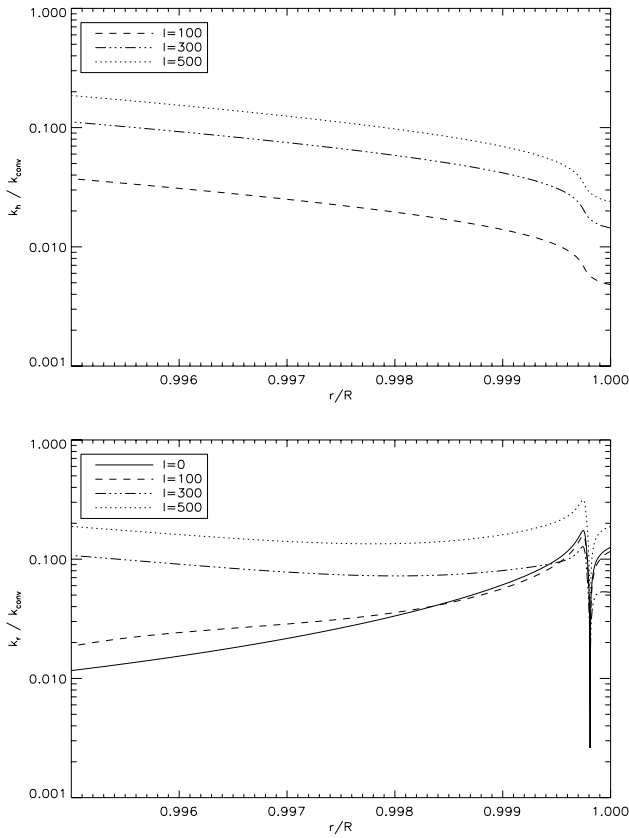


Fig. 3. *Top:* ratio of the horizontal oscillation wavenumber to the convective wavenumber (k_h/k_{conv}), versus the normalized radius (r/R). k_{conv} is computed using the mixing length theory such that $k_{\text{conv}} = 2\pi/L_c$ (L_c is the mixing length) and k_r is computed using the dispersion relation Eq. (66). Note that the ratio k_h/k_{conv} is computed for a frequency of around $\nu = 3$ mHz, depending on the angular degree (ℓ). *Bottom:* the same as in the top but for the ratio k_r/k_{conv} .

In Fig. 3 the ratios k_r/k_{conv} and k_h/k_{conv} are plotted. Those plots focus on the uppermost part of the solar convection zone where most of the excitation takes place. The assumption of separation of scale is valid for the horizontal component of the oscillation, since one has $k_h/k_{\text{conv}} \ll 1$ (for $\ell \leq 500$) in the region where excitation is dominant. However, we must recall that our criterion is based on the mixing length for computing k_{conv} . As shown by Samadi et al. (2003a) using 3D numerical simulations, the convective length scale (computed using the CESAM code, see Sect. 5.1) must be multiplied by a factor around five to reproduce the injection scale (L_c) in the superadiabatic layers. Hence, for a more conservative criterion, we must then multiply the ratio k_h/k_{conv} by a factor of five, which leads to a ratio near unity for $\ell \approx 500$ (see Fig. 3). Thus, for higher values of the angular degree, the separation-of-scale hypothesis becomes doubtful.

Concerning the radial component of the oscillation wavenumber, the limiting value of ℓ seems to be the same (i.e. $\ell = 500$). Thus, we conclude that, for modes of angular degree lower than 500 one can use the separation of scales assumption. For $\ell > 500$, the characteristic length of the mode becomes shorter than the characteristic length L_c of the energy bearing eddies. Those modes will then be excited by turbulent eddies with a length-scale smaller than L_c , i.e. lying in the turbulent cascade. These eddies inject less energy into the mode than the energy

bearing eddies do, since they have less kinetic energy. We can then expect that – at fixed frequency – they received less energy from the turbulent eddies than the low-degree modes. A theoretical development is currently underway to properly treat the case of very high ℓ modes.

6.2. The closure model

A second approximation in the present formalism is the use of a closure model. The uppermost part of the convection zone is a turbulent convective system composed of two flows (upward and downward), and the probability distribution function of the fluctuations of the vertical velocity and temperature does not obey a Gaussian law (Lesieur 1997). Thus, the use of the quasi-normal approximation (QNA, Millionshchikov 1941), which is exact for a normal distribution, is no longer rigorously correct. A more realistic closure model has been developed in Belkacem et al. (2006a) and can be easily adapted for high- ℓ modes. This alternative approach takes the existence of two flows (the up- and downdrafts) within the convection zone into account. However, the QNA is nevertheless often used for the sake of simplicity as is the case here. Note that, when using the closure model with plumes, it is no longer consistent to assume that the third-order velocity moments strictly vanish; however, as shown by Belkacem et al. (2006a,b), their contribution is negligible in the sense that their effect is weaker than the accuracy of the presently available observational data.

6.3. Mode inertia

We have shown that the excitation rates for high- ℓ and n modes are sensitive to the variation in the mode inertia (I). The value of I depends on the structure of the stellar model and the properties of the eigenfunctions in these external regions. Samadi et al. (2006) have shown that different local formulations of convection can change the mode inertia by a small amount. This sensitivity then affects the computed excitation rates (P). However, the changes induced in P are found to be smaller than the accuracy to which the mode excitation rates are derived from the current observations (see Baudin et al. 2005; Belkacem et al. 2006b). Furthermore, concerning the way the modes are obtained, we have computed non-adiabatic eigenfunctions using the time-dependent formalism of Gabriel for convection (see Grigahcène et al. 2005). The mode inertia obtained with these non-adiabatic eigenfunctions exhibits a ν dependency different from those obtained using adiabatic eigenfunctions (the approximation adopted in the present paper). On the other hand, the mode inertia using non-adiabatic eigenfunctions (see Houdek et al. 1999, for details) obtained according to Gough’s time-dependent formalism of convection (Gough 1977) shows smaller differences with the adiabatic mode inertia. Accordingly, the way the interaction of oscillation and time-dependent convection is modelled affects the eigenfunctions differently. As explained in Sect. 5.3, the formalism developed in this paper can be an efficient tool for deriving constraints on the mode inertia to distinguish between the different treatments of convection. Further work is thus needed on that issue.

7. Conclusions

We extended the Samadi & Goupil (2001) formalism in order to predict the amount of energy that is supplied to non-radial modes. In this paper, we focused on high- ℓ acoustic modes

with a particular emphasis on the solar case. The validity of the present formalism is limited to values of the angular degree lower than $\ell = 500$, due to the separation of scale assumption that is discussed above in Sect. 6.1. We have demonstrated that non-radial effects are due to two contributions, namely the effect of inertia that prevails for high-order modes ($n > 3$) and non-radial contributions in the Reynolds source term in C_R^2 (see Eq. (22)) that dominate the radial one for low-order modes ($n < 3$).

Contrary to Belkacem et al. (2006b) who used 3D simulations to build an equilibrium model, we restricted ourselves to the use of a simple classical 1D MLT equilibrium model. Indeed, we were interested in deriving qualitative conclusions on nonradial contributions. Forthcoming quantitative studies will have to use more realistic equilibrium models, particularly for the convection description, such as models including turbulent pressure (e.g. Balmforth 1992) or patched models (e.g. Rosenthal et al. 1999).

From a theoretical point of view, several improvements and extensions of the present formalism remain to be carried out. For instance, one must relax the assumption of the separation of scales if one wants to model very high- ℓ modes. Such an investigation (which is currently underway) should enable us to draw conclusions about the observational evidence that, beyond some value of ℓ the energy supplied to the modes decreases with frequency (see Woodard et al. 2001, Fig. 2). Another hypothesis is the isotropic turbulence that has been assumed in the present work as a first approximation. Such an assumption needs to be given up to get a better description of the nonradial excitation of modes by turbulent convection, which requires further theoretical developments.

The present work focuses on p modes, but the formalism is valid for both p and g modes. We will address the analysis of gravity modes in a forthcoming paper.

Appendix A: Detailed expressions for source terms

The eigenfunctions (ξ) are developed in spherical coordinates ($\mathbf{e}_r, \mathbf{e}_\theta, \mathbf{e}_\phi$) and expanded in spherical harmonics. Hence, the fluid displacement eigenfunction for a mode with given n, ℓ, m is written as

$$\xi(\mathbf{r}) = (\xi_r \mathbf{e}_r + \xi_h \nabla_H) Y_{\ell,m} \quad (\text{A.1})$$

with

$$\nabla_H = \begin{cases} \mathbf{e}_\theta \frac{\partial}{\partial \theta} \\ \mathbf{e}_\phi \frac{1}{\sin \theta} \frac{\partial}{\partial \phi} \end{cases} \quad (\text{A.2})$$

where the spherical harmonics ($Y_{\ell,m}(\theta, \phi)$) are normalized according to

$$\int \frac{d\Omega}{4\pi} Y_{\ell,m} Y_{\ell,m}^* = 1 \quad (\text{A.3})$$

with Ω being the solid angle ($d\Omega = \sin \theta d\theta d\phi$).

The large-scale gradient ∇_0 appearing in Eqs. (13) and (14) for instance is given, in the local spherical coordinates, by

$$\nabla_0 = \mathbf{e}_r \frac{\partial}{\partial r} + \frac{1}{r} \nabla_H. \quad (\text{A.4})$$

A.1. Contribution of the turbulent Reynolds stress

The Reynolds stress contribution can be written as (see Sect. 2.1)

$$C_R^2 = \pi^2 \int d^3 x_0 (\rho_0^2 b_{ij}^* b_{lm}) \int d^3 k \int d\omega \\ \times (T^{ijlm} + T^{ijml}) \frac{E^2(k)}{k^4} \chi_k(\omega_0 + \omega) \chi_k(\omega) \quad (\text{A.5})$$

where

$$T^{ijlm} = \left(\delta^{il} - \frac{k^i k^l}{k^2} \right) \left(\delta_{jm} - \frac{k^j k^m}{k^2} \right). \quad (\text{A.6})$$

and

$$b_{ij} \equiv \mathbf{e}_i \cdot (\nabla_0 : \xi) \cdot \mathbf{e}_j \quad (\text{A.7})$$

where the double dot denotes the tensor product.

We now consider the covariant ($\mathbf{a}^r, \mathbf{a}^\theta, \mathbf{a}^\phi$) and the contravariant ($\mathbf{a}_r, \mathbf{a}_\theta, \mathbf{a}_\phi$) natural base coordinates where the eigenfunction can be expanded:

$$\xi = \hat{\xi}^k \mathbf{e}_k = q_k \mathbf{a}^k \quad k = \{r, \theta, \phi\}. \quad (\text{A.8})$$

The natural and physical coordinates are related to each other by

$$\mathbf{e}_i = \frac{1}{\sqrt{|g_{ii}|}} \mathbf{a}_i, \quad (\text{A.9})$$

where g_{ij} is the metric tensor in spherical coordinates (see Table 6.5-1 in Korn & Korn 1968), i.e.,

$$g_{rr} = 1, \quad g_{\theta\theta} = r^2, \quad g_{\phi\phi} = r^2 \sin^2 \theta, \\ g_{ij} = 0 \quad \text{for } i \neq j. \quad (\text{A.10})$$

Equation (A.7), with the help of Eq. (A.8), can then be developed in covariant coordinates

$$\nabla_0 : \xi = \mathbf{a}^i \frac{\partial \xi}{\partial x^i} = \mathbf{a}^i \mathbf{a}^j \left(\frac{\partial q_j}{\partial x^i} \right) + \mathbf{a}^i q_j \left(\frac{\partial \mathbf{a}^j}{\partial x^i} \right) \\ = \mathbf{a}^i \mathbf{a}^j \left(\frac{\partial q_j}{\partial x^i} \right) - q_j \Gamma_{pi}^j \mathbf{a}^i \mathbf{a}^p \quad (\text{A.11})$$

where Γ_{pi}^j is the Christoffel three-index symbol of the second kind (Korn & Korn 1968). According to Eqs. (A.11) and (A.9), b_{ij} (Eq. (A.7)) can be written as

$$b_{ij} = \frac{1}{\sqrt{|g_{ii} g_{jj}|}} \left(\frac{\partial q_j}{\partial x^i} - q_p \Gamma_{ji}^p \right). \quad (\text{A.12})$$

To proceed, one has to express Eq. (A.12) in terms of the physical coordinates ($\hat{\xi}^k$). With the help of Eqs. (A.8) and (A.9), we relate the covariant coordinates q_i to the physical (contravariant) components $\hat{\xi}^j$

$$q_j = \frac{g_{ij}}{\sqrt{|g_{jj}|}} \hat{\xi}^j, \quad (\text{A.13})$$

where the component $\hat{\xi}^k$ are derived from Eq. (A.1)

$$\hat{\xi}^r = \xi_r Y_{\ell,m}; \quad \hat{\xi}^\theta = \xi_h \frac{\partial Y_{\ell,m}}{\partial \theta}; \quad \hat{\xi}^\phi = \xi_h \frac{1}{\sin \theta} \frac{\partial Y_{\ell,m}}{\partial \phi}. \quad (\text{A.14})$$

Hence Eq. (A.12) becomes

$$\begin{aligned}
b_{rr} &= \left(\frac{d\xi_r}{dr} \right) Y_{\ell,m} \\
b_{r\theta} &= \left(\frac{d\xi_h}{dr} \right) \frac{\partial Y_{\ell,m}}{\partial \theta} \\
b_{r\phi} &= \left(\frac{d\xi_h}{dr} \right) \frac{1}{\sin \theta} \frac{\partial Y_{\ell,m}}{\partial \phi} \\
b_{\theta r} &= \frac{1}{r} (\xi_r - \xi_h) \frac{\partial Y_{\ell,m}}{\partial \theta} \\
b_{\theta\theta} &= \frac{\xi_h}{r} \left(\frac{\partial^2 Y_{\ell,m}}{\partial \theta^2} \right) + \frac{\xi_r}{r} Y_{\ell,m} \\
b_{\theta\phi} &= b_{\phi\theta} = \frac{\xi_h}{r} \frac{\partial}{\partial \theta} \left[\frac{1}{\sin \theta} \frac{\partial Y_{\ell,m}}{\partial \phi} \right] \\
b_{\phi r} &= \frac{1}{r} (\xi_r - \xi_h) \frac{1}{\sin \theta} \frac{\partial Y_{\ell,m}}{\partial \phi} \\
b_{\phi\phi} &= \frac{\xi_r}{r} Y_{\ell,m} + \frac{\xi_h}{r} \left[\frac{1}{\sin^2 \theta} \left(\frac{\partial^2 Y_{\ell,m}}{\partial \phi^2} \right) + \frac{\cos \theta}{\sin \theta} \left(\frac{\partial Y_{\ell,m}}{\partial \theta} \right) \right].
\end{aligned}$$

The contribution of the Reynolds stress can thus be written as

$$\begin{aligned}
C_R^2 &= 4\pi^3 \int dm \int dk \int d\omega R(r, k) \\
&\times \frac{E^2(k)}{k^2} \chi_k(\omega + \omega_0) \chi_k(\omega), \quad (A.16)
\end{aligned}$$

where we have defined $dm = 4\pi r^2 \rho_0 dr$, and

$$R(r, k) \equiv \int \frac{d\Omega}{4\pi} \int \frac{d\Omega_k}{4\pi} b_{ij}^* b_{lm} (T^{ijlm} + T^{ijml}). \quad (A.17)$$

Because $T^{ijlm} = T^{jilm}$, it is easy to show that

$$R(r, k) \equiv \int \frac{d\Omega}{4\pi} \int \frac{d\Omega_k}{4\pi} B_{ij}^* B_{lm} (T^{ijlm} + T^{ijml})$$

where $B_{ij} \equiv (1/2)(b_{ij} + b_{ji})$.

Using the expression Eq. (A.6) for T^{ijlm} , we write

$$R(r, k) \equiv R_1 - R_2 + R_3 \quad (A.18)$$

where

$$\begin{aligned}
R_1 &= 2 \int \frac{d\Omega}{4\pi} \int \frac{d\Omega_k}{4\pi} \left(\sum_{i,j} B_{ij}^* B_{ij} \right) \\
R_2 &= 4 \int \frac{d\Omega}{4\pi} \int \frac{d\Omega_k}{4\pi} \left(\sum_{i,j} B_{ij}^* B_{ii} \frac{k_j k_l}{k^2} \right) \\
R_3 &= 2 \int \frac{d\Omega}{4\pi} \int \frac{d\Omega_k}{4\pi} \left(\sum_{i,j} B_{ij}^* B_{lm} \frac{k_i k_j k_l k_m}{k^4} \right). \quad (A.19)
\end{aligned}$$

We assume isotropic turbulence, hence the \mathbf{k} components satisfy

$$\int d\Omega_k \frac{k_i k_j}{k^2} = \delta_{ij} \int d\Omega_k \frac{k_r^2}{k^2}$$

with δ_{ij} as the Kronecker symbol for $i, j = r, \theta, \phi$. Then we obtain

$$R_1 = 2 \int \frac{d\Omega}{4\pi} \left(\sum_{i,j} |B_{ij}|^2 \right)$$

$$\begin{aligned}
R_2 &= 4 \int \frac{d\Omega}{4\pi} \int \frac{d\Omega_k}{4\pi} \frac{k_r^2}{k^2} \left(\sum_{i,j} |B_{ij}|^2 \right) = 2\alpha R_1 \\
R_3 &= 2\beta \int \frac{d\Omega}{4\pi} \left(\sum_{i,j} |B_{ij}|^2 + \sum_{i \neq j} (B_{ii}^* B_{jj} + c.c) \right) \\
&= \beta R_1 + 2\beta \left(\int \frac{d\Omega}{4\pi} \sum_{i \neq j} (B_{ii}^* B_{jj} + c.c) \right), \quad (A.20)
\end{aligned}$$

where we have set

$$\alpha \equiv \int \frac{d\Omega_k}{4\pi} \frac{k_r^2}{k^2}; \quad \beta \equiv \int \frac{d\Omega_k}{4\pi} \frac{k_r^4}{k^4}. \quad (A.21)$$

To compute R_1, R_2 , and R_3 , we write

$$\begin{aligned}
B_{rr} &= b_{rr}; \quad B_{\theta\theta} = b_{\theta\theta}; \quad B_{\phi\phi} = b_{\phi\phi} \\
B_{r\theta} &= \frac{1}{2} \zeta_r \frac{\partial Y_{\ell,m}}{\partial \theta} \\
B_{r\phi} &= \frac{1}{2} \zeta_r \frac{1}{\sin \theta} \frac{\partial Y_{\ell,m}}{\partial \phi} \\
B_{\theta\phi} &= b_{\theta\phi} = b_{\phi\theta}
\end{aligned} \quad (A.22)$$

with

$$\zeta_r = \frac{d\xi_h}{dr} + \frac{1}{r} (\xi_r - \xi_h). \quad (A.23)$$

Using the expression Eq. (A.22) for the quantities B_{ij} , we obtain, after some manipulation,

$$\begin{aligned}
R_1 &= 2 \left| \frac{d\xi_r}{dr} \right|^2 + 4 \left| \frac{\xi_r}{r} \right|^2 + 2L^2(L^2 - 1) \left| \frac{\xi_h}{r} \right|^2 \\
&+ L^2 \left(|\zeta_r|^2 - 2 \left(\frac{\xi_r^* \xi_h}{r^2} + c.c \right) \right). \quad (A.24)
\end{aligned}$$

For R_3 , some lengthy manipulation leads to:

$$\begin{aligned}
R_3/\beta &= 2 \left| \frac{d\xi_r}{dr} \right|^2 + 8 \left| \frac{\xi_r}{r} \right|^2 + 2(L^4 + 4\mathcal{F}_{\ell,|m|}) \left| \frac{\xi_h}{r} \right|^2 \\
&+ L^2 \left(2|\zeta_r|^2 - 2 \left(\frac{d\xi_r^*}{dr} \frac{\xi_h}{r} + 2 \frac{\xi_r^* \xi_h}{r^2} + c.c \right) \right) \\
&+ 4 \left(\frac{\xi_r^*}{r} \frac{d\xi_r}{dr} + c.c \right) \quad (A.25)
\end{aligned}$$

where we have defined

$$\mathcal{F}_{\ell,|m|} = \frac{(2\ell + 1)}{2} \quad (A.26)$$

$$\times \left((|m| + 1) A_{\ell,|m|}^2 + (|m| - 1) B_{\ell,|m|}^2 \right)$$

$$A_{\ell,m}^2 = \frac{1}{4} (\ell(\ell + 1) - m(m + 1)) \quad (A.27)$$

$$B_{\ell,m}^2 = \frac{1}{4} (\ell(\ell + 1) - m(m - 1)). \quad (A.28)$$

To derive R_1, R_2 , and R_3 , the following relations have been used

$$\frac{\partial^2 Y_{\ell,m}}{\partial \theta^2} + \frac{\cos \theta}{\sin \theta} \frac{\partial Y_{\ell,m}}{\partial \theta} + \frac{1}{\sin^2 \theta} \frac{\partial^2 Y_{\ell,m}}{\partial \phi^2} = -L^2 Y_{\ell,m} \quad (A.29)$$

$$-m \frac{\cos \theta}{\sin \theta} Y_{\ell,m} = A_{\ell,m} Y_{\ell,m+1} e^{-i\phi} + B_{\ell,m} Y_{\ell,m-1} e^{i\phi} \quad (A.30)$$

$$\frac{\partial Y_{\ell,m}}{\partial \theta} = A_{\ell,m} Y_{\ell,m+1} e^{-i\phi} - B_{\ell,m} Y_{\ell,m-1} e^{i\phi} \quad (A.31)$$

$$\int \frac{d\Omega}{4\pi} (\nabla_H Y_{\ell,m}^* \cdot \nabla_H Y_{\ell,m}) = L^2 \quad (\text{A.32})$$

$$- \int \frac{d\Omega}{4\pi} (\nabla_H^2 Y_{\ell,m}^*) Y_{\ell,m} = L^2 \quad (\text{A.33})$$

$$\int \frac{d\Omega}{4\pi} \left| \partial_\theta \left(\frac{1}{\sin\theta} \frac{\partial Y_{\ell,m}}{\partial \phi} \right) \right|^2 = \mathcal{F}_{\ell,|m|}. \quad (\text{A.34})$$

Combining Eqs. (A.24), (A.20), (A.20), and (A.18), with $\alpha = 1/3, \beta = 1/5$ (isotropic turbulence, see Paper I for details), yields

$$\begin{aligned} R(r) = & \frac{16}{15} \left| \frac{d\xi_r}{dr} \right|^2 + \frac{44}{15} \left| \frac{\xi_r}{r} \right|^2 + \frac{4}{5} \frac{1}{r} \frac{d|\xi_r|^2}{dr} \\ & + L^2 \left(\frac{11}{15} |\zeta_r|^2 - \frac{22}{15} \left(\frac{\xi_r^* \xi_h}{r^2} + c.c. \right) \right) \\ & - \frac{2}{5} L^2 \left(\frac{d\xi_r^*}{dr} \frac{\xi_h}{r} + c.c. \right) \\ & + \left| \frac{\xi_h}{r} \right|^2 \left(\frac{16}{15} L^4 + \frac{8}{5} \mathcal{F}_{\ell,m} - \frac{2}{3} L^2 \right). \end{aligned} \quad (\text{A.35})$$

For radial modes, this reduces to

$$R(r) = \frac{16}{15} \left| \frac{d\xi_r}{dr} \right|^2 + \frac{44}{15} \left| \frac{\xi_r}{r} \right|^2 + \frac{4}{5} \frac{d|\xi_r|^2}{dr}. \quad (\text{A.36})$$

The final expression for the Reynolds source term is then given by

$$C_R^2 = 4\pi^3 \int dm R(r) S_R(\omega_0), \quad (\text{A.37})$$

with

$$S_R(\omega_0) = \int \frac{dk}{k^2} E^2(k) \int d\omega \chi_k(\omega + \omega_0) \chi_k(\omega) \quad (\text{A.38})$$

and $R(r)$ by Eq. (A.35).

A.2. Contribution of entropy fluctuations

We start from Eq. (28), and to proceed further in the derivation of the entropy fluctuation source term, one has to compute

$$\int d\Omega_k h^{ij} T_{ij}. \quad (\text{A.39})$$

Then, ξ and \mathbf{k} are expanded in spherical coordinates $(\mathbf{a}_r, \mathbf{a}_\theta, \mathbf{a}_\phi)$. We assume an isotropic turbulence; as a consequence, the quantities $k_r k_\theta, k_r k_\phi, k_\theta k_\phi$ vanish when integrated over Ω_k . One next obtains

$$\int d\Omega_k h^{ij} T_{ij} = 2\pi \mathcal{H} (h_{rr} + h_{\theta\theta} + h_{\phi\phi}) \quad (\text{A.40})$$

where \mathcal{H} is the anisotropy factor introduced in Paper I, which in the current assumption (isotropic turbulence) is equal to 4/3. Assuming that $\alpha_s = \alpha_s(r)$, we have, according to Eq. (A.4),

$$\begin{cases} h_{rr} = \left| C \frac{d \ln |\alpha_s|}{dr} - \frac{\partial C}{\partial r} \right|^2 \\ h_{\theta\theta} = \frac{1}{r^2} \left| \frac{\partial C}{\partial \theta} \right|^2 \\ h_{\phi\phi} = \frac{1}{r^2 \sin^2 \theta} \left| \frac{\partial C}{\partial \phi} \right|^2. \end{cases} \quad (\text{A.41})$$

To proceed, it is necessary to express the divergence of the eigenfunction

$$C \equiv \nabla_0 \cdot \xi = D_\ell Y_\ell^m \quad (\text{A.42})$$

with

$$D_\ell(r, \ell) \equiv D_r - \frac{L^2}{r} \xi_h; \quad D_r \equiv \frac{1}{r^2} \frac{\partial}{\partial r} (r^2 \xi_r), \quad (\text{A.43})$$

where again $L^2 = \ell(\ell + 1)$.

We next integrate Eq. (28) over $d\Omega/4\pi$, the solid angle associated with the eigenfunctions ξ . One obtains, with the help of Eq. (A.42) and according to Eq. (A.41),

$$\begin{aligned} & \int \frac{d\Omega}{4\pi} \int d\Omega_k h^{ij} T_{ij} = \\ & \frac{2\pi \mathcal{H}}{r^2} \left(L^2 |D_\ell|^2 + \left| D_\ell \frac{d \ln |\alpha_s|}{d \ln r} - \frac{d D_\ell}{d \ln r} \right|^2 \right). \end{aligned} \quad (\text{A.44})$$

The final expression for the contribution of entropy fluctuations reduces to

$$C_S^2 = \frac{4\pi^3 \mathcal{H}}{\omega_0^2} \int d^3 x_0 \alpha_s^2 (A_\ell + B_\ell) S_S(\omega_0), \quad (\text{A.45})$$

where \mathcal{H} is the anisotropy factor introduced in Paper I that in the current assumption (isotropic turbulence) is equal to 4/3. In addition,

$$A_\ell \equiv \frac{1}{r^2} \left| D_\ell \frac{d(\ln |\alpha_s|)}{d \ln r} - \frac{d D_\ell}{d \ln r} \right|^2 \quad (\text{A.46})$$

$$B_\ell \equiv \frac{1}{r^2} L^2 |D_\ell|^2 \quad (\text{A.47})$$

$$\begin{aligned} S_S(\omega_0) \equiv & \int \frac{dk}{k^4} E(k) E_s(k) \\ & \times \int d\omega \chi_k(\omega_0 + \omega) \chi_k(\omega). \end{aligned} \quad (\text{A.48})$$

References

- Alexander, D. R., & Ferguson, J. W. 1994, *ApJ*, 437, 879
 Balmforth, N. J. 1992, *MNRAS*, 255, 639
 Barban, C., Hill, F., & Kras, S. 2004, *ApJ*, 602, 516
 Baudin, F., Samadi, R., Goupil, M.-J., et al. 2005, *A&A*, 433, 349
 Belkacem, K., Samadi, R., Goupil, M. J., & Kupka, F. 2006a, *A&A*, 460, 173
 Belkacem, K., Samadi, R., Goupil, M. J., Kupka, F., & Baudin, F. 2006b, *A&A*, 460, 183
 Boury, A., Gabriel, M., Noels, A., Scuflaire, R., & Ledoux, P. 1975, *A&A*, 41, 279
 Christensen-Dalsgaard, J. 2002, *Inter. J. Mod. Phys. D*, 11, 995
 Christensen-Dalsgaard, J. & Daepfen, W. 1992, *A&ARv*, 4, 267
 Dintrans, B., Brandenburg, A., Nordlund, Å., & Stein, R. F. 2005, *A&A*, 438, 365
 Goldreich, P., & Keeley, D. A. 1977, *ApJ*, 212, 243
 Goldreich, P., Murray, N., & Kumar, P. 1994, *ApJ*, 424, 466
 Gough, D. O. 1977, *ApJ*, 214, 196
 Gough, D. O. 1985, *Theory of Solar Oscillations*, Tech. Rep.
 Grigahcène, A., Dupret, M.-A., Gabriel, M., Garrido, R., & Scuflaire, R. 2005, *A&A*, 434, 1055
 Houdek, G. 2006, [[arXiv:astro-ph/0612024](https://arxiv.org/abs/astro-ph/0612024)]
 Houdek, G., Balmforth, N. J., Christensen-Dalsgaard, J., & Gough, D. O. 1999, *A&A*, 351, 582
 Iglesias, C. A., & Rogers, F. J. 1996, *ApJ*, 464, 943
 Korn, G. A., & Korn, T. M. 1968, *Mathematical handbook for scientists and engineers. Definitions, theorems, and formulas for reference and review* (New York: McGraw-Hill, 2nd enl. and rev. edition)
 Korzennik, S. G., Rabello-Soares, M. C., & Schou, J. 2004, *ApJ*, 602, 481
 Kumar, P., Quataert, E. J., & Bahcall, J. N. 1996, *ApJ*, 458, L83

- Kurucz, R. 1993, ATLAS9 Stellar Atmosphere Programs and 2 km/s grid. Kurucz CD-ROM No. 13. Cambridge, Mass.: Smithsonian Astrophysical Observatory
- Lesieur, M. 1997, *Turbulence in Fluids* (Kluwer Academic Publishers)
- Millionshchikov, M. D. 1941, *Doklady Acad. Nauk SSSR*, 32, 611
- Morel, P. 1997, *A&AS*, 124, 597
- Rosenthal, C. S., Christensen-Dalsgaard, J., Nordlund, Å., Stein, R. F., & Trampedach, R. 1999, *A&A*, 351, 689
- Samadi, R., & Goupil, M. . 2001, *A&A*, 370, 136
- Samadi, R., Nordlund, Å., Stein, R. F., Goupil, M. J., & Roxburgh, I. 2003a, *A&A*, 404, 1129
- Samadi, R., Nordlund, Å., Stein, R. F., Goupil, M. J., & Roxburgh, I. 2003b, *A&A*, 403, 303
- Samadi, R., Goupil, M.-J., Alecian, E., et al. 2005, *J. Astrophys. Atr.*, 26, 171
- Samadi, R., Kupka, F., Goupil, M. J., Lebreton, Y., & van't Veer-Menneret, C. 2006, *A&A*, 445, 233
- Stein, R., Georgobiani, D., Trampedach, R., Ludwig, H.-G., & Nordlund, Å. 2004, *Sol. Phys.*, 220, 229
- Stein, R. F., & Nordlund, Å. 2001, *ApJ*, 546, 585
- Unno, W., Osaki, Y., Ando, H., Saio, H., & Shibahashi, H. 1989, *Nonradial oscillations of stars* (University of Tokyo Press, 2nd ed.)
- Woodard, M. F., Korzennik, S. G., Rabello-Soares, M. C., et al. 2001, *ApJ*, 548, L103

Stochastic excitation of nonradial modes

II. Are solar asymptotic gravity modes detectable?

K. Belkacem¹, R. Samadi¹, M. J. Goupil¹, M. A. Dupret¹, A. S. Brun^{2,3}, and F. Baudin⁴

¹ Observatoire de Paris, LESIA, CNRS UMR 8109, 92195 Meudon, France
e-mail: Kevin.Belkacem@obspm.fr

² DSM/IRFU/SaP, CEA Saclay & AIM, UMR 7158, CEA – CNRS – Université Paris 7, 91191 Gif-sur-Yvette, France

³ Observatoire de Paris, LUTH, CNRS UMR 8102, 92195 Meudon, France

⁴ Institut d’Astrophysique Spatiale, CNRS – Université Paris XI UMR 8617, 91405 Orsay Cedex, France

Received 18 August 2008 / Accepted 3 October 2008

ABSTRACT

Context. Detection of solar gravity modes remains a major challenge to our understanding of the inner parts of the Sun. Their frequencies would enable the derivation of constraints on the core physical properties, while their amplitudes can put severe constraints on the properties of the inner convective region.

Aims. Our purpose is to determine accurate theoretical amplitudes of solar g modes and estimate the SOHO observation duration for an unambiguous detection of individual modes. We also explain differences in theoretical amplitudes derived from previous works.

Methods. We investigate the stochastic excitation of modes by turbulent convection, as well as their damping. Input from a 3D global simulation of the solar convective zone is used for the kinetic turbulent energy spectrum. Damping is computed using a parametric description of the nonlocal, time-dependent, convection-pulsation interaction. We then provide a theoretical estimation of the intrinsic, as well as apparent, surface velocity.

Results. Asymptotic g -mode velocity amplitudes are found to be orders of magnitude higher than previous works. Using a 3D numerical simulation from the ASH code, we attribute this to the temporal-correlation between the modes and the turbulent eddies, which is found to follow a Lorentzian law rather than a Gaussian one, as previously used. We also find that damping rates of asymptotic gravity modes are dominated by radiative losses, with a typical life time of 3×10^5 years for the $\ell = 1$ mode at $\nu = 60 \mu\text{Hz}$. The maximum velocity in the considered frequency range (10–100 μHz) is obtained for the $\ell = 1$ mode at $\nu = 60 \mu\text{Hz}$ and for the $\ell = 2$ at $\nu = 100 \mu\text{Hz}$. Due to uncertainties in the modeling, amplitudes at maximum i.e. for $\ell = 1$ at 60 μHz can range from 3 to 6 mm s^{-1} . The upper limit is too high, as g modes would have been easily detected with SOHO, the GOLF instrument, and this sets an upper constraint mainly on the convective velocity in the Sun.

Key words. convection – turbulence – Sun: oscillations

1. Introduction

The pioneer works of Ulrich (1970) and Leibacher & Stein (1971) led to the identification of the solar five-minutes oscillations as global acoustic standing waves (p modes). Since then, successful works have determined the Sun internal structure from the knowledge of its oscillation frequencies (e.g., Christensen-Dalsgaard 2004). However, p modes are not well-suited to probing the deepest inner part of the Sun. On the other hand, g modes are mainly trapped in the radiative region and are thus able to provide information on the properties of the central part of the Sun ($r < 0.3 R_{\odot}$) (e.g., Turck-Chièze et al. 2001; Christensen-Dalsgaard 2006). As g modes are evanescent in the convective region, their amplitudes are expected to be very low at the photosphere and above, where observations are made, their detection is thus quite a challenge for more than 30 years.

The first claims of detection of solar gravity modes began with the work of Severnyi et al. (1976) and Brookes et al. (1976). Even after more than ten years of observations from SOHO, there is still no consensus about detection of solar g modes. Most of the observational efforts have been focused on low-order g modes motivated by a low the granulation noise (Appourchaux et al. 2006; Elsworth et al. 2006) and by previous theoretical

estimates of g -mode amplitudes (e.g., Turck-Chièze et al. 2004; Kumar et al. 1996). Recently, García et al. (2007) have investigated the low-frequency domain, with the hope of detecting high radial-order g modes. The method looked for regularities in the power spectrum, and the authors claim to detect a periodicity in accordance with what is expected from simulated power spectra. The work of García et al. (2007) present the advantage of exploring a different frequency domain ($\nu \in [25; 140] \mu\text{Hz}$) more favorable to a reliable theoretical estimation of the g -mode amplitudes, as we will explain later on.

Amplitudes of g modes, as p modes, are believed to result from a balance between driving and damping processes in the solar convection zone. Two major processes have been identified as stochastically driving the resonant modes in the stellar cavity. The first is related to the Reynolds stress tensor, the second is caused by the advection of turbulent fluctuations of entropy by turbulent motions. Theoretical estimations based on stochastic excitation have been previously obtained by Gough (1985) and Kumar et al. (1996). Gough (1985) made an order of magnitude estimate based on an assumption of equipartition of energy as proposed by Goldreich & Keeley (1977b). He found a maximum velocity around 0.5 mm s^{-1} for an $\ell = 1$ mode at $\nu \approx 100 \mu\text{Hz}$. Kumar et al. (1996) used a different approach based on the Goldreich et al. (1994) modeling of stochastic

excitation by turbulent convection, as well as an estimating of the damping rates (Goldreich & Kumar 1991) that led to a surface velocity near 0.01 mm s^{-1} for the $\ell = 1$ mode at $\nu \approx 100 \mu\text{Hz}$. The results differ from each other by orders of magnitude, as pointed out by Christensen-Dalsgaard (2002b). Such differences remain to be understood. One purpose of the present work is to carry out a comprehensive study of both the excitation and damping rates of asymptotic g modes. Our second goal is to provide theoretical oscillation mode velocities, as reliably as possible. Note, however, that penetrative convection is another possible excitation mechanism (Andersen 1996; Dintrans et al. 2005), but it is beyond the scope of this paper.

Damping rates are computed using the Grigahcène et al. (2005) formalism that is based on a non-local time-dependent treatment of convection. We will show that, contrary to p modes and high frequency g modes, asymptotic g -mode (i.e. low frequency) damping rates are insensitive to the treatment of convection. This then removes most of the uncertainties in the estimated theoretical oscillation mode velocities. Consequently, we restrict our investigation to low-frequency gravity modes. Stochastic excitation is modeled in the same way as in Belkacem et al. (2008), which is a generalization to non-radial modes of the formalism developed by Samadi & Goupil (2001) and Samadi et al. (2003b,a), for radial modes. As in the case of p -modes, the excitation formalism requires knowing the turbulent properties of the convection zone, but unlike p modes, the excitation of gravity modes is not concentrated towards the uppermost surface layers. One must then have some notion about the turbulent properties across the whole convection zone. Those properties will be inferred from a 3D numerical simulation provided by the ASH code (Miesch et al. 2008).

The paper is organized as follows. Section 2 briefly recalls our model for the excitation by turbulent convection and describes the input from a 3D numerical simulation. Section 3 explains how the damping rates are computed. Section 4 gives our theoretical results on the surface velocities of asymptotic g modes and compares them with those from previous works. Section 5 provides the apparent surface velocities, which take disk integrated effects and line formation height into account. These quantities can be directly compared with observations. We then discuss our ability to detect these modes using data from the GOLF instrument onboard SOHO as a function of the observing duration. The discussion is based on estimations of detection threshold and numerical simulations of power spectra. In Sect. 6, uncertainties on the estimated theoretical and apparent velocities, due to the main uncertainties in our modeling, are discussed. Finally, conclusions are provided in Sect. 7.

2. Excitation by turbulent convection

The formalism we used to compute excitation rates of non-radial modes was developed by Belkacem et al. (2008) who extended the work of Samadi & Goupil (2001) developed for radial modes to non-radial modes. It takes the two sources into account that drive the resonant modes of the stellar cavity. The first is related to the Reynolds stress tensor and the second one is caused by the advection of the turbulent fluctuations of entropy by the turbulent motions (the ‘‘entropy source term’’). Unlike for p modes, the entropy source term is negligible for g modes. We numerically verified that it is two to four orders of magnitude lower than the Reynolds stress contribution depending on frequency. This is explained by the entropy contribution being sensitive to second-order derivatives of the displacement eigenfunctions in the superadiabatic region where entropy fluctuations are

localized. As the gravity modes are evanescent in the convection zone, the second derivatives of displacement eigenfunctions are negligible and so is the entropy contribution.

The excitation rate, P , then arises from the Reynolds stresses and can be written as (see Eq. (21) of Belkacem et al. 2008)

$$P = \frac{\pi^3}{2I} \int_0^M dm \rho_0 R(r) \int_0^{+\infty} dk \mathcal{S}_k \quad (1)$$

$$\mathcal{S}_k = \frac{1}{k^2} \int_{-\infty}^{+\infty} d\omega E^2(k) \chi_k(\omega + \omega_0) \chi_k(\omega) \quad (2)$$

where m is the local mass, ρ_0 the mean density, ω_0 the mode angular frequency, I the mode inertia, \mathcal{S}_k the source function, $E(k)$ the spatial kinetic energy spectrum, χ_k the eddy-time correlation function, and k the wavenumber. The term $R(r)$ depends on the eigenfunction, its expression is given in Eq. (23) of Belkacem et al. (2008), i.e.

$$\begin{aligned} R(r) = & \frac{16}{15} \left| \frac{d\xi_r}{dr} \right|^2 + \frac{44}{15} \left| \frac{\xi_r}{r} \right|^2 + \frac{4}{5} \left(\frac{\xi_r^*}{r} \frac{d\xi_r}{dr} + c.c \right) \\ & + L^2 \left(\frac{11}{15} |\zeta_r|^2 - \frac{22}{15} \left(\frac{\xi_r^* \xi_h}{r^2} + c.c \right) \right) \\ & - \frac{2}{5} L^2 \left(\frac{d\xi_r^*}{dr} \frac{\xi_h}{r} + c.c \right) \\ & + \left| \frac{\xi_h}{r} \right|^2 \left(\frac{16}{15} L^4 + \frac{8}{5} \mathcal{F}_{\ell,|m|} - \frac{2}{3} L^2 \right), \end{aligned} \quad (3)$$

where we have defined

$$L^2 = \ell(\ell + 1) \quad (4)$$

$$\zeta_r \equiv \frac{d\xi_h}{dr} + \frac{1}{r}(\xi_r - \xi_h) \quad (5)$$

$$\mathcal{F}_{\ell,|m|} = \frac{|m|(2\ell + 1)}{2} (L^2 - (m^2 + 1)), \quad (6)$$

and ξ_r, ξ_h are the radial and horizontal components of the fluid displacement eigenfunction (ξ), and ℓ, m represent the degree and azimuthal number of the associated spherical harmonics.

2.1. Numerical computation of theoretical excitation rates

In the following, we compute the excitation rates of g modes for a solar model. The rate (P) at which energy is injected into a mode per unit time is calculated according to Eq. (1). Eigenfrequencies and eigenfunctions are computed using the adiabatic pulsation code OSC (Boury et al. 1975). The solar structure model used for these computations is obtained with the stellar evolution code CESAM (Morel 1997) for the interior and a Kurucz (1993) model for the atmosphere. The interior-atmosphere matching point is chosen at $\log \tau = 0.1$ (above the convective envelope). The pulsation computations use the full model (interior+atmosphere). In the interior model, we used the OPAL opacities (Iglesias & Rogers 1996) extended to low temperatures with the opacities of Alexander & Ferguson (1994) and the CEFF equation of state (Christensen-Dalsgaard & Däppen 1992). Convection is included according to a Böhm-Vitense mixing-length (MLT) formalism (see Samadi et al. 2006, for details), from which the convective velocity is computed. Turbulent pressure is not included (but see discussion in Sect. 6).

Apart from the eigenfunctions and the density stratification, Eq. (1) involves both the convective velocity and the turbulent kinetic energy spectrum. To get some insight into the turbulent properties of the inner part of the solar convection zone,

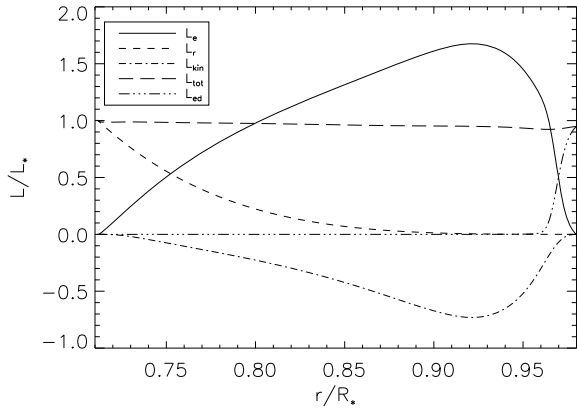


Fig. 1. Luminosity flux contributions versus radius, averaged over horizontal surfaces and in time. The solid line corresponds to the enthalpy luminosity (L_e), the short dashed-line to the radiative luminosity (L_r), the dotted-dashed line to the kinetic energy luminosity (L_{kin}), the long-dashed line to the total luminosity (L_{tot}), and the dot-dashed line correspond to the unresolved eddy luminosity (L_{ed}) (Brun et al. 2004). We particularly emphasize the negative kinetic-energy flux that results in a larger convective flux (see text for details).

we chose to use results from (ASH) 3D numerical simulations. Such a choice was motivated by the uncertainties inherent in the treatment of turbulence by the MLT. The MLT indeed only gives us an estimation of the convective flux but is not able to assess the contributions of all scales involved in turbulent convection. Thus, in the following, the rms convective velocity is taken from the mixing-length theory, while both the spatial and temporal turbulent properties are inferred from the 3D simulation. Then, velocity from the numerical simulation is not used in our calculation. This choice is motivated by the rigid boundary condition at the top of the simulation that results in an unrealistic decrease in the vertical velocity for $r > 0.93 R_\odot$.

2.2. The 3D convection simulation

One way of assessing the dynamical properties of the deep solar turbulent convection zone is to exploit a high resolution numerical simulation such as those performed with the anelastic spherical harmonic (ASH) code (Miesch et al. 2008; Brun et al. 2004). The simulation of global scale turbulent convection used in the present work is discussed in detail in Miesch et al. (2008). The ASH code solves the hydrodynamic anelastic equations within a spherical shell extending from $r = 0.71$ up to $r = 0.98 R_\odot$, yielding an overall radial density contrast of 132. Solar values were assumed for the rotation rate and the imposed luminosity. Figure 1 represents the energy flux balance (converted to luminosity and normalized to the solar luminosity) in the simulation. We clearly see how dominant, and overluminous, the convective (enthalpy) flux is in carrying the heat outward. This is mostly due to the strong density contrast and to the corresponding strong asymmetry between up- and downflows yielding a large inward kinetic energy flux (see Miesch et al. 2008, for more details). We have seen above that, in order to compute the excitation rate of the waves, one needs some well-defined physical quantities, such as the kinetic energy spectrum (E_k) and the eddy time function (χ_k). It is straightforward to deduce these quantities from the 3D simulation as explained in Appendix B. We then directly use E_k in Eq. (2) to compute the source function, whereas for χ_k we perform a fit of the 3D results with a simple analytical

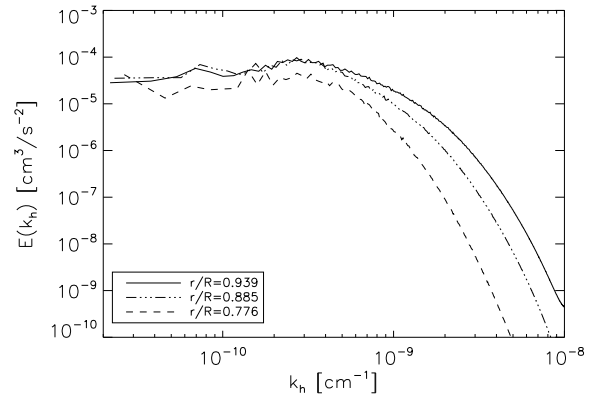


Fig. 2. $E(k_h)$ computed as explained in Appendix B, for three shell radii that sample the convection zone, as a function of the local horizontal wave number k_h .

expression. In the ASH code, the set of anelastic equations is projected onto spherical harmonics for the horizontal dimensions. This implies that the kinetic energy spectrum is obtained as a function of the spherical degree l . The local wavenumber k_h is obtained via the simple expression $k_h = \sqrt{l(l+1)}/r$, with r the shell radius.

2.2.1. Kinetic energy spectrum and time-correlation function

The kinetic energy spectrum of the total velocity (i.e. the horizontal and vertical components), $E(k_h)$, is plotted in the top panel of Fig. 2 as a function of the local horizontal wave number k_h . The rms convective velocity (u) increases with r , thus explaining that the deeper the layers, the smaller $E(k)$ since $\int dk E(k) = 1/2 u^2$. In terms of excitation rates, an important issue is the scale at which the spectrum peaks. As pointed out by Miesch et al. (2008), the scale at which the kinetic energy spectrum is maximum is the scale between the downflows. It is about 58 Mm at the top of the simulation ($r = 0.98 R_\odot$) up to 300 Mm at the bottom. This is quite different from what is found in the uppermost layers in 3D numerical simulations of the Sun (e.g., Stein & Nordlund 1998), in which the maximum of $E(k)$ is found on a scale around 1 Mm. Such a difference is explained by the density that strongly decreases in the upper layers.

The time-correlation function (χ_k) also plays an important role. Usually, a Gaussian time-correlation function is used (Goldreich et al. 1994; Chaplin et al. 2005). Samadi et al. (2003a) demonstrate that χ_k is reproduced better by a Lorentzian function. They argue that the departure from a Gaussian function can be explained by the presence of plumes in the uppermost part of the convection zone. This result, obtained with 3D numerical simulations, was then confirmed by confronting solar- p modes excitation rates, computed with Gaussian and Lorentzian functions, with the observational data. It turns out that the Lorentzian function greatly improves the agreement between models and observations. However, the time-correlation function is unknown at deeper layers. The eddy-time correlation function derived from the 3D numerical simulation provided by the ASH code is therefore compared to Gaussian and Lorentzian functions that are respectively defined as

$$\chi_k(\omega) = \frac{1}{\omega_k \sqrt{\pi}} e^{-(\omega/\omega_k)^2} \quad (7)$$

$$\chi_k(\omega) = \frac{1}{\pi \omega_k / 2} \frac{1}{1 + (2\omega/\omega_k)^2} \quad (8)$$

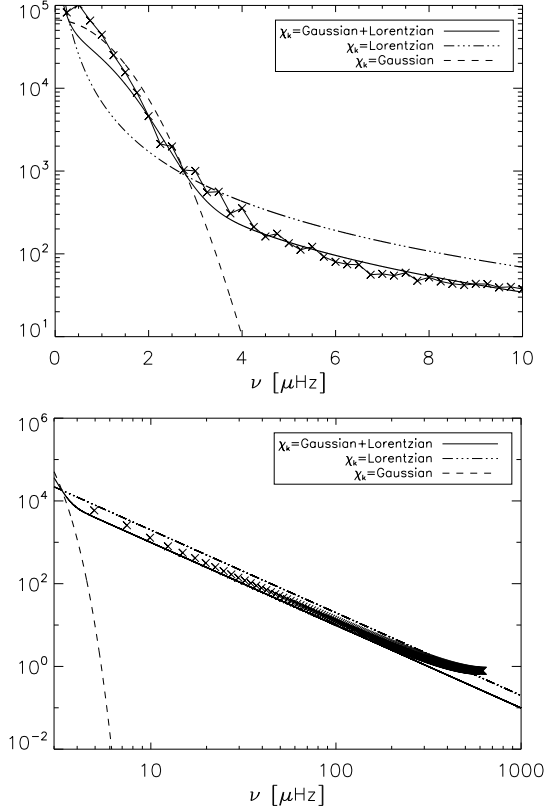


Fig. 3. *Top:* crosses represent $\chi_k(\omega)$ obtained from the 3D simulation at the wave number k_0 that corresponds to the maximum of $E(k)$, and at the radius $r/R_\odot = 0.89$. Data are obtained with a time series of duration ≈ 45.83 days with a sampling time of 4×10^4 s. Analytical functions are normalized so that their integrals are equal to unity. *Bottom:* the same as the upper panel except that data are obtained with a time series of duration ~ 4.68 days with a sampling time of 800 s. The theoretical curves are normalized so that their integrals over frequency equal that of the simulated data.

with the condition

$$\int_{-\infty}^{+\infty} \chi_k(\omega) d\omega = 1 \quad (9)$$

where ω_k is its linewidth, defined as

$$\omega_k \equiv \frac{2k u_k}{\lambda}. \quad (10)$$

where λ is a parameter as in [Balmforth \(1992\)](#), the velocity u_k of the eddy with wavenumber k is related to the kinetic energy spectrum $E(k_h)$ by ([Stein 1967](#))

$$u_k^2 = \int_k^{2k} dk E(k). \quad (11)$$

Figure 3 presents the comparison between analytical time-correlation functions, computed following the set of Eqs. (7)–(11), and χ_k computed from the 3D numerical simulation. The latter is calculated as described in Appendix B. The Lorentzian function represents the eddy-time correlation function better than a Gaussian function in the frequency range we are interested in ($\nu \in [20 \mu\text{Hz}; 110 \mu\text{Hz}]$).

The best fit is found using a sum of a Lorentzian function with $\lambda = 3$ and a Gaussian with $\lambda = 1/3$ as shown in the top

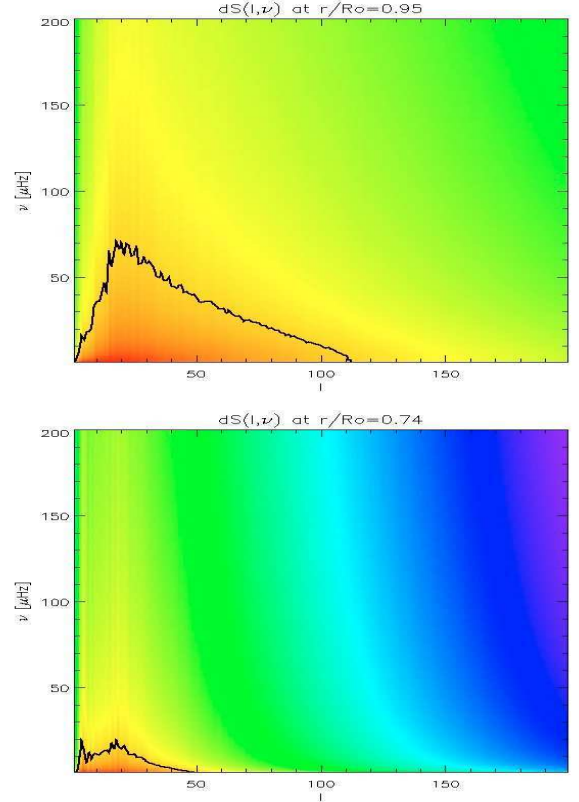


Fig. 4. The source function is plotted versus the spherical angular degree (l), and the frequency for two radii: $r = 0.95 R_\odot$ (*top panel*) and $r = 0.74 R_\odot$ (*bottom panel*). Bright (red) and dark (blue) tones indicate the high and low intensity of the source function, respectively. The color table is logarithmic. The black line corresponds to an arbitrary contour line that is the same for *both panels*.

panel of Fig. 3. In the frequency range we are interested in, i.e. at frequencies corresponding to the gravity modes (*bottom panel* of Fig. 3) the fit reproduces the time-correlation given by the 3D numerical simulation. We also clearly see that the eddy-time correlation function is very poorly represented by a Gaussian function, which only reproduces very low frequencies that do not significantly contribute to the excitation, then it fails and underestimates χ_k by many order of magnitudes (see Sect. 4.2.2).

The results presented in Fig. 3 are for the depth $r \approx 0.8 R_\odot$, where excitation is dominant, and for an angular degree corresponding to the maximum of the kinetic energy spectrum ($\ell = 40$), whose contribution is dominant in the excitation rates. Those results do not depend on the shell considered but instead on the wavenumber. For very high angular degree ($\ell > 300$) we find that χ_k becomes more and more Gaussian. Nevertheless, as shown by Fig. 2, those contributions are negligible compared to large-scale ones.

The value of the parameter λ is also of interest. Contrary to the upperlayers where $\lambda = 1$ ([Samadi et al. 2003b](#)), we find a higher value, $\lambda = 3$, that accords with the result of [Samadi et al. \(2003b\)](#) who find that the deeper the layers, the higher this parameter.

2.2.2. The source function

Figure 4 displays the source function (\mathcal{S}_k , Eq. (1)) as a function of both the angular degree l involved in the summation

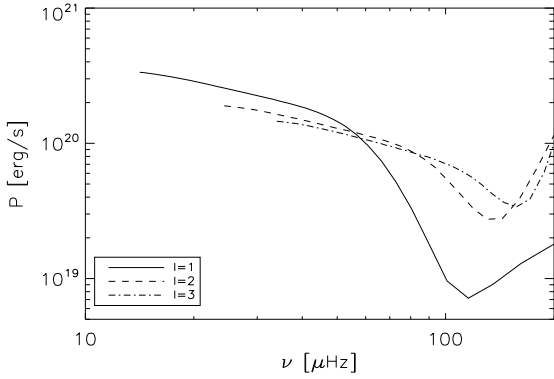


Fig. 5. Rate (P) at which energy is supplied to the modes versus the frequency for modes with angular degree $\ell = 1, 2$, and 3. The computation is performed as detailed in Sect. 2.1, using a Lorentzian eddy-time correlation function.

Eq. (B.1) and the mode frequency. The function S_k evaluated at two levels, $r = 0.95 R_\odot$ and $r = 0.74 R_\odot$, is shown in order to emphasize the dependence of S_k with the radius. Near the top of the convection zone, S_k is non-negligible at high frequencies ($\nu > 50 \mu\text{Hz}$) and on small scales. From top to bottom, the intensity of the source function decreases such that at the bottom, significant intensities exist only on large scales (small l values) and low frequencies. This behavior corresponds to the evolution of convective elements, i.e. turbulent eddies evolve on larger time and spatial scales with depth. Thus, we conclude that *high-frequency g modes are mainly excited in the upper layers, whereas low ones are excited deeper*; however, the net excitation rate, Eq. (1), is a balance between the eigenfunction shape and the source function.

2.3. Excitation rates

Anticipating the following (see Sect. 3), we stress that modes with high angular degree will be highly damped, making their amplitudes very small; hence, we restrict our investigation to low- ℓ degrees ($\ell < 4$). In Fig. 5, we present the excitation rates for low-frequency gravity modes (i.e., $\ell = 1, 2, 3$). By asymptotic modes we denote low-frequency modes ($\nu < 100 \mu\text{Hz}$, i.e. high- $|n|$ modes) while high frequencies ($\nu > 100 \mu\text{Hz}$) correspond to low- $|n|$ modes. At low frequencies ($\nu < 100 \mu\text{Hz}$), the excitation rate (P) decreases with increasing ν , it reaches a minimum and then at high frequency increases with the frequency. This can be explained by considering the two major contributions to the excitation rate P (Eqs. (1) and (3)) which are the inertia I (in Eq. (1)) and mode compressibility ($\nabla \cdot \xi$, appearing in $R(r)$, Eq. (3)).

Mode inertia decreases with frequency as shown by Fig. 6 since the higher the frequency, the higher up the mode is confined in the upper layers. This then tends to decrease the efficiency of the excitation of low-frequency modes. On the other hand, mode compressibility (Fig. 6) increases with frequency and consequently competes and dominates the effect of mode inertia. Mode compressibility can be estimated as

$$\left| \int_{\Omega} d\Omega Y_{\ell}^m \nabla \cdot \xi \right| \approx \left| \frac{d\xi_r}{dr} - \ell(\ell+1) \frac{\xi_h}{r} \right|. \quad (12)$$

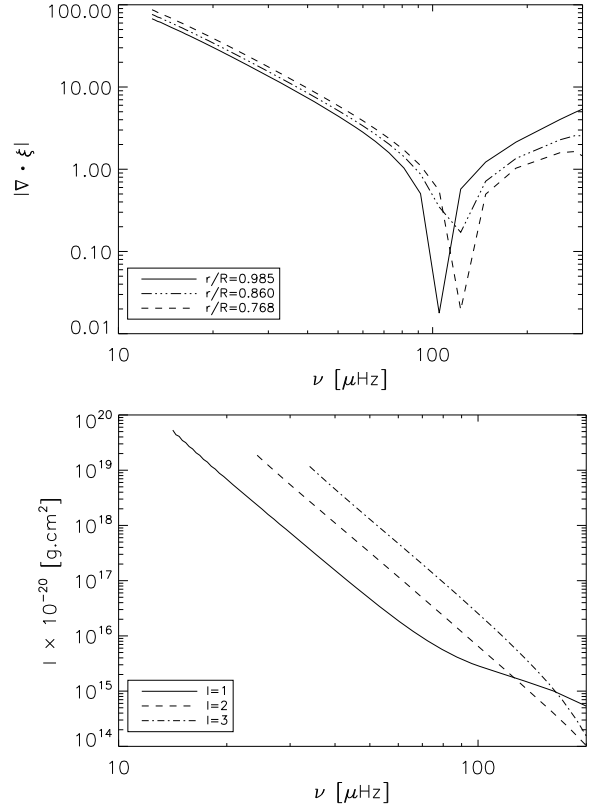


Fig. 6. *Top:* absolute value of mode compressibility for $\ell = 1$ modes versus the frequency, computed for three different layers in the convection zone. *Bottom:* mode inertia versus frequency for modes with angular degree $\ell = 1, 2, 3$.

The mode compressibility is minimum when both terms in Eq. (12) are of the same order. Following Belkacem et al. (2008), one has

$$\left| \frac{d\xi_r}{dr} \right| / \frac{\ell(\ell+1)\xi_h}{r} \approx \frac{\sigma^4}{\ell(\ell+1)} \quad \text{with} \quad \sigma^2 = \frac{R^3}{GM} \omega_0^2 \quad (13)$$

where σ is the dimensionless frequency, ω_0 is the angular frequency of the mode, R the Sun radius, and M its mass. According to Eq. (13), mode compressibility is minimum for $\nu \approx 100 \mu\text{Hz}$ depending on ℓ , as shown by Fig. 6. In contrast, in the asymptotic regime ($\nu < 100 \mu\text{Hz}$), the modes are compressible and this compressibility increases with decreasing frequency.

It is important to stress that for the asymptotic g modes, in the frequency range $[20; 110] \mu\text{Hz}$, the horizontal contributions in Eq. (3) are dominant. For low- ℓ g modes, the dominant contributions come, in Eq. (3), from the component of the mode divergence (see Eq. (12)). Then the ratio of the horizontal to the vertical contributions to Eq. (1) is around a factor five, imposing the use of a non-radial formalism.

3. Damping rates

To compute theoretical (surface velocities) amplitudes of g modes, knowledge of the damping rates is required.

3.1. Physical input

Damping rates have been computed with the non-adiabatic pulsation code MAD (Dupret 2002). This code includes a time-dependent convection (TDC) treatment described in

Grigahcène et al. (2005): it takes into account the role played by the variations of the convective flux, the turbulent pressure, and the dissipation rate of turbulent kinetic energy. This TDC treatment is non-local, with three free parameters a , b , and c corresponding to the non-locality of the convective flux, the turbulent pressure and the entropy gradient. We take here the values $a = 10$, $b = 3$, and $c = 3.5$ obtained by fitting the convective flux and turbulent pressure of 3D hydrodynamic simulations in the upper overshooting region of the Sun (Dupret et al. 2006c). According to Grigahcène et al. (2005), we introduced a free complex parameter β in the perturbation of the energy closure equation. This parameter is introduced to prevent non-physical spatial oscillation of the eigenfunctions. We use here the value $\beta = -0.5i$, which leads to a good agreement between the theoretical and observed damping rates and phase lags in the range of solar pressure modes (Dupret et al. 2006a). The sensitivity of the damping rates to β is discussed in Sect. 3.2.1, and we show in next sections that the values of those parameters have no influence on the results since we are interested in low-frequency g modes.

We use the TDC treatment as described in Dupret et al. (2006b), in which the 1D model reproduces exactly the mean convective flux, the turbulent pressure and the mean superadiabatic gradient obtained from a 3D hydrodynamic simulation by Stein & Nordlund (1998), by introducing two fitting parameters, the mixing-length, and a closure parameter (see Dupret et al. 2006b, for details). We also stress that, for low-frequency g modes, particular attention is to be paid to the solution of the energy equation near the center as explained in Appendix A for the $\ell = 1$ modes since those dipolar modes present a peculiar behavior near the center that must be properly treated.

3.2. Numerical results for a solar model

3.2.1. Sensibility to the time-dependent treatment of convection

To understand the contribution of each layer of the Sun in the damping of the g modes, we give the normalized work integral in Fig. 7 in such a way that the surface value is the damping rate η (in μHz)¹. Results obtained with our TDC treatment (solid lines) and with frozen convection (FC, dashed line) are compared for 4 different modes with $\nu \approx 60 \mu\text{Hz}$ (top panel) and $\nu \approx 20 \mu\text{Hz}$ (bottom panel). We see that most of the damping occurs in the inner part of the radiative core. The work integrals obtained with TDC and FC treatments are not very different; hence, the uncertainties inherent in the treatment of the coherent interaction between convection and oscillations do not significantly affect the theoretical damping rates of solar asymptotic g modes. This means that the frozen convection is adapted to low-frequency g modes. This can be explained by paying attention to the ratio $Q = \omega_0/\omega_c$, where ω_0 is the oscillation frequency and ω_c the convective frequency, defined to be $\omega_c = 2\pi\Lambda/u_{\text{mlt}}$ where Λ is the mixing length and u_{mlt} the convective velocity. In the whole solar convective zone Q is higher than unity except near the surface (the superadiabatic region). However contributions of the surface layer remain small in comparison with the radiative ones for asymptotic g modes (see Fig. 7).

One can thus draw some conclusions:

- for high-frequency g modes ($\nu > 110 \mu\text{Hz}$), the work integrals and thus the damping rates are sensitive to the

¹ Note that, regions where the work decreases outwards have a damping effect on the mode, or a driving effect when it increases outwards.

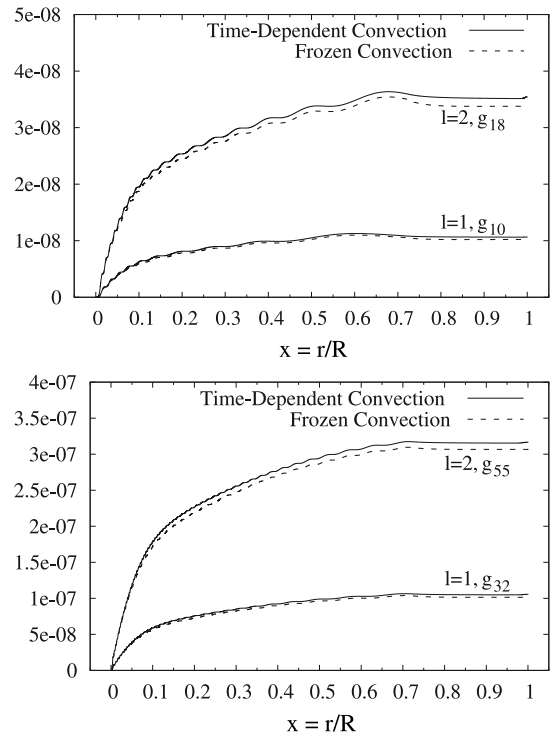


Fig. 7. Work integrals for $\ell = 1$ and $\ell = 2$ modes at $\nu \approx 60 \mu\text{Hz}$ (top panel) and $\nu \approx 20 \mu\text{Hz}$ (bottom panel), the surface values give the damping rates η in μHz .

parameter β that is introduced to model the convection/pulsation interactions because the role of the surface layers in the work integrals becomes important. As a result, the results on the damping rates are questionable for high frequencies since the value of β is derived from the observed p modes and that there is no evidence it can be applied *safely* for g modes;

- in contrast, for low-frequency g modes ($\nu < 110 \mu\text{Hz}$), we find that the work integrals and then the damping rates are *insensitive* to parameter β . Also, we numerically checked that the damping rates are insensitive to the non-local parameters introduced in Sect. 3.1.

3.2.2. Contributions to the work integral

Figure 8 allows us to investigate the respective roles played by different terms in the damping of the mode. More precisely we consider two modes ($\ell = 1, g_{10}, \nu \approx 60 \mu\text{Hz}$ and $\ell = 1, g_{32}, \nu \approx 20 \mu\text{Hz}$) in the frequency interval of interest here and give in Fig. 8 the modulus of:

- the contribution to the work by the radial part of the radiative flux divergence variations (solid line)

$$dW_{\text{FRr}} = \Re \left\{ \left(\frac{\delta T}{T} \right)^* \frac{\partial \delta L_{\text{R}}}{\partial x} \right\} \frac{R}{GM^2 \sigma}, \quad (14)$$

where T is the temperature, L_{R} the radiative luminosity, R the solar radius, M the solar mass, x the normalized radius, σ the real part of the normalized frequency $\sigma = \omega_0/(GM/R^3)^{1/2}$, and x the normalized radius (see Appendix A). Note that δ denotes the wave Lagrangian perturbations, \Re the real part, and $*$ the complex conjugate;

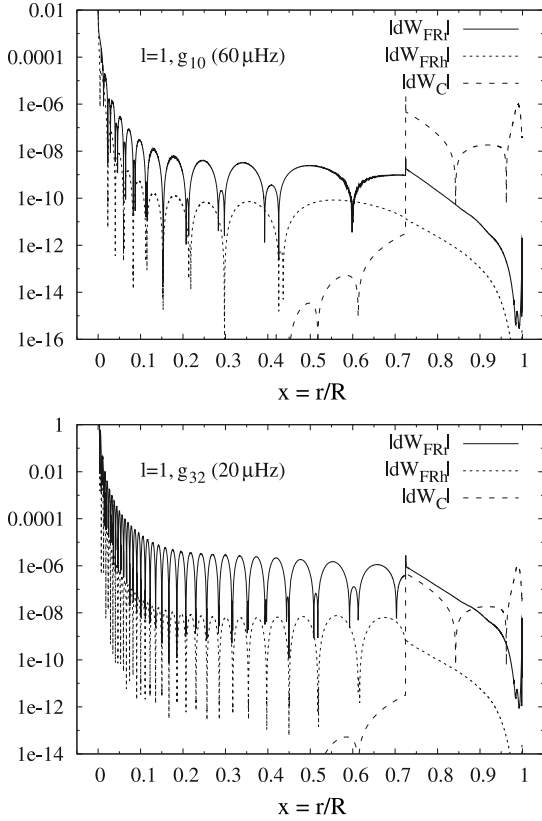


Fig. 8. Contributions to the work by the radial radiative flux variation (solid line), the transverse radiative flux variation (dotted line), and the time-dependent convection terms (dashed line), for the mode $\ell = 1, g_{10}$ (top panel) and $\ell = 1, g_{32}$ (bottom panel). Details are given in the text.

- the contribution to the work by the transversal part of the radiative flux divergence variations (dotted line):

$$dW_{FRh} = -\ell(\ell + 1) \Re \left\{ \frac{\delta T^*}{T} \left(\frac{\delta T}{x dT/dx} - \frac{\xi_r}{r} \right) \right\} \frac{RL}{GM^2 \sigma x}; \quad (15)$$

- the contribution to the work by the time-dependent convection terms (dashed line): dW_C (see Sect. 4 of Grigahcène et al. 2005).

Integration of these terms over the normalized radius gives their global contribution to the work performed during one pulsation cycle.

The time-dependent convection terms have a very low weight for both modes in the frequency range $\nu < 110 \mu\text{Hz}$. It confirms the conclusion of Sect. 3.2.1 that the damping rates of low-frequency g modes are not dominated by the perturbation of the convective flux, i.e. the interaction convection/oscillation (through the parameter β). The higher the mode frequency, the higher the integrated convective contribution of the work (W_C), which becomes dominant for $\nu > 110 \mu\text{Hz}$.

While the transverse radiative flux term plays a significant role near the center, the major contribution to the work comes from the radial component of the radiative flux variations. As a result, the radiative damping is the dominant contribution for low-frequency gravity modes.

In Fig. 9, we give the theoretical damping rates η of g -modes of degree $\ell = 1, 2, 3$, as a function of the oscillation frequency in μHz . We see that for $\nu < 110 \mu\text{Hz}$, η is a decreasing function

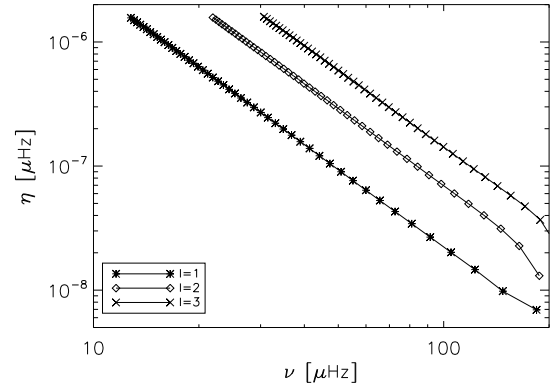


Fig. 9. Theoretical damping rates η of g modes of degree $\ell = 1, 2, 3$ as a function of the oscillation frequency in μHz .

of frequency. We find that the frequency dependence is $\eta \propto \omega_0^{-3}$. To understand this behavior, we express the integral expression of the damping rate (see Grigahcène et al. 2005, for details) as

$$\eta = \frac{1}{2\omega_0 I} \int_0^M \text{Im} \left(\frac{\delta \rho^*}{\rho} T \delta S \right) (\Gamma_3 - 1) dm \quad (16)$$

with

$$I = \int_0^M dm |\xi|^2 \quad \text{and} \quad (\Gamma_3 - 1) = \left(\frac{\partial \ln T}{\partial \ln \rho} \right)_s \quad (17)$$

where $\delta \rho, \delta S$ are the perturbations of the density and entropy, respectively, ρ, T are the density and temperature, ξ the eigenfunction, and the star denotes the complex conjugate.

Keeping only the radial contribution of the radiative flux in the energy equation (Eq. (A.1)) because it is the dominant contribution, and neglecting the production of nuclear energy ($\epsilon = 0$), one gets

$$T \delta S = \frac{i}{\omega_0} \frac{\partial \delta L}{\partial m}. \quad (18)$$

This approximation comes from the dominance of the radial contribution of the radiative flux. In addition, in the diffusion approximation

$$\frac{\delta L}{L} = \left(\frac{1}{dT/dr} \frac{\partial \delta T}{\partial r} + 2 \frac{\xi_r}{r} + 3 \frac{\delta T}{T} - \frac{\delta \kappa}{\kappa} - \frac{\delta \rho}{\rho} - \frac{\partial \xi_r}{\partial r} \right). \quad (19)$$

Because of the high wavenumber for low-frequency g modes, the term in $\partial \delta T / \partial r$ is very high in Eq. (14), dominates in Eq. (19), and is the main source of damping. This term appears as a second-order derivative in the work integral, and introduces a factor k_r^2 ($k_r \approx \sqrt{\ell(\ell+1)N}/(\omega_0 r)$ is the vertical local wavenumber). Thus, from Eqs. (19), (18), and (16) one obtains $\eta \propto \omega_0^{-5}/I$. By using an asymptotic expansion of the eigenfunctions (Christensen-Dalsgaard 2002a), one gets $I \propto \omega_0^{-2}$, which permits $\eta \propto \omega_0^{-3}$ and explains the behavior of η in Fig. 9. The argument is the same for the variation of η with the angular degree at fixed frequency because it comes from the wave-number dependence k_r^2 .

Above $110 \mu\text{Hz}$, the role of the radiative zone in the mode damping is smaller. There, the damping rates begin to increase with frequency simply because the kinetic energy of the modes decreases faster than the mechanical work.

4. Surface velocities of g modes

4.1. Theoretical (intrinsic) velocities

We compute the mean-squared surface velocity (v_s^2) for each mode as

$$v_s^2(h) = \left\langle \int_{\Omega} \left(\mathbf{v}(\mathbf{r}, t) \cdot \mathbf{v}(\mathbf{r}, t) \right) d\Omega \right\rangle (h) \quad (20)$$

where h is the height in the stellar atmosphere, $\langle \rangle$ the time average. Using the expression Eq. (C.3) in Appendix C, one then has

$$v_s^2(h) = A^2 \left[v_r^2(h) + \ell(\ell + 1)v_h^2(h) \right]. \quad (21)$$

The amplitude $A^2 = (1/2)\langle |a(t)|^2 \rangle$ is given by (Eq. (C.6)):

$$A^2 = \frac{P}{2\eta I\omega_0^2} \quad (22)$$

where $\langle \rangle$ denotes the time average, I the mode inertia, η the damping rate, and $v_{r,h}(h) = \omega_0 \xi_{r,h}(h)$ with $\xi_r(h)$ and $\xi_h(h)$ respectively the radial and horizontal displacement eigenmode components.

In this section, we consider the level of the photosphere $h = R$ with R the radius at the photosphere. Figure 10 presents *intrinsic* values of the velocities. The behavior of the surface velocities as a function of the angular degree (ℓ) is mainly due to the damping rates, which rapidly increase with ℓ ; hence, at fixed frequency, the higher the angular degree, the lower the surface velocities. As a consequence, amplitudes are very low for $\ell > 3$. At fixed ℓ , v_s increases with frequency with a slope resulting from a balance between the excitation and damping rates. Nevertheless, modes of angular degree $\ell = 1$ exhibit a singular behavior, i.e. a maximum at $\nu \approx 60 \mu\text{Hz}$. This is due to the variation of the slope in the excitation rates (see Fig. 5). In terms of amplitudes, the maximum is found to be $\approx 5 \text{ mm/s}$ for $\ell = 1$ at $\nu \approx 60 \mu\text{Hz}$, which corresponds to the mode with radial order $|n| = 10$. It is important to stress that the velocities shown in Fig. 10, are *intrinsic* values of the modulus that must not be confused with the *apparent* surface velocities (see Sect. 5), which are the values that can be compared with observed ones.

4.2. Comparison with previous estimations

The theoretical intrinsic velocities obtained in the present work must be compared to previous estimations based on the same assumption that modes are stochastically excited by turbulent convection. All works cited in the next sections deal with intrinsic velocities, i.e. ones not corrected for visibility effects.

4.2.1. Estimation based on the equipartition of energy

The first estimation of g -mode amplitudes was performed by Gough (1985), who found a maximum of velocity of about 0.5 mm s^{-1} for the $\ell = 1$ mode at $\nu \approx 100 \mu\text{Hz}$. Gough (1985) used the principle of equipartition of energy, which consists in equating the mode energy (\mathcal{E}) with the kinetic energy of resonant eddies whose lifetimes are close to the modal period. This ‘‘principle’’ has been theoretically justified for p modes, by Goldreich & Keeley (1977b) assuming that the modes are damped by eddy viscosity. They found that the modal energy to be inversely proportional to the damping rate, η , and proportional to an integral involving the term $E_\lambda v_\lambda \lambda$ where $E_\lambda \equiv (1/2)m_\lambda v_\lambda^2$ is the kinetic energy of an eddy with

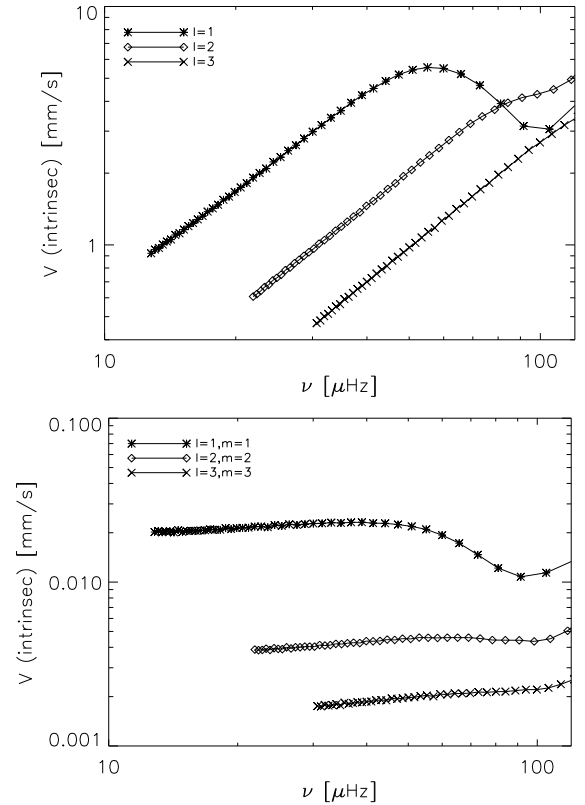


Fig. 10. *Top:* theoretical *intrinsic* surface velocities of g -modes of degree $\ell = 1, 2, 3$ as a function of the oscillation frequency in μHz , computed as described in Sect. 4.1 using a Lorentzian χ_k . *Bottom:* surface velocities of gravity modes of angular degree $\ell = 1$ and $\ell = 2$ computed using a Gaussian χ_k and a Kolmogorov spectrum to reproduce the results of Kumar et al. (1996).

size λ , velocity v_λ , and mass $m_\lambda = \rho \lambda^3$ (see Eq. (46) of Goldreich & Keeley 1977b). Using a solar model, they show that the damping rates of solar p modes are dominated by turbulent viscosity and that the damping rates are accordingly proportional to the eddy-viscosity, that is, $\eta \propto v_\lambda \lambda$ (see Eq. (6) of Goldreich & Keeley 1977a). Hence, after some simplifying manipulations, Goldreich & Keeley (1977b) found the modal energy to be (see their Eq. (52))

$$\mathcal{E} \approx 0.26 E_\lambda = 0.13 m_\lambda v_\lambda^2. \quad (23)$$

This principle then was used by Christensen-Dalsgaard & Frandsen (1983) for p modes and Gough (1985) for solar g modes. However, as mentioned above, the result strongly depends on the way the modes are damped, and for asymptotic g modes there is no evidence that this approach can be used and in particular, as shown in this work, if the damping is dominated by radiative losses.

4.2.2. Kumar et al. (1996)’s formalism

Another study was performed by Kumar et al. (1996), which was motivated by a claim of g -mode detection in the solar wind (Thomson et al. 1995). Computations were performed using the Goldreich et al. (1994) formalism; both turbulent and radiative contributions to the damping rates were included as derived by Goldreich & Kumar (1991) who obtained mode lifetimes around 10^6 yrs. This is not so far from our results (see Fig. 9).

Kumar et al. (1996) found that the theoretical (i.e. not corrected for visibility factors) surface velocity is around $10^{-2} \text{ cm s}^{-1}$ near $\nu = 200 \mu\text{Hz}$ for $\ell = 1$ modes. However, as shown in Sect. 3, the results for this frequency range are very sensitive to the convective flux perturbation in the damping rate calculations. Thus, we do not discuss the result obtained for those frequencies.

More interesting for our study, Kumar et al. (1996) also found very low velocities ($10^{-2} \text{ mm s}^{-1}$) for $\nu < 100 \mu\text{Hz}$. This is significantly lower than what we find. However, the efficiency of the excitation strongly depends on how the eddies and the waves are temporally-correlated. As already explained in Sect. 2.1, the way the eddy-time correlation function is modeled is crucial since it leads to major differences between, for instance, a Gaussian and a Lorentzian modeling. The Goldreich & Keeley (1977b) approach, from which Kumar et al. (1996)'s formulation is derived, implicitly assumes that the time-correlation between the eddies is Gaussian. The present work (as explained in Sect. 2.1) assumes a Lorentzian for the time correlation function χ_k , which results in $v = 3 \text{ mm s}^{-1}$ in amplitude for $\ell = 1$ mode at $\nu \approx 60 \mu\text{Hz}$ (Sect. 4.1).

We performed the same computation but now assuming χ_k to be Gaussian (Eq. (7)) and using a Kolmogorov spectrum as in Kumar et al. (1996). In that case (see Fig. 10), we find velocities of the order of $10^{-2} \text{ mm s}^{-1}$ for $\ell = 1$ which agree with the result of Kumar et al. (1996), which is significantly lower than when assuming a Lorentzian.

5. Apparent surface velocities

We denote as *disk-integrated apparent velocities* the values of amplitudes that take both geometrical and limb darkening effects into account. Contrary to solar p modes, one cannot neglect the horizontal component of ξ compared to the vertical one. The observed velocity (V_{obs}) is given by the apparent surface velocity $\langle |V_{\text{app}}(r, t)|^2 \rangle^{1/2}$ (see Appendix C) evaluated at the observed line formation height h :

$$V_{\text{obs}} = \left(\frac{P}{2\eta I \omega_0^2} \right)^{1/2} \left(\alpha_\ell^m v_r(h) + \beta_\ell^m v_h(h) \right) \quad (24)$$

where α_ℓ^m and β_ℓ^m are the visibility factors defined in Appendix C.

In Appendix C we follow the procedure first derived by Dziembowski (1977) and for asymptotic g modes by Berthomieu & Provost (1990). We use a quadratic limb-darkening law following Ulrich et al. (2000) for the Sun with an angle between the rotation axis and the Equator of 83 degrees. As mentioned above, the apparent velocities are evaluated at the level h , i.e. the height above the photosphere where oscillations are measured. Then h is set so as to correspond to the SoHO/GOLF measurements that use the NaD1 and D2 spectral lines, formed at the optical depth $\tau = 5 \times 10^{-4}$ (see Bruls & Rutten 1992). The results are presented in Tables 1 and 2 for angular degrees $\ell = 1, 2, 3$.

Figure 11 displays the apparent velocities for modes $\ell = 1, 2, 3$ and $\ell = m$. For a given angular degree, the azimuthal order degree is chosen such that the apparent velocity is maximal. The velocities of the $m = 0$ modes are strongly attenuated by the visibility effects, while the $m = \ell$ modes are less sensitive to them. For $\ell = 1$ modes, the amplitudes are divided by a factor of two with respect to the intrinsic velocities, while the $\ell = 2, 3$ mode velocities remain roughly the same. Consequently, our calculations show that both the $\ell = 1$ and $\ell = 2$ ($m = \ell$) are the most probable candidates for detection with amplitudes $\approx 3 \text{ mm s}^{-1}$.

Table 1. Values of the visibility coefficient α_ℓ^m of the radial component of the velocity, corresponding to an inclination angle of $\theta_0 = 83^\circ$.

m	0	1	2	3
$\ell = 1$	0.117	0.675		
$\ell = 2$	0.346	0.107	0.437	
$\ell = 3$	0.06	0.164	0.0552	0.184

Table 2. Values of the visibility coefficient β_ℓ^m of the radial component of the velocity, corresponding to an inclination angle of $\theta_0 = 83^\circ$.

m	0	1	2	3
$\ell = 1$	0.094	0.540		
$\ell = 2$	0.833	0.258	1.053	
$\ell = 3$	0.291	0.649	0.268	0.892

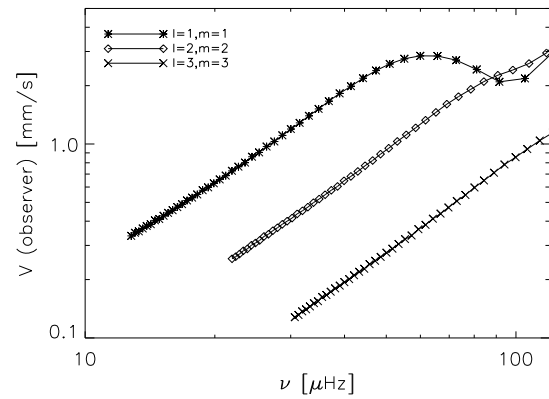


Fig. 11. Apparent surface velocities for g modes of degree $\ell = 1, 2, 3$ as a function of the oscillation frequency in μHz (visibility factors are taken into account).

5.1. Detectability of g modes; only a matter of time

To compare our calculated apparent velocities with observations, we used data from the GOLF spectrometer (Gabriel et al. 2002) onboard the SOHO platform, which performed Doppler-like measurements on the disk-integrated velocity of the Sun, using the Na D lines. We used here a series of 3080 days to estimate the background noise level and compare it to the apparent velocities determined in this work.

A first possible approach is to use some analytical and statistical calculations such as the ones developed by Appourchaux et al. (2000) (Eq. (10)). Once a length of observation T (in units of 10^6 s), a frequency range $\Delta\nu$ (in μHz), and a level of confidence p_{det} are set, this gives the corresponding signal-to-noise ratio

$$\frac{s_{\text{det}}}{\langle s \rangle} \approx \ln(T) + \ln(\Delta\nu) - \ln(1 - p_{\text{det}}), \quad (25)$$

where s_{det} is the power of the signal to be detected, and $\langle s \rangle$ the local power of the noise. This means that any peak in the frequency range $\Delta\nu$ above this ratio has a probability p_{det} of not being due to noise. Choosing a frequency range of $\Delta\nu = 10 \mu\text{Hz}$ centered on the frequency of the highest expected velocities ($60 \mu\text{Hz}$) sets the background level at $\approx 500 (\text{m s}^{-1})^2/\text{Hz}$. Equation (25) gives an amplitude of 5.2 mm s^{-1} for a detection with a confidence level p_{det} of 90% for 15 years of observation, 4.6 mm s^{-1} for 20 years, and 3.8 mm s^{-1} for 30 years.

However, this approach has to be repeated for each mode (with its own proper noise level) to have a global view of detection possibilities. To do so, we used simulations. Again relying

Table 3. Number of peaks above the detection level in the simulated power spectra versus the duration of observation in three cases. In the simulated signal, the modes are given an amplitude A_{\max} . The 3 cases respectively correspond to A_{\max} being the apparent amplitudes A readily stemmed from our calculation, $A_{\max} = 1.5A$ and $A_{\max} = 2A$. The last two cases take into account that uncertainties in the modeling globally tend to underestimate the amplitudes as discussed in Sect. 6.

A_{\max}	10 years	15 years	20 years	25 years	30 years
A	0.8	1.6	0.8	1.4	1.7
$1.5A$	1.4	2.9	4.5	6.5	8.8
$2A$	4.6	8.5	13.4	20.0	21.7

on the GOLF data to estimate the noise spectrum, we simulated synthetic data including noise and g modes with the apparent velocities as above (and with random phases). Several durations of observation were simulated, from 10 to 30 years. A hundred simulations were performed in each case. The noise level is estimated locally and so is the detection level, following Eq. (25), on the frequency range $[30 \mu\text{Hz}, 100 \mu\text{Hz}]$. Thus, with a confidence level of 90% and with 7 independent subsets of $10 \mu\text{Hz}$, noise is expected to show no peak above the global detection level with a probability of 48%, and to show 1 peak above the global detection level with a probability of 32% (and even 2 peaks in 12% of the realizations). Table 3 lists the average (over 100 simulations) number of peaks detected above the detection level for different observation durations. These simulations were performed using amplitudes A_{\max} assuming three different cases:

- Case 1: we assumed for A_{\max} the apparent surface velocity amplitudes calculated above, A .
Due to uncertainties in the theoretical modeling (as discussed in Sect. 6), we also assume:
- Case 2: that amplitudes are larger than the amplitudes estimated above by 50% i.e. $A_{\max} = 1.5A$;
- Case 3: that amplitudes are larger than the amplitudes estimated above by a factor 2 i.e. $A_{\max} = 2A$.

Cases 1 and 3 are the two limits of this exercise. The number of detected peaks in case 3 shows that the predicted amplitudes cannot be overestimated by a factor of two, because in this case, the solar g modes would have already been detected without doubt. Case 1 sets a lower limit, because in this case, even with longer (30 years) observation, g modes would not be detected. Case 2 shows that if real solar amplitudes are just a few tens of percent higher than the present estimations, then g modes could be detected no doubt after say 15 to 20 years of observation (to be compared to the present status of observation: 12 years). The results are summarized in Figs. 12.

We must stress that, apart from visibility effects and height of line formation, we took no other instrumental effects on the apparent amplitude determination into account, because they depend on the instrument. The impact is probably a decrease in the measured amplitudes compared to the apparent amplitudes as computed here. This does not change the above conclusion for Case 1. We expect that the instrumental uncertainty is less than the theoretical uncertainties discussed in Sect. 6 below, which led to case 2 and 3.

6. Discussion

In Sect. 5 above, we explained why estimates of g -mode amplitudes obtained by previous authors differ from each other by orders of magnitude (Christensen-Dalsgaard 2002b). We propose

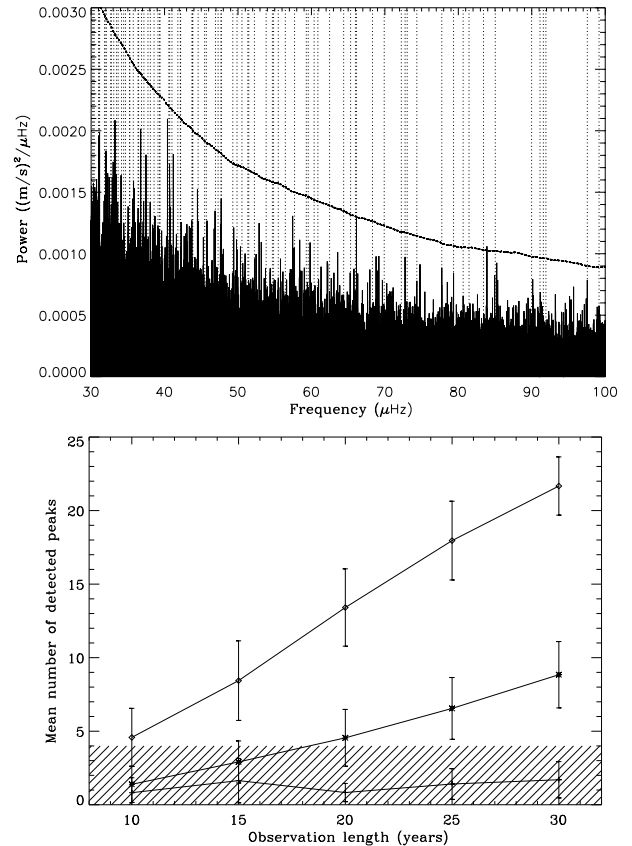


Fig. 12. Simulated spectrum for an observation length of 30 years, in Case 1. The dashed line indicates the level of detection (see text and Eq. (25)). The vertical lines indicate the frequencies of the simulated modes. Here, only one mode is above the detection level. *Bottom:* average number and standard deviation (from the 100 realizations) of modes detected in simulations versus the length of observation for the three cases (see text). Above the hashed region (less than four peaks detected), one can consider the detection to be unambiguous. The upper curve corresponds to the case 3 ($A_{\max} = 2A$), the *middle one* to case 2 ($A_{\max} = 1.5A$), and the *lower one* to case 1 ($A_{\max} = A$).

an improved modeling based on the input of 3D numerical simulations and on a formalism that had successfully reproduced the observations for p modes (Belkacem et al. 2006). Nevertheless, several approximations remain, and they lead to uncertainties that can reach a factor two in the estimation of g -mode apparent velocities (overestimation). We next discuss the most important ones.

6.1. Equilibrium model: description of convection

Convection is implemented in our equilibrium models according to the classical Böhm-Vitense mixing-length (MLT) formalism (see Samadi et al. 2006, for details).

6.1.1. Convective velocities

Values of the MLT convective velocity, u , are by far the most important contributions to mode amplitude uncertainties because the mode surface velocities depend on u^3 . First, we verified that a non-local description of turbulence does not modify the convective velocities by more than a few per cent except near the uppermost part of the convection zone, which does not play any role

here. Second, we compared the rms velocities from the 3D numerical simulation with MLT velocities to estimate of the uncertainties. The MLT underestimates the velocity, relative to the more realistic numerical simulation (far from the boundaries). Indeed, it comes from the negative kinetic energy flux that results in a larger enthalpy flux in order to carry the solar flux to the surface. A direct consequence is that in 3D simulations the velocities are higher than the ones computed by MLT by a factor of about 50%. This may in turn result in a possible underestimation of the amplitudes of the modes by a factor 2, when, as here, MLT is used to estimate the velocities.

6.1.2. Anisotropy

The value for the velocity anisotropy, which is the ratio between the square of the vertical velocity to the square of the rms velocity parameter, Φ , is derived from the MLT: its value is 2. However, this is not fully consistent since we assume, in the excitation model, isotropic turbulence (i.e. $\Phi = 3$). Nevertheless, increasing the value of Φ from two to three results in an increase of only 15% in the mode surface velocities. This is lower than the uncertainties coming from χ_k (see Sect. 6.2).

6.1.3. Turbulent pressure

Our solar equilibrium model does not include turbulent pressure. However, unlike p modes, low-frequency (high radial order) gravity modes, i.e. those considered in this work, are only slightly affected by turbulent pressure. The reason is that such modes are excited in the deepest layers of the convection zone, i.e. between $r = 0.7 R_\odot$ and $r = 0.9 R_\odot$ where turbulent pressure has little influence on the equilibrium structure since the ratio of the turbulent pressure to the gas pressure increases with the radius.

6.2. Stochastic excitation: the role of the eddy-time correlation function

A Gaussian function is commonly used to describe the frequency dependence of the turbulent kinetic energy spectrum, χ_k , (e.g., Samadi & Goupil 2001; Chaplin et al. 2005). However, Samadi et al. (2003a) show that, for p modes, a Lorentzian function represents the results obtained using 3D numerical simulations better. Furthermore, the latter function yields a theoretical modeling in accordance with observations, while using a Gaussian function fails (Samadi et al. 2003b). This led us to investigate $\chi_k(\omega)$ for g modes. We find that different choices of the functional form for $\chi_k(\omega)$ result in order of magnitude differences for the mode amplitudes.

Uncertainties inherent in the eddy-time correlation function are related to the value of the λ parameter (Sect. 2.2.1) and to the contribution of low frequency components in the 3D simulation. As a rough estimate, decreasing λ from 3 to 2 leads to an increase of 20% for the surface velocity. Figure 3 shows that low-frequency components in the turbulent kinetic energy spectrum are better-fitted using a Gaussian function. However, the source of such low-frequency components remains unclear, because they can originate from rotation; in particular, it is not clear whether they must be taken into account when estimating the mode excitation rates. By removing those contributions, the resulting surface velocities decrease by around 25%.

6.3. Mode damping: the convection-pulsation coupling

Last but not least, modeling damping rates of damped, stochastically excited modes remains one of the most challenging issues. The strong coupling between convection and oscillation in solar-like stars makes the problem difficult and still unsolved, since all approaches developed so far failed to reproduce the solar damping rates without the use of unconstrained free parameters (e.g., Dupret et al. 2005; Houdek 2006). Such descriptions fail to correctly describe the interaction between convection and oscillations when both are strongly coupled, i.e. when the characteristic times associated with the convective motions are the same order of magnitude as the oscillation periods. This explains why we do not use an extrapolation based on a fit of p mode damping rates, but instead consider a frequency domain in which the damping is dominated by radiative contributions. A reliable computation of the damping rates at higher frequencies, beyond this paper's scope, would require a sophisticated analytical or semi-analytical theory of the convection-oscillation interaction, which will not be limited to the first order in the convective fluctuations and which will take the contribution of different spatial scales into account.

7. Conclusions

We performed a theoretical computation of the surface oscillation velocities of asymptotic gravity modes. This calculation requires knowing excitation rates, which were obtained as described in Belkacem et al. (2008) with input from 3D numerical simulations of the solar convective zone (Miesch et al. 2008). Damping rates, η , are also needed. As mentioned in Sect. 6, we restricted our investigation to the frequency domain for which η is dominated by radiative contributions (i.e. $\nu \in [20; 110] \mu\text{Hz}$). For higher frequencies, the coupling between convection and oscillation becomes dominant, making the theoretical predictions doubtful. For asymptotic g -modes, we find that damping rates are dominated by the modulation of the radial component of the radiative flux by the oscillation. In particular for the $\ell = 1$ mode near $\nu \approx 60 \mu\text{Hz}$, η is around $10^{-7} \mu\text{Hz}$, then the mode life time is $\approx 3 \times 10^5$ yrs. Maximum velocity amplitude at the photosphere arises for this same mode and is found at the level of 3 mm s^{-1} (see Fig. 11). Modes with higher values of the angular degree ℓ present smaller amplitudes since the damping is proportional to ℓ^2 .

Amplitudes found in the present work are orders of magnitude larger than those from previous works, which themselves showed a large dispersion between their respective results. In one of these previous works, the estimation was based on an equipartition principle derived from the work of Goldreich & Keeley (1977a,b) and designed for p modes. Its use for asymptotic g modes is not adapted as the damping rates of these modes are not dominated by turbulent viscosity. Kumar et al. (1996) have carried another investigation of g mode amplitudes, and its calculation is rather close to our modeling. Most of the quantitative disagreement with our result lies in the use of a different eddy-time correlation function. Kumar et al. (1996) assumed a Gaussian function as is commonly used. Our choice relies on results from 3D simulations and is closer to a Lorentzian function.

Taking visibility factors, as well as the limb-darkening, into account we finally found that the maximum of apparent surface velocities of asymptotic g -modes is $\approx 3 \text{ mm s}^{-1}$ for $\ell = 1$ at $\nu \approx 60 \mu\text{Hz}$ an $\ell = 2$ at $\nu \approx 100 \mu\text{Hz}$. Due to uncertainties in the theoretical modeling, amplitudes at maximum, i.e. for $\ell = 1$ at $60 \mu\text{Hz}$, can range from 3 to 6 mm s^{-1} . By performing numerical

simulations of power spectra, it is shown that, with amplitudes of 6 mm s^{-1} , the modes would have been already detected by the GOLF instrument, while in the case of an amplitude of 3 mm s^{-1} the g modes would remain undetected even with 30 years of observations. The theoretical amplitudes found in this work are then close to the actual observational limit. When detected, the amplitude detection threshold of these modes will, for instance, establish a strict upper limit to the convective velocities in the Sun.

Acknowledgements. We are indebted to J. Leibacher for his careful reading of the manuscript and his helpful remarks. We also thank J. P. Zahn for its encouragements.

Appendix A: Energy equation near the center

For the full non-adiabatic computation of g -mode damping rates, much care must be given to the solution of the energy equation near the center of the Sun for the modes of angular degree $\ell = 1$. We give in Eqs. (A.1) and (A.2) the perturbed energy and transfer equations in a purely radiative zone:

$$i\omega_0 T \delta S = -\frac{d\delta L}{dm} + \epsilon \left(\frac{\delta\epsilon}{\epsilon} + \frac{\delta\rho}{\rho} + \frac{1}{r^2} \frac{d(r^2\xi_r)}{dr} \right) + \ell(\ell+1) \frac{L}{4\pi\rho r^3} \left(\frac{\delta T}{r dT/dr} - \frac{\xi_r}{r} \right), \quad (\text{A.1})$$

$$\frac{\delta L}{L} = 2 \frac{\xi_r}{r} + 3 \frac{\delta T}{T} - \frac{\delta\kappa}{\kappa} - \frac{\delta\rho}{\rho} + \frac{1}{dT/dr} \frac{d\delta T}{dr} - \frac{d\xi_r}{dr}. \quad (\text{A.2})$$

The radial (first term of Eq. (A.1)) and transverse parts (last term of Eq. (A.1)) of the perturbed flux divergence are both singular at the center. But this singularity is lifted when the two terms are joined and an appropriate change of variables is carried out:

$$\begin{aligned} \sigma &= \frac{\omega_0}{\sqrt{GM/R^3}} \\ \frac{\xi_r}{r} &= \zeta x^{\ell-2} \\ \frac{\delta S}{c_v} &= \eta x^\ell \quad ; \quad \frac{\delta T}{T} = \vartheta x^\ell \quad ; \quad \frac{\delta\rho}{\rho} = \gamma x^\ell \\ \frac{\delta\epsilon}{\epsilon} &= \delta\epsilon_x x^\ell \\ k &= (GM/R^3)^{-1/2} \frac{L(r)}{4\pi\rho r^3 c_v} \\ \epsilon_1 &= \left(\frac{4\pi\rho r^3}{3} \frac{\epsilon}{L(r)} - 1 \right) \frac{3}{x^2} \\ T_1 &= \frac{d \ln T / dx}{x} \\ T_2 &= \frac{x^2}{L} \frac{d}{dx} \left(\frac{L}{x^2} \frac{1}{d \ln T / dx} \right) \\ x &= \frac{r}{R}. \end{aligned} \quad (\text{A.3})$$

All of these variables and quantities are regular at the solar center, where the perturbed energy equation takes the form

$$\begin{aligned} \frac{i\sigma\eta}{k} &= 3\delta\epsilon_x + 2\gamma \\ &\quad -(\ell+3) \left((4 - \kappa_T) \vartheta - (1 + \kappa_\rho) \gamma \right) \\ &\quad -\ell T_2 \vartheta - (2\ell+3) T_1 \frac{d^2\vartheta}{dx^2} \\ &\quad + 2(\ell-1)\epsilon_1 \zeta + (2\ell+3) \frac{d^2\zeta}{dx^2}. \end{aligned} \quad (\text{A.4})$$

For a precise solution of the non-adiabatic problem by a finite difference method, it is crucial to use a discrete scheme that tends continuously towards Eq. (A.4) at the center. If not, the eigenfunctions diverge towards the center; in the particular case of the solar g modes, this can lead to an overestimate of the damping rates by a factor of about 2.

Appendix B: Computation of the kinetic energy spectrum from the ASH code

The ASH code solves the hydrodynamical equations in spherical coordinates (r, θ, ϕ) . Each component of the velocity is decomposed in terms of spherical harmonics as

$$V_p(t, r, \theta, \phi) = \sum_{l,m} V_{l,m,p}(t, r) Y_{l,m}(\theta, \phi) \quad (\text{B.1})$$

where $p = r, \theta, \phi$. The spherical harmonic $Y_{l,m}(\theta, \phi)$ is defined as

$$Y_l^m(\theta, \phi) \equiv N_{l,m} P_l^m(\cos\theta) e^{im\phi} \quad (\text{B.2})$$

where P_l^m is the associated Legendre function, and the normalization constant $N_{l,m}$

$$N_{l,m} = \sqrt{\frac{2l+1}{4\pi}} \sqrt{\frac{(l-m)!}{(l+m)!}} \quad (\text{B.3})$$

is chosen such that

$$\int d\Omega Y_{l,m}(\theta, \phi) Y_{l',m'}(\theta, \phi) = \delta_{l,l'} \delta_{m,m'} \quad (\text{B.4})$$

where $d\Omega = \sin\theta d\theta d\phi$.

The kinetic energy spectrum that is averaged over time and the solid angle is defined following Samadi et al. (2003b) as

$$E(\ell, r) \equiv \frac{1}{2} \sum_{m,p} \left\langle \left(V_{l,m,p} - \langle V_{l,m,p} \rangle \right)^2 \right\rangle \quad (\text{B.5})$$

where $\langle (\cdot) \rangle$ refers to time average. As in Samadi et al. (2003b), density does not enter into the definition of the kinetic energy spectrum. Indeed, the Samadi & Goupil (2001)' formalism assumes a homogeneous turbulence. This assumption is justified when the turbulent Mach number is low. This is the case in most parts of the convective zone except at the top of convective region.

The mean kinetic energy spectrum, $E(l, r)$, verifies the relation

$$\sum_l E(l, r) = \frac{1}{2} u^2(r) \quad (\text{B.6})$$

where $u(r)$ is the root mean square velocity at the radius r .

Following Samadi et al. (2003a), we also define a kinetic energy spectrum as a function of frequency (ν) and averaged over the solid angle, $E(l, \nu, r)$ such that

$$\sum_l E(l, \nu, r) \equiv \frac{1}{2} \int \frac{d\Omega}{4\pi} \sum_p \left\| \hat{V}_p(\nu, r, \theta, \phi) \right\|^2 \quad (\text{B.7})$$

where $\hat{V}_p(\nu, r, \theta, \phi)$ is the time Fourier transform of $V_p(t, r, \theta, \phi) - \langle V_p \rangle$. Using Eqs. (B.1) and (B.4), Eq. (B.7) yields:

$$E(l, \nu, r) = \frac{1}{2} \sum_{m,p} \left\| \hat{V}_{l,m,p}(\nu, r) \right\|^2 \quad (\text{B.8})$$

where $\hat{V}_{l,m,p}(v, r)$ is the time Fourier transform of $V_{l,m,p}(t, r) - \langle V_{l,m,p} \rangle$. As in Samadi et al. (2003a), we decompose $E(l, v, r)$ as

$$E(l, v, r) = E(l, r) \chi_l(v, r) \quad (\text{B.9})$$

where the function $\chi_l(v, r)$ satisfies the normalization condition

$$\int_{-\infty}^{+\infty} dv \chi_l(v, r) = 1. \quad (\text{B.10})$$

According to the Parseval-Plancherel relation, one has

$$\sum_l \int_{-\infty}^{+\infty} dv E(l, v, r) = \sum_l E(l, r) = \frac{1}{2} u^2(r), \quad (\text{B.11})$$

We consider a short time series of duration ≈ 4.68 days with a sampling time of 800 s. Accordingly the Nyquist frequency is ≈ 1 mHz and the frequency resolution reaches ≈ 2.5 μ Hz. In addition, we use a longtime series of duration ≈ 45.83 days with a sampling time of 4×10^4 s that permits us to get χ_k at very low frequencies. In practice, $E(l)$ is derived from Eq. (B.5) and is directly implemented into Eq. (1), while $\chi_k(v)$ inferred from the simulation is computed using Eqs. (B.9) and (B.5).

By using $E(l)$ from the numerical simulation, we assume a planparallel approximation ($E(k) dk = E(l) dl$) since the maximum of the kinetic energy spectrum occurs on scales ranging between $l \approx 20$ and $l \approx 40$.

Appendix C: Visibility factors

Visibility factors have been computed first by Dziembowski (1977). Berthomieu & Provost (1990) studied the case of g modes which, for convenience, we recall below in our own notation. We denote the spherical coordinate system in the observer's frame by (r, θ, ϕ) where $r = 0$ corresponds to the center of the star and the $\theta = 0$ axis coincides with the observer's direction. At a surface point (r, θ, ϕ) , the unit vector directed toward the observer is $\mathbf{n} = \cos \theta \mathbf{e}_r - \sin \theta \mathbf{e}_\theta$. The apparent surface velocity is obtained as

$$V_{\text{app}}(r, t) = \frac{\int h(\mu) (\mathbf{v}(r, t) \cdot \mathbf{n}) d\Omega}{\int h(\mu) d\Omega}, \quad (\text{C.1})$$

where $\mathbf{v}(r, t)$ is the intrinsic mode velocity and $h(\mu)$ the limb-darkening function, which is normalized such that:

$$\int_0^1 \mu h(\mu) d\mu = 1. \quad (\text{C.2})$$

To first order in linearized quantities in Eq. (C.1), the effect of the distorted surface is neglected, and $d\Omega = R^2 \sin \theta d\theta d\phi$ is the solid angle around the direction of the observer \mathbf{n} with R the stellar radius.

For slow rotation, the oscillation velocity can be described in a pulsation frame with a single spherical harmonic. The coordinate system (r, Θ, Φ) in the pulsation frame is chosen such that the pulsation polar axis coincides with the rotation polar axis. The velocity vector at a level r in the atmosphere of the star for a mode with given ℓ, m and pulsation frequency ω_0 can then be written with no loss of generality as

$$\mathbf{v}(r, t) = \frac{1}{2} a(t) \omega_0 \boldsymbol{\xi}(r) e^{i\omega_0 t} + c.c. \quad (\text{C.3})$$

where $c.c.$ means complex conjugate and with the displacement eigenvector defined as

$$\boldsymbol{\xi}(r) = \xi_r(r) Y_\ell^m(\Theta, \Phi) \mathbf{e}_r + \xi_h(r) \nabla_H Y_\ell^m(\Theta, \Phi) \quad (\text{C.4})$$

with

$$\nabla_H = \left(0, \frac{\partial}{\partial \Theta}, \frac{1}{\sin \Theta} \frac{\partial}{\partial \Phi} \right). \quad (\text{C.5})$$

The dimensionless complex velocity amplitude $a_\nu(t)$ is assumed to be a slowly varying function of time for a damped stochastically excited mode (Samadi & Goupil 2001; Samadi et al. 2003b; Belkacem et al. 2008). The theoretical expression is given by

$$\langle |a(t)|^2 \rangle = \frac{P}{\eta I \omega_0^2} \quad (\text{C.6})$$

where the power P is defined in Eq. (1), I is the mode inertia, η the damping rate and $\langle \rangle$ represents a statistical average, or equivalently here a time average.

To obtain the apparent velocity from Eq. (C.1) using Eqs. (C.3) and (C.4), one must compute the scalar product: $\boldsymbol{\xi}(r) \cdot \mathbf{n}$.

$$\boldsymbol{\xi}(r) \cdot \mathbf{n} = \xi_r(r) Y_\ell^m(\Theta, \Phi) (\mathbf{e}_r \cdot \mathbf{n}) + \xi_h(r) (\nabla_H Y_\ell^m \cdot \mathbf{n}). \quad (\text{C.7})$$

A change in coordinate system shows that $\mathbf{e}_r \cdot \mathbf{n} = \cos \theta$ and

$$\nabla_H Y_\ell^m(\Theta, \Phi) \cdot \mathbf{n} = -\sin \theta \frac{\partial Y_\ell^m(\Theta, \Phi)}{\partial \theta}.$$

We use the spherical harmonics as defined in Eq. (B.2) and the following property

$$P_\ell^m(\cos \Theta) e^{im\Phi} = \sum_{m'=-\ell}^{\ell} q_{m,m'}^\ell(\Theta_0, \Phi_0) P_\ell^{m'}(\cos \theta) e^{im'\phi}, \quad (\text{C.8})$$

which for convenience, we use under the form

$$Y_\ell^m(\Theta, \Phi) = N_{\ell,m} \sum_{m'=-\ell}^{\ell} q_{m,m'}^\ell(\Theta_0, \Phi_0) P_\ell^{m'}(\cos \theta) e^{im'\phi} \quad (\text{C.9})$$

where $N_{\ell,m}$ is defined in Eq. (B.3), and (Θ_0, Φ_0) are the coordinates of the line-of-sight direction in the pulsation frame. The scalar product Eq. (C.7) becomes

$$\begin{aligned} \boldsymbol{\xi}(r) \cdot \mathbf{n} &= N_{\ell,m} \sum_{m'=-\ell}^{\ell} q_{m,m'}^\ell(\Theta_0, \Phi_0) e^{im'\phi} \\ &\times \left(\xi_r(r) P_\ell^{m'} \cos \theta - \xi_h(r) \sin \theta \frac{dP_\ell^{m'}}{d\theta} \right). \end{aligned} \quad (\text{C.10})$$

As emphasized by Dziembowski (1977), only the $q_{m,0}^\ell$ coefficients survive the ϕ integration in Eq. (C.1). Its expression is

$$q_{m,0}^\ell(\Theta_0, \Phi_0) = P_\ell^m(\cos \Theta_0) e^{im\Phi_0}. \quad (\text{C.11})$$

The angle Θ_0 between the observer and the rotation axis is often denoted i . Integration over the solid angle leads to:

$$\begin{aligned} \int h(\mu) (\boldsymbol{\xi}(r) \cdot \mathbf{n}) d\Omega &= Y_\ell^m(\Theta_0, \Phi_0) \\ &\times \left(\xi_r(r) \int_0^1 \mu^2 h(\mu) P_\ell(\mu) d\mu \right. \\ &\left. + \xi_h(r) \int_0^1 \mu h(\mu) (1 - \mu^2) \frac{dP_\ell(\mu)}{d\mu} d\mu \right). \end{aligned} \quad (\text{C.12})$$

Finally, using properties of spherical harmonics, one obtains

$$\frac{\int h(\mu) (\boldsymbol{\xi}(r) \cdot \mathbf{n}) d\Omega}{\int h(\mu) d\Omega} = Y_\ell^m(\Theta_0, \Phi_0) (\xi_r(r) u_\ell + \xi_h(r) w_\ell) \quad (\text{C.13})$$

where we have defined

$$u_\ell = \int_0^1 d\mu \mu^2 \tilde{h}(\mu) P_\ell(\mu) \quad (\text{C.14})$$

$$w_l = \ell \int_0^1 d\mu \mu \tilde{h}(\mu) (P_{\ell-1} - \mu P_\ell) \quad (\text{C.15})$$

with

$$\tilde{h}(\mu) = \frac{h(\mu)}{\int_0^1 h(\mu) d\mu}. \quad (\text{C.16})$$

Collecting Eq. (C.3) and Eq. (C.13), the apparent velocity is then given by

$$V_{\text{app}}(r, t) = \frac{1}{2} a(t) \omega_0 N_{\ell, m} P_\ell(\cos \Theta_0) \quad (\text{C.17})$$

$$\times (\xi_r(r) u_l + \xi_h(r) w_l) e^{i(\omega_0 t + m \phi_0)} + c.c. \quad (\text{C.18})$$

We assume a quadratic limb-darkening law of the form

$$h(\mu) = 1 + c_1 X^2 + c_2 X^2 + c_3 X^3 \quad (\text{C.19})$$

where $X = 1 - \mu$, $c_{i=\{1,2,3\}}$ are the associated limb-darkening coefficients, which respective values are -0.466 , -0.06 and -0.29 for the NaD1 spectral line, as derived by [Ulrich et al. \(2000\)](#). We find that our conclusion depends neither on the adopted limb-darkening law nor on the limb-darkening coefficients, results in accordance with [Berthomieu & Provost \(1990\)](#).

Using Eq. (C.6), the rms velocity is obtained as:

$$\begin{aligned} \langle (|V_{\text{app}}(r, t)|^2) \rangle^{1/2} &= \left(\frac{P}{2\eta I \omega_0^2} \right)^{1/2} \omega_0 N_{\ell, m} |P_\ell(\cos \Theta_0)| \\ &\times |\xi_r(r) u_l + \xi_h(r) w_l| \end{aligned} \quad (\text{C.20})$$

which we finally rewrite as

$$\langle (|V_{\text{app}}(r, t)|^2) \rangle^{1/2} = \left(\frac{P}{2\eta I \omega_0^2} \right)^{1/2} \times |v_r(r) \alpha_\ell^m + v_h(r) \beta_\ell^m|, \quad (\text{C.21})$$

where we have defined

$$\alpha_\ell^m = N_{\ell, m} P_\ell(\cos \Theta_0) u_l \quad (\text{C.22})$$

$$\beta_\ell^m = N_{\ell, m} P_\ell(\cos \Theta_0) w_l, \quad (\text{C.23})$$

and

$$v_r(r) = \omega_0 \xi_r(r) ; \quad v_h(r) = \omega_0 \xi_h(r). \quad (\text{C.24})$$

References

Alexander, D. R., & Ferguson, J. W. 1994, *ApJ*, 437, 879
 Andersen, B. N. 1996, *A&A*, 312, 610
 Appourchaux, T., Fröhlich, C., Andersen, B., et al. 2000, *ApJ*, 538, 401

Appourchaux, T., Andersen, B., Baudin, F., et al. 2006, in *SOHO-17. 10 Years of SOHO and Beyond*, ESA SP, 617
 Balmforth, N. J. 1992, *MNRAS*, 255, 639
 Belkacem, K., Samadi, R., Goupil, M. J., Kupka, F., & Baudin, F. 2006, *A&A*, 460, 183
 Belkacem, K., Samadi, R., Goupil, M.-J., & Dupret, M.-A. 2008, *A&A*, 478, 163
 Berthomieu, G., & Provost, J. 1990, *A&A*, 227, 563
 Boury, A., Gabriel, M., Noels, A., Scuflaire, R., & Ledoux, P. 1975, *A&A*, 41, 279
 Brookes, J. R., Isaak, G. R., & van der Raay, H. B. 1976, *Nature*, 259, 92
 Bruls, J. H. M. J., & Rutten, R. J. 1992, *A&A*, 265, 257
 Brun, A. S., Miesch, M. S., & Toomre, J. 2004, *ApJ*, 614, 1073
 Chaplin, W. J., Houdek, G., Elsworth, Y., et al. 2005, *MNRAS*, 360, 859
 Christensen-Dalsgaard, J. 2002a, *Rev. Mod. Phys.*, 74, 1073
 Christensen-Dalsgaard, J. 2002b, *Int. J. Mod. Phys. D*, 11, 995
 Christensen-Dalsgaard, J. 2004, in *SOHO 14 Helio- and Asteroseismology: Towards a Golden Future*, ed. D. Danesy, ESA SP, 559, 1
 Christensen-Dalsgaard, J. 2006, in *Proceedings of SOHO 18/GONG 2006/HELAS I, Beyond the spherical Sun*, ESA SP, 624
 Christensen-Dalsgaard, J., & Frandsen, S. 1983, *Sol. Phys.*, 82, 469
 Christensen-Dalsgaard, J., & Däppen, W. 1992, *A&AR*, 4, 267
 Dintrans, B., Brandenburg, A., Nordlund, Å., & Stein, R. F. 2005, *A&A*, 438, 365
 Dupret, M.-A. 2002, *Bull. Soc. Roy. Sc. Liège*, 5-6, 249
 Dupret, M. A., Barban, C., Goupil, M.-J., et al. 2006a, in *Proceedings of SOHO 18/GONG 2006/HELAS I, Beyond the spherical Sun*, ESA SP, 624
 Dupret, M.-A., Goupil, M.-J., Samadi, R., Grigahcène, A., & Gabriel, M. 2006b, in *Proceedings of SOHO 18/GONG 2006/HELAS I, Beyond the spherical Sun*, ESA SP, 624
 Dupret, M.-A., Samadi, R., Grigahcène, A., Goupil, M.-J., & Gabriel, M. 2006c, *Communications in Asteroseismology*, 147, 85
 Dziembowski, W. 1977, *AcA*, 27, 203
 Elsworth, Y. P., Baudin, F., Chaplin, W., et al. 2006, in *Proceedings of SOHO 18/GONG 2006/HELAS I, Beyond the spherical Sun*, ESA SP, 624
 Gabriel, A. H., Baudin, F., Boumier, P., et al. 2002, *A&A*, 390, 1119
 García, R. A., Turck-Chièze, S., Jiménez-Reyes, S. J., et al. 2007, *Science*, 316, 1591
 Goldreich, P., & Keeley, D. A. 1977a, *ApJ*, 211, 934
 Goldreich, P., & Keeley, D. A. 1977b, *ApJ*, 212, 243
 Goldreich, P., & Kumar, P. 1991, *ApJ*, 374, 366
 Goldreich, P., Murray, N., & Kumar, P. 1994, *ApJ*, 424, 466
 Gough, D. O. 1985, *Theory of Solar Oscillations*, Tech. Rep.
 Grigahcène, A., Dupret, M.-A., Gabriel, M., Garrido, R., & Scuflaire, R. 2005, *A&A*, 434, 1055
 Iglesias, C. A., & Rogers, F. J. 1996, *ApJ*, 464, 943
 Kumar, P., Quataert, E. J., & Bahcall, J. N. 1996, *ApJ*, 458, L83
 Kurucz, R. 1993, *ATLAS9 Stellar Atmosphere Programs and 2 km/s grid* Kurucz CD-ROM No. 13 (Cambridge, Mass.: Smithsonian Astrophysical Observatory)
 Leibacher, J. W., & Stein, R. F. 1971, *ApJ*, 7, L191
 Miesch, M. S., Brun, A. S., DeRosa, M. L., & Toomre, J. 2008, *ApJ*, 673, 557
 Morel, P. 1997, *A&AS*, 124, 597
 Samadi, R., & Goupil, M. 2001, *A&A*, 370, 136
 Samadi, R., Nordlund, Å., Stein, R. F., Goupil, M. J., & Roxburgh, I. 2003a, *A&A*, 404, 1129
 Samadi, R., Nordlund, Å., Stein, R. F., Goupil, M. J., & Roxburgh, I. 2003b, *A&A*, 403, 303
 Samadi, R., Kupka, F., Goupil, M. J., Lebreton, Y., & van't Veer-Menneret, C. 2006, *A&A*, 445, 233
 Severnyi, A. B., Kotov, V. A., & Tsap, T. T. 1976, *Nature*, 259, 87
 Stein, R. F. 1967, *Sol. Phys.*, 2, 385
 Stein, R. F., & Nordlund, A. 1998, *ApJ*, 499, 914
 Thomson, D. J., MacLennan, C. G., & Lanzerotti, L. J. 1995, *Nature*, 376, 139
 Turck-Chièze, S., Couvidat, S., Kosovichev, A. G., et al. 2001, *ApJ*, 555, L69
 Turck-Chièze, S., García, R. A., Couvidat, S., et al. 2004, *ApJ*, 604, 455
 Ulrich, R. K. 1970, *ApJ*, 162, 993
 Ulrich, R. K., Boumier, P., Robillot, J.-M., et al. 2000, *A&A*, 364, 816

Intrinsic photometric characterisation of stellar oscillations and granulation

Solar reference values and CoRoT response functions

E. Michel¹, R. Samadi¹, F. Baudin², C. Barban¹, T. Appourchaux², and M. Auvergne¹

¹ Observatoire de Paris-LESIA, CNRS (UMR 8109), Université Pierre et Marie Curie, Université Denis Diderot, Pl. J. Janssen, 92195 Meudon, France
e-mail: eric.michel@obspm.fr

² Institut d'Astrophysique Spatiale, UMR8617, Université Paris X, Bât.121, 91405 Orsay, France

Received 9 June 2008 / Accepted 6 December 2008

ABSTRACT

Context. Measuring amplitudes of solar-like oscillations and the granulation power spectral density constitute two promising sources of information to improve our understanding and description of the convection in outer layers of stars. However, different instruments, using different techniques and different bandpasses, give measurements that cannot be directly compared to each other or to theoretical values.

Aims. In this work, we define simple response functions to derive intrinsic oscillation amplitudes and granulation power densities, from photometry measurements obtained with a specific instrument on a specific star.

Methods. We test this method on different photometry data sets obtained on the Sun with two different instruments in three different bandpasses.

Results. We show that the results are in good agreement and we establish reference intrinsic values for the Sun with photometry. We also compute the response functions of the CoRoT instrument for a range of parameters representative of the Main Sequence solar-like pulsators to be observed with CoRoT. We show that these response functions can be conveniently described by simple analytic functions of the effective temperature of the target star.

Key words. Sun: oscillations – Sun: granulation – stars: oscillations – techniques: photometric – convection

1. Introduction

Solar-like oscillations are being detected in a rapidly growing number of stars (see e.g. [Bedding & Kjeldsen 2007](#)). The excitation of these oscillations, first observed in the Sun, is attributed to the acoustic noise generated by convection in the outer layers of stars and the measurement of their amplitude is a source of information on the convection process (see e.g. [Samadi et al. 2007a,b](#)). The existing theoretical works generally consider parametric scaling laws calibrated on the Sun. However, as noticed by [Kjeldsen et al. \(2005\)](#), measurements made on different stars with different instruments using different techniques in velocimetry or photometry, in different spectral lines or bandpasses, have different sensitivity to the oscillations. They cannot be directly compared to each other, or to theoretical values. The comparison to the Sun is not straightforward either, since the different existing data sets obtained on the Sun have not been translated into a proper standard reference suitable for comparison with stars. [Kjeldsen et al. \(2005\)](#) initiated such a normalization work and a comparison between several stars. [Kjeldsen et al. \(2008\)](#) measured the solar oscillation amplitude with stellar techniques, aiming at setting up a consistent reference for stellar oscillation measurements. This was done with velocimetry, since until now the vast majority of solar-like oscillations measured in other stars has been obtained with this technique. However, CoRoT ([Baglin et al. 2006](#)) has started photometric measurements of oscillations in solar-like pulsators which will need to be

measured quantitatively and compared with those of the Sun and with those obtained in velocimetry. In addition to oscillations, rapid photometry might allow us to measure, in approximately the same domain of frequency, the power density spectrum contribution associated with the stellar granulation. Granulation being a manifestation of the convective motion at the photosphere level, the profile of its power density spectrum is expected to reflect characteristic time scales and geometric scales associated with the convection process as described by heavy 3D numerical simulations (see e.g. [Ludwig 2006](#); [Trampedach et al. 1998](#)) or by parametrized models (see e.g. [Baudin et al. 2007](#)).

In the present work, we consider measurements of solar photometric variations obtained with two different instruments in four different bandpasses (SOHO/VIRGO/PMO6 and SPM three channels). In the corresponding instrumental power density spectra, we fit contributions from the solar background and from the acoustic oscillations (Sect. 2). In Sect. 3, we establish a simple instrumental response function relating the instrumental power density measurement to the intrinsic bolometric luminosity relative variation. These response functions can be applied to infer the intrinsic (bolometric) power density of the solar background from specific photometry measurements. They also can be used to derive intrinsic amplitudes of solar radial oscillations from the same data. We discuss how they can be adapted for non-radial modes. Following [Kjeldsen et al. \(2005\)](#) and [Kjeldsen et al. \(2008\)](#), we also propose to relate the oscillation mean power density measurement to an intrinsic amplitude

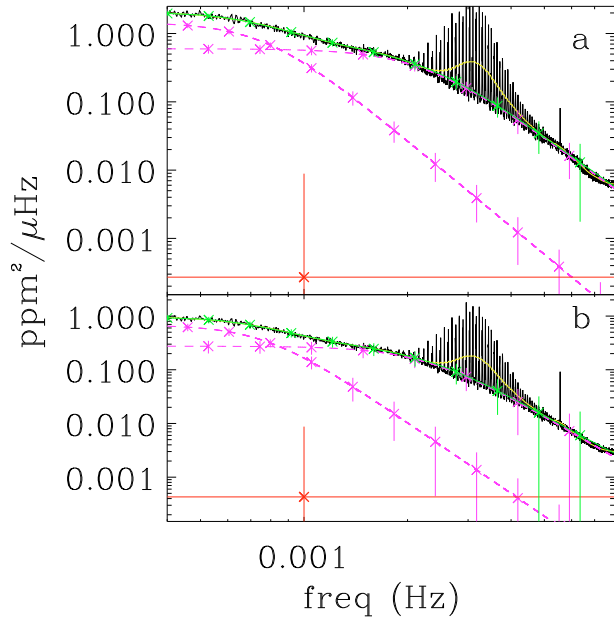


Fig. 1. Observational power density spectrum obtained for: SPM-blue **a**) and SPM-green **b**) data over 700 days; a moving mean is applied with a $4 \mu\text{Hz}$ boxcar (plain black line); the same spectrum highly smoothed with a 0.405 mHz boxcar (3Δ) is superimposed (plain light grey line [yellow]); individual powerlaws associated with granulation and meso-granulation are shown (dash lines [purple]); the white noise component (horizontal line [red]); the global fit of solar background + white noise components is represented (plain grey line [green]) but differs from the mean power density only in the domain of oscillations. Vertical error bars associated with the fit precision are illustrated at different frequencies for each component of the fit. For clarity, in the case of the white noise component, the error bar is represented only once at 1 mHz .

chosen here to be the bolometric amplitude for radial modes. In Sect. 4, we show that the results obtained with the different data sets considered here are consistent to a good approximation and allow us to produce a reference value of bolometric radial oscillation amplitude for the Sun observed as a star, and a reference bolometric power density spectrum for Solar granulation. Then (Sect. 5), we compute the response functions adapted to the CoRoT instrument for stars representative of potential solar-like pulsators on the Main Sequence in terms of effective temperatures, $\log g$ values and chemical compositions. We show that to a great extent, the dependency on $\log g$ and chemical composition can be neglected and that the CoRoT response functions can be conveniently described with good precision by analytic functions of T_{eff} .

2. Observational material and power density spectra

We consider four data sets obtained on the Sun with different techniques and different band pass by SOHO/VIRGO/PMO6 (essentially bolometric variations) and by SOHO/VIRGO/SPM (photon counting) in three narrow (5 nm) bands at 402 nm (blue), 500 nm (green) and 862 nm (red) (Frohlich et al. 1997). For each of these time series, we compute the power density spectrum shown in Figs. 1 and 2. Following the technique proposed by Kjeldsen et al. (2005) for stellar oscillation measurements, we smooth these spectra with a boxcar of width $405 \mu\text{Hz}$ corresponding to 3 times the solar large separation ($135 \mu\text{Hz}$).

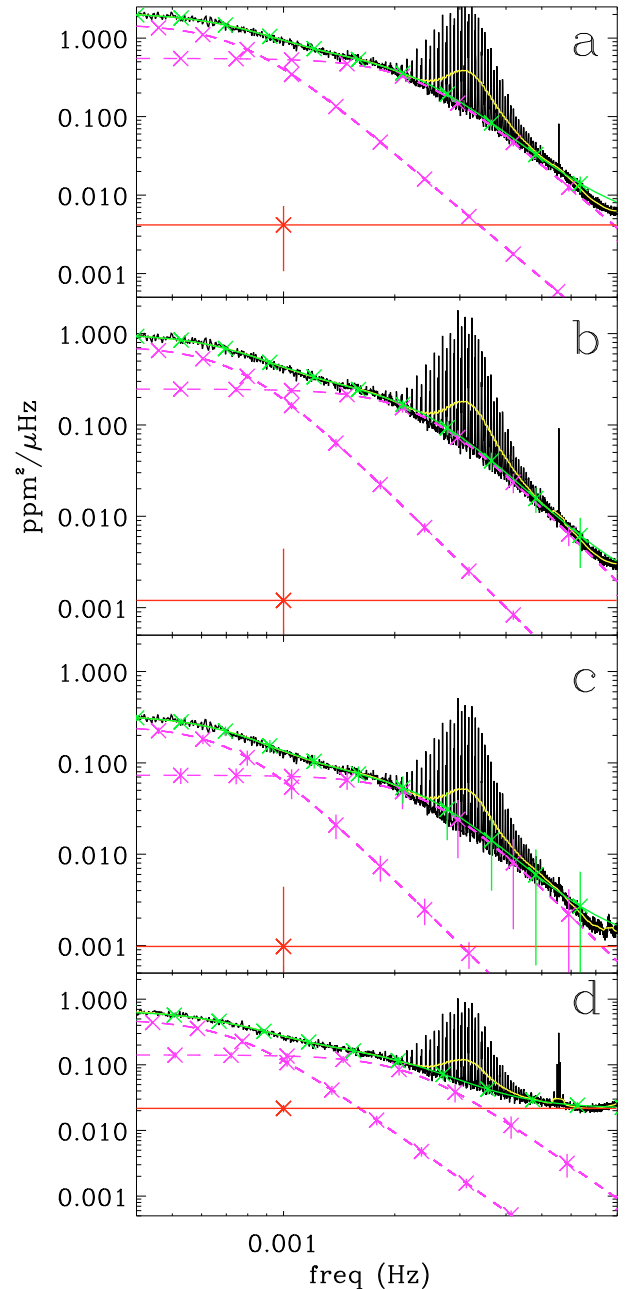


Fig. 2. Same as Fig. 1 for, from top to bottom: SPM-blue **a**), SPM-green **b**), SPM-red **c**) data over 700 days and PMO6 **d**) data over 800 days, but here we forced $C_i = 4$.

Then, we perform a least square fit of each spectrum with three components: a flat white noise contribution essentially due to photon counting noise, the solar background contribution detailed hereafter, and on top, the stellar oscillation spectrum contribution. For the solar background contribution, following Harvey (1985) and Andersen et al. (1998a), we consider a sum of powerlaws: $P(\nu) = \sum_i P_i(\nu)$, and $P_i(\nu) = a_i \zeta_i^2 \tau_i / (1 + (2\pi\tau_i\nu)^{C_i})$ (also noted $P_i(\nu) = A_i / (1 + (B_i\nu)^{C_i})$ for convenience hereafter), with ν the frequency, τ_i the characteristic time scale and C_i the slope at high frequency associated with each powerlaw, and a_i a normalizing factor such as $\zeta_i^2 = \int P_i(\nu) d\nu$ corresponding to the variance of the time series. Note that in the case of

Table 1. Fit with seven parameters. Values of the parameters are given as well as the associated one-sigma error estimates.

Data	A_1	B_1	A_2	B_2	D	C_1	C_2
	σ_{A1}	σ_{B1}	σ_{A2}	σ_{B2}	σ_D	σ_{C1}	σ_{C2}
	$\left(\frac{\text{ppm}^2}{\mu\text{Hz}}\right)$	(s)	$\left(\frac{\text{ppm}^2}{\mu\text{Hz}}\right)$	(s)	$\left(\frac{\text{ppm}^2}{\mu\text{Hz}}\right)$		
SPMb	1.46	1297	0.60	444	3×10^{-4}	4.2	3.7
	0.12	22	0.09	27	8.6×10^{-3}	0.4	0.5
SPMg	0.69	1300	0.28	438	4×10^{-4}	4.4	3.8
	0.10	41	0.07	50	8.3×10^{-3}	0.8	1.1
SPMr	0.23	1320	0.09	438	-2×10^{-4}	4.6	3.4
	0.10	117	0.08	185	1×10^{-2}	2.4	3.0
PMO6	0.54	1350	0.13	409	1.87×10^{-2}	3.6	3.8
	0.20	110	0.12	156	1.20×10^{-2}	1.6	3.0

Harvey (1985), C_i being set to 2, $a_i = 2$. This corresponds to a signal whose autocorrelation in time has a decreasing exponential behaviour. However, as mentioned by Harvey (1985), other values for the decay rate power over time might be found for different types of data probing the atmosphere at different heights (see e.g. Andersen et al. 1998a).

The physical processes most commonly considered in the solar background and represented by such power laws are: activity (predominant up to $\sim 10 \mu\text{Hz}$), supergranulation (up to $\sim 100 \mu\text{Hz}$), mesogranulation (up to $\sim 1 \text{ mHz}$), and granulation (see e.g. Andersen et al. 1998b; Anclin et al. 1998; Aigrain et al. 2004). In the present study, we will focus on the two latter processes showing significant contribution above $100 \mu\text{Hz}$, in the frequency domain where oscillations are found.

An estimate of the two first contributions (white noise and solar background) is obtained by a simultaneous fit of the spectrum outside the domain where the oscillation signal is seen with function $D + \sum_i P_i(\nu)$, where D represents the white noise contribution. After subtraction of these two components, we isolate the one due to stellar oscillations.

The two powerlaw components (7 parameters: A_i , B_i , C_i , and D) give a satisfactory fit of the background for our purpose and we do not find it necessary to include other components like supergranulation or activity.

As shown by error values in Table 1, the fit gives satisfactory results in the case of SPM data, especially for the blue and green channels. In the case of SPM/red channel, the coefficients are obtained with very large error bars and in the case of PMO6, the convergence precision is even worse, due to the larger white noise component. We note that these fits all suggest a value of C_i around 4, in agreement with the results obtained by Andersen et al. (1998a). We thus decided to fit again the previous function, but forcing the C_i coefficients to the value 4, thus reducing the number of free parameters to 5 and obtaining a more precise determination of them.

The results shown in Fig. 2 (see also Table 2) are very satisfactory, and we will refer to these values hereafter.

As could be expected, the level of the intensity components (A_1 and A_2) attributed to granulation and mesogranulation is very different in the measurements associated with different techniques and different bandpasses (see Fig. 3 top). The same is true for the contribution associated to the oscillations (Fig. 3 bottom), stressing the necessity to establish a reference independent of the instrument for the Sun oscillations and for comparison with other stars to be observed with other instruments.

Table 2. Fit with five parameters.

Data set	A_1	B_1	A_2	B_2	D
	σ_{A1}	σ_{B1}	σ_{A2}	σ_{B2}	σ_D
	$\left(\frac{\text{ppm}^2}{\mu\text{Hz}}\right)$	(s)	$\left(\frac{\text{ppm}^2}{\mu\text{Hz}}\right)$	(s)	$\left(\frac{\text{ppm}^2}{\mu\text{Hz}}\right)$
SPMb	1.52	1292	0.55	433	4×10^{-3}
	0.02	18	0.02	12	3×10^{-3}
SPMg	0.74	1302	0.25	419	1×10^{-3}
	0.02	37	0.02	27	3×10^{-3}
SPMr	0.26	1321	0.07	403	1×10^{-3}
	0.02	105	0.01	89	3×10^{-3}
PMO6	0.50	1349	0.14	439	20×10^{-3}
	0.02	55	0.02	42	3×10^{-3}

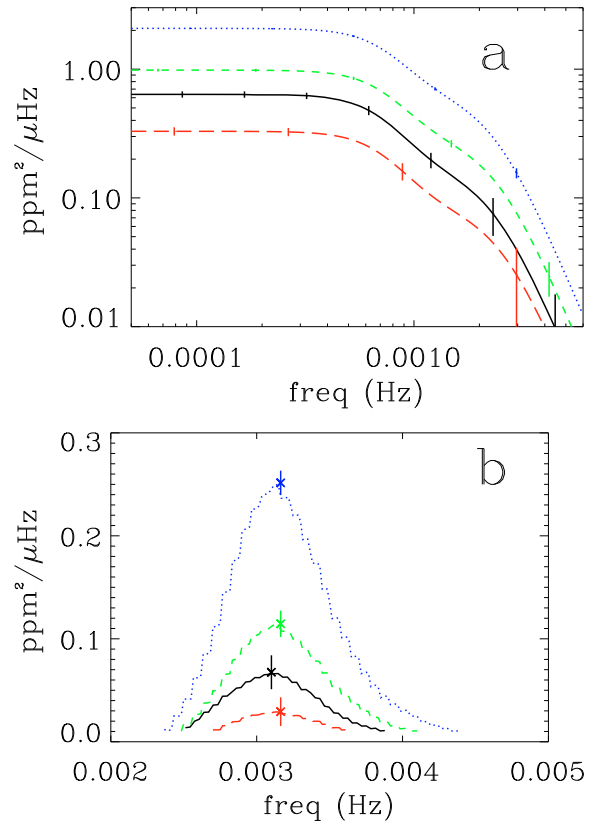


Fig. 3. a) Observational instrumental power density spectrum associated with the stellar background contribution and estimated as described in the text, for PMO6 data (plain black line), SPM-blue (dot [blue]), SPM-green (dash [green]), SPM-red (long dash [red]); b) same for the oscillation contribution.

3. Instrumental response functions

In this section we establish a relation between intensity variation observed with a given instrument (hereafter “instrumental flux variation”) and an intrinsic quantity defined as the “bolometric luminosity variation”. This relation features a response function characteristic of the instrument.

We derive the response function for an individual non-radial mode (Sect. 3.2), then for a smoothed power density spectrum (Sect. 3.3), and finally for the granulation (Sect. 3.4).

This is done taking into account both the band-width of the instrument, the spectral energy distribution of the given star (approximated by a black body law) and the dependence of the

stellar limb-darkening with the wavelength (given by stellar atmosphere models).

3.1. Instrumental flux variation and local temperature variation

Here, we express the relative instrumental flux variation $\delta I/\bar{I}$ as a function of the local relative variation of the temperature at the stellar photosphere $\delta T(\theta, \phi)/\bar{T}$.

First we define the relative variation of the instrumental flux I :

$$\left(\frac{\delta I}{\bar{I}}\right)(t) = \frac{\int_{\lambda} d\lambda E(\lambda) \delta F_{\lambda}}{\int_{\lambda} d\lambda E(\lambda) F_{\lambda}} \quad (1)$$

where $E(\lambda)$ is the global efficiency in terms of energy of the instrument at the wavelength λ , F_{λ} the flux received from the star at the wavelength λ and δF_{λ} its variation.

Then, following the approach of [Berthomieu & Provost \(1990\)](#), we show (see Appendix A) that F_{λ} and δF_{λ} can be approximated as

$$F_{\lambda} = 2\pi H_{\lambda} G_{\lambda} B_{\lambda} \quad (2)$$

where B_{λ} is the black body law evaluated at the photosphere, i.e. at $T = T_{\text{eff}}$ and where we have defined

$$H_{\lambda} \equiv 2 \left(\int_{-1}^1 d\mu g_{\lambda}(\mu) \right)^{-1} \quad (3)$$

and

$$G_{\lambda} \equiv \int_0^1 d\mu \mu g_{\lambda}(\mu). \quad (4)$$

with g_{λ} the limb-darkening function, $\mu = \cos(\theta)$ and θ and ϕ refer to the spherical coordinates for a z -axis pointing toward the observer (observer reference frame) and

$$\delta F_{\lambda} = H_{\lambda} \left(\frac{dB_{\lambda}}{d \ln T} \right) \int_0^{2\pi} d\phi \int_0^1 d\mu \mu g_{\lambda}(\mu) \left(\frac{\delta T}{\bar{T}} \right) \quad (5)$$

where T is the temperature, δT its variation, the meaning of other terms staying the same.

At this stage, we have expressed the instrumental flux relative variation $\delta I/\bar{I}$ as a function of $\delta T/\bar{T}$ the local (μ, ϕ) relative variation of the temperature at the photosphere.

3.2. Response function for an individual non-radial mode

Here, in the case of an individual oscillation mode, we show that we can relate $\delta T(\theta, \phi)/\bar{T}$ to a “bolometric luminosity relative variation” $(\delta L/\bar{L})_{\ell, m}$, defined as an extension of the specific case of radial modes where $(\delta L/\bar{L}) = 4\delta T_{\text{eff}}/\bar{T}_{\text{eff}}$.

As detailed in Appendix A, we consider the relative temperature fluctuations associated with a mode with degree ℓ and azimuthal order m :

$$\left(\frac{\delta T}{\bar{T}}\right)(t, \theta, \phi) = \Theta_{\ell, m}(t) Y_{\ell}^m(\theta', \phi') \quad (6)$$

where $\Theta_{\ell, m}(t)$ is the *intrinsic* and *instantaneous* mode amplitude in terms of temperature fluctuation, Y_{ℓ}^m is the spherical harmonic associated with the mode with degree ℓ and azimuthal order m , and (r, θ', ϕ') (resp. (r, θ, ϕ)) the spherical coordinate system in the pulsation frame (resp. in the observer frame). As discussed

in Appendix A, $(\delta T/\bar{T})$ and hence $\Theta_{\ell, m}(t)$ are evaluated at the photosphere.

For a radial mode, the *bolometric* and *intrinsic* luminosity fluctuation is related to the relative intrinsic temperature fluctuation as:

$$\left(\frac{\delta L}{\bar{L}}\right)_{\ell=0}(t) = 4 \left(\frac{\delta T_{\text{eff}}}{T_{\text{eff}}}\right)_0 = 4 \Theta_0(t) \quad (7)$$

where T_{eff} is the effective temperature and L the luminosity of the star. Then, by extension of the radial case, we define, in the general case, the *bolometric* and *intrinsic* mode amplitude in terms of luminosity:

$$\left(\frac{\delta L}{\bar{L}}\right)_{\ell, m}(t) \equiv 4 \Theta_{\ell, m}(t). \quad (8)$$

Note that, in the present case, since the mode excitation is a random process, we rather consider the rms quantities

$$\left(\frac{\delta L}{\bar{L}}\right)_{\ell, m}^{\text{rms}} \equiv \sqrt{\left(\frac{\delta L}{\bar{L}}\right)_{\ell, m}^2}(t) = 4 \sqrt{\Theta_{\ell, m}^2(t)}. \quad (9)$$

The rms label will however be generally omitted in the following for conciseness of the notation.

Then, we establish the relation between $(\delta I/\bar{I})_{\ell, m, i}$ (the observed relative intensity fluctuations due to a given mode (ℓ, m) , for a given inclination i) and the intrinsic mode amplitude:

$$\left(\frac{\delta I}{\bar{I}}\right)_{\ell, m, i} = R_{\ell, m, i} \Theta_{\ell, m} = \frac{R_{\ell, m, i}}{4} \left(\frac{\delta L}{\bar{L}}\right)_{\ell, m} \quad (10)$$

with $R_{\ell, m, i}$ the instrumental response function associated with the mode with degree ℓ and azimuthal order m and inclination i . The expression for $R_{\ell, m, i}$ is:

$$R_{\ell, m, i} \equiv \frac{\int_{\lambda} d\lambda E(\lambda) \frac{dB_{\lambda}}{d \ln T} S_{\ell, m, i}(\lambda)}{\int_{\lambda} d\lambda E(\lambda) B_{\lambda}} \quad (11)$$

where $S_{\ell, m, i}(\lambda)$ is the so-called “visibility” coefficient associated with the mode.

The visibility coefficient, $S_{\ell, m, i}$, measures the contribution of the mode integrated over the projected stellar surface, taking into account the effect of the limb-darkening (see e.g. [Dziembowski 1977](#); [Berthomieu & Provost 1990](#)). An expression for $S_{\ell, m, i}$ is given in Eq. (A.19). Note that in the case of radial modes, S_0 is independent of λ and $S_0 = 1$ by definition.

An interesting property of the visibility coefficients $S_{\ell, m, i}$ is that, assuming equipartition of energy among different modes of a same multiplet, the global visibility contribution of each multiplet (composed of modes of the same radial order n , same degree ℓ , and different azimuthal order m) is independent of the inclination i ([Dziembowski 1977](#); [Toutain & Gouttebroze 1993](#)). It is thus possible to compute a global visibility function $S_{\ell} = \sqrt{\sum_m S_{\ell, m, i}^2}$, which is independent of i for the different multiplets. This property will be useful in the next section.

3.3. Response function for smoothed oscillation power density spectrum

In the case of stellar observations, as remarked by [Kjeldsen et al. \(2005\)](#) the measurement of individual modes or even individual

multiplets might be delicate and it might give more precise results to estimate oscillation amplitudes from the smoothed oscillation power density contribution as represented in Sect. 1. In this case, as suggested by Kjeldsen et al. (2005), the oscillation power density contribution (P_{osc} , in $\text{ppm}^2/\mu\text{Hz}$) is smoothed over typically three or four times the large separation (Δ); then, once multiplied by the estimate of the large separation (in μHz), it is representative of P_n^I , the total power (in ppm^2) concentrated in all modes present in one large separation (of order n). Accordingly, we have

$$P_n^I \simeq 2 P_{\text{osc}} \Delta \quad (12)$$

where Δ is the large separation and the factor 2 multiplying P_{osc} is introduced to take into account the power density spread in the negative part of the spectrum.

Let define $P_{\ell,m,i}$ as the observed power (in ppm^2) associated with a mode (ℓ, m) , with inclination i . Assuming that $\Theta_{\ell,m}$ is the same for all the modes that are within the same separation and using Eq. (7), it can easily be shown that :

$$P_n^I = \sum_{\ell,m} P_{\ell,m}^I = R_{\text{osc}}^2 \overline{\Theta_0^2(t)} = \frac{R_{\text{osc}}^2}{16} \overline{\left(\frac{\delta L}{L}\right)_0^2(t)} \quad (13)$$

with

$$R_{\text{osc}} \equiv \sqrt{\sum_{\ell} R_{\ell}^2} \quad (14)$$

$$R_{\ell} \equiv \frac{\int_{\lambda} d\lambda E(\lambda) \frac{dB_{\lambda}}{d\ln T} S_{\ell}(\lambda)}{\int_{\lambda} d\lambda E(\lambda) B_{\lambda}} \quad (15)$$

and $\overline{\Theta_0^2(t)}$ (resp. $\overline{\left(\frac{\delta L}{L}\right)_0^2(t)}$) is the mean square value of $\Theta_0(t)$ (resp. $(\delta L/L)_0(t)$) for a radial mode. Note that in Eq. (13) the sum over (ℓ, m) is performed among all the multiplets within the same separation. The expression for the visibility coefficient S_{ℓ} is given by Eq. (A.22). The visibility factor associated with modes $\ell > 4$ can be neglected. Accordingly, Eq. (14) can be simplified as:

$$R_{\text{osc}} = \sqrt{R_0^2 + R_1^2 + R_2^2 + R_3^2}. \quad (16)$$

In practice, we consider P_{osc} , the smoothed power density component associated with oscillations derived from observations, as in Sect. 1. Using Eqs. (12), 13 and (9), one obtains the (rms) bolometric amplitude normalised to radial mode given by

$$A_{\text{bol},\ell=0} \equiv \left(\frac{\delta L}{L}\right)_0^{\text{rms}} = \frac{4}{R_{\text{osc}}} \sqrt{2 P_{\text{osc}} \Delta} \quad (17)$$

where R_{osc} is the response function given by Eq. (16) and computed for each data set using Eqs. (15) and (A.22).

In the present work, the $S_{\ell}(\lambda)$ coefficients (Eq. (A.22)) are computed taking into account monochromatic specific intensities derived from stellar atmosphere models (see Barban et al. 2003) with relevant T_{eff} , $[\text{Fe}/\text{H}]$, and $\log g$.

3.4. Response function for granulation

As detailed in Appendix A, since we are interested in rms values with time and assuming that these values are identical all over the stellar surface, the granulation component can be treated in a similar way as a radial mode. Accordingly, the relation between

Table 3. Response functions for different sets of solar data.

Resp. Func.	SPM _b	SPM _g	SPM _r	PMO6
$R_{\text{osc}}(T_{\text{eff,Sun}})$	11.63	9.02	5.26	7.15
$R_g(T_{\text{eff,Sun}})$	6.24	5.02	3.06	4.00

the observed relative intensity fluctuations and the associated intrinsic fluctuations is

$$\left(\frac{\delta I}{I}\right)_g(t) = R_g \Theta_g(t) = \frac{R_g}{4} \left(\frac{\delta L}{L}\right)_g(t) \quad (18)$$

where the quantities have the same meaning as previously for radial modes but subscript g refers to the granulation and

$$R_g = R_{\ell=0,m=0} = \frac{\int_{\lambda} d\lambda E(\lambda) \frac{dB_{\lambda}}{d\ln T}}{\int_{\lambda} d\lambda E(\lambda) B_{\lambda}}. \quad (19)$$

As for the radial modes, we define the rms and intrinsic relative luminosity fluctuation due to granulation as the quantity

$$\left(\frac{\delta L}{L}\right)_g^{\text{rms}} \equiv \sqrt{\overline{\left(\frac{\delta L}{L}\right)_g^2(t)}} = 4 \sqrt{\overline{\Theta_g^2(t)}} = \frac{4}{R_g} \left(\frac{\delta I}{I}\right)_g^{\text{rms}}(t). \quad (20)$$

If we consider the power density contribution associated with granulation (P_g) determined in Sect. 1, we can derive the corresponding bolometric power density spectrum according to

$$P_{g,\text{bol}} = 16 P_g / R_g^2 \quad (21)$$

which is expected to characterize granulation independently of the instrument considered. The application to the different data sets obtained on the Sun (R_g values are given in Table 3) with different instrumental techniques and with different bandpasses shows a good agreement (see Sect. 4).

4. Results for different data sets

4.1. A reference solar bolometric oscillation amplitude

The resulting estimates of the bolometric amplitude per radial mode are shown in Fig. 4 (R_{osc} values computed for the different data sets considered here are given in Table 3). We compare the curves obtained for each data set, with special attention to the value at maximum often taken as a convenient characteristic measurement of the oscillations amplitudes in stars (see also Table 4). Although some residuals of the initial difference seem to subsist (suggesting that our response function might be refined further), we notice a reasonable agreement of the different curves, within one-sigma error bar estimates. This allows us to propose as a reference for the Sun a 2.53 ± 0.11 ppm of maximum bolometric amplitude per radial mode (mean of the four values weighted by $1/\sigma_i$). We checked that this result was not affected significantly by changing the smoothing boxcar width from 2 times to 4 times Δ .

4.2. A reference bolometric granulation power density spectrum

The different mean profiles of bolometric background power density spectra are shown in Fig. 5. Here again, we notice the good agreement of the different curves. Coefficients characterizing the different curves are given in Table 4 as well as reference values proposed for the Sun background contribution. Here again, the influence of the size of the smoothing boxcar (between 0.1 to 4 times Δ) has been tested and found negligible within the present error bars.

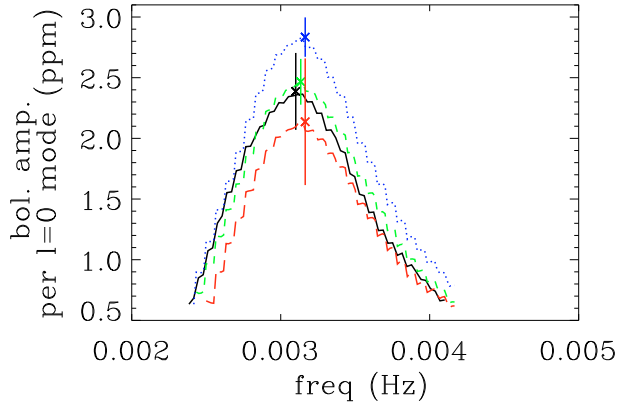


Fig. 4. Observational bolometric amplitude per radial mode estimated as described in the text, for PMO6 data (plain black line), SPM-blue (dot [blue]), SPM-green (dash [green]), SPM-red (long dash [red]). Error bars are given for the estimate of the maximum (boxcar: 3 times Large Separation taken as 135 μ Hz).

Table 4. Bolometric parameters. The last line corresponds to reference values resulting from a mean of the values given in the other lines, weighted by $1/\sigma_i$.

Data	$A_{1,\text{bol}}$	ζ_1	τ_1	$A_{2,\text{bol}}$	ζ_2	τ_2	$A_{\text{bol},\ell=0}$
set	$\sigma_{A_{1,\text{bol}}}$ ($\frac{\text{ppm}^2}{\mu\text{Hz}}$)	σ_{ζ_1}	σ_{τ_1} (s)	$\sigma_{A_{2,\text{bol}}}$ ($\frac{\text{ppm}^2}{\mu\text{Hz}}$)	σ_{ζ_2}	σ_{τ_2} (s)	$\sigma_{A_{\text{bol},\ell=0}}$ (ppm)
SPMb	0.62	8.2×10^{-3}	206	0.23	8.5×10^{-3}	69	2.83
	0.01	1.0×10^{-4}	3	0.01	2.0×10^{-4}	2	0.16
SPMg	0.47	7.1×10^{-3}	207	0.16	7.2×10^{-3}	67	2.47
	0.01	1.0×10^{-4}	6	0.01	3.0×10^{-4}	4	0.19
SPMr	0.44	6.8×10^{-3}	210	0.13	6.6×10^{-3}	64	2.14
	0.03	4.0×10^{-4}	17	0.02	1.0×10^{-3}	14	0.52
PMO6	0.50	7.2×10^{-3}	215	0.14	6.7×10^{-3}	70	2.36
	0.02	2.0×10^{-4}	9	0.02	5.0×10^{-4}	7	0.23
Ref.	0.52	7.6×10^{-3}	208	0.18	7.6×10^{-3}	68	2.53
	0.01	1.0×10^{-4}	3	0.01	2.0×10^{-4}	2	0.11

5. Response functions of CoRoT for objects on the Main Sequence

Stellar atmosphere models are computed with the Atlas 9 code (Kurucz 1993) in a modified version including the CGM convection (see Heiter et al. 2002). Considering the CoRoT total efficiency shown in Fig. 6, we compute the CoRoT response functions for stellar atmosphere models characterized by different values of T_{eff} , $\log g$ and chemical compositions illustrative of possible solar-like candidates on the Main Sequence ($-1 < [\text{Fe}/\text{H}] < +1$, $3.9 < \log g < 4.5$, $5800 < T_{\text{eff}} < 6750$ K).

As shown in Fig. 7, the dependency of the CoRoT response function R_{osc} on $\log g$ and chemical composition is small in the considered range. To a great extent (within 0.6%), it can be neglected and R_{osc} as R_g can be described as simple polynomial functions of T_{eff} only:

$$R_{\text{osc}}(T_{\text{eff}}) = R_{\text{osc}}(T_{\text{eff},\text{Sun}}) + A(T_{\text{eff}} - T_{\text{eff},\text{Sun}}) + B(T_{\text{eff}} - T_{\text{eff},\text{Sun}})^2.$$

We proceed in the same way for R_g .

Values of the parameters obtained for the fit are given in Table 5.

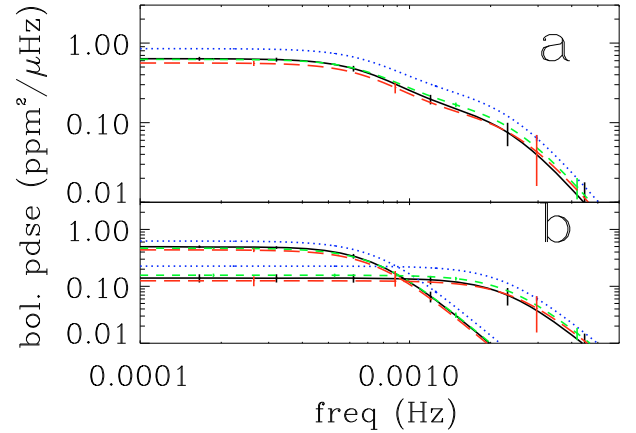


Fig. 5. Observational bolometric power density spectrum estimated as described in the text, for PMO6 data (plain black line), SPM-blue (dot [blue]), SPM-green (dash [green]), SPM-red (long dash [red]). **a**): granulation+ mesogranulation components; **b**): granulation and mesogranulation individual components.

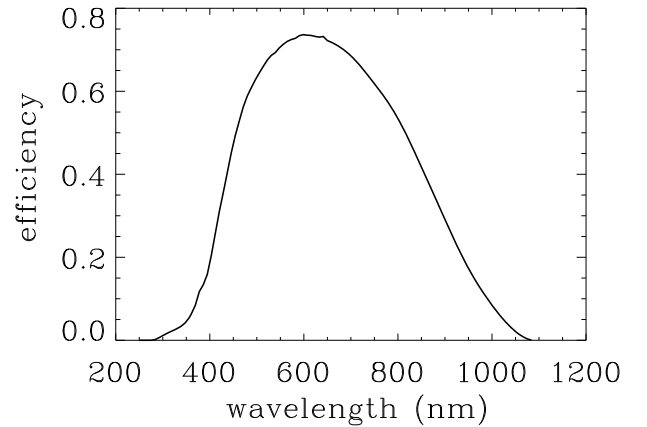


Fig. 6. CoRoT total efficiency.

6. Conclusions

Measurement of stellar oscillations or granulation provides instrumental values which depend on the instrumental technique and bandpass and on the star considered. In this work, with the purpose of helping future comparisons between stars observed in photometry,

1. We propose a simple expression for response functions connecting specific instrumental photometric measurements with intrinsic bolometric values for oscillation amplitudes and granulation power density.
2. We test and validate this expression on four sets of data obtained on the Sun, in four different bandpasses and with two different instrumental techniques.
3. We establish reference bolometric measurements for the Solar oscillation amplitudes (2.53 ± 0.11 ppm) and for the Solar granulation power density.
4. We compute the response functions for the CoRoT instrument and give an analytic expression for it.

Acknowledgements. SOHO is a mission of international collaboration between ESA and NASA.

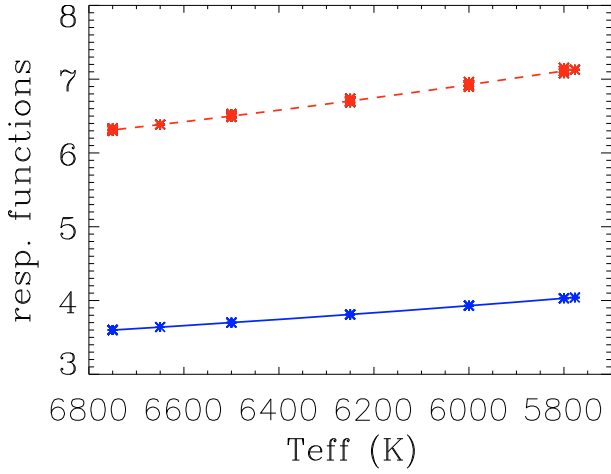


Fig. 7. Polynomial fit of the CoRoT response function R_{osc} (dash [red]) and R_g (plain [blue]) for different stellar atmosphere models mentioned in the text.

Table 5. Fit of CoRoT response functions.

Resp. Func.	$R(T_{\text{eff,Sun}})$ $\sigma_{R(T_{\text{eff,Sun}})}$	$A(K^{-1})$ σ_A	$B(K^{-2})$ σ_B	χ^2
$R_{\text{osc}}(T_{\text{eff}})$	7.134 9×10^{-3}	-96.8×10^{-5} 4.4×10^{-5}	13×10^{-8} 4×10^{-8}	8×10^{-3}
$R_g(T_{\text{eff}})$	4.0420 4×10^{-4}	-523×10^{-6} 2×10^{-6}	71×10^{-9} 2×10^{-9}	1.3×10^{-5}

Appendix A: Derivation of the instrumental response functions

Here we derive the relation between the *observed* flux fluctuation and the *intrinsic* temperature fluctuations induced by the presence of non-radial modes or granulation on the surface of the star. We proceed in the manner of Berthomieu & Provost (1990). We summarize the main steps and emphasize the approximations that we adopt in the present study. The flux, F_λ , received from the star at the wavelength λ is given by (see Berthomieu & Provost 1990):

$$F_\lambda = \int_{\mathcal{A}} d\mathcal{A} I_\lambda(\tau = 0, \mu) \quad (\text{A.1})$$

where \mathcal{A} is the total observed surface, $d\mathcal{A} = d\mathbf{A} \cdot \mathbf{n}$ the elementary observed surface around the direction of the observer, \mathbf{n} a unit vector in the direction of the observer, $d\mathbf{A}$ the differential surface element perpendicular to the stellar surface, τ the optical depth, $\mu = \cos(\theta)$, and $I_\lambda(\mu)$ the specific intensity at the wavelength λ . We adopt a spherical coordinate system with the z -axis pointing toward the observer. The specific intensity is assumed to be invariant with respect to any rotation along the z -axis; this is why here I_λ depends only on μ . Note that the integral of Eq. (A.1) is evaluated at the optical depth $\tau = 0$.

We define the limb-darkening function, g_λ , as

$$g_\lambda \equiv \frac{I_\lambda(\mu)}{I_\lambda(1)} \quad (\text{A.2})$$

where $I_\lambda(1) \equiv I_\lambda(\mu = 1)$. Finally, we define the mean intensity as the quantity

$$J_\lambda \equiv \frac{1}{4\pi} \int d\Omega I_\lambda(\mu) \quad (\text{A.3})$$

where $d\Omega$ is the elementary solid angle. Using Eqs. (A.2) and (A.3) we then derive the relation:

$$J_\lambda = I_\lambda(1)/H_\lambda \quad (\text{A.4})$$

where we have defined

$$H_\lambda \equiv 2 \left(\int_{-1}^1 d\mu g_\lambda(\mu) \right)^{-1}. \quad (\text{A.5})$$

According to Eqs. (A.1), (A.2) and (A.4), a small variation of F_λ is given by

$$\delta F_\lambda = \int_{\mathcal{A}} d\mathcal{A} \left(\bar{g}_\lambda \bar{H}_\lambda \delta J_\lambda + \bar{J}_\lambda \bar{H}_\lambda \delta g_\lambda + \bar{J}_\lambda \bar{g}_\lambda \delta H_\lambda \right) + \delta(d\mathcal{A}) \bar{J}_\lambda \bar{g}_\lambda \quad (\text{A.6})$$

where $\bar{(\)}$ refers to the equilibrium quantity. The first term on the RHS of Eq. (A.6) corresponds to the perturbations of the mean intensity evaluated at an effective optical depth $\tau = \tau_0$ in the atmosphere. This effective optical depth corresponds to the layer that contributes predominantly to the variation of the emergent flux (see Berthomieu & Provost 1990). As in Berthomieu & Provost (1990), we assume that g_λ and hence H_λ do not depend on τ_0 and are evaluated at $\tau = 0$.

The three last terms in RHS of Eq. (A.6) are the perturbation of the limb-darkening function and the surface distortion (for details see Berthomieu & Provost 1990). All these perturbations are shown to have a negligible contribution to δF_λ compared to that of δJ_λ . Accordingly, Eq. (A.6) can be simplified as:

$$\delta F_\lambda = \int_0^{2\pi} d\phi \int_0^1 d\mu \mu g_\lambda(\mu) H_\lambda \delta J_\lambda, \quad (\text{A.7})$$

where we have dropped $\bar{(\)}$ from g_λ and H_λ .

We place ourself in Local Thermodynamic Equilibrium and assume adiabatic perturbations for linearisation, accordingly $\delta J_\lambda = \delta B_\lambda$ where B_λ is the black body law whose expression is

$$B_\lambda = \frac{2hc^2}{\lambda^5} \frac{1}{e^{hc/\lambda kT} - 1} \quad (\text{A.8})$$

where T is the local temperature, c the speed of the light, h Planck's constant, and k Boltzmann's constant.

The local variation of B_λ is induced by a local variation of T . Assuming small perturbations, we have

$$\delta J_\lambda = \delta B_\lambda = \left(\frac{dB_\lambda}{d \ln T} \right) \left(\frac{\delta T}{T} \right) (\tau_0, t, \theta, \phi). \quad (\text{A.9})$$

Using Eqs. (A.9) and (A.15), Eq. (A.7) can then be written as:

$$\delta F_\lambda = H_\lambda \left(\frac{dB_\lambda}{d \ln T} \right) \int_0^{2\pi} d\phi \int_0^1 d\mu \mu g_\lambda(\mu) \left(\frac{\delta T}{T} \right). \quad (\text{A.10})$$

Finally, we approximate Eq. (A.1) as

$$F_\lambda = 2\pi H_\lambda G_\lambda B_\lambda, \quad (\text{A.11})$$

where B_λ is evaluated at the photosphere, i.e. at $T = T_{\text{eff}}$ and where we have defined

$$G_\lambda \equiv \int_0^1 d\mu \mu g_\lambda(\mu). \quad (\text{A.12})$$

The relative variation of the total flux I received by the instrument is finally given by

$$\left(\frac{\delta I}{I} \right) (t) = \frac{\int_\lambda d\lambda E(\lambda) \delta F_\lambda}{\int_\lambda d\lambda E(\lambda) F_\lambda} \quad (\text{A.13})$$

where $E(\lambda)$ is the global efficiency in terms of energy of the instrument at a given wavelength. The function $E(\lambda)$ is normalised as

$$\int_0^{+\infty} d\lambda E(\lambda) = 1. \quad (\text{A.14})$$

A.1. Non-radial oscillations

In the case of a non-radial spheroidal mode, $\delta T/T$ is by definition:

$$\left(\frac{\delta T}{T}\right)(\tau_0, t, \theta, \phi) = \Theta_\ell(t, \tau_0) Y_\ell^m(\theta', \phi') \quad (\text{A.15})$$

where $\Theta_\ell(t, \tau_0)$ is the *intrinsic* and *instantaneous* mode amplitude in terms of temperature fluctuation, Y_ℓ^m is the spherical harmonic associated with the mode with a degree ℓ and azimuthal order m , and (r, θ', ϕ') the spherical coordinate system in the pulsation frame. The pulsation frame is chosen such that its polar axis coincides with the star rotation axis. The spherical harmonic, Y_ℓ^m , is normalized here as:

$$\int d\Omega' \|Y_\ell^m(\theta', \phi')\|^2 = 4\pi \quad (\text{A.16})$$

where Ω' is the elementary solid angle associated with the pulsation coordinate system. Note that for low ℓ degree, $\Theta_\ell(t, \tau_0)$ is expected to negligibly depend on ℓ (Belkacem et al. 2008).

As shown by Berthomieu & Provost (1990), for low ℓ degree, τ_0 marginally depends on ℓ . Furthermore, they show that – in the Sun – the optical depth τ_0 is very close to the photosphere, which by definition corresponds to the layer $T = T_{\text{eff}}$ and $\tau = 2/3$. Then, from here, we will assume that τ_0 coincides with the photosphere ($\tau = 2/3$).

Using Eqs. (A.10), (A.11), (A.13), (A.12), and (A.15), we then derive the flux variation due to the mode:

$$\left(\frac{\delta I}{I}\right)(t) = R_{\ell,m,i} \Theta_\ell(t) \quad (\text{A.17})$$

with

$$R_{\ell,m,i} \equiv \frac{\int_\lambda d\lambda E(\lambda) \frac{dB_\lambda}{d \ln T} G_\lambda H_\lambda S_{\ell,m,i}(\lambda)}{\int_\lambda d\lambda E(\lambda) B_\lambda G_\lambda H_\lambda} \quad (\text{A.18})$$

where we have defined the “visibility” coefficient, $S_{\ell,m,i}$, as the quantity:

$$S_{\ell,m,i}(\lambda) \equiv \frac{\int_0^{2\pi} d\phi \int_0^1 d\mu \mu g_\lambda(\mu) Y_\ell^m(\theta', \phi')}{2\pi \int_0^1 d\mu \mu g_\lambda(\mu)}. \quad (\text{A.19})$$

Note that, from the definition of $S_{\ell,m,i}$, we have for a radial mode $S_0 = 1$.

By using stellar atmosphere models, we find that – in the domain of T_{eff} and gravity we are interested here – $G_\lambda H_\lambda$ varies slowly with λ compared to B_λ and $dB_\lambda/d \ln T$. Accordingly, Eq. (A.18) can be simplified as:

$$R_{\ell,m,i} \equiv \frac{\int_\lambda d\lambda E(\lambda) \frac{dB_\lambda}{d \ln T} S_{\ell,m,i}(\lambda)}{\int_\lambda d\lambda E(\lambda) B_\lambda}. \quad (\text{A.20})$$

Following Dziembowski (1977), we can decompose $S_{\ell,m,i}(\lambda)$ as:

$$S_{\ell,m,i} = q_{\ell,m}(i) S_\ell \quad (\text{A.21})$$

with

$$S_\ell(\lambda) = \frac{\int_0^1 d\mu \mu g_\lambda(\mu) Y_\ell^0(\mu)}{\int_0^1 d\mu \mu g_\lambda(\mu)} \quad (\text{A.22})$$

$$q_{\ell,m}(i) = \sqrt{\frac{(l-m)!}{(l+m)!}} |P_\ell^m| \cos(i) \quad (\text{A.23})$$

where i is the angle between the observer and the rotation axis and P_ℓ^m the associated Legendre function.

The bolometric flux variation, $(\delta I/\bar{I})^{\text{bol}}$, is obtained from Eq. (A.17) by assuming in Eq. (A.20) a constant $E(\lambda)$, this gives

$$\left(\frac{\delta I}{\bar{I}}\right)^{\text{bol}}(t) = R_{\ell,m,i}^{\text{bol}} \Theta_\ell(t) \quad (\text{A.24})$$

with

$$R_{\ell,m,i}^{\text{bol}} \equiv \frac{\pi}{\sigma T_{\text{eff}}^4} \int_\lambda d\lambda \frac{dB_\lambda}{d \ln T} S_{\ell,m,i}(\lambda). \quad (\text{A.25})$$

For a radial mode, $S_{0,0} = 1$ and $R_{\text{bol},0,0} = 4$. We have then for a radial mode:

$$\left(\frac{\delta I}{\bar{I}}\right)^{\text{bol}}(t) = 4 \Theta_0(t). \quad (\text{A.26})$$

By definition of the effective temperature (T_{eff}) and the stellar radius R_* , the total luminosity of the star, L , is given by Steffan’s law:

$$L = 4\pi \sigma T_{\text{eff}}^4 R_*^2 \quad (\text{A.27})$$

where σ is Steffan’s constant. Variation of the stellar radius due to the mode can be neglected. Accordingly, the relative variation of L due to a radial mode is given by the relation

$$\left(\frac{\delta L}{L}\right) = 4 \left(\frac{\delta T_{\text{eff}}}{T_{\text{eff}}}\right). \quad (\text{A.28})$$

We have again for a radial mode:

$$\left(\frac{\delta I}{\bar{I}}\right)^{\text{bol}} = \left(\frac{\delta L}{L}\right) \quad (\text{A.29})$$

Then, according to Eqs. (A.26) and (A.28), we have

$$\left(\frac{\delta T_{\text{eff}}}{T_{\text{eff}}}\right) = \Theta_0. \quad (\text{A.30})$$

Thus, for a radial mode, Θ_0 (resp. $(\delta I/\bar{I})^{\text{bol}}$) is then directly related to a variation of T_{eff} (resp. L). On the other hand, for a *non-radial* mode, $(\delta I/\bar{I})^{\text{bol}}$ is related to the intrinsic mode amplitude in terms of temperature, Θ_ℓ , through the coefficient given by Eq. (A.25) that depends on the mode geometry and the limb-darkening law. However, by extension of the radial case, we define, in the general case, the *bolometric* and *intrinsic* mode amplitude in terms of luminosity as the quantity:

$$\left(\frac{\delta L}{L}\right)_\ell \equiv 4 \Theta_\ell. \quad (\text{A.31})$$

Now, according to Eqs. (A.17) and (A.31), we can write:

$$\left(\frac{\delta I}{\bar{I}}\right)(t) = R_{\ell,m,i} \Theta_\ell = \frac{R_{\ell,m,i}}{4} \left(\frac{\delta L}{L}\right)_\ell. \quad (\text{A.32})$$

Eq. (A.32) then relates the observed intensity fluctuations to the bolometric and intrinsic mode amplitude in terms of luminosity.

A.2. Granulation

We define $(\delta T/T)_g = \Theta_g(t, \mu, \phi)$ as the relative temperature perturbation due to the granulation at the instant t and the position (θ, ϕ) .

As for the mode, we derive the flux perturbation, $\delta I_{g,\lambda}$, due to the granulation:

$$\left(\frac{\delta I}{\bar{I}}\right)_g(t) = \frac{\int_{\lambda} d\lambda E(\lambda) \delta F_{g,\lambda}}{\int_{\lambda} d\lambda E(\lambda) F_{\lambda}} \quad (\text{A.33})$$

with

$$\delta F_{g,\lambda} = \left(\frac{dB_{\lambda}}{d \ln T}\right) \int_0^{2\pi} d\phi \int_0^1 d\mu \mu g_{\lambda}(\mu) \Theta_g(t, \mu, \phi). \quad (\text{A.34})$$

To go further, one needs to know how temperature fluctuations due to the granules are distributed along the star surface. We note that we are only interested in the time averaged intensity fluctuations. As a simplification, we assume that distribution of the temperature fluctuations is – in time average – homogeneous. Accordingly, we can ignore the dependence of Θ_g with (μ, ϕ) . This is formally equivalent to assuming in Eq. (A.15) that $Y_{\ell}^m = 1$, as for a radial mode $((\ell, m) = (0, 0))$. Then, the expression for $(\delta I/\bar{I})_g$ is derived from Eqs. (A.32) and (A.20) by assuming $(\ell, m) = (0, 0)$. Accordingly, $\delta(I/\bar{I})_g$ can be written as

$$\left(\frac{\delta I}{\bar{I}}\right)_g(t) = R_g \Theta_g(t) = \frac{R_g}{4} \left(\frac{\delta L}{\bar{L}}\right)_g(t) \quad (\text{A.35})$$

with

$$R_g = R_{\ell=0, m=0} = \frac{\int_{\lambda} d\lambda E(\lambda) \frac{dB_{\lambda}}{d \ln T}}{\int_{\lambda} d\lambda E(\lambda), B_{\lambda}} \quad (\text{A.36})$$

$$\left(\frac{\delta L}{\bar{L}}\right)_g = 4 \Theta_g. \quad (\text{A.37})$$

As for the radial modes, $(\delta L/\bar{L})_g$ represents the bolometric and intrinsic luminosity variation due to the granulation.

References

- Aigrain, S., Favata, F., & Gilmore, G. 2004, *A&A*, 414, 1139
- Andersen, B., Appourchaux, T., & Crommelynck, D. 1998a, in *Sounding solar and stellar interiors*, ed. Provost, & F. Schieder, 181, 147
- Andersen, B., Leifsen, T., Appourchaux, T., et al. 1998b, in *Structure and Dynamics of the Interior of the Sun and Sun-like Stars*, ed. S. Korzenik, ESA SP, 418, 83
- Anklin, M., Frohlich, C., Wehrli, C., & Finsterle, W. 1998, in *Structure and Dynamics of the Interior of the Sun and Sun-like Stars*, ed. S. Korzenik, ESA SP, 418, 91
- Baglin, A., Michel, E., Auvergne, M., & The COROT Team. 2006, in *Proceedings of SOHO 18/GONG 2006/HELAS I, Beyond the spherical SunESA*, Special Publication, 624,
- Barban, C., Goupil, M. J., Van't Veer-Menneret, C., et al. 2003, *A&A*, 405, 1095
- Baudin, F., Samadi, R., Appourchaux, T., & Michel, E. 2007, *ArXiv e-prints*, 710
- Bedding, T. R., & Kjeldsen, H. 2007, in *Unsolved Problems in Stellar Physics: A Conference in Honor of Douglas Gough*, ed. R. J. Stancilffe, J. Dewi, G. Houdek, R. G. Martin, & C. A. Tout, *Amer. Inst. Phys. Conf. Ser.*, 948, 117
- Belkacem, K., Samadi, R., Goupil, M.-J., & Dupret, M.-A. 2008, *A&A*, 478, 163
- Berthomieu, G., & Provost, J. 1990, *A&A*, 227, 563
- Dziembowski, W. 1977, *Acta Astron.*, 27, 203
- Frohlich, C., Andersen, B. N., Appourchaux, T., et al. 1997, *Sol. Phys.*, 170, 1
- Harvey, J. 1985, in *Future Missions in Solar, Heliospheric, & Space Plasma Physics*, ed. E. Rolfe, & B. Battrock, ESA SP, 235, 199
- Heiter, U., Kupka, F., van't Veer-Menneret, C., et al. 2002, *A&A*, 392, 619
- Kjeldsen, H., Bedding, T. R., Butler, R. P., et al. 2005, *ApJ*, 635, 1281
- Kjeldsen, H., Bedding, T. R., Arentoft, T., et al. 2008, *ArXiv e-prints*, 804
- Kurucz, R. L. 1993, *SYNTHE spectrum synthesis programs and line data (Kurucz CD-ROM, Cambridge, MA: Smithsonian Astrophysical Observatory)*
- Ludwig, H.-G. 2006, *A&A*, 445, 661
- Samadi, R., Belkacem, K., Goupil, M.-J., Kupka, F., & Dupret, M.-A. 2007a, in *IAU Symposium*, ed. F. Kupka, I. Roxburgh, & K. Chan, 239, 349
- Samadi, R., Georgobiani, D., Trampedach, R., et al. 2007b, *A&A*, 463, 297
- Toutain, T., & Gouttebroze, P. 1993, *A&A*, 268, 309
- Trampedach, R., Christensen-Dalsgaard, J., Nordlund, A., & Stein, R. F. 1998, in *The First MONS Workshop: Science with a Small Space Telescope*, held in Aarhus, Denmark, June 29–30, ed. H. Kjeldsen, T. R. Bedding, Aarhus Universitet, 59

The CoRoT^{*} target HD 49933

I. Effect of the metal abundance on the mode excitation rates

R. Samadi¹, H.-G. Ludwig², K. Belkacem^{1,3}, M. J. Goupil¹, and M.-A. Dupret^{1,3}

¹ Observatoire de Paris, LESIA, CNRS UMR 8109, Université Pierre et Marie Curie, Université Denis Diderot, 5 pl. J. Janssen, 92195 Meudon, France
e-mail: Reza.Samadi@obspm.fr

² Observatoire de Paris, GEPI, CNRS UMR 8111, 5 pl. J. Janssen, 92195 Meudon, France

³ Institut d'Astrophysique et de Géophysique de l'Université de Liège, Allée du 6 Août 17, 4000 Liège, Belgium

Received 17 February 2009 / Accepted 27 October 2009

ABSTRACT

Context. Solar-like oscillations are stochastically excited by turbulent convection at the surface layers of the stars.

Aims. We study the role of the surface metal abundance on the efficiency of the stochastic driving in the case of the CoRoT target HD 49933.

Methods. We compute two 3D hydrodynamical simulations representative – in effective temperature and gravity – of the surface layers of the CoRoT target HD 49933, a star that is rather metal poor and significantly hotter than the Sun. One 3D simulation has a solar metal abundance, and the other has a surface iron-to-hydrogen, [Fe/H], abundance ten times smaller. For each 3D simulation we match an associated global 1D model, and we compute the associated acoustic modes using a theoretical model of stochastic excitation validated in the case of the Sun and α Cen A.

Results. The rate at which energy is supplied per unit time into the acoustic modes associated with the 3D simulation with [Fe/H] = -1 is found to be about three times smaller than those associated with the 3D simulation with [Fe/H] = 0. As shown here, these differences are related to the fact that low metallicity implies surface layers with a higher mean density. In turn, a higher mean density favors smaller convective velocities and hence less efficient driving of the acoustic modes.

Conclusions. Our result shows the importance of taking the surface metal abundance into account in the modeling of the mode driving by turbulent convection. A comparison with observational data is presented in a companion paper using seismic data obtained for the CoRoT target HD 49933.

Key words. convection – turbulence – stars: oscillations – stars: individual: HD 49933 – Sun: helioseismology

1. Introduction

Using the measured linewidths and the amplitudes of the solar acoustic modes, it has been possible to infer the rate at which energy is supplied per unit time into the solar acoustic modes. Using these constraints, different models of mode excitation by turbulent convection have been extensively tested in the case of the Sun (see e.g. recent reviews by Samadi et al. 2008b; and Houdek 2006). Among the different approaches, we can distinguish pure theoretical approaches (e.g. Samadi & Goupil 2001; Chaplin et al. 2005), semi-analytical approaches (e.g. Samadi et al. 2003b,a) and pure numerical approaches (e.g. Nordlund & Stein 2001; Stein et al. 2004; Jacoutot et al. 2008). The advantage of a theoretical approach is that it easily allows massive computation of the mode excitation rates for a wide variety of stars with different fundamental parameters (e.g. effective temperature, gravity) and different surface metal abundance. However, pure theoretical approaches are based on crude or simplified descriptions of turbulent convection. On the other hand, a semi-analytical approach is generally more realistic since the quantities related to turbulent convection are obtained from 3D hydrodynamical simulation. 3D hydrodynamical simulations are

at this point in time too time consuming, so that a fine grid of 3D models with a sufficient resolution in effective temperature (T_{eff}), gravity ($\log g$) and surface metal abundance (Z) is not yet available. In the present paper, we study and provide a procedure to interpolate for any value of Z the mode excitation rates \mathcal{P} between two 3D simulations with different Z but the same T_{eff} and $\log g$. With such interpolation procedure it is no longer required to have at our disposal a fine grid in Z of 3D simulations.

The semi-analytical mode that we consider here is based on Samadi & Goupil (2001)'s theoretical model with the improvements proposed by Belkacem et al. (2006a). This semi-analytical model satisfactorily reproduces the solar seismic data (Samadi et al. 2003a; Belkacem et al. 2006b). Recently, the seismic constraints obtained for α Cen A (HD 128620) have provided an additional validation of the basic physical assumptions of this theoretical model (Samadi et al. 2008a). The star α Cen A has a surface gravity ($\log g = 4.305$) lower than that of the Sun ($\log g_{\odot} = 4.438$), but its effective temperature ($T_{\text{eff}} = 5810$ K) does not significantly differ from that of the Sun ($T_{\text{eff},\odot} = 5780$ K). The higher T_{eff} , the more vigorous the convective velocity at the surface and the stronger the driving by turbulent convection (see e.g. Houdek et al. 1999). For main sequence stars with a mass $M \lesssim 1.6 M_{\odot}$, an increase of the convective velocity is expected to be associated with a larger turbulent Mach number, M_t (Houdek et al. 1999). However, the theoretical

* The CoRoT space mission, launched on December 27, 2006, has been developed and is operated by CNES, with the contribution of Austria, Belgium, Brasil, ESA, Germany and Spain.

models of stochastic excitation are strictly valid in a medium where M_t is – as in the Sun and α Cen A – rather small. Hence, the higher M_t , the more questionable the different approximations and the assumptions involved in the theory (see e.g. Samadi & Goupil 2001). It is therefore important to test the theory with another star characterized by a T_{eff} significantly higher than in the Sun.

Furthermore, the star α Cen A has an iron-to-hydrogen abundance slightly larger than the Sun, namely $[\text{Fe}/\text{H}] = 0.2$ (see Neuforge-Verheecke & Magain 1997). However, the modeling performed by Samadi et al. (2008a) for α Cen A assumes a solar iron abundance ($[\text{Fe}/\text{H}] = 0$). According to Houdek et al. (1999), the mode amplitudes are expected to change with the metal abundance. However, Houdek et al. (1999)’s result was obtained on the basis of a mixing-length approach involving several free parameters and by using a theoretical model of stochastic excitation in which a free multiplicative factor is introduced in order to reproduce the maximum of the solar mode excitation rates. Therefore, it is important to extend Houdek et al. (1999)’s study by using a more realistic modeling based on 3D hydrodynamical simulation of the surface layers of stars and a theoretical model of mode driving that reproduces – without the introduction of free parameters – the available seismic constraints.

To this end, the star HD 49933 is an interesting case for three reasons: first, this star has $T_{\text{eff}} = 6780 \pm 130$ K (Bruntt et al. 2008), $\log g \simeq 4.25 \pm 0.13$ (Bruntt et al. 2008) and $[\text{Fe}/\text{H}] \simeq -0.37$ dex (Solano et al. 2005; Gillon & Magain 2006). The properties of its surface layers are thus significantly different from those of the Sun and α Cen A. Second, HD 49933 was observed in Doppler velocity with the HARPS spectrograph. A seismic analysis of these data performed by Mosser et al. (2005) has provided the maximum of the mode surface velocity (V_{max}). Third, the star was more recently observed continuously in intensity by CoRoT during 62 days. Apart from observations for the Sun, this is the longest seismic observation ever performed both from the ground and from space. This long term and *continuous* observation provides a very high frequency resolution (~ 0.19 μHz). The seismic analysis of these observations undertaken by Appourchaux et al. (2008) or more recently by Benomar et al. (2009) have provided the *direct* measurements of the mode amplitudes and the mode linewidths with an accuracy not previously achieved for a star other than the Sun.

We consider two 3D hydrodynamical simulations representative – in effective temperature and gravity – of the surface layers of HD 49933. One 3D simulation has $[\text{Fe}/\text{H}] = 0$, while the second has $[\text{Fe}/\text{H}] = -1$. For each 3D simulation, we match an associated global 1D model and compute the associated acoustic modes and mode excitation rates, \mathcal{P} . This permits us to quantify the variation of \mathcal{P} induced by a change of the surface metal abundance Z . From these two sets of calculation, we then deduce \mathcal{P} for HD 49933 by taking into account the observed iron abundance of the star (i.e. $[\text{Fe}/\text{H}] = -0.37$). In a companion paper (Samadi et al. 2010, hereafter Paper II), we will use these theoretical calculations of \mathcal{P} and the mode linewidths obtained from the seismic analysis of HD 49933 performed with the CoRoT data to derive the expected mode amplitudes in HD 49933. These computed mode amplitudes will then be compared with the observed ones. This comparison will then constitute a test of the stochastic excitation model with a star significantly different from the Sun and α Cen A. It will also constitute a test of the procedure proposed here for deriving \mathcal{P} for any value of Z between two 3D simulations with different Z .

The present paper is organised as follows: we first describe in Sect. 2 the method to compute the theoretical mode excitation

rates associated with the two 3D hydrodynamical simulations. Next, the effects on \mathcal{P} of a different surface metal abundance are presented in Sect. 3. Then, by taking into account the actual iron abundance of HD 49933, we derive theoretical values of \mathcal{P} expected for HD 49933. Finally, Sect. 5 is dedicated to our conclusions.

2. Calculation of mode excitation rates

2.1. Model of stochastic excitation

The energy injected into a mode per unit time \mathcal{P} is given by the relation (see Samadi & Goupil 2001; Belkacem et al. 2006b):

$$\mathcal{P} = \frac{1}{8I} (C_R^2 + C_S^2), \quad (1)$$

where C_R^2 and C_S^2 are the turbulent Reynolds stress and entropy contributions, respectively, and

$$I = \int_0^M dm |\xi_r|^2 \quad (2)$$

is the mode inertia, ξ_r is the adiabatic radial mode displacement and M is the mass of the star. The expressions for C_R^2 and C_S^2 are given for a radial mode with frequency ω_{osc} by

$$C_R^2 = \frac{64\pi^3}{15} \int dm \frac{\bar{\rho} \tilde{u}^4}{k_0^3 \omega_0} \frac{\mathcal{K}_w}{3} f_r S_R(r, \omega_{\text{osc}}), \quad (3)$$

$$C_S^2 = \frac{16\pi^3}{3\omega_{\text{osc}}^2} \int dm \frac{(\alpha_s \tilde{s} \tilde{u})^2}{\bar{\rho} k_0^3 \omega_0} g_r S_S(r, \omega_{\text{osc}}) \quad (4)$$

where we have defined the ‘‘source functions’’:

$$S_R(r, \omega_{\text{osc}}) = \frac{k_0^3 \omega_0}{\tilde{u}^4} \int \frac{dk}{k^2} E^2(k) \times \int d\omega \chi_k(\omega + \omega_{\text{osc}}) \chi_k(\omega) \quad (5)$$

$$S_S(r, \omega_{\text{osc}}) = \frac{k_0^3 \omega_0}{\tilde{u}^2 \tilde{s}^2} \int \frac{dk}{k^2} E(k) E_s(k) \times \int d\omega \chi_k(\omega + \omega_{\text{osc}}) \chi_k(\omega) \quad (6)$$

where P is the gas pressure, ρ the density, s the entropy, $\bar{\rho}$ the equilibrium density profile, $\alpha_s \equiv (\partial P / \partial s)_\rho$, $f_r \equiv (d\xi_r / dr)^2$ and g_r are two functions that involve the first and second derivatives of ξ_r respectively, k is the wavenumber, $E(k)$ is the turbulent kinetic energy spectrum, $E_s(k)$ is the spectrum associated with the entropy fluctuations (s), \tilde{s} is the rms of s , χ_k is the time-correlation function associated with the velocity, \tilde{u} is a characteristic velocity defined in a way that $3\tilde{u}^2 = \langle u^2 \rangle$, $\langle \cdot \rangle$ refers to horizontal and time average, \mathbf{u} is the turbulent velocity field, and finally $\mathcal{K}_w \equiv \langle u_z^4 \rangle / \langle u_z^2 \rangle^2$ is the Kurtosis (see Belkacem et al. 2006a,b, for details). Furthermore, we have introduced for convenience the characteristic frequency ω_0 and the characteristic wavenumber k_0 :

$$\omega_0 \equiv k_0 \tilde{u} \quad (7)$$

$$k_0 \equiv \frac{2\pi}{\Lambda} \quad (8)$$

where Λ is a characteristic size derived from $E(k)$ as explained in Samadi et al. (2003b). Note that the introduction of the term $k_0^3 \omega_0 \tilde{u}^{-4}$ in the RHS of Eq. (5) and the term $k_0^3 \omega_0 \tilde{u}^{-2} \tilde{s}^{-2}$ in the RHS of Eq. (6) ensure dimensionless source functions.

The kinetic spectrum $E(k)$ is derived from the 3D simulation as detailed in Samadi et al. (2003b). As shown by Samadi et al. (2003b), the k -dependence of $E_s(k)$ is similar to that of the $E(k)$. Accordingly, we assume $E_s \propto \bar{E}$.

In Samadi et al. (2008a), two different analytical functions for $\chi_k(\omega)$ have been considered, namely a Lorentzian function and a Gaussian one. In the present study we will in addition derive $\chi_k(\omega)$ directly from the 3D simulations as detailed in Samadi et al. (2003a). Once $\chi_k(\omega)$ is derived from the 3D simulation, it is implemented in Eqs. (5) and (6).

We compute the mode excitation as detailed in Samadi et al. (2008a): all required quantities – except ξ_r , I and ω_{osc} – are obtained directly from two 3D hydrodynamical simulations representative of the outer layers of HD 49933, whose characteristics are described in Sect. 2.2 below.

The quantities related to the modes (ω_{osc} , I and ξ_r) are calculated using the adiabatic pulsation code ADIPLS (Christensen-Dalsgaard & Berthomieu 1991) from 1D global models. The outer layers of these 1D models are derived from the 3D simulation as described in Sect. 2.3.

2.2. The 3D simulations

We computed two 3D radiation-hydrodynamical model atmospheres with the code CO⁵BOLD (Freytag et al. 2002; Wedemeyer et al. 2004). One 3D simulation had a solar iron-to-hydrogen [Fe/H] = 0.0 while the other had [Fe/H] = -1.0. The 3D model with [Fe/H] = 0 (resp. [Fe/H] = -1) will be hereafter referred to as model S0 (resp. S1). The assumed chemical composition is similar (in particular for the CNO elements) to that of the solar chemical composition proposed by Asplund et al. (2005). The abundances of the α -elements in model S1 were assumed to be enhanced by 0.4 dex. For S0 we obtain $Z/X = 0.01830$ and $Y = 0.249$, and for S1 $Z/X = 0.0036765$ and $Y = 0.252$. Both 3D simulations have exactly the same gravity ($\log g = 4.25$) and are very close in effective temperature (T_{eff}). Both models employ a spatial mesh with $140 \times 140 \times 150$ grid points, and a physical extent of the computational box of $16.4 \times 16.4 \times 24.2 \text{ Mm}^3$. The equation of state takes into account the ionisation of hydrogen and helium as well as the formation of H₂ molecules according to the Saha-Boltzmann statistics. The wavelength dependence of the radiative transfer is treated by the opacity binning method (Nordlund 1982; Ludwig 1992; Vögler et al. 2004) using five wavelength bins for model S0 and six for model S1. Detailed wavelength-dependent opacities were obtained from the MARCS model atmosphere package (Gustafsson et al. 2008). Table 1 summarizes the characteristics of the 3D models. The effective temperature and surface gravity correspond to the parameters of HD 49933 within the observational uncertainties, while the two metallicities bracket the observed value.

For each 3D simulation, two time series were built. One has a long duration (38h and 20h for S0 and S1, respectively) and a low sampling frequency (10 mn). This time series is used to compute time averaged quantities ($\bar{\rho}$, $E(k)$, etc.). The second time series is shorter (8.8 h and 6.8 h for S0 and S1, respectively), but has a high sampling frequency (1 mn). Such high sampling frequency is required for the calculation of $\chi_k(\omega)$. Indeed, the modes we are looking at lie between $\nu \approx 1.25 \text{ mHz}$ and $\nu \approx 2.4 \text{ mHz}$.

The two 3D simulations extend up to $T = 100\,000 \text{ K}$. However, for $T \gtrsim 30\,000 \text{ K}$, the 3D simulations are not completely realistic. First of all, the MARCS-based opacities are provided only up to a temperature of $30\,000 \text{ K}$; for higher

Table 1. Characteristics of the 3D simulations.

Label	[Fe/H]	Y	Z	Z/X	T_{eff} [K]
S0	0	0.249	13.5×10^{-3}	0.018305	6725 ± 17
S1	-1	0.252	2.74×10^{-3}	0.003676	6730 ± 12

temperatures the value at $30\,000 \text{ K}$ is assumed. Note that we refer to the opacity per unit mass here. For the radiative transfer the opacity per unit volume is the relevant quantity, i.e. the product of opacity per mass unit and density. Since in the simulation the opacity is still multiplied at each position with the correct local density, the actual error we make when extrapolating the opacity is acceptable.

Another limitation of the simulations is the restricted size of the computational box which does not allow for a full development of the largest flow structures, again in the layers above $T \approx 30\,000 \text{ K}$. Two hints make us believe that the size of the computational domain is not fully sufficient: i) in the deepest layers of the simulations there is a tendency that structures align with the computational grid; ii) the spatial spectral power P of scalar fields in a horizontal layer does not tend towards the expected asymptotic behaviour $P \times k$ for low spatial wavenumber k . We noticed this shortcoming only after the completion of the simulation runs. To mitigate its effect in our analysis, we will later by default integrate the mode excitation rates up to $T = 30\,000 \text{ K}$. However, for comparison purposes, some computations have been extended down to the bottom of the 3D simulations. For S0, the layers located below $T \approx 30\,000 \text{ K}$ contribute only by $\lesssim 10\%$ to the excitation of the modes lying in the frequency range where modes have the most chance to be detected ($\nu \approx 1.2\text{--}2.5 \text{ mHz}$). For S1, the contribution of the deep layers is even smaller ($\sim 5\%$).

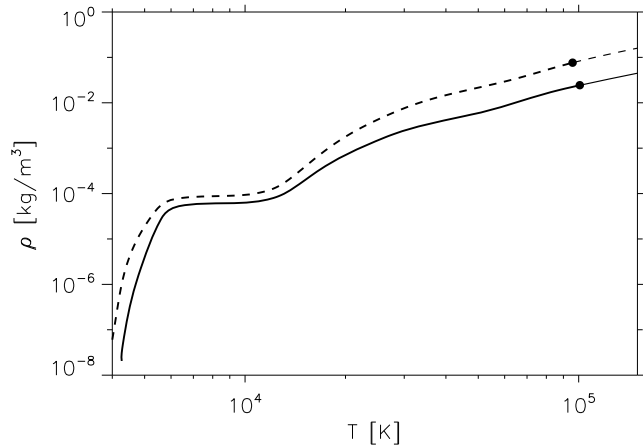
Finally, one may wonder how the treatment of the small-scales or the limited spatial resolution of the simulation can influence our calculations. Dissipative processes are handled in CO⁵BOLD on the one hand side implicitly by the numerical scheme (Roe-type approximate Riemann solver), and on the other hand explicitly by a sub-grid model according to the classical Smagorinsky (1963) formulation. Jacoutot et al. (2008) found that computed mode excitation rates significantly depend on the adopted sub-grid model. Samadi et al. (2007) have found that solar mode excitation rates computed in the manner of Nordlund & Stein (2001), i.e., using data directly from the 3D simulation, decrease as the spatial resolution of the solar 3D simulation decreases. As a conclusion the spatial resolution or the sub-grid model can influence computed mode excitation rates (see a discussion in Samadi et al. 2008a). However, concerning the spatial resolution and according to Samadi et al. (2007)'s results, the present spatial resolution (1/140 of the horizontal size of the box and about 1/150 of the vertical extent of the simulation box) is high enough to obtain accurate computed energy rates. The increased spatial resolution of our models in comparison to the work of Jacoutot et al. (2008) reduces the impact of the unresolved scales.

2.3. The 1D global models

For each 3D model we compute an associated 1D global model. The models are built in the manner of Trampedach (1997) as detailed in Samadi et al. (2008a) in such way that their outer layers are replaced by the averaged 3D simulations described in Sect. 2.2. The interior of the models are obtained with the CESAM code assuming standard physics: Convection is

Table 2. Characteristics of the 1D “patched” models. α is the mixing-length parameter.

[Fe/H]	Y	Z	T_{eff} [K]	R/R_{\odot}	M/M_{\odot}	α
0	0.249	13.5×10^{-3}	6726	1.473	1.408	1.677
-1	0.252	2.74×10^{-3}	6732	1.261	1.033	1.905

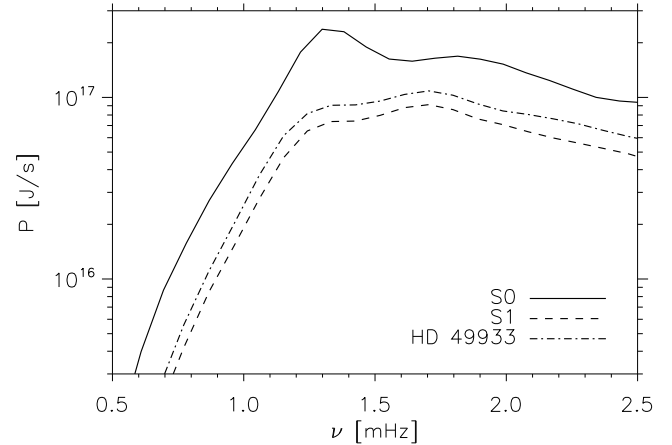
**Fig. 1.** Mean density $\bar{\rho}$ as a function of temperature, T . The solid line corresponds to the 3D model with the metal abundance (S0) and the dashed line to metal poor 3D model (S1). The filled dots show the location where the 1D models have been matched to the associated 3D simulation.

described according to Böhm-Vitense (1958)’s local mixing-length theory of convection (MLT), and turbulent pressure is ignored. Microscopic diffusion is not included. The OPAL equation of state is assumed. The chemical mixture of the heavy elements is similar to that of Asplund et al. (2005)’s mixture. As in Samadi et al. (2008a), we will refer to these models as “patched” models hereafter.

The two models have the effective temperature and the gravity of the 3D simulations. One model is matched with S0 and has [Fe/H] = 0, while the second is matched with S1 and has [Fe/H] = -1. The 1D models have the same chemical mixture as their associated 3D simulations. The parameters of the 1D patched models are given in Table 2. The stratification in density and temperature of the patched 1D models are shown in Fig. 1. At any given temperature the density is larger in S1 as a consequence of its lower metal abundance. Indeed, the lower the metal abundance, the lower the opacity; then, at a given optical depth (τ), the density is larger in S1 compared to S0. The photosphere corresponds to the optical depth $\tau = 2/3$. Since the two 3D simulations have approximately the same effective temperature, the density in S1 is larger at optical depth $\tau = 2/3$. Since the density in S1 increases with depth even more rapidly than in S0, the density in S1 remains larger for $\tau > 2/3$ than in S0.

3. Effects of the metal abundance on excitation rates

The mode excitation rates (\mathcal{P}) are computed for the two 3D simulations according to Eqs. (1)–(6). The integration is performed from the top of the simulated domains down to $T = 30\,000$ K (see Sect. 2.2). In the following, \mathcal{P}_1 (resp. \mathcal{P}_0) corresponds to the mode excitation rates associated with the 3D model with [Fe/H] = -1 (resp. [Fe/H] = 0).

**Fig. 2.** Mode excitation rates \mathcal{P} as a function of the mode frequency, ν . The solid line corresponds to the 3D model with the canonical metal abundance (S0) and the dashed line to the metal poor 3D model (S1). The dot-dashed line corresponds to the mode excitation rates derived for the specific case of HD 49933 as explained in Appendix A.

3.1. Results

Figure 2 shows the effect of the assumed metal abundance of the stellar model on the mode excitation rates. \mathcal{P}_1 is found to be three times smaller than \mathcal{P}_0 , i.e. p modes associated with the metal poor 3D model (S1) receive approximately three times less energy per unit time than those associated with the 3D model with the solar metal abundance (S0).

For both 3D models, the dominant part of the driving is ensured by the Reynolds stresses. The entropy fluctuations contribute by only $\sim 30\%$ of the total power for both S0 and S1. By comparison, in the case of the Sun and α Cen A it contributes by only $\sim 15\%$. Furthermore, we find that the contribution of the entropy source term is – as for the Reynolds stress term – about three times smaller in S1 than in S0. We conclude that the effect of the metal abundance on the excitation rates is almost the same for the Reynolds stress contribution and the entropy source term.

3.2. Interpretation

From Eqs. (1), (2), (3), (7) and (8) we show that at a given layer the power supplied to the modes – per unit mass – by the Reynolds stress is proportional to $F_{\text{kin}} \Lambda^4 S_R / \mathcal{M}$, where F_{kin} is the flux of the kinetic energy, which is proportional to $\bar{\rho} \bar{u}^3$, Λ is a characteristic length (see Sect. 2.1) and \mathcal{M} is the mode mass defined as:

$$\mathcal{M} = \frac{I}{\xi_r^2} \quad (9)$$

where ξ_r is the mode displacement evaluated at the layer in the atmosphere where the mode is measured.

The power supplied to the modes – per unit mass – by the entropy source term is proportional to $\bar{\rho} \bar{u}^3 \Lambda^4 \mathcal{R}^2 S_s$ where ω_{osc} is the mode frequency, $\mathcal{R} \propto F_{\text{conv}} / F_{\text{kin}}$, where $F_{\text{conv}} \propto w \alpha_s \bar{s}$ is the convective flux, and finally \bar{s} is the rms of the entropy fluctuations (see Samadi et al. 2006). We recall that the higher \mathcal{R} , the higher the relative contribution of the entropy source to the excitation. We study below the role of \mathcal{M} , F_{kin} , Λ , S_R , S_s and \mathcal{R} :

- *Mode mass (\mathcal{M}):* The frequency domain, where modes are strongly excited, ranges between $\nu \approx 1.2$ mHz and

- $\nu \approx 2.5$ mHz. In this frequency domain, the mode masses \mathcal{M} associated with S0 are quite similar to those associated with S1 (not shown). Consequently the differences between \mathcal{P}_1 and \mathcal{P}_0 do not arise from the (small) differences in \mathcal{M} .
- *Kinetic energy flux* (F_{kin}): The larger F_{kin} , the larger the driving by the Reynolds stress. However, we find that the two 3D models have very similar F_{kin} . This is not surprising since the two 3D models have very similar effective temperatures. This means that the differences between \mathcal{P}_1 and \mathcal{P}_0 do not arise from the (small) differences in F_{kin} .
 - *Characteristic length* (Λ): In the manner of Samadi et al. (2003b) we derive from the kinetic energy spectra $E(k)$ of the two 3D simulations the characteristic length Λ ($\Lambda = 2\pi/k_0$, see Eq. (8)) for each layer of the simulated domain. We find that the differences in Λ between the two 3D simulations is small and does not play a significant role in the differences in \mathcal{P} . This can be understood by the fact that S0 and S1 have the same gravity. Indeed, as shown by Samadi et al. (2008a) – at a fixed effective temperature – Λ scales as the inverse of g . We conclude that the differences between \mathcal{P}_1 and \mathcal{P}_0 do not originate from the (small) differences in Λ .
 - *Source functions* (S_R and S_S): The dimensionless source functions S_R and S_S are defined in Eqs. (5) and (6) respectively. Both source functions involve the eddy time-correlation function $\chi_k(\omega)$. We define ω_k as the frequency width of $\chi_k(\omega)$. As shown by Samadi et al. (2003a) and as verified in the present case, ω_k can be evaluated as the product $k u_k$ where u_k is given by the relation (Stein 1967):

$$u_k^2 = \int_k^{2k} dk E(k) \quad (10)$$

where $E(k)$ is normalised as:

$$\int_0^{+\infty} dk E(k) = \frac{1}{2} \langle u^2 \rangle \equiv \frac{1}{2} \tilde{u}^2. \quad (11)$$

According to Eqs. (10) and (11), u_k is directly proportional to \tilde{u} . At a fixed k/k_0 , we then have $\omega_k \propto \tilde{u} k_0 = \omega_0$.

As seen above, ω_0 controls ω_k , the frequency width of χ_k . Then, at fixed ω_{osc} , we can easily see from Eqs. (5) and (6) that the smaller ω_0 , the smaller $S_R(\omega_{\text{osc}})$ and $S_S(\omega_{\text{osc}})$. Since $\omega_0 = \tilde{u} k_0 = 2\pi \tilde{u} / \Lambda$ and since both 3D simulations have approximately the same Λ , smaller \tilde{u} results directly in smaller ω_0 and hence in smaller source functions.

We have plotted in Fig. 3 the characteristic velocity \tilde{u} . This quantity is found to be up to 15% smaller for S1 compared with S0. In other words, the metal poor 3D model is characterized by lower convective velocities. Consequently, the source functions are smaller for S1 compared to S0. Although the convective velocities differ between S0 and S1 by only 15%, the excitation rates differ by a factor ~ 3 . The reason for this is that the source functions, which are non-linear functions of \tilde{u} , decrease very rapidly with \tilde{u} . This is the consequence of the behavior of the eddy-time correlation χ_k . Indeed, this function varies with the ratio $\omega_{\text{osc}}/\omega_k$ approximately as a Lorentzian function. This is why χ_k varies rapidly with \tilde{u} (we recall that $\omega_k \propto \tilde{u} k_0$).

In conclusion, the differences between \mathcal{P}_1 and \mathcal{P}_0 are mainly due to differences in the characteristic velocity \tilde{u} . In turn, the low convective velocity in S1 is a consequence of the larger density compared to S0. Indeed, as shown in Fig. 1, the density is systematically higher in S1. At the layer where the modes are the most excited (i.e. at $T \sim 10\,000$ K), the density is $\sim 50\%$ higher. Since the two 3D models have a similar kinetic energy flux (see

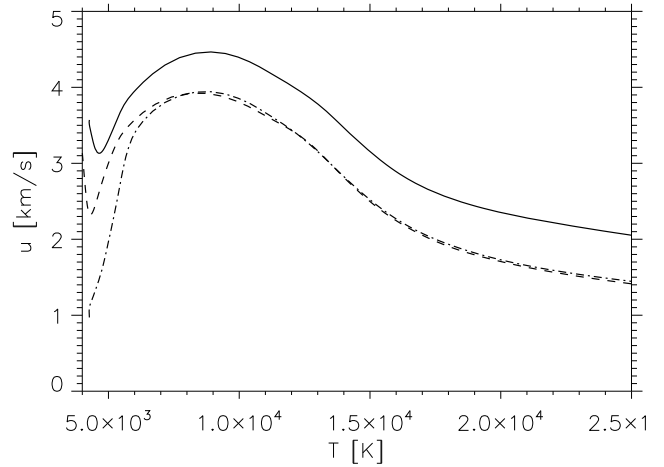


Fig. 3. Characteristic velocity \tilde{u} defined in Eq. (7) as a function of temperature, T . The solid and dashed lines have the same meaning as in Fig. 2. The dot-dashed line corresponds to the solid line multiplied by γ_1 , where $\gamma_1(T) \equiv (\bar{\rho}_0/\bar{\rho}_1)^{1/3}$ and $\bar{\rho}_0$ (resp. $\bar{\rho}_1$) is the mean density stratification of S0 (resp. S1) (see Appendix A).

above), it follows that a larger density for S1 then implies lower convective velocities.

Relative contribution of the entropy source term (\mathcal{R}): The convective flux F_{conv} in S1 is almost identical to that of S0. This is due to the fact that the two 3D simulations have almost the same effective temperature. Furthermore, as pointed out above, the differences in F_{kin} between S1 and S0 are small. As a consequence, the ratio $\mathcal{R} \propto F_{\text{conv}}/F_{\text{kin}}$ does not differ between the two 3D simulations. Accordingly, as for the Reynolds contribution, the variation of the excitation rates with the metal abundance is only due to the source term S_S . The latter varies with ω_0 in the same manner as S_R , which is in turn the reason for the contribution of the entropy fluctuations to show the same trend with the metal abundance as the Reynolds stress term.

4. Theoretical calculation of \mathcal{P} for HD 49933

We derive the mode excitation rates \mathcal{P} for HD 49933. According to Gillon & Magain (2006), HD 49933 has $[\text{Fe}/\text{H}] = -0.37 \pm 0.03$ dex, while we only have two 3D simulations with values of $[\text{Fe}/\text{H}]$, respectively $[\text{Fe}/\text{H}] = 0$ and $[\text{Fe}/\text{H}] = -1$.

As seen in Sect. 3.2, differences in \mathcal{P} between S0 and S1 are a direct consequence of the differences in the source functions S_R and S_S . It follows that in order to derive \mathcal{P} for HD 49933, we only have to derive the expected values for S_R and S_S . As seen in Sect. 3.2, differences in S_R (or in S_S) between S0 and S1 are related to the surface metal abundance through the surface densities that impact the convective velocities (\tilde{u}). The determination of the HD 49933 convective velocities allows us to determine its source function. To this end, we use the fact that the kinetic flux is almost unchanged between S1 and S0 (see Sect. 3.2) to derive the profile of $\tilde{u}(T)$, expected at the surface layers of HD 49933. This is performed by interpolating in Z between S0 and S1, the surface density stratification representative of the surface layers of HD 49933. The whole procedure is described in Appendix A.

In order to compute \mathcal{P} for HD 49933, we then need to know Z for this star. Since we do not know its surface helium abundance, we will assume by default the solar value for Y : $Y = 0.249 \pm 0.003$ (Basu 1997). Gillon & Magain (2006)'s

analysis shows that the chemical mixture of HD 49933 does not significantly differ from that of the Sun. According to [Asplund et al. \(2005\)](#), the new solar metal to hydrogen ratio is $(Z/X)_\odot = 0.0165$. Accordingly, since $[\text{Fe}/\text{H}] = -0.37 \pm 0.03$ dex, we derive $Z = 5.3 \times 10^{-3} \pm 0.4 \times 10^{-3}$ for HD 49933. Note that assuming [Grevesse & Noels \(1993\)](#)'s chemical mixture yields $Z = 7.8 \times 10^{-3} \pm 0.5 \times 10^{-3}$.

The result of the calculation is shown in Fig. 2. The maximum \mathcal{P} is $1.08 \pm 0.05 \times 10^{17}$ J/s when [Asplund et al. \(2005\)](#)'s chemical composition is assumed (see Appendix A). This is about 30 times larger than in the Sun and about 14 times larger than in α Cen A. When [Grevesse & Noels \(1993\)](#)'s chemical mixture is assumed, the maximum in \mathcal{P} is in that case equal to $1.27 \pm 0.05 \times 10^{17}$ J/s, that is about 30% larger than with [Asplund et al. \(2005\)](#)'s solar chemical mixture.

We note that the uncertainties in the knowledge of $[\text{Fe}/\text{H}]$ set uncertainties on \mathcal{P} which are on the order of 10% in the frequency domain of interest.

5. Conclusion

We have built two 3D hydrodynamical simulations representative in effective temperature (T_{eff}) and gravity (g) of the surface layers of an F type star on the main sequence. One model has a solar iron-to-hydrogen abundance ($[\text{Fe}/\text{H}] = 0$) and the other has $[\text{Fe}/\text{H}] = -1$. Both models have the same T_{eff} and g . For each 3D simulation, we have computed an associated ‘‘patched’’ 1D full model. Finally, we have computed the mode excitation rates \mathcal{P} associated with the two ‘‘patched’’ 1D models.

Mode excitation rates associated with the metal poor 3D simulation are found to be about three times smaller than those associated with the 3D simulation which has a solar surface metal abundance. This is explained by the following connections: the lower the metallicity, the lower the opacity. At fixed effective temperature and surface gravity, the lower the opacity, the denser the medium at a given optical depth. The higher the density, the smaller are the convective velocities to transport the same amount of energy by convection. Finally, smaller convective velocities result in a less efficient driving. On the other hand, a surface metal abundance higher than the solar metal abundance will result in a lower surface density, which in turn will result in a higher convective velocity and then in a more efficient driving. Our result can then be qualitatively generalised for any surface metal abundance.

By taking into account the observed surface metal abundance of the star HD 49933 (i.e. $[\text{Fe}/\text{H}] = -0.37$), we have derived, using two 3D simulations and the interpolation procedure developed here, the rates at which acoustic modes are expected to be excited by turbulent convection in the case of HD 49933. These excitation rates \mathcal{P} are found to be about two times smaller than for a model built assuming a solar metal abundance. These theoretical mode excitation rates will be used in Paper II to derive the expected mode amplitudes from measured mode linewidths. We will then be able to compare these amplitudes with those derived for HD 49933 from different seismic data. This will constitute an indirect test of our procedure which permits us to interpolate for any value of Z the mode excitation rates \mathcal{P} between two 3D simulations with different Z but the same T_{eff} and $\log g$. We must stress that a more direct validation of this interpolation procedure will be to compute a third 3D model with the surface metal abundance of the star HD 49933 and to compare finally the mode excitation rates obtained here with the interpolation procedure with that obtained with this third 3D model. This represents a long term work since several months (about three to

four months) are required for the calculation of this additional 3D model, which is in progress.

Acknowledgements. We thank C. Catala for useful discussions concerning the spectrometric properties of HD 49933. We are indebted to J. Leibacher for his careful reading of the manuscript. K.B. acknowledged financial support from Liège University through the Subside Fédéral pour la Recherche 2009.

Appendix A: Theoretical calculation of the mode excitation rates for HD 49933

The mode excitation rate \mathcal{P} is inversely proportional to the mode mass \mathcal{M} (see Eqs. (9), (2) and (2)). This is why we can derive \mathcal{M} and $\mathcal{M}\mathcal{P}$ separately in order to derive \mathcal{P} for HD 49933.

A.1. Derivation of $\mathcal{M}\mathcal{P}$

As pointed out in Sect. 3.2, the kinetic flux $F_{\text{kin}} = \bar{\rho} \tilde{u}^3$ is almost unchanged between S1 and S0 because both 3D models have the same T_{eff} . This has also to be the case for HD 49933 (same T_{eff} and same $\log g$ than S0 and S1). Therefore, the calculation of $\mathcal{M}\mathcal{P}$ for HD 49933 relies only on the evaluation of the values reached – at a fixed mode frequency – by the source functions \mathcal{S}_R and \mathcal{S}_S .

As seen in Sect. 3.2, $\omega_0 = k_0 \tilde{u}$ controls the width of χ_k in a way that the source functions $\mathcal{S}_R(\omega_{\text{osc}})$ and $\mathcal{S}_S(\omega_{\text{osc}})$ can be seen as functions of the dimensionless ratio $\omega_{\text{osc}}/\omega_0$. The variation of E with k as well as the variation of χ_k with ω/ω_0 are shown to be similar in the two 3D simulations. Furthermore, S0 and S1 have approximately the same characteristic length Λ and hence approximately the same $k_0 \equiv 2\pi/\Lambda$. Therefore, the source function \mathcal{S}_R (resp. \mathcal{S}_S) associated with S0 only differs from that of S1 by the characteristic velocity \tilde{u} . This must then also be the case for HD 49933. Further, in order to evaluate the source functions in the case of HD 49933, we only need to know the factor γ by which \tilde{u} is modified in HD 49933 with respect to S1 or S0. According to Eq. (5) (resp. Eq. (6)), multiplying \tilde{u} by γ is equivalent to replace $\mathcal{S}_R(\omega_{\text{osc}})$ (reps. $\mathcal{S}_S(\omega_{\text{osc}})$) by $\gamma \mathcal{S}_R(\omega_{\text{osc}}/\gamma)$ (resp. $\gamma \mathcal{S}_S(\omega_{\text{osc}}/\gamma)$).

Since the kinetic flux F_{kin} in HD 49933 must be the same for S0 or S1, the characteristic velocity \tilde{u} can be derived for HD 49933 according to $\tilde{u}_*(T) = \tilde{u}_1 \gamma_*$ with $\gamma_*(T) \equiv (\bar{\rho}_1/\bar{\rho}_*)^{1/3}$ where $\bar{\rho}_1(T)$ is the mean density stratification of S1, $\tilde{u}_1(T)$ the characteristic velocity of S1 and $\bar{\rho}_*$ the mean density of HD 49933. Once γ_* and then \tilde{u}_* are derived for HD 49933, we then compute the source functions associated with HD 49933. Finally, we compute $\mathcal{M}\mathcal{P}$ by keeping F_{kin} constant. We now turn to the derivation of the factor γ_* .

A.2. Derivation of γ_*

To derive γ_* at a given T , we need to know how the mean density $\bar{\rho}$ varies with the metal abundance Z . In order to this we consider five ‘‘standard’’ 1D models with five different values of Z . These 1D models are built using the same physics as described in Sect. 2.3. Two of these models have the same abundance as S0 and S1. All of the 1D models have approximately the same gravity ($\log g \approx 4.25$) and the same effective temperature ($T_{\text{eff}} \approx 6730$ K).

The set of 1D models shows that – at any given temperature within the excitation region – $\bar{\rho}$ varies with Z rather linearly. In order to derive $\bar{\rho}$ for HD 49933, we apply – at fixed T and between S0 and S1 – a linear interpolation of $\bar{\rho}(T)$ with respect to Z .

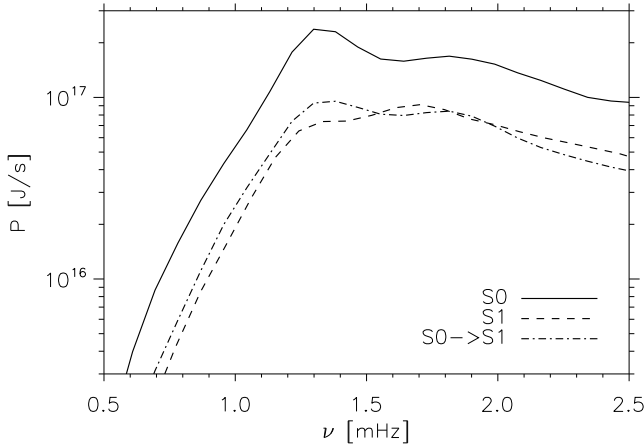


Fig. A.1. Mode excitation rates \mathcal{P} as a function of the mode frequency ν . The thin dot-dashed line corresponds to \mathcal{P}_{01} , the mode excitation rates derived for S1 from S0 (see Appendix A4). The other lines have the same meaning as in Fig. 2.

A.3. Derivation of \mathcal{M}

As shown in Sect. 3.2 above in the frequency domain where modes are detected in HD 49933, \mathcal{M} does not change significantly between S0 and S1. This suggests that the mode masses associated with a patched 1D model with the metal abundance expected for HD 49933 would be very similar to those associated with S0 or S1. Consequently we will assume for the case of HD 49933 the same mode masses as those associated with S1, since this 3D model has a Z abundance closer to that of HD 49933.

A.4. Derivation of \mathcal{P}

Before deriving \mathcal{P} for HD 49933, we check that, from S0 and the knowledge of \mathcal{P}_0 , we can approximately reproduce \mathcal{P}_1 , the mode excitation rates, associated with S1 following the procedure described above. Let $\gamma_1 \equiv (\bar{\rho}_0/\bar{\rho}_1)^{1/3}$. As seen in Fig. 3, when we multiply \tilde{u}_0 by $\gamma_1(T)$ we match \tilde{u}_1 . Then, using $\gamma_1(T)$ and following the procedure described above, we derive \mathcal{P}_{01} , the mode excitation rates associated with S1 but derived from S0. The result is shown in Fig. A.1. \mathcal{P}_{01} matches \mathcal{P}_1 rather well. However, there are differences remaining in particular in the frequency domain $\nu = 1.2\text{--}1.5$ mHz. Nevertheless, the differences between \mathcal{P}_{01} and \mathcal{P}_∞ are in any case not significant compared to the accuracy at which the mode amplitudes are measured with the CoRoT data (see Paper II). This validates the procedure, at least at the level of the current seismic precisions.

Since the metal abundance Z of HD 49933 is closer to that of S1 than that of S0, we derive the mode excitation rates \mathcal{P} associated with HD 49933 from S1 following the procedure detailed above. The result is shown in Fig. 2. As expected, the mode excitation rates \mathcal{P} associated with HD 49933 lie between those of

S0 and S1, while remaining closer to S1 than to S0. Note that the differences between \mathcal{P}_1 and the excitation rates derived for HD 49933 (\mathcal{P}) are of the same order as the differences seen locally between \mathcal{P}_1 and \mathcal{P}_{01} . These differences remain small compared to the current seismic precisions. On the other hand the differences between \mathcal{P} and \mathcal{P}_0 are significant and have an important impact on the mode amplitudes (see Paper II).

References

- Appourchaux, T., Michel, E., Auvergne, M., et al. 2008, *A&A*, 488, 705
 Asplund, M., Grevesse, N., & Sauval, A. J. 2005, in *Cosmic Abundances as Records of Stellar Evolution and Nucleosynthesis*, ed. T. G. Barnes, III, & F. N. Bash, Conf. Ser., 336, 25
 Basu, S. 1997, *MNRAS*, 288, 572
 Belkacem, K., Samadi, R., Goupil, M. J., & Kupka, F. 2006a, *A&A*, 460, 173
 Belkacem, K., Samadi, R., Goupil, M. J., Kupka, F., & Baudin, F. 2006b, *A&A*, 460, 183
 Benomar, O., Baudin, F., Campante, T., et al. 2009, *A&A*, 507, L13
 Böhm-Vitense, E. 1958, *Z. Astrophys.*, 46, 108
 Bruntt, H., De Cat, P., & Aerts, C. 2008, *A&A*, 478, 487
 Chaplin, W. J., Houdek, G., Elsworth, Y., et al. 2005, *MNRAS*, 360, 859
 Christensen-Dalsgaard, J., & Berthomieu, G. 1991, *Theory of solar oscillations, Solar interior and atmosphere*, A92-36201 14-92 (Tucson: AZ university of Arizona Press), 401
 Freytag, B., Steffen, M., & Dorch, B. 2002, *Astron. Nachr.*, 323, 213
 Gillon, M., & Magain, P. 2006, *A&A*, 448, 341
 Grevesse, N., & Noels, A. 1993, in *Origin and Evolution of the Elements*, ed. N. Prantzos, E. Vangioni-Flam, & M. Cassé (Cambridge University Press), 15
 Gustafsson, B., Edvardsson, B., Eriksson, K., et al. 2008, *A&A*, 486, 951
 Houdek, G. 2006, in *Proceedings of SOHO 18/GONG 2006/HELAS I, Beyond the spherical Sun*, Published on CDROM, ESA SP, 624, 28.1
 Houdek, G., Balmforth, N. J., Christensen-Dalsgaard, J., & Gough, D. O. 1999, *A&A*, 351, 582
 Jacoutot, L., Kosovichev, A. G., Wray, A. A., & Mansour, N. N. 2008, *ApJ*, 682, 1386
 Ludwig, H.-G. 1992, Ph.D. Thesis, University of Kiel
 Mosser, B., Bouchy, F., Catala, C., et al. 2005, *A&A*, 431, L13
 Neuforge-Verheecke, C., & Magain, P. 1997, *A&A*, 328, 261
 Nordlund, A. 1982, *A&A*, 107, 1
 Nordlund, Å., & Stein, R. F. 2001, *ApJ*, 546, 576
 Samadi, R., & Goupil, M. J. 2001, *A&A*, 370, 136
 Samadi, R., Nordlund, Å., Stein, R. F., Goupil, M. J., & Roxburgh, I. 2003a, *A&A*, 404, 1129
 Samadi, R., Nordlund, Å., Stein, R. F., Goupil, M. J., & Roxburgh, I. 2003b, *A&A*, 403, 303
 Samadi, R., Kupka, F., Goupil, M. J., Lebreton, Y., & van't Veer-Menneret, C. 2006, *A&A*, 445, 233
 Samadi, R., Georgobiani, D., Trampedach, R., et al. 2007, *A&A*, 463, 297
 Samadi, R., Belkacem, K., Goupil, M. J., Dupret, M.-A., & Kupka, F. 2008a, *A&A*, 489, 291
 Samadi, R., Belkacem, K., Goupil, M.-J., Ludwig, H.-G., & Dupret, M.-A. 2008b, *Commun. Asteroseismol.*, 157, 130
 Samadi, R., Ludwig, H., Belkacem, K., et al. 2010, *A&A*, 509, A16 (Paper II)
 Smagorinsky, J. 1963, *Monthly Weather Rev.*, 91, 99
 Solano, E., Catala, C., Garrido, R., et al. 2005, *AJ*, 129, 547
 Stein, R., Georgobiani, D., Trampedach, R., Ludwig, H.-G., & Nordlund, Å. 2004, *Sol. Phys.*, 220, 229
 Stein, R. F. 1967, *Sol. Phys.*, 2, 385
 Trampedach, R. 1997, Master's thesis, Aarhus University
 Vögler, A., Bruls, J. H. M. J., & Schüssler, M. 2004, *A&A*, 421, 741
 Wedemeyer, S., Freytag, B., Steffen, M., Ludwig, H.-G., & Holweger, H. 2004, *A&A*, 414, 1121

The CoRoT target HD 49933[★]

II. Comparison of theoretical mode amplitudes with observations

R. Samadi¹, H.-G. Ludwig², K. Belkacem^{1,3}, M. J. Goupil¹, O. Benomar⁴, B. Mosser¹, M.-A. Dupret^{1,3}, F. Baudin⁴,
T. Appourchaux⁴, and E. Michel¹

¹ Observatoire de Paris, LESIA, CNRS UMR 8109, Université Pierre et Marie Curie, Université Denis Diderot, 5 Pl. J. Janssen, 92195 Meudon, France
e-mail: Reza.Samadi@obspm.fr

² Observatoire de Paris, GEPI, CNRS UMR 8111, 5 Pl. J. Janssen, 92195 Meudon, France

³ Institut d'Astrophysique et de Géophysique de l'Université de Liège, Allé du 6 Août 17, 4000 Liège, Belgium

⁴ Institut d'Astrophysique Spatiale, CNRS UMR 8617, Université Paris XI, 91405 Orsay, France

Received 17 February 2009 / Accepted 27 October 2009

ABSTRACT

Context. The seismic data obtained by CoRoT for the star HD 49933 enable us for the first time to measure *directly* the amplitudes and linewidths of solar-like oscillations for a star other than the Sun. From those measurements it is possible, as was done for the Sun, to constrain models of the excitation of acoustic modes by turbulent convection.

Aims. We compare a stochastic excitation model described in Paper I with the asteroseismology data for HD 49933, a star that is rather metal poor and significantly hotter than the Sun.

Methods. Using the seismic determinations of the mode linewidths detected by CoRoT for HD 49933 and the theoretical mode excitation rates computed in Paper I for the specific case of HD 49933, we derive the expected surface velocity amplitudes of the acoustic modes detected in HD 49933. Using a calibrated quasi-adiabatic approximation relating the mode amplitudes in intensity to those in velocity, we derive the expected values of the mode amplitude in intensity.

Results. Except at rather high frequency, our amplitude calculations are within 1- σ error bars of the mode surface velocity spectrum derived with the HARPS spectrograph. The same is found with respect to the mode amplitudes in intensity derived for HD 49933 from the CoRoT data. On the other hand, at high frequency ($\nu \gtrsim 1.9$ mHz), our calculations depart significantly from the CoRoT and HARPS measurements. We show that assuming a solar metal abundance rather than the actual metal abundance of the star would result in a larger discrepancy with the seismic data. Furthermore, we present calculations which assume the “new” solar chemical mixture to be in better agreement with the seismic data than those that assumed the “old” solar chemical mixture.

Conclusions. These results validate in the case of a star significantly hotter than the Sun and α Cen A the main assumptions in the model of stochastic excitation. However, the discrepancies seen at high frequency highlight some deficiencies of the modelling, whose origin remains to be understood. We also show that it is important to take the surface metal abundance of the solar-like pulsators into account.

Key words. convection – turbulence – stars: oscillations – Sun: helioseismology – stars: individual: HD 49933

1. Introduction

The amplitudes of solar-like oscillations result from a balance between excitation and damping. The mode linewidths are directly related to the mode damping rates. Once we can measure the mode linewidths, we can derive the theoretical value of the mode amplitudes from theoretical calculations of the mode excitation rates, which in turn can be compared to the available seismic constraints. This comparison allows us to test the model of stochastic mode excitation investigated in a companion paper (Samadi et al. 2010, hereafter Paper I).

As shown in Paper I, a moderate deficit of the surface metal abundance results in a significant decrease of the mode driving by turbulent convection. Indeed, by taking into account the measured iron-to-hydrogen abundance ($[\text{Fe}/\text{H}]$) of HD 49933

($[\text{Fe}/\text{H}] = -0.37$), we have derived the theoretical values of the mode excitation rates \mathcal{P} expected for this star. The resulting value of \mathcal{P} is found to be about two times smaller than for a model with the same gravity and effective temperature, but with a solar metal abundance (i.e. $[\text{Fe}/\text{H}] = 0$).

The star HD 49933 was first observed in Doppler velocity by Mosser et al. (2005) with the HARPS spectrograph. More recently, this star has been observed twice by CoRoT. A first time this was done continuously during about 61 days (initial run, IR) and a second time continuously during about 137 days (first long run in the center direction, LRc01). The combined seismic analysis of these data (Benomar et al. 2009) has provided the mode linewidths as well as the amplitudes of the modes in intensity. Then, using mode linewidths obtained for HD 49933 with the CoRoT data and the theoretical mode excitation rates (obtained in Paper I), we derive the expected values of the mode surface velocity amplitudes. We next compare these values with the mode velocity spectrum derived following

[★] The CoRoT space mission, launched on December 27 2006, has been developed and is operated by CNES, with the contribution of Austria, Belgium, Brasil, ESA, Germany and Spain.

Kjeldsen et al. (2005) with seismic data from the HARPS spectrograph (Mosser et al. 2005).

Mode amplitudes in terms of *luminosity* fluctuations have also been derived from the CoRoT data for 17 radial orders. These data provide us with not only a constraint on the maximum of the mode amplitude but also with the frequency dependence. The relative luminosity amplitudes $\delta L/L$ are linearly related to the velocity amplitudes. This ratio is determined by the solution of the *non-adiabatic* pulsation equations and is independent of the stochastic excitation model (see Houdek et al. 1999). Such a non-adiabatic calculation requires us to take into account, not only the radiative damping, but also the coupling between the pulsation and the turbulent convection. However, there are currently very significant uncertainties concerning the modeling of this coupling (for a recent review see Houdek 2008). We relate further for the sake of simplicity the mode luminosity amplitudes to computed mode velocity amplitudes by assuming adiabatic oscillations as Kjeldsen & Bedding (1995). Such a relation is calibrated in order to reproduce the helioseismic data.

The comparison between theoretical values of the mode amplitudes (both in terms of surface velocity and intensity) constitutes a test of the stochastic excitation model with a star significantly different from the Sun and α Cen A. In addition it is also possible to test the validity of the calibrated quasi-adiabatic relation, since both mode amplitudes, in terms of surface velocity and intensity, are available for this star.

This paper is organized as follows: we describe in Sect. 2 the way mode amplitudes in terms of surface velocity v_s are derived from the theoretical values of \mathcal{P} and from the measured mode linewidths (Γ). Then, we compare the theoretical values of the mode surface velocity with the seismic constraint obtained from HARPS observations. We describe in Sect. 3 the way mode amplitudes in terms of intensity fluctuations $\delta L/L$ are derived from theoretical values of v_s and compare $\delta L/L$ with the seismic constraints obtained from the CoRoT observations. Finally, Sects. 4 and 5 are dedicated to a discussion and conclusion respectively.

2. Surface velocity mode amplitude

2.1. Derivation of the surface velocity mode amplitude

The intrinsic rms mode surface velocity v_s is related to the mode excitation rate $\mathcal{P}(\nu)$ and the mode linewidth $\Gamma(\nu)$ according to (see, e.g., Baudin et al. 2005):

$$v_s(r_h, \nu) = \sqrt{\frac{\mathcal{P}}{2\pi \mathcal{M}_h \Gamma}} \quad (1)$$

where \mathcal{P} is the mode excitation rate derived as described in Paper I, Γ is the mode full width at half maximum (in ν), $\nu = \omega_{\text{osc}}/2\pi$ the mode frequency and \mathcal{M}_h is the mode mass defined as:

$$\mathcal{M}_h = \frac{I}{\xi_r^2(r_h)} \quad (2)$$

where I is the mode inertia (see Eq. (2) of Paper I), ξ_r the radial mode eigendisplacement, $r_h \equiv R + h$ the layer in the atmosphere where the mode is measured in radial velocity, R the radius at the photosphere (i.e. at $T = T_{\text{eff}}$) and h the height above the photosphere.

In Sect. 2.2 we will compare estimated values of v_s with the seismic constraint obtained by Mosser et al. (2005) with the HARPS spectrograph. We therefore need to estimate v_s at the layer h where the HARPS spectrograph is the most sensitive to

the mode displacement. As discussed by Samadi et al. (2008a), the seismic measurements obtained with HARPS spectrograph are likely to arise from the optical depth $\tau_{500 \text{ nm}} \approx 0.013$, which corresponds to the depth where the potassium (K) spectral line is formed. We then compute the mode mass at the layer h associated with the optical depth $\tau_{500 \text{ nm}}$ (Christensen-Dalsgaard & Gough 1982). For the model with $[\text{Fe}/\text{H}] = 0$ (resp. $[\text{Fe}/\text{H}] = -1$) this optical depth corresponds to $h \approx 390$ km (resp. $h \approx 350$ km).

For the mode linewidth Γ we use the seismic measurement obtained from the seismic analysis of the CoRoT data performed by Benomar et al. (2009). This seismic analysis combined the two CoRoT runs available for HD 49933. Two different approaches were considered in this analysis: one based on the maximum likelihood estimator and the second one using the Bayesian approach coupled with a Markov Chains Monte Carlo algorithm. The Bayesian approach remains in general more reliable even in low signal-to-noise conditions. Nevertheless, in terms of mode amplitudes, mode heights and mode linewidths, both methods agree within $1-\sigma$. We will consider here the seismic parameters and associated error bars obtained on the basis of the Bayesian approach.

2.2. Comparison with the HARPS measurements

The seismic analysis in velocity has been performed by Mosser et al. (2005) using data from the HARPS spectrograph. The quality of these data is too poor to perform a direct comparison between the observed spectrum and the calculated amplitude spectrum (v_s , Eq. (1)). Indeed, the observed spectrum is highly affected by the day aliases. Furthermore, the quality of the data does not allow to isolate individual modes, in particular modes of a different angular degree (ℓ). A consequence is that energies of modes which are close in frequency are mixed.

In order to measure the oscillation amplitude in a way that is independent of these effects, we have followed the method introduced by Kjeldsen et al. (2005, see also Kjeldsen et al. 2008). This method consists in deriving the oscillation amplitudes from the oscillation power density spectrum smoothed over typically four times the large separation (i.e. four radial orders). Next, we multiply this smoothed spectrum by a coefficient in order to convert the *apparent* amplitudes into *intrinsic* amplitudes. This coefficient takes into account the spatial response function of the angular degrees $\ell = 0-3$ (see Kjeldsen et al. 2008). We have checked that the sensitivity of the visibility factor with the limb-darkening law is significantly smaller in comparison with the error associated with the Mosser et al. (2005) seismic measurements. The amplitude spectrum v_{HARPS} derived following Kjeldsen et al. (2005) is shown in Fig. 1. The $1-\sigma$ error bar associated with each values of v_{HARPS} is constant and equal to $\Delta v_{\text{HARPS}} = 7$ cm/s.

The maximum of v_{HARPS} reaches $V_{\text{max}} = 50.2 \pm 7$ cm/s. By comparison, Mosser et al. (2005) found a maximum of 40 ± 10 cm/s, which once converted into *intrinsic* amplitude represents a maximum of 42 ± 10 cm/s. The difference between the two values is within the $1-\sigma$ error bars. The different value found by Mosser et al. (2005) can be explained by the way the maximum of the mode amplitude was derived. Indeed, Mosser et al. (2005) have constructed synthetic time series based on a theoretical low degree p-modes eigenfrequency pattern and theoretical mode lines widths (Houdek et al. 1999). The maximum amplitudes were assumed to follow a Gaussian distribution in frequency. Using a Monte-Carlo approach, the maximum amplitude was then determined in order to obtain comparable energy per frequency bin in the synthetic and observed spectra. On the

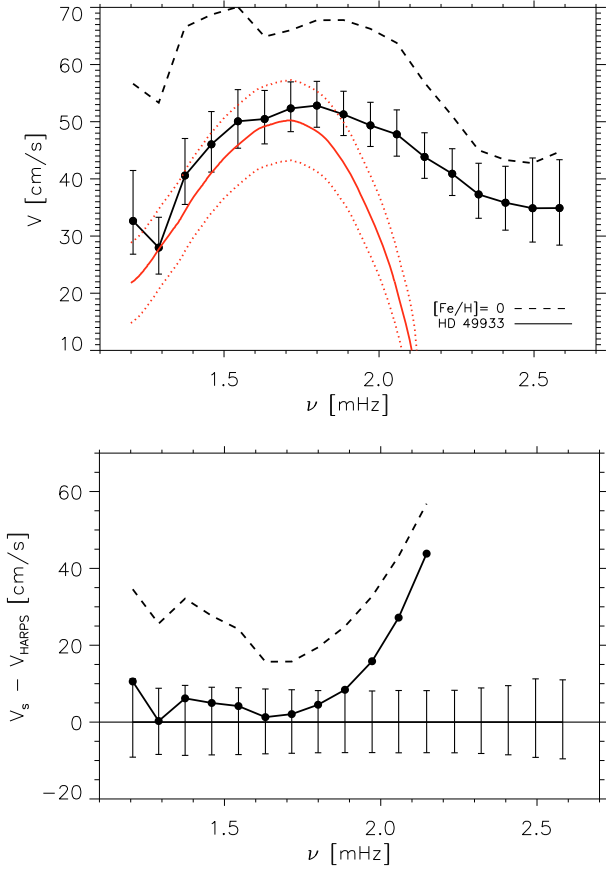


Fig. 1. *Top:* intrinsic mode surface velocity as a function of the mode frequency (ν). The filled circles connected by the thick solid line correspond to the mode surface velocity (v_s) derived for HD 49933 according to Eq. (1), where the mode excitation rates \mathcal{P} are derived as explained in Paper I and the mode linewidths and their associated error bars are derived by Benomar et al. (2009) from the CoRoT data. The thick dashed line corresponds to the mode velocity associated with the model with $[\text{Fe}/\text{H}] = 0$. The thick and red solid line corresponds to the amplitude spectrum derived from the seismic observations obtained with the HARPS spectrograph (see text). The dotted line corresponds to the $1\text{-}\sigma$ domain associated with this measurement. *Bottom:* differences between v_s and v_{HARPS} . The $1\text{-}\sigma$ error bars correspond to $\sigma_v \equiv \sqrt{\Delta v_s^2 + \Delta v_{\text{HARPS}}^2}$ (see text).

other hand, except for the mode response function, the method by Kjeldsen et al. (2005) does not impose a priori constraints concerning the modes. This method can then be considered to be more reliable than the method by Mosser et al. (2005).

We compare in Fig. 1 v_{HARPS} with the calculated mode surface velocity v_s (Eq. (1)). However, in order to have a consistent comparison, we have smoothed v_s quadratically over four radial orders. We note Δv_s the $1\text{-}\sigma$ error bars associated with v_s . They are derived from $\Delta\Gamma$, the $1\text{-}\sigma$ error bars associated with Γ . As pointed out in Paper I, the uncertainty related to our knowledge of the metal abundance Z for HD 49933 results in an uncertainty about the determination of \mathcal{P} . However, in terms of amplitude, this uncertainty is of the order of 5%; this is negligible compared to the uncertainty that arises from $\Delta\Gamma$ (ranging between 25% to 50% in terms of amplitude).

The difference between computed values and observations is shown in the bottom panel of Fig. 1. This difference must be

compared with σ_v , the $1\text{-}\sigma$ interval resulting from the errors associated with v_s and this in turn associated with v_{HARPS} , that is $\sigma_v \equiv \sqrt{\Delta v_s^2 + \Delta v_{\text{HARPS}}^2}$. As seen in Fig. 1, except at high frequency ($\nu \gtrsim 1.9$ mHz), the theoretical v_s lie well in the $1\text{-}\sigma$ domain. However, there is a clear disagreement at high frequencies where the computed mode surface velocities overestimate the observations. This disagreement is attributed to the assumptions in the theoretical model of stochastic excitation (see Sect. 4.5).

Assuming the 3D model with the solar abundance results in significantly larger v_s . In that case the differences between computed v_s and the seismic constraint are in general larger than $2\text{-}\sigma_v$. This shows that ignoring the metal abundance of HD 49933 would result in a larger discrepancy between v_s and v_{HARPS} .

3. Amplitudes of mode in intensity

3.1. Derivation of mode amplitudes in intensity

Fluctuations of the luminosity L due to variations of the stellar radius can be neglected since we are looking at high n order modes; accordingly the bolometric mode intensity fluctuations δL are mainly due to variations of the effective temperature, that is:

$$\frac{\delta L}{L} = 4 \frac{\delta T_{\text{eff}}}{T_{\text{eff}}}. \quad (3)$$

As in Kjeldsen & Bedding (1995), we now assume that δT_{eff} is proportional to the variation of the temperature induced by the modes at the photosphere (i.e. at $T = T_{\text{eff}}$). This assumption is discussed in Sect. 4.3. Assuming further low degree ℓ and *adiabatic* oscillations, one can derive a relation between $\delta T_{\text{eff}}/T_{\text{eff}}$ and the radial mode velocity v that is:

$$\frac{\delta T_{\text{eff}}}{T_{\text{eff}}} = (\Gamma_3 - 1) \left| \frac{1}{\omega_{\text{osc}} \xi_r} \frac{d\xi_r}{dr} \right| v \quad (4)$$

where $\Gamma_3 = \nabla_{\text{ad}} \Gamma_1 + 1$, ∇_{ad} is the adiabatic temperature gradient, $\Gamma_1 = \left(\frac{\partial \ln P_y}{\partial \ln \rho} \right)_s$, ξ_r the radial mode eigendisplacement, and v the mode velocity at the photosphere. Finally, according to Eqs. (3) and (4), one has:

$$\left(\frac{\delta L}{L} \right) = 4\beta (\Gamma_3 - 1) \left| \frac{1}{\omega_{\text{osc}} \xi_r} \frac{d\xi_r}{dr} \right| v \quad (5)$$

where v is computed using Eq. (1) with $h = 0$ (the photosphere), that is:

$$v = \sqrt{\frac{\mathcal{P}}{2\pi \mathcal{M}_0 \Gamma}} \quad (6)$$

where \mathcal{M}_0 is the mode mass evaluated at the photosphere ($h = 0$).

In Eq. (5), β is a free parameter introduced so that Eq. (5) gives, in the case of the solar p modes, the correct maximum in $\delta L/L$. Indeed, Eq. (5) applied to the case of the solar p modes, overestimates by ~ 10 times the mode amplitudes in intensity. This important discrepancy is mainly a consequence of the adiabatic approximation.

From the SOHO/GOLF seismic data (Baudin et al. 2005), we derive the maximum of the solar mode (intrinsic) surface velocity, that is 32.6 ± 2.6 cm/s. Then, using ξ_r , we infer the maximum of mode velocity at the photosphere, that is 18.5 ± 1.5 cm/s. According to Michel et al. (2009), the maximum of the solar mode (bolometric) amplitude in intensity is equal to

2.53 ± 0.11 ppm. Then, by applying Eq. (5) in the case of the Sun, we derive the scaling factor $\beta = 0.103 \pm 10\%$. We have checked that this calibration depends very little on the choice of the chemical mixture (see also Sect. 4.3). We then adopt this value for the case of HD 49933.

3.2. The mode intensity fluctuations measured by CoRoT

The seismic analysis by Benomar et al. (2009) provides the apparent amplitude A_ℓ of the $\ell = 0-2$ modes and the associated error bars. However, the CoRoT measurements A_ℓ correspond to relative intensity fluctuations in the CoRoT pass-band. Furthermore, the *observed* (apparent) mode amplitudes depend on the degree ℓ . Therefore, to transform them into *bolometric* and *intrinsic* intensity fluctuations normalised to the radial modes, we divide them by the CoRoT response function, R_ℓ , derived here for $\ell = 0-2$, following Michel et al. (2009). The adopted values for R_ℓ are: $R_0 = 0.90$, $R_1 = 1.10$, and $R_2 = 0.66$. We finally derive the bolometric intensity fluctuations normalised to the radial modes according to:

$$(\delta L/L)_{\text{CoRoT}} = \sqrt{\frac{1}{3} \left(\left(\frac{A_0}{R_0} \right)^2 + \left(\frac{A_1}{R_1} \right)^2 + \left(\frac{A_2}{R_2} \right)^2 \right)}. \quad (7)$$

We shall stress that the differences between the amplitudes derived by Benomar et al. (2009) and by Appourchaux et al. (2008) are smaller than the $1-\sigma$ error bars. Furthermore, these amplitudes are in agreement with those found by Michel et al. (2008), using a different technique.

3.3. Comparison with the CoRoT measurements

We compute the mode amplitudes in terms of bolometric intensity fluctuations, $\delta L/L$, according to Eqs. (5) and (6) (see Sect. 3.1). As for v_s , the uncertainty associated with the measured mode linewidths, Γ , put uncertainties on the theoretical values of $\delta L/L$. Furthermore, the uncertainty associated with the calibrated factor β (see Sect. 3.1) also puts an additional uncertainty on $\delta L/L$. From here on, $\Delta(\delta L/L)$ will refer to the $1-\sigma$ uncertainties associated with $\delta L/L$. Accordingly, we have $\Delta(\delta L/L) = (\delta L/L) \sqrt{\left(\frac{1}{2} \Delta\Gamma/\Gamma\right)^2 + (\Delta\beta/\beta)^2}$, where $\Delta\Gamma$ (reps. $\Delta\beta$) is the $1-\sigma$ uncertainty associated with Γ (resp. β).

Figure 2 compares, as a function of the mode frequency, $\delta L/L$ to the CoRoT measurements: $(\delta L/L)_{\text{CoRoT}}$. The difference between our calculations and the observations is shown in the bottom panel. As for the velocity, this difference must be compared with σ_L , the $1-\sigma$ interval resulting from the association of the $1-\sigma$ error bars $\Delta(\delta L/L)$ and the $1-\sigma$ error, $\Delta(\delta L/L)_{\text{CoRoT}}$, associated with the CoRoT measurements. Accordingly, we have $\sigma_L \equiv \sqrt{a^2 + b^2}$ where $a \equiv \Delta(\delta L/L)$ and $b \equiv \Delta(\delta L/L)_{\text{CoRoT}}$.

As seen in Fig. 2, below $\nu \lesssim 1.9$ mHz, values of $\delta L/L$ are within approximately $1-\sigma_L$ in agreement with $(\delta L/L)_{\text{CoRoT}}$. However, above $\nu \sim 1.9$ mHz, the differences between $\delta L/L$ and $(\delta L/L)_{\text{CoRoT}}$ exceed $2-\sigma_L$.

Assuming a solar abundance ($[\text{Fe}/\text{H}] = 0$) results in a clear overestimation of $\Delta(\delta L/L)_{\text{CoRoT}}$. Furthermore, calculations which assume the Grevesse & Noels (1993) chemical mixture result in mode amplitudes larger by $\sim 15\%$.

Both in terms of intensity and velocity, differences between the calculated mode amplitudes and those derived from the observations (CoRoT and HARPS) are approximately within the $1-\sigma$ domain below $\nu \sim 1.9$ mHz. This then validates the

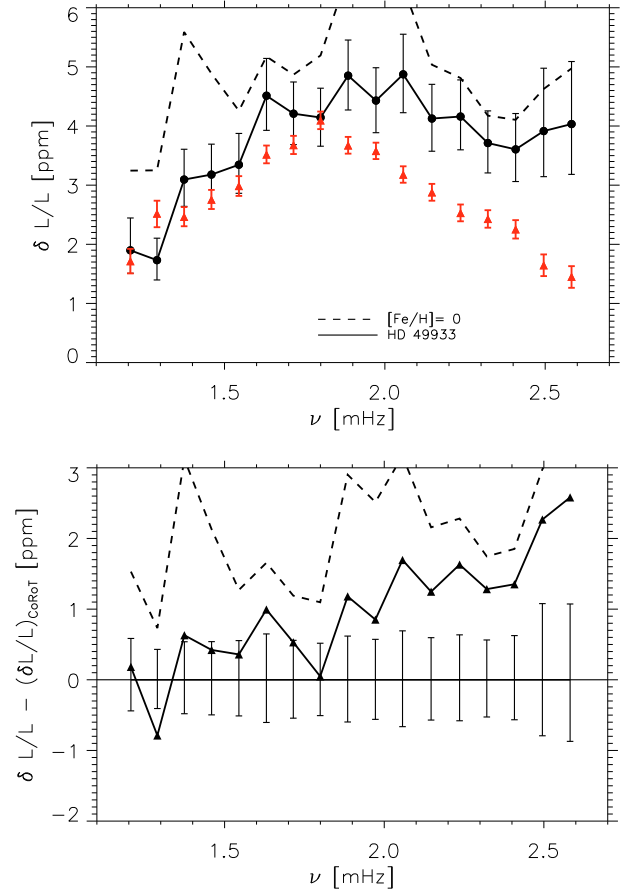


Fig. 2. *Top:* mode bolometric amplitude in intensity as a function of the mode frequency (ν). The filled circles connected by the thick solid line correspond to the mode amplitudes in intensity, $\delta L/L$, derived for HD 49933 according to Eqs. (5) and (1) where the mode surface velocity v is evaluated at the photosphere. The thick dashed solid line corresponds to the mode amplitude in intensity associated with the model with $[\text{Fe}/\text{H}] = 0$. The red triangles and associated error bars correspond to the mode amplitudes in intensity, $(\delta L/L)_{\text{CoRoT}}$, obtained from the CoRoT data (Benomar et al. 2009). These measurements have been translated into bolometric amplitudes following Michel et al. (2009). *Bottom:* same as top for the difference between $\delta L/L$ and $(\delta L/L)_{\text{CoRoT}}$. The $1-\sigma$ error bars correspond here to $\sqrt{a^2 + b^2}$ where $a \equiv \Delta(\delta L/L)$ and $b \equiv \Delta(\delta L/L)_{\text{CoRoT}}$ (see text).

intensity-velocity relation given by Eq. (5) at the level of the current seismic precision.

The maximum $(\delta L/L)$ peaks at $\nu_{\text{max}} \approx 1.9$ mHz and the maximum of v_s at $\nu_{\text{max}} \approx 1.8$ mHz. By comparison, $(\delta L/L)_{\text{CoRoT}}$ peaks at $\nu_{\text{max}} \approx 1.8$ mHz and v_{HARPS} peaks at $\nu_{\text{max}} \approx 1.7$ mHz. The difference in ν_{max} between the observations (CoRoT and HARPS) and the model can be partially a consequence of the clear tendency at high frequency toward over-estimated amplitudes compared to the observations.

4. Discussion

4.1. Uncertainties in the knowledge of the fundamental parameters of HD 49933

Uncertainties in the knowledge of T_{eff} and $\log g$ place uncertainties on the theoretical values of \mathcal{P} and hence on the mode

amplitudes (v_s and $\delta L/L$). However, estimating these uncertainties would require the consideration of 3D models with a T_{eff} and a $\log g$ that depart more than $1\text{-}\sigma$ from the values adopted in our modeling, i.e. $T_{\text{eff}} = 6750$ K and $\log g = 4.25$. This is beyond the scope of our efforts since such 3D models are not yet available.

4.2. Influence of the mode mass

As discussed in details in Samadi et al. (2008a), the computed mode surface velocities v_s significantly depend on the choice of the height h in the atmosphere where the mode masses are evaluated. According to Samadi et al. (2008a), seismic measurements performed with the HARPS spectrograph reflect conditions slightly below the formation depth of the K line. Accordingly, we have evaluated by default the mode masses at the optical depth where the K line is expected to be formed (i.e. $\tau_{500\text{ nm}} \simeq 0.013$), which corresponds, for our 3D models, to a height of about 350 km above the photosphere. We can evaluate how sensitive we are to the choice of h . Indeed, evaluating the mode mass at the photosphere results in values of v_s which are about 15% lower and hence would reduce the discrepancy with the HARPS observations. On the other hand, evaluating the mode mass one pressure scale height (~ 300 km at the photosphere) above $h = 350$ km results in an increase of v_s of about 10%. A more rigorous approach to derive the different heights in the atmosphere where the measurements are sensitive would require a dedicated modeling (see a discussion in Samadi et al. 2008a).

4.3. The intensity-velocity relation

Sensitivity to the location: the derivation of Eq. (4) (or equivalently Eq. (5)) is based on the assumption that $\delta T_{\text{eff}} \propto \delta T|_{T=T_{\text{eff}}}$ (see Sect. 3.1). This is quite a arbitrary simplification. In order to check how sensitive our results are to this assumption, we have computed Eqs. (5) and (6) for two different positions in the atmosphere. The first position, $h = h_1$, is chosen one pressure scale height ($\simeq 300$ km) above the photosphere, which corresponds to an optical depth of $\tau \sim 0.02$. The second position, $h = h_2$, is chosen one pressure scale height beneath the photosphere, that is around $\tau \sim 200$. For both positions, the mode amplitudes with frequencies below ~ 1.9 mHz are almost unchanged. Concerning the amplitudes of modes with frequencies above ~ 1.9 mHz, they are increased by up to $\sim 20\%$ when $h = h_1$ and are in turn almost unchanged when $h = h_2$. Since the fluctuations of L induced by the oscillations are mostly due to temperature changes that occur around an optical depth of the order of the unit, we can conclude that our calculations are almost insensitive to the choice of the layer in the visible atmosphere where δT is evaluated.

Non-adiabatic effects: the modes are measured at the surface of the star where non-adiabatic interactions between the modes and convection as well as radiative losses of the modes are important. Assuming Eq. (4) is then a crude approximation. In fact, it is clearly non-valid in the case of the Sun since it results in a severe over-estimation of the solar mode amplitudes in intensity (see Sect. 3.1). Avoiding this approximation requires non-adiabatic eigenfunctions computed with a time-dependent convection model. However, such models (e.g. Grigahcène et al. 2005; Balmforth 1992) are subject to large uncertainties, and there is currently no consensus about the non-adiabatic mechanisms that play a significant role (see e.g. the recent review by

Houdek 2008). For instance, parameters are usually introduced in the theories so that they cannot be used in a predictive way.

In the present study, we adopt by default the adiabatic approximation and introduce in Eq. (5) the parameter β calibrated with helioseismic data. We show here that despite the deficiency of the quasi-adiabatic approximation, it nevertheless provides the correct scaling, at least at low frequency and at the level of the present seismic precisions.

As an alternative approach, comparing the spectrum obtained from the 3D models in intensity with that obtained in velocity can provide valuable information concerning the intensity-velocity relation, in particular concerning the departure from the adiabatic approximation and the sensitivity to the surface metal abundance. We have started to carry out such a study. For the velocity, the (few) acoustic modes trapped in the simulated boxes can be extracted and their properties measured. But this was impossible to do for the intensity with the simulations at our disposal because the computed spectrum for the intensity is dominated by the granulation background. As a consequence it is not possible to extract the mode amplitudes in intensity with sufficient accuracy. A comparison between the spectra obtained from the 3D models requires a much longer time series (work in progress).

Sensitivity to the metal abundance: we have shown in this study how the mode amplitudes in the velocity are sensitive to the surface metal abundance. An open question is how sensitive is the intensity-velocity relation in general to the metal abundance? A theoretical answer to this question would require a realistic and validated non-adiabatic treatment. The pure numerical approach mentioned above can also in principle provide some answers to this question. However, as discussed above, this approach is not applicable with the time series at our disposal. Concerning the quasi-adiabatic relation of Eq. (5): a change of the metal abundance has a direct effect on Γ_3 and an indirect effect on the properties of the (radial) eigen-displacement ξ_r . However, the comparison between the metal-poor 3D model (S1) and the 3D model with the solar abundances (S0) shows that – at a fixed frequency ω_{osc} – the ratio $(\delta L/L)/v$, which is equal to $4\beta(\Gamma_3 - 1)(d\xi_r/dr)/(\xi_r \omega_{\text{osc}})$, is almost unchanged between S0 and S1 (the differences are less than $\sim 1\%$). In conclusion, the quasi-adiabatic relation of Eq. (5) depends very weakly on the surface metal abundance. Accordingly, the choice of the solar chemical mixture has a negligible impact on the value of the calibration factor β .

4.4. The solar case

As seen in this study, the surface metal abundance has a pronounced effect on the mode excitation rates. One may then wonder about the previous validation of the theoretical model of stochastic excitation in the case of the Sun (Belkacem et al. 2006; Samadi et al. 2008b). Indeed, this validation was carried out with the use of a solar 3D model based on an “old” solar chemical mixture (namely those proposed by Anders & Grevesse 1989) while the “new” chemical mixture by Asplund et al. (2005) is characterized by a significantly lower metal abundance.

In order to address this issue, we have first considered two global 1D solar models. One model has an “old” solar abundance (Grevesse & Noels 1993, model M_{old} hereafter) while the second one has the “new” abundances (Asplund et al. 2005, model M_{new} hereafter). At the surface where the excitation

occurs, the density of the solar model M_{new} is only $\sim 5\%$ lower compared to the model M_{old} . According to the arguments developed in Paper I, this difference in the density must imply a difference in the convective velocities (\bar{u}) of the order of $\sim (\rho_{\text{old}}/\rho_{\text{new}})^{1/3}$, where ρ_{old} (resp. ρ_{new}) is the surface density associated with M_{old} (resp. M_{new}). Accordingly, \bar{u} is expected to be $\sim 1.7\%$ higher for M_{new} compared to M_{old} .

The next question is what is the change in the solar mode excitation rates induced by the above difference in \bar{u} ? We have computed the solar mode excitation rates exactly in the same manner as for HD 49333 by using a solar 3D simulations based on the “old” abundances. We obtained a rather good agreement with the different helioseismic data (see the result in Samadi et al. 2008b). To derive the solar mode excitations expected with the “new” solar abundance, we have proceeded in a similar way as the one done in Paper I: we have increased the convective velocity \bar{u} derived from the solar 3D model by 2% while keeping the kinetic flux constant (see details in Paper I). This increase of $\sim 2\%$ of \bar{u} results in an increase of $\sim 10\%$ of the mode excitation rates. This increase is significantly lower than the current uncertainties associated with the different helioseismic data (Baudin et al. 2005; Samadi et al. 2008b).

4.5. Discrepancy at high frequency

The discrepancy between theoretical calculations and observations is particularly pronounced at high frequency. This discrepancy may be attributed to a canceling between the entropy and the Reynolds stress contributions (see Sect. 4.5.1) or the “scale length separation” assumption (see Sect. 4.5.2).

4.5.1. Canceling between the entropy and the Reynolds stress contributions

The relative contribution of the entropy fluctuations to the excitation is found to be about 30% of the total excitation. This is two times larger than in the case of the Sun ($\sim 15\%$). This can be explained by the fact HD 49933 is significantly hotter than the Sun and, as pointed-out by Samadi et al. (2007), the larger $(L/M) \propto T_{\text{eff}}^4/g$, the more important the relative contribution of the entropy. Although more important than in the Sun, the contribution of the entropy fluctuations remains relatively smaller than the uncertainties associated with the current seismic data. This is illustrated in Fig. 3: the difference between theoretical mode amplitudes which take into account only the Reynolds stress contribution (C_R^2 , see Eq. (3) of Paper I) and those that include both contributions (entropy and Reynolds stress) is lower than σ_v . In terms of amplitudes, the entropy fluctuations contribute only $\sim 15\%$ of the global amplitude. This is significantly smaller than the uncertainties associated with the current seismic measurements. Seismic data of a better quality are then needed to constrain the entropy contribution and its possible canceling with the Reynolds stress.

Numerical simulations show some cancellation between the entropy source term and the one due to the Reynolds stress (Stein et al. 2004). However, in the present theoretical model of stochastic excitation, the cross terms between the entropy fluctuations and the Reynolds stresses vanish (see Samadi & Goupil 2001). This is a consequence of the different assumptions concerning the entropy fluctuations (see Samadi & Goupil 2001; see also the recent discussion in Samadi et al. 2008b). Accordingly, the entropy source term is included as a source independent from the Reynolds stress contribution. As suggested by

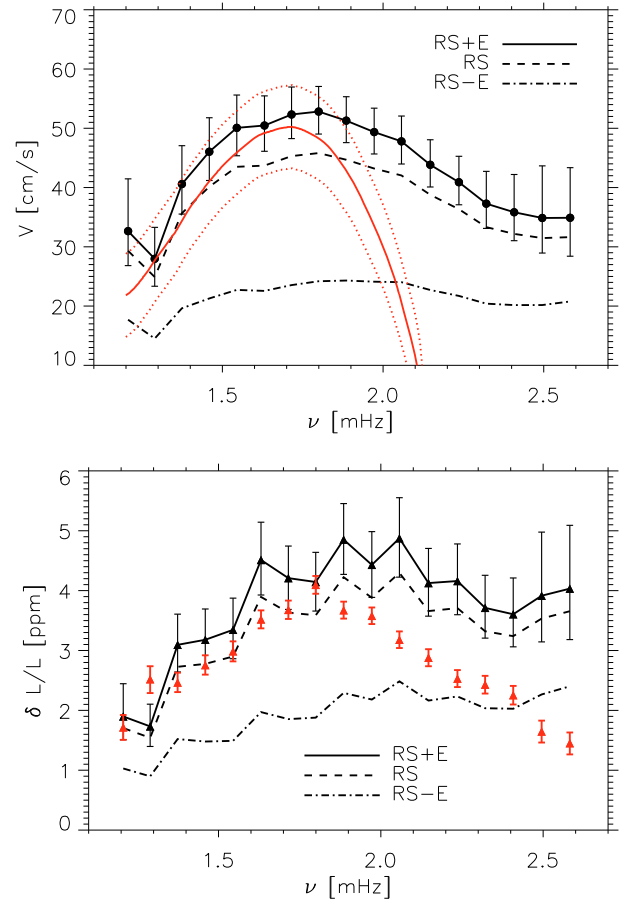


Fig. 3. *Top:* same as Fig. 1. The thin dashed line corresponds to a calculation that takes only the contribution of the Reynolds stress into account. The dot-dashed line corresponds to a calculation in which we have assumed that the contribution of the Reynolds stress interferes totally with that of the entropy fluctuations (see text). The thick solid line has the same meaning as in Fig. 1. *Bottom:* same as top for $\delta L/L$. The triangles and associated error bars have the same meaning as in Fig. 2.

Houdek (2006), a partial canceling between the entropy fluctuations and the Reynolds stress can decrease the mode amplitudes of F-type stars and reduce the discrepancy between the theoretical calculations and the observations.

There is currently no theoretical description of these interferences. In order to have an upper limit of the interferences, we assume that both contributions *locally* and *fully* interfere. This assumption leads to the computation of the excitation rates per unit mass as:

$$\frac{d\mathcal{P}}{dm} = \left(\frac{d\mathcal{P}}{dm}\right)_{\text{RS}} + \left(\frac{d\mathcal{P}}{dm}\right)_{\text{E}} - 2\sqrt{\left(\frac{d\mathcal{P}}{dm}\right)_{\text{RS}} \left(\frac{d\mathcal{P}}{dm}\right)_{\text{E}}} \quad (8)$$

where $(d\mathcal{P}/dm)_{\text{RS}}$ and $(d\mathcal{P}/dm)_{\text{E}}$ are the contributions per unit mass of the Reynolds stress and entropy respectively. The result is presented in Fig. 3 in terms of velocity (top panel) and in terms of intensity (bottom panel). The mode amplitudes are decreased by up to $\sim 55\%$. In that case, $(\delta L/L)_{\text{CoRoT}}$ is systematically under-estimated. Obviously, a partial canceling between the entropy contribution and the Reynolds stress would result in a smaller decrease.

We have assumed here that the cancellation between the two terms is independent of the mode frequency (see Eq. (8)).

However, according to [Stein et al. \(2004\)](#), the level of the cancellation depends on the frequency (see their Fig. 8). In particular, for F-type stars, the cancellation is expected to be more important around and above the peak frequency.

As a conclusion, the existence of a partial canceling between the entropy fluctuations and the Reynolds stress can decrease the mode amplitude and could improve the agreement with the seismic observations at high frequency. However, there is currently no theoretical modeling of the interference between these two terms. Further theoretical developments are required.

4.5.2. The “scale length separation” assumption

The “scale length separation” assumption (see the review by [Samadi et al. 2008b](#)) consists of the assumption that the eddies contributing effectively to the driving have a characteristic length scale smaller than the mode wavelength. This assumption is justified for a low Mach number (M_t). However, this approximation is less valid in the super-adiabatic region where M_t reaches a maximum (for the Sun M_t is up to 0.3) and accordingly affects the high-frequency modes more. This approximation is then expected to be even more questionable for stars hotter than the Sun, since M_t increases with T_{eff} . This spatial separation can be avoided, however if the kinetic energy spectrum associated with the turbulent elements ($E(k)$) is properly coupled with the spatial dependence of the modes (work in progress). In that case, we expect a more rapid decrease of the driving efficiency with increasing frequency than in the present formalism where the spatial dependence of the modes is totally decoupled from $E(k)$ (i.e. “scale length separation”).

5. Conclusion

From the mode linewidths measured by CoRoT and theoretical mode excitation rates derived for HD 49933, we have derived the expected mode surface velocities v_s which we have compared with v_{HARPS} , the mode velocity spectrum derived from the seismic observations obtained with the HARPS spectrograph ([Mosser et al. 2005](#)). Except at high frequency ($\nu \gtrsim 1.9$ mHz), the agreement between computed v_s and v_{HARPS} is within the $1\text{-}\sigma$ domain associated with the seismic data from the HARPS spectrograph. However, there is a clear tendency to overestimate v_{HARPS} above $\nu \sim 1.9$ mHz.

Using a *calibrated* quasi-adiabatic approximation to relate the mode velocity to the mode amplitude in intensity (Eq. (5)), we have derived for the case of HD 49933 the expected mode amplitudes in intensity. Computed mode intensity fluctuations, $\delta L/L$, are within $1\text{-}\sigma$ in agreement with the seismic constraints derived from the CoRoT data ([Benomar et al. 2009](#)). However, as for the velocity, there is a clear tendency at high frequency ($\nu \gtrsim 1.9$ mHz) towards over-estimated $\delta L/L$ compared to the CoRoT observations.

Calculations that assume a solar surface metal abundance result, both in velocity and in intensity, in amplitudes larger by $\sim 35\%$ around the peak frequency ($\nu_{\text{max}} \simeq 1.8$ mHz) and by up to a factor of two at lower frequency. It follows that, ignoring the current surface metal abundance of the star results in a more severe over-estimation of the computed amplitudes compared with observations. This illustrates the importance of taking the surface metal abundance of the solar-like pulsators into account when modeling the mode driving. In addition, we point out that the [Grevesse & Noels \(1993\)](#) solar chemical mixture results in mode amplitudes larger by about 15% with respect to calculations that assume the “new” solar abundance by

[Asplund et al. \(2005\)](#). However, this increase remains significantly smaller than the uncertainties associated with current seismic measurements.

Since both mode amplitudes in terms of surface velocity and intensity are available for this star, it was possible to test the validity of the calibrated quasi-adiabatic relation (Eq. (5)). Our comparison shows that this relation provides the correct scaling, at least at the level of the present seismic precisions.

Both in terms of surface velocity and of intensity, the differences between predicted and observed mode amplitudes are within the $1\text{-}\sigma$ uncertainty domain, except at high frequency. This result then validates for low frequency modes the basic underlying physical assumptions included in the theoretical model of stochastic excitation for a star significantly different in effective temperature, surface gravity, turbulent Mach number (M_t) and metallicity compared to the Sun or α Cen A.

As discussed in Sect. 4, the clear discrepancy between predicted and observed mode amplitudes seen at high frequency may have two possible origins: first, a canceling between the entropy contribution and the Reynolds stress is expected to occur and to be important around and above the frequency of the maximum of the mode excitation rates (see Sect. 4.5.1). Second, the assumption called the “scale length separation” ([Samadi et al. 2008b](#)) may also result in an over-estimation of the mode amplitudes at high frequency (see Sect. 4.5.2). These issues will be investigated in a forthcoming paper.

Acknowledgements. The CoRoT space mission, launched on December 27 2006, has been developed and is operated by CNES, with the contribution of Austria, Belgium, Brasil, ESA, Germany and Spain. We are grateful to the referee for his pertinent comments. We are indebted to J. Leibacher for his careful reading of the manuscript. K.B. acknowledged financial support from Liège University through the Subside Fédéral pour la Recherche 2009.

References

- Anders, E., & Grevesse, N. 1989, *Geochim. Cosmochim. Acta*, 53, 197
 Apourchoux, T., Michel, E., Auvergne, M., et al. 2008, *A&A*, 488, 705
 Asplund, M., Grevesse, N., & Sauval, A. J. 2005, in *Cosmic Abundances as Records of Stellar Evolution and Nucleosynthesis*, ed. T. G. Barnes, III, & F. N. Bash, ASP Conf. Ser., 336, 25
 Balmforth, N. J. 1992, *MNRAS*, 255, 603
 Baudin, F., Samadi, R., Goupil, M.-J., et al. 2005, *A&A*, 433, 349
 Belkacem, K., Samadi, R., Goupil, M. J., Kupka, F., & Baudin, F. 2006, *A&A*, 460, 183
 Benomar, O., Baudin, F., Campante, T., et al. 2009, *A&A*, 507, L13
 Christensen-Dalsgaard, J., & Gough, D. O. 1982, *MNRAS*, 198, 141
 Grevesse, N., & Noels, A. 1993, in *Origin and Evolution of the Elements*, ed. N. Prantzos, E. Vangioni-Flam, & M. Cassé (Cambridge University Press), 15
 Grigahcène, A., Dupret, M.-A., Gabriel, M., Garrido, R., & Scuflaire, R. 2005, *A&A*, 434, 1055
 Houdek, G. 2006, in *Proceedings of SOHO 18/GONG 2006/HELAS I, Beyond the spherical Sun*, Published on CDROM, ESA SP, 624, 28.1
 Houdek, G. 2008, *Commun. Asteroseismol.*, 157, 137
 Houdek, G., Balmforth, N. J., Christensen-Dalsgaard, J., & Gough, D. O. 1999, *A&A*, 351, 582
 Kjeldsen, H., & Bedding, T. R. 1995, *A&A*, 293, 87
 Kjeldsen, H., Bedding, T. R., Butler, R. P., et al. 2005, *ApJ*, 635, 1281
 Kjeldsen, H., Bedding, T. R., Arentoft, T., et al. 2008, *ApJ*, 682, 1370
 Michel, E., Baglin, A., Auvergne, M., et al. 2008, *Science*, 322, 558
 Michel, E., Samadi, R., Baudin, F., et al. 2009, *A&A*, 495, 979
 Mosser, B., Bouchy, F., Catala, C., et al. 2005, *A&A*, 431, L13
 Samadi, R., & Goupil, M. 2001, *A&A*, 370, 136
 Samadi, R., Georgobiani, D., Trampedach, R., et al. 2007, *A&A*, 463, 297
 Samadi, R., Belkacem, K., Goupil, M. J., Dupret, M.-A., & Kupka, F. 2008a, *A&A*, 489, 291
 Samadi, R., Belkacem, K., Goupil, M.-J., Ludwig, H.-G., & Dupret, M.-A. 2008b, *Commun. Asteroseismol.*, 157, 130
 Samadi, R., Ludwig, H.-G., Belkacem, K., Goupil, M., & Dupret, M.-A. 2010, *A&A*, 509, A15 (Paper I)
 Stein, R., Georgobiani, D., Trampedach, R., Ludwig, H.-G., & Nordlund, Å. 2004, *Sol. Phys.*, 220, 229

Stochastic excitation of gravity modes in massive main-sequence stars

R. Samadi · K. Belkacem · M.J. Goupil · M.-A. Dupret ·
A.S. Brun · A. Noels

Received: 28 September 2009 / Accepted: 17 November 2009 / Published online: 1 December 2009
© Springer Science+Business Media B.V. 2009

Abstract We investigate the possibility that gravity modes can be stochastically excited by turbulent convection in massive main-sequence (MS) stars. We build stellar models of MS stars with masses $M = 10 M_{\odot}$, $15 M_{\odot}$, and $20 M_{\odot}$. For each model, we then compute the power supplied to the modes by turbulent eddies in the convective core (CC) and the outer convective zones (OCZ). We found that, for asymptotic gravity modes, the major part of the driving occurs within the outer iron convective zone, while the excitation of low n order modes mainly occurs within the CC. We compute the mode lifetimes and deduce the expected mode amplitudes. We finally discuss the possibility of detecting such stochastically-excited gravity modes with the CoRoT space-based mission.

Keywords Turbulence · Convection · Oscillations · Mode driving · Massive stars

1 Introduction

Stochastic excitation of *solar* gravity modes by turbulent convection has been recently studied in detail by Belkacem

et al. (2009b). The modelling performed by these authors put the theoretical amplitudes of solar gravity modes close to the SoHO/GOLF detection threshold. A new issue then arises: can we expect such stochastically-excited gravity modes to be more easily detectable in other stars than the Sun?

Main-sequence stars significantly more massive than the Sun are potentially interesting for seeking stochastically-excited modes. Indeed, stochastically-excited p modes have recently been detected in a massive star (Belkacem et al. 2009a). The question remains: can gravity modes be stochastically excited in such stars? Stars with mass above $M \approx 1.2 M_{\odot}$ have a convective core (CC hereafter) and the more massive the star, the higher is the eddies' kinetic energy in the CC. We therefore consider here the illustrative cases of massive main-sequence stars with masses $M = 10 M_{\odot}$, $15 M_{\odot}$, and $20 M_{\odot}$. Amplitudes of stochastically-excited gravity modes are computed following Belkacem et al. (2009b) as explained in Sect. 2. We describe in Sect. 3 the efficiency of the different driving regions. The results of our calculations are presented and commented on in Sect. 4, and our conclusions are summarized in Sect. 5. We finally discuss in Sect. 5 the possibility of detecting stochastically-excited gravity modes with the CoRoT space-based mission.

2 Mode amplitudes

We compute the mean-squared surface velocity for each *non-radial* mode according to (see e.g. Belkacem et al. 2009b, and references therein):

$$v_s^2 = \frac{\mathcal{P}}{2\eta\mathcal{M}} \quad (1)$$

R. Samadi (✉) · M.J. Goupil
Observatoire de Paris, LESIA, CNRS UMR 8109,
92195 Meudon, France
e-mail: reza.samadi@obspm.fr

K. Belkacem · M.-A. Dupret · A. Noels
Institut d'Astrophysique et de Géophysique, Université de Liège,
Allée du 6 Août 17-B, 4000 Liège, Belgium

A.S. Brun
DSM/DAPNIA/SAP, CEA Saclay, 91191 Gif-sur-Yvette Cedex,
France

where \mathcal{P} is the mode excitation rate, η the mode damping rate (which is equal to the inverse of the mode lifetime τ) and \mathcal{M} the mode mass. The latter is defined as

$$\mathcal{M} = \frac{I}{\xi_r^2(R_*) + \ell(\ell + 1)\xi_h^2(R_*)} \quad (2)$$

where I is the mode inertia, ℓ the mode angular degree, ξ_r and ξ_h respectively are the radial and the horizontal components of the mode eigendisplacement. Both quantities are evaluated here at the photosphere, i.e. at the radius $r = R_*$ where R_* is the stellar radius. The mode inertia is defined as $I = \int dm (\xi_r^2(r) + \ell(\ell + 1)\xi_h^2(r))$.

The mode amplitude in terms of the *intensity* (or brightness fluctuations) is then deduced at the photosphere according to (Dziembowski 1977; Pesnell 1990)

$$\frac{\delta L}{L} = 4 \frac{\delta T_{\text{eff}}}{T_{\text{eff}}} + 2 \frac{\delta R_*}{R_*} \quad (3)$$

where δL is the bolometric intensity fluctuation, δT_{eff} the effective temperature fluctuation, and δR_* the variation of the stellar radius for each given mode. As seen in (1), the modal amplitude is a balance between driving (\mathcal{P}) and damping (η). Determination of the mode amplitude then requires knowledge of \mathcal{P} (see Sect. 2.1) and η (see Sect 2.2).

2.1 Excitation rates (\mathcal{P})

Mode excitation rates are computed on the basis of the formalism due to Belkacem et al. (2008). This formalism is a generalization of the work of Samadi and Goupil (2001, SG01 hereafter) to non-radial modes. Two sources of driving are taken into account: the Reynolds stress tensor and the advection of the turbulent fluctuations of entropy by the turbulent motions (the “entropy source term”).

In the CC, the entropy contribution represents less than $\sim 10\%$ of the total excitation rates. This is because the gravity modes are evanescent within the CC. Accordingly, the second derivative of displacement eigenfunction is negligible and so is the entropy source term (see details in Belkacem et al. 2008, 2009b). On the other hand, in the outer convective zone (OCZ hereafter), this source term is not negligible since it represents up to $\sim 50\%$. This is a consequence of the fact that energy is inefficiently transported by convection within the OCZ. As a consequence, non-adiabatic fluctuations of the gas pressure are important compared to the turbulent pressure. For the sake of brevity we will not discuss further the entropy contribution.

When limited to Reynolds stresses, the excitation rates, \mathcal{P} , can be written as (see (21) of Belkacem et al. 2008)

$$\mathcal{P} = \frac{\pi^3}{2I} \int_0^M dm \frac{\rho_0 u_0^4}{k_0^3 \omega_0} \mathcal{R}(\vec{r}, m) \mathcal{S}_R(\omega_{\text{osc}}, m) \quad (4)$$

$$\begin{aligned} \mathcal{S}_R &= \frac{k_0^3 \omega_0}{u_0^4} \int_0^{+\infty} \frac{dk}{k^2} E^2(k) \\ &\times \int_{-\infty}^{+\infty} d\omega \chi_k(\omega + \omega_{\text{osc}}) \chi_k(\omega) \end{aligned} \quad (5)$$

where m is the local mass, ρ_0 the mean density, ω_{osc} the mode angular frequency, u_0 a characteristic velocity associated with the energy bearing eddies, \mathcal{S}_R the dimensionless source function associated with the Reynolds stress, $E(k)$ the spatial kinetic energy spectrum, χ_k the eddy-time correlation function, and k the wave number. The term $\mathcal{R}(r)$ depends on the eigenfunction, its expression is given in (23) of Belkacem et al. (2008). We have introduced, for convenience, the characteristic frequency $\omega_0 \equiv k_0 u_0$ and the characteristic wave number $k_0 \equiv 2\pi/\Lambda$ where Λ is the characteristic size of the energy bearing eddies.

2.2 Damping rates (η)

Mode damping rates (η) are computed using the full non-adiabatic and non-radial pulsation code MAD (Dupret 2002; Dupret et al. 2003). This code includes a time-dependent convection (TDC) treatment described in Grigahcène et al. (2005), which allows us to take into account the role played by the variations of the convective flux, the turbulent pressure, and the dissipation rate of the turbulent kinetic energy. Actually, the damping of the gravity modes is dominated by the perturbation of the radiative flux. We have numerically verified that the interaction between convection and pulsation does not affect the damping rates.

2.3 Computational details and assumptions

We consider main-sequence stellar models computed with the stellar evolution code CLÉS (Scuflaire et al. 2008). These models use standard physics, in particular convection is treated according to the Böhm–Vitense mixing-length (MLT) formalism, but overshoot is not included. Details of the physical inputs used are given in (Belkacem et al. 2009c). Three models are computed; one with a mass $M = 10 M_\odot$ (M10 hereafter), the second with $M = 15 M_\odot$ (M15 hereafter), and the third with $M = 20 M_\odot$ (M20 hereafter). All models are at the same evolutionary stage, namely $X_c = 0.5$ where X_c is the hydrogen core abundance.

The mode damping rates (η) or equivalently the mode lifetimes ($\tau = 1/\eta$), as well as the relation between δT_{eff} and δR_* are obtained using the pulsation code MAD (see Sect. 2.2).

The rate (\mathcal{P}) at which energy is injected into a mode per unit time is then computed according to (4). The density

stratification, ρ_0 , is obtained from the equilibrium model. Mode eigenfrequencies and eigenfunctions are computed using the adiabatic pulsation code OSC (Scuflaire et al. 2008). We consider modes with angular degree $\ell = 1$ and radial orders between $n = -2$ and $n = -21$ (asymptotic g mode). Modes with $\ell > 1$ are not considered, since those modes are expected to have lower amplitudes. Modes below $n = -21$ are not considered for several reasons: the calculation of gravity modes with lower values of n requires models with a much denser mesh-grid than those at our disposal. Furthermore, in the limit where $n \rightarrow -\infty$, the density of gravity modes becomes very high in frequency. Below a given value of n , it is then no longer possible to distinguish in the Fourier spectrum one mode from another.

Apart from the eigenfunctions and ρ_0 , (4) involves both the eddy-time correlation function (χ_k) and the turbulent kinetic energy spectrum (E). However, the properties of turbulent convection are poorly known for main-sequence massive stars, in particular in the CC (see the discussion in Sect. 5). We therefore need to set a priori χ_k , the k dependence of E and the characteristic wave number (k_0) or equivalently the characteristic length scale (Λ) at which energy is injected into the turbulent cascade.

- χ_k : It has been shown that the use of a Lorentzian function for χ_k results for the Sun (Samadi et al. 2003; Belkacem et al. 2006) and α Cen A (Samadi et al. 2008) in good agreement between observed mode amplitudes and computed ones. We will then by default consider a Lorentzian for χ_k . However, in order to probe the sensitivity of our results to this choice we will also consider for comparison a Gaussian for χ_k (see Sect. 5).
- $E(k)$: Among the different analytical functions tested so far for E (see e.g. Samadi et al. 2003; Chaplin et al. 2005), the best agreement with a solar 3D simulation was found with the so-called “Extended Kolmogorov Spectrum” defined by Musielak et al. (1994). We will then use by default this analytical empirical spectrum.
- Λ : One usually assumes by default that Λ is proportional to the classical mixing length (Λ_{MLT}), i.e. $\Lambda = \beta \Lambda_{\text{MLT}}$ where Λ_{MLT} is the mixing length, and β is a free parameter introduced in order to probe the sensitive of our results to this definition of Λ (see SG01). According to Samadi et al. (2003), one must assume $\beta = 5$ in order that—in the case of the Sun— Λ_{MLT} matches the characteristic length Λ derived from the numerical simulations of the upper part of the solar convection zone. However, in the CC, Λ_{MLT} and hence Λ exceeds the size of the CC (Λ_c). In the CC, we will therefore assume the upper limit $\Lambda = \Lambda_c$. In order to probe our sensitivity to Λ , other choices will be investigated in Sect. 5.

3 Efficiency of the driving regions

At a given layer, the power supplied to the modes by the Reynolds stress is proportional—per unit mass—to $F_{\text{kin}} \Lambda^4 S_R \mathcal{R}(\xi, m)/I$ where F_{kin} is the vertical flux of kinetic energy, which is proportional to $\rho_0 u_0^3$ (for details see Samadi 2010). It is important to stress that the value taken by the dimensionless source function, S_R , depends on the way mode and turbulent eddies are time-correlated: S_R is maximum for $p_{\text{osc}} \gtrsim \tau_0$ (resonance) where $\tau_0 \equiv 2\pi/\omega_0$ is the characteristic eddy turn-over time and $p_{\text{osc}} = 2\pi/\omega_{\text{osc}}$ is the period of the mode. On the other hand S_R decreases very rapidly for $p_{\text{osc}} < \tau_0$ (off-resonance). F_{kin} , Λ and S_R depend directly on the properties of the convective regions. The efficiency of the driving will then depend on the balance between these three terms. We discuss below the efficiency of the different convective regions.

We distinguish three convective regions.

- The convective zone associated with the *helium* opacity bump: this region is located at $T \approx 40000$ K, and is inefficient to transport energy with a negligible ratio of the convective heat flux to the radiative one. This region is located near the star surface, where density and, as a consequence, F_{kin} are low. The mixing length, Λ_{MLT} , is more than hundred times smaller than the size of the CC (Λ_c). Furthermore, the characteristic eddy turn-over time (τ_0) is very long compared to the period (p_{osc}) of the modes we are interested in here. Driving of the gravity modes is then expected to be negligible in the helium CZ.
- The convective zone associated with the *iron* opacity bump, located at $T \approx 200000$ K: as for the helium convective region, the transport of energy by convection is still inefficient. However, this region is located deeper than the helium one, where density is higher. F_{kin} is still negligible compared to the total flux, but the ratio of the kinetic energy flux of the iron convective zone to the helium one is $\sim 10^8$ for e.g. M10. Furthermore, τ_0 is of the order of p_{osc} . The excitation in this region is then expected to be much stronger than in the helium CZ.
- The convective *core* (CC): convection is fully efficient, meaning that most of the flux is transported by convection. The kinetic energy is several magnitudes higher than for the iron convective zone (ICZ hereafter), due to the high densities. For instance in M10, F_{kin} is about 10^5 larger than in the ICZ. Furthermore, Λ is several magnitudes higher than in the ICZ. The driving is then expected to be potentially stronger in the CC than in the OCZ. However, τ_0 is significantly longer than p_{osc} . In other words, excitation lies off-resonance within the CC. In this region, the final efficiency of the driving will depend on the net balance between F_{kin} , S_R , and Λ .

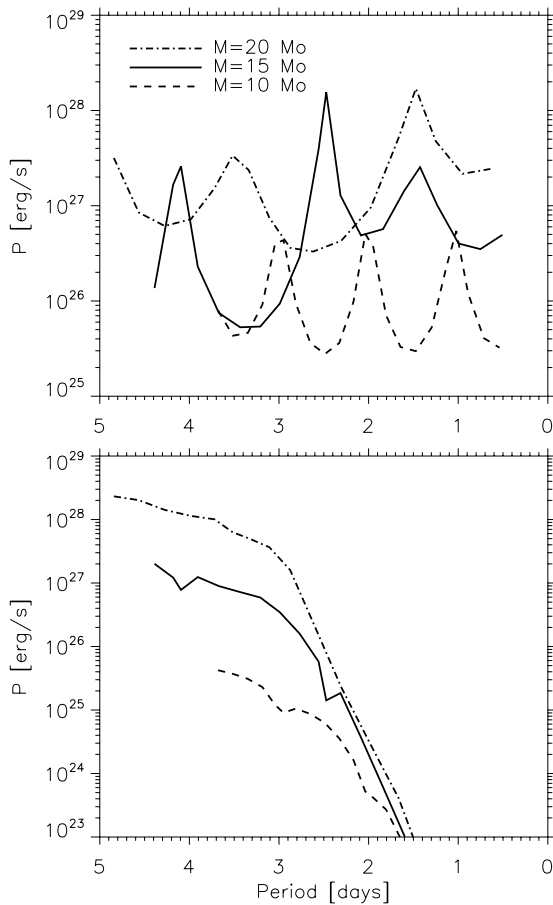


Fig. 1 *Top*: contribution of the CC to the mode excitation rates (\mathcal{P}_C) as a function of the mode period (p_{osc}). \mathcal{P}_C is shown for the three models: $M = 10 M_\odot$ (dashed line), $M = 15 M_\odot$ (solid line) and $M = 20 M_\odot$ (dot-dashed line). *Bottom*: contribution of the outer convective zones (OCZ) to the mode excitation rates (\mathcal{P}_S) as a function of the mode period (p_{osc}). The line style is the same as in the top panel.

4 Result

4.1 Excitation in the convective core

The contribution of the CC to the mode excitation rates (\mathcal{P}_C hereafter) are presented in Fig. 1 (top) for the three models. Important wiggles are seen on \mathcal{P}_C . They are due to the behavior of the mode eigendisplacements in the vicinity of the CC. More precisely, mode amplitude in the CC depends on the phase of the eigenfunction at the frontier of the CC.

The values reached by \mathcal{P}_C are larger for M15 compared to M10. On the other hand, the values reached by \mathcal{P}_C for M15 are as high as for M20. These results are explained as follows: the larger F_{kin} , the stronger the driving. However, \mathcal{P} is inversely proportional to I (see 4). Hence—at fixed F_{kin} —the larger I , the lower is \mathcal{P} . Generally, the larger M , the higher is I . On the other hand, the larger M , the higher is F_{kin} in the CC. There is then a balance between F_{kin} and I .

4.2 Excitation in the outer convective zones

The contribution of the outer convective zones (OCZ) to the mode excitation rates (\mathcal{P}_S hereafter) are presented in Fig. 1 (bottom). We find that, within the OCZ, the excitation predominantly occurs within the iron convective zone. This is a direct consequence of the arguments developed in Sect. 3.

As clearly seen in Fig. 1 (bottom), the larger M the higher \mathcal{P}_S . This is because the larger M , the higher the temperature at the surface. Now, the higher the temperature, the larger the energy transported by convection and accordingly the larger F_{kin} .

At low frequency ($p_{\text{osc}} \gtrsim 3$ days), \mathcal{P}_S is in general larger than \mathcal{P}_C . On the other hand, this contribution decreases more rapidly with decreasing p_{osc} than does \mathcal{P}_C . This is because \mathcal{P}_S depends on the mode compressibility, which decreases with increasing frequency (i.e. decreasing n), while \mathcal{P}_C depends on the amplitude of the mode displacement in the vicinity of the CC, which increases with increasing frequency. At high frequency ($p_{\text{osc}} \lesssim 3$ days), the excitation turns out to be dominated by the contribution of the CC (\mathcal{P}_C).

4.3 Mode amplitudes

We sum the contribution of the CC (\mathcal{P}_C) with that of the OCZ (\mathcal{P}_S); this gives the total mode excitation rates $\mathcal{P} = \mathcal{P}_S + \mathcal{P}_C$. From \mathcal{P} and η , we then derive the mode amplitudes in terms of surface velocity (v_s , (1)) and intensity ($\delta L/L$, (3)). The result is shown in Fig. 2. We have not taken the mode visibility factor into account; in other words, the amplitudes shown in Fig. 2 correspond to *intrinsic* (in opposition to *apparent*) rms amplitudes.

5 Conclusion and discussion

We have computed, for three main-sequence stellar models, the power (\mathcal{P}) supplied by turbulent convection into gravity modes. According to our theoretical calculations and associated assumptions, gravity modes are expected to be efficiently excited both in the CC and the iron convective zone. On the other hand, the driving within the helium CZ is found to be negligible compared to the driving taking place in the other driving regions.

We have next computed the mode damping rates (equivalently, the mode lifetimes). We found that the mode damping is dominated by the perturbation of the radiative flux. The computed η are then more reliable than if the coupling between pulsation and convection were at the origin of the damping.

We have finally derived the mode amplitudes. The amplitudes of asymptotic g-modes are mainly fixed by the driving

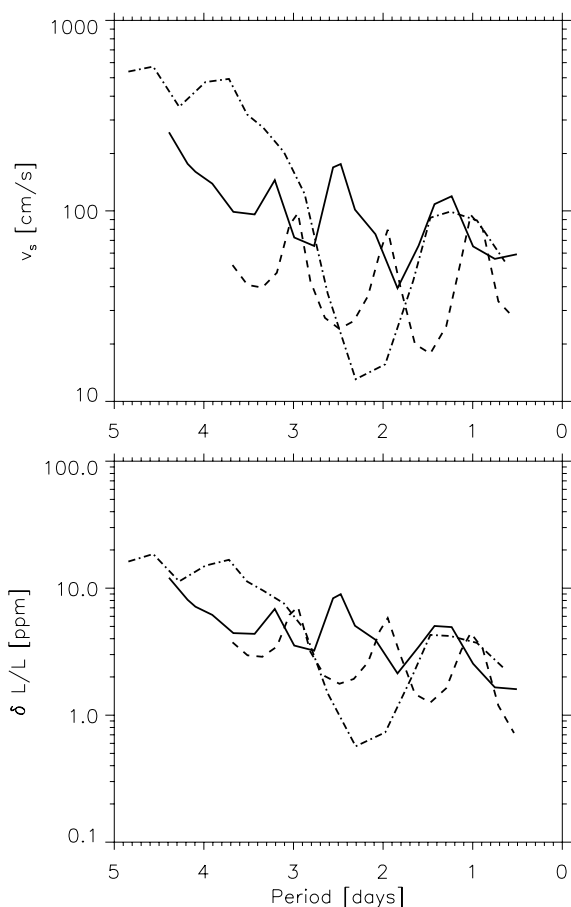


Fig. 2 Intrinsic mode amplitudes as a function of p_{osc} . The line style is the same as in Fig. 1. *Top*: mode amplitudes in terms of surface velocity, v_s (see (1)). *Bottom*: mode amplitudes in terms of intensity, $\delta L/L$ (see (3)).

taking place within the iron convective zone. On the other hand, the amplitudes of the low n order modes are expected to be predominantly fixed by the driving within the CC. However, the relative contribution of the CC and the iron convective zone to the mode excitation rates significantly depends on the assumptions concerning the characteristic length Λ and the eddy-time correlation function χ_k .

The theoretical mode amplitudes in surface velocity (v_s) are found in general to be significantly larger than those of the solar p-modes (~ 30 cm/s). Mode amplitudes in intensity are found to be of the same order as for the solar p-modes (≈ 2.5 ppm, see Michel et al. 2009).

For asymptotic g-modes, the larger M , the larger are the mode amplitudes. This is because the higher M , the higher is the energy transported by convection and hence the stronger the driving within the OCZ. For low n order modes, the maximum of the mode amplitudes depends weakly on M . Indeed, the square of the mode amplitude is inversely proportional to the mode inertia (I). Furthermore, the driving within the CC results from the balance between the kinetic flux (F_{kin}) in the CC and I . F_{kin} in the CC increases with

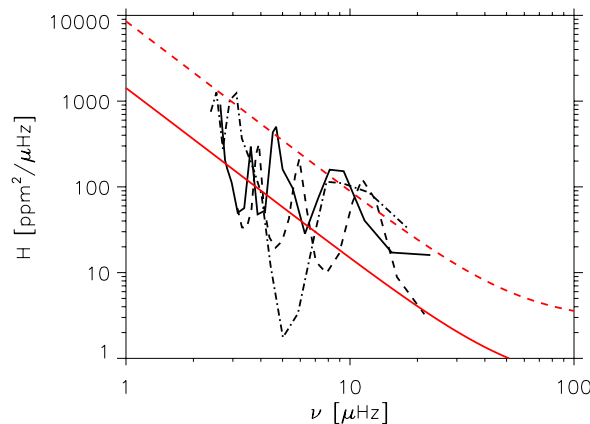


Fig. 3 Mode heights in terms of intensity and as a function of the period. The *black curves* have the same meaning as in Fig. 1. The *red curve* corresponds to an estimate of the upper limit of the CoRoT instrumental noise level (see text). The *dashed red curve* corresponds to the associated detection threshold (see text)

increasing M . For low n order modes, I also increases with increasing M . Therefore, the increase of F_{kin} with M is partially compensated by the increase of I with M .

At this point several issues arise.

- (i) How reliable are our amplitude estimates?
- (ii) Can we detect such stochastically-excited gravity modes with CoRoT?

We now address these two questions.

Uncertainties: Among the different assumptions adopted in the present model concerning the properties of turbulent convection, the major sources of uncertainty are the characteristic length Λ , the adopted prescription for χ_k , and the wave-number dependence of $E(k)$.

Concerning Λ , in the absence of other physical consideration, it is usually assumed—by default—that Λ is proportional to the mixing length (which is by definition proportional to the pressure scale height). The coefficient of proportionality, β , was—as in the case of the Sun—set to 5 (see Sect. 2.3). However, in the CC, Λ cannot be larger than Λ_c . Therefore, we have assumed by default $\Lambda = \Lambda_c$ in the CC. Accordingly, our theoretical calculation of the excitation in the CC then corresponds to an upper limit. Assuming $\Lambda = \Lambda_c/10$ in the CC results in significantly lower mode amplitudes. Concerning the OCZ, assuming as in the Sun $\beta = 5$ is rather arbitrary. In order to probe the sensitivity of our results to this choice we performed a calculation for which $\Lambda = \Lambda_{MLT}$ in the OCZ and $\Lambda = \Lambda_c/10$ in the CC. In that case the computed mode amplitudes are found to be about 20 times lower compared to our default case.

Concerning χ_k and $E(k)$, we have chosen the analytical forms that match hydrodynamical 3D simulations of the outer layer of stars analogues to the Sun and that result—in

the case of the Sun and α Cen A—in good agreement between computed and observed \mathcal{P} . However, whether these analytical forms remain valid in the present case is an open question.

Finally, we point out that some 3D hydrodynamical models of stars with CC have been performed (see e.g. Browning et al. 2004; Meakin and Arnett 2007). These 3D models can provide some hints about the properties of turbulent convection in the CC. This will be investigated in future work.

Detection: The noise level of the CoRoT instrument in the Fourier domain can be estimated by considering the Fourier spectrum of a CoRoT star that is almost constant. We thus consider the CoRoT target HD 50170 (F2, $m_v = 6.82$), which almost does not show intrinsic variability. We have fitted the power spectrum of this target using a Lorentzian function. The result is shown in Fig. 3. This fitted spectrum then represents an estimate of the upper limit of the CoRoT instrumental noise. From this limit we can then derive a detection threshold for a given confidence level. This threshold is presented in Fig. 3 for a confidence level of 95%. This threshold must be compared with the mode height and not with the mode amplitude (see the definition of the mode height in e.g. Lochard et al. 2005). This comparison is shown in Fig. 3. The mode heights are all found below the CoRoT detection threshold associated with individual modes. We point out that taking into account the mode visibility factor would result in lower mode height. As a conclusion, the detection of stochastically-excited gravity modes with CoRoT seems to be challenging. However, an open question is whether or not the current Kepler mission or the future PLATO mission will be able to detect such modes.

Acknowledgements This work was supported by the Centre National d'Etudes Spatiales (CNES). It is based on observations with CoRoT. K.B. acknowledges financial support through a postdoctoral fellowship from the "Subside fédéral pour la recherche 2009", University of Liège. A.N is grateful to HELAS for financial support.

References

- Belkacem, K., Samadi, R., Goupil, M.J., Kupka, F., Baudin, F.: *Astron. Astrophys.* **460**, 183 (2006)
- Belkacem, K., Samadi, R., Goupil, M.J., Dupret, M.A.: *Astron. Astrophys.* **478**, 163 (2008)
- Belkacem, K., Samadi, R., Goupil, M.J., Lefèvre, L., Baudin, F., Deheuvels, S., Dupret, M.A., Appourchaux, T., Scuflaire, R., Auvergne, M., Catala, C., Michel, E., Miglio, A., Montalbán, J., Thoul, A., Talon, S., Baglin, A., Noels, A.: *Science* **324**, 1540 (2009a)
- Belkacem, K., Samadi, R., Goupil, M.J., Dupret, M.A., Brun, A.S., Baudin, F.: *Astron. Astrophys.* **494**, 191 (2009b)
- Belkacem, K., Dupret, M.A., Noels, A.: *Astron. Astrophys.* (2009c, in press). [arXiv:0911.0908](https://arxiv.org/abs/0911.0908)
- Browning, M.K., Brun, A.S., Toomre, J.: *Astrophys. J.* **601**, 512 (2004)
- Chaplin, W.J., Houdek, G., Elsworth, Y., Gough, D.O., Isaak, G.R., New, R.: *Mon. Not. R. Astron. Soc.* **360**, 859 (2005)
- Dupret, M.A.: *Bull. Soc. R. Sci. Liège* **5–6**, 249 (2002)
- Dupret, M.A., Scuflaire, R., Noels, A., Thoul, A., Garrido, R., Moya, A., De Ridder, J., De Cat, P., Aerts, C.: *Astrophys. Space Sci.* **284**, 129 (2003)
- Dziembowski, W.: *Acta Astron.* **27**, 95 (1977)
- Grigahcène, A., Dupret, M.A., Gabriel, M., Garrido, R., Scuflaire, R.: *Astron. Astrophys.* **434**, 1055 (2005)
- Lochard, J., Samadi, R., Goupil, M.J.: *Astron. Astrophys.* **438**, 939 (2005)
- Meakin, C.A., Arnett, D.: *Astrophys. J.* **667**, 448 (2007)
- Michel, E., Samadi, R., Baudin, F., Barban, C., Appourchaux, T., Auvergne, M.: *Astron. Astrophys.* **495**, 979 (2009)
- Musielak, Z.E., Rosner, R., Stein, R.F., Ulmschneider, P.: *Astrophys. J.* **423**, 474 (1994)
- Pesnell, W.D.: *Astrophys. J.* **363**, 227 (1990)
- Samadi, R.: In: Rozelot, J.P., Neiner, C. (eds.) *Lecture Notes in Physics*. Springer, Berlin (2010, in press)
- Samadi, R., Goupil, M.: *Astron. Astrophys.* **370**, 136 (2001) (SG01)
- Samadi, R., Nordlund, Å., Stein, R.F., Goupil, M.J., Roxburgh, I.: *Astron. Astrophys.* **404**, 1129 (2003)
- Samadi, R., Nordlund, Å., Stein, R.F., Goupil, M.J., Roxburgh, I.: *Astron. Astrophys.* **403**, 303 (2003)
- Samadi, R., Belkacem, K., Goupil, M.J., Dupret, M.A., Kupka, F.: *Astron. Astrophys.* **489**, 291 (2008)
- Scuflaire, R., Théado, S., Montalbán, J., Miglio, A., Bourge, P.O., Godard, M., Thoul, A., Noels, A.: *Astrophys. Space Sci.* **316**, 83 (2008)
- Scuflaire, R., Montalbán, J., Théado, S., Bourge, P.O., Miglio, A., Godard, M., Thoul, A., Noels, A.: *Astrophys. Space Sci.* **316**, 149 (2008)

L E

Turbulent eddy-time-correlation in the solar convective zone

K. Belkacem^{1,2}, R. Samadi², M. J. Goupil², F. Baudin³, D. Salabert^{4,5}, and T. Appourchaux³

¹ Institut d'Astrophysique et de Géophysique, Université de Liège, Allée du 6 août 17, 4000 Liège, Belgium

² LESIA, UMR8109, Université Pierre et Marie Curie, Université Denis Diderot, Obs. de Paris, 92195 Meudon Cedex, France
e-mail: Kevin.belkacem@obspm.fr

³ Institut d'Astrophysique Spatiale, CNRS-Université Paris XI UMR 8617, 91405 Orsay Cedex, France

⁴ Instituto de Astrofísica de Canarias, 38200 La Laguna, Tenerife, Spain

⁵ Departamento de Astrofísica, Universidad de La Laguna, 38206 La Laguna, Tenerife, Spain

Received 7 September 2010 / Accepted 6 October 2010

ABSTRACT

Theoretical modeling of the driving processes of solar-like oscillations is a powerful way of understanding the properties of the convective zones of solar-type stars. In this framework, the description of the temporal correlation between turbulent eddies is an essential ingredient to model mode amplitudes. However, there is a debate between a Gaussian or Lorentzian description of the eddy-time correlation function (Samadi et al. 2003b, A&A, 403, 303; Chaplin et al. 2005, MNRAS, 360, 859). Indeed, a Gaussian description reproduces the low-frequency shape of the mode amplitude for the Sun, but is unsatisfactory from a theoretical point of view (Houdek 2010, Ap&SS, 328, 237) and leads to other disagreements with observations (Samadi et al. 2007, A&A, 463, 297). These are solved by using a Lorentzian description, but there the low-frequency shape of the solar observations is not correctly reproduced. We reconcile the two descriptions by adopting the sweeping approximation, which consists in assuming that the eddy-time-correlation function is dominated by the advection of eddies, in the inertial range, by energy-bearing eddies. Using a Lorentzian function together with a cut-off frequency derived from the sweeping assumption allows us to reproduce the low-frequency shape of the observations. This result also constitutes a validation of the sweeping assumption for highly turbulent flows as in the solar case.

Key words. convection – turbulence – Sun: oscillations

1. Introduction

Excitation of solar-like oscillations is attributed to turbulent motions that excite p modes (for a recent review, see Samadi 2009). Their amplitudes result from a balance between excitation and damping and crucially depend on the way the eddies are temporally correlated as shown for solar *p* and *g* modes (Samadi et al. 2003b; Belkacem et al. 2009b; Appourchaux et al. 2010), for main-sequence stars (Samadi et al. 2010b,a), for red giants (Dupret et al. 2009), or for massive stars (Belkacem et al. 2009a, 2010). Hence, the improvement of our understanding and modeling of the temporal correlation of turbulent eddies, hereafter denoted in the Fourier domain as $\chi_k(\omega)$, is fundamental to infer turbulent properties in stellar convection zones.

There are two ways to compute the eddy-time correlation function. A direct computation from 3D numerical simulations is possible and was performed by Samadi et al. (2008a). Nevertheless, Samadi (2009) pointed out that the results depend on the spatial resolution, and therefore dedicated high-resolution 3D numerical simulations are required. This then becomes an important limitation when computing mode amplitudes for a large number of stars, preventing us from applying statistical asteroseismology.

The second way to compute χ_k consists in using appropriate analytical descriptions. Most of the theoretical formulations of mode excitation explicitly or implicitly assume a Gaussian functional form for $\chi_k(\omega)$ (Goldreich & Keeley 1977; Dolginov & Muslimov 1984; Goldreich et al. 1994; Balmforth 1992; Samadi et al. 2001; Chaplin et al. 2005). However, 3D hydrodynamical simulations of the outer layers of the Sun show that at the length-scales close to those of the energy-bearing eddies (around 1 Mm), χ_k is a Lorentzian function (Samadi et al. 2003a;

Belkacem et al. 2009b). As pointed out by Chaplin et al. (2005), a Lorentzian χ_k is also a result predicted for the largest, most-energetic eddies by the time-dependent mixing-length formulation derived by Gough (1977). Therefore, there is numerical, theoretical, and also observational evidence (Samadi et al. 2007) that χ_k is Lorentzian.

However, Chaplin et al. (2005), Samadi (2009), and Houdek (2010) found that a Lorentzian χ_k , when used with a mixing-length description of the whole convection zone, results in a severe over-estimate for the low-frequency modes. In this case, low-frequency modes ($\nu < 2$ mHz) are excited deep in the solar convective region by large-scale eddies that give a substantial fraction of the energy injected to the modes. Chaplin et al. (2005) and Samadi (2009) then suggested that most contributing eddies situated deep in the Sun have a χ_k more Gaussian than Lorentzian because at a fixed frequency, a Gaussian χ_k decreases more rapidly with depth.

We therefore propose a refined description of the eddy-time correlation function based on the sweeping approximation to overcome this issue. This consists in assuming that the temporal correlation of the eddies, in the inertial subrange, is dominated by the advection by energy-bearing eddies. This assumption was first proposed by Tennekes (1975), and was subsequently investigated by Kaneda (1993) and Kaneda et al. (1999). In this letter, we demonstrate that the low-frequency shape of the observed energy injection rates into the solar modes is very sensitive to this assumption and more precisely to the Eulerian microscale, defined as the curvature of the time-correlation function at the origin. Hence, modeling of the solar p-mode amplitudes is shown to constitute an efficient test for temporal properties in highly turbulent flows.

The paper is organized as follows: Sect. 2 defines the eddy-time correlation function. In Sect. 3, we propose a short-time expansion of the eddy-time correlation function. The use of the Eulerian microscale as a cut-off is introduced in the computation of solar p mode amplitudes and the result is compared to the observations in Sect. 4. Finally, Sect. 5 is dedicated to conclusions and discussions.

2. The Eulerian eddy time-correlation function

For a turbulent fluid, one defines the Eulerian eddy time-correlation function as

$$\langle \mathbf{u}(\mathbf{x} + \mathbf{r}, t + \tau) \cdot \mathbf{u}(\mathbf{x}, t) \rangle = \int \mathcal{E}(\mathbf{k}, t, \tau) e^{i\mathbf{k} \cdot \mathbf{x}} d^3 \mathbf{k}, \quad (1)$$

where \mathbf{u} is the Eulerian turbulent velocity field, \mathbf{x} and t the space and time position of the fluid element, \mathbf{k} the wave number vector, τ the time-correlation length, and \mathbf{r} the space-correlation length. The function \mathcal{E} in the RHS of Eq. (1) represents the time-correlation function associated with an eddy of wave-number \mathbf{k} .

We assume an isotropic and stationary turbulence, accordingly \mathcal{E} is only a function of k and τ . The quantity $\mathcal{E}(k, \tau)$ is related to the turbulent energy spectrum according to

$$\mathcal{E}(k, \tau) = \frac{E(k, \tau)}{2\pi k^2}, \quad (2)$$

where $E(k, \tau)$ is the turbulent kinetic energy spectrum whose temporal Fourier transform is

$$E(k, \omega) \equiv \frac{1}{2\pi} \int_{-\infty}^{+\infty} E(k, \tau) e^{i\omega\tau} d\tau, \quad (3)$$

where ω is the eddy frequency, and $E(k, \omega)$ is written following an approximated form proposed by Stein (1967)

$$E(k, \omega) = E(k) \chi_k(\omega) \quad \text{with} \quad \int_{-\infty}^{+\infty} \chi_k(\omega) d\omega = 1, \quad (4)$$

where $\chi_k(\omega)$ is the frequency component of $E(k, \omega)$. In other words, $\chi_k(\omega)$ represents – in the frequency domain – the temporal correlation between eddies of wave-number k .

As already discussed in Sect. 1, theoretical and observational evidence show that $\chi_k(\omega)$ is Lorentzian, i.e.

$$\chi_k(\omega) = \frac{1}{\pi\omega_k} \frac{1}{1 + (\omega/\omega_k)^2}, \quad (5)$$

where ω_k is by definition the width at half maximum of $\chi_k(\omega)$. In the framework of Samadi & Goupil (2001)'s formalism, this latter quantity is evaluated as:

$$\omega_k = k u_k \quad \text{with} \quad u_k^2 = \int_k^{2k} E(k) dk, \quad (6)$$

where $E(k)$ is defined by Eq. (4). However, in the high-frequency regime ($\omega \gg \omega_k$), corresponding to the short-time correlation ($\tau \approx 0$), the situation is less clear. We next investigate short-time correlations ($\tau \approx 0$).

3. The sweeping assumption for the Eulerian time-correlation function

3.1. Short-time expansion of the eddy-time correlation function

The function $\mathcal{E}(k, t, \tau)$ (Eq. (1)) can be expanded for short-time scales, in the inertial sub-range (i.e. for $k > k_0$ and $k < k_d$, where

k_0 is the wave number of energy-bearing eddies and k_d is the wave-number of viscous dissipation), using the Navier-Stokes equations and the sweeping assumption, as (see Kaneda 1993, for a derivation)

$$\mathcal{E}(k, \tau) = \mathcal{E}(k, \tau = 0) \left(1 - \alpha_k |\tau| - \frac{1}{2} (\omega_E \tau)^2 + \dots \right), \quad (7)$$

where the characteristic frequency α_k is defined by the relation

$$\epsilon = -\frac{1}{2} \frac{d}{dt} \langle \mathbf{u} \cdot \mathbf{u} \rangle = \int \alpha_k \mathcal{E}(k, \tau = 0) d^3 \mathbf{k} \quad (8)$$

with ϵ the dissipation rate of energy. Hence, α_k is the typical frequency of energy dissipation at the scale k . It can be estimated by assuming that a large fraction of the kinetic energy of eddies is lost within one turnover time (Tennekes & Lumley 1972). Hence, α_k is approximated by the turn-over frequency $\alpha_k = k u_k = \omega_k$ (see Eq. (6)).

The second characteristic frequency, $\omega_E(k)$, is the curvature of the correlation function near the origin (Kaneda 1993), and is defined by

$$\omega_E = k u_0. \quad (9)$$

The associated characteristic time $\tau_E(k) = 2\pi \omega_E^{-1}$ is also referred to as the Eulerian micro-scale¹ (Tennekes & Lumley 1972). An approximate expression for $\omega_E(k)$ can be obtained by assuming the random sweeping effect of large eddies on small eddies. This assumption consists in assuming that the velocity field $\mathbf{u}(k)$ associated with an eddy of wave-number \mathbf{k} lying in the inertial-subrange (i.e. large \mathbf{k} compared to \mathbf{k}_0) is advected by the energy-bearing eddies with velocity \mathbf{u}_0 (i.e. of wave-number \mathbf{k}_0). This time-scale is obtained by assuming uniform density, which is valid in the Sun for $\mathbf{k} > \mathbf{k}_0$ (i.e. in the inertial sub-range) since the density scale-height approximately equals the length-scale of energy-bearing eddies ($(d \ln \rho / dr)^{-1} \approx 2\pi / k_0$). It also assumes the quasi-normal approximation (see Kaneda 1993; Kaneda et al. 1999; Rubinstein & Zhou 2002, for details). The Eulerian micro-scale then corresponds to the timescale over which the energy-bearing eddies of velocity \mathbf{u}_0 advect eddies of size $2\pi k^{-1}$. It is the lowest time-scale (highest frequency) on which those eddies can be advected.

3.2. Eulerian time micro-scale as a cut-off frequency

The issue is now to estimate to what extent ω_E can be considered as a cut-off frequency, i.e. that there is a sharp change in the slope of χ_k at high ω .

To this end, we first remark that the zero-th- and first-order terms in Eq. (7) are consistent with an exponential decrease of width α_k (i.e. a Lorentzian in the frequency domain of width ω_k , Eq. (5)) for small τ . In contrast, the zero-th-order term together with the second order term in Eq. (7) are consistent with a Gaussian behavior of width τ_E . Hence, the relative importance of those two regimes depends on the relative magnitude of the second and third terms in Eq. (7). Let us define the ratio (\mathcal{R}) of the first to the second order term in the expansion of \mathcal{E} (Eq. (7))

$$\mathcal{R} = 2 (\omega_E \tau)^{-1} \left(\frac{\omega_k}{\omega_E} \right), \quad (10)$$

To evaluate this ratio, we compare the typical frequencies ω_k and ω_E using Eq. (9) together with Eq. (6). Adopting a Kolmogorov

¹ It is the time equivalent of the Taylor micro-scale, which corresponds to the largest scale at which viscosity affects the dynamic of eddies.

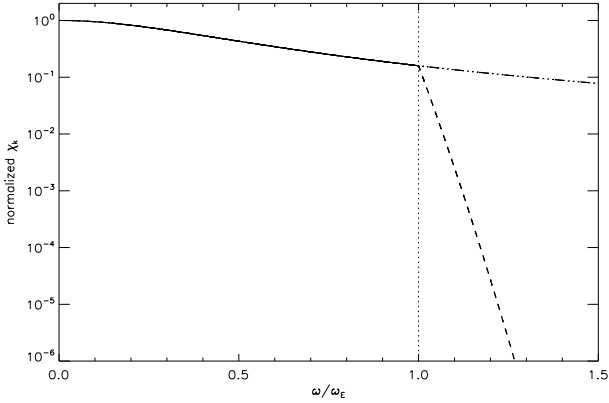


Fig. 1. Schematic time-correlation (χ_k) versus normalized eddy frequency (ω/ω_E) at $k = 5k_0$ (i.e. in the inertial subrange such as $k_d \gg k > k_0$), where $k_0 = 6.28 \times 10^{-6} \text{ m}^{-1}$. Note that the value of k_0 does not influence the result. The solid line (resp. dashed triple dot line) corresponds to the Lorentzian functional form of χ_k for $\omega < \omega_E$ (resp. $\omega > \omega_E$). The dashed line corresponds to a Gaussian modeling ($\chi_k \propto e^{-(\omega/\omega_E)^2}$) of characteristic frequency ω_E . (we numerically verified that $e^{-(\tau/\tau_E)^2}$ is a good approximation of Eq. (7), see also Sect. 3.2). We stress that the sharp decrease the functional form given by Eq. (7), in the temporal Fourier domain, then justifies to consider ω_E as a cut-off frequency. In other words, χ_k is computed according to Eq. (12).

spectrum $E(k) = C_K \epsilon^{2/3} k^{-5/3}$, with C_K the Kolmogorov universal constant (close to 1.72), we have $u_k^2 = \beta u_0^2 (k/k_0)^{-2/3}$, where $\beta = 0.555$. Hence

$$\frac{\omega_E}{\omega_k} = \frac{u_0}{u_k} = \beta^{-1/2} \left(\frac{k}{k_0} \right)^{1/3}. \quad (11)$$

From Eq. (11) we conclude that for $k \gg k_0$ (i.e. at small scale) we have $\omega_E/\omega_k \approx \beta^{-1/2} (k/k_0)^{1/3} \gg 1$, then $\tau_E \ll \tau_k$. And for $k \approx k_0$ (i.e. at large scale), we have $\omega_E/\omega_k = \beta^{-1/2} \approx 1.4$. Hence, we always are in the situation where $\omega_E > \omega_k$.

From Eq. (10), it immediately follows that for $\omega \gtrsim \omega_E$ the second order term dominates over the first order one in Eq. (7), at all length-scales. We then conclude that for frequencies near the micro-scale frequency ($\omega \gtrsim \omega_E$), the eddy-time correlation function behaves as a Gaussian function ($e^{-(\omega/\omega_E)^2}$) instead of a Lorentzian function, resulting in a sharp decrease with ω (see Fig. 1). Hence, the contributions for $\omega > \omega_E$ are negligible and the temporal correlation is computed as follows

$$\chi_k(\omega) = \begin{cases} \frac{1}{1 + (\omega/\omega_k)^2} & \text{if } \omega \leq \omega_E \\ 0 & \text{if } \omega > \omega_E. \end{cases} \quad (12)$$

4. Computation of the p -mode energy injection rates

4.1. Computation of the energy injection rate

The formalism we used to compute excitation rates of radial modes was developed by Samadi & Goupil (2001) and Samadi et al. (2005) (see Samadi 2009, for a thorough discussion)

For a radial mode of frequency $\omega_0 = 2\pi \nu_0$, the excitation rate (or equivalently, the energy injection rate), P , mostly arises

from the Reynolds stresses and can be written as (see Eq. (21) of Belkacem et al. 2008)

$$P(\omega_0) = \frac{\pi^3}{2I} \int_0^M \left[\rho_0 \left(\frac{16}{15} \right) \left(\frac{\partial \xi_r}{\partial r} \right)^2 \int_0^{+\infty} S_k dk \right] dm \quad (13)$$

$$S_k = \frac{E^2(k)}{k^2} \int_{-\infty}^{+\infty} \chi_k(\omega + \omega_0) \chi_k(\omega) d\omega, \quad (14)$$

where ξ_r is the radial component of the fluid displacement eigenfunction (ξ), m is the local mass, ρ_0 the mean density, ω_0 the mode angular frequency, I the mode inertia, S_k the source function, $E(k)$ the spatial kinetic energy spectrum, χ_k the eddy-time correlation function, and k the wave-number.

The rate (P) at which energy is injected into a mode is computed according to Eq. (13). In this letter, we consider two theoretical models, namely:

- an analytical approach: the 1D calibrated solar structure model used for these computations is obtained with the stellar evolution code CESAM2k (Morel 1997; Morel & Lebreton 2008). The atmosphere is computed assuming an Eddington grey atmosphere. Convection is included according to a Böhm-Vitense mixing-length (MLT) formalism (see Samadi et al. 2006, for details), from which the convective velocity is computed. The mixing-length parameter α is adjusted in a way that the model reproduces the solar radius and the solar luminosity at the solar age. This calibration gives $\alpha = 1.90$, with an helium mass fraction of 0.245, and a chemical composition following Grevesse & Noels (1993). The equilibrium model also includes turbulent pressure;
- a semi-analytical approach: calculation of the mode excitation rates is performed essentially in the manner of Samadi et al. (2008a,b). All required quantities, except the eddy-time correlation function, the mode eigenfunctions (ξ_r) and mode inertia (I), are directly obtained from a 3D simulation of the outer layers of the Sun (see Samadi 2009, for details on the numerical simulation).

In both cases, the eigenfrequencies and eigenfunctions are computed with the adiabatic pulsation code ADIPLS (Christensen-Dalsgaard 2008). We stress again that in both cases χ_k is implemented as an analytical function.

4.2. Results on mode amplitudes

When the frequency range of χ_k is extended toward infinity, computation of P according to Eq. (13) and Eq. (14) fails to reproduce the observations, in particular the low-frequency shape. In order to illustrate this issue, we have computed the solar model excitation rates, using the solar global model described in Sect. 4.1. The turbulent kinetic energy spectrum ($E(k)$) is assumed to be a Kolmogorov spectrum to be consistent with the derivation of τ_E as proposed by Kaneda (1993). In addition, the eddy-time correlation function is supposed to be Lorentzian as described by Eq. (5) for all $\omega > 0$. In agreement with the results of Chaplin et al. (2005) and Samadi (2009), it results in an over-estimate of the excitation rates at low frequency (see Fig. 2 top).

In contrast, by assuming that the time-dynamic of eddies in the Eulerian point of view is dominated by the sweeping, the Eulerian time micro-scale arises as a cut-off frequency (see Sect. 3.2). Hence, $\chi_k(\omega)$ is modeled following Eq. (5) for $\omega < \omega_E$ and $\chi_k(\omega) = 0$ elsewhere. Using this procedure to model $\chi_k(\omega)$

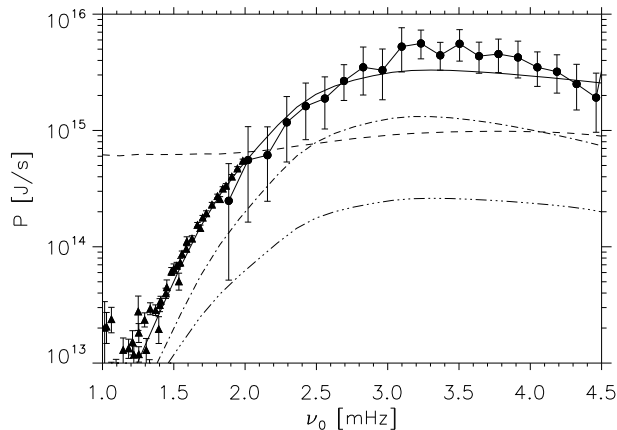


Fig. 2. Solar p -mode excitation rates as a function of the frequency ν . The dots correspond to the observational data obtained by the GONG network, as derived by Baudin et al. (2005), and the triangles corresponds to observational data obtained by the GONG network as derived by Salabert et al. (2009) for $\ell = 0$ to $\ell = 35$. The dashed line corresponds to the computation of the excitation rates using the analytical approach together with a Lorentzian description of χ_k without any cut-off frequency. Note that this modeling is similar to that mentioned by Chaplin et al. (2005). The solid line corresponds to the computation of mode excitation rates using the semi-analytical approach as described in Sect. 4.1 and using a Lorentzian χ_k together with a cut-off frequency at $\omega = \omega_E$. The dashed triple dot line corresponds to the analytical approach using a Lorentzian description of χ_k down to the cut-off frequency ω_E . Finally, the dashed-dot line corresponds to a semi-analytical approach using a Gaussian description of χ_k . Note that both solid (Lorentzian χ_k) and dashed-dot (Gaussian χ_k) lines present a similar frequency dependence, and since both are computed using the 3D numerical simulations for the convective motions the differences only comes from the way turbulence is temporally correlated.

(i.e. by introducing ω_E as a cut-off frequency) permits us to reproduce the low-frequency ($\nu < 3$ mHz) shape of the mode excitation rates as observed by the GONG network (see Fig. 2). This is explained as follows: for large-scale eddies near k_0^{-1} , situated deep in the convective region, the cut-off frequency ω_E is close to ω_k as shown by Eq. (11). As a consequence, the frequency range over which χ_k is integrated in Eq. (14) is limited, resulting in lower injection rates into the modes.

Note that the absolute values of mode excitation rates are not reproduced by using a mixing-length description of convection, this is in agreement with Samadi (2009), and arises because that it underestimates the convective velocities as well as convective length-scales. It then explains the differences between the computation of mode excitation rates using the MLT and the 3D numerical simulations (Fig. 2).

5. Conclusion and discussion

By using a short-time analysis and the sweeping assumption, we have shown that there is a frequency (ω_E the micro-scale frequency) beyond the temporal correlation χ_k sharply decreases with frequency. Including this frequency as a cut-off in our modeling of χ_k and assuming a Lorentzian shape we are able to reproduce the observed low-frequency ($\nu < 3$ mHz) excitation rates.

These results then re-conciliate the theoretical and observational evidence that the frequency dependence of the eddy-time correlation may be Lorentzian in the whole solar convective

region down to the cut-off frequency ω_E . Finally, it also represents a validation of the sweeping assumption in highly turbulent flows.

We note, however, that one must remove several theoretical shortcomings to go further. For instance, a rigorous treatment of the energy-bearing eddies is needed. The short-time analysis and the computation of the Eulerian micro-scale must be reconsidered by including the effect of buoyancy that mainly affects large scales. Furthermore, some discrepancies remain at high-frequency ($\nu > 3$ mHz), and to go beyond these one has to remove the separation of scales assumption (see Belkacem et al. 2008, for a dedicated discussion) and include non-adiabatic effects.

Eventually, we note that the modeling of amplitudes under the sweeping assumption is to be extended. In particular, the investigation of the effect of the sweeping assumption on solar gravity mode amplitudes is desirable.

Acknowledgements. We are indebted to J. Leibacher for his careful reading of the manuscript and his helpful remarks. K.B. acknowledges financial support through a postdoctoral fellowship from the Subside fédéral pour la recherche 2010, University of Liège. The authors also acknowledge financial support from the French National Research Agency (ANR) for the SIROCO (Seismology, ROTation and CONvection with the COROT satellite) project.

References

- Appourchaux, T., Belkacem, K., Broomhall, A., et al. 2010, A&AR, 18, 197
 Balmforth, N. J. 1992, MNRAS, 255, 639
 Baudin, F., Samadi, R., Goupil, M.-J., et al. 2005, A&A, 433, 349
 Belkacem, K., Samadi, R., Goupil, M.-J., & Dupret, M.-A. 2008, A&A, 478, 163
 Belkacem, K., Samadi, R., Goupil, M., et al. 2009a, Science, 324, 1540
 Belkacem, K., Samadi, R., Goupil, M. J., et al. 2009b, A&A, 494, 191
 Belkacem, K., Dupret, M. A., & Noels, A. 2010, A&A, 510, A6
 Chaplin, W. J., Houdek, G., Elsworth, Y., et al. 2005, MNRAS, 360, 859
 Christensen-Dalsgaard, J. 2008, Ap&SS, 316, 113
 Dolginov, A. Z., & Muslimov, A. G. 1984, Ap&SS, 98, 15
 Dupret, M., Belkacem, K., Samadi, R., et al. 2009, A&A, 506, 57
 Goldreich, P., & Keeley, D. A. 1977, ApJ, 212, 243
 Goldreich, P., Murray, N., & Kumar, P. 1994, ApJ, 424, 466
 Gough, D. O. 1977, ApJ, 214, 196
 Grevesse, N., & Noels, A. 1993, in Origin and Evolution of the Elements, ed. N. Prantzos, E. Vangioni-Flam, & M. Casse, 15
 Houdek, G. 2010, Ap&SS, 328, 237
 Kaneda, Y. 1993, Phys. Fluids, 5, 2835
 Kaneda, Y., Ishihara, T., & Gotoh, K. 1999, Phys. Fluids, 11, 2154
 Morel, P. 1997, A&AS, 124, 597
 Morel, P., & Lebreton, Y. 2008, Ap&SS, 316, 61
 Rubinstein, R., & Zhou, Y. 2002, ApJ, 572, 674
 Salabert, D., Leibacher, J., Appourchaux, T., & Hill, F. 2009, ApJ, 696, 653
 Samadi, R. 2009, Stochastic excitation of acoustic modes in stars, [arXiv:0912.0817]
 Samadi, R., & Goupil, M. J. 2001, A&A, 370, 136
 Samadi, R., Goupil, M., & Lebreton, Y. 2001, A&A, 370, 147
 Samadi, R., Nordlund, Å., Stein, R. F., Goupil, M. J., & Roxburgh, I. 2003a, A&A, 404, 1129
 Samadi, R., Nordlund, Å., Stein, R. F., Goupil, M. J., & Roxburgh, I. 2003b, A&A, 403, 303
 Samadi, R., Goupil, M.-J., Alecian, E., et al. 2005, J. Astrophys. Atr., 26, 171
 Samadi, R., Kupka, F., Goupil, M. J., Lebreton, Y., & van't Veer-Menneret, C. 2006, A&A, 445, 233
 Samadi, R., Georgobiani, D., Trampedach, R., et al. 2007, A&A, 463, 297
 Samadi, R., Belkacem, K., Goupil, M., Ludwig, H., & Dupret, M. 2008a, Commun. Asteroseismol., 157, 130
 Samadi, R., Belkacem, K., Goupil, M. J., Dupret, M., & Kupka, F. 2008b, A&A, 489, 291
 Samadi, R., Ludwig, H., Belkacem, K., et al. 2010a, A&A, 509, A16
 Samadi, R., Ludwig, H., Belkacem, K., Goupil, M. J., & Dupret, M. 2010b, A&A, 509, A15
 Stein, R. F. 1967, Sol. Phys., 2, 385
 Tennekes, H. 1975, J. Fluids Mech., 67, 561
 Tennekes, H., & Lumley, J. L. 1972, First Course in Turbulence, ed. H. Tennekes, & J. L. Lumley

Amplitudes of solar-like oscillations in red giant stars

Evidence for non-adiabatic effects using CoRoT observations

R. Samadi¹, K. Belkacem¹, M.-A. Dupret², H.-G. Ludwig^{3,4}, F. Baudin⁵, E. Caffau^{3,4},
M.-J. Goupil¹, and C. Barban¹

¹ LESIA, CNRS UMR 8109, Observatoire de Paris, Université Pierre et Marie Curie, Université Denis Diderot, Place Jules Janssen, 92195 Meudon Cedex, France
e-mail: reza.samadi@obspm.fr

² Institut d'Astrophysique et de Géophysique de l'Université de Liège, Allée du 6 Août 17, 4000 Liège, Belgium

³ Zentrum für Astronomie der Universität Heidelberg, Landessternwarte, Königstuhl 12, 69117 Heidelberg, Germany

⁴ GEPI, CNRS, Observatoire de Paris, Université Denis Diderot, Place Jules Janssen, 92195 Meudon Cedex, France

⁵ Institut d'Astrophysique Spatiale, CNRS, Université Paris XI, 91405 Orsay Cedex, France

Received 21 March 2012 / Accepted 18 May 2012

ABSTRACT

Context. A growing number of solar-like oscillations has been detected in red giant stars thanks to the CoRoT and *Kepler* space-crafts. In the same way as for main-sequence stars, mode driving is attributed to turbulent convection in the uppermost convective layers of those stars.

Aims. The seismic data gathered by CoRoT on red giant stars allow us to test the mode driving theory in physical conditions different from main-sequence stars.

Methods. Using a set of 3D hydrodynamical models representative of the upper layers of sub- and red giant stars, we computed the acoustic mode energy supply rate (\mathcal{P}_{\max}). Assuming adiabatic pulsations and using global stellar models that assume that the surface stratification comes from the 3D hydrodynamical models, we computed the mode amplitude in terms of surface velocity. This was converted into intensity fluctuations using either a simplified adiabatic scaling relation or a non-adiabatic one.

Results. From L and M (the luminosity and mass), the energy supply rate \mathcal{P}_{\max} is found to scale as $(L/M)^{2.6}$ for both main-sequence and red giant stars, extending previous results. The theoretical amplitudes in velocity under-estimate the Doppler velocity measurements obtained so far from the ground for red giant stars by about 30%. In terms of intensity, the theoretical scaling law based on the adiabatic intensity-velocity scaling relation results in an under-estimation by a factor of about 2.5 with respect to the CoRoT seismic measurements. On the other hand, using the non-adiabatic intensity-velocity relation significantly reduces the discrepancy with the CoRoT data. The theoretical amplitudes remain 40% below, however, the CoRoT measurements.

Conclusions. Our results show that scaling relations of mode amplitudes cannot be simply extended from main-sequence to red giant stars in terms of intensity on the basis of adiabatic relations because non-adiabatic effects for red giant stars are important and cannot be neglected. We discuss possible reasons for the remaining differences.

Key words. stars: solar-type – stars: oscillations – sun: oscillations – turbulence – convection – waves

1. Introduction

Before CoRoT (launched in December 2006), solar-like oscillations had been detected for a dozen of bright red giant stars either from the ground or from space with MOST (e.g., Barban et al. 2007). Thanks to CoRoT and *Kepler*, it is now possible to detect and measure solar-like oscillations in many more (several thousands) red giant stars (e.g., de Ridder et al. 2009; Huber et al. 2010; Bedding et al. 2010; Kallinger et al. 2010; Stello et al. 2011; Mosser et al. 2012). With such a large set of stars, it is possible to perform ensemble asteroseismology by deriving scaling relations that relate seismic parameters to a few fundamental stellar parameters (e.g. masses, radii, luminosities etc.). These approaches are now commonly applied to global seismic parameters, such as the cutoff-frequency or peak frequency (e.g., Miglio et al. 2009; Stello et al. 2009; Kallinger et al. 2010; Mosser et al. 2010). However, scaling relation is used only infrequently for mode amplitudes. The main reason for this is our poor theoretical understanding of the underlying physical mechanisms for mode driving and damping.

Using a large set of red giant stars observed by CoRoT, Baudin et al. (2011) have derived scaling relations in terms of mode lifetimes and amplitudes. These authors have found that the scaling relation proposed by Samadi et al. (2007) for the mode amplitude significantly departs from the measured one. This result was recently confirmed by Huber et al. (2011), Stello et al. (2011) and Mosser et al. (2012) with *Kepler* observations, and is easily understood by noting that Samadi et al. (2007) established the scaling for *main-sequence stars* only, and only for *mode surface velocity*. Indeed, those results point out that a dedicated theoretical investigation of mode amplitudes in intensity for red giants is needed to provide an adequate theoretical background.

Towards the end of their lives, low-mass stars greatly expand their envelope to become red giant stars. As a consequence, the low density of the envelope favours a vigorous convection such that excitation of solar-like oscillations occurs in a medium with very different physical conditions than encountered in the Sun. This introduces new problems about the physical mechanism

related to mode driving. For instance, the higher the turbulent Mach number, the more questionable the assumptions involved in the theory (Goldreich & Keeley 1977; Goldreich et al. 1994; Samadi & Goupil 2001; Chaplin et al. 2005; Belkacem et al. 2010).

In addition, red giant stars are characterised by high luminosities and hence have relatively short convective thermal time-scales at the upper most part of their convective envelope. One can therefore expect a stronger departure from adiabatic oscillations because the perturbation of entropy fluctuations related to the oscillations dimensionally depends on the ratio L/M (where L is the luminosity and M the mass). Thus, extreme physical conditions in the uppermost convective regions of red giants raise new questions about the energetic aspects of damped stochastically excited oscillations (more precisely mode driving and damping). In the present paper, we focus on modelling mode driving. We derive scaling relations for red giant stars in terms of mode amplitude (in velocity and intensity) and compare them with the available CoRoT observations.

This paper is organised as follows: from a grid of 3D hydrodynamical models representative for the upper layers of red giant stars, we derive in Sect. 2 theoretical scaling laws for the mode amplitudes in velocity (Sect. 2.1) and in intensity (Sect. 2.4). These scaling laws are then compared in Sect. 3 with seismic data. Finally, Sect. 4 is dedicated to conclusions.

2. Theoretical scaling relations for mode amplitudes

In this section our objective is to compute theoretical scaling relations of mode amplitudes both in terms of surface velocity and intensity. To this end, the mode amplitude will be computed with the help of hydrodynamical 3D numerical simulations.

2.1. Surface velocity mode amplitude, v

The mean-squared surface velocity for each *radial* mode is given by (e.g. Samadi 2011, and references therein)

$$v^2(\nu, r) = \frac{\tau(\nu)}{2} \frac{\mathcal{P}(\nu)}{\mathcal{M}(\nu, r)}, \quad (1)$$

where ν is the mode frequency, \mathcal{P} the mode excitation rate, τ the mode life-time (which is equal to the inverse of the mode damping rate η), \mathcal{M} the mode mass, and r the radius in the atmosphere where the mode velocity is evaluated. The mode mass \mathcal{M} is defined for radial modes as

$$\mathcal{M}(\nu, r) = \frac{1}{|\xi_r(\nu, r)|^2} \int_0^M |\xi_r(\nu, m)|^2 dm, \quad (2)$$

where ξ_r is the radial component of the mode eigendisplacement. The quantities v , \mathcal{M} and ξ_r are evaluated at two relevant layers:

- the photosphere, i.e. at $r = R_*$ where R_* is the stellar radius;
- at a layer where spectrographs dedicated to stellar seismology are the most sensitive. According to Samadi et al. (2008), for the Sun and solar-type stars, this layer is close to the depth where the potassium (K) spectral line is formed, that is at the optical depth $\tau_{500 \text{ nm}} \approx 0.013$. For stars with different spectral type this layer may vary, but by an as yet unknown manner (see the discussion in Samadi et al. 2008). By default we therefore adopt this reference optical depth to be representative for the Doppler velocity measurements for red giant stars. This assumption is discussed in Sect. 3.2.

Table 1. Characteristics of the 3D models.

Label	$\log g$	T_{eff} [K]
S1	2.50	4964 ± 22
S2	2.50	4475 ± 10
S3	2.00	4551 ± 16
S4	3.50	4931 ± 20
S5	3.50	5431 ± 23
S6	3.50	5885 ± 16
S7	3.00	5039 ± 11

Notes. T_{eff} is the effective temperature, and g the surface gravity.

In Eq. (1), \mathcal{P} and \mathcal{M} are computed in the manner of Samadi et al. (2008) using a set of 3D hydrodynamical models of the upper layers of sub- and red giant stars. However, this calculation differs from Samadi et al. (2008) in two aspects. First, instead of adopting a pure Lorentzian function for the eddy-time correlation in the Fourier domain, we introduce, following Belkacem et al. (2010), a cut-off frequency derived from the sweeping assumption. Second, the 3D models at our disposal have a limited vertical extent that results in an under-estimation by up to ~10% of the maximum of \mathcal{P} . To take into account the driving that occurs at deeper layers we extend the calculation to deeper layers using standard 1D stellar models (see below).

The 3D hydrodynamical models were built with the CO⁵BOLD code (Freytag et al. 2002; Wedemeyer et al. 2004; Freytag et al. 2012). All 3D models have a solar metal abundance. The chemical mixture is based on Asplund et al. (2005). The characteristics of these 3D models are given in Table 1. All models have a helium abundance of $Y = 0.249$ and a metal abundance of $Z = 0.0135$. The 3D models S1, S2, S3, and S7 correspond to red giant stars while S4, S5 and S6 to sub-giant stars.

For each 3D model, an associated complete 1D model (interior+surface) is computed in such a way that the outer layers are obtained from the 3D model (see Samadi et al. 2008, for details) while the interior layers are computed using the CESAM2K code (Morel & Lebreton 2008). In these 1D models, convection is treated according to the Canuto et al. (1996) local formulation of convection. This formulation requires a prescription for the size Λ of the strongest eddies. We assume that $\Lambda = \alpha H_p$ where H_p is the pressure scale height and α a parameter adjusted such that the interior model matches the associated 3D model as detailed in Samadi et al. (2008). The complete models (interior+surface) are from now on referred to as *patched* models.

The characteristics of the patched models are given in Table 2. We then computed the global acoustic modes associated with each of the patched models using the adiabatic pulsation code ADIPLS (Christensen-Dalsgaard 2008). Finally, the mode lifetimes τ are evaluated using the measurements performed by Baudin et al. (2011, see Sect. 3.1).

Our objective is to establish a scaling for the maximum of v (Eq. (1), V_{max} hereafter) as a function of stellar parameters and assuming that the mode lifetime τ is known. As shown by Belkacem et al. (2011), the mode lifetime τ is expected to reach a plateau at a characteristic frequency, ν_{max} . As we will see in Sect. 2.2, the maximum of $(\mathcal{P}/\mathcal{M})$ also peaks at ν_{max} . Accordingly, to derive a scaling law for V_{max} , one needs to determine how the ratio $(\mathcal{P}/\mathcal{M})_{\text{max}}$ scales with stellar parameters (see Sect. 2.2).

Among these parameters, apart from the classical fundamental parameters (luminosity L , mass M , effective temperature T_{eff} , gravity g , etc.), we in addition considered the acoustic cut-off

Table 2. Characteristics of the 1D “patched” models.

Label	M [M_{\odot}]	α	$\log g$	T_{eff} [K]	L [L_{\odot}]	$\Delta\nu$ [μHz]	ν_c [μHz]
M1	3.74	0.565	2.51	4962	172.5	3.43	63
M2	0.98	0.621	2.50	4463	30.4	4.77	67
M3	4.20	0.610	1.99	4551	444	1.40	21
M4	1.39	0.636	3.53	4927	5.86	25.11	637
M5	1.74	0.596	3.50	5392	11.5	23.30	607
M6	1.73	0.576	3.51	5856	15.9	23.30	583
M7	2.49	0.615	3.00	5040	39.3	9.00	199

Notes. L is the luminosity, M the mass, $\Delta\nu$ the large separation, and ν_c the acoustic cut-off frequency.

frequency ν_c and the large frequency separation $\Delta\nu$ (see e.g. Christensen-Dalsgaard 1982), since the former is related to the properties of the surface and the latter to the mean density of the star. These parameters scale as

$$\nu_c = \nu_{c,\odot} \frac{g}{g_{\odot}} \sqrt{\frac{T_{\text{eff},\odot}}{T_{\text{eff}}}} \quad (3)$$

$$\Delta\nu = \Delta\nu_{\odot} \sqrt{\frac{M}{M_{\odot}} \left(\frac{R_{\odot}}{R}\right)^3}, \quad (4)$$

where quantities labelled with the symbol \odot refer to solar values, $\nu_{c,\odot} = 5100 \mu\text{Hz}$ (see Jiménez 2006, and references therein), and $\Delta\nu_{\odot} = 134.9 \mu\text{Hz}$ (Toutain & Froehlich 1992). The values of ν_c and $\Delta\nu$ associated with each model are given in Table 2.

Finally, we stress that the characteristic frequency ν_{max} , at which τ reaches a plateau and \mathcal{P}/M is maximum, is related to a resonance in the uppermost layers of solar-like stars between the thermal time-scale and the modal period (see Belkacem et al. 2011, and reference therein). This is why it scales as the acoustic cut-off frequency ν_c in very good approximation:

$$\nu_{\text{max}} = \nu_{\text{max},\odot} \frac{\nu_c}{\nu_{c,\odot}}, \quad (5)$$

where $\nu_{\text{max},\odot} = 3101 \mu\text{Hz}$.

2.2. Scaling relation for $(\mathcal{P}/M)_{\text{max}}$

The maximum of \mathcal{P} is plotted in Fig. 1 (top) as a function of the ratio $L/M \propto T_{\text{eff}}^4/g$. This dependence with T_{eff} and g was already highlighted and explained by Stein et al. (2004) and Samadi et al. (2007; see also the review by Samadi 2011), and is nicely confirmed by Fig. 1 (top). Indeed, \mathcal{P}_{max} follows a power law of the form

$$\mathcal{P}_{\text{max}} = \mathcal{P}_{\text{max}}^0 \left(\frac{L}{L_{\odot}} \frac{M_{\odot}}{M}\right)^s \quad \text{with} \quad s = 2.60 \pm 0.08, \quad (6)$$

where $\mathcal{P}_{\text{max}}^0 = (4.2^{+1.0}_{-0.8}) \times 10^{15} \text{ J/s}$. The maximum of \mathcal{P} is found to peak at a frequency close to ν_{max} . We note also that the value of the exponent and the constant $\mathcal{P}_{\text{max}}^0$ in Eq. (6) are compatible with the results of Samadi et al. (2007) established on the basis of a small set of 3D models of the surface layers of main-sequence (MS) stars. We thus confirm the validity of this relation from MS to red giant stars.

We turn now to the mode mass, M . Because we aim to compare theoretical mode velocities with measurements made from the ground with spectrographs dedicated to stellar seismology, we evaluate M at the optical depth $\tau_{500 \text{ nm}} = 0.013$ (see Sect. 2.1

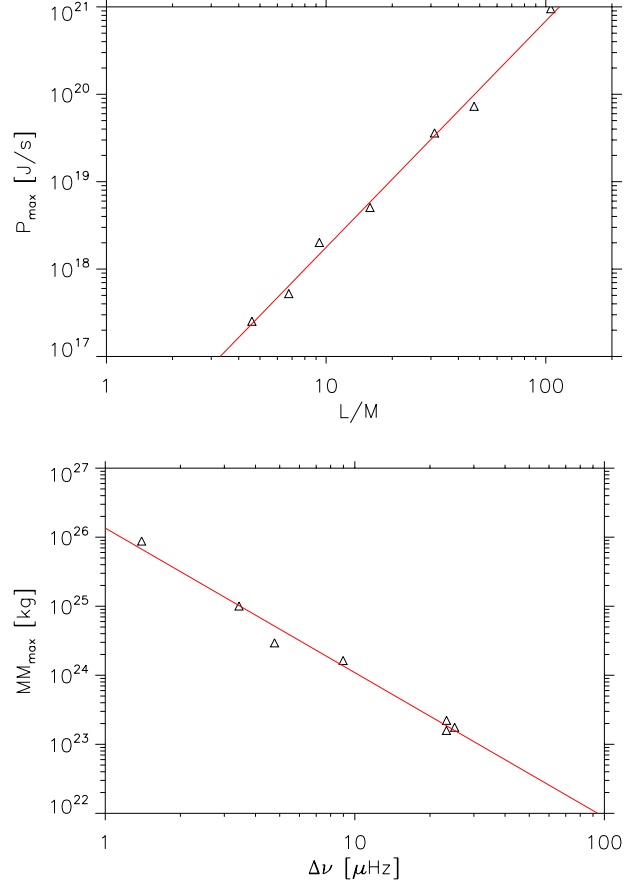


Fig. 1. Top: \mathcal{P}_{max} as a function of L/M . The triangles are associated with the 3D models. The red line is a power law of the form $(L/M)^s$ with $s = 2.6$. Bottom: mode mass at $\nu = \nu_{\text{max}}$ (M_{max}) as a function of the large separation $\Delta\nu$. The mode masses are evaluated here at the layer corresponding to the optical depth $\tau_{500 \text{ nm}} = 0.013$ (see text). The triangles are associated with the 3D models. The red line is a power law of the form $(\Delta\nu/\Delta\nu_{\odot})^{-p}$ with $p = 2.1$.

and Samadi et al. 2008). For a given model, the mode mass (M) decreases rapidly with ν , but above a characteristic frequency close to ν_{max} it decreases more slowly. Although M does not have a minimum, we found that, as \mathcal{P} , the ratio (\mathcal{P}/M) reaches a maximum close to ν_{max} , which scales as given by Eqs. (3) and (5). Therefore, we evaluate M at $\nu = \nu_{\text{max}}$. From now on we label this quantity as M_{max} .

Among the different stellar parameters mentioned in Sect. 2.1, a clear correlation of M_{max} is found with g , (L/M) , ν_c or $\Delta\nu$. However, the more pronounced correlation is found with $\Delta\nu$. We therefore adopt the scaling with $\Delta\nu$. The variation of M_{max} with $\Delta\nu$ is shown in Fig. 1 (bottom). M_{max} can be nicely fitted by a power law of the form

$$M_{\text{max}} = M_{\text{max}}^0 \left(\frac{\Delta\nu}{\Delta\nu_{\odot}}\right)^{-p} \quad \text{with} \quad p = 2.1 \pm 0.1, \quad (7)$$

where $M_{\text{max}}^0 = (4.5^{+1.8}_{-1.3}) \times 10^{21} \text{ kg}$, and $\Delta\nu$ is given by the scaling relation of Eq. (4).

By using Eqs. (6) and (7), the maximum of the ratio \mathcal{P}/M then varies according to:

$$(\mathcal{P}/M)_{\text{max}} = (\mathcal{P}_{\text{max}}^0/M_{\text{max}}^0) \left(\frac{L}{L_{\odot}} \frac{M_{\odot}}{M}\right)^s \left(\frac{\Delta\nu}{\Delta\nu_{\odot}}\right)^p. \quad (8)$$

2.3. Scaling relation for V_{\max}

Equation (8) now permits us to proceed by considering the scaling law for mode amplitudes, in terms of surface velocities. The maximum of the mode surface velocity, by using Eq. (8) together with Eq. (1), reads

$$V_{\max} = v_0 \sqrt{\frac{\tau_{\max}}{\tau_0} \left(\frac{L}{L_{\odot}} \frac{M_{\odot}}{M} \right)^s \left(\frac{\Delta v}{\Delta v_{\odot}} \right)^p}, \quad (9)$$

where τ_{\max} is the characteristic lifetime at $v = v_{\max}$, and

$$v_0 = \sqrt{\frac{\tau_0}{2} \left(\frac{\mathcal{P}_{\max}^0}{\mathcal{M}_{\max}^0} \right)}, \quad (10)$$

with τ_0 a reference mode lifetime whose values are arbitrary fixed to the lifetime of the solar radial modes at the peak frequency, that is $\tau_0 = 3.88$ days. Accordingly, we have $v_0 = 0.41$ m/s.

It is worthwhile to note that our scaling relation (Eq. (9)) differs from the result of Kjeldsen & Bedding (2011). This is explained by the fact that the postulated relation of Kjeldsen & Bedding (2011) for mode amplitudes in velocity (their Eq. (16)) does not take the mode masses into account, while this is definitively necessary as seen in Eq. (1).

2.4. Scaling relation for bolometric amplitude

The instantaneous bolometric mode amplitude is deduced at the photosphere according to (Dziemkowski 1977; Pesnell 1990)

$$\frac{\delta L(t)}{L} = 4 \frac{\delta T_{\text{eff}}(t)}{T_{\text{eff}}} + 2 \frac{\delta R_*(t)}{R_*}, \quad (11)$$

where $\delta L(t)$ is the mode Lagrangian (bolometric) luminosity perturbation, $\delta T_{\text{eff}}(t)$ the effective temperature fluctuation, and $\delta R_*(t)$ the variation of the stellar radius.

Since the second term of Eq. (11) is found negligible in front of $\delta T_{\text{eff}}(t)$, one obtains the rms bolometric amplitudes according to

$$\left(\frac{\delta L}{L} \right)_{\text{rms}} = 4 \left(\frac{\delta T_{\text{eff}}}{T_{\text{eff}}} \right)_{\text{rms}}, \quad (12)$$

where the subscript rms denotes the root mean-square.

We now need a relation between $(\delta T_{\text{eff}}/T_{\text{eff}})_{\text{rms}}$ (or equivalently $(\delta L/L)_{\text{rms}}$) and the rms mode velocity V_{\max} . For convenience we introduce the dimensionless coefficient ζ defined according to

$$(\delta L/L)_{\text{rms}} = 4 \left(\frac{\delta T_{\text{eff}}}{T_{\text{eff}}} \right)_{\text{rms}} = \zeta \left(\frac{\delta L}{L} \right)_{\text{rms}}^{\odot} \left(\frac{v_{\text{rms}}}{v_{\odot}} \right), \quad (13)$$

where $(\delta L/L)_{\text{rms}}^{\odot} = 2.53 \pm 0.11$ ppm is the maximum of the solar bolometric mode amplitude (Michel et al. 2009), $T_{\text{eff}}^{\odot} = 5777$ K the effective temperature of the Sun, and $v_{\text{rms}}^{\odot} = 18.5 \pm 1.5$ cm/s the maximum of the solar mode (intrinsic) surface velocity evaluated at the photosphere as explained in Samadi et al. (2010).

The quantity ζ in Eq. (13) is defined at an arbitrary layer, which is generally the photosphere (i.e. at $r = R_*$). Accordingly, we must evaluate the velocity and hence the mode mass \mathcal{M} at that layer. This implies the following scaling for \mathcal{M}_{\max} :

$$\mathcal{M}_{\max,*} = \mathcal{M}_{\max,*}^0 \left(\frac{\Delta v}{\Delta v_{\odot}} \right)^{-p_*}, \quad (14)$$

where $p_* = 2.0 \pm 0.10$, $\mathcal{M}_{\max,*}^0 = (8.0_{-2.1}^{+2.8}) \times 10^{21}$ kg and Δv is given by the scaling relation of Eq. (4).

Combining Eq. (13) with (9) gives the scaling for the bolometric amplitude

$$\begin{aligned} \left(\frac{\delta L}{L} \right)_{\text{max}} &= \zeta \left(\frac{\delta L}{L} \right)_{\text{rms}}^{\odot} \left(\frac{v_{0,*}}{v_{\text{rms}}^{\odot}} \right) \\ &\times \sqrt{\frac{\tau_{\max}}{\tau_0} \left(\frac{L}{L_{\odot}} \frac{M_{\odot}}{M} \right)^s \left(\frac{\Delta v}{\Delta v_{\odot}} \right)^{p_*}}, \end{aligned} \quad (15)$$

where $v_{0,*} \equiv \sqrt{\frac{\tau_0}{2} \left(\frac{\mathcal{P}_{\max}^0}{\mathcal{M}_{\max,*}^0} \right)} = 0.31$ m/s.

2.4.1. Adiabatic case

Within the adiabatic approximation, it is possible to relate the mode surface velocity to intensity perturbations (e.g., Kjeldsen & Bedding 1995); this give:

$$\zeta_{\text{K95}} = \sqrt{\frac{T_{\text{eff}}^{\odot}}{T_{\text{eff}}}}, \quad (16)$$

which assumes that the modes are quasi-adiabatic, but not only. It supposes that the modes propagate at the surface where they are measured. This approximation is not valid in the region where the modes are measured since in this region they are evanescent. Furthermore, it assumes an isothermal atmosphere. A more sophisticated quasi-adiabatic approach has been proposed by Severino et al. (2008). The authors went beyond the approximation of isothermal atmosphere by taking into account the temperature gradient as well as the fact that the intensity is measured at constant instantaneous optical depth. Both effects are taken into account by the method described in Sect. 2.4.2, which in addition considers non-adiabatic modes.

We present in Fig. 2 ζ_{K95} as a function of (L/M) . The adiabatic coefficient remains almost constant for the type of stars investigated here (sub- and red giant stars). This is obviously because ζ_{K95} varies as the inverse of the square root of T_{eff} .

2.4.2. Non-adiabatic case

We also computed ζ using the MAD non-adiabatic pulsation code (Grigahcène et al. 2005). This code includes the time-dependent convection (TDC) treatment described in Grigahcène et al. (2005).

This TDC formulation involves a free parameter β , which takes complex values and enters the perturbed energy equation. This parameter was introduced to prevent the occurrence of non-physical spatial oscillations in the eigenfunctions (see Grigahcène et al. 2005, for details). To constrain this parameter we used the scaling relation between the frequency of the maximum height in the power spectrum (ν_{\max}) and the cut-off frequency (ν_c). When scaled to the Sun, one can use this scaling to infer ν_{\max} for the models we used and the parameter β is then adjusted so that the plateau (or depression) of the computed damping rates coincides (see Belkacem et al. 2012).

Note also that TDC is a non-local formulation of convection and is based on the Gabriel (1996) formalism as explained in Dupret et al. (2006b) and Dupret et al. (2006a). In this framework, non-local parameters related to the convective flux (a) and the turbulent pressure (b) are chosen in the same way as in Dupret et al. (2006b, see their Eqs. (17) and (18), see also

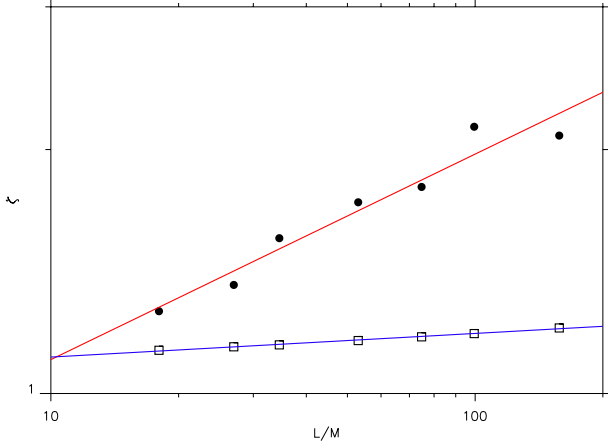


Fig. 2. Coefficient ζ (see Eq. (13)) as a function of L/M for sub- and red giants. The filled circles correspond to the values, ζ_{nad} , obtained with the MAD non-adiabatic pulsation code (see details in the text). The empty squares correspond to the adiabatic coefficient Kjeldsen & Bedding (1995) (see Eq. (16)). The red line corresponds to a power law of the form $\zeta_0 (L/M)^k$ with $k = 0.25$. Both intensity-velocity relations ζ have been calibrated so that for the Sun $\zeta = 1$ (see text).

Dupret et al. 2006c) so that it fits the solar 3D numerical simulation. This calibration results in $a = 10.4$ and $b = 2.9$ (assuming a mixing-length parameter $\alpha = 1.62$).

For sub- and red giant stars ($L/M \gtrsim 10 L_{\odot}/M_{\odot}$), the non-adiabatic intensity-velocity relation obtained with the MAD code can quite well be fitted by a power law of the form

$$\zeta_{\text{nad}} = \zeta_0 \left(\frac{L}{L_{\odot}} \frac{M_{\odot}}{M} \right)^k, \quad (17)$$

where $k = 0.25 \pm 0.05$ and $\zeta_0 = 0.59 \pm 0.07$. For main-sequence stars ($L/M \lesssim 10 L_{\odot}/M_{\odot}$), ζ_{nad} remains almost constant (not shown). For the Sun, we find $\zeta_{\text{nad}} \simeq 0.95$, which is close to the value expected by definition for the Sun. Therefore, we are then led to multiply ζ_{nad} by only a factor 1.05 so that, for the Sun, theoretical $(\delta L/L)_{\text{max}}$ matches the helioseismic measurements. The result is shown in Fig. 2 for the sub- and red giant stars ($L/M \gtrsim 10 (L_{\odot}/M_{\odot})$). The non-adiabatic coefficient increases rapidly with increasing (L/M) while ζ_{K95} remains almost constant. Hence, the higher (L/M) , the larger the difference between the non-adiabatic and the adiabatic coefficient (ζ_{K95}).

3. Comparison with the observations

We compare in this section theoretical mode amplitudes with seismic measurements made from the ground in terms of Doppler velocity (Sect. 3.2) and from space by CoRoT in terms of intensity (Sect. 3.3). We recall that computing the theoretical mode amplitudes requires knowledge of τ_{max} (see Eqs. (9) and (15)), which is obtained from a set of CoRoT targets as explained in Sect. 3.1.

3.1. The CoRoT data set

Baudin et al. (2011) have measured the mode amplitudes for 360 CoRoT red giant targets. Among those targets, many show very narrow peaks, close to the frequency resolution of the spectrum, while the others have resolved peaks. About 65% of those targets have a highest mode whose width is sufficiently broad to

be fitted with a Lorentzian profile. For those targets, the height of the highest mode, H_{max} , and its lifetime τ_{max} are thus derived from the fit procedure. However, it is not excluded that some modes with a width more narrow than the frequency resolution may have been fitted with a Lorentzian profile because of the low signal-to-noise ratio. To exclude those modes, we only considered modes with a width $\Gamma_{\text{max}} = 1/(\pi\tau_{\text{max}})$ broader than twice the frequency resolution of the spectra (which is $0.081 \mu\text{Hz}$). This subset represents about 170 targets for which we have an estimate of the mode lifetime (τ_{max}) at the peak frequency. For each target of this subset, the maximum of the mode amplitude in intensity (A_{max}) was obtained according to the relation $A_{\text{max}} = \sqrt{H_{\text{max}}/\tau_{\text{max}}}$. Finally, a bolometric correction was applied in the manner of Michel et al. (2009) to convert the apparent intensity fluctuation A_{max} into a bolometric amplitude $(\delta L/L)_{\text{max}}$.

3.2. Maximum velocity amplitude (V_{max})

The mode amplitude in terms of velocity is given by Eq. (9). Calculating V_{max} requires to know the mode life time τ_{max} at the peak frequency. We used the values of τ_{max} available for our set of CoRoT targets (see Sect. 3.1). We also determined the ratio L/M as well as $\Delta\nu$. The luminosity and mass of these targets are unknown. However, Baudin et al. (2011) have proposed to derive an estimate of the ratio L/M using the following scaling:

$$\frac{L}{M} \propto \frac{T_{\text{eff}}^{7/2}}{\nu_{\text{max}}}, \quad (18)$$

where ν_{max} is the frequency of the maximum mode height H_{max} and T_{eff} is determined from photometric broad-band measurements as explained in Baudin et al. (2011). Note that the scaling law of Eq. (18) assumes that ν_{max} scales as ν_c , which scales as $g/\sqrt{T_{\text{eff}}}$ (see Eq. (3)). Concerning $\Delta\nu$, as first established by Stello et al. (2009), Hekker et al. (2009) and Kallinger et al. (2010), there is a clear scaling relation between this quantity and ν_{max} . We derived this quantity here according to the relation derived by Mosser et al. (2010) from a large set of CoRoT red giant stars:

$$\Delta\nu = 0.280 \nu_{\text{max}}^{0.747}. \quad (19)$$

Theoretical values of V_{max} were compared with the stars whose V_{max} has been measured so far in Doppler velocity from the ground. We considered the different measurements published in the literature (Frandsen et al. 2002; Barban et al. 2004; Bouchy et al. 2005; Carrier et al. 2005a,b; Mosser et al. 2005, 2008; Arentoft et al. 2008; Kjeldsen et al. 2008; Teixeira et al. 2009; Ando et al. 2010). The values quoted in the literature are generally given in terms of peak amplitudes. In that case they were converted into *root-mean-square* (rms) amplitudes. Furthermore, we rescaled all amplitudes into *intrinsic* (by opposition to observed) amplitudes. Measured values of V_{max} are shown in Fig. 3 (top panel) as a function of L/M . We have an estimate of the ratio L/M for only a few stars while for almost all of them we have a seismic measure of ν_{max} , which is typically more accurate than the determination of the ratio L/M . Therefore, we also show V_{max} in Fig. 3 (bottom) as a function of ν_{max} . The theoretical values of V_{max} obtained for our subset of red giants are found to be close to the measurements obtained for the red giant stars observed in Doppler velocity from the ground. Note that the considerable dispersion seen in the theoretical values of V_{max} comes from the dispersion in the measured value of τ_{max} .

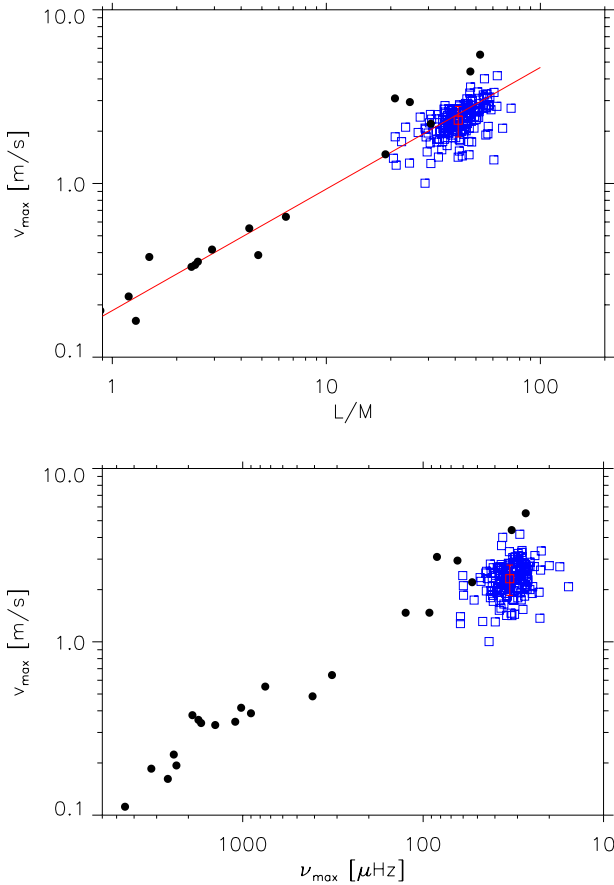


Fig. 3. *Top:* maximum of the mode velocity V_{\max} as a function of L/M . The filled circles correspond to the MS stars observed in Doppler velocity from the ground and the red line to the power law of the form $(L/M)^{0.7}$ obtained by Samadi et al. (2007) using 3D models of MS stars. The blue squares correspond to the theoretical V_{\max} derived according to Eq. (9) (see Sect. 3.2). The red square corresponds to the median value of the theoretical V_{\max} and the associated vertical bar corresponds to bias introduced by the $1-\sigma$ error associated with the parameters p , s , \mathcal{P}_0 , and M_0 (Eq. (8)). *Bottom:* same as top as a function of ν_{\max} .

Furthermore, we point out that the parameters p , s , \mathcal{P}_0 , and M_0 , which appear in Eq. (8), are mostly determined with quite a large error. The errors associated with the parameters introduce a bias on the theoretical V_{\max} , which is shown in Fig. 3 by a red vertical bar. As seen in Fig. 3, the theoretical V_{\max} are found, on average, to be about 30% lower than the measurements.

Using several 3D simulations of the surface of main-sequence stars, Samadi et al. (2007) have found that V_{\max} scales as $(L/M)^{sv}$ with $sv = 0.7$. As seen in Fig. 3, this scaling law reproduces the MS stars quite well. When extrapolated to the red giant domain ($L/M \gtrsim 10 L_{\odot}/M_{\odot}$), this scaling law results for V_{\max} in values very close to our present theoretical calculations.

The mode masses M_{\max} were so far evaluated at the reference optical depth $\tau_{500 \text{ nm}} = 0.013$ (see Sect. 2.1). We now discuss the sensitivity M_{\max} to the optical depth at which they are computed. To evaluate our sensitivity to this choice, we alternatively computed the theoretical V_{\max} at the photosphere and at an optical depth ten times lower than our reference level, that is at $\tau_{500 \text{ nm}} = 10^{-3}$. Theoretical V_{\max} are found to be $\sim 30\%$ lower at the photosphere and higher by $\sim 20\%$ at the optical depth

$\tau_{500 \text{ nm}} = 10^{-3}$. This result illustrates at which level V_{\max} is sensitive to the depth where the acoustic modes are supposed to be measured. This depth is not well known, however, but we believe that it should be located between the photosphere and our reference optical depth.

3.3. Maximum bolometric amplitude $(\delta L/L)_{\max}$

3.3.1. Adiabatic case

We computed $(\delta L/L)_{\max}$ according to Eq. (15) using the scaling law given by Eq. (9) for ν and assuming the adiabatic coefficient ζ_{K95} (Eq. (16)). Figure 4 (top) shows $(\delta L/L)_{\max}$ as a function of ratio (L/M) , where this ratio is estimated according to Eq. (18). We also plotted the mode amplitudes measured for a small sample of CoRoT main-sequence stars (see Baudin et al. 2011, and references therein). Theoretical $(\delta L/L)_{\max}$ underestimates the amplitudes measured on the CoRoT red giant stars by a factor of about 2.5.

3.3.2. Non-adiabatic case

We computed $(\delta L/L)_{\max}$ according to Eq. (15) assuming the non-adiabatic scaling law established in Sect. 2.4.2 (see Eq. (17)) for ζ . The result is shown in Fig. 4 (bottom). Using the non-adiabatic coefficient results in an increase of the bolometric amplitude by a factor ~ 1.5 compared to the calculations based on the adiabatic coefficient. This renders the theoretical bolometric amplitude closer to the observations.

We have plotted in Fig. 5 the histogram of the relative difference between observed and theoretical $(\delta L/L)_{\max}$, that is, the histogram of the quantity $\gamma \equiv (A^{\text{obs}} - A)/A$, where A is the theoretical amplitude and A^{obs} the observed one. The dispersion seen in the histogram is due both to the errors associated with the data and the fact that we observe a heterogeneous population of stars with different chemical abundance.

The red horizontal bar shows the bias introduced by the $1-\sigma$ errors associated with the determination of the parameters p , s , \mathcal{P}_0 , $M_{0,*}$, k , and ζ_0 as well the measurement of $(\delta L/L)_{\text{rms}}^{\odot}$ and ν_{rms}^{\odot} (see Eq. (13)). The median of γ is close to 0.8 (the vertical dashed line). This means that theoretical amplitudes remains, on average, $\sim 40\%$ below the CoRoT measurements.

4. Conclusion

4.1. Theoretical scaling relation for the velocity mode amplitude

We have extended the calculations performed by Samadi et al. (2007) for main-sequence stars to sub- and red giant stars. We found that the maximum of the mode excitation rate, \mathcal{P}_{\max} , scales approximately as $(L/M)^s$ with $s = 2.60 \pm 0.08$. Accordingly, for sub- and red giant stars, theoretical \mathcal{P}_{\max} scales in same way as for the main-sequence stars.

We also found that the mode mass at the peak frequency, M_{\max} , which was evaluated at a reference level in the atmosphere, scales as $\Delta\nu^{-p}$ where $\Delta\nu \propto (M/R^3)^{1/2}$, with $p = 2.1 \pm 0.1$. Since (M/R^3) represents also the mean density, we have that M_{\max} scales almost linearly as the inverse of the star mean density. This tight relation still remains to be understood, however.

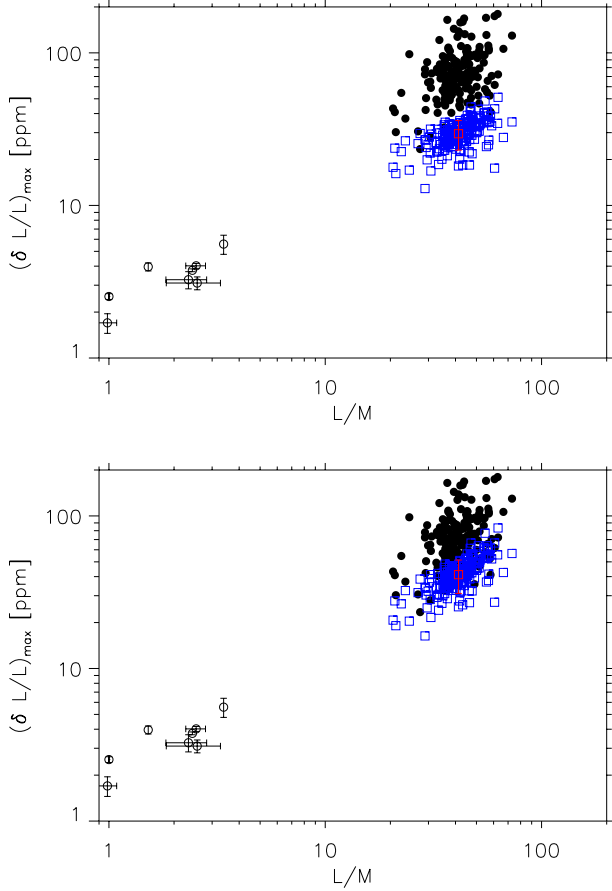


Fig. 4. *Top:* maximum of the mode intensity fluctuation $(\delta L/L)_{\max}$ as a function of L/M . The filled circles correspond to the seismic measurements performed by Baudin et al. (2011) on a large number of CoRoT red giant stars (~ 170 targets). We only considered the targets for which the mode line width is broader than twice the frequency resolution (see Sect. 3.1). The empty circles correspond to the MS stars observed so far by CoRoT (see Baudin et al. 2011), and the blue squares are the theoretical $(\delta L/L)_{\max}$ computed according to the Kjeldsen & Bedding (1995) adiabatic coefficient (Eq. (16), see Sect. 3.3.1). The red square corresponds to the median value of the theoretical $(\delta L/L)_{\max}$ and the associated vertical bar corresponds to the bias introduced by the $1\text{-}\sigma$ error associated with the parameters p_* , s , \mathcal{P}_0 , and $\mathcal{M}_{0,*}$, $(\delta L/L)_{\text{rms}}^{\circ}$ and v_{rms}° (see Eq. (15)). *Bottom:* same as top, the theoretical $(\delta L/L)_{\max}$ are computed here assuming for ζ the non-adiabatic scaling relation established in Sect. 2.4.2 (see also Fig. 2). The red error bar here also accounts for the $1\text{-}\sigma$ error associated with the parameters k and ζ_0 (see Eq. (17) and Sect. 2.4.2).

From the scaling laws for \mathcal{M}_{\max} and \mathcal{P}_{\max} , we finally derived a scaling law for the maximum of the mode velocity, which has the following form:

$$V_{\max} \propto (\tau_{\max})^{1/2} \left(\frac{L}{M}\right)^{s/2} \left(\frac{M}{R^3}\right)^{p/4}, \quad (20)$$

where τ_{\max} is the mode lifetime at the peak frequency.

Using CoRoT data, Baudin et al. (2011) have found that τ_{\max} scales approximately as T_{eff}^{-m} where $m = 16.2 \pm 2$ for the main-sequence and sub-giant stars. Recently, Appourchaux et al. (2012) have found a slope $m = 15.5 \pm 1.6$ with *Kepler* data, which is hence compatible with that of Baudin et al. (2011). Such a power law is also supported by the theoretical calculations of Belkacem et al. (2012) performed for main-sequence,

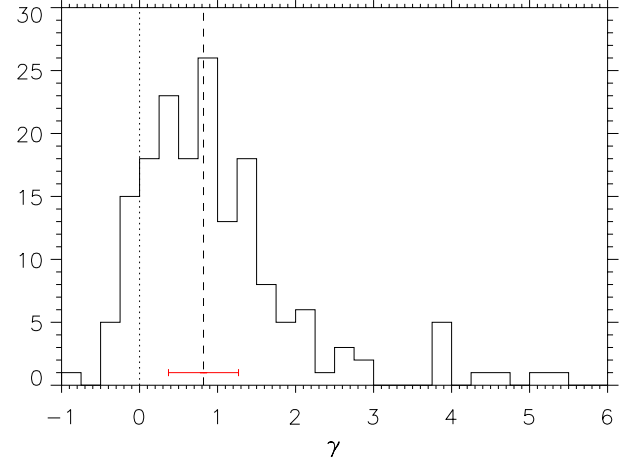


Fig. 5. Histogram of the relative difference (γ) between observed and theoretical $(\delta L/L)_{\max}$ (see text). The vertical dashed line shows the position of the median value. The horizontal error bar corresponds to the bias introduced by the $1\text{-}\sigma$ error associated with the determination of the parameters p_* , s , \mathcal{P}_0 , $\mathcal{M}_{0,*}$, k , and ζ_0 and the measurement of $(\delta L/L)_{\text{rms}}^{\circ}$ and v_{rms}° .

sub- and red giant stars. Furthermore, although \mathcal{M}_{\max} scales better with Δv , it also scales well as $g^{-p'}$ with $p' = 1.66 \pm 0.15$ (note the larger uncertainty for p' compared to p). Accordingly, since $L/M \propto T_{\text{eff}}^4/g$, we can rewrite the scaling for V_{\max} (Eq. (20)) as a function of the star spectroscopic parameters only:

$$V_{\max} \propto T_{\text{eff}}^{(2s-m/2)} g^{(p'/2-s/2)}. \quad (21)$$

Using a set of CoRoT red giant stars for which the mode lifetimes have been measured (Baudin et al. 2011), we derived from the scaling law of Eq. (20) theoretical values of V_{\max} . These values were found to be close to the measurements made from the ground in terms of Doppler velocity for red giant stars. However, the Doppler measurements remain on average under-estimated by a about 30%. We discuss in Sect. 5 possible reasons for this under-estimation.

4.2. Theoretical scaling relation for the bolometric mode amplitude

When converted in terms of intensity using the Kjeldsen & Bedding (1995) adiabatic relation, the theoretical amplitudes under-estimate the bolometric mode amplitudes measured by Baudin et al. (2011) on a set of CoRoT red giant stars by a factor about 2.5. Alternatively, we have considered the MAD non-adiabatic pulsation code (Grigahcène et al. 2005) to establish a non-adiabatic relation between intensity and velocity. We found that this relation scales as $(L/M)^k$ with $k = 0.25 \pm 0.05$. We finally established for the mode amplitude in *intensity* the following scaling law:

$$(\delta L/L)_{\max} \propto (\tau_{\max})^{1/2} \left(\frac{L}{M}\right)^{s/2+k} \left(\frac{M}{R^3}\right)^{p_*/4}, \quad (22)$$

where $p_* = 2.0 \pm 0.1$. As for the scaling relation for V_{\max} , the one for $(\delta L/L)_{\max}$ can be rewritten as a function of the star spectroscopic parameters only:

$$(\delta L/L)_{\max} \propto T_{\text{eff}}^{(2s-m/2+4k)} g^{(p_*/2-s/2-k)}, \quad (23)$$

where $p'_* = 1.63 \pm 0.15$.

Using the non-adiabatic scaling law for $(\delta L/L)_{\max}$ reduces the difference between theoretical and measured amplitudes by a factor ~ 1.5 . Our analysis hence explains qualitatively the recent results obtained for red giant stars using photometric CoRoT and *Kepler* observations (Baudin et al. 2011; Huber et al. 2011; Stello et al. 2011; Mosser et al. 2012). Indeed, we stress that the theoretical relation obtained for mode amplitudes in velocity cannot be simply extrapolated into photometry because non-adiabatic effects dominate the relation between mode amplitude in velocity and intensity.

However, while the non-adiabatic treatment implemented in the MAD code (Grigahcène et al. 2005) reduces the discrepancy with the CoRoT measurements, the latter are still underestimated on average by about 40%. Possible reasons for this discrepancy are discussed in Sect. 5.

5. Discussion

The mode masses are sensitive to the layer at which they are evaluated, which must in principle correspond to the height in the atmosphere at which spectrographs dedicated to stellar seismology are the most sensitive (see Sects. 2.1, 3.2, and Samadi et al. 2008). However, the uncertainty associated with the lack of knowledge of this layer introduces an uncertainty on the computed amplitudes that should not exceed $\sim 30\%$ (see Sect. 3.2).

The discrepancy with the velocity measurements can also be attributed to the under-estimation of the mode driving. It is not clear which part of the excitation model might be incorrect or incomplete. Nevertheless, we believe that a possible bias can arise from the way oscillations are currently treated in the region where the driving is the most efficient (i.e. the uppermost part of the convective region). Indeed, in this region the oscillation period, the thermal time-scale and the dynamical time-scale are of the same order, making the coupling between pulsation and convection stronger and energy losses more significant (see e.g. Belkacem et al. 2011, and references therein). We have compared non-adiabatic and adiabatic eigenfunctions computed for the global standard 1D model. The non-adiabatic eigenfunctions obtained with the MAD pulsation code differ from the adiabatic ones only in a small fraction of the excitation region. We found a negligible difference between excitation rates computed with non-adiabatic eigenfunctions and those computed with adiabatic eigenfunctions. However, we point out that the underlying theory is based on a time-dependent version of the mixing-length theory, which is well known to be a crude formulation of convection. Therefore a more realistic and consistent non-adiabatic approach that does not rely on free parameters and that includes constraints from 3D hydrodynamical models is required.

Finally, part of the differences with amplitudes $(\delta L/L)_{\max}$ measured by CoRoT can be attributed to the intensity-velocity relation. Indeed, if we suppose that the mode masses are correct, then we must multiply the mode excitation rates \mathcal{P}_{\max} by a factor $\sim 1.5^2 = 2.25$ to match the velocity measurements. In that case only a difference of about 20% with the observed $(\delta L/L)_{\max}$ remains, which must then be attributed to the intensity-relation. The intensity-relation strongly depends on the way non-adiabatic effects are treated, and as mentioned above, the current non-adiabatic treatment is based on a crude description of the convection and its inter-action with pulsation.

Acknowledgements. The CoRoT space mission, launched on December 27, 2006, has been developed and is operated by CNES, with the contribution of Austria, Belgium, Brasil, ESA, Germany and Spain.

References

- Ando, H., Tsuboi, Y., Kambe, E., & Sato, B. 2010, PASJ, 62, 1117
- Appourchaux, T., Benomar, O., Gruberbauer, M., et al. 2012, A&A, 537, A134
- Arentoft, T., Kjeldsen, H., Bedding, T. R., et al. 2008, ApJ, 687, 1180
- Asplund, M., Grevesse, N., & Sauval, A. J. 2005, in Cosmic Abundances as Records of Stellar Evolution and Nucleosynthesis, eds. T. G. Barnes, III, & F. N. Bash, ASP Conf. Ser., 336, 25
- Barban, C., de Ridder, J., Mazumdar, A., et al. 2004, in Proceedings of the SOHO 14/GONG 2004 Workshop, ESA SP-559, Helio- and Asteroseismology: Towards a Golden Future 12–16 July, New Haven, Connecticut, USA, ed. D. Danesy, 113
- Barban, C., Matthews, J. M., de Ridder, J., et al. 2007, A&A, 468, 1033
- Baudin, F., Barban, C., Belkacem, K., et al. 2011, A&A, 529, A84
- Bedding, T. R., Huber, D., Stello, D., et al. 2010, ApJ, 713, L176
- Belkacem, K., Samadi, R., Goupil, M. J., et al. 2010, A&A, 522, L2
- Belkacem, K., Goupil, M. J., Dupret, M. A., et al. 2011, A&A, 530, A142
- Belkacem, K., Dupret, M. A., Baudin, F., et al. 2012, A&A, 540, L7
- Bouchy, F., Bazot, M., Santos, N. C., Vauclair, S., & Sosnowska, D. 2005, A&A, 440, 609
- Canuto, V. M., Goldman, I., & Mazzitelli, I. 1996, ApJ, 473, 550
- Carrier, F., Eggenberger, P., & Bouchy, F. 2005a, A&A, 434, 1085
- Carrier, F., Eggenberger, P., D'Alessandro, A., & Weber, L. 2005b, New A, 10, 315
- Chaplin, W. J., Houdek, G., Elsworth, Y., et al. 2005, MNRAS, 360, 859
- Christensen-Dalsgaard, J. 1982, MNRAS, 199, 735
- Christensen-Dalsgaard, J. 2008, Ap&SS, 316, 113
- de Ridder, J., Barban, C., Baudin, F., et al. 2009, Nature, 459, 398
- Dupret, M. A., Barban, C., Goupil, M.-J., et al. 2006a, in Proceedings of SOHO 18/GONG 2006/HELAS I, Beyond the spherical Sun, ESA Spec. Publ., 624
- Dupret, M.-A., Goupil, M.-J., Samadi, R., Grigahcène, A., & Gabriel, M. 2006b, in Proceedings of SOHO 18/GONG 2006/HELAS I, Beyond the spherical Sun, ESA Spec. Publ., 624
- Dupret, M.-A., Samadi, R., Grigahcène, A., Goupil, M.-J., & Gabriel, M. 2006c, Commun. Asteroseismol., 147, 85
- Dziemblowski, W. 1977, Acta Astron., 27, 95
- Fransen, S., Carrier, F., Aerts, C., et al. 2002, A&A, 394, L5
- Freytag, B., Steffen, M., & Dorch, B. 2002, Astron. Nachr., 323, 213
- Freytag, B., Steffen, M., Ludwig, H.-G., et al. 2012, J. Comput. Phys., 231, 919
- Gabriel, M. 1996, BASI, 24, 233
- Goldreich, P., & Keeley, D. A. 1977, ApJ, 212, 243
- Goldreich, P., Murray, N., & Kumar, P. 1994, ApJ, 424, 466
- Grigahcène, A., Dupret, M.-A., Gabriel, M., Garrido, R., & Scuflaire, R. 2005, A&A, 434, 1055
- Hekker, S., Kallinger, T., Baudin, F., et al. 2009, A&A, 506, 465
- Huber, D., Bedding, T. R., Stello, D., et al. 2010, ApJ, 723, 1607
- Huber, D., Bedding, T. R., Stello, D., et al. 2011, ApJ, 743, 143
- Jiménez, A. 2006, ApJ, 646, 1398
- Kallinger, T., Weiss, W. W., Barban, C., et al. 2010, A&A, 509, A77
- Kjeldsen, H., & Bedding, T. R. 1995, A&A, 293, 87
- Kjeldsen, H., & Bedding, T. R. 2011, A&A, 529, L8
- Kjeldsen, H., Bedding, T. R., Arentoft, T., et al. 2008, ApJ, 682, 1370
- Michel, E., Samadi, R., Baudin, F., et al. 2009, A&A, 495, 979
- Miglio, A., Montalbán, J., Baudin, F., et al. 2009, A&A, 503, L21
- Morel, P., & Lebreton, Y. 2008, Ap&SS, 316, 61
- Mosser, B., Bouchy, F., Catala, C., et al. 2005, A&A, 431, L13
- Mosser, B., Deheuvels, S., Michel, E., et al. 2008, A&A, 488, 635
- Mosser, B., Belkacem, K., Goupil, M.-J., et al. 2010, A&A, 517, A22
- Mosser, B., Elsworth, Y., Hekker, S., et al. 2012, A&A, 537, A30
- Pesnell, W. D. 1990, ApJ, 363, 227
- Samadi, R. 2011, in Lect. Notes Phys., 832, 305
- Samadi, R., & Goupil, M. J. 2001, A&A, 370, 136
- Samadi, R., Georgobiani, D., Trampedach, R., et al. 2007, A&A, 463, 297
- Samadi, R., Belkacem, K., Goupil, M. J., Dupret, M.-A., & Kupka, F. 2008, A&A, 489, 291
- Samadi, R., Ludwig, H.-G., Belkacem, K., et al. 2010, A&A, 509, A16
- Severino, G., Straus, T., & Steffen, M. 2008, Sol. Phys., 251, 549
- Stein, R., Georgobiani, D., Trampedach, R., Ludwig, H.-G., & Nordlund, Å. 2004, Sol. Phys., 220, 229
- Stello, D., Chaplin, W. J., Basu, S., Elsworth, Y., & Bedding, T. R. 2009, MNRAS, 400, L80
- Stello, D., Huber, D., Kallinger, T., et al. 2011, ApJ, 737, L10
- Teixeira, T. C., Kjeldsen, H., Bedding, T. R., et al. 2009, A&A, 494, 237
- Toutain, T., & Froehlich, C. 1992, A&A, 257, 287
- Wedemeyer, S., Freytag, B., Steffen, M., Ludwig, H.-G., & Holweger, H. 2004, A&A, 414, 1121

Annexe B

CURRICULUM VITAE

Nom, prénoms : **SAMADI, Davoud Réza**

Date et lieu de naissance : 31/12/71 à Meched (Iran)

Nationalité : Française

Coordonnées :

Observatoire de Paris - section Meudon

Bat. 14, 5 place Jules Janssen

92 195 Meudon

France

Tél : +33 1 45 07 78 48

Fax : +33 1 45 07 79 59

e-mail : Reza.Samadi@obspm.fr

Carrière professionnelle

01/2004-	Astronome adjoint à l'Observatoire de Paris dans le Laboratoire d'études spatiales et d'instrumentation en astrophysique (LESIA, UMR8109), Université Pierre et Marie Curie, Université Denis Diderot
06/2003-12/2003	Boursier de la Fondation portugaise pour la Science et la Technologie (FCT) à l'Observatoire de Coimbra (Coimbra, Portugal)
02/2003-05/2003	Boursier de la Société de Secours des Amis des Sciences au LESIA (Observatoire de Paris)
10/2002-01/2003	Vacataire de recherche au LESIA (Observatoire de Paris)
10/2000-09/2002	Chercheur Assistant au Queen Mary University of London (Londres, Royaume-Uni) sous la responsabilité de I. Roxburgh
10/1997-09/2000	Allocataire de recherche au DESPA (Observatoire de Paris)

Séjours à l'étranger

09/2001 [3 mois]	Niels Bohr Institut for Astrophysics, Physics and Geophysics, Copenhagen, Denmark
01/2003 [5 semaines]	Michigan State University, Lansing, Michigan, USA
10/2004 [2 semaines]	Standford University, Standford, California, USA

Diplomes et qualifications

2001 1997-2000	Qualifié par la section 34 de la Commission Nationale des Universités (CNU) Thèse de doctorat de l'Université Pierre et Marie Curie (Paris 6) <ul style="list-style-type: none">• Spécialité : «Méthodes instrumentales en Astrophysique et leurs applications spatiales».• Sujet : «Excitation stochastique des oscillations stellaires. Application à la mission spatiale COROT».• Laboratoire : DESPA, Observatoire de Paris.• Date et lieu de soutenance : 8 décembre 2000, Observatoire de Meudon.• Directeurs de thèse : Annie BAGLIN, Directeur de recherche à l'Observatoire de Paris et Marie-Jo GOUPIL, Astronome à l'Observatoire de Paris• Mention : Très honorable avec les félicitations du Jury.• Financement : allocation de recherche MESR.
1996-1997	DEA «Méthodes instrumentales en Astrophysique et leurs applications spatiales», Paris 6, mention Bien
1994-1995	Maîtrise de Physique Fondamentale, Paris 6, mention Assez Bien
1993-1994	Licence de Physique, Paris 6, mention Bien
1992-1993	DEUG A, Paris 6, mention Bien
1991-1992	Classe Préparatoire Maths Sup., au lycée Fénélon (Paris 5)
1990-1991	Baccalauréat série C au lycée Gustave Eiffel (Cachan, Val de Marne)

Enseignements ponctuels

01/2011	1 h de cours dispensé dans le cadre du module «conduite de projet» de l'Ecole Doctorale d'Astronomie et d'Astrophysique d'Ile-de-France. Titre du cours : «PLATO : Objectifs et besoins scientifiques»
10/2008	1 h de cours dispensé dans le cadre de l'Ecole Internationale CoRoT. Titre du cours : «The CoRoT data»
10/2008	2 h de TP dispensés dans le cadre de l'Ecole Internationale CoRoT. Titre du cours : «Practice : asteroseismology data analysis»
10/2008	1 h de cours dispensé lors de l'Ecole St Flour du CNRS «Les pulsations du Soleil et des étoiles». Titre du cours : «Processus d'excitation des modes par la convection turbulente»

Enseignements

2011-	Licence 2eme année : «Électrostatique, Magnétostatique et Induction» (UE LP 203), Université Pierre et Marie Curie (Paris 6). Travaux dirigés et travaux pratiques
2005-2010	Licence 1ere année : «Electrocinétique et optique par l'expérience» (UE LP 103), Université Pierre et Marie Curie (Paris 6). Cours magistraux, travaux dirigés et travaux pratiques. Co-direction d'un amphi avec Eric Michel. Mise en place d'un site internet dédié (http://www.edu.upmc.fr/physique/lp103ElectOpt/). Mise en ligne des cours, énoncés de TD et sujets d'examen
2004-	Module de méthodologie, Master Astronomie Astrophysique et Sciences de l'Espace de l'Observatoire de Paris
2004-	Enseignement de post-master «TP de méthodes inverses», Ecole Doctorale Astronomie et Astrophysique d'Ile de France
2002-2003	6 heures d'encadrement de TP d'électronique à l'université Paris 6 18 heures d'encadrement de TP de sismologie à des doctorants de l'Ecole Doctorale d'Astronomie et d'Astrophysique d'Ile-de-France
2001-2002	26 heures de TP/TD d'informatique dispensées à des étudiants en 1ième année de DEUG SM de l'université Versailles-Saint Quentin-En-Yvelines (UVSQ)
2000-2001	28 heures de TP/TD d'informatique dispensées à des étudiants en 2ième année de DEUG SM de l'UVSQ 15 heures de TP de modélisation numérique en astrophysique dans le cadre des enseignements du DEA «Mathématique de la modélisation, simulation et application de la physique» de l'UVSQ
1999-2000	8 heures de colles en Physique dispensées à des étudiants en 2ième année de DEUG préparant les concours ENSI à l'université Paris 7

Encadrements de thèses

10/2005-10/2008	Co-encadrement avec M. Goupil de la thèse de K. Belkacem
09/2004-12/2007	Implication sur la thèse de Fabio Fialho (Directeur : M. Auvergne)
09/2002-12/2005	Implication sur la thèse de Jérémie Lochard (Directeurs : M.J Goupil et P. Boumier)

Encadrements de stagiaires

01/06/2012- 30/08/2012	[3 mois] Direction d'ingénieur de Florian Ferreira de l'Ecole d'Ingénieur Denis Diderot EIDD, Spécialité Architecture des Systèmes Physiques. Sujet : «Mission spatiale PLATO : simulation de la réponse instrumentale et traitement photométrique bord»
23/04/2012- 15/06/2012	[7 semaines effectives] Direction du stage de M1 de Maylis Dozieres de l'Université Pierre et Marie Curie. Sujet : «Modélisation du spectre de la granulation stellaire dans une variété d'étoiles»
01/04/2011- 30/08/2011	[73 mois] Direction du stage de M2R de Julien Auriac de l'Université Pierre et Marie Curie. Sujet : «Étude de la réponse instrumentale des télescopes à bord du satellite PLATO (ESA)». Soutenu le 20/09/2011
01/04/2010- 15/05/2010	[7 semaines] Direction du stage de M1 de F. ZHANG & Y. CAO (binôme) de l'Université Pierre et Marie Curie. Sujet : «Transport convectif dans les étoiles : un modèle théorique et son implémentation» Soutenu le 14/06/2010
04/01/2010- 15/01/2010	(2 semaines) Stage de L3, Guichard Marc & Rodriguez Diego (binôme). Sujet : «Transport convectif dans les étoiles : étude d'un modèle théorique et son implémentation»
01/04/2005- 30/06/2005	[3 mois] Direction du stage de M2R de Kévin Belkacem de l'Ecole Doctorale d'Astronomie et d'Astrophysique d'Ile-de-France, Sujet : «Modèle de fermeture avec panaches. Application à l'excitation stochastique des oscillations stellaires»

Responsabilités scientifiques et techniques

09/2010-	Au sein du PLATO Data Center (PDC) : responsable du groupe de travail «Data Processing Algorithms» (WP 32). Responsable des études et des définitions détaillées des algorithmes scientifiques de traitement bord et sol. Animation et gestion du groupe de travail (12 collaborateurs ingénieurs et chercheurs). Évaluation des performances attendues. Rédaction de notes techniques et rapports d'avancement. Encadrement d'un ingénieur CDD de 18 mois financé par le CNES
09/2007-	Maintenance de la chaîne de traitement des données scientifiques CoRoT. Validation et surveillance des traitements
6/2008- 10/2010	Participation au groupe système PLATO (phase Assesment Study). Responsabilité de l'étude et de la définition des algorithmes scientifiques du projet de mission spatiale PLATO (ESA - Cosmic Vision). Participation à la rédaction des documents définissant l'architecture complète de la charge utile, documents sur la base desquels la mission a été sélectionnée pour une étude approfondie
2007-2011	co-I de l'ANR blanc SIROCO (SIsmologie, ROTation et CONvection stellaire avec le satellite COROT)
01/2004- 08/2007	Direction et coordination des travaux du groupe responsable de la mise en place de la chaîne de traitement scientifique sol de la mission spatiale CoRoT. Définition et développement de la chaîne de traitement. Encadrement de trois CDD
01/2002- 12/2006	Participation aux activités du groupe de travail (CoRoT - Seismology Working Group) en charge de la préparation scientifique à l'interprétation des données CoRoT

Encadrement ingénieurs et post-doctorants

07/2010-12/2011	Encadrement de Dr. J. Green dans le cadre du groupe de travail WP32 de la mission PLATO. CCD financé par le CNES
06/2005-03/2007	Encadrement de P. Journoud dans le cadre du développement de la chaîne de traitement des données scientifiques CoRoT. CCD financé par le CNES
01/2006-06/2010	Encadrement (mi-temps) de Dr. L. Lefevre dans le cadre du développement d'outils d'analyse et de caractérisation des données CoRoT et de la réduction photométrique sol. CCD financé par le CNES
01/2004-12/2006	Encadrement (mi-temps) de Dr. E. Costa dans le cadre du développement des algorithmes de correction du fond de ciel et d'outils de visualisation des données CoRoT. CCD financé par le ministère brésilien de la recherche.

Responsabilités administratives et électives

2010-2012	Secrétaire de la Société Française d'Astronomie et d'Astrophysique (SF2A) (2nd mandat de 2ans)
2008-2010	Secrétaire de la SF2A (1er mandat de 2 ans)
2008-2012	Membre élu du conseil de la SF2A (2nd mandat de 4 ans)
2004-2008	Membre élu du conseil de la SF2A (1er mandat de 4 ans)
1999-2007	Membre de la Commission Jeunes Chercheurs de l'Observatoire de Paris. Diffusion de l'information auprès des jeunes chercheurs et des étudiants en DEA. Gestion du serveur internet et de la liste de diffusion de la commission jeune chercheur.

Organisation de conférences internationales et nationales

2008	Membre du comité local d'organisation et du comité scientifique de la Semaine 2008 de l'Astrophysique Française, 30 juin - 4 juillet, 2008, Paris
2009	Membre du comité scientifique de la Semaine 2009 de l'Astrophysique Française, 29 juin - 4 juillet 2009, Besançon
2010	Membre du comité scientifique de la Semaine 2010 de l'Astrophysique Française, 21-24 juin, 2010, Marseille
2011	Responsable du comité local d'organisation et membre du comité scientifique de la Semaine 2011 de l'Astrophysique Française, juin 2011, Paris
2011	Membre du comité scientifique de l'atelier « Helio et asterosismologie, avancées et perspectives dans le contexte des nouvelles missions spatiales et instruments terrestres », 20 Juin 2011, Paris 2011
2011	Membre du comité scientifique de l'atelier « SIROCO Workshop », 8-9 juin 2011, Paris
2012	Membre du comité scientifique de la Semaine 2012 de l'Astrophysique Française, 5-8 juin 2012, Nice
2012	Membre du comité scientifique de l'atelier « CoRoT/Kepler : contribution to stars characterization », 5 juin 2012, Nice

Edition scientifique

-
- 2012 S. Boissier, P. de Laverny, N. Nardetto, R. Samadi R. (chair), Valls-Gabaud D., H. Wozniak, 2012, «SF2A 2012 : Semaine de l’Astrophysique Française», mise en ligne en cours
- 2011 Alecian G., Belkacem K., R. Samadi R. (chair), Valls-Gabaud D., 2011, «SF2A 2011 : Semaine de l’Astrophysique Française», <http://sf2a.cesr.fr/php/spip/spip.php?article350>
- 2010 Boissier S., Heydari-Malayeri, M. ; Samadi, R. (chair), Valls-Gabaud D., «SF2A 2010 : Semaine de l’Astrophysique Française», <http://sf2a.cesr.fr/php/spip/spip.php?article279>
- 2009 Heydari-Malayeri, M. ; Reylé C., Samadi, R. (chair), «SF2A 2009 : Semaine de l’Astrophysique Française», <http://sf2a.cesr.fr/php/spip/spip.php?article205>
- 2008 Charbonnel C., Combes F. (chair), Samadi R., «SF2A 2008 : Semaine de l’Astrophysique Française», <http://sf2a.cesr.fr/2008/proceedings2008.html>

Autre experience professionnelle

- 09/1995-09/1996 Informatique, dépouillement de données et traitement du signal au DESPA (Observatoire de Paris) dans le cadre du Service National. Travail sur le projet spatial EVRIS (MARS 96) en collaboration avec M. Auvergne et G.Epstein.

Autres responsabilités

- 01/2004- Gestion des serveurs de calculs et des codes numériques de l’équipe

Informatique

- Langages C/C++, JAVA, IDL, Matlab, Fortran 77, Python.
Environnements Unix, Linux (utilisation et administration), Windows XP
Logiciels Word, L^AT_EX, Excell

Annexe C

Publications

C.1 Journaux à comité de lecture

1. Degroote, P., Aerts, C., Michel, E., Briquet, M., Pápics, P. I., and 12 colleagues, The CoRoT B-type binary HD50230 : a prototypical hybrid pulsator with g-mode period and p-mode frequency spacings, 2012, *A&A*, 542, 88
2. Samadi, R., Belkacem, K., Dupret, M.-A., Ludwig, H.-G., Baudin, F., and 3 colleagues, Amplitudes of solar-like oscillations in red-giant stars : Evidences for non-adiabatic effects using CoRoT observations, 2012, *A&A*, 543, 120
3. Pápics, P. I., Briquet, M., Baglin, A., Poretti, E., Aerts, C., and 12 colleague(s), Gravitational and pressure modes detected in the B3 IV CoRoT target HD 43317, 2012, *A&A*, 542, A55
4. Mantegazza, L., Poretti, E., Michel, E., Rainer, M., Baudin, F., and 12 colleague(s), Pulsation spectrum of δ Scuti stars : the binary HD 50870 as seen with CoRoT and HARPS, 2012, *A&A*, 542, A24
5. Belkacem, K., Dupret, M. A., Baudin, F., Appourchaux, T., Marques, J. P., and 1 colleague(s), Damping rates of solar-like oscillations across the HR diagram. Theoretical calculations confronted to CoRoT and Kepler observations, 2012, *A&A*, 540, L7
6. Mosser, B., Goupil, M. J., Belkacem, K., Michel, E., Stello, D., and 13 colleague(s), Probing the core structure and evolution of red giants using gravity-dominated mixed modes observed with Kepler, 2012, *A&A*, 540, A143
7. Baudin, F., Barban, C., Goupil, M. J., Samadi, R., Lebreton, Y., and 13 colleague(s), Modelling a high-mass red giant observed by CoRoT, 2012, *A&A*, 538, A73
8. Mosser, B., Elsworth, Y., Hekker, S., Huber, D., Kallinger, T., and 13 colleague(s), Characterization of the power excess of solar-like oscillations in red giants with Kepler, 2012, *A&A*, 537, A30
9. Degroote, P., Acke, B., Samadi, R., Aerts, C., Kurtz, D. W., and 9 colleague(s), CoRoT's view on variable B8/9 stars : spots versus pulsations. Evidence for differential rotation in HD 174648, 2011, *A&A*, 536, A82
10. Baudin, F., Barban, C., Belkacem, K., Hekker, S., Morel, T., and 10 colleague(s), Amplitudes and lifetimes of solar-like oscillations observed by CoRoT (Corrigendum). Red-giant versus main-sequence stars, 2011, *A&A*, 535, 1

11. Blomme, R., Mahy, L., Catala, C., Cuypers, J., Gosset, E., and 13 colleague(s), Variability in the CoRoT photometry of three hot O-type stars. HD 46223, HD 46150, and HD 46966, 2011, A&A, 533, A4
12. Mosser, B., Barban, C., Montalbán, J., Beck, P. G., Miglio, A., and 13 colleague(s), Mixed modes in red-giant stars observed with CoRoT, 2011, A&A, 532, A86
13. Belkacem, K., Goupil, M. J., Dupret, M. A., Samadi, R., Baudin, F., and 2 colleague(s), The underlying physical meaning of the $\nu_{max} - \nu_c$ relation, 2011, A&A, 530, A142
14. Ballot, J., Gizon, L., Samadi, R., Vauclair, G., Benomar, O., and 25 colleague(s), Accurate p-mode measurements of the G0V metal-rich CoRoT target HD 52265, 2011, A&A, 530, A97
15. Baudin, F., Barban, C., Belkacem, K., Hekker, S., Morel, T., and 10 colleague(s), Amplitudes and lifetimes of solar-like oscillations observed by CoRoT. Red-giant versus main-sequence stars, 2011, A&A, 529, A84
16. Pápics, P. I., Briquet, M., Auvergne, M., Aerts, C., Degroote, P., and 11 colleague(s), CoRoT high-precision photometry of the B0.5 IV star HD 51756, 2011, A&A, 528, A123
17. Briquet, M., Aerts, C., Baglin, A., Nieva, M. F., Degroote, P., and 11 colleague(s), An asteroseismic study of the O9V star HD 46202 from CoRoT space-based photometry, 2011, A&A, 527, A112
18. Belkacem, K., Samadi, R., and Goupil, M. J., Amplitudes of solar p modes : Modelling of the eddy time-correlation function, 2011, Journal of Physics Conference Series, 271, 012047
19. Goupil, M. J., Lebreton, Y., Marques, J. P., Samadi, R., and Baudin, F., Open issues in probing interiors of solar-like oscillating main sequence stars 1. From the Sun to nearly suns, 2011, Journal of Physics Conference Series, 271, 012031
20. Mosser, B., Belkacem, K., Goupil, M. J., Michel, E., Elsworth, Y., and 10 colleague(s), The universal red-giant oscillation pattern. An automated determination with CoRoT data, 2011, A&A, 525, L9
21. Mahy, L., Gosset, E., Baudin, F., Rauw, G., Godart, M., and 11 colleague(s), Plaskett's star : analysis of the CoRoT photometric data, 2011, A&A, 525, A101
22. Chapellier, E., Rodríguez, E., Auvergne, M., Uytterhoeven, K., Mathias, P., and 16 colleague(s), The γ Doradus CoRoT target HD 49434. II. Frequency analysis of the CoRoT data, 2011, A&A, 525, A23
23. Degroote, P., Aerts, C., Samadi, R., Miglio, A., Briquet, M., and 5 colleague(s), Asteroseismology of OB stars with CoRoT, 2010, Astronomische Nachrichten, 331, 1065
24. Barban, C., Baudin, F., Mosser, B., Goupil, M. J., De Ridder, J., and 5 colleague(s), Frequency spacings of p-modes in red giants observed by CoRoT, 2010, Astronomische Nachrichten, 331, 1016
25. Gaulme, P., Deheuvels, S., Weiss, W. W., Mosser, B., Moutou, C., and 11 colleague(s), HD 46375 : seismic and spectropolarimetric analysis of a young Sun hosting a Saturn-like planet, 2010, A&A, 524, A47
26. Belkacem, K., Samadi, R., Goupil, M. J., Baudin, F., Salabert, D., and 1 colleague(s), Turbulent eddy-time-correlation in the solar convective zone, 2010, A&A, 522, L2
27. Suárez, J. C., Goupil, M. J., Reese, D. R., Samadi, R., Lignières, F., and 2 colleague(s), On the Interpretation of Echelle Diagrams for Solar-like Oscillations Effect of Centrifugal Distortion, 2010, ApJ, 721, 537

28. Degroote, P., Briquet, M., Auvergne, M., Simón-Díaz, S., Aerts, C., and 13 colleague(s), Detection of frequency spacings in the young O-type binary HD 46149 from CoRoT photometry, 2010, *A&A*, 519, A38
29. Samadi, R., Belkacem, K., Goupil, M. J., Dupret, M.-A., Brun, A. S., and 1 colleague(s), Stochastic excitation of gravity modes in massive main-sequence stars, 2010, *Ap&SS*, 328, 253
30. Carrier, F., Morel, T., Miglio, A., Montalbán, J., Auvergne, M., and 17 colleague(s), The red-giant CoRoT target HR 7349, 2010, *Ap&SS*, 328, 83
31. Gaulme, P., Vannier, M., Guillot, T., Mosser, B., Mary, D., and 17 colleague(s), Possible detection of phase changes from the non-transiting planet HD 46375b by CoRoT, 2010, *A&A*, 518, L153
32. Mathur, S., García, R. A., Catala, C., Bruntt, H., Mosser, B., and 20 colleague(s), The solar-like CoRoT target HD 170987 : spectroscopic and seismic observations, 2010, *A&A*, 518, A53
33. Mosser, B., Belkacem, K., Goupil, M.-J., Miglio, A., Morel, T., and 8 colleague(s), Red-giant seismic properties analyzed with CoRoT, 2010, *A&A*, 517, A22
34. Charpinet, S., Green, E. M., Baglin, A., van Grootel, V., Fontaine, G., and 8 colleague(s), CoRoT opens a new era in hot B subdwarf asteroseismology. Detection of multiple g-mode oscillations in KPD 0629-0016, 2010, *A&A*, 516, L6
35. Deheuvels, S., Bruntt, H., Michel, E., Barban, C., Verner, G., and 14 colleague(s), Seismic and spectroscopic characterization of the solar-like pulsating CoRoT target HD 49385, 2010, *A&A*, 515, A87
36. Aerts, C., Lefever, K., Baglin, A., Degroote, P., Oreiro, R., and 13 colleague(s), Periodic mass-loss episodes due to an oscillation mode with variable amplitude in the hot supergiant HD 50064, 2010, *A&A*, 513, L11
37. Kallinger, T., Weiss, W. W., Barban, C., Baudin, F., Cameron, C., and 8 colleague(s), Oscillating red giants in the CoRoT exofield : asteroseismic mass and radius determination, 2010, *A&A*, 509, A77
38. Carrier, F., De Ridder, J., Baudin, F., Barban, C., Hatzes, A. P., and 11 colleague(s), Non-radial oscillations in the red giant HR 7349 measured by CoRoT, 2010, *A&A*, 509, A73
39. Lüftinger, T., Fröhlich, H.-E., Weiss, W. W., Petit, P., Aurière, M., and 13 colleague(s), Surface structure of the CoRoT CP2 target star HD 50773, 2010, *A&A*, 509, A43
40. Samadi, R., Ludwig, H.-G., Belkacem, K., Goupil, M. J., Benomar, O., and 5 colleague(s), The CoRoT target HD 49933 . II. Comparison of theoretical mode amplitudes with observations, 2010, *A&A*, 509, A16
41. Samadi, R., Ludwig, H.-G., Belkacem, K., Goupil, M. J., and Dupret, M.-A., The CoRoT target HD 49933 . I. Effect of the metal abundance on the mode excitation rates, 2010, *A&A*, 509, A15
42. Maceroni, C., Montalbán, J., Michel, E., Harmanec, P., Prsa, A., and 10 colleague(s), HD 174884 : a strongly eccentric, short-period early-type binary system discovered by CoRoT, 2009, *A&A*, 508, 1375
43. Belkacem, K., Mathis, S., Goupil, M. J., and Samadi, R., Mode excitation by turbulent convection in rotating stars. I. Effect of uniform rotation, 2009, *A&A*, 508, 345
44. Benomar, O., Baudin, F., Campante, T. L., Chaplin, W. J., García, R. A., and 16 colleague(s), A fresh look at the seismic spectrum of HD49933 : analysis of 180 days of CoRoT photometry, 2009, *A&A*, 507, L13

45. Debosscher, J., Sarro, L. M., López, M., Deleuil, M., Aerts, C., and 25 colleague(s), Automated supervised classification of variable stars in the CoRoT programme. Method and application to the first four exoplanet fields, 2009, *A&A*, 506, 519
46. Degroote, P., Aerts, C., Ollivier, M., Miglio, A., Debosscher, J., and 16 colleague(s), CoRoT's view of newly discovered B-star pulsators : results for 358 candidate B pulsators from the initial run's exoplanet field data, 2009, *A&A*, 506, 471
47. Auvergne, M., Bodin, P., Boissard, L., Buey, J.-T., Chaintreuil, S., and 105 colleague(s), The CoRoT satellite in flight : description and performance, 2009, *A&A*, 506, 411
48. Léger, A., Rouan, D., Schneider, J., Barge, P., Fridlund, M., and 156 colleague(s), Transiting exoplanets from the CoRoT space mission. VIII. CoRoT-7b : the first super-Earth with measured radius, 2009, *A&A*, 506, 287
49. Ludwig, H.-G., Samadi, R., Steffen, M., Appourchaux, T., Baudin, F., and 4 colleague(s), Hydrodynamical simulations of convection-related stellar micro-variability. II. The enigmatic granulation background of the CoRoT target HD 49933, 2009, *A&A*, 506, 167
50. Dolez, N., Vauclair, S., Michel, E., Hui-Bon-Hoa, A., Vauclair, G., and 11 colleague(s), HD 51106 and HD 50747 : an ellipsoidal binary and a triple system observed with CoRoT, 2009, *A&A*, 506, 159
51. Neiner, C., Gutiérrez-Soto, J., Baudin, F., de Batz, B., Frémat, Y., and 23 colleague(s), The pulsations of the B5IVe star HD 181231 observed with CoRoT and ground-based spectroscopy, 2009, *A&A*, 506, 143
52. Gutiérrez-Soto, J., Floquet, M., Samadi, R., Neiner, C., Garrido, R., and 18 colleague(s), Low-amplitude variations detected by CoRoT in the B8IIIe star HD 175869, 2009, *A&A*, 506, 133
53. Diago, P. D., Gutiérrez-Soto, J., Auvergne, M., Fabregat, J., Hubert, A.-M., and 20 colleague(s), Pulsations in the late-type Be star HD 50 209 detected by CoRoT, 2009, *A&A*, 506, 125
54. Huat, A.-L., Hubert, A.-M., Baudin, F., Floquet, M., Neiner, C., and 17 colleague(s), The B0.5IVe CoRoT target HD 49330. I. Photometric analysis from CoRoT data, 2009, *A&A*, 506, 95
55. Poretti, E., Michel, E., Garrido, R., Lefèvre, L., Mantegazza, L., and 19 colleague(s), HD 50844 : a new look at δ Scuti stars from CoRoT space photometry, 2009, *A&A*, 506, 85
56. García Hernández, A., Moya, A., Michel, E., Garrido, R., Suárez, J. C., and 11 colleague(s), Asteroseismic analysis of the CoRoT δ Scuti star HD 174936, 2009, *A&A*, 506, 79
57. Alecian, G., Gebran, M., Auvergne, M., Richard, O., Samadi, R., and 2 colleague(s), Looking for pulsations in HgMn stars through CoRoT lightcurves, 2009, *A&A*, 506, 69
58. Dupret, M.-A., Belkacem, K., Samadi, R., Montalbán, J., Moreira, O., and 8 colleague(s), Theoretical amplitudes and lifetimes of non-radial solar-like oscillations in red giants, 2009, *A&A*, 506, 57
59. Barban, C., Deheuvels, S., Baudin, F., Appourchaux, T., Auvergne, M., and 16 colleague(s), Solar-like oscillations in HD 181420 : data analysis of 156 days of CoRoT data, 2009, *A&A*, 506, 51
60. García, R. A., Régulo, C., Samadi, R., Ballot, J., Barban, C., and 21 colleague(s), Solar-like oscillations with low amplitude in the CoRoT target HD 181906, 2009, *A&A*, 506, 41
61. Mosser, B., Michel, E., Appourchaux, T., Barban, C., Baudin, F., and 15 colleague(s), The CoRoT target HD 175726 : an active star with weak solar-like oscillations, 2009, *A&A*, 506, 33
62. Appourchaux, T., Samadi, R., and Dupret, M.-A., On posterior probability and significance level : application to the power spectrum of HD 49 933 observed by CoRoT, 2009, *A&A*, 506, 1

63. Belkacem, K., Goupil, M. J., Dupret, M. A., and Samadi, R., Theoretical amplitudes of solar-like oscillations in classical pulsators, 2009, *Communications in Asteroseismology*, 158, 269
64. Degroote, P., Miglio, A., Debosscher, J., Montalbán, J., Cuypers, J., and 18 colleague(s), Space observations of B stars with CoRoT, 2009, *Communications in Asteroseismology*, 158, 167
65. Belkacem, K., Samadi, R., Goupil, M.-J., Lefèvre, L., Baudin, F., and 13 colleague(s), Solar-Like Oscillations in a Massive Star, 2009, *Science*, 324, 1540
66. De Ridder, J., Barban, C., Baudin, F., Carrier, F., Hatzes, A. P., and 8 colleague(s), Non-radial oscillation modes with long lifetimes in giant stars, 2009, *Nature*, 459, 398
67. Kupka, F., Belkacem, K., Goupil, J.-M., and Samadi, R., Using p-mode excitation rates for probing convection in solar-like stars, 2009, *Communications in Asteroseismology*, 159, 24
68. Michel, E., Samadi, R., Baudin, F., Barban, C., Appourchaux, T., and 1 colleague(s), Intrinsic photometric characterisation of stellar oscillations and granulation. Solar reference values and CoRoT response functions, 2009, *A&A*, 495, 979
69. Belkacem, K., Samadi, R., Goupil, M. J., Dupret, M. A., Brun, A. S., and 1 colleague(s), Stochastic excitation of nonradial modes. II. Are solar asymptotic gravity modes detectable ?, 2009, *A&A*, 494, 191
70. Garcia, R. A., Appourchaux, T., Baglin, A., Auvergne, M., Barban, C., and 5 colleague(s), Solar-like stars as seen by CoRoT, 2008, *Communications in Asteroseismology*, 157, 288
71. Michel, E., Baglin, A., Weiss, W. W., Auvergne, M., Catala, C., and 18 colleague(s), First asteroseismic results from CoRoT, 2008, *Communications in Asteroseismology*, 157, 69
72. Michel, E., Baglin, A., Weiss, W. W., Auvergne, M., Catala, C., and 62 colleague(s), First asteroseismic results from CoRoT, 2008, *Communications in Asteroseismology*, 156, 73
73. Michel, E., Baglin, A., Auvergne, M., Catala, C., Samadi, R., and 39 colleague(s), CoRoT Measures Solar-Like Oscillations and Granulation in Stars Hotter Than the Sun, 2008, *Science*, 322, 558
74. Hekker, S., Arentoft, T., Kjeldsen, H., Bedding, T. R., Christensen-Dalsgaard, J., and 43 colleague(s), Oscillations in Procyon A : First results from a multi-site campaign, 2008, *Journal of Physics Conference Series*, 118, 012059
75. Chaplin, W. J., Appourchaux, T., Arentoft, T., Ballot, J., Baudin, F., and 25 colleague(s), Asteroseismology from the Sun to the stars, 2008, *Journal of Physics Conference Series*, 118, 012048
76. Belkacem, K., Samadi, R., and Goupil, M. J., Amplitudes of non-radial oscillations driven by turbulence, 2008, *Journal of Physics Conference Series*, 118, 012028
77. Samadi, R., Belkacem, K., Goupil, M. J., Dupret, M.-A., and Kupka, F., Modeling the excitation of acoustic modes in α Centauri A, 2008, *A&A*, 489, 291
78. Appourchaux, T., Michel, E., Auvergne, M., Baglin, A., Toutain, T., and 17 colleague(s), CoRoT sounds the stars : p-mode parameters of Sun-like oscillations on HD 49933, 2008, *A&A*, 488, 705
79. Mosser, B., Deheuvels, S., Michel, E., Thévenin, F., Dupret, M. A., and 3 colleague(s), HD 203608, a quiet asteroseismic target in the old galactic disk, 2008, *A&A*, 488, 635
80. Drummond, R., Lapeyrere, V., Auvergne, M., Vandenbussche, B., Aerts, C., and 2 colleague(s), Correcting for background changes in CoRoT exoplanet data, 2008, *A&A*, 487, 1209
81. Belkacem, K., Samadi, R., Goupil, M.-J., and Dupret, M.-A., Stochastic excitation of non-radial modes. I. High-angular-degree p modes, 2008, *A&A*, 478, 163

82. Michel, E., Baglin, A., Samadi, R., Baudin, F., and Auvergne, M., CoRoT data contribution to stellar seismology, 2007, *Communications in Asteroseismology*, 150, 341
83. Belkacem, K., Samadi, R., Goupil, M.-J., Kupka, F., and Dupret, M.-A., Two-scale mass-flux closure models for turbulence : p-mode amplitudes in solar-like stars, 2007, *Communications in Asteroseismology*, 150, 153
84. Barban, C., Matthews, J. M., De Ridder, J., Baudin, F., Kuschnig, R., and 8 colleague(s), Detection of solar-like oscillations in the red giant star ϵ Ophiuchi by MOST spacebased photometry, 2007, *A&A*, 468, 1033
85. Samadi, R., Georgobiani, D., Trampedach, R., Goupil, M. J., Stein, R. F., and 1 colleague(s), Excitation of solar-like oscillations across the HR diagram, 2007, *A&A*, 463, 297
86. Belkacem, K., Samadi, R., Goupil, M. J., Kupka, F., and Baudin, F., A closure model with plumes. II. Application to the stochastic excitation of solar p modes, 2006, *A&A*, 460, 183
87. Belkacem, K., Samadi, R., Goupil, M. J., and Kupka, F., A closure model with plumes. I. The solar convection, 2006, *A&A*, 460, 173
88. Dupret, M.-A., Samadi, R., Grigahcene, A., Goupil, M.-J., and Gabriel, M., Non-local time-dependent treatments of convection in A-G type stars, 2006, *Communications in Asteroseismology*, 147, 85
89. Samadi, R., Kupka, F., Goupil, M. J., Lebreton, Y., and van't Veer-Menneret, C., Influence of local treatments of convection upon solar p mode excitation rates, 2006, *A&A*, 445, 233
90. Lochard, J., Samadi, R., and Goupil, M. J., Rotation profile inversion in solar-like stars. In the COROT framework, 2005, *A&A*, 438, 939
91. Goupil, M.-J., Dupret, M. A., Samadi, R., Boehm, T., Alecian, E., and 3 colleague(s), Asteroseismology of δ Scuti Stars : Problems and Prospects, 2005, *Journal of Astrophysics and Astronomy*, 26, 249
92. Samadi, R., Goupil, M.-J., Alecian, E., Baudin, F., Georgobiani, D., and 3 colleague(s), Excitation of Solar-like Oscillations : From PMS to MS Stellar Models, 2005, *Journal of Astrophysics and Astronomy*, 26, 171
93. Baudin, F., Samadi, R., Goupil, M.-J., Appourchaux, T., Barban, C., and 3 colleague(s), Inferred acoustic rates of solar p modes from several helioseismic instruments, 2005, *A&A*, 433, 349
94. Mosser, B., Bouchy, F., Catala, C., Michel, E., Samadi, R., and 5 colleague(s), Seismology and activity of the F type star HD 49933, 2005, *A&A*, 431, L13
95. Lochard, J., Samadi, R., and Goupil, M.-J., ϵ Boo Inversion of simulated rotational profile, 2004, *Solar Physics*, 220, 199
96. Samadi, R., Nordlund, Å., Stein, R. F., Goupil, M. J., and Roxburgh, I., Numerical 3D constraints on convective eddy time-correlations : Consequences for stochastic excitation of solar p modes, 2003, *A&A*, 404, 1129
97. Samadi, R., Nordlund, Å., Stein, R. F., Goupil, M. J., and Roxburgh, I., Numerical constraints on the model of stochastic excitation of solar-type oscillations, 2003, *A&A*, 403, 303
98. Samadi, R., Goupil, M. J., Lebreton, Y., Nordlund, Å., and Baudin, F., Seismic Diagnostics on Stellar Convection Treatment from Oscillation Amplitudes of p-modes, 2003, *Ap&SS*, 284, 221
99. Samadi, R., Goupil, M.-J., and Houdek, G., Solar-like oscillations in Delta Scuti stars, 2002, *Communications in Asteroseismology*, 142, 37

100. Samadi, R., Goupil, M.-J., and Houdek, G., Solar-like oscillations in delta Scuti stars, 2002, *A&A*, 395, 563
101. Samadi, R., Goupil, M.-J., and Lebreton, Y., Excitation of stellar p-modes by turbulent convection. II. The Sun, 2001, *A&A*, 370, 147
102. Samadi, R. and Goupil, M.-J., Excitation of stellar p-modes by turbulent convection. I. Theoretical formulation, 2001, *A&A*, 370, 136
103. Samadi, R., Stochastic excitation of stellar oscillations. Application for the space mission CO-ROT., 2000, Ph.D. Thesis,
104. Samadi, R., Photometric microlensing and stellar mass determination, 1998, *Academie des Sciences Paris Comptes Rendus Serie B Sciences Physiques*, 326, 939

C.2 **Autres journaux**

1. Suárez, J. C., Goupil, M.-J., Reese, D. R., Samadi, R., Lignières, F., and 2 colleagues, Rotation on the oscillation spectrum of solar-like stars, 2011, SF2A-2011 : Proceedings of the Annual meeting of the French Society of Astronomy and Astrophysics, 249
2. Alecian, G., Belkacem, K., Samadi, R., and Valls-Gabaud, D., SF2A-2011 : Semaine de l'Astrophysique Francaise, 2011, SF2A-2011 : Proceedings of the Annual meeting of the French Society of Astronomy and Astrophysics,
3. Uytterhoeven, K., Mathias, P., Baglin, A., Rainer, M., Poretti, E., and 13 colleagues, The variability of the CoRoT target HD171834 : gamma Dor pulsations and/or activity ?, 2011, arXiv :1111.1840
4. Blomme, R., Briquet, M., Degroote, P., Mahy, L., Aerts, C., and 24 colleagues, CoRoT observations of O stars : diverse origins of variability, 2011, arXiv :1109.1999
5. Hulot, J. C., Baudin, F., Samadi, R., and Goupil, M. J., A quantitative analysis of stellar activity based on CoRoT photometric data, 2011, arXiv :1104.2185
6. Boissier, S., Heydari-Malayeri, M., Samadi, R., and Valls-Gabaud, D., SF2A-2010 : Semaine de l'Astrophysique Francaise, 2010, SF2A-2010 : Proceedings of the Annual meeting of the French Society of Astronomy and Astrophysics,
7. Aerts, C., Debosscher, J., Sarro, L., Degroote, P., Neiner, C., and 7 colleagues, Discovery of New Hot Pulsators in the CoRoT Exoplanet Database and Their Potential for Asteroseismology, 2009, *Solar-Stellar Dynamos as Revealed by Helio- and Asteroseismology : GONG 2008/SOHO 21*, 416, 401
8. Heydari-Malayeri, M., Reyl'E, C., and Samadi, R., SF2A-2009 : Semaine de l'Astrophysique Francaise, 2009, SF2A-2009 : Proceedings of the Annual meeting of the French Society of Astronomy and Astrophysics,
9. Poretti, E., Mantegazza, L., Rainer, M., Uytterhoeven, K., Michel, E., and 17 colleagues, The tip of the iceberg : the frequency content of the δ Sct star HD 50844 from CoRoT space photometry, 2009, *American Institute of Physics Conference Series*, 1170, 435
10. Kallinger, T., Weiss, W. W., De Ridder, J., Hekker, S., and Barban, C., Oscillating Red Giants in the CoRoT Exo-field : An Asteroseismic Radius and Mass Determination, 2009, *The Eighth Pacific Rim Conference on Stellar Astrophysics : A Tribute to Kam-Ching Leung*, 404, 307
11. Poretti, E., Michel, E., Garrido, R., Lefevre, L., Mantegazza, L., and 19 colleagues, HD 50844 : the new look of Delta Sct stars from CoRoT space photometry, 2009, arXiv :0906.2628

12. Leibacher, J. W., Baudin, F., Belkacem, K., Dupret, M., Goupil, M., and 2 colleagues, Helioseismic Spectral Diagnostics - An Update, 2009, AAS/Solar Physics Division Meeting, 40, 7.16
13. Gondoin, P., Fridlund, M., Goupil, M. J., Baudin, F., Samadi, R., and 14 colleagues, CoRoT observations of active giants : preliminary results, 2009, American Institute of Physics Conference Series, 1094, 864
14. Charbonnel, C., Combes, F., and Samadi, R., SF2A-2008 : Semaine de l'Astrophysique Française, 2008, SF2A-2008,
15. Baudin, F., Samadi, R., Appourchaux, T., and Michel, E., Simu-LC : a Light-Curve simulator for CoRoT, 2007, arXiv :0710.3378
16. Bedding, T. R., Brun, A. S., Christensen-Dalsgaard, J., Crouch, A., De Cat, P., and 14 colleagues, Joint Discussion 17 Highlights of recent progress in the seismology of the Sun and Sun-like stars, 2007, Highlights of Astronomy, 14, 491
17. Belkacem, K., Samadi, R., Goupil, M.-J., Kupka, F., and Baudin, F., A closure model for turbulent convection. Application to the excitation of p modes, 2007, IAU Symposium, 239, 376
18. Samadi, R., Fialho, F., Costa, J. E. S., Drummond, R., Pinheiro Da Silva, L., and 3 colleagues, The Corot Book : Chap. V.5/ Extraction of the photometric information : corrections, 2007, arXiv :astro-ph/0703354
19. Goupil, M. J., Lochard, J., Samadi, R., Barban, C., Dupret, M. A., and 1 colleagues, Rotational Splittings with CoRoT, Expected Number of Detections and Measurement Accuracy, 2006, ESA Special Publication, 1306, 453
20. Appourchaux, T., Berthomieu, G., Michel, E., Ballot, J., Barban, C., and 16 colleagues, Evaluation of the Scientific Performances for the Seismology Programme, 2006, ESA Special Publication, 1306, 429
21. Baudin, F., Samadi, R., Appourchaux, T., and Michel, E., SIMU-LC : A Light-Curve Simulator for CoRoT, 2006, ESA Special Publication, 1306, 403
22. Appourchaux, T., Berthomieu, G., Michel, E., Aerts, C., Ballot, J., and 16 colleagues, Data Analysis Tools for the Seismology Programme, 2006, ESA Special Publication, 1306, 377
23. Samadi, R., Fialho, F., Costa, J. E. S., Drummond, R., Pinheiro da Silva, L., and 3 colleagues, Extraction of the Photometric Information : Corrections, 2006, ESA Special Publication, 1306, 317
24. Goupil, M. J., Moya, A., Suarez, J. C., Lochard, J., Barban, C., and 16 colleagues, Why Bothering to Measure Stellar Rotation with CoRoT ?, 2006, ESA Special Publication, 1306, 51
25. Michel, E., Baglin, A., Auvergne, M., Catala, C., Aerts, C., and 60 colleagues, The Seismology Programme of CoRoT, 2006, ESA Special Publication, 1306, 39
26. Dupret, M. A., Barban, C., Goupil, M.-J., Samadi, R., Grigahcène, A., and 1 colleagues, Theoretical damping rates and phase-lags for solar-like oscillations, 2006, Proceedings of SOHO 18/GONG 2006/HELAS I, Beyond the spherical Sun, 624,
27. Dupret, M.-A., Goupil, M.-J., Samadi, R., Grigahcène, A., and Gabriel, M., A non-local MLT treatment fitting 3D simulations, 2006, Proceedings of SOHO 18/GONG 2006/HELAS I, Beyond the spherical Sun, 624,
28. Barban, C., Matthews, J., De Ridder, J., Baudin, F., Kuschnig, R., and 8 colleagues, Studying solar-like oscillations in red giants : MOST spacebased photometry of epsilon Ophiuchi, 2006, Proceedings of SOHO 18/GONG 2006/HELAS I, Beyond the spherical Sun, 624,

29. Samadi, R., Belkacem, K., Goupil, M.-J., and Kupka, F., Seismic diagnostics inferred from the amplitudes of stochastically-excited modes, 2006, IAU Joint Discussion, 17,
30. Belkacem, K., Samadi, R., Goupil, M. J., Kupka, F., and Baudin, F., Excitation of solar p modes. Effect of the asymmetry of the convection zone, 2006, SF2A-2006 : Semaine de l'Astrophysique Francaise, 523
31. Michel, E., Samadi, R., Baudin, F., Auvergne, M., and CoRoT Team, CoRoT - a so near future ., 2006, Memorie della Società Astronomica Italiana, 77, 539
32. Samadi, R., Georgobiani, D., Trampedach, R., Goupil, M. J., Stein, R. F., and 1 colleagues, Excitation rates of p modes : mass luminosity relation across the HR diagram, 2004, SF2A-2004 : Semaine de l'Astrophysique Francaise, 323
33. Lochard, J., Samadi, R., and Goupil, M. J., Rotational inversion for selected solar-like stars, 2004, SF2A-2004 : Semaine de l'Astrophysique Francaise, 299
34. Mosser, B., Bouchy, F., Catala, C., Michel, E., Baglin, A., and 2 colleagues, Asteroseismology with HARPS : observation of a COROT target, 2004, SF2A-2004 : Semaine de l'Astrophysique Francaise, 255
35. Samadi, R., Goupil, M. J., Baudin, F., Georgobiani, D., Trampedach, R., and 2 colleagues, Oscillation Power Spectra of the Sun and of CEN a : Observations Versus Models, 2004, SOHO 14 Helio- and Asteroseismology : Towards a Golden Future, 559, 615
36. Samadi, R., Goupil, M. J., Lebreton, Y., van't Veer, C., and Kupka, F., Effect of Local Treatments of Convection upon the Solar P-Mode Excitation Rates, 2004, SOHO 14 Helio- and Asteroseismology : Towards a Golden Future, 559, 611
37. Goupil, M. J., Samadi, R., Lochard, J., Dziembowski, W. A., and Pamyatnykh, A., Inferring information about rotation from stellar oscillations, 2004, Stellar Structure and Habitable Planet Finding, 538, 133
38. Heiter, U., Kupka, F., Samadi, R., Barban, C., van't-Veer Menneret, C., and 4 colleagues, Application of New ATLAS9 Model Atmosphere Grids, 2003, Modelling of Stellar Atmospheres, 210, 10P
39. Samadi, R., Nordlund, Å., Stein, R. F., Goupil, M.-J., and Roxburgh, I., Characterizing the Dynamic Properties of the Solar Turbulence with 3-D Simulations : Consequences in Term of p-mode Excitation, 2003, Modelling of Stellar Atmospheres, 210, 2P
40. Baudin, F., Goupil, M.-J., and Samadi, R., Amplitude and Inferred Excitation Rates of P-Modes, 2003, IAU Joint Discussion, 12,
41. Samadi, R., Nordlund, A., Stein, R. F., Goupil, M.-J., and Roxburgh, I., Consequences of the non gaussian character of the stochastic excitation for solar-type oscillations, 2002, SF2A-2002 : Semaine de l'Astrophysique Francaise, 489
42. Samadi, R., Houdek, G., Goupil, M.-J., Lebreton, Y., and Baglin, A., Oscillation power across the H-R diagram : sensitivity to the convection treatment, 2002, Stellar Structure and Habitable Planet Finding, 485, 87
43. Baglin, A., Auvergne, M., Catala, C., Michel, E., Goupil, M. J., and 3 colleagues, The COROT Mission and its Seismology Programme (invited paper), 2002, IAU Colloq. 185 : Radial and Non-radial Pulsations as Probes of Stellar Physics, 259, 626
44. Samadi, R., Stochastic excitation of stellar oscillations, 2001, SF2A-2001 : Semaine de l'Astrophysique Francaise, 117

45. Samadi, R., Goupil, M.-J., Lebreton, Y., and Baglin, A., Oscillation power as a test of stellar turbulence : scanning the HR diagram, 2001, SOHO 10/GONG 2000 Workshop : Helio- and Asteroseismology at the Dawn of the Millennium, 464, 451
46. Samadi, R. and Houdek, G., Oscillation power as a diagnostic tool for stellar turbulent spectra, 2001, arXiv :astro-ph/0101128
47. Samadi, R. and Houdek, G., Oscillation power as a diagnostic tool for stellar turbulent spectra, 2000, The Third MONS Workshop : Science Preparation and Target Selection, 27

C.3 Contributions invitées et revues

1. Samadi, R., Belkacem, K., Goupil, M.-J., Ludwig, H.-G., and Dupret, M.-A., Modeling stochastic excitation of acoustic modes in stars : present status and perspectives, 2008, Communications in Asteroseismology, 157, 130 (revue invitée)
2. Samadi, R., Belkacem, K., Goupil, M.-J., Kupka, F., and Dupret, M.-A., Solar-like oscillation amplitudes and line-widths as a probe for turbulent convection in stars, 2007, IAU Symposium, 239, 349 (contribution invitée)

C.4 Ouvrages et chapitres d'ouvrages

1. Samadi, R., Stochastic Excitation of Acoustic Modes in Stars, 2011, Lecture Notes in Physics, Berlin Springer Verlag, 832, 305
2. Belkacem, K., Samadi, R., Connections between stellar oscillations and turbulent convection , 2013, Lecture Notes in Physics, Berlin Springer Verlag, in press

C.5 Diffusion des connaissances

1. Baglin, A., Samadi, R., and Barban, C., Les tremblements de Procyon., 2005, La Recherche, 383, 40

C.6 Notes techniques

1. Samadi, R. & Green, J., Synopsis of on-board processing algorithms, novembre 2011, ref : PLATO-GS-TN-244-LESIA
2. Samadi, R., Spécification des simulateurs des traitements bords et sols, novembre 2011, ref : PLATO-GS-SP-225-LESIA
3. Samadi, R., A statistical numerical tool for assessing the expected performance, mars 2011, ref : PLATO-GS-TN-234-LESIA
4. Samadi, R., PLATO - Phase A assessment study, mars 2011, ref : PLATO-GS-TN-235-LESIA
5. Samadi, R., Effect of the differential cinematic aberration and possible correction, mars 2011, ref : PLATO-GS-TN-236-LESIA
6. Samadi, R., Comparison of different photometry methods, mars 2011, ref : PLATO-GS-TN-237-LESIA

7. Samadi, R., On-board numerical precision and data precision, mars 2011, ref : PLATO-GS-TN-238-LESIA
8. Samadi, R. et al, PLATO SCIENCE GROUND SEGMENT DEFINITION PHASE A REPORT-WP 32- WP Data Processing Algorithms, mars 2011, ref : PLATO-GS-TN-241-LESIA
9. Samadi, R., PLATO Data Processing Algorithms, juin 2009, ref : PLATO.LESIA.DPR.SW.1040
10. Samadi, R., Description of the N1 Products Generated at the Mission Control Center (CMC), décembre 2007, ref : COR.LESIA.06.008
11. Samadi, R., Description des corrections N0-N1 en mode observation, juillet 2007, ref : COR.LESIA.06.025
12. Samadi, R. & Lefevre, L. ; Contenu et fonctionnalités de la boîte à outil (BAO) du Segment Sol CoRoT, mars 2006, ref : COR.LESIA.06.026

Résumé

Alors que les oscillations solaires n'ont pas fini de nous révéler tous leurs secrets, des oscillations acoustiques analogues sont détectées dans un nombre croissant d'étoiles. Comme sur le Soleil, ces oscillations (dite de type solaire) sont amorties par des mécanismes complexes et encore mal connus et excitées par la turbulence dans l'enveloppe convective supérieure des étoiles. Grâce à la qualité photométrique exceptionnelle des missions spatiales CoRoT (CNES) et *Kepler* (NASA) ainsi qu'à la continuité long terme des observations qu'elles fournissent, on mesure maintenant précisément fréquences, amplitudes et durées de vie de ces oscillations dans une variété d'étoiles dotées de caractéristiques diverses concernant leur stade évolutif, paramètres fondamentaux, composition chimique, champ magnétique, rotation ... etc.

Plus que ne le fait la mesure de leurs fréquences, la mesure des amplitudes et durées vies des modes de type solaire nous fournit des contraintes sur les propriétés statiques et dynamiques de la convection, sur la physique des modes et enfin sur la stratification en surface des étoiles. Le jeu conséquent d'étoiles pulsantes détectées par CoRoT et *Kepler* nous révèle aussi que les amplitudes et durées de ces oscillations varient d'une étoile à l'autre selon des lois d'échelles caractéristiques qui dépendent d'un nombre restreint de paramètres stellaires (masse, luminosité, température effective ... etc).

Ce mémoire de thèse résume les travaux que j'ai menés dans ce contexte depuis plus de dix ans en collaboration avec mes collègues et avec les étudiants que j'ai encadré. Ces travaux ont cherché à comprendre et mieux modéliser les amplitudes des oscillations excitées par la convection turbulente, notamment les lois d'échelles observées. Ce faisant, ils ont visé à établir des diagnostics sur les propriétés statiques et dynamiques des régions convectives, avec pour objectif à plus long terme d'améliorer la modélisation des processus de transport convectif dans les intérieurs stellaires.

Mots-clés: Turbulence - convection - oscillations - excitation stochastique